AFRL-AFOSR-UK-TR-2011-0050

# Experimental and Numerical Investigation of Conjugate Heat Transfer in Rib-roughened Duct

**Tony Arts**
**Carlos Benocci**

**von Karman Institute**
**Turbomachinery and Propulsion**
**Chaussee de Waterloo, 72**
**Rhode Saint Genese, Belgium 1640**

EOARD GRANT 08-3048

October 2011

Final Report for 01 August 2008 to 01 August 2011



**Air Force Research Laboratory**
**Air Force Office of Scientific Research**
**European Office of Aerospace Research and Development**
**Unit 4515 Box 14, APO AE 09421**

# REPORT DOCUMENTATION PAGE

Form Approved OMB No. 0704-0188



| 1. REPORT DATE *(DD-MM-YYYY)* | 2. REPORT TYPE | 3. DATES COVERED *(From – To)* |
|---|---|---|
| 26-10-2011 | Final Report | 1 August 2008 – 01 August 2011 |

**4. TITLE AND SUBTITLE**

**Experimental and Numerical Investigation of Conjugate Heat Transfer in Rib-roughened Duct**

**5a. CONTRACT NUMBER**

FA8655-08-1-3048

**5b. GRANT NUMBER**

Grant 08-3048

**5c. PROGRAM ELEMENT NUMBER**

**6. AUTHOR(S)**

Tony Arts
Carlos Benocci

**5d. PROJECT NUMBER**

**5d. TASK NUMBER**

**5e. WORK UNIT NUMBER**

**7. PERFORMING ORGANIZATION NAME(S) AND ADDRESS(ES)**

von Karman Institute
Turbomachinery and Propulsion
Chaussee de Waterloo, 72
Rhode Saint Genese, Belgium 1640

**8. PERFORMING ORGANIZATION REPORT NUMBER**

N/A

**9. SPONSORING/MONITORING AGENCY NAME(S) AND ADDRESS(ES)**

EOARD
Unit 4515 BOX 14
APO AE 09421

**10. SPONSOR/MONITOR'S ACRONYM(S)**

AFRL/AFOSR/RSW (EOARD)

**11. SPONSOR/MONITOR'S REPORT NUMBER(S)**

**AFRL-AFOSR-UK-TR-2011-0050**

**12. DISTRIBUTION/AVAILABILITY STATEMENT**

Approved for public release; distribution is unlimited.

**13. SUPPLEMENTARY NOTES**

**14. ABSTRACT**

The final report for this effort is divided into two parts. The first is the Experimental activity and the second the numerical activity. Each of these parts is covered separately in the following report.

The purpose of the experimental project is to have a deeper understanding of the conjugate heat transfer phenomenon by conducting experiments for the fundamental understanding, as well as creating a baseline database for numerical investigations. The targeted application is the ribbed internal cooling channels used in turbine blades. A test section is built to model the underlying physics of the conjugate heat transfer phenomena in a turbine blade. The investigation focuses on measurements conducive to turbulence characterization of the channel by means of a hotwire, and local heat flux calculations over flat, ribbed and ribbed/film cooled slab configurations through local temperature measurements made by Infrared Thermography. The turbulence characterization of the channel is not only important for the interpretation of the experimental based local heat flux calculations, but also crucial for the conjugate numerical models that predict the cooling performance in parallel to the experimental work conducted.

The numerical part of this project has be executed investigating a generic configuration, namely a straight duct of square test section roughened by square sharp angled ribs. A metallic slab simulates one of the rib-roughened cooling duct walls. An uniform heat flux is applied at the bottom face of this slab, allowing the conduction heat transfer through its thickness; at the interface solid-fluid this heat flux is removed and transported by the cooling flow. In a further phase cooling holes was introduced to investigate film cooling. This approach simulates the heat transfer occurring from the free-stream hot gas side, through the blade thickness, towards the internal cooling channels and it can be considered to be similar to internal cooling channels in turbine blades. The first part was devoted to demonstrate the capability and the usefulness of the LES technique for this class of problems. In the second part of the investigation, the phenomenology of the CS(s) in the flow has been investigated in depth, post-processing the LES fields so obtained. Advanced post-processing tools were developed/applied to put in evidence the role of CS(s) in heat transfer. In the last third part of investigation, the effect of cooling holes flow and heat transfer in the ribbed duct.

**15. SUBJECT TERMS**

EOARD, Fluid Mechanics, Heat & Mass Transfer

| 16. SECURITY CLASSIFICATION OF: | | | 17. LIMITATION OF ABSTRACT | 18, NUMBER OF PAGES | 19a. NAME OF RESPONSIBLE PERSON |
|---|---|---|---|---|---|
| a. REPORT | b. ABSTRACT | c. THIS PAGE | | | Gregg Abate |
| UNCLAS | UNCLAS | UNCLAS | SAR | 371 | 19b. TELEPHONE NUMBER *(Include area code)* +44 (0)1895 616021 |

# EXPERIMENTAL AND NUMERICAL INVESTIGATION OF CONJUGATE HEAT TRANSFER IN RIB-ROUGHENED DUCT

## *Numerical Activity*

*Principal Investigators Prof. Carlo Benocci, Prof. Patrick Rambaud*
*Researchers: D. Nakhle, S. Le Clainche Martinez, F. J. García Soto;*
*Senior Research Assistants: A. Parente, P. Planquart*

*Author of the report: Carlo Benocci*

*von Karman Institute*
*Belgium*

# Table of contents

# List of Figures

# List of Tables

# List of Symbols

BR: blowing ratio: ratio between bulk velocity in the orifice and at the inlet of the duct
*Cf* friction factor
CS(s) Coherent structure(s)
U average velocity in x direction (m/s)
V average velocity in y direction (m/s)
W average velocity in z direction (m/s)
P average pressure (Pa)
T average temperature (K)
u' resolved fluctuation of velocity in x direction (m/s)
v'=resolved fluctuation of velocity in y direction (m/s)
w'=resolved fluctuation of velocity in z direction (m/s)
p'= resolved fluctuation of pressure (Pa)
T'=resolved fluctuation of temperature (K)
<U> Mean velocity in x direction (m/s)
<V> Mean velocity in y direction (m/s)
<W> Mean velocity in z direction (m/s)
<P> Mean pressure (Pa)
<T> Mean temperature (K)
UV Instantaneous velocity correlation
<UV> Mean velocity correlation
u=U-<U> resolved fluctuation of velocity in x direction (m/s)
v=V-<V> resolved fluctuation of velocity in y direction (m/s)
w=W -<W> resolved fluctuation of velocity in z direction (m/s)
p=P-<P> resolved fluctuation of pressure (Pa)
T'=T-<T> resolved fluctuation of temperature (K)
$U_b$ bulk velocity in the duct (m/s)
$V_b$ bulk velocity in the in the orifice (m/s)
$u_\tau$ shear velocity
*I* Indicator of condition
<*I*> I time averaged
Pr Prandtl number
Re Reynolds number
Nu Nusselt number in a ribbed channel
$Nu_0$ Nusselt number in a smooth pipe
EF Enhancement Factor
$D_h$ Hydraulic diameter (m)
H side of the duct (m)
*h*, $H_{rib}$ height of the rib (m)
*s* height of the bottom slab (m)
*p* pitch length (m)
*k, Tke* resolved turbulent kinetic (m2/s2)
N Number of time steps
*q* input heat flux

$Q$, $Q_{ins}$ $Q$ of the instantaneous field
$\langle Q \rangle$, $Q_{mean}$ $Q$ of the averaged field
SPB Symmetry Plane Bifurcation mechanism
$\varphi$ generic scalar
$\Phi$ heat flux
$\Gamma$ heat coefficient

# *Part I: Modeling and Mathematical Aspects*

# CHAPTER 1 Introduction

## *1.1 Overall plan of the research program*

The efficiency of a gas turbine can be improved increasing its operating temperature. This objective could be achieved by internal cooling, which prevent the blade from operating at temperatures higher than the melting point of the blade material. This aim can be achieved having a cooling fluid flowing within the blade through a network of ducts. Heat transfer between the body of the blade and the cooling fluid can then be enhanced by ribs located on the wall(s) of the cooling duct. The ribs act as turbulence promoters and increase the turbulent heat transfer in the fluid and the wall of the blade. This cooling process, therefore, represents a problem of conjugate heat transfer between ***blade shell-cooling fluid*.** The objective of this numerical study is to investigate the fundamental aspects of this process and, in particular, the interaction between turbulence and the heat transfer at interface solid-fluid and the of the role of turbulent coherent structures (CS). The relevant information will be extracted post-processing the flow and thermal fields obtained by the set of Large Eddy Simulations.

This task has be executed investigating a generic configuration, namely a straight duct of square test section roughened by square sharp angled ribs. A metallic slab simulates one of the rib-roughened cooling duct walls. An uniform heat flux is applied at the bottom face of this slab, allowing the conduction heat transfer through its thickness; at the interface solid-fluid this heat flux is removed and transported by the cooling flow. In a further phase **cooling holes** was introduced to investigate film cooling. This approach simulates the heat transfer occurring from the free-stream hot gas side, through the blade thickness, towards the internal cooling channels and it can be considered to be similar to internal cooling channels in turbine blades (*figure 1.1*).

The first part was devoted to demonstrate the capability and the usefulness of the LES technique for this class of problems. The von Karman Institute for Fluid Dynamics has gained deep experience [1-4] in use of LES [5, 6] and MILES [7] (Monotonically Integrated Large-Eddy Simulation) technique to the simulation of flow in rib-roughened ducts and this experience will be applied to the conjugate problem. An attempt to model the conjugate heat transfer has already been performed by the VKI and this research will be the starting point of the present investigation. This approach was applied to simulate the different cases of the experimental database in order to assess and quantify the performance and to highlight the influence of grid refinement, numerical algorithms and sub-grid models on the prediction of the dynamics of the flow and of the thermal field in the flow and in the solid.

In the second part of the investigation, the phenomenology of the CS(s) in the flow has been investigated in depth, post-processing the LES fields so obtained. Advanced post-processing tools were developed/applied to put in evidence the role of CS(s) in heat transfer.

In the last third part of investigation, the effect of cooling holes flow and heat transfer in the ribbed duct.

.

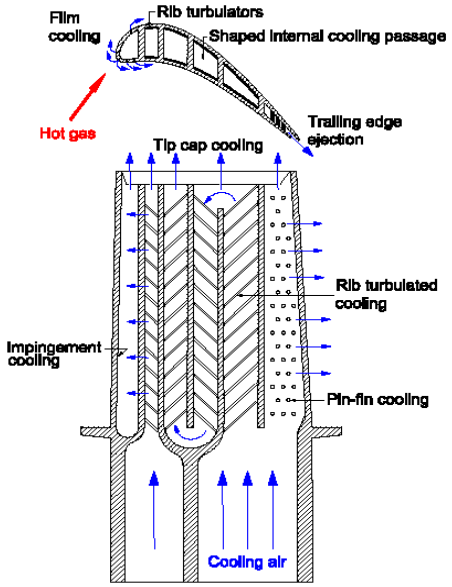


*Figure 1.1 conceptual view of Internal Cooling Passage in a Gas Turbine*

## *1.2 Test cases*

The main effort was focused on the simulation of the ribbed square duct. The corresponding case of the smooth square duct was studied to finalize and tune the main simulation. Previous investigations have show that the problem cannot be fully simulated by a computational field made of a SINGLE pitch length (length between two successive ribs) and closed with periodic boundary condition in the longitudinal direction [1-3]
This conclusion was motivated, under the fundamental point of view by the potential existence of long scale flow structures extending over more than one pitch and under the practical point of view, by the fact it was found impossible to study the instantaneous heat transfer, because the present solver (FLUENT 6.2 and 6.3) does not support periodic boundary conditions for heat transfer in a fluid only.

It was therefore proposed to overcome this limitation performing the simulations of ribbed ducts over a domain made of number of successive ribs and closed with classical inlet-outlet boundary conditions, taking into account the evolution of the thermal field along the stream-wise direction. Previous experiments [8, 9] had shown that the flow achieved fully developed state (and itself ) over the 4$^{th}$ rib and simulations over a domain of successive ribs had shown the simulated flow was not developed over the 3$^{rd}$ rib.
Therefore, it was decided to perform the future simulations over a domain of 5 pitch lengths
The initial hypothesis was that, applying a realistic description of the developed flow at the inlet, the computed flow would have stabilized itself over the first 2 pitch lengths, the solution over the 3$^{rd}$ and 4$^{th}$ second pitch length would have been representative of the full periodic

flow, while the last 5$^{th}$ pitch would have damped the perturbation introduced by the outlet boundary condition.
The same length for the domain was maintained for the simulations without ribs.
A further advantage of this choice is that is fully compatible with the test section developed for the part of the experimental of the present research program, which contains 5 consecutive ribs [10].

The conceptual set-up for the planned simulations, without or with ribs, is presented in *figure 1.2* together with its boundary conditions.

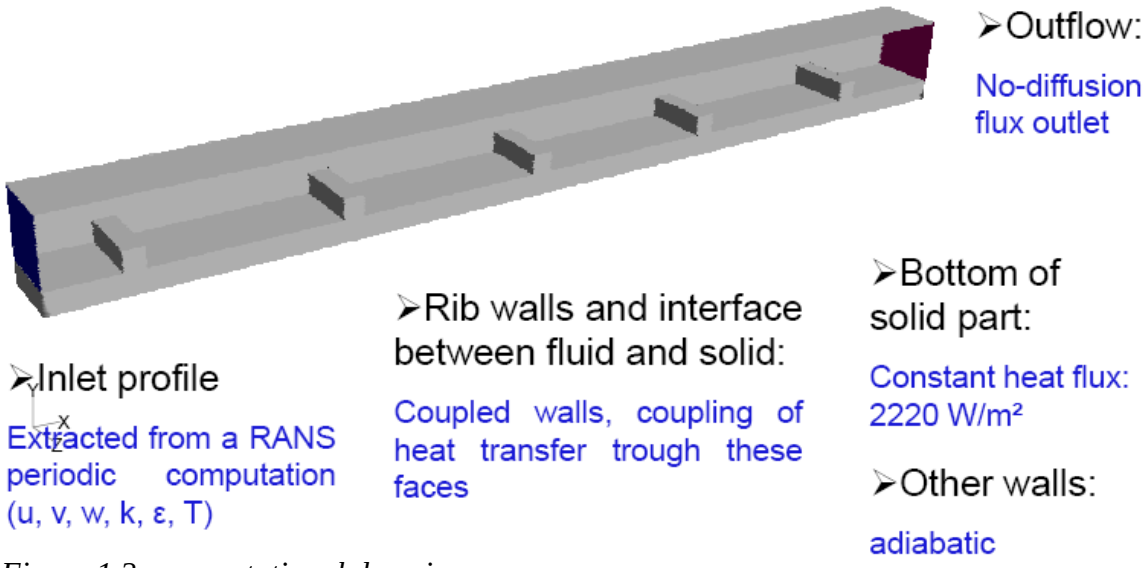


*Figure 1.2 computational domain*

The relevant geometrical parameters to be considered are:

- L is the length of the Duct
- $D_h$ is the hydraulic diameter of the fluid zone
- H is the side of the duct
- p is the pitch (length between two successive ribs)
- *h* is the height of the rib (square ribs)
- *s* is the thickness of the solid domain (steel)

The values applied for the present simulations are:

- L=1.125 m
- H=0.075 m

- $\frac{h}{D_h} = 0.3$ $\frac{s}{h} = 1.1$ $\frac{p}{h} = 10$

values which match the present experimental set-up.

The general flow conditions and the properties of the materials applied for the simulations are listed in *Table 1.1*:

| ***General flow conditions*** | | | |
|---|---|---|---|
| Reynolds number: ***Re*** | | ***40 000*** | |
| Prandtl number : ***Pr*** | | ***0.7*** | |
| Rotation number: ***Ro*** | | ***0 (stationary blade)*** | |
| ***Fluid properties (Air)*** | | ***Solid properties (Steel)*** | |
| Density: [ kg.m$^{-3}$] ***ρ*** | 1.225 | Density: [ kg.m$^{-3}$] ***ρ*** | 8030 |
| Specific heat: [J/kg.K] ***Cp*** | 1006.43 | Specific heat: [J/kg.K] ***Cp*** | 502.48 |
| Thermal conductivity: [W/m.K] ***k*** | 0.0242 | Thermal conductivity: [W/m.K] ***k*** | 16.27 |
| Dynamic viscosity: [kg.m$^2$/s] ***μ*** | 1.7894e-5 | | |

*Table 1.1 Physical parameters*

# CHAPTER 2 Governing equations and models

## *2.1 Governing equations*

The equations that govern fluid motion and heat transfer are the continuity, momentum and energy equations. These equations were independently constructed by Navier (1827) and Stokes (1845) and are referred to as the Navier-Stokes equations. The equations are written below, in a Cartesian coordinate form for a Newtonian fluid with constant material properties

as density (ρ), dynamic viscosity (η), specific heat ($C_p$) and thermal conductivity (k).The conventional summation of Einstein is used.

### *2.1.1 Continuity equation*

The continuity equation for an incompressible flow (ρ=constant) represents the conservation of mass and it is given by:

$$\boxed{\frac{\partial U_i}{\partial x_j} = 0}$$

### *2.1.2 Momentum equation*

The momentum equation is a force balance derived from Newton's second law. For Newtonian incompressible fluid the momentum equation is written as follows:

$$\boxed{\frac{\partial U_i}{\partial t} + \frac{\partial U_j U_i}{\partial x_j} = -\frac{1}{\rho}\frac{\partial P}{\partial x_j} + \frac{\partial}{\partial x_j}(2\nu S_{ij}) + g_i + F_i}$$

Where:
- $\nu = \frac{\mu}{\rho}$ $\mu$ is the dynamic viscosity and $\nu$ is the kinematic viscosity.
- $S_{ij} = \frac{1}{2}\left(\frac{\partial U_i}{\partial x_j} + \frac{\partial U_j}{\partial x_i}\right)$ is the strain tensor.
- $g_i$ is the gravitational force: in our case $g_i$ is negligible.
- $F_i$ are the additional body-forces such as rotation or magnetic field.

For incompressible flow we can show that $\frac{\partial}{\partial x_j}(2\nu S_{ij}) = \nu\frac{\partial^2 Ui}{\partial x_j \partial x_j}$, so the new momentum equation will become:

$$\boxed{\frac{\partial U_i}{\partial t} + \frac{\partial U_j U_i}{\partial x_j} = -\frac{1}{\rho}\frac{\partial P}{\partial x_j} + \nu\frac{\partial^2 Ui}{\partial x_j \partial x_j}}$$

### *2.1.3 Energy equation*

Since the presence of heat transfer in the flow, it is obvious to set energy equation. The total energy equation is more particularly used in compressible flow, but in the present case the energy equation results in simple transport of temperature scalar (T):

$$\frac{\partial T}{\partial t}+\frac{\partial U_j T}{\partial x_j}=\frac{\partial}{\partial x_j}\left(\alpha_f \frac{\partial T}{\partial x_j}\right)+Q_f$$

Where:

- $\alpha_f = \frac{\lambda}{\rho C_p}$ Where $\alpha_f$ is the fluid thermal diffusivity
- $\rho$ is the air density.
- $\lambda$ is the thermal conductivity ($W.m^{-1}.K^{-1}$).
- $C_p$ is the specific heat capacity.
- $Q_f = \frac{q}{\rho C_p}$ is the fluid heat source: in our case $Q_f$ =0

### *2.1.4 Solid heat transfer equation*

For coupled fluid/solid thermal problems, the temperature field and heat transfer in solid structure is represented with the solid heat transfer equation

$$\frac{\partial T}{\partial t}=\frac{\partial}{\partial x_j}\left(\alpha_s \frac{\partial T}{\partial x_j}\right)+Q_s$$

Where:

- $\alpha_s$ is the solid thermal diffusivity
- $Qs$ is the solid heat source: in our case $Qs$ =0

## *2.2 Turbulence modeling*

### *2.2.1 Choice of Turbulence model*

The key of any simulation of flows at high Reynolds number is obviously the choice of the suitable turbulence model. Direct Numerical Simulation (DNS) being obviously unaffordable of the present case the choice would between Reynolds Average Navier Stokes (RANS] modeling and Large-eddy Simulation (LES) ( the reader is referred to [5,6] for a fundamental discussion).
In the present case, the LES approach has been chosen because:
-In general terms, LES can be expected to yield a better performance than RANS in the simulation of complex flows; even in the case approximate wall conditions were applied [11].
-In particular, the literature (see [12] for an example and [2, 3] for a full review) shows that RANS approach is not able to reproduce the complex aspect of this flow case. This trend was confirmed, among others, by the tests from the present authors [2, 3].
It must be remarked that LES, besides yielding a better estimation of the Eulerian statistics, is the only tool capable of investigating the unsteady field and, in particular, to put in evidence

the presence of vortex structures [13] in the flow and their potential role in heat transfer. The LES capabilities of the commercial finite volume solver Fluent [14] were applied in the present case.

### *2.2.2 LES- Large Eddy Simulation*

Turbulent flow are characterized by eddies (structures) with a wide range of length and time scales. The main idea of the large-eddy simulation (LES) approach consists in getting rid of the small (and high-frequency) components of turbulence in space. Indeed, in LES the Navier-Stokes equations are filtered in space and only the scales larger than the filter width are directly simulated. Thus, the large scales of motion, which are the most interesting for engineering applications, since they are responsible of most of momentum and energy transport, are directly resolved. On the other hand, the smallest scales which are responsible for the dissipation of turbulence kinetic energy have to be modeled.

### *2.2.3 Filtering Functions*

In LES, a space filtering function is applied, in order to separate large structures from small ones. In a mathematical point of view this filtering operation can be obtained through the convolution with a filter function $G_\Delta(\mathbf{x}, t)$, where $\Delta$ is the filter width which depends on geometry mesh spacing and flow characteristics. The resolved part $\overline{\varphi}(\vec{x},t)$ of a space-time variable $\varphi(\vec{x},t)$, whose scale is larger than the filter width, is defined by the relation:

$$\overline{\varphi}(\vec{x},t)=\int_{-\infty}^{+\infty}\int_{-\infty}^{+\infty}\varphi(\vec{\xi},t')G(\vec{x}-\vec{\xi},t-t')dt'\,d^3\vec{\xi}$$

Where $G$ is the kernel filter which satisfies the normalization condition:

$$\int_{-\infty}^{+\infty}\int_{-\infty}^{+\infty}G(\vec{x}-\vec{\xi},t-t')d^3\vec{\xi}dt'=1$$

So the unresolved part of $\varphi(\vec{x},t)$, denoted $\varphi'(\vec{x},t)$ which represents the fluctuations at scales smaller than the filter width, is defined by:

$$\varphi'(\vec{x},t)=\varphi(\vec{x},t)-\overline{\varphi}(\vec{x},t)$$

The three most commonly used filter functions in LES are listed as follows:

► Fourier cut off filter ► Gaussian filter ► Top hat filter

In order to manipulate the Navier-Stokes equations applying a filter, the latter must verify these following properties:

● Conservation of constants: $\overline{a}=a$

- Linearity: $\overline{\varphi+\psi}=\overline{\varphi}+\overline{\psi}$
- Spatial and temporal derivation commuting $\overline{\frac{\partial\varphi}{\partial s}}=\frac{\partial\overline{\varphi}}{\partial s}$ with $s=x, t$

### 2.2.4 Filtered Navier-Stoke equations

In this section the Navier-Stokes equations, introduced at the beginning of this chapter, are filtered in the physical space using a filtering function with the properties described in Sec. 2.2.3. The new equations are:

### 2.2.5 Continuity equation

The filtered continuity equation is written as follows:

$$\boxed{\frac{\partial\overline{U}_i}{\partial x_j}=0}$$

### 2.2.6 Momentum equation

The filtered momentum equation is written as follows:

$$\boxed{\frac{\partial\overline{U}_i}{\partial t}+\frac{\partial\overline{U}_j\overline{U}_i}{\partial x_j}=-\frac{1}{\rho}\frac{\partial\overline{P}}{\partial x_j}+\frac{\partial}{\partial x_j}\left(2\nu\overline{S}_{ij}+\overline{\tau}_{ij}\right)}$$

Where: • $\overline{S}_{ij}=\frac{1}{2}\left(\frac{\partial\overline{U}_i}{\partial x_j}+\frac{\partial\overline{U}_j}{\partial x_i}\right)$ is the resolved strain tensor.

• $\overline{\tau}_{ij}=\overline{U_iU_j}-\overline{U}_i\overline{U}_j$ called the Sub grid scale stress (SGS) tensor (equivalent to Reynolds tensor in RANS). It represents the new unknown quantities in the equation that need to be modeled.

### 2.2.7 Energy equation

The filtered energy equation is written as follows:

$$\frac{\partial \overline{T}}{\partial t}+\frac{\partial \overline{U}_j \overline{T}}{\partial x_j}=\frac{\partial}{\partial x_j}\left(\alpha_f \frac{\partial \overline{T}}{\partial xj}+\overline{\theta}_j\right)$$

Where: • $\overline{\theta}_j = \overline{UjT} - \overline{U}_j\overline{T}$ called the sub grid scale heat flux and need to be modelled too.

### *2.2.8 Sub grid scale $\overline{\tau}_{ij}$ modeling*

As it is said in the section before, the sub grid scale stresses resulting from the filtering operation are unknown, and require modeling. The sub grid scale turbulence models in FLUENT employ an approach analogous to the RANS models, namely the Boussinesq hypothesis which expresses the sub grid scale turbulent stresses from:

$$\overline{\tau}_{ij} = \frac{1}{3}\overline{\tau}_{kk}\delta_{ij} - 2\mu_t \overline{S}_{ij}$$

Where: • $\mu_t \sim u' l_t$ is the sub grid scales turbulent viscosity (or eddy viscosity) and it is unknown and need to be modeled. Now the new momentum equation is written as follows:

$$\frac{\partial \overline{U}_i}{\partial t}+\frac{\partial \overline{U}_j \overline{U}_i}{\partial x_j}=-\frac{1}{\rho}\frac{\partial(\overline{P}-\frac{1}{3}\rho\overline{\tau}_{kk})}{\partial x_j}+\frac{\partial}{\partial x_j}(2(\nu+\nu_t)\overline{S}_{ij})$$

***Fluent*** offers four models (see [14] for details and [5, 6] for the related theory) for $\mu_t$ :

- The Smagorinsky-Lilly model
- The dynamic Smagorinsky-Lilly model
- The WALE model
- The dynamic kinetic energy sub grid scale model

***Smagorinsky-Lilly model:*** Smagorinsky proposed the first usable sub-grid model. It is based on a simple Zero-equation model. The eddy viscosity $\mu_t$ is modeled:

$$\mu_t = \rho L_s^2 |S|$$

Where: • $L_s$ is the mixing length for sub grid scales and it is computed in Fluent:

$$L_s = \min(\kappa d, Cs, Vol^{1/3})$$

- $\kappa$ : Von Kármán constant
- $d$ : distance to the closest wall
- $Cs$ : Smagorinsky constant.
- $Vol$ : Volume of the computational cell

$$|S| \equiv \sqrt{2\overline{S}_{ij}\overline{S}_{ij}}$$

It has been found that 0.1 as a value of $Cs$ yields to best results for a wide range of flows and it is the default value in Fluent. Practical experience shows that, for complex geometries and affordable grid, Smagorinsky model yields results comparable to more advanced sub-grid models [13]. This finding was confirmed by further tests, for the present case (Annex A) and was therefore retained for the present application.

### *2.2.9 Sub grid scale heat flux $\overline{\theta}_j$ modeling*

With analogy to the Fourier law, the sub grid scale heat flux $\overline{\theta}_j$ in the filtered energy equation is related to the resolved gradient of temperature and the turbulent eddy diffusivity $\alpha_t$ , which is unknown and need to be modeled:

$$\boxed{\overline{\theta}_j = \alpha_t \frac{\partial \overline{T}}{\partial x_j}}$$

The sub grid scale Prandtl number (or the Turbulent Prandtl number), $Pr_t$ defined as follows*:*

$$\boxed{Pr_t = \frac{\nu_t}{\alpha_t}}$$

Allows defining $\alpha_t$ in terms of $\nu_t$ .

***Constant turbulent Prandtl number model***: With this simple model one can define the unknown turbulent eddy diffusivity $\alpha_t$. In general the value of turbulent Prandtl number is around 1 but it can be varied according to the authors between (0.5 -1.1). For the case of channel flow, DNS experiences suggest values in the order of $Pr_t = 0.5$ and this value was, therefore applied in the present investigation. With this value of $Pr_t$ and the calculated $\nu_t$ from the SGS model the filtered energy equation can be closed.

# CHAPTER 3 Introduction to code Fluent

## *3.1 Overall description*

Fluent Version 6.3 [14] is a CFD computer code developed and marketed by Fluent Inc. The code solves the equations for conservation of mass, momentum, energy and other relevant fluid variables using a Finite Volume technique. The procedure of solution of the equations is the following:

● The fluid domain is divided into a large number of discrete control volumes (also known as cells) using a pre-processor code which creates a computational mesh over which the equations can be solved.

● Once the fluid domain has been meshed, the governing equations (in integral form) for the conservation of mass, momentum, energy and any other relevant variables are applied to each discrete control volume and used to construct a set of non-linear algebraic equations for the discrete dependent variables(‘’unknowns’’) such as velocities, pressure, temperature, and others scalar. The unknowns then are the values of the fluid variables at the centre of each cell. Fluent then solves the complete set of coupled equations for all the control volumes on the mesh using either a pressure-based solver (segregated solver) or a density based solver (coupled solver).

● In the present study the pressure-based solver (segregated solver) has been used, because this approach is the most adequate one for low-speed incompressible flows. In the pressure-based approach, the pressure field is extracted solving a pressure correction equation which is obtained by manipulating continuity and momentum equations. In this approach the governing equations are solved sequentially. Since these equations are non-linear they must be linearized first. In principle, this could be done either implicitly or explicitly, although, in the case of segregated solution method Fluent automatically linearizes each discrete governing equation implicitly with respect to that equation’s dependent variable. This produces a scalar system of equations containing only one equation per computational cell. Since the equations are non-linear, several iterations of the solution loop must be performed before a converged solution is obtained. The segregated solver thus solves for a given fluid variable (for example U – the *x* component of velocity) by considering all cells at a same time livel. It then solves for the next fluid variable (for example V – the *y* component of velocity) by again considering all cells at the same time level. Each iteration of the solution loop consists of the following steps:

**1.** The values of the fluid variables at the cell centre are updated based on the current solution values.

**2.** The U, V and W velocity components of the momentum equation are each solved in turn using the current values for the pressure and the mass fluxes through each of the cell faces.

**3.** The pressure correction equation (a form of the continuity equation) is solved to obtain the necessary corrections to the pressure and velocity fields so that the continuity equation is satisfied.

**4.** Where appropriate, additional scalar equations (such as those describing transport of turbulence quantities) are solved.

**5.** A check for convergence is made.

**6.** The above steps are repeated until the convergence criteria are met (all residuals less than $10^{-6}$).

## *3.2 Numerical methods*

In this section, the steps of the current simulation are given. Then specified solver parameters are set.

### *3.2.1 Steps of simulation*

Before launching the ''LES'' calculation a periodic RANS simulation with 5 ribs was run to generate a profile at the inlet. This profile can be generated by different methods, either by writing a profile from another CFD simulation or by using a User Defined Function (UDF). In fluent profiles can be manipulated through the command define → profiles. Here are the steps for the simulation:

**1.** Periodic simulation→ inlet profiles for RANS simulation see section 3.6.3 - 1
**2.** RANS simulation → initial conditions for LES see section 3.6.3 -2
**3.** LES simulations → see section 3.6.3 - 3 – 4 – 5

### *3.2.2 Solver parameters*

### *A- Boundary conditions*

To define a problem that results in a unique solution, specific information must be given on the dependent (flow) variables at the domain boundaries. Wide range of boundary conditions type permits the flow to enter and exit the solid domain: in the following boundaries are used in the present case:

● Inlet: Velocity Inlet: The current simulation was performed using an inlet profile with velocity and temperature profiles obtained from a RANS simulation over 5 ribs with periodic boundary conditions in the stream-wise direction.

● Outlet: Outflow condition assumes the flow to have a linear evolution ($\partial^2/\partial n^2=0$ in the direction $n$ normal to the boundary). Generally this would require flow not far to equilibrium, but, in the present case the reversed flow at the exit of the duct actually caused by the recirculation zone does not have a serious effect on the solution.

### *B-Inflow boundary condition*

When simulating turbulent flows using Large-Eddy Simulations (LES) or Direct Numerical Simulations (DNS), the specification of realistic instantaneous flow quantities at the inlet boundary conditions is a challenge and plays a major role in the accuracy of a numerical simulation [6]. The main objective of generating synthetic turbulence is to reduce the length between the inlet and the region where physical turbulence is established and shortens the required computational domain so that reduces the cost of the simulation. Fluent 6.3 offers three turbulent inflow velocity boundary condition methods for more realistic predictions of the downstream flow:

● ***No perturbation:*** individual instantaneous velocity components set equal to their mean velocity counterparts

● ***Spectral synthesiser:*** Random flow generation technique [15].

● ***Vortex method:*** Time-dependent inlet condition. The velocity component normal to streamlines at the inlet is perturbed by discrete vortices. In our case this method was used for a number of vortices=190 generated from the inlet boundary condition.

*C- Near wall treatment for wall bounded turbulent flows*

Turbulent flows are significantly affected by the presence of walls and a special near wall treatment is therefore required. In the case, no-slip condition (stationary wall) must be applied on all the walls. In Fluent [14], this condition is implemented assuming the flow to follow the classical linear –logarithmic (lin-log) law close the wall [5, 6]:

$$u^+ = \begin{cases} y^+ \quad if \quad y^+ \le 11.25 \\ \frac{1}{\kappa} ln E y^+ \quad if \quad y^+ \ge 11.25 \end{cases}$$

Where E =9.793, $\kappa$ is the Von Karman constant and $y^+$ is the distance from the wall made non-dimensional defined by:

$$y^+ = \frac{u_\tau y}{\nu} \quad \text{With} \quad u_\tau = \sqrt{\frac{\tau_w}{\rho}} \text{ is the friction velocity}$$

***Wall boundary conditions for the thermal field:***

● Constant heat flux boundary condition is applied at the bottom wall.
● The boundaries between fluid and solid domains, including the bottom wall of the fluid and the rib surfaces are coupled.
● Adiabatic boundary condition is defined on the top and lateral walls of the duct.

***D-Solver***

As it was said before, a Pressure Based (segregated) solver is applied which provides flexibility in solution procedure and lower memory requirements than coupled solver.

***E-Discretization***

LES requires as small numerical error as possible. The basic points to be kept in mind are:

● The solution needs to capture the main eddies (refined solution of gradients)

● Upwind schemes are too diffusive for LES and should be avoided [5, 6 and 11].
● Central differencing ***(CD)*** gives minimum numerical diffusion and best accuracy but sometimes it can become unstable, giving unphysical oscillations (wiggles) for high-Re flows. So instead Bounded Central Differencing ***(BCD)***, implemented in Fluent [14] is used. For the current simulation, the applied discretizations are resumed in *Table 3.1*:

| Spatial discretization | | Temporal Discretization |
|---|---|---|
| Pressure: | ***Standard*** | ***2nd order implicit*** |
| Momentum: | ***BCD*** | ***Iterative Time Advancement ITA*** |
| Energy: | ***BCD*** | ***ITA*** |

*Table 3.1 Numerical algorithms*

### *F- Pressure velocity coupling*

Pressure-Velocity Coupling fix the way mass continuity is accounted for when using the segregated solver. Three methods are available in Fluent [14]:
● SIMPLE
● SIMPLEC
● PISO
The present choice for the pressure velocity coupling is the default scheme SIMPLE because it is robust.
G- Under Relaxation Factors URF

Under-relaxation factor, $\alpha$, is included to stabilize the iterative process for the segregated solver. It controls the update of computed variables at each iteration.

$$\varphi_p = \varphi_{p,old} + \underline{\alpha} \Delta \varphi_p$$

### *H-Unsteady flow parameters*

In the case of DNS and LES simulations, the solution must be advanced in time and a time step $\Delta t$ must be fixed. The time step $\Delta t$ corresponds to physical advancement time and its value should be inferior to the stability criterions of the solution algorithm.

Fluent applies an implicit algorithm and the time step is not, therefore, limited by stability limits. The choice of our time step is then driven by accuracy reasons. $\Delta t$ should be defined

to ensure that the flow does not pass through cross more than one cell per time step; this is what is the Courant-Friedrich-Lewy (CFL=1) condition.

$$\Delta t = \frac{(CFL)\Delta x_{min}}{U_b}$$

# CHAPTER 4 Grid Creation

## *4.1 Creation of the present grid*

### 4.1.1 Gambit software mesh generator

The meshing software available with Fluent is Gambit [18]. This software can create a two-dimensional (2D) surface mesh using triangular or quadrilateral elements, or a three-dimensional (3D) volume mesh using a combination of hexahedral, tetrahedral or prism elements. The procedures to create a good mesh can be listed as follow (*figure 4.1*):

- **Create the geometry:**
  -Vertices
  -Edges
  -Faces
  -Volume
- **Mesh:**
  -hexahedral
  -tetrahedral
- **Examine the mesh**
  -skewness
  -show the worst elements
- **Define Boundary conditions**
  -Velocity inlet
  -walls
  -outflow…
  -symmetry…
- **Define continuum regions:**
  -Fluid zone
  -Solid zone
- **Export the mesh file**
  When the mesh is ready, **Gambit** can export it into a **.msh** file so it can be read by Fluent software.
- **Mesh steps are over.**

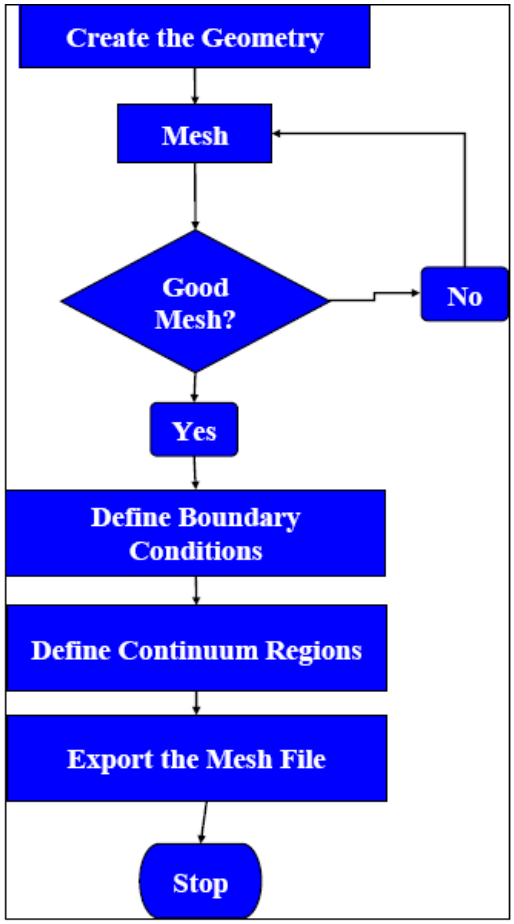


*Figure 4.1: meshing procedures*

### *4.1.2 Boundary layer mesh*

With Gambit, boundary layers zone scan be created, with ease in very complex geometries to increase the resolution of the zone close to a wall. The *figure 4.2* shows the over grid of a rib pitch span and the boundary layer mesh created in the present case, whose characteristics are listed as follows:

| | | ***Top fluid wall*** | ***Bottom Fluid wall*** | ***Top Solid wall*** |
|---|---|---|---|---|
| Length 1st row: | a | 0.002$D_h$ | 0.002$D_h$ | 0.002$D_h$ |
| Growth factor: | b/a | 1.2 | 1.2 | 1.2 |
| Number of rows: | N | 20 | 18 | 10 |

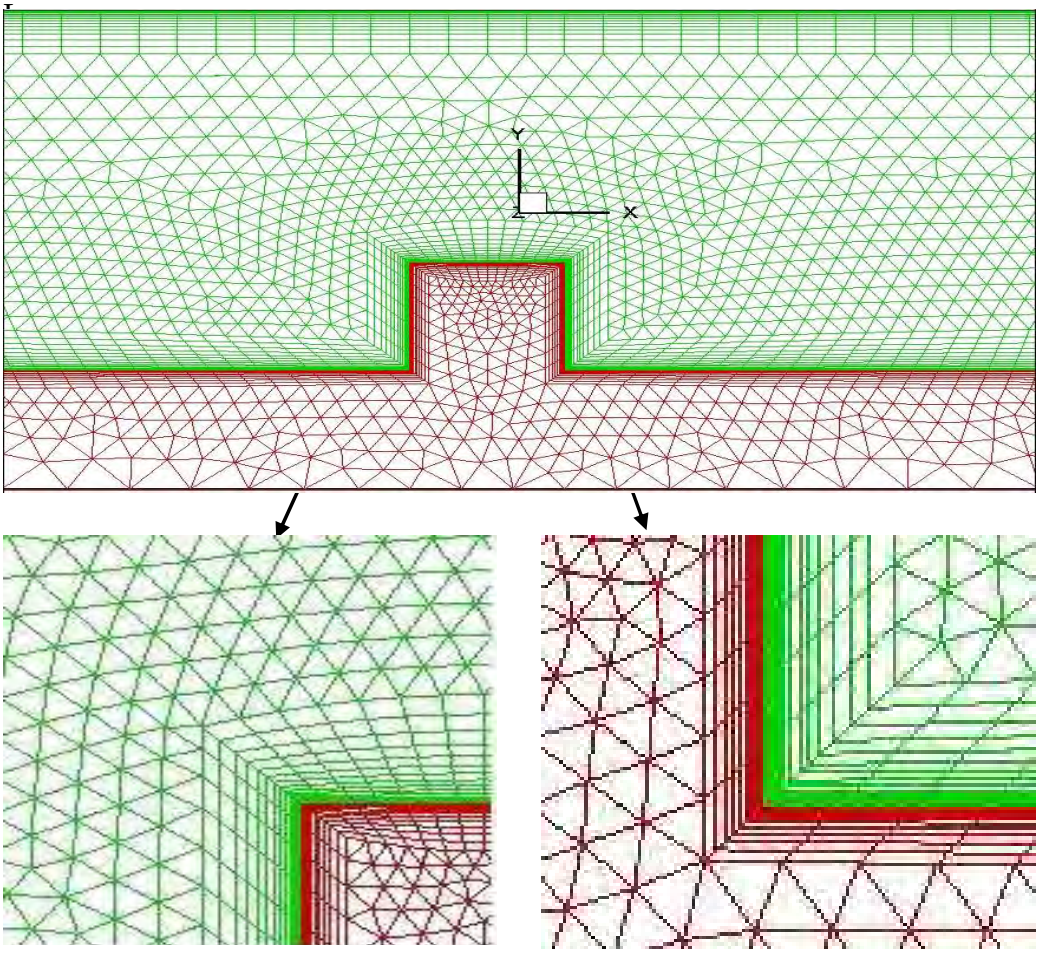


*Figure 4.2 Structured boundary layers mesh and Unstructured TRI-face mesh*

**N.B** as it can be seen the in *figure 4.2* the grid cells do not interact above that on the corners of the rib. This can be done in Gambit by a simple procedure before starting the boundary layer mesh: the type of the vertex on the ribs is switched from *CORNER* to *SIDE* and then the number of cells in the front face is reduced effectively. The maximum skewness cell is around 0.5.

### *4.1.3 Front face mesh*

Once the boundary layer's mesh is created on the walls of the front face, the unstructured Tri-Mape mesh can be created in the fluid (Air) and solid (Steel) zones. The mesh in the X-Y plane is refined on the 3rd and 4th rib as it is shown below and the maximum number of cells in the front face X-Y plane for the fluid and the solid zone is **14706 cells (***figure 4.3***).**

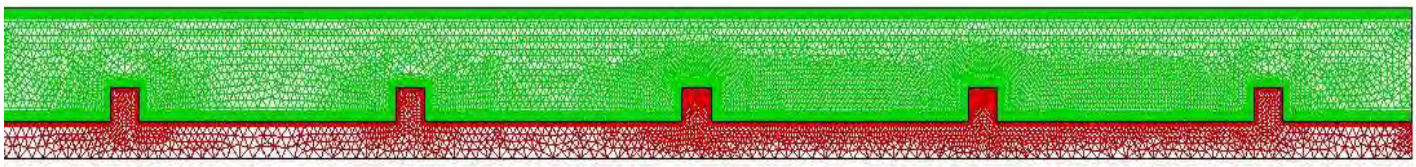

*Figure 4.3 refined mesh on 3rd and 4th rib of the fluid (air) and solid (steel) zones.*

### *4.1.4 Volume mesh*

After meshing the front XY plane, an edge in the Z direction is created and then the face is extruded to 3D volume geometry on this Z direction edge. Besides, in Gambit, the option is available to extrude it with the mesh. So a structured volume mesh was generated with 70 points in the span-wise direction. The *figure 4.4* shows the structured mesh in the YZ plane.

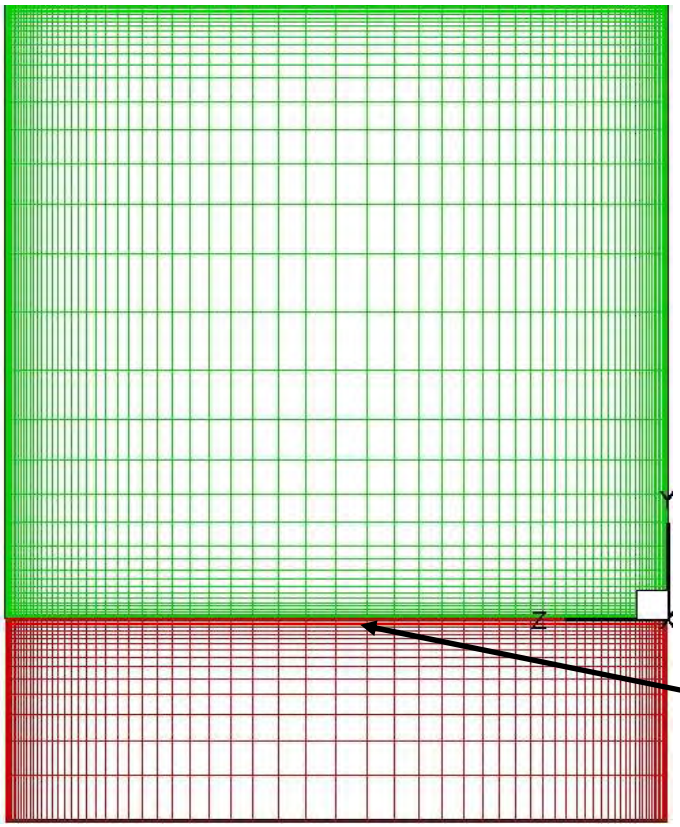


Total cell volume mesh:

**1.455 090 cells**

3D geometry mesh extrusion on this edge.

*Figure 4.4 Z-Y plane structured mesh*

### *4.1.5 Boundary conditions*

Before exporting the mesh to fluent software, boundary conditions should be applied in Gambit. The boundary conditions applied in our case are:

***Fluid inlet:*** Velocity Inlet
***Fluid Outlet:*** Outflow
***On the rest of the boundaries:*** Wall boundary condition is applied.

## *4.2 Checking of the present grid*

### *4.2.1 Comparison between grids*

Another mesh was generated by another member of the team [16] applying a unstructured quad - Mape mesh in the X-Y plane direction. The big differences in these two meshes (*figures 5.5* and *5.6*) are:

- Different boundary layers characteristics.
- Different number of nodes in the Z-Y direction.
- Refined mesh in the solid (steel) zone near the bottom wall of the fluid.

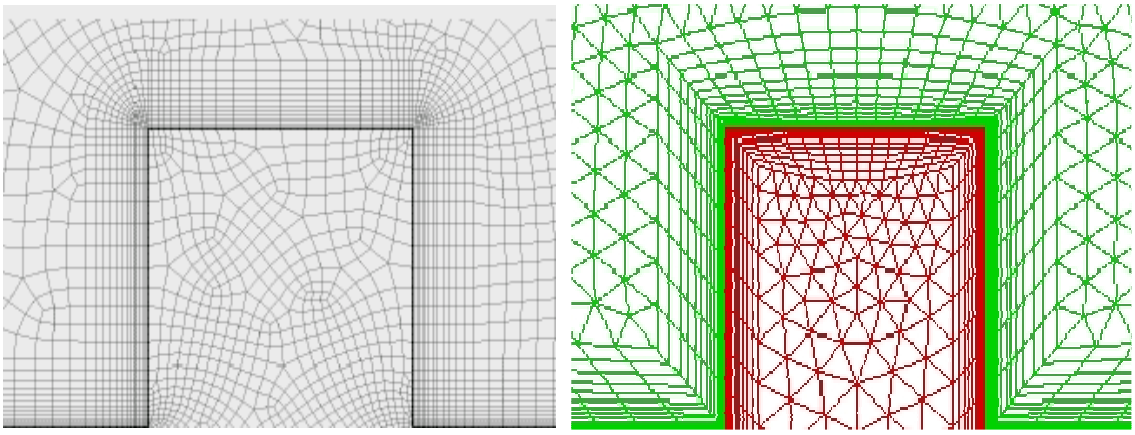

*Figure 4.5 Boundary layers mesh (left [16]) and (right: present grid)*

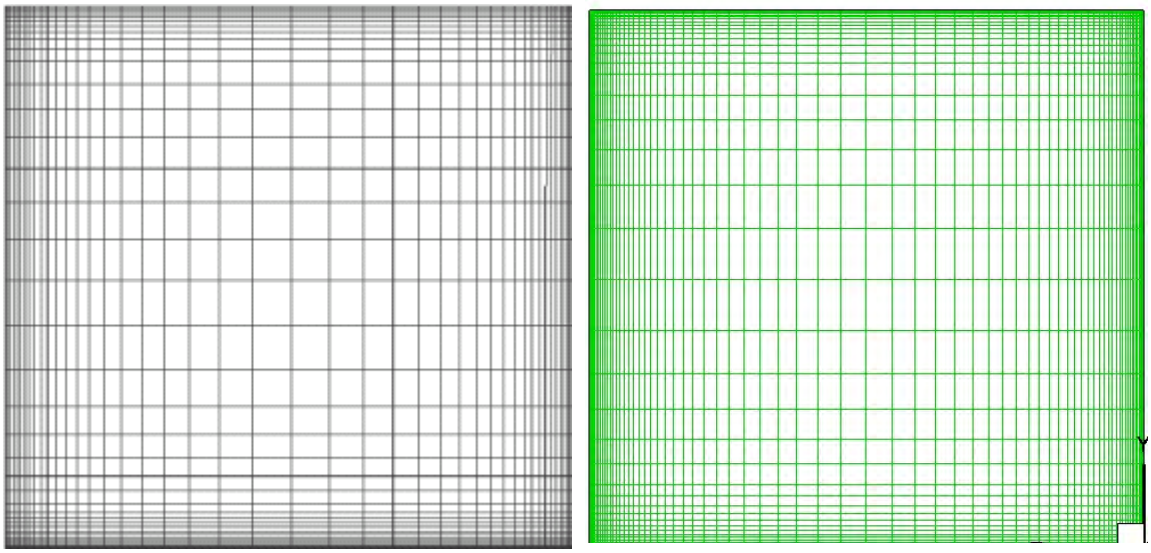

*Figure 4.6 Z-Y plane mesh (48 nodes .Left: [16]) – (70 nodes right: present grid)*

No important difference between preliminary results was remarked and the present grid was therefore adopted for the following investigation

### *4.2.2 **Resolution of the wall layer***

The quality of LES simulations is critically dependent on the resolution of the wall layer [6, 7]. Therefore, the present grid was checked "a priori" estimating the distance from the wall for the first inner grid point in the fluid region.
The shear velocity was estimated from the skin friction coefficient based on approximate correlations for pipe flows:

$$u_\tau = \sqrt{\frac{\tau_w}{\rho}} \sim U_\infty \sqrt{\frac{Cf}{2}} \quad \text{With} \quad \frac{Cf}{2} \sim 0.023 Re_D^{-0.2}$$

A contour of instantaneous $y^+$ on the bottom and back wall of the geometry is shown in the *figure 4.7* and next to it a plot of instantaneous $y^+$ (x) on a center line extracted from the bottom ribbed wall at the symmetry plane Z/h=

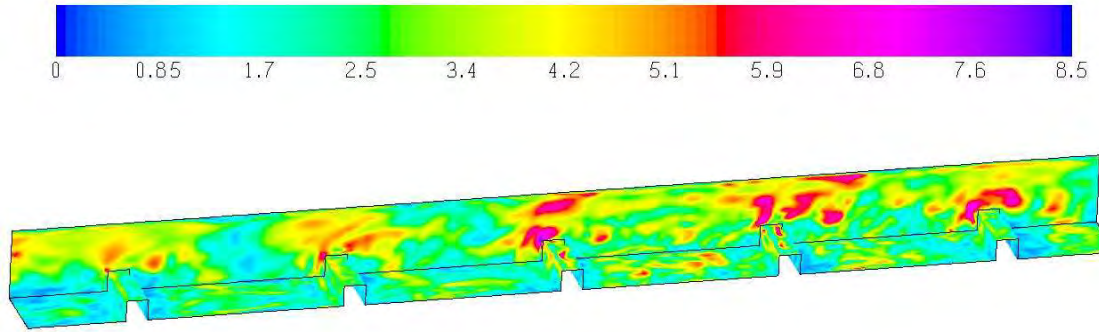


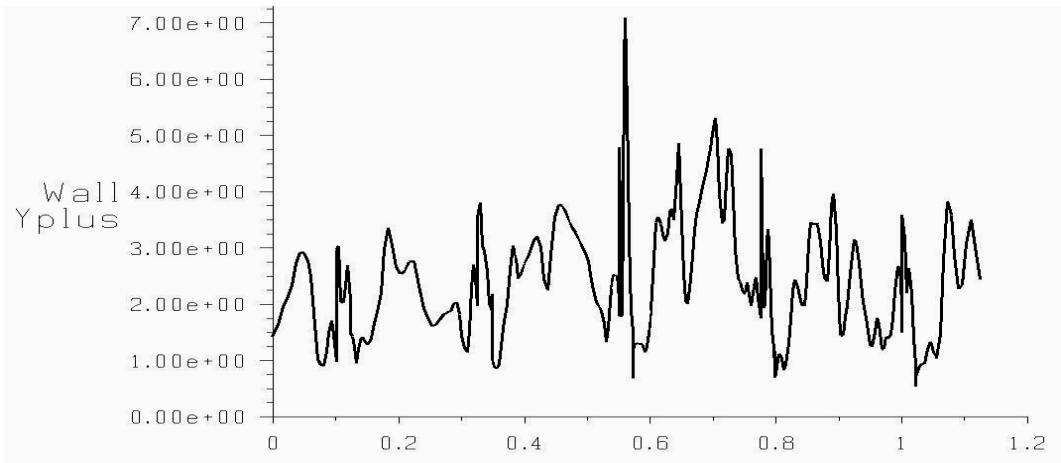


*Figure 4.7 contours and maximum plot values of instantaneous y+*

$y^+$ was found to vary between 1 and 7 wall units with an average of

$$y^+ \simeq 5$$

Therefore, the first inner node can be expected to fall within the viscous sub-layer (linear part of the lin-log low) and the present boundary condition can be expected to yield a satisfactory estimation of the wall layer and wall heat flux.

# CHAPTER 5 Procedure for LES simulations

## *5.1 Options for the solver*

The present choice for the pressure velocity coupling is the default scheme SIMPLE because past use [1 to 14] had proved the most robust one among the available solvers (See Chapter 3).

As anticipated, the solution of the present equations is obtained by a segregated solver, which achieves convergence (be it the final solution for a steady case of for each time-step for an unsteady case). The under-relaxation factor, $\alpha$ was optimized on the basis of the previous investigations of the present authors:

The values adopted for the computed variables are:

| | |
|---|---|
| Pressure | 0.6 |
| Momentum | 0.55 |
| Energy | 0.55 |

## *5.2 Options for unsteady executions*

The general criterion for the choice of $\Delta t$ for LES simulations was discussed in Chapter 3. For the present simulations the target was that $\Delta t$ should be small enough to resolve time dependant features and to ensure convergence within 20 iterations. Following preliminary tests, the chosen parameters are:

- $\Delta t$ =3.10$^{-5}$ s
- Z=14 ↔ maximum iterations per time step.

*Figure 5.1* shows that the present simulation the maximum value of CFL is around 0.85 at the upstream edge of the rib, otherwise it is far below that [0-0.3]. These results can be considered to be satisfactory since they are lower than 1 and well lower than the limit suggested in the literature [17].

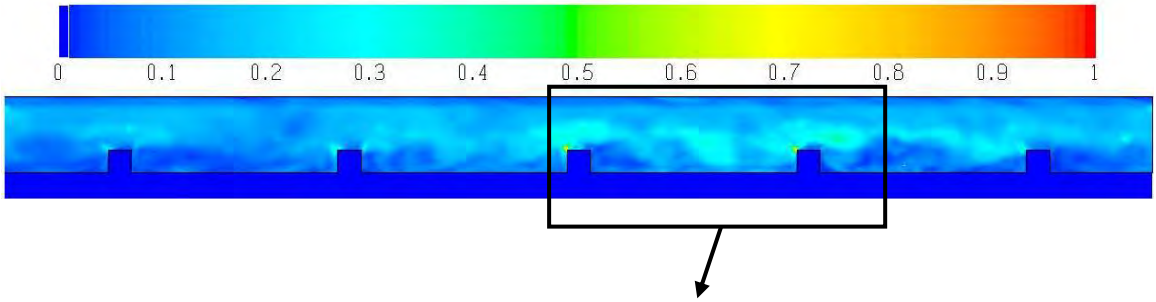

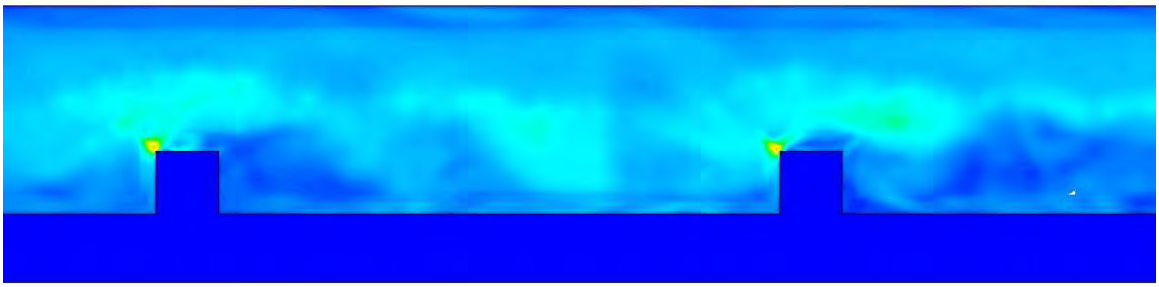

*Figure 5.1 Contours of the Courant cell number on the vertical symmetry plane*

## *5.3 LES-Specific Solution Strategies (Fluent-User's-Guide-6.3)*

Large eddy simulation involves running a transient solution from some initial condition, on an appropriately fine grid, using an appropriate time step size. The solution must be run long enough to become independent of the initial unphysical condition and to enable the statistics of the flow field to be determined. The following descriptions are the steps which have been followed for the current large eddy simulation:

1. The simulation begins running a steady state flow simulation using the Realizable k-ε Reynolds-averaged turbulence model with enhanced wall treatment EWT. The simulation is run until the flow field converged (*figure 5.2*).

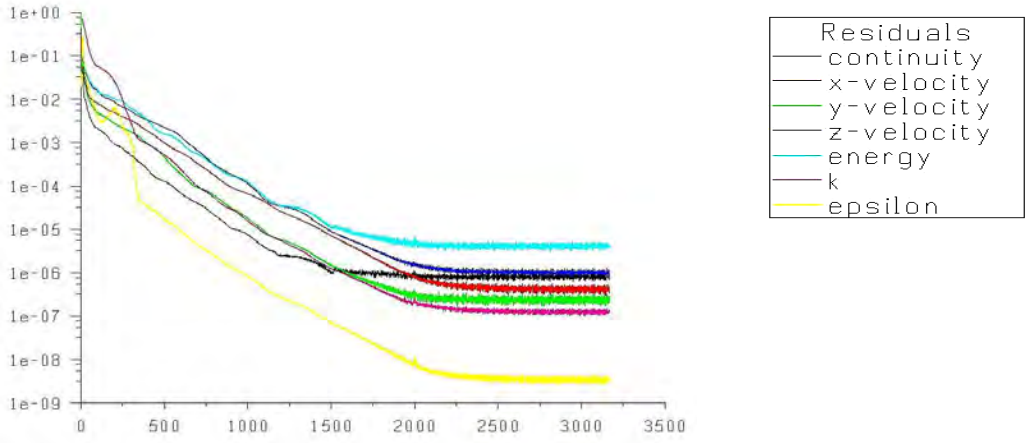


*Figure 5.2 Evolution of residuals versus iterations*

The profiles of the solution at half-pitch-length are extracted to be use as average inlet profiles for the LES execution. An example is shown *figure 5.3* for the average stream-wise velocity $<U>$ cast in non dimensional terms against the bulk velocity *Ub*. It can be remarked that flow is here attached, but not at the equilibrium.

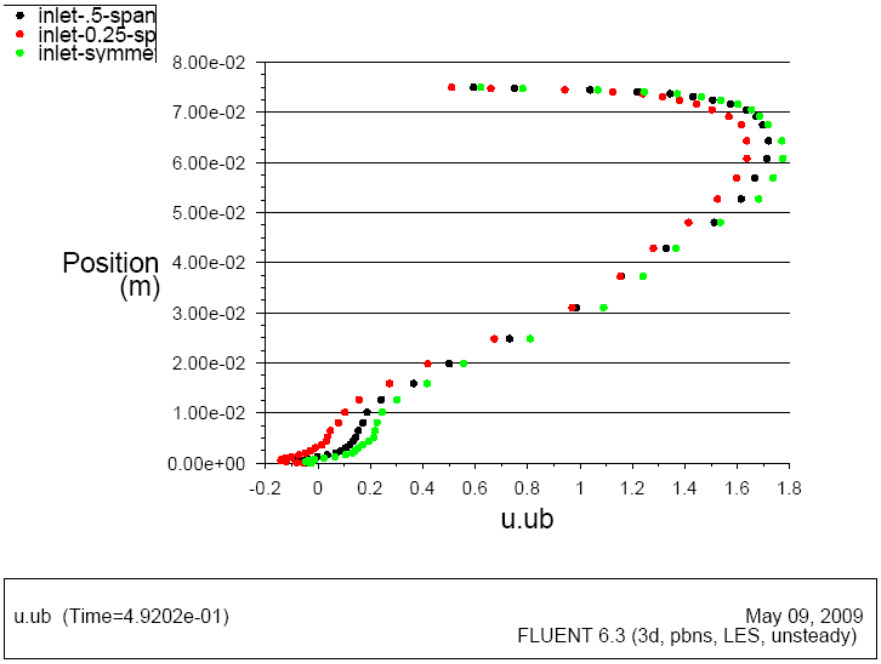


*Figure 5.3 profiles of average stream-wise velocity <$U/U_b$> for inlet condition for the LES execution.*

2. Once the RANS calculation had converged, the solve/ initialize/ init-instantaneous-vel text command is used to generate initial instantaneous velocity field out of the steady-state RANS results. This command must be executed before LES is enabled. This option is available for all RANS-based models and it will create a much more realistic initial field for the LES run. Additionally, the choice of this initial condition does not influence the accuracy of the final solution, although it will help in reducing the time needed for the LES simulation to reach a statistically stable mode. (N.B. This step is optional). The numerical parameters for the present simulation are resumed in *Table 5.1*.

3. After setting the solver parameters described section 5.1 before, the LES calculation is run in order to evacuate the initial, non-physical, condition. That is the ‘’Transient run’’. This calculation was run for ~ 10 000 times steps which correspond to a time ~ $2*T_{flow-th}$

$T_{flow-th} = \frac{L = 1.125}{U_b = 7.791} \sim 0.144s$ where $T_{flow-th}$ is the “flow-through” time, or the time spent for one particle transported with the bulk velocity to pass through the whole ribbed duct.

4. After the Transient run was reached, the Data Sampling for Time Statistics option is enabled in the Iterate pane of the menu of Fluent. With this option enabled, Fluent will gather data for time statistics while performing a large eddy simulation. We set the Sampling Interval to 1 so that Data Sampling for Time Statistics can be performed every one time step. The

statistics collected at each sampling interval can be post-processed to analyze both the mean and the root-mean-square (RMS) values in Fluent.

5. The simulation was initially run for 7.5*T (the mean flow residence time) to obtain statistically stable data; further checking (Annex A) shown the flow field statistics being fully converged by then. Then the post-processing undertaken and its results are given in the following chapters.

| **UNSTEADY PARAMETERS** | |
|---|---|
| Time Step | $3*10^{-5}$ s |
| CFL | [0-1] |
| Nb of Iteration/ time step | 15 |
| CPU time (8nodes) | 55s/Time step |

*Table5.1. Numerical parameters for unsteady simulations*

# *Part II: Simulation of the flow field*

# CHAPTER 6 Simulations of smooth duct

## *6.1 Scope of the simulation of the smooth duct*

At the beginning of this research the Data Bank did not contained experimental data for the conjugate heat transfer for the case of no-ribbed duct, as the investigation fluid dynamic characteristics of the new test section had being investigated. Therefore, a limited investigation of this case with performed and used to assess the influence of the inlet boundary condition and to calibrate the parameters of the LES simulations of the ribbed duct.

### *6.1.1 Computational field.*

There is no agreement in the literature concerning the entrance length over the state of established flow is attained. Available values range between $L/D_h$=10 to $L/D_h$=100, depending on the different inlet conditions. The last value is well above the limit of computational power available for the present research and the computational field (*figure 6.1*) was chosen equal to the one for the ribbed duct ($L/D_h$=15) to ensure full compatibility with the case of main interest (see Chapter 1).


*Figure 6.1 Computational field (blue fluid field; red solid wall)*

### *6.1.2 Effect of the inflow boundary condition*

As remarked in Chapter 3, in general terms, the inflow boundary condition can have an important effect on LES of space developing flows. This point is more important for the case of the ribbed duct, where the expected computational field contains no region of flow close to equilibrium state. The methodology developed in the previous work of the present team is to impose boundary condition on the XZ plane at the midway of a pitch. This location corresponds to non-equilibrium ***attached*** flow. On this plane the result of a RANS simulation is imposed for the mean field and a time-dependent three-dimensional perturbation to it, to trigger the development of the turbulent fluctuations. Among the three models for turbulent inflow perturbations available in Fluent 6.3, the option of ***No perturbation*** was neglected because it is unable to trigger the development of the turbulent fluctuations and the ***Spectral synthesiser*** (*ss*) and ***Vortex method*** (*vm*) (see Chapter 3 and [14]) has been applied on the case of smooth duct to assess their respective behaviors.

An instantaneous field of velocity perturbation for the two cases is presented in *figure 6.2.*

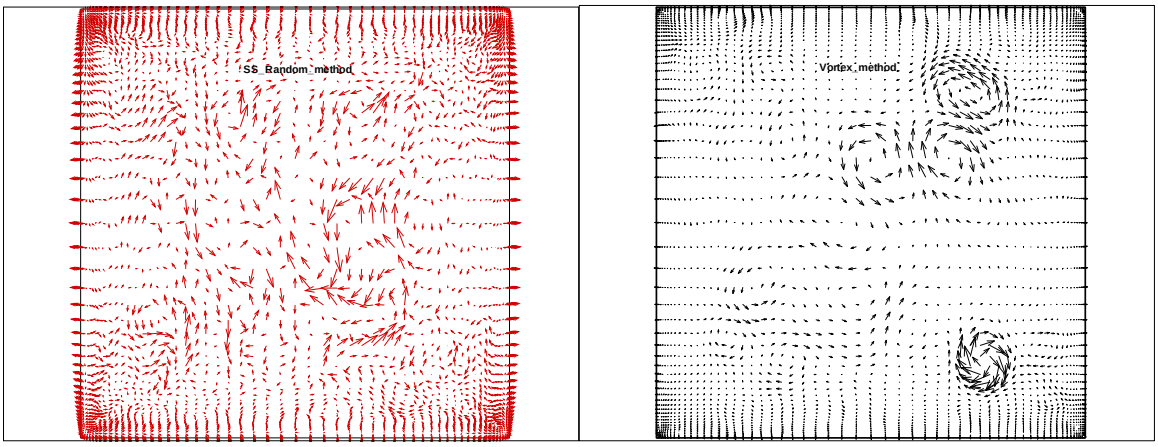


***(a)*** ***(b)***

*Figure 6.2 Instantaneous field of perturbation at the inlet, (a) Spectral synthesizer ; (b) Vortex method.*

The stronger organization of field created by the Vortex Method can be remarked.
*Figure 6.3* which compares the resolved kinetic energy (***k***), made non dimensional against the bulk velocity ***Ub***, on a symmetry line of the inlet plane ( X=0; Z=H/2); it can be noted that, qualitatively, *vm* produces a more realistic distribution of the fluctuations ( the presence of 2 maxima of kinetic energy in the wall region as expected) .

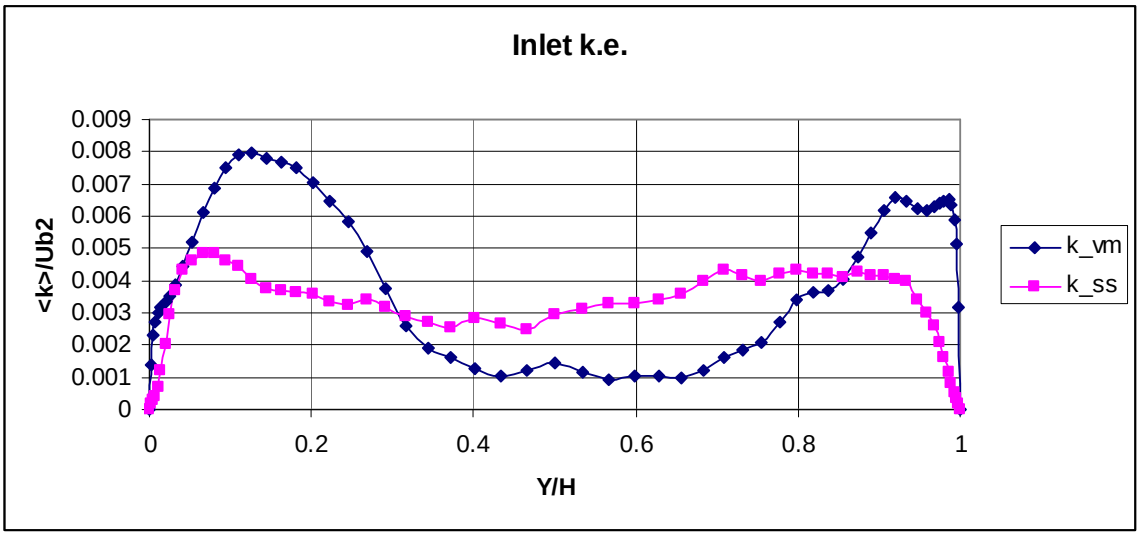


*Figure 6.3 Resolved kinetic energy (k) a symmetry line of the inlet plane ( X=0; Z=H/2). Instantaneous field of perturbation at the inlet, (ss) Spectral synthesizer ; (vm) Vortex method.*

The following figures show the evolution of the flow in the stream-wise direction and put in evidence the importance of the inlet perturbation on the development of the flow. *Figure 6.4*

to *figure 6.7* which present profiles of the symmetry line (X=constant, Z=H/2) at X locations separated by 1 pitch length, which, respectively, correspond to the locations of the 3rd, 4th, 5th rib.

Considering the *vm* perturbation, *figure 6.4* shows the evolution of the mean velocity ***U*** cast in non-dimensional terms against the bulk velocity while *figure 6.5* shows the corresponding resolved kinetic energy.
It can be that the mean flow has reached equilibrium between the positions 35, 45 (which correspond to locations of the 4th and 5th rib) the turbulent field is close to equilibrium by the last location.

The intensity of *TI* of the turbulence $\frac{\sqrt{<u'^2>}}{U_{bulk}}$ takes the values:

X_35: 0.097
X_45: 0.1
X_outlet : 0.103

This result supports the present conclusion.

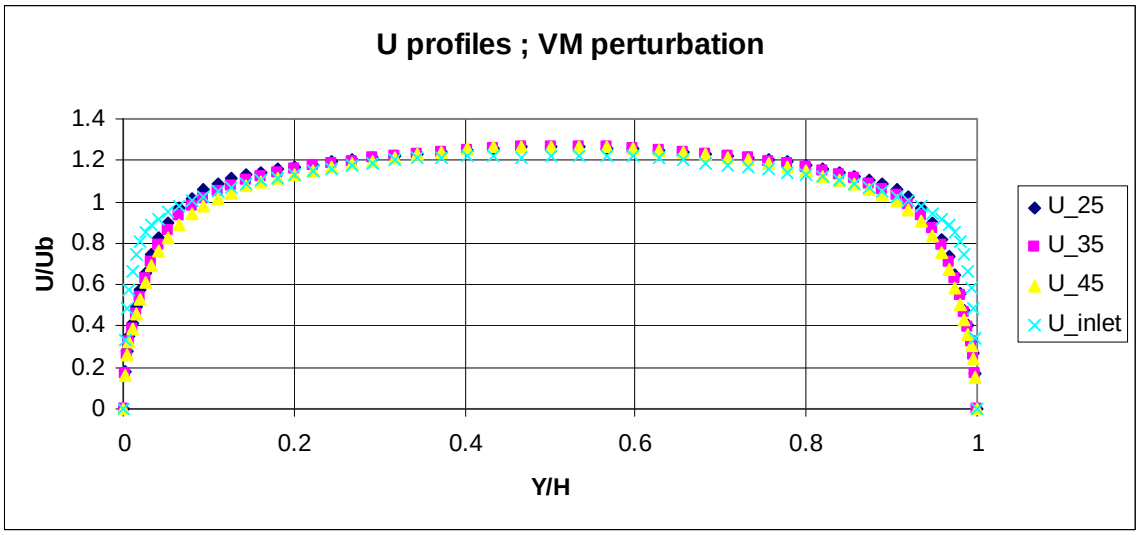


*Figure 6.4 Evolution of the average longitudinal velocity U on the symmetry plane (Z=H/2) along X. Perturbation at the inlet: (vm).*

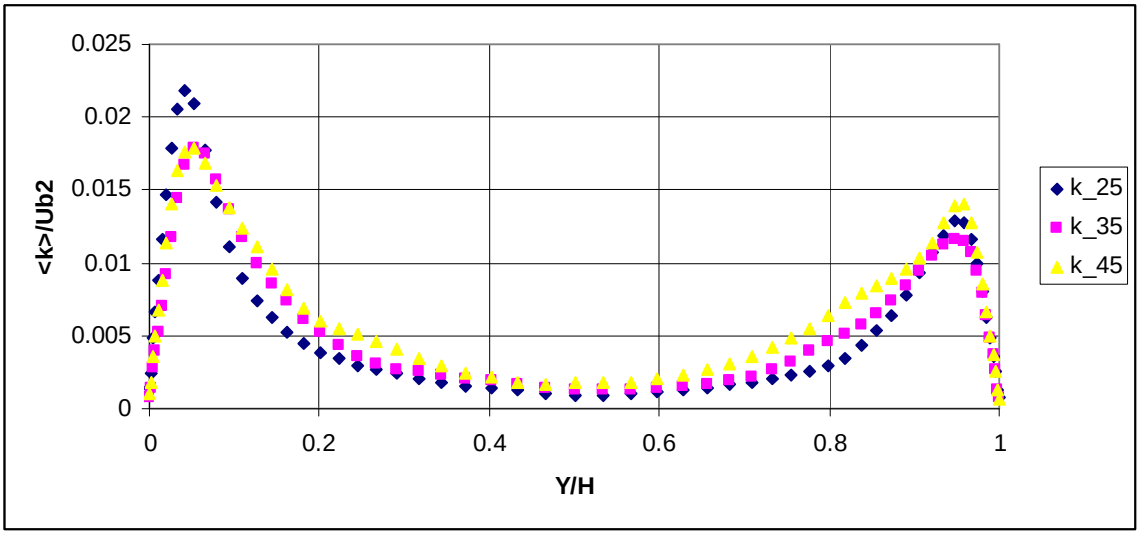


*Figure 6.5 Evolution of the resolved kinetic energy (k) on the symmetry plane (Z=H/2) along X. Perturbation at the inlet: (vm)*

The corresponding results for the **ss** perturbation are, respectively, presented in *figures 6.6 and 6.7*. These graphs show that, in this case the level of turbulence is lower and the turbulent field has not yet reached the established state. This is show by the corresponding ***TI*** is:

X_35: 0.066
X_45: 0.080
X_outlet : 0.085

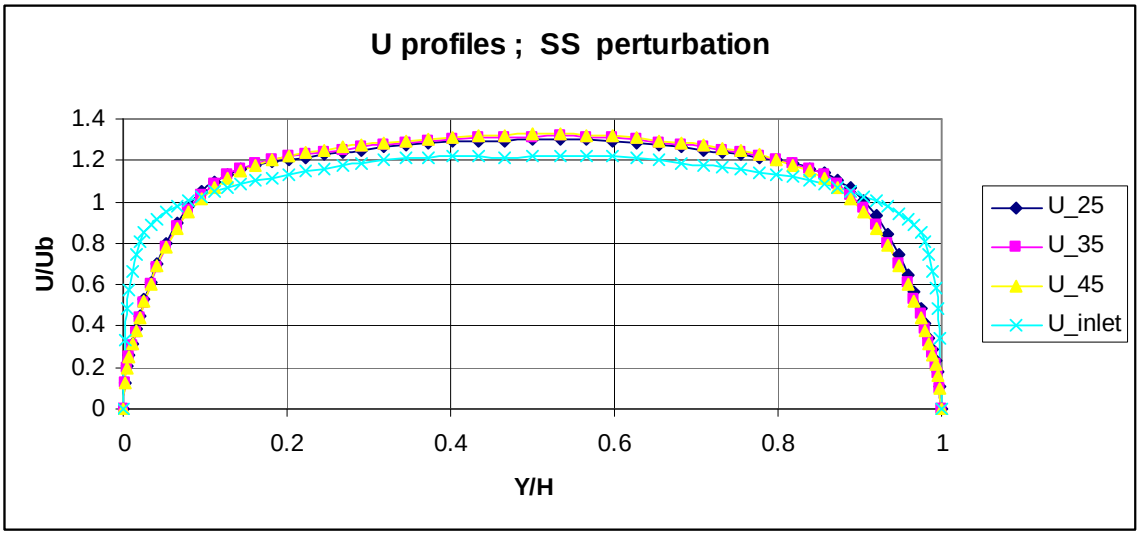


*Figure 6.6 Evolution of the average longitudinal velocity U on the symmetry plane (Z=H/2) along X . Perturbation at the inlet: (ss).*

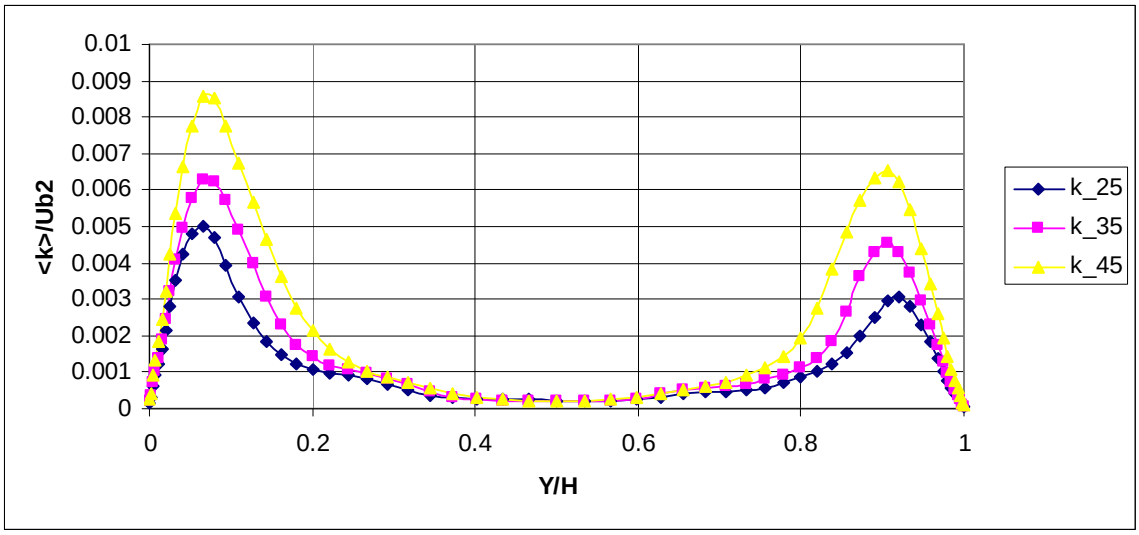


*Figure 6.7 Evolution of the resolved kinetic energy (k) on the symmetry plane (Z=H/2) along X. Perturbation at the inlet: (ss)*

It can be concluded that the Vortex method is able to produce an established flow within the range $L/D_h$=15 t is a more practical inlet condition for flow case where a long establishment length is forbidden by the geometry, as is the case of the following simulation of ribbed ducts.

The contours in the region where flow was established itself (*vm*) are presented in the following figures. *Figure 6.8* shows the average velocity made non-dimensional against *Ub*

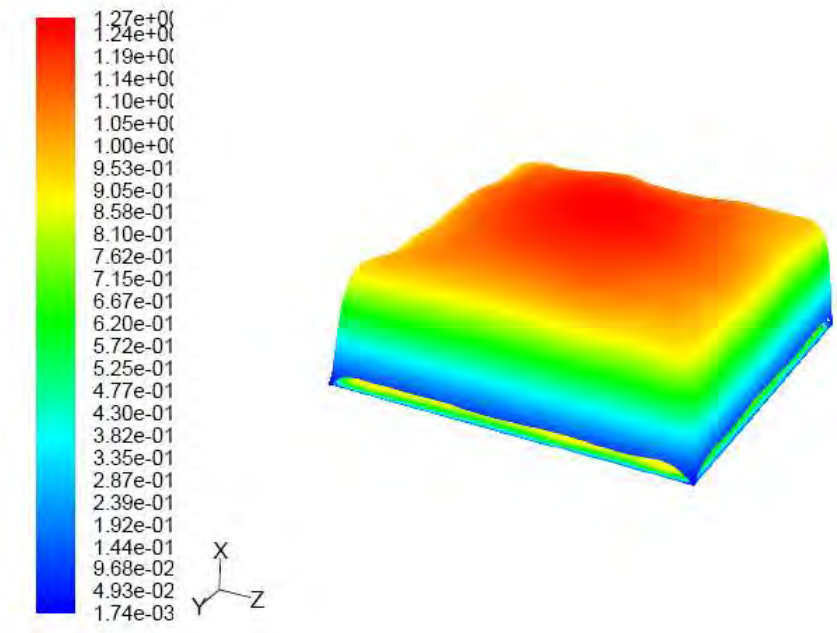


*Figure 6.8 Contours of average velocity in a cross-plane in the region of established flow (vm)*

*Figure 6.9* shows the in-plane secondary flow in the same non-dimensional form. The typical patterns of secondary motions are recovered.

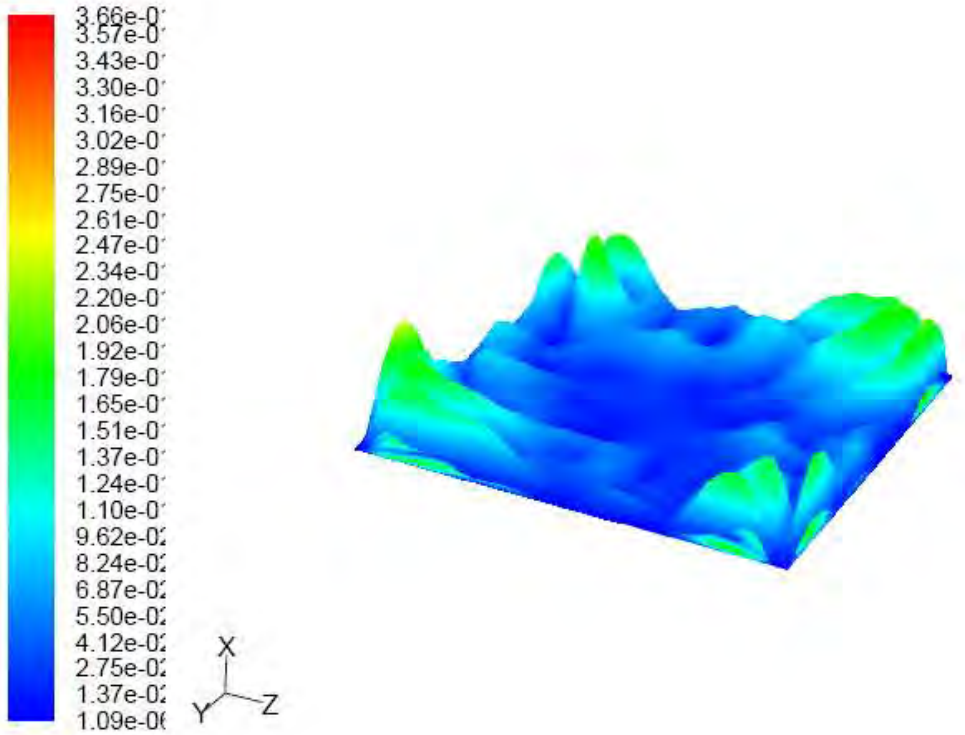


*Figure 6.9 Contours of secondary flow in a cross-plane in the region of established flow* (*vm*)

*Figure 6.10* presents the contours of the turbulent intensity and puts in evidence the regions of high turbulence close to the walls.

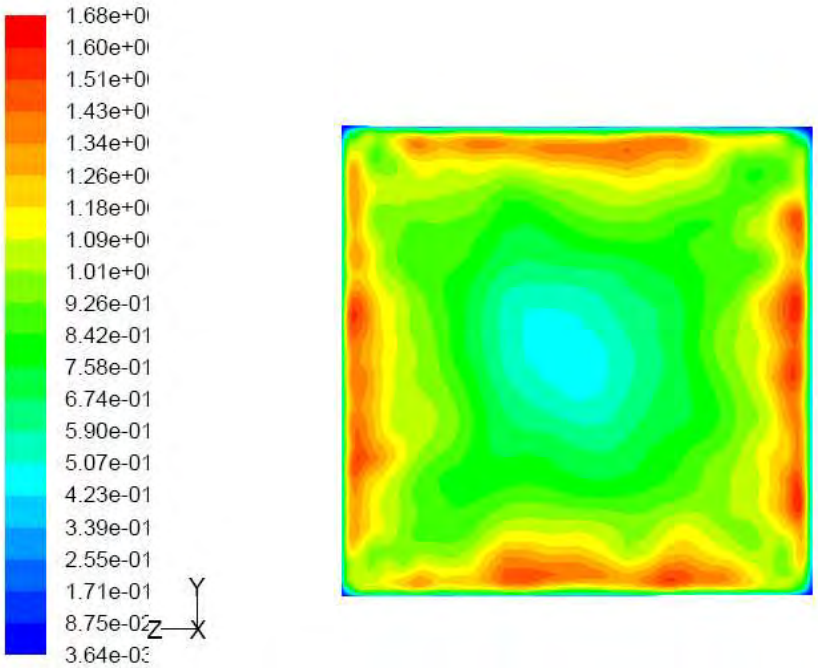


*Figure 6.10 Contours of the turbulent intensity* (*vm*)

It can be concluded that the typical behavior of established flow in square duct is recovered and the present methodology can be applied to the simulation of the flow in the ribbed duct.

# CHAPTER 7 Aerodynamic Results and Discussion

## *7.0 Introduction*

This chapter compares the results of the Large Eddy Simulation technique with PIV and Infra Red thermography measurements of former experimental researches performed at the von Karman Institute. [8 to 10].

## *7.1 Measurement and validation planes*

The coordinate system used in the present simulation is given in the chapter 1 In order to compare with the experimental data, the numerical results for every rib pitch have been reported to a single pitch and all the geometrical dimensions are normalized with the rib height *h* (*figures 7.1 to 7.3*).
Data for different quantities are available for the nine different mutually perpendicular planes (*figures 7.1 to 7.3).*

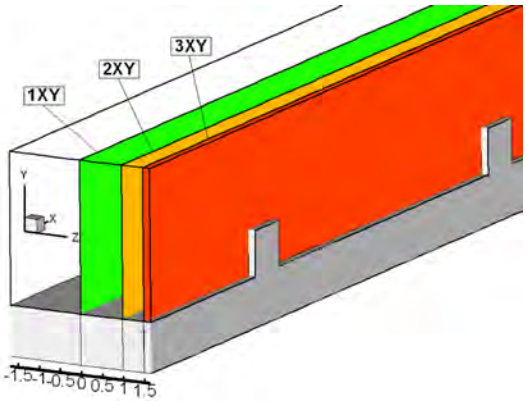


*Figure 7.1 XY planes position*

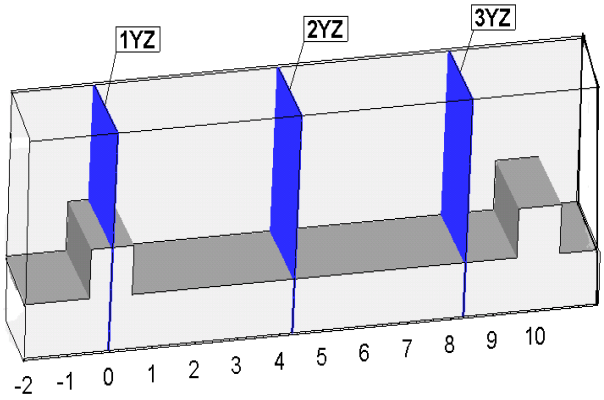


*Figure 7.2 YZ planes position*

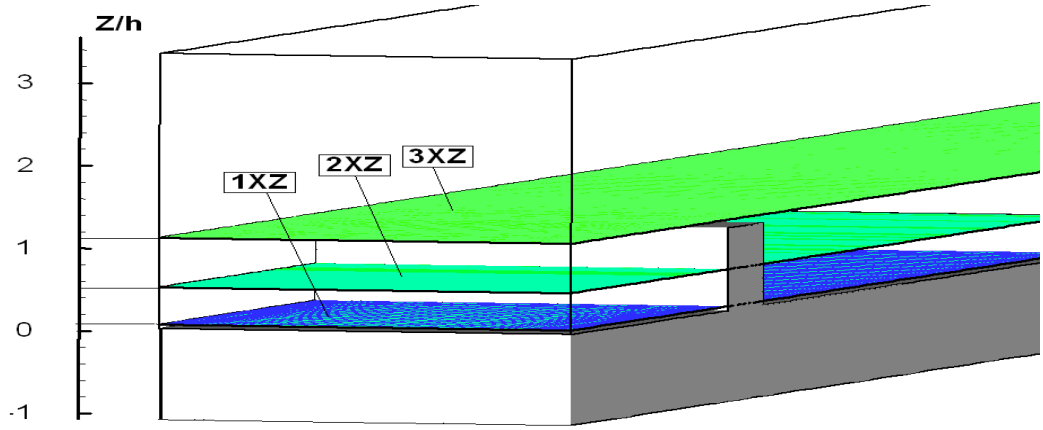


*Figure 7.3. XZ planes position*

The nomenclature and the coordinates of each measurement plane are given in the following *Table 7.1*. In the case of simulation the same planes were analyzed for every rib pitch *p*.

| *Name* | *X/h extension* | *Y/h extension* | *Z/h extension* |
|---|---|---|---|
| **1XY or Z/h=0** | (-2)-(8) | (0)-(3.33) | **0=symmetry plane** |
| **2XY or Z/h=1** | (-2)-(8) | (0)-(3.33) | **1** |
| **3XY or Z/h=1.5** | (-2)-(8) | (0)-(3.33) | **1.5** |
| **1XZ or Y/h=0.05** | (-2)-(8) | **0.05** | (-1.66)-(1.66) |
| **2XZ or Y/h=0.5** | (-2)-(8) | **0.5** | (-1.66)-(1.66) |
| **3XZ or Y/h=1.05** | (-2)-(8) | **1.05** | (-1.66)-(1.66) |
| **1YZ or X/h=0** | **0** | (0)-(3.33) | (-1.66)-(1.66) |
| **2YZ or X/h=3** | **4.3** | (0)-(3.33) | (-1.66)-(1.66) |
| **3YZ or X/h=8.3** | **8.3** | (0)-(3.33) | (-1.66)-(1.66) |

*Table 7.1Llocation of the measurement planes in non-dimensional units*

## 7.2 Definition of measurement and validation lines

For every rib pitch, numerical and experimental results are compared along vertical and horizontal lines as shown in *figure 7.4*.
4 horizontal Lines at: Y/h = 0.05 / 0.5 / 1.1 / 1.66 /
12 vertical lines: X/h = -2 / -1 / -0.25 / 0 / 0.25 / 1 / 2 / 3 / 4 / 5 / 6 / 7

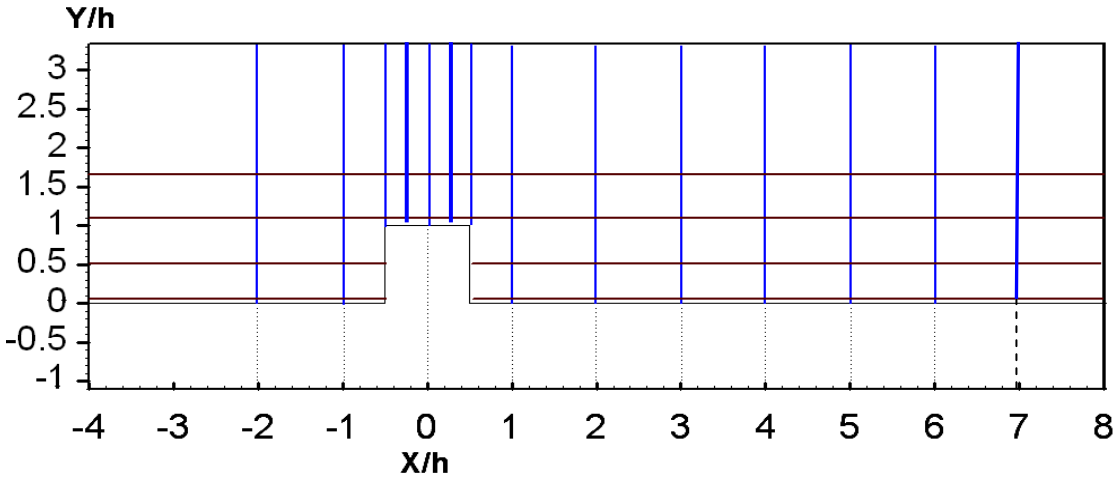

*Figure 7.4 Lines along which profiles where extracted in each XY plane*

## 7.3 Investigation of the flow field

The description and investigation of the mean flow field and the one of resolved turbulence are presented in the next sections below. Comparisons between numerical simulation (3rd, 4th and 5th rib) and experimental data are presented in form of contours and profiles plots. All the velocity components shown in the contours and profiles plots are normalized with the inlet bulk velocity ($U_b$=7.791 m/s).

## 7.4 Macroscopic quantities and topology of the flow field

### 7.4.1 Pressure drop

As it was already written in the first chapter, the pressure drop ***Δp*** over one rib is one of the most important parameters in the internal cooling channel. This parameter, related to the skin friction coefficient, is given by the formula:

$$C_f = \frac{D_h \Delta p}{2 p \rho U_b^2}$$

In order to compare the numerical results with the available experimental data, the skin friction coefficient is normalized with by the expression of *Blasius* for a fully developed flow in a smooth duct for the same hydraulic diameter and the same Reynolds number. $C_{f_0} = 0.046 Re^{-0.2}$

***Δp*** was evaluated as the difference of area weighted averages of static pressure between two surfaces separate by one pitch upstream and downstream the rib. Otherwise, since there are 5 pitches between the inlet and the outlet $C_f$ was divided by 5 to give also the average pressure drop in the entire channel. Thus, the ratio $C_f / C_{f_0}$, computed from both experimental and the simulation results, is given in the *Table 7.2* :

| | $C_f / C_{f_0}$ |
|---|---|
| Experimental (Casarsa and Arts) | 12.3±0.25 |
| **(RANS)** | 8.56 |
| **(LES-3rd RIB)** | **12.05** |
| **(LES-4th RIB)** | **13.91** |
| **(LES-entire channel)** | **12.2412** |

*Table 7.2 Pressure drop comparison between experimental and numerical*

The difference found between experimental and LES numerical result is less than 5 % which represents a rather encouraging validation.

### *7.4.2 Identification of structures around the ribs*

The flow around a rib is characterized by the presence of several recirculation zones and by an increase the turbulence level and, hence the heat transfer, by a factor 2-4 with respect to a smooth duct.

These separation zones (*figure 7.5*) are generated due to the adverse pressure gradients, caused by the high blockage of the ribs, which deforms and inverses the velocity profile in the boundary layer near the wall and separates the latter one and to create a recirculation bubble. The average streamlines in the symmetry plane (Z/h=0) clearly show the different structures of the separated regions: ($V_{big}$ $V_1$ ,$V_2$ ,$V_3$) and the (*Table 7.3*) gives the length of each bubble separation region: ($L_{big}$, $L_{v1}$, $L_{v2}$, $L_{v3}$).From the *figure 7.5* four different recirculation regions can be identified and are listed as follow:

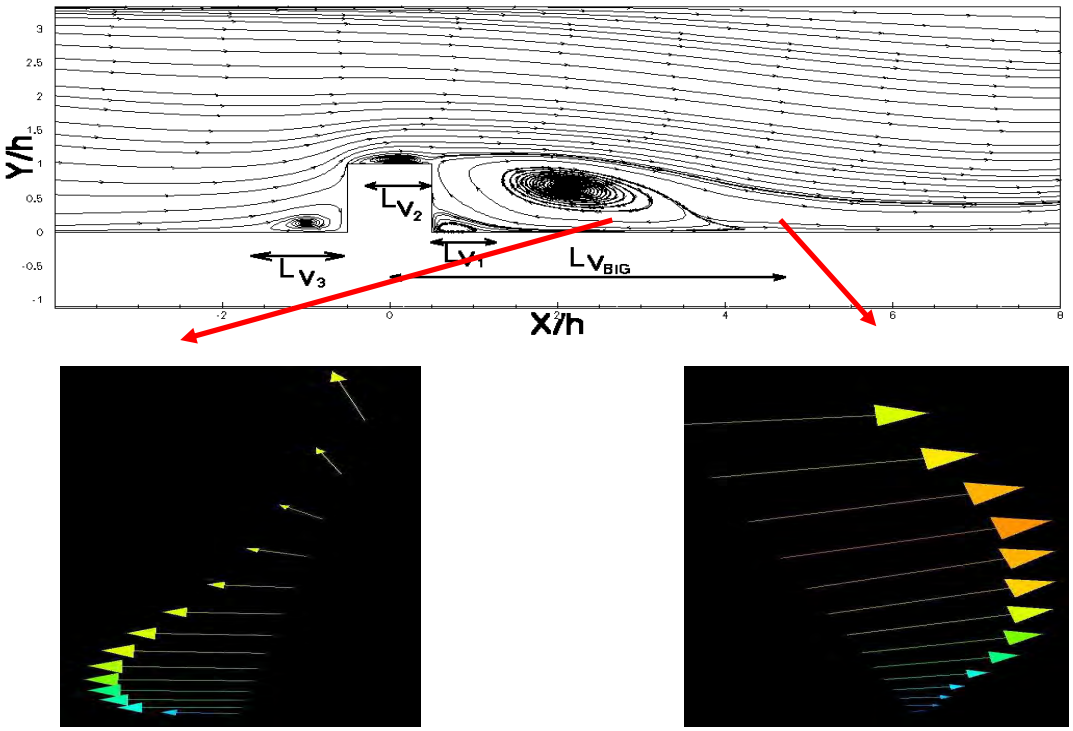


*Figure 7.5 Flow structures in the symmetrical plane 1XY (Z/h=0)*

● **The structure $V_{big}$ downstream the rib:**

The biggest recirculation zone or primary recirculation zone ($V_{big}$) is located downstream the rib. The physics within this region is similar to one behind a backward-facing-step and it is the most important one since it is responsible for the increase of the heat transfer in the ribbed channel.

● **The structure $V_1$ downstream the rib**:

Imbedded within structure $V_{big}$ is the counter-rotating corner vortex $V_1$. *Figure 7.6* presents the streamlines for this region, for the three available **XY** planes. It can be remarked that the recirculation zones produced by the calculation are larger than ones deduced from the PIV data.

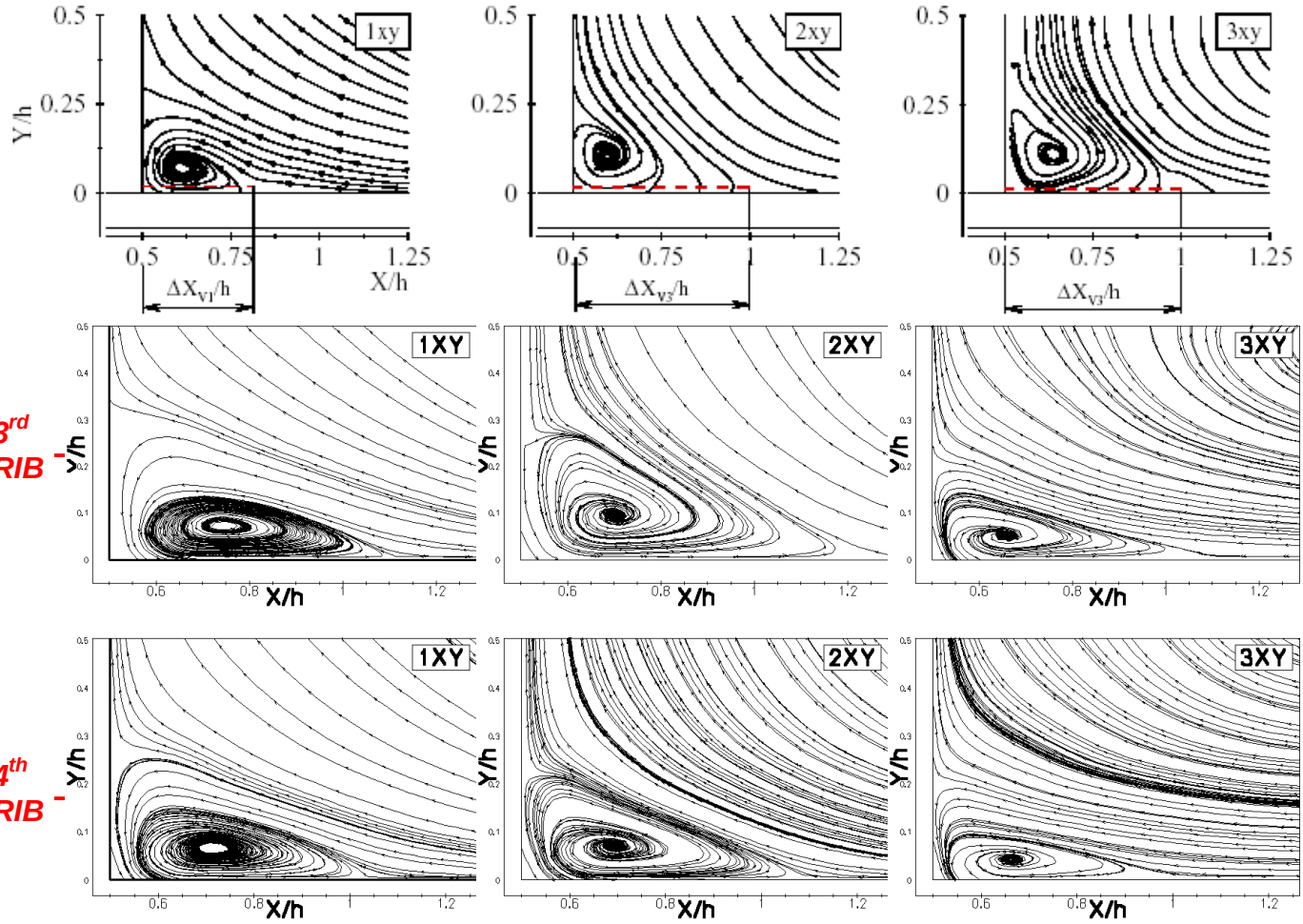


*Figure 7.6. Comparison of the secondary recirculation downstream of the rib the rib*

- **The structure $V_2$ located over the top of the rib:**

Flow separates itself on the upstream corner of the rib creating the separate region $V_2$. *Figure 7.7* presents the streamlines for the region above the rib and for the three **XY** planes of reference. It can be remarked that the recirculation zones produced by the calculation are again larger than ones deduced from the PIV data.

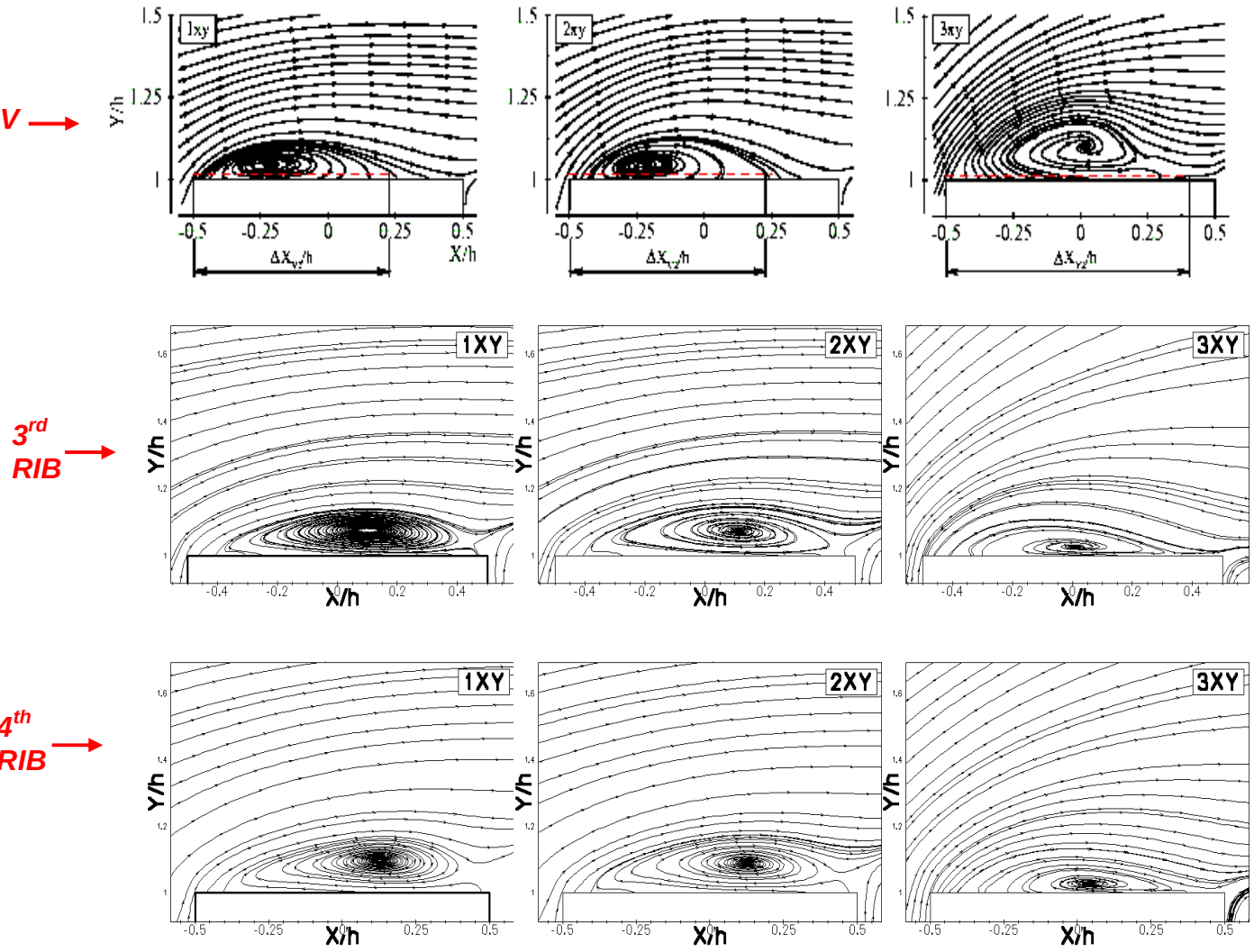


*Figure 7.7 Comparison of the separate zone on the top of the rib*

- **The structure $V_3$ upstream of the rib:**

The separated region upstream the rib, $V_3$ is presented in *figure 7.8*. It can be remarked that the size of this region is larger at **2XY** (Z/*h*=1) plane than in the at 1XY plane. This behaviour is caused by flow moving from the interior of the flow to the corner formed by the rib and the lateral wall, where is uplifted by the corner vortex.

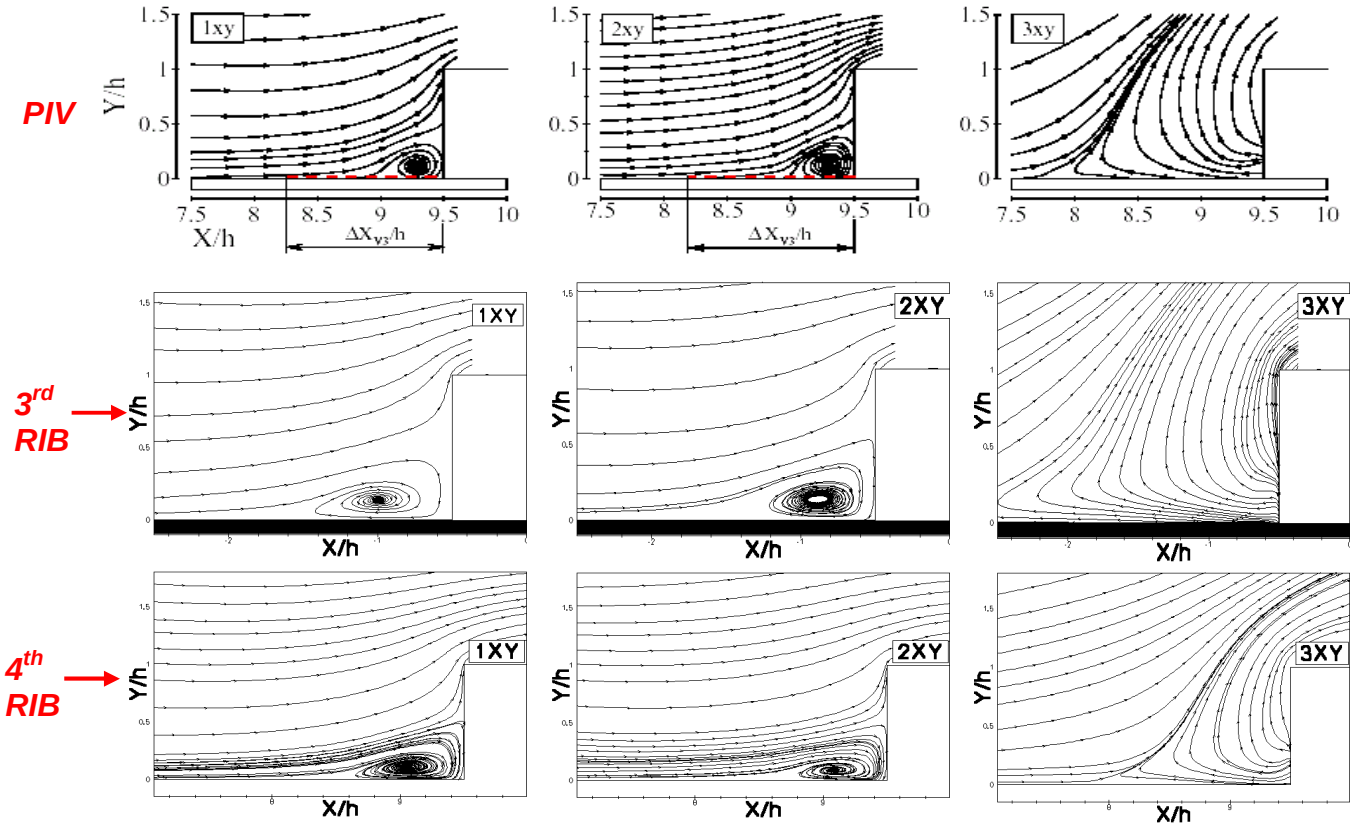


*Figure 7.8 Comparison of the separate region upstream the rib*

In all the cases, the topology of the flow, as deduced from the experimental data is reproduced.

● **Mean skin friction coefficient (details about the recirculation zones)**

**Definition**: In 3D, the friction (wall shear stress) is a two dimension vector which represents the force applied by the fluid on the surface:

$$\vec{\tau}_w = \mu\left(\frac{\partial U}{\partial y}\right)\vec{i} + \mu\left(\frac{\partial W}{\partial y}\right)\vec{j}$$

In 2D, the non dimensional mean skin friction coefficient in $C_f$ is defined as the ratio between the mean x-wall shear stress and the dynamic pressure:

$$C_f = \frac{\mu\left(\frac{\partial U}{\partial y}\right)}{\frac{1}{2}\rho U^2}$$

To obtain a quantity easy-to-plot and giving more details about the recirculation zones (**S**eparation and **R**eattachment points), $C_f$ is plotted in *figure 7.9* for the 3rd and 4th pitch. This figure shows the location of singular points where $C_f = 0$. The zones of negative values indicate the recirculation regions and the local minimum of $C_f$ correspond to the flow rolling up at the centre of the vortex.

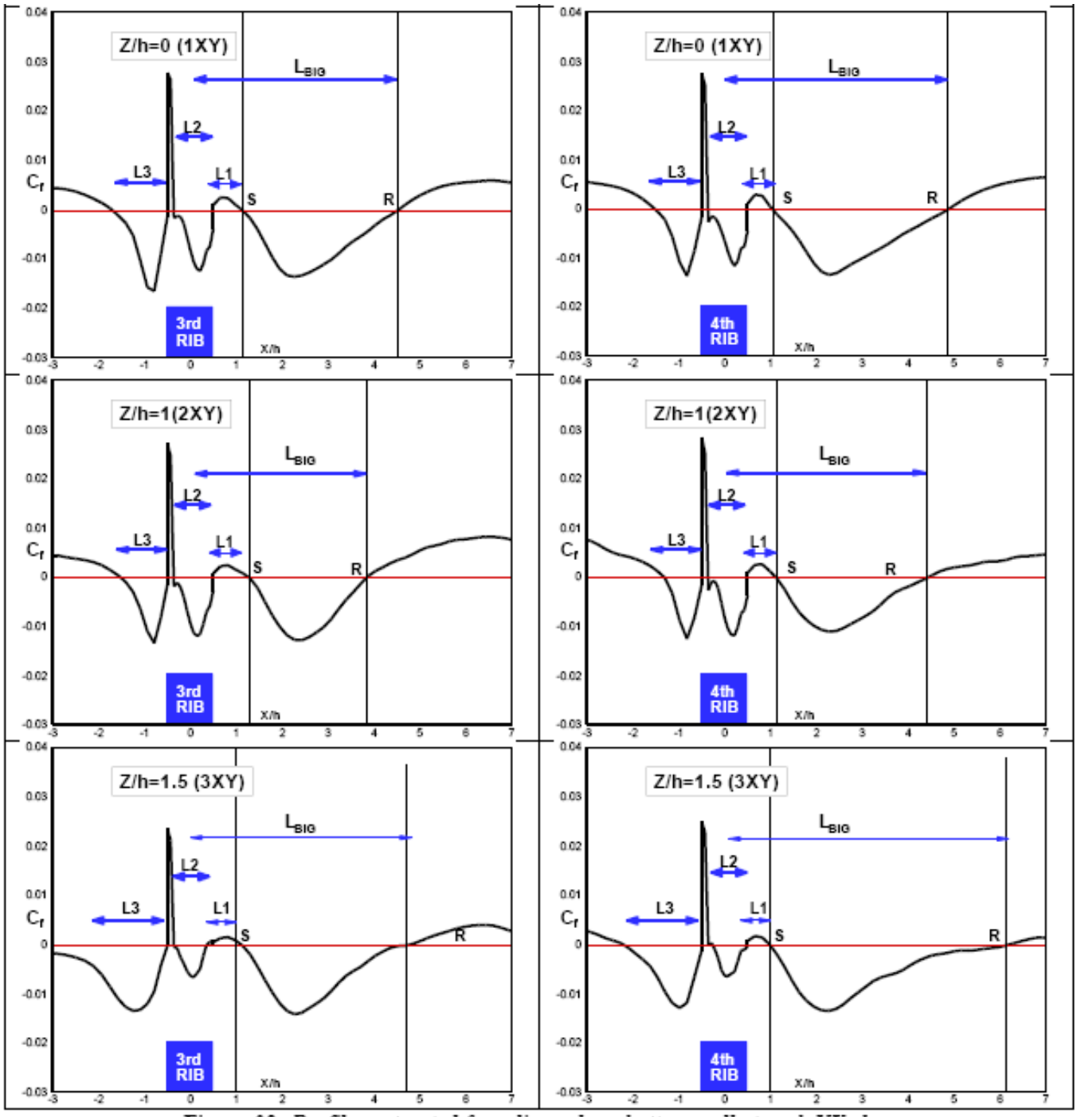


*Figure 7.9 Profiles extracted from lines along bottom wall at each XY plan*

From the information from *figure 7.9* the lengths of each separation zone for the 3 vertical planes can be grouped in the *table 7.3*. In the **3XY** plane (Z/h=1.5) RANS result was found unphysical (no reattachment over the bottom rib ) at was not reported.

| ***1XY(Z/h=0)*** | ***L big*** | ***L v1*** | ***L v2*** | ***L v3*** |
|---|---|---|---|---|
| ***PIV*** | 4.26h-4.34h | 0.255h-0.28h | 0.6h-0.9h | 1.04h-1.5h |
| ***RANS 3rd RIB*** | 4.76h | 1.3h | 0.5521h | 1.1274h |
| ***RANS 4th RIB*** | 4.825h | 1.3h | 0.5536h | 1.11h |
| ***LES 3rd RIB*** | 4.5h | 0.62h | 0.868h | 1.243h |
| ***LES 4th RIB*** | 4.85h | 0.55h | 0.872h | 1.02h |

| ***2XY(Z/h=1)*** | ***L big*** | ***L v1*** | ***L v2*** | ***L v3*** |
|---|---|---|---|---|
| ***PIV*** | 4.29h-4.36h | 0.18h-0.47h | 0.65h-0.9h | 1.51h-2.1 |
| ***RANS 3rd RIB*** | 6.85h | 0.625h | 0.65h | 1.35h |
| ***RANS 4th RIB*** | 7h | 0.635h | 0.7h | 1.3h |
| ***LES 3rd RIB*** | 3.822h | 0.8h | 0.872h | 1.02h |
| ***LES 4th RIB*** | 4.38h | 0.7h | 0.872h | 0.82h |

| ***3XY(Z/h=1.5)*** | ***L big*** | ***L v1*** | ***L v2*** | ***L v3*** |
|---|---|---|---|---|
| ***PIV*** | 4.54h-4.62h | 0.22h-0.44h | 0.7h-0.97h | N.A |
| ***RANS 3rd RIB*** | N.A | N.A | N.A | N.A |
| ***RANS 4th RIB*** | N.A | N.A | N.A | N.A |
| ***LES 3rd RIB*** | 4.65h | 0.63h | 0.707h | N.A |
| ***LES 4th RIB*** | 5.1h | 0.467h | 0.7587h | 1.7h |

*Table 7.3 Length of the recirculation zones in the 3 different vertical plane*

Concerning plane **1XY**, it can be remarked that the results of the simulation fall within the uncertainty of the PIV measurements, with the exception of the length ***L v1*** which is

overestimated. It can be noted that the results for the ribs 3rd and 4th are very near each to other, leading to assume that flow is reaching the stationary state.
The picture is different for **2XY** plane, where the values for $L_{big}$ and $L_{v3}$ are different by an important amount, even if the most important discrepancy with the experiment remains the one for $L_{v1}$. This result leads to suspect a different development of the exchange of momentum between longitudinal and span-wise direction.
The experimental results for **3XY** plane are incomplete, due to the difficulty to measure close to the side wall, but similar trends can be detected.

The wall treatment turbulence model, the refinement of the grid and the generation of the synthetic turbulence at the inlet might be the reasons for inaccurately predicted reattachment point. However, the present results represent a clear improvement with respect to RANS and, in most cases, within the uncertainty of the experimental data.

## *7.5 Flow field in XY planes*

### *7.5.0 Effect of ribs*

To conclude, the ribs introduce in the smooth duct increase the friction (pressure drop). The presence of these ribs develops a complicated flow structure characterized by the presence of repeated separation zones. It also reduces the free cross section of the flow passage causing the flow accelerates above these obstacles.
This behavior will first be studied focusing on the **XY** planes.
Results for all the 3 available planes (*figure 7.1*) have been processed, but, to avoid a too heavy text, only the full symmetry plane (**1XY**) will discussed in the main text. Selected results for the other 2 planes will be presented where needed to complete the understanding of the flow field. The main behavior of the flow in the (**2XY**) plane was found similar to the one in the symmetry one (**1XY**), while the results of the further plane (**3XY**) are perturbed by the presence of the wall. Maps of the different quantities were presented in the following figures together with the corresponding PIV result.

### *7.5.1 Results in the channel symmetry plane 1XY(Z/h)=0*

#### A- Time averaged stream-wise-velocity (<U>)

The mean streamwise velocity component *<U>* in the symmetry plane is reported in *figure 7.10*. Only contours around the 3rd and 4th rib are compared to experimental results because it is expected that the flow becomes developed after the 3rd rib-pitch. In matter of fact the contours of *<U>* field around both the 3rd and 4th rib in the numerical results match well the PIV experiences. Examining the flow field three different regions can be clearly distinguished:

● High velocity region (red): the high velocity region over the rib, where the mean stream-wise velocity accelerates and reaches values which are practically twice the inlet bulk velocity. This is due to the section reduction.
● Medium velocity region (green): This region in the center of the duct represents values of velocity near to the inlet bulk velocity.
● Low velocity region (blue): The blue region downstream the ribs corresponds to the main recirculation zone (***big)*** where the mean stream-wise velocity has negative values. The three other smaller separated (*figure 7.5*) regions can be also observed.

## PLANE 1XY

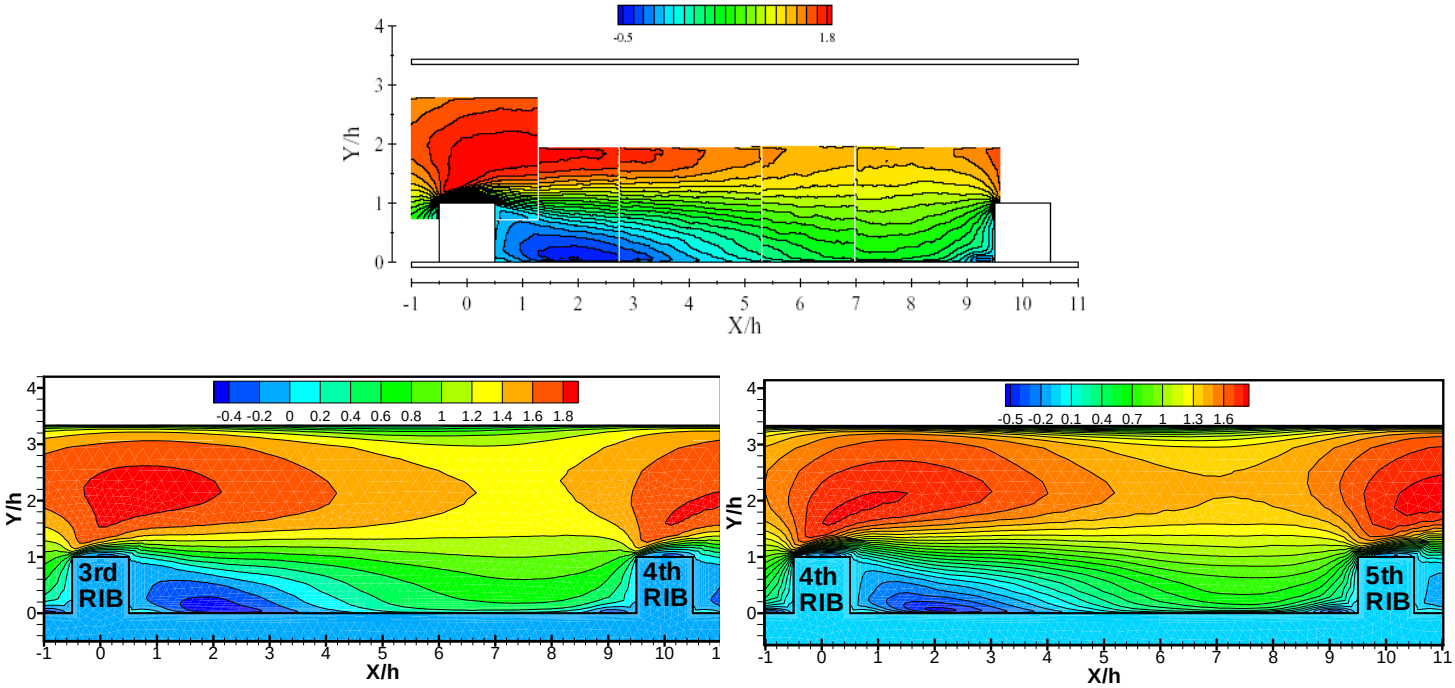


*Figure 7.10 Contours of mean <U>/$U_b$ in the plane 1XY*

A more detailed comparison can be performed by the examination of the profiles of the mean stream-wise velocity (*figure 7.11*) extracted from the fluid domain at different locations (from X/h=-2 to X/*h*=+7). It can be remarked the presence of regions of negative <***U***>, which correspond to the recirculation zones. The maximum of the negative velocities reaches a magnitude in the order of half the inlet bulk velocity (~0.5 $U_b$) at X/*h*=+2. The highest positive values are located in the upper part of the channel with a value near to 1.9 $U_b$ *at X/h=0, +0.25 and +1*. On the ribbed wall the boundary layer redevelops downstream of the reattachment point 4<X/*h*<5, (no more negative values). However, an inflection point exists in the profiles after X/*h*=+5, which indicates that the redeveloping boundary layer is not stable. Actually, this can be due to the presence of big structures which had not been yet dissipated themselves. The numerical results show a satisfactory agreement with the PIV measurement. The single important difference is found in the wall region on the top of the rib, (region around X/h=0): the measurements do not show the presence of a recirculation bubble at this

location (no negative values) while the numerical results at the same locations show negative values of the velocity near the wall. At the beginning it was we thought that the wall condition for the wall treatment was not appropriate, but after further examination of the data it was concluded that this difference may be due to the fact that the PIV measurements on the top of the rib are probably inaccurate as will be shown in the next section.

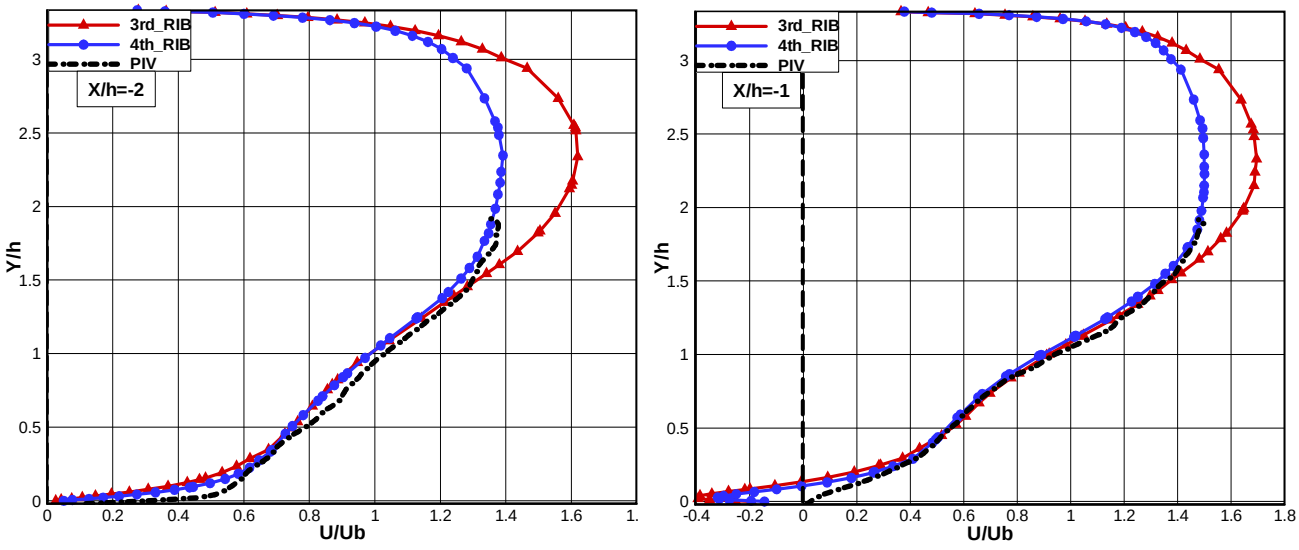


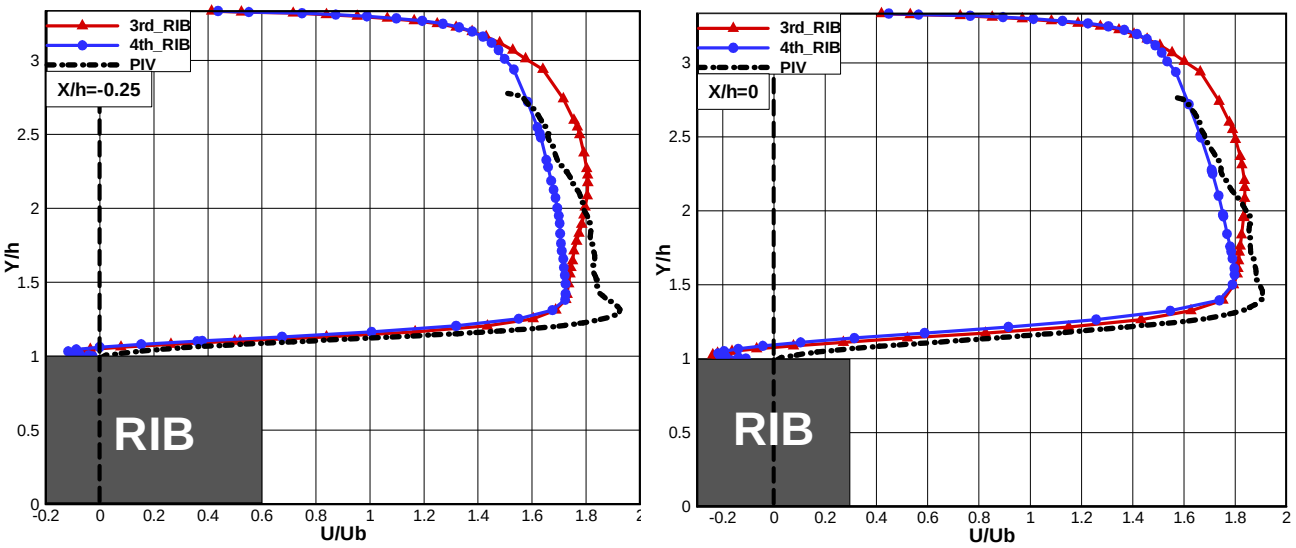


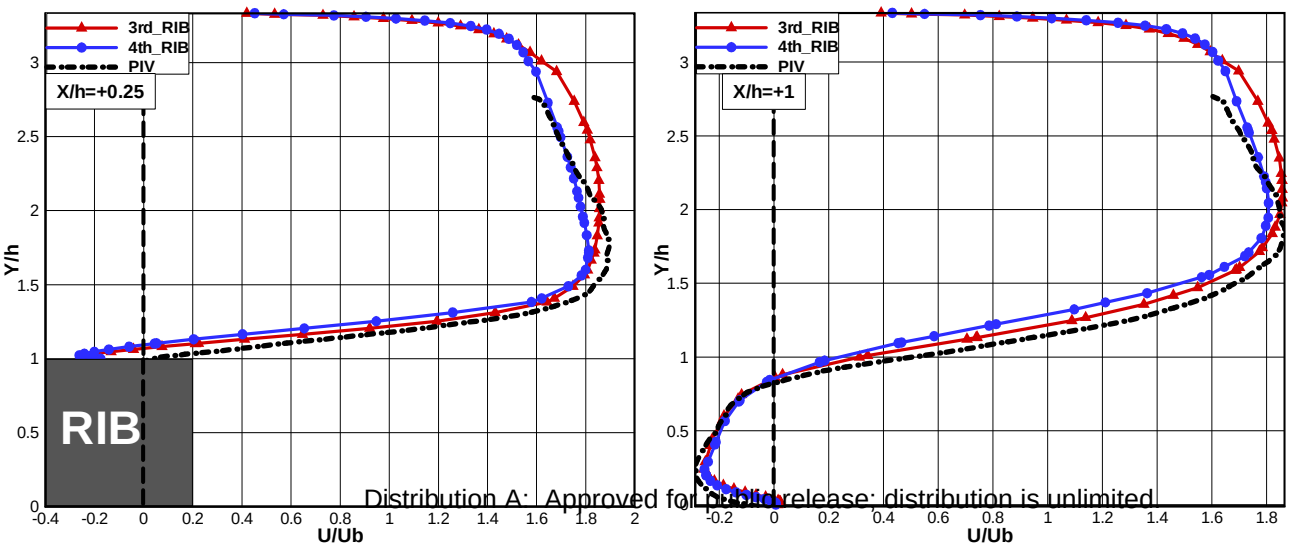

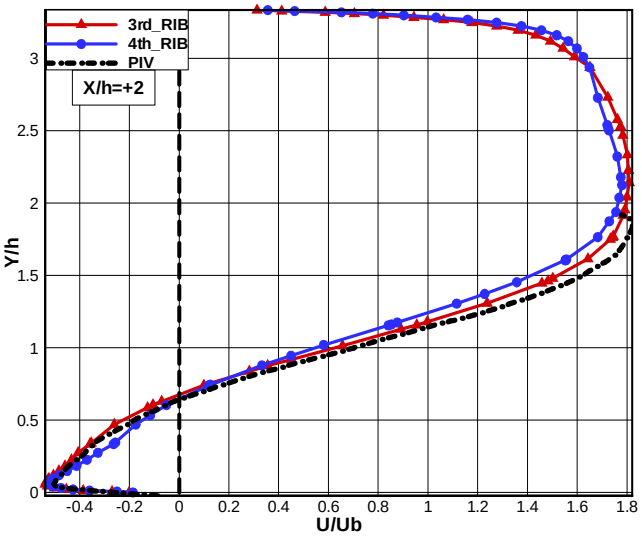


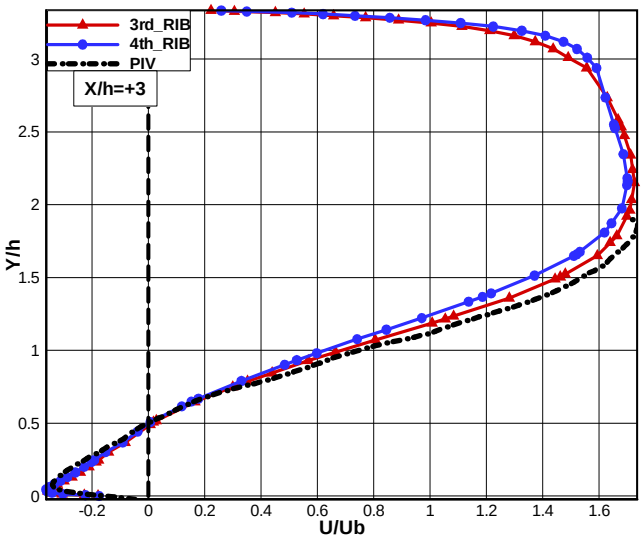


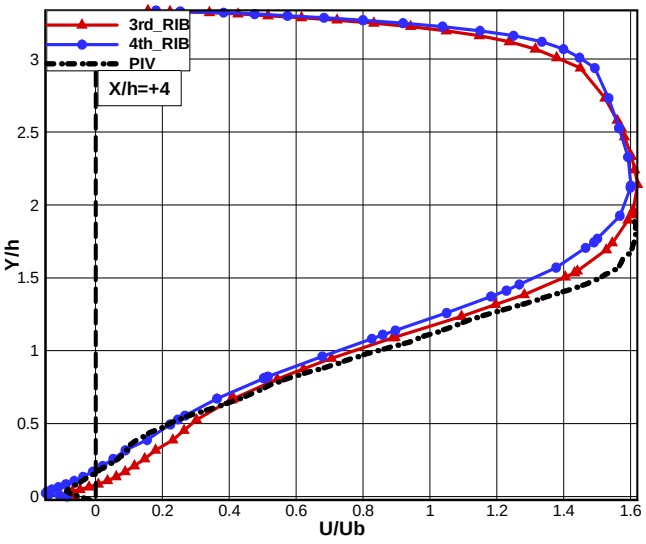


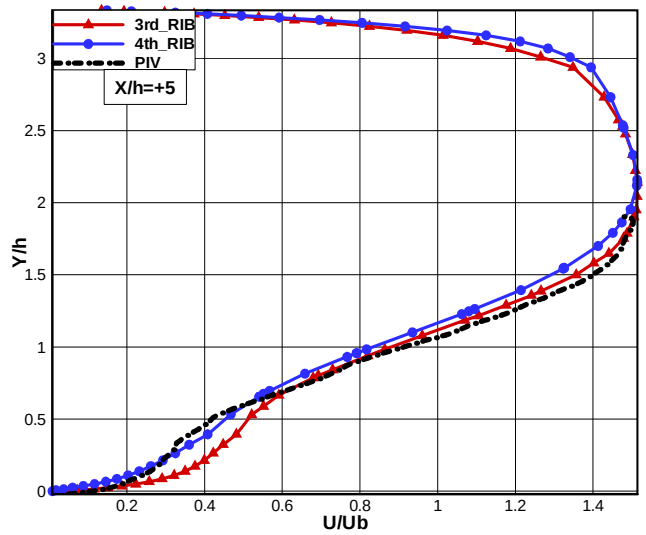


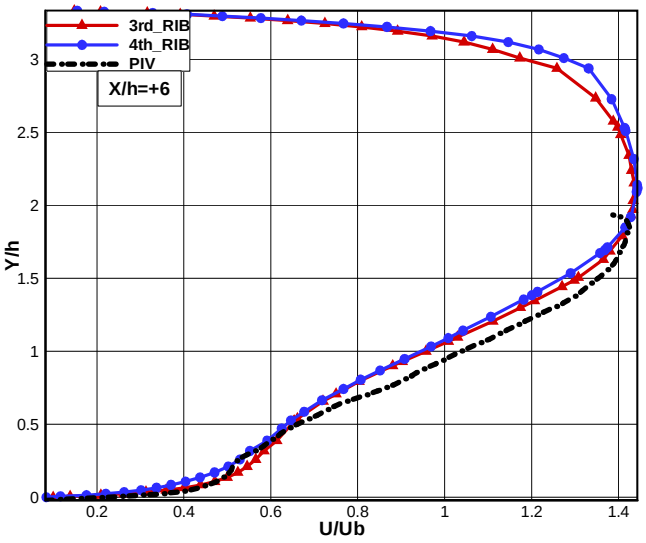


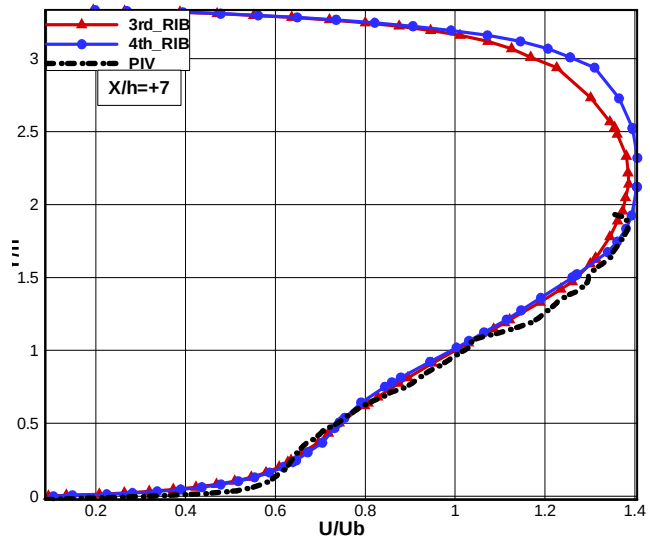

*Figure 7.11 Mean streamwise velocity in 1XY extracted from every vertical line*

Considering the spatial development of the simulated flow, it can remarked that the main difference between the 2 profiles is found in the core flow upstream of the rib ( locations X/*h*=-2, -1) which would be consistent with the hypothesis that the flow will stabilizes itself at the 4$^{th}$ pitch length.

**B- Time averaged normal-velocity (<*V*>)**

The contours of the mean vertical velocity component <V> are shown in the *figure 7.12*. Two different regions are distinguished:

● On the leading edge corner of the rib, <V> accelerates and can reach positive values of a magnitude similar to the bulk inlet velocity $U_b$.

● A large region of negative <V> values is found downstream the ribs, as it could be also observed by the streamstraces shown in the *figure 7.5*. The velocity profiles in (*fig.7.13*) indicate positive values of <V> near the wall and negative ones close to the entire upper side of the ribbed duct. One can see a notable difference between the results of the 3$^{rd}$ and 4$^{th}$ rib, which is more important upstream of the rib. This observation would be is consistent with the previous observation that only the results obtained in the 4$^{th}$ pitch are representative of the established state, even if it could be due to the short computational domain and the fact the mean normal velocity might need a longer length to become developed and periodic. In general, the agreement between experiment and simulation is worse than found for <U>. On the top of the wall (region around X/*h*=0) the experiments show a negative values near the rib bottom wall while the numerical results show positive ones. This difference is also seen in the streamstraces in YZ plane (vertical plane at X/h=0. See section 7.6.1) and it is due to the fact that the position of the centre of the recirculation bubble is different for numerical and PIV results. The maxima positive values near the wall on the top of the ribs are over predicted in numerical solutions. These maximum values are located near the leading edge corner and their magnitude is in the order of half the bulk velocity at X/*h*=-0.25. The positive values decrease downstream the ribs until they disappear at X/*h*=+3. Negative values are found downstream the big recirculation region and the maximum negative values can reach 0.25 the bulk velocity. It can be again remarked that the agreement is better downstream of the rib, consistent with the present interpretation of the development of the mean flow.

# <V> (1XY) Z/h=0

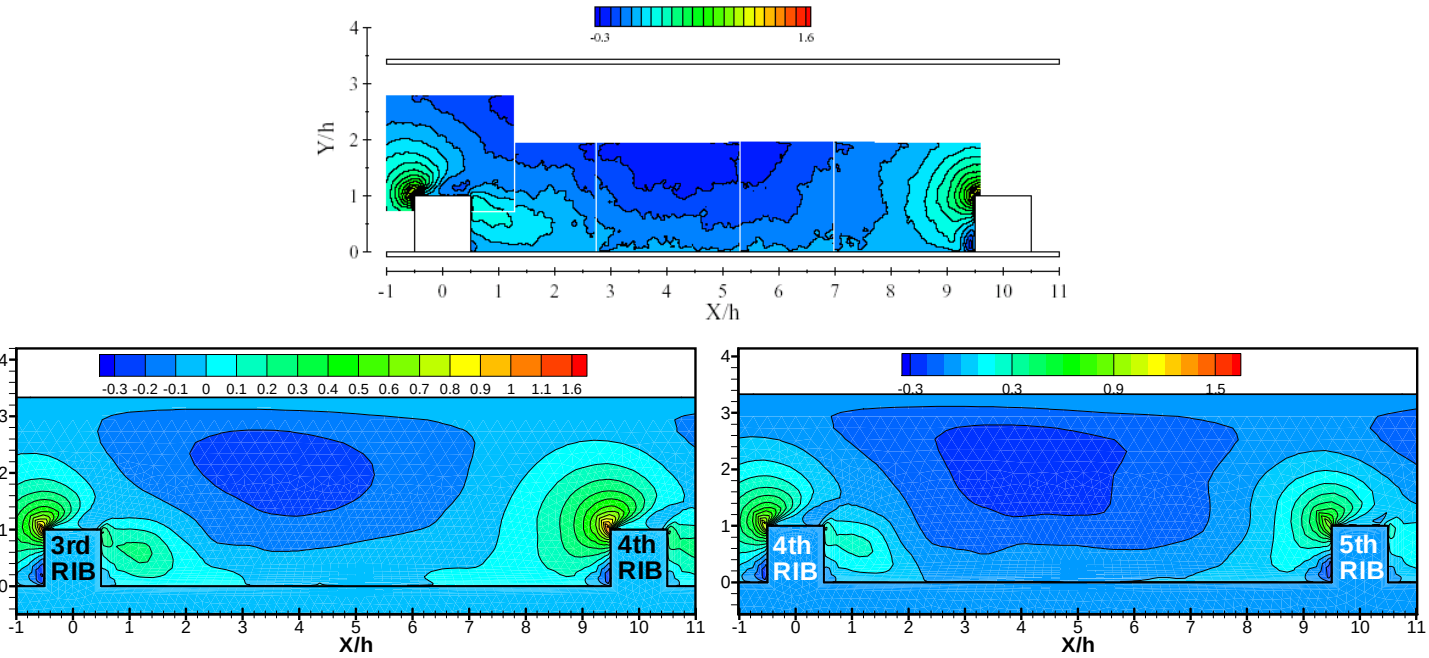


*Figure 7.12 Contours of mean <V >/$U_b$ in the plane 1XY*

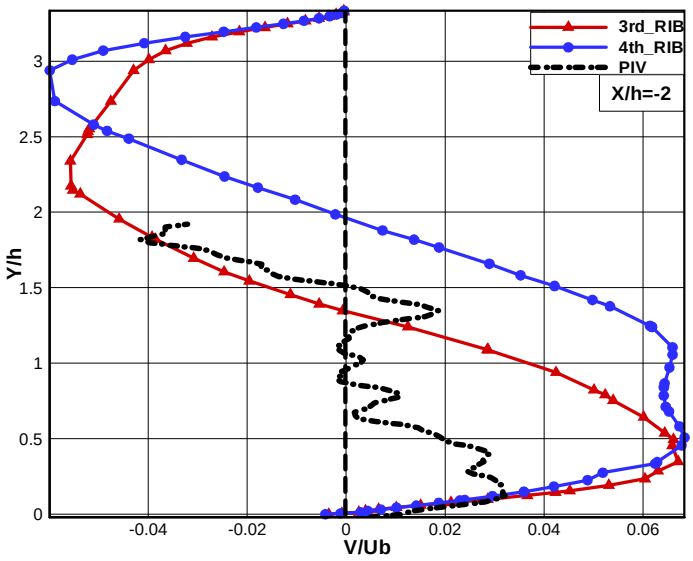
3rd_RIB
4th_RIB
PIV
X/h=-2
Y/h
V/Ub

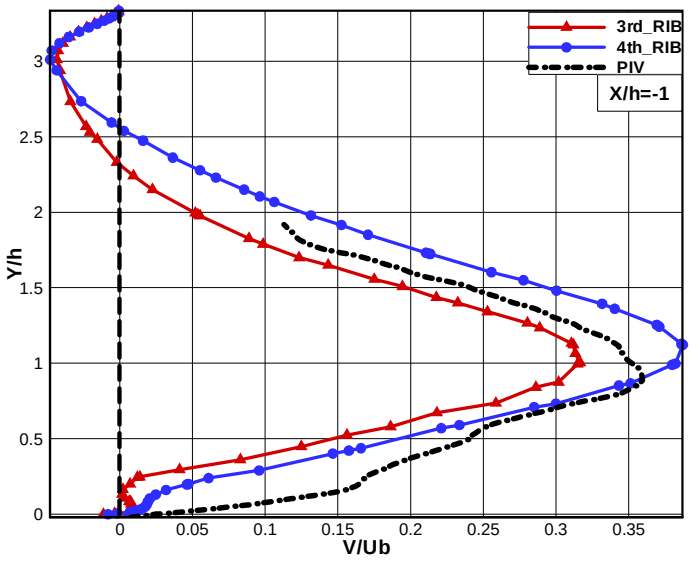
3rd_RIB
4th_RIB
PIV
X/h=-1
Y/h
V/Ub

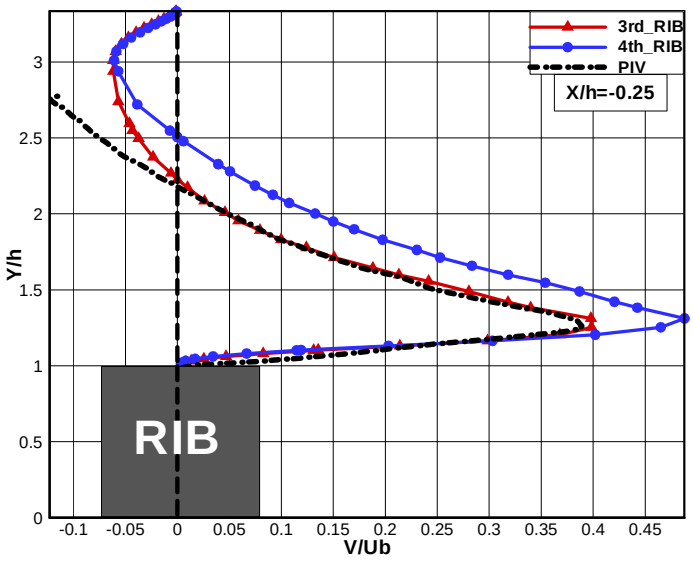
3rd_RIB
4th_RIB
PIV
X/h=-0.25
RIB
Y/h
V/Ub

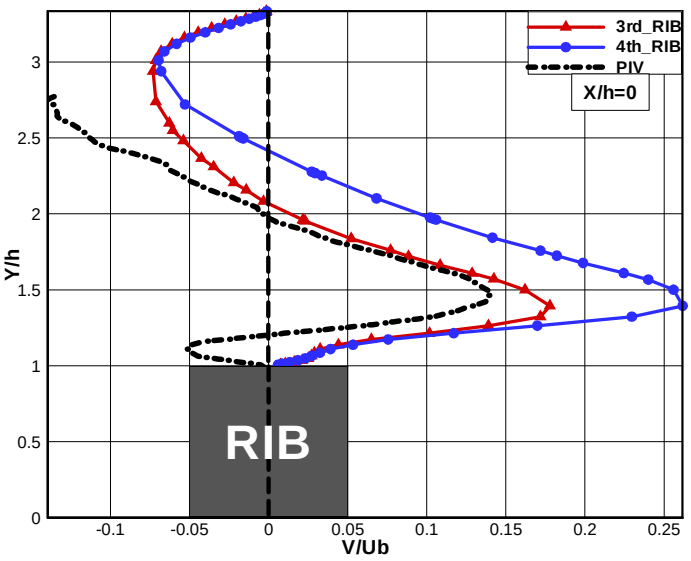
3rd_RIB
4th_RIB
PIV
X/h=0
RIB
Y/h
V/Ub

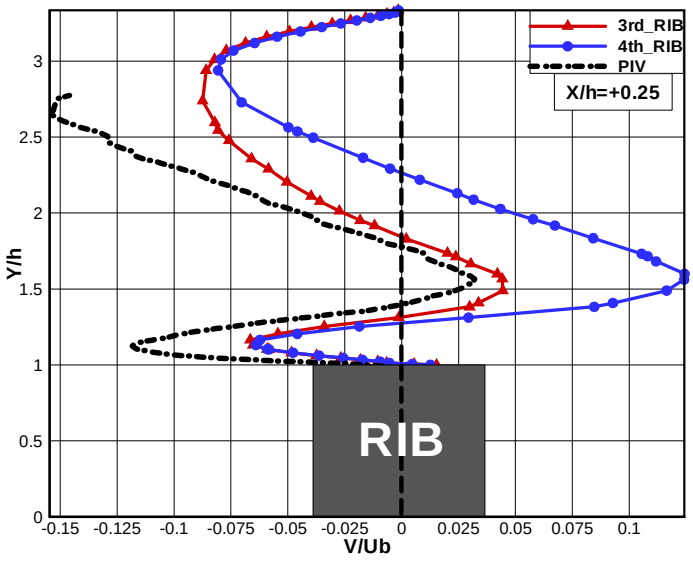
3rd_RIB
4th_RIB
PIV
X/h=+0.25
RIB
Y/h
V/Ub

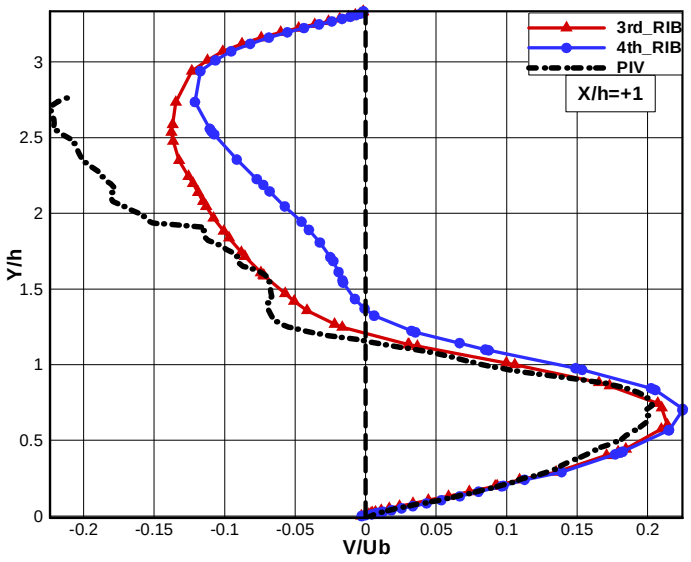
3rd_RIB
4th_RIB
PIV
X/h=+1
Y/h
V/Ub

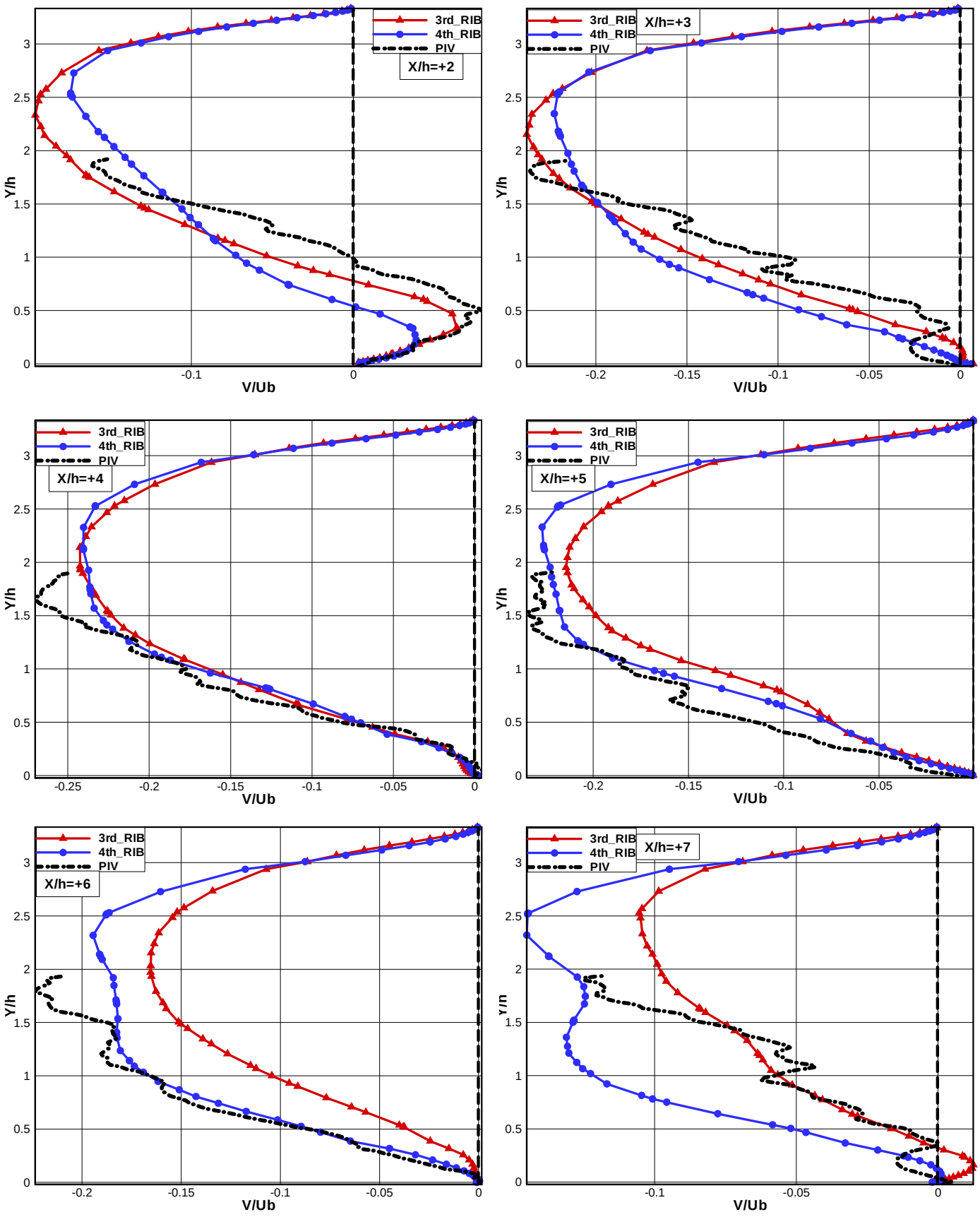

*Figure 7.13 Mean normal velocity <V> in 1XY extracted from every vertical line*

**C- Stream-wise normal stress (<u'u'>)**

The best way to evaluate the intensity of a turbulent flow is to measure its turbulent fluctuations. In the present analysis, the stream-wise normal stress<u'u'>, (variance of the stream-wise velocity) is normalized with $U_b^2$. This variance can also be regarded as the squared turbulent streamwise intensity $I_x^2$.
The distribution of <u'u'> is presented in *figure 7.14*, while the corresponding profiles are presented in *figure 7.15*.
In *Figure 7.14*, it is evident the region of high <u'u'> downstream of the separation on the upstream corner of the rib. In the simulation, the shape and intensity of this region is similar of the one put in evidence by PIV.
*Figure 7.15* shows again an important differences at location X/*h*=-2 between the 2 numerical profiles and the experimental one (although the irregularity of the experimental profile rises doubts on this accuracy). Over the rib itself, there is a good agreement between the 2 numerical profiles, due to the fact that turbulence is locally created downstream of the corner separation and is independent of the upstream history. The maximum of turbulent intensity is well predicted for location, but the value is underestimated. This effect can be associated with the imprecision of the wall model.
Good agreement is found between numerical profiles and with the experimental one. This result is due the good resolution of the grid and the good simulation of the turbulence above the rib. The agreement becomes gradually worse, probably due to the insufficiency of the wall model in the not-equilibrium boundary layer developing itself on the wall.

## <u'u'> (1 XY) Z/h=0

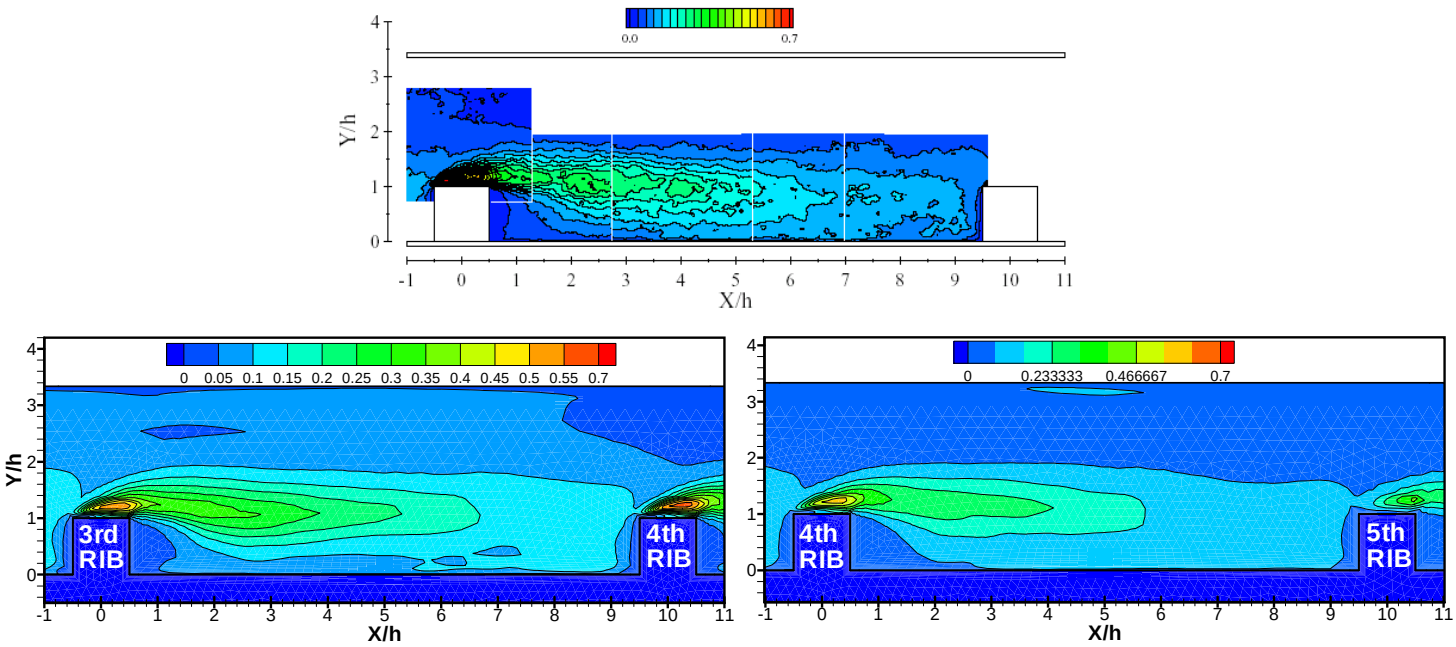


*Figure 7.14 Contours of mean< u'u'>/$U_b^2$ in the plane 1XY*

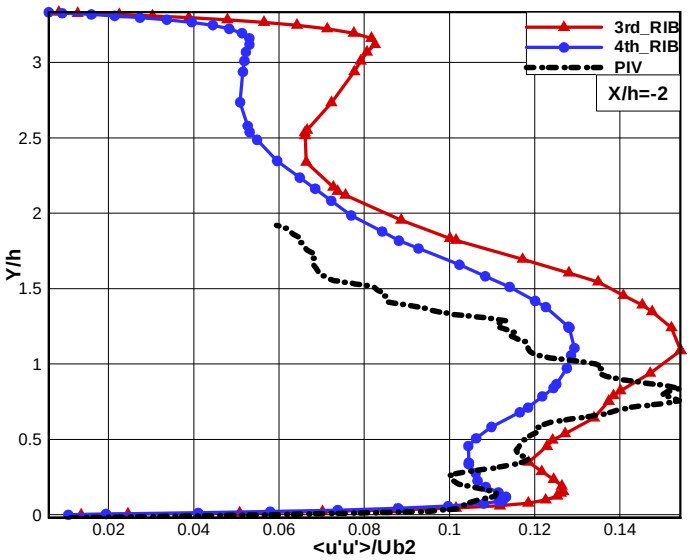


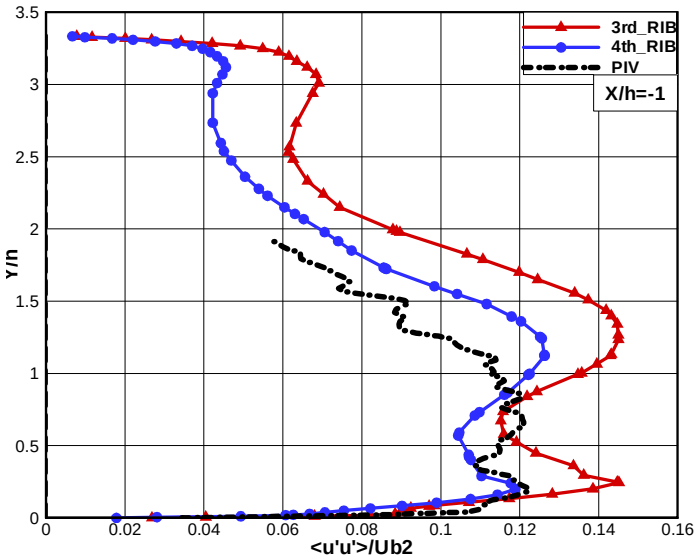


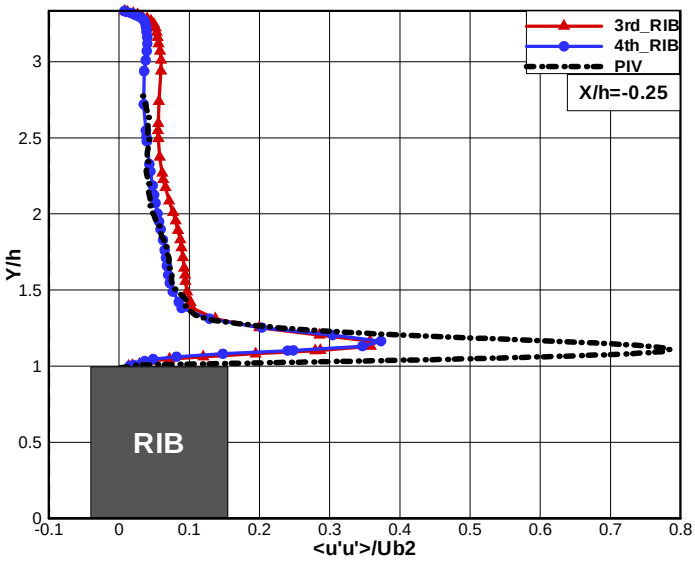


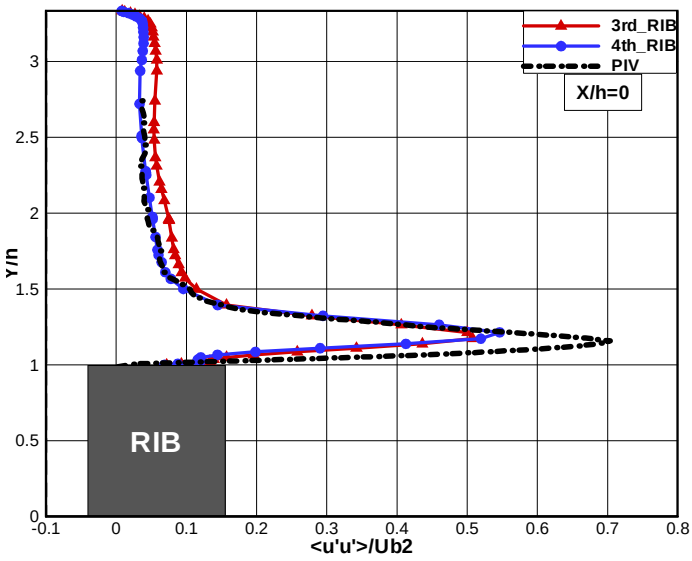


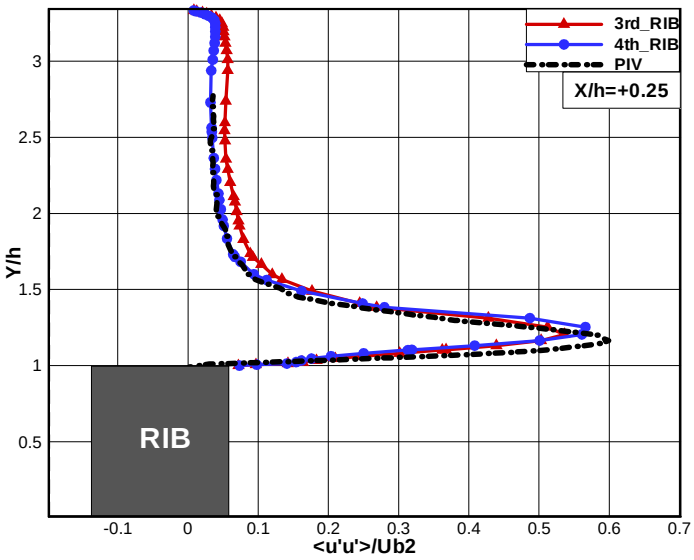


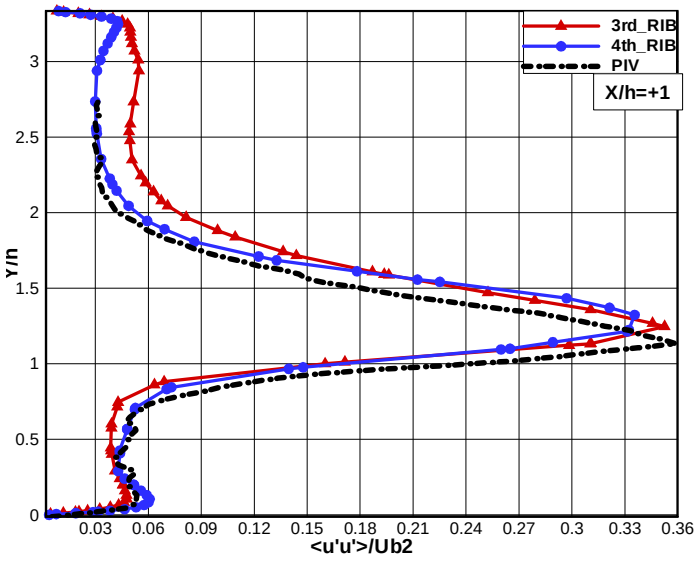

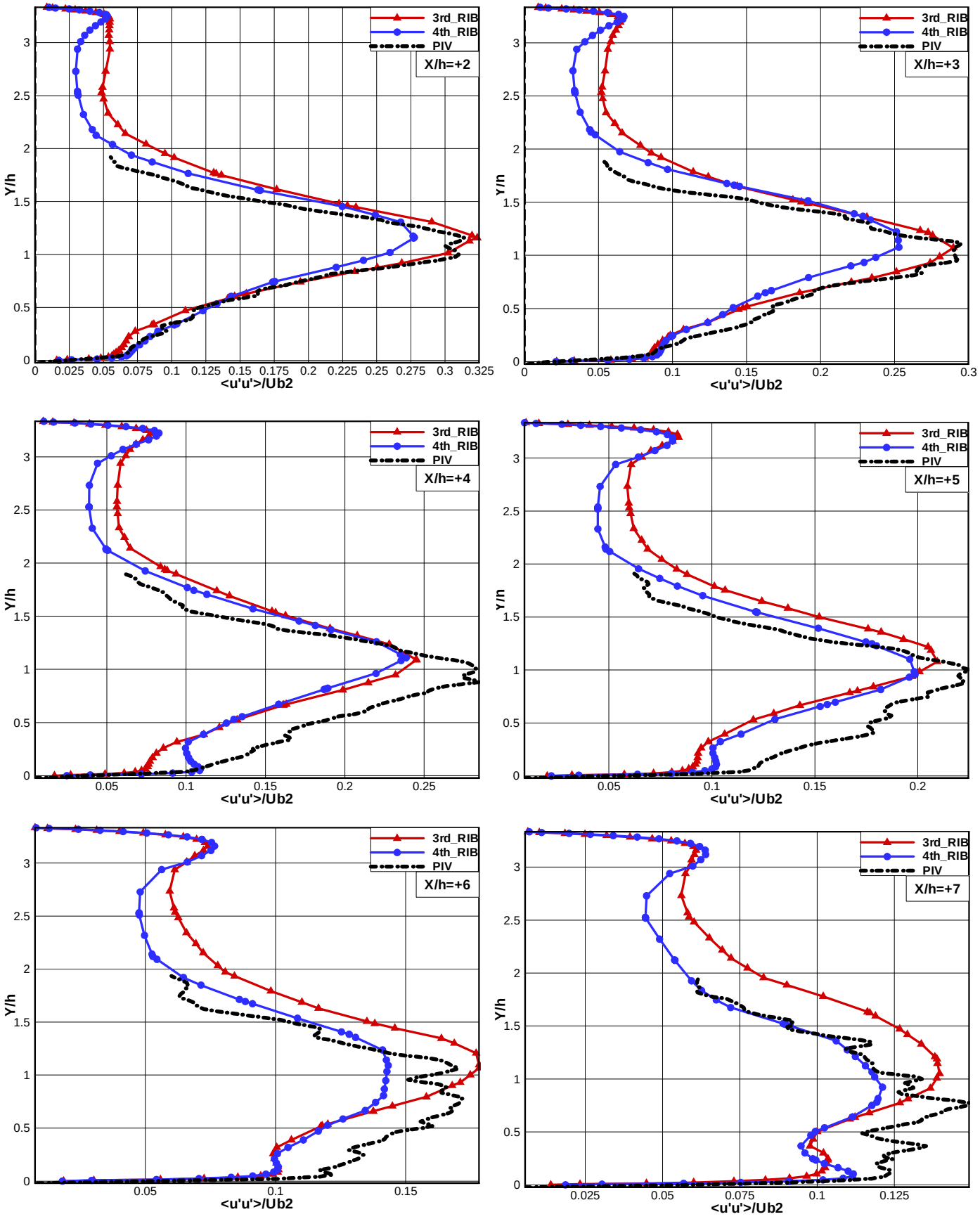

*Figure 7.15 Streamwise turbulent intensity < u'u'>/$U_b^2$ in 1XY plane.*

**D- Cross-stream normal stress (<v'v'>)**

The component of the resolved turbulence in the vertical direction <v'v'> (turbulent intensity in the normal direction $I_y$) is presented in *figures 7.16* and *7.17*. The iso-contours presented in *figure 7.17* show that the maximum values are found downstream of the rib and at distance from the bottom wall similar to the height of the rib itself. The process is that the flow hits the rib and is transported over it; turbulent stresses are created over the rib and transported in the wake region. The examination of the profiles (*figure 7.17*) shows acceptable agreement between the 2 numerical profiles, excepted at the X/*h* =7. Comparing with PIV result the trend is different of the one observed for <u'u'>: at locations X/*h*,=-1 and X/*h*,=-2, while, over the rib, the value of the maximum intensity is underestimated and its distance from the top of rib is not very well reproduced, even if that the noisiness of the PIV results makes the comparison difficult. It is visible that the current computation under predicts the magnitude of the peak over most of the domain.
The behavior rises the possibility that the present sub-grid model might be unable to fully reproduce the complex interchange between different components of the Reynolds stress tensor.

**<v'v'> (1XY) Z/h=0**

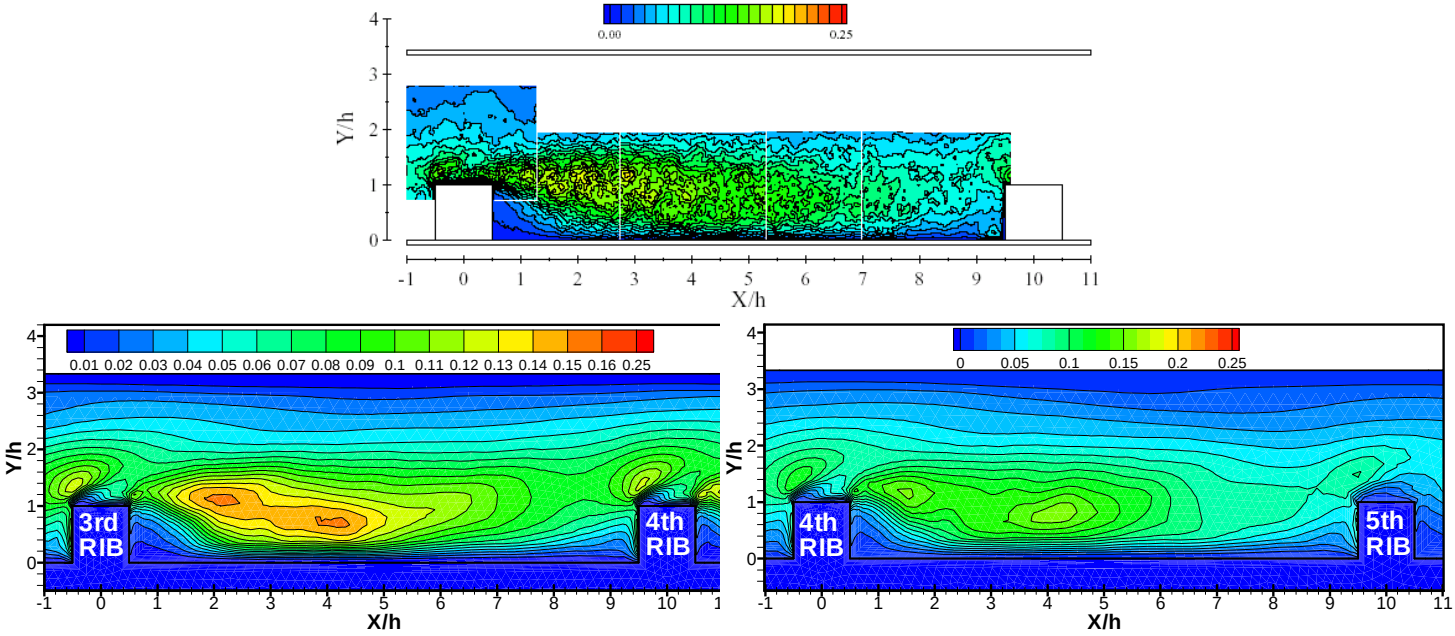


*Figure 7.16 Contours of mean <v'v'>/$U_b^2$ in the plane 1XY*

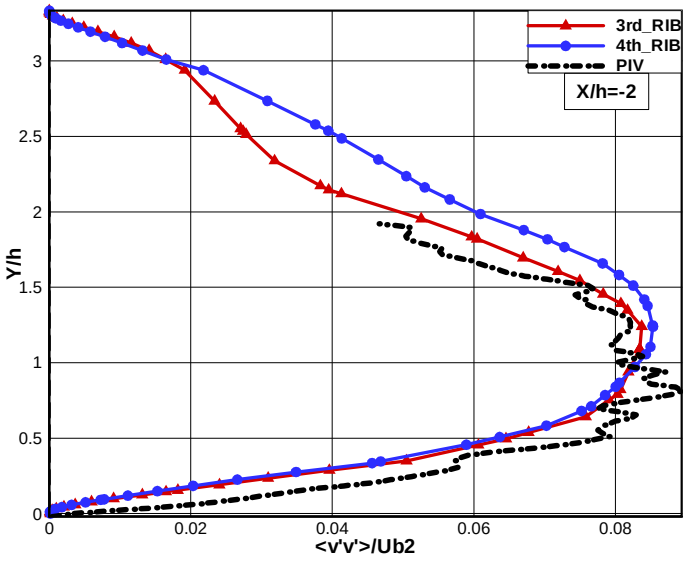


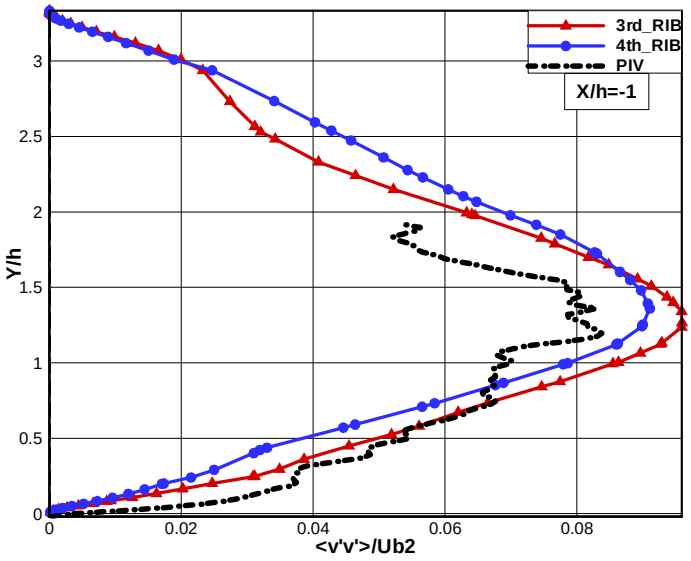


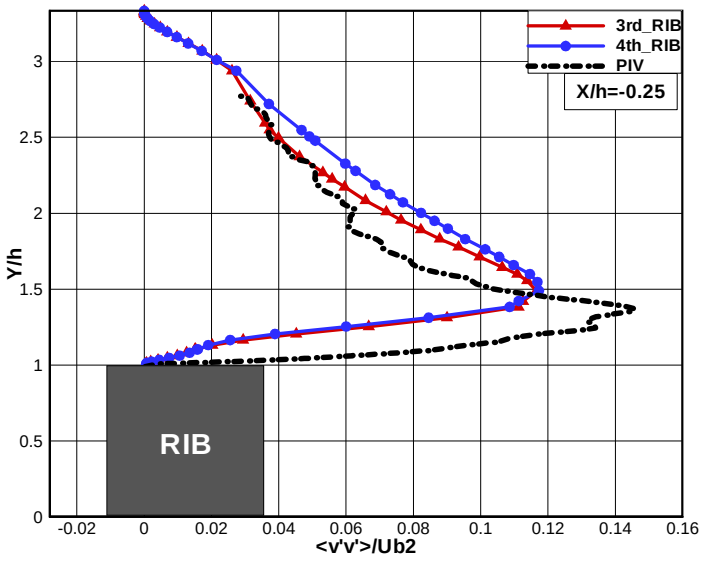


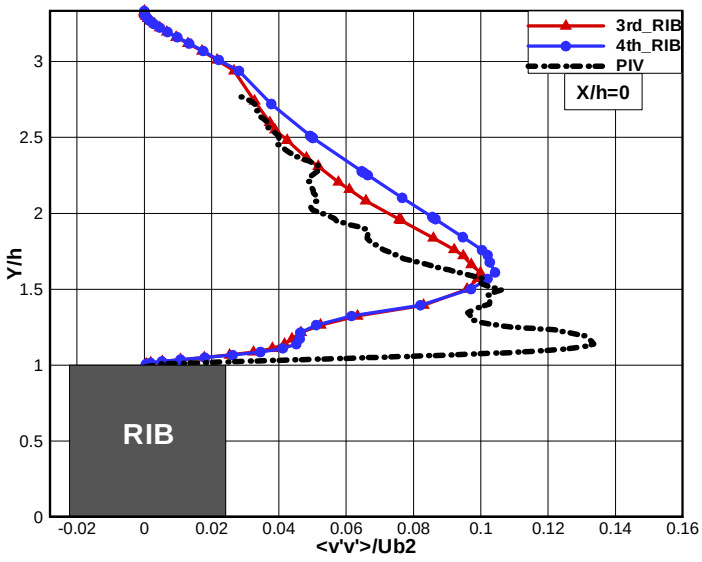


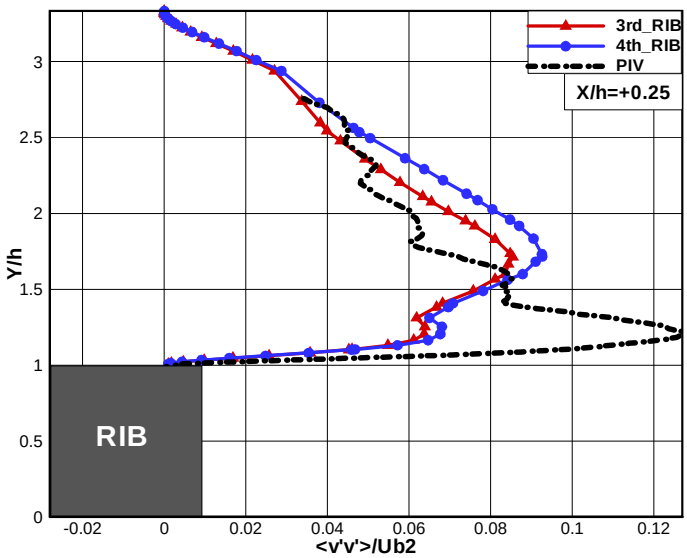


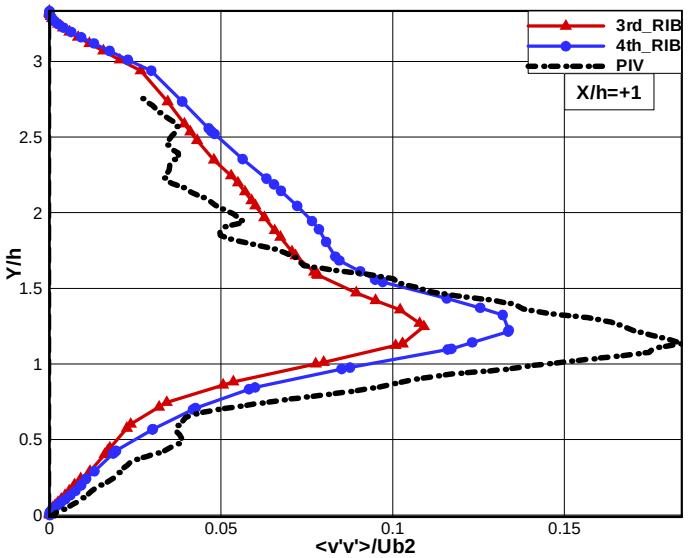

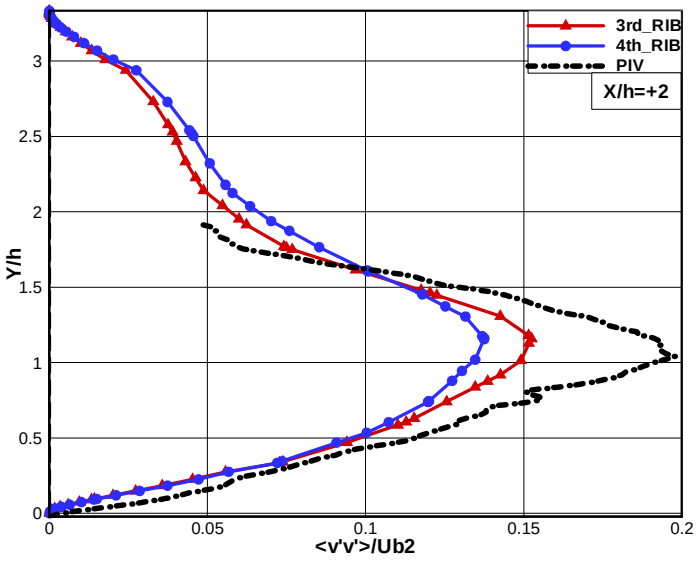


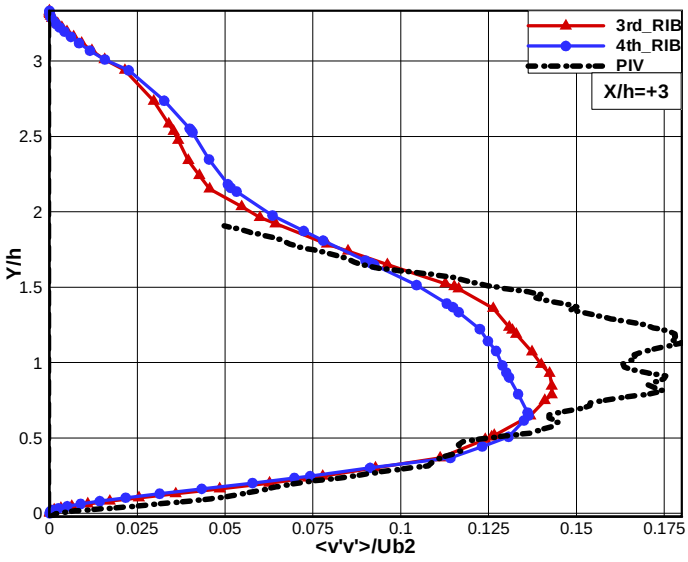


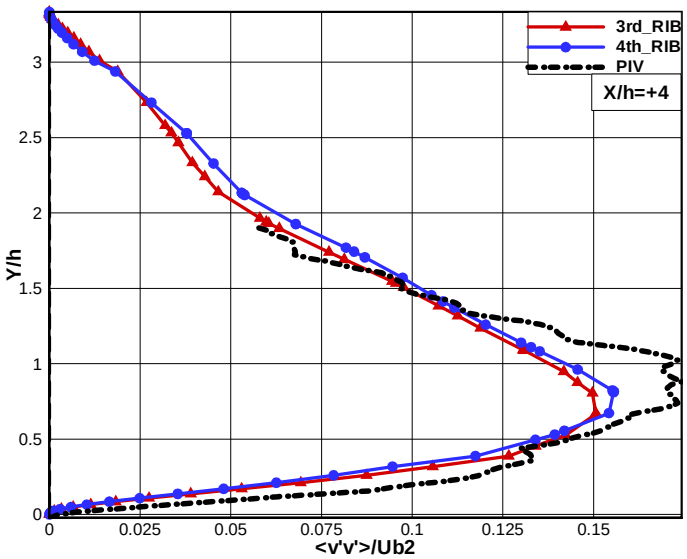


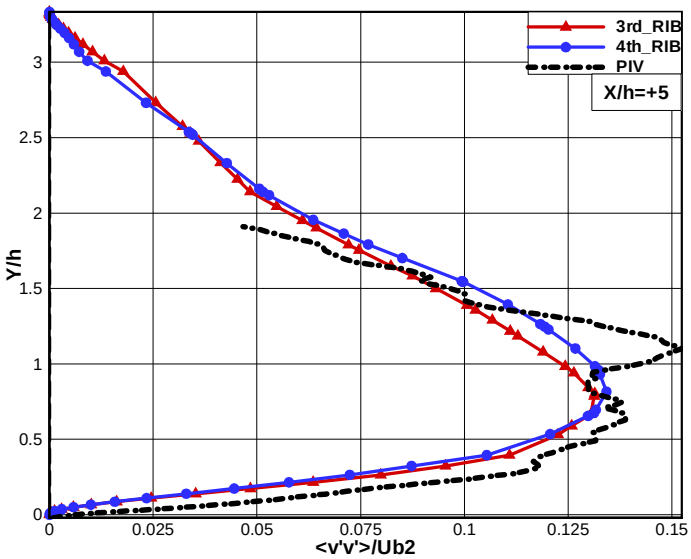


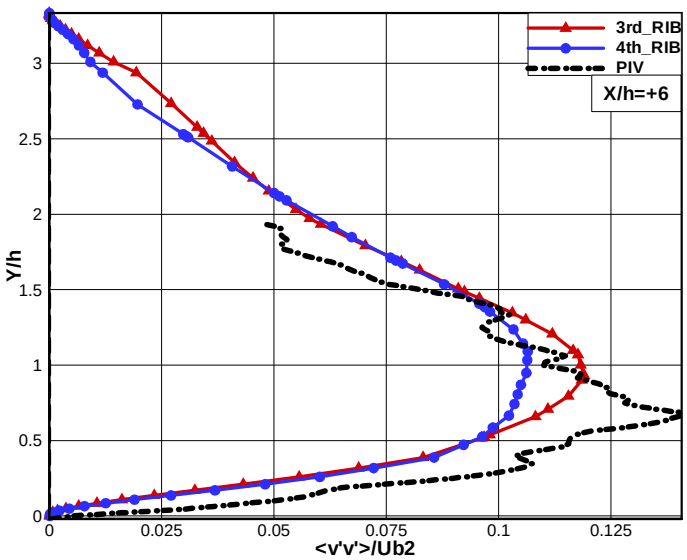


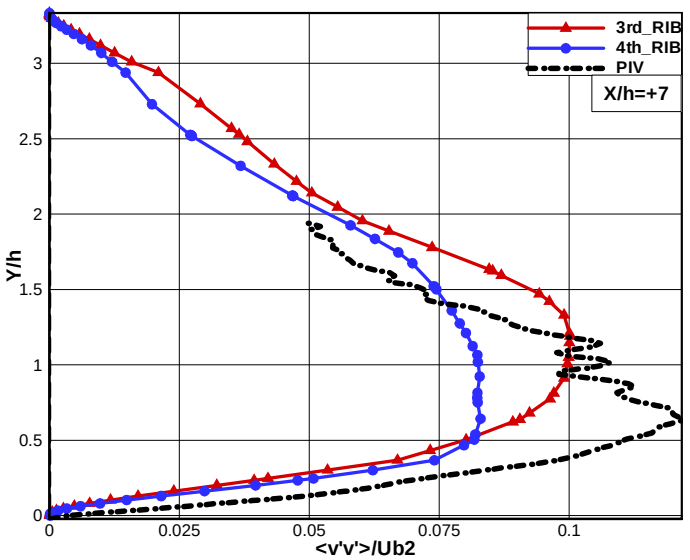

*Figure 7.17 Normal turbulent intensity <v'v'>/$U_b^2$ in 1XY plane.*

**F- Mean Shear stress- (<u'v'>)**

The isolines and the profiles for the shear stress <u'v'>, (mean covariance of the fluctuating velocity) are respectively presented in *figure 7.18* and *figure 7.19.* <u'v'> is a measure of the extent of correlation between $u'$ and $v'$ fluctuations and it also represents the most important component of the Reynolds stress in terms of its influence on the mean flow. It plays a fundamental role in the momentum transfer by turbulent motion (mixing layer) and also in the turbulent increase of the heat transfer. It is visible in *figure 7.19*: after passing over the obstacle, the flow separates downstream the rib and generates a strong shear layer. Maximum positive values are located at the leading edge of the rib while the maximum negative values are at the trailing edge of the latter one. In *figure 7.19* the numerical profiles show an acceptable agreement upstream of the rib, but from numerical results under predict the magnitude of the shear stress peak value on the top of the rib at X/*h*=0. Good agreement is found in correspondence with main downstream separation, but the agreement deteriorates once the non-equilibrium boundary layer redevelops itself on the bottom wall. These numerical results could be improved by refining the mesh in the boundary layer near the wall region.

**< u'v'> (1XY) Z/h=0**

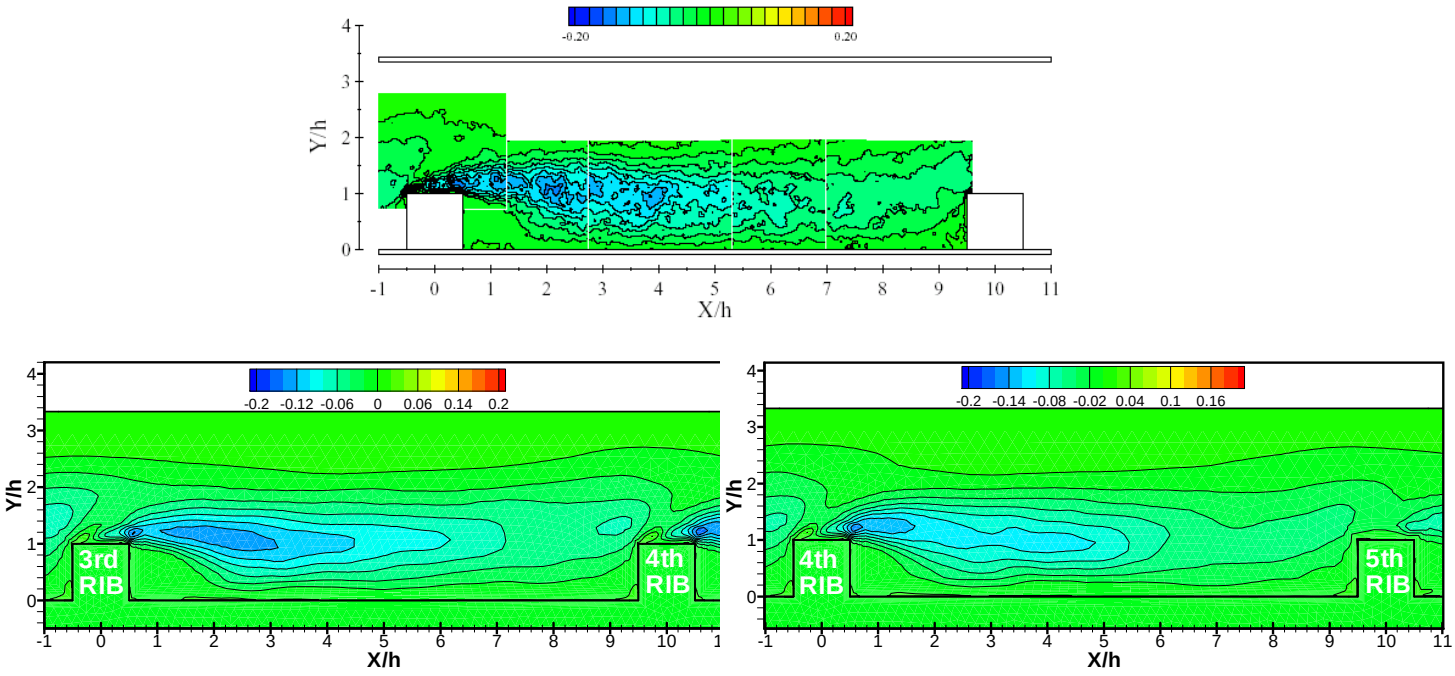


*Figure 7.18 Contours of mean < u'v'>/$U_b^2$ in the plane 1XY*

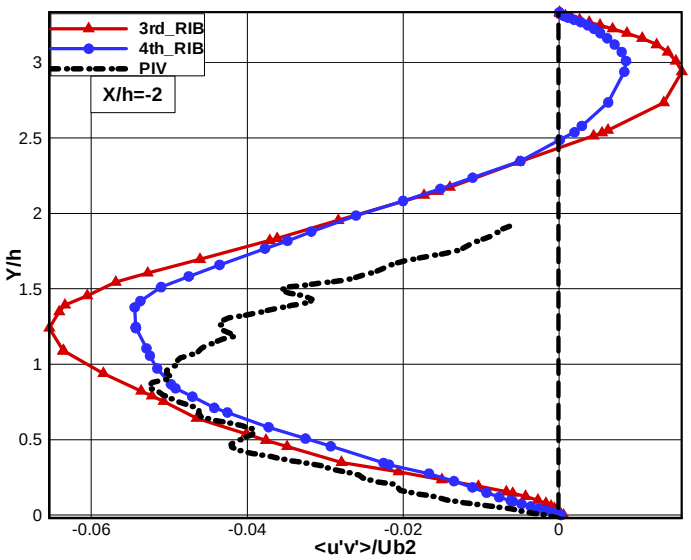


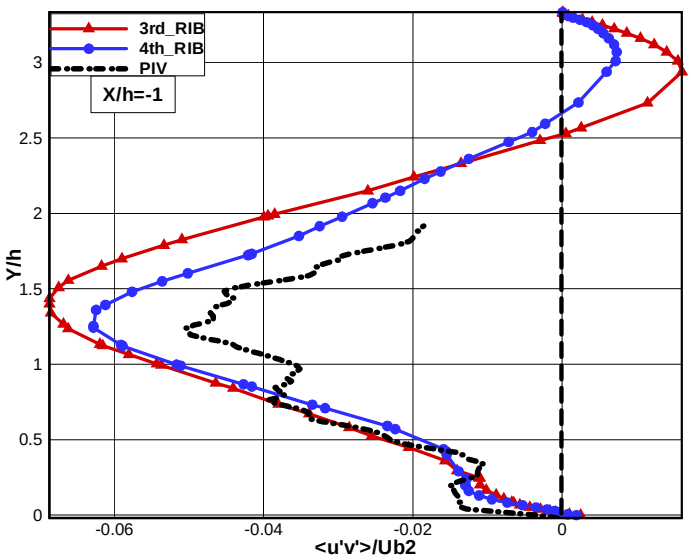


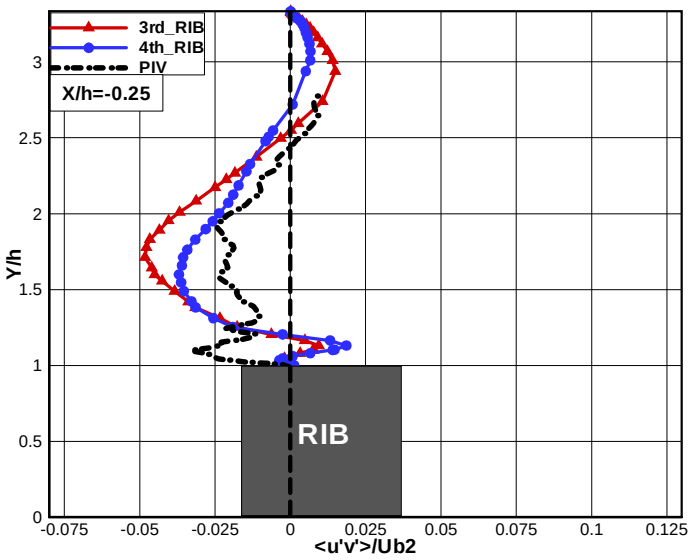


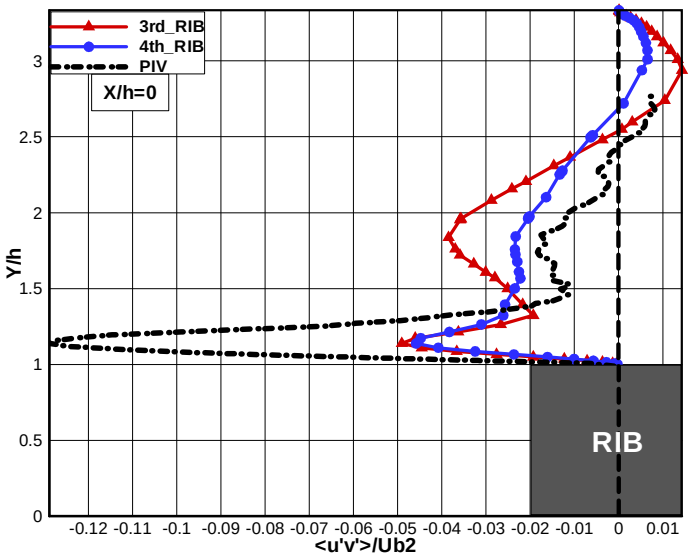


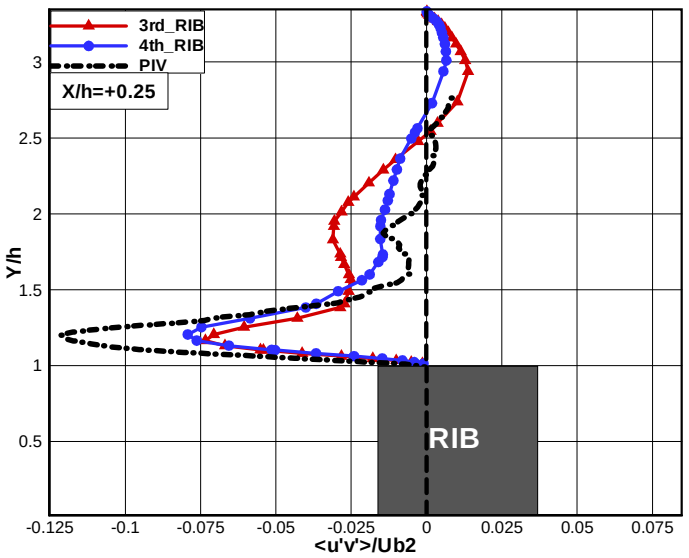


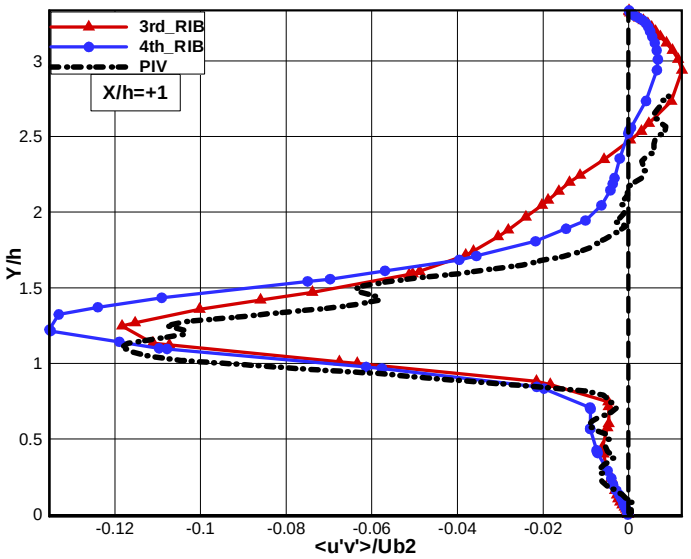

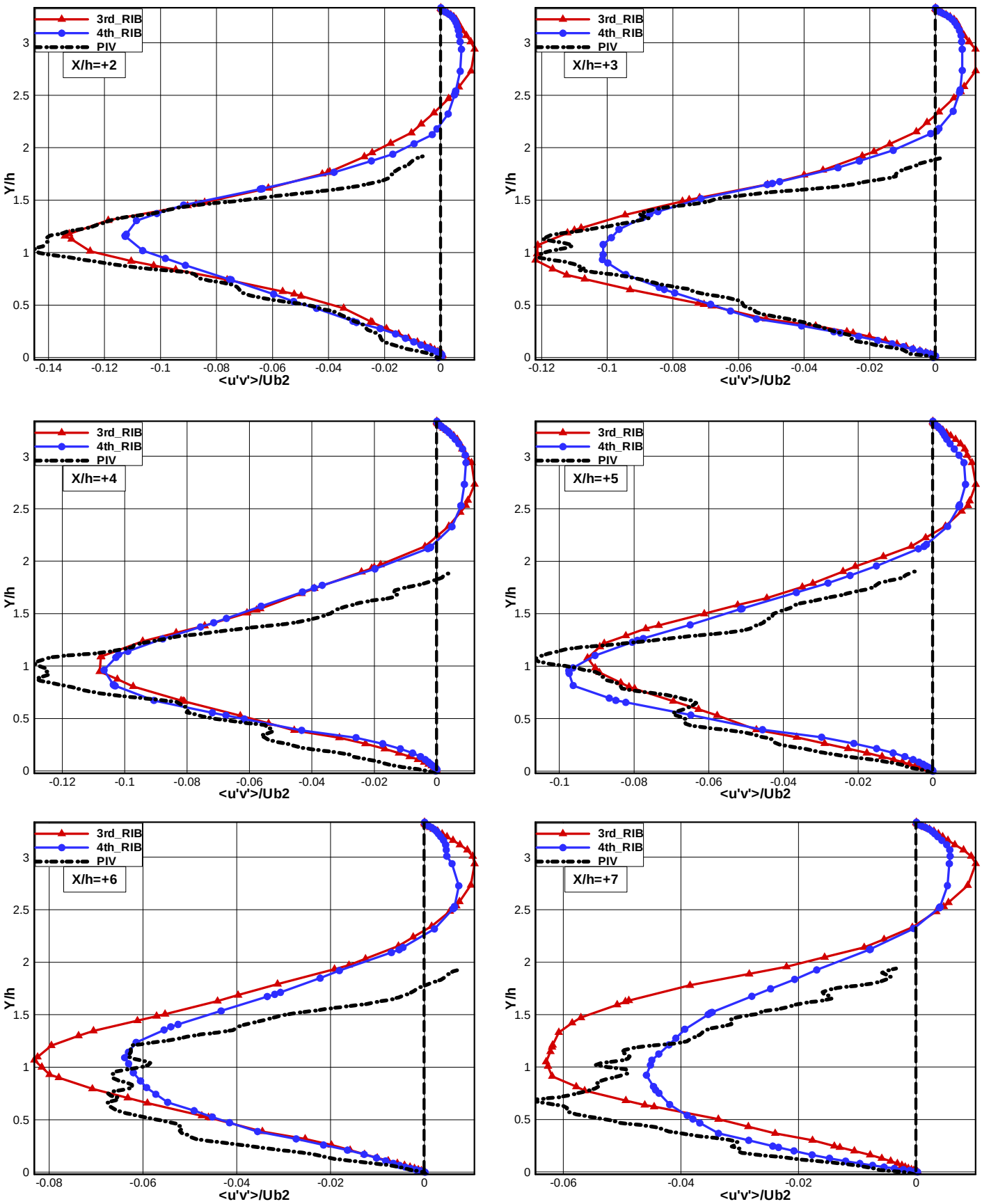

*Figure 7.19. Turbulent shear stress $< u'v' >/U_b^2$ in 1XY*

***N.B As a conclusion it can be said that the contours show qualitatively similar points between the 3rd and the 4th rib. But, since we have time average data for 7 entire cycles ~ 350 rib height cycle, a 13% uncertainty can be expected, which justify the different turbulent profiles over the 3rd and 4th rib. Finally, similar shapes and differences less than 15% could be considered acceptable.***

## 7.6 Flow field in XZ planes

### 7.6.0 Results in the planes XZ planes

In order to reveal the three dimensional character of the flow we also performed some investigations in the horizontal XZ planes defined in *figure 7.3*.

### 7.6.1 Results in the plane 1XZ (Y/h=0.05)

The first plane considered (1XZ, Y/*h*=.05) is localized very close to the wall, (y+~30- close to the expected the transition between buffer layer and region of developed turbulence). The information concerning this plane is very useful to investigate the correlation between flow and heat transfer (See chapter 8). The visualization of the time averaged flow field in this plane by means of streamstraces [23] is compared to experimental data in the *figure 7.20* below. ( patterns deduced from PIV measurements are given in the upper half of the plane). It can be observed that the average flow is divided into two main regions:

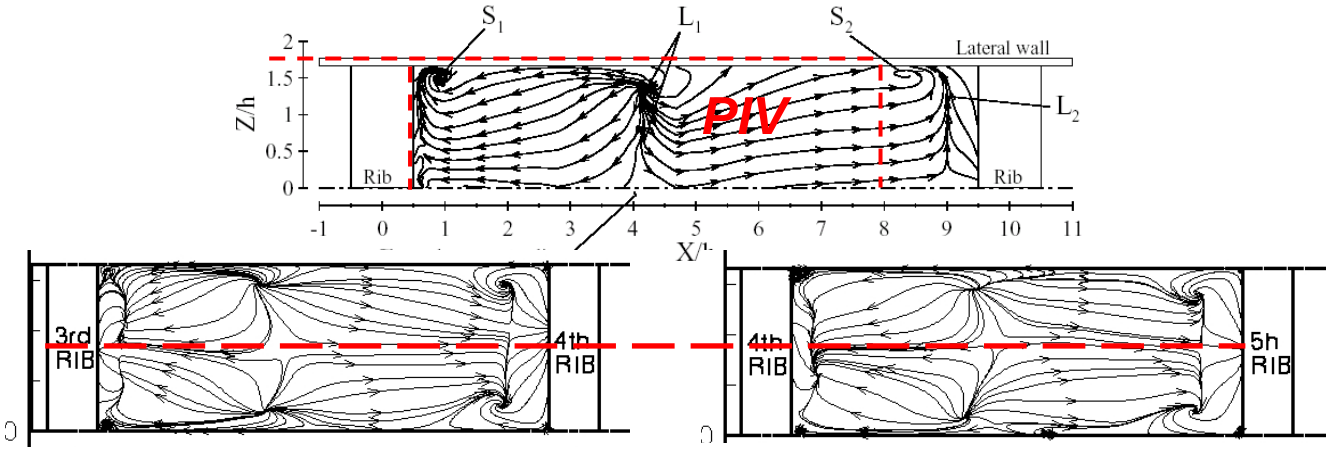


*Figure 7.20 streamstraces in the 1XZ horizontal plane (Y/h=0.05)*

***Region A: upstream L1***

This region showed negative values of the mean streamwise velocity U. It corresponds to the zone where the biggest recirculation region is situated after the ribs. The position of the reattachment line $L_1$ is situated between ($4 < X/h < 4.5$).
$S_1$ is a Horseshoe vortex [24] placed behind the rib in the corner near the lateral wall. It is characterized by positive U (rotating clockwise).

***Region B: downstream L1***

After the reattachment line, the mean streamwise velocity becomes positive which is obvious. The flow reattaches then moves forward till it separates again, on the line $L_2$ just upstream the rib. Again a second structure $S_2$ similar to $S_1$ is located upstream the rib. $S_2$ is characterized by negative U (rotating anticlockwise) where the flow accumulates and then it accelerates above the corner to feed $S_1$ structure.

It can also be observed from the contours (*figure 7.21*) of the average stream-wise velocity that the flow in the horizontal plane is not completely symmetric. In PIV the maximum is on the centerline but in LES it is shifted away between the 3rd and 4th rib. However, span-wise velocity seems to be symmetric and corresponds to PIV. It can be noted the trace of the corner vortex structures developed upstream the rib.

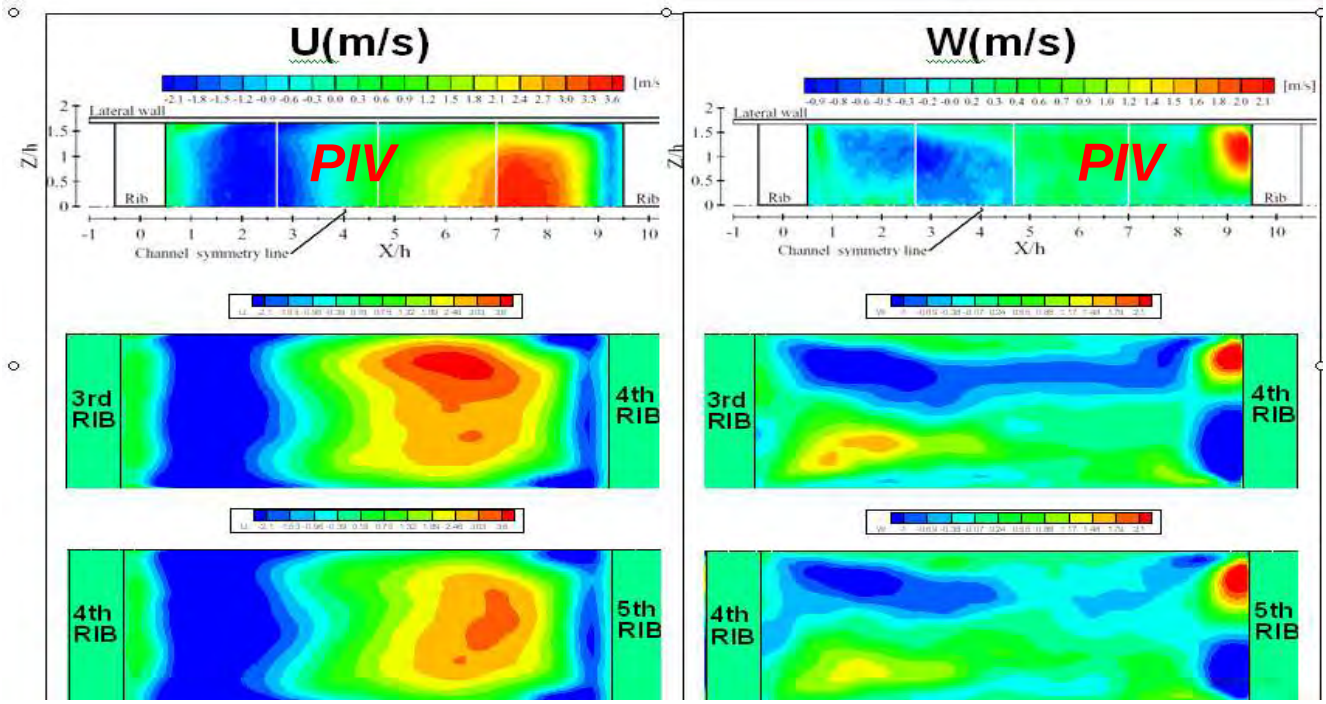


*Figure 7.21 Contours comparison of the stream-wise and span-wise velocity*

To assist on the understanding of the flow in this plane, the results for the symmetry line are presented in *figure 7.22*. The average velocity components U, V, the resolved turbulent quantities <u'u'> and <u'v'> are presented. It can be remarked that the stream-wise velocity shows negative values downstream the rib and upstream the rib, representing the main separations upstream and downstream of the rib. For the average velocity the numerical results show a good agreement between themselves and with the PIV data. The two profiles of numerical turbulent stresses also show a satisfactory internal agreement. The agreement with PIV is acceptable of <u'u'> although <u'v'> is overestimated, even if the noisy experimental profile allows to suspect and important measurement uncertainty. Simulation and experimental results both show maximum results around the reattachment point where maximum heat transfer is present (see chapter 8). A good match can be remarked for shape between the results of experiment and the numerical studies even if the magnitude of numerical turbulent stresses differ from experimental ones. Improved and more precise results are given by running the numerical simulation two more channel cycles.

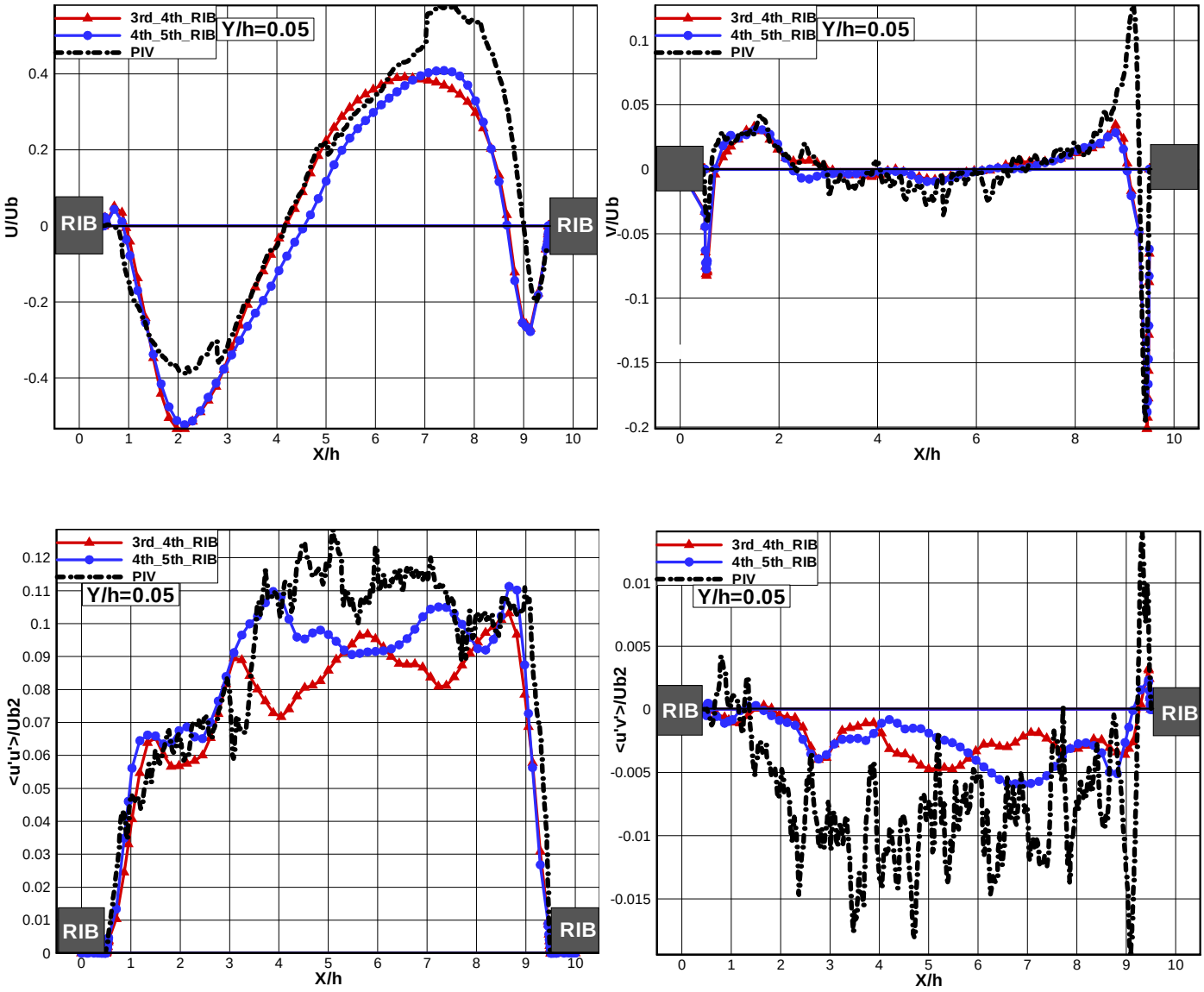

*Figure 7.22 Profiles of the mean and turbulent quantities on the symmetry line at Y/h=0.05*

### *7.6.2 Results in the plane 2XZ (Y/h=0.5)*

The plane 2XZ (Y/*h*=0.5) is located at one half height of the rib. This mid-height rib Y/*h*=0.5 position is chosen because it crosses the core of the separation bubble, as t has been shown by the experimental results that this line. The mean flow is visualized by means of streamstraces (*figure 7.23*) while the contours for stream-wise and span-wise velocity component are given in *figure 7.24*

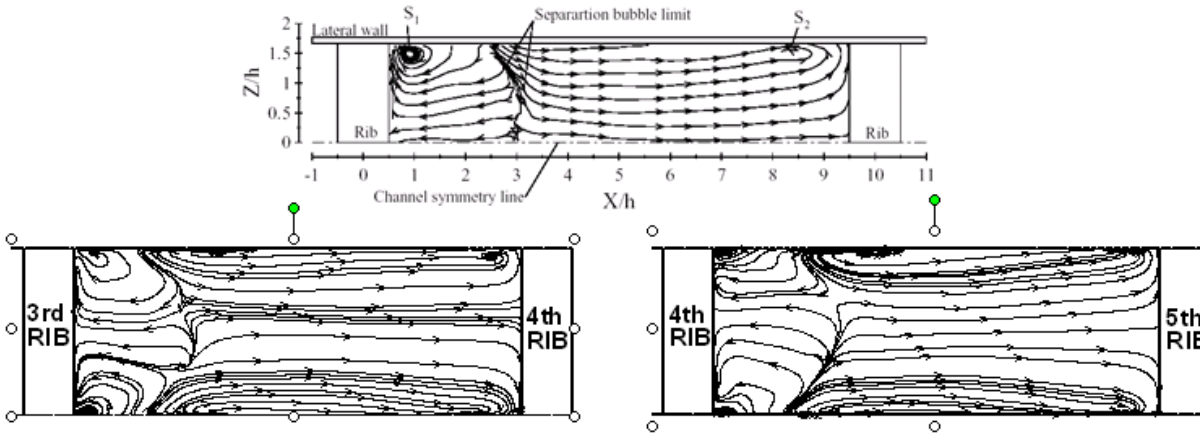


*Figure 7.23 streamstraces in the 1XZ horizontal plane (Y/h=0.5)*

*Figure 7.23* highlights the three-dimensional nature of the flow and the corner vortex.
*Figure 7.24* puts in evidence the separation region downstream the rib and the important region of high velocity downstream of it.

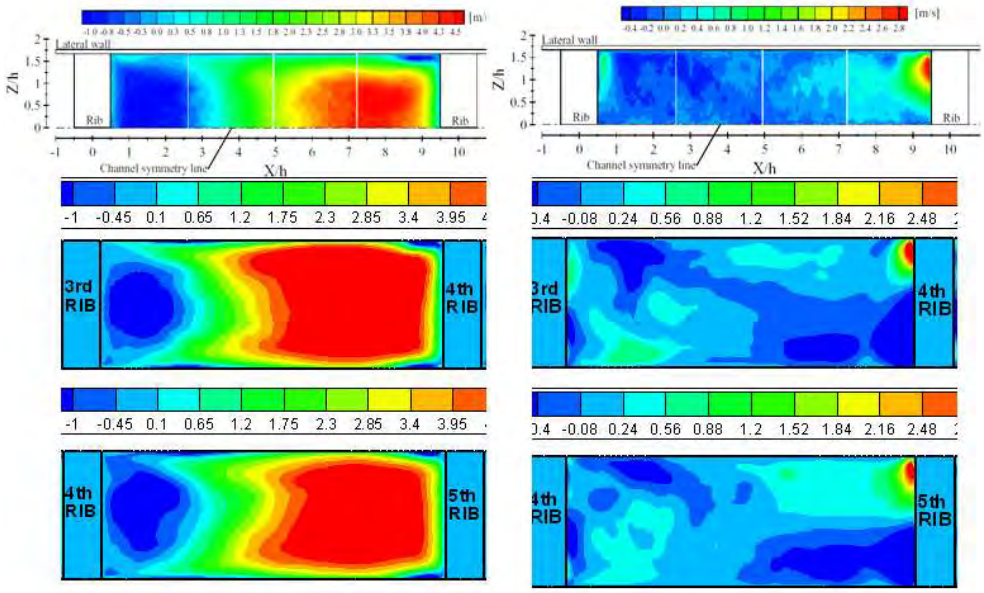

*Figure 7.24. Stream-wise and span-wise velocity in 2YZ plane*

The results for the symmetry line are presented in *figure 7.25*. The average velocity components <U>, <V>, the resolved turbulent quantities <u'u'> and <u'v'> are presented. The two numerical profiles for mean stream-wise and normal velocities agree well between themselves and match quite well the measurements. The variance<u'u'> under predict the PIV results, while the agreement is satisfactory for but <u'v'>.

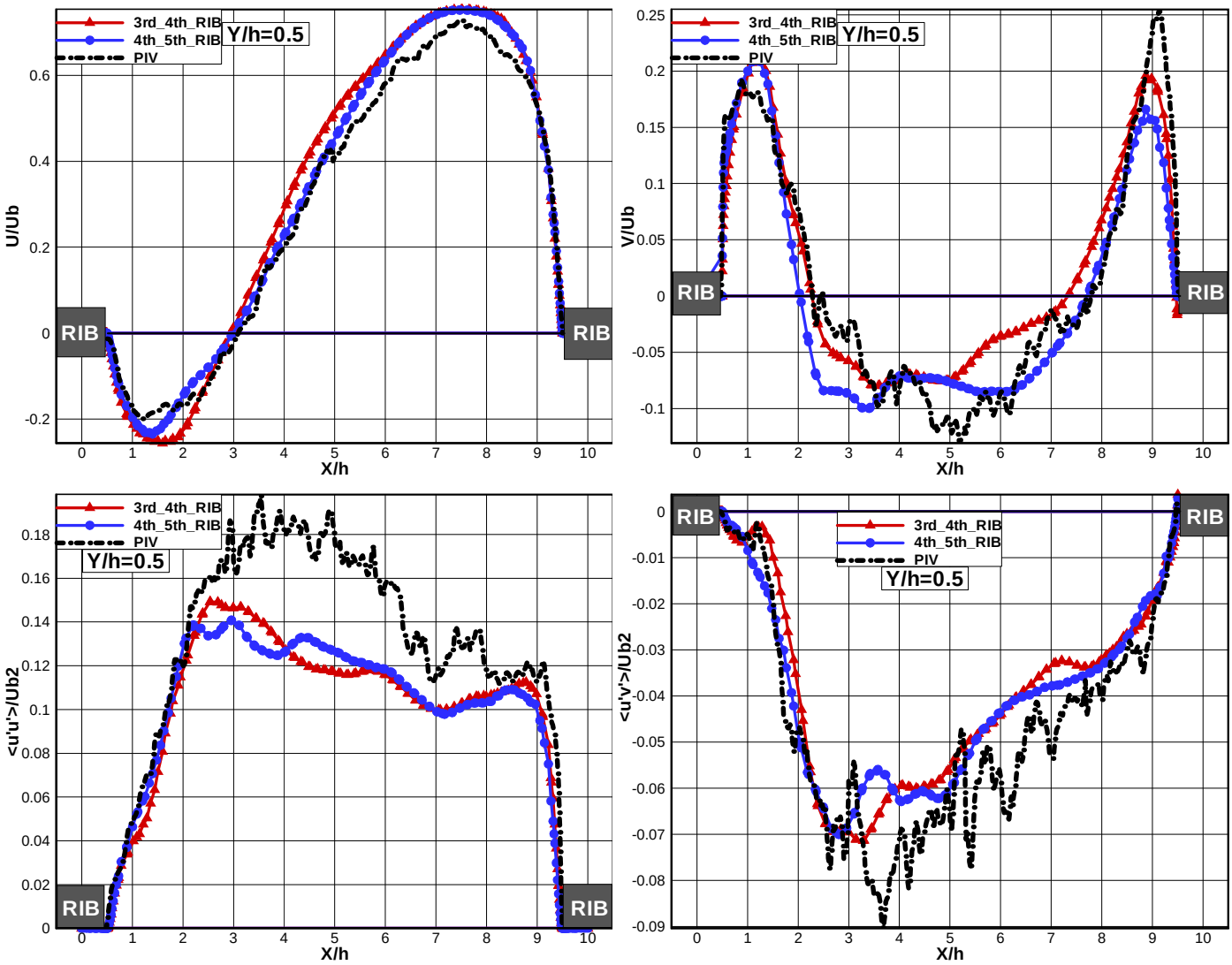


*Figure 7.25 Profiles of the mean and turbulent quantities on the symmetry line at height Y/h=0.5*

### *7.6.3 Results in the plane 3XZ (Y/h=1.05~1.1*)

The measurement plane is situated at Y/*h*=1.05, above the rib's surface at th. The mean flow is visualized by means of streamstraces while the contours for stream-wise and span-wise velocity component are given in *figure 7.26*.

Here it can be again remarked the presence of the recirculation region on the top of the rib exists and it can be concluded that the profile of the PIV mean streamwise data are inaccurate at X/h=0

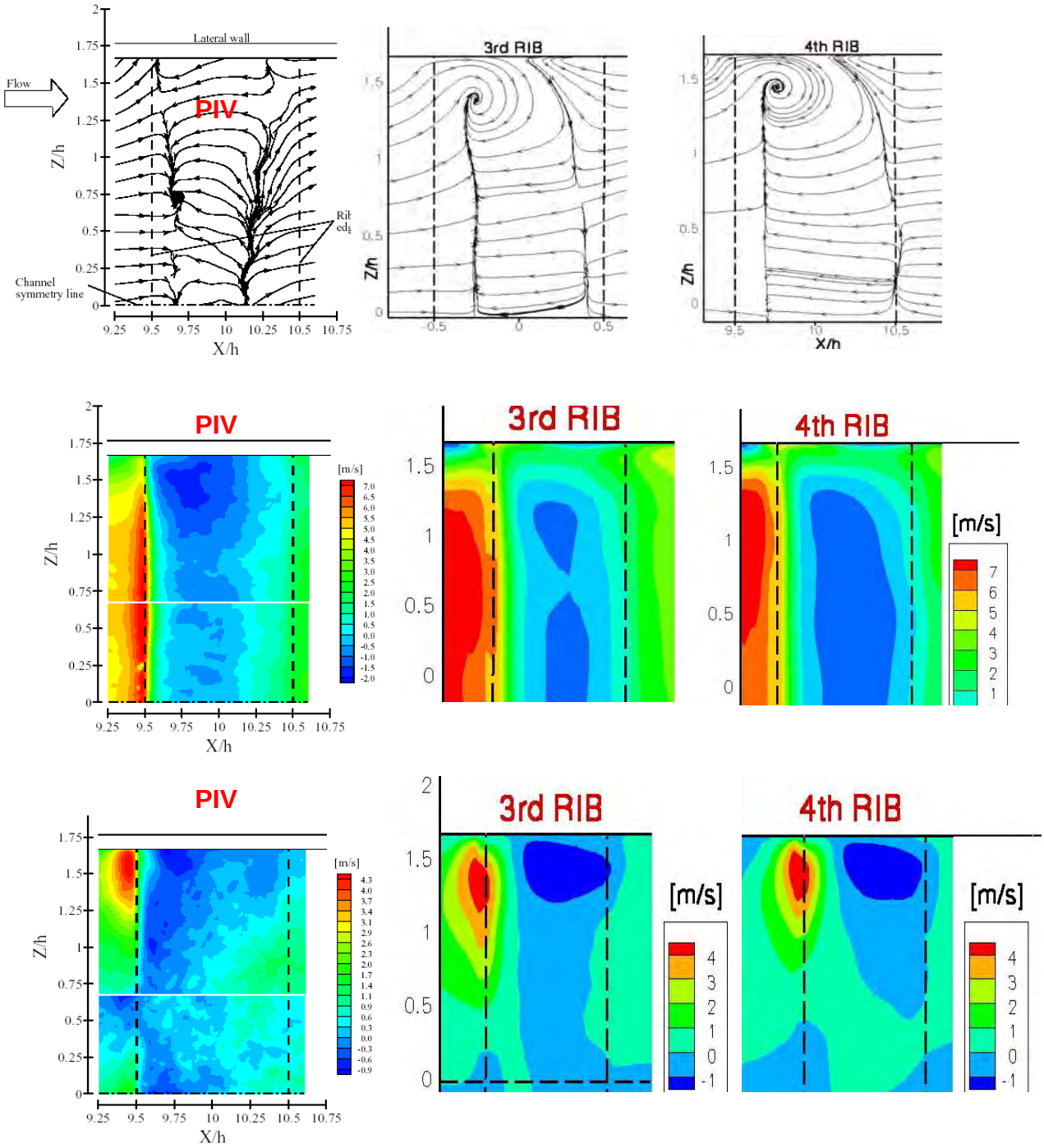


*Figure 7.26 Streamlines and contours in the horizontal plane (Y/h=1.05)*

## *7.7 Flow field in YZ planes (cross-vertical planes)*

### *7.7.0 Secondary flow features characterization*

The cross-vertical planes (YZ) are characterized by the presence of secondary flows [25]. In general terms, these motions can be generated by either geometrical constraints (eg: ribs) or imposed forces (eg: Coriolis forces). The magnitude of these secondary vortices is very weak and it is of the order of 1% to 3 % of the streamwise bulk velocity. According to *Prandtl* there are two types of secondary flows:

- Secondary flows generated by viscous effects. (First type secondary flows).
- Secondary flows generated by Reynolds stress. (Second type secomdary flows).

*The first type secondary flows* are generated when a stream-wise component of vorticity (X-vorticity) is developed by the deflection of an initially sheared flow. When the flow is deviated by the rib, the boundary layer is also deviated and generates a stream-wise vortex, which makes the flow rolls on itself as shown in the *figure 7.27* below. In the present case the main re-circulating bubble is not a secondary flow, as the ribs only generate span-wise vorticity (Z-vorticity).

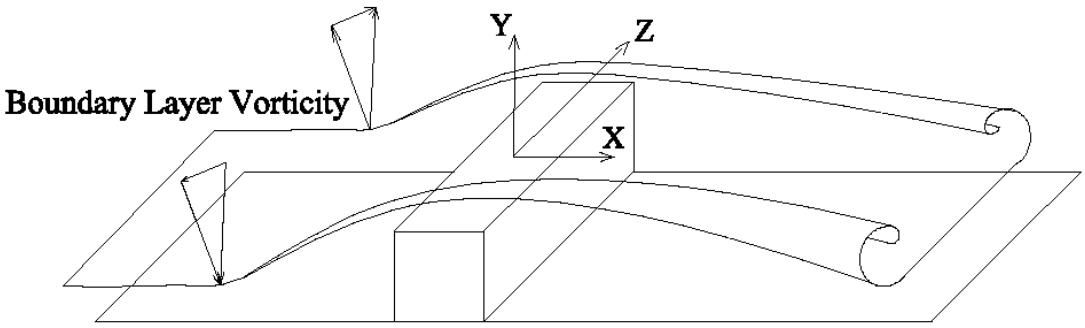


*Figure 7.27 Deflection of the boundary layer due to the pressure gradient*

*The second type secondary flow* generated by Reynolds stresses develops itself in the corners of the duct, where there is an increase in the wall shear stress towards the corner. Moreover, significant influence on the heat transfer was observed by the secondary motion.

These behaviors will be seen in the following figures, which shows the stream traces and the velocity contours in the cross-vertical plane. In the next 3 figures ( *figure 7.28-30*) the left-side column shows the experimental result; the middle column shows the numerical result corresponding to the 3rd pitch while the right column presents the numerical result corresponding to the 4th pitch; the upper row presents the stream trace and the middle row presents the contours of the <V> velocity component and the bottom one shows the contours of the <W> velocity component . A general remark, common the following figures, is that the insufficient resolution of PIV does not capture the vortices generated in the corners, which are, on the contrary, captured by the simulation.

### *7.7.1 Results in the plane 1YZ (X/h=0)*

*Figure 7.28* shows the behaviour of the cross flow in the plane 1YZ, which corresponds to middle line of the rib. The examination of the stream traces shows that in the central bottom part of the plane the PIV data suggests that the flow moves up, while the numerical LES results show a different pattern. This behaviour has been remarked in the section 7.4.1-B where it can be seen that the profiles of the mean normal velocity extracted from a vertical line at the top of the rib (X/h=0) show positive values <V> instead of negative ones. The reason of this difference is that, in LES, the centre of the recirculation bubble located on the top of the rib is shifted downward than the one shown in PIV *(figure 7.7)*

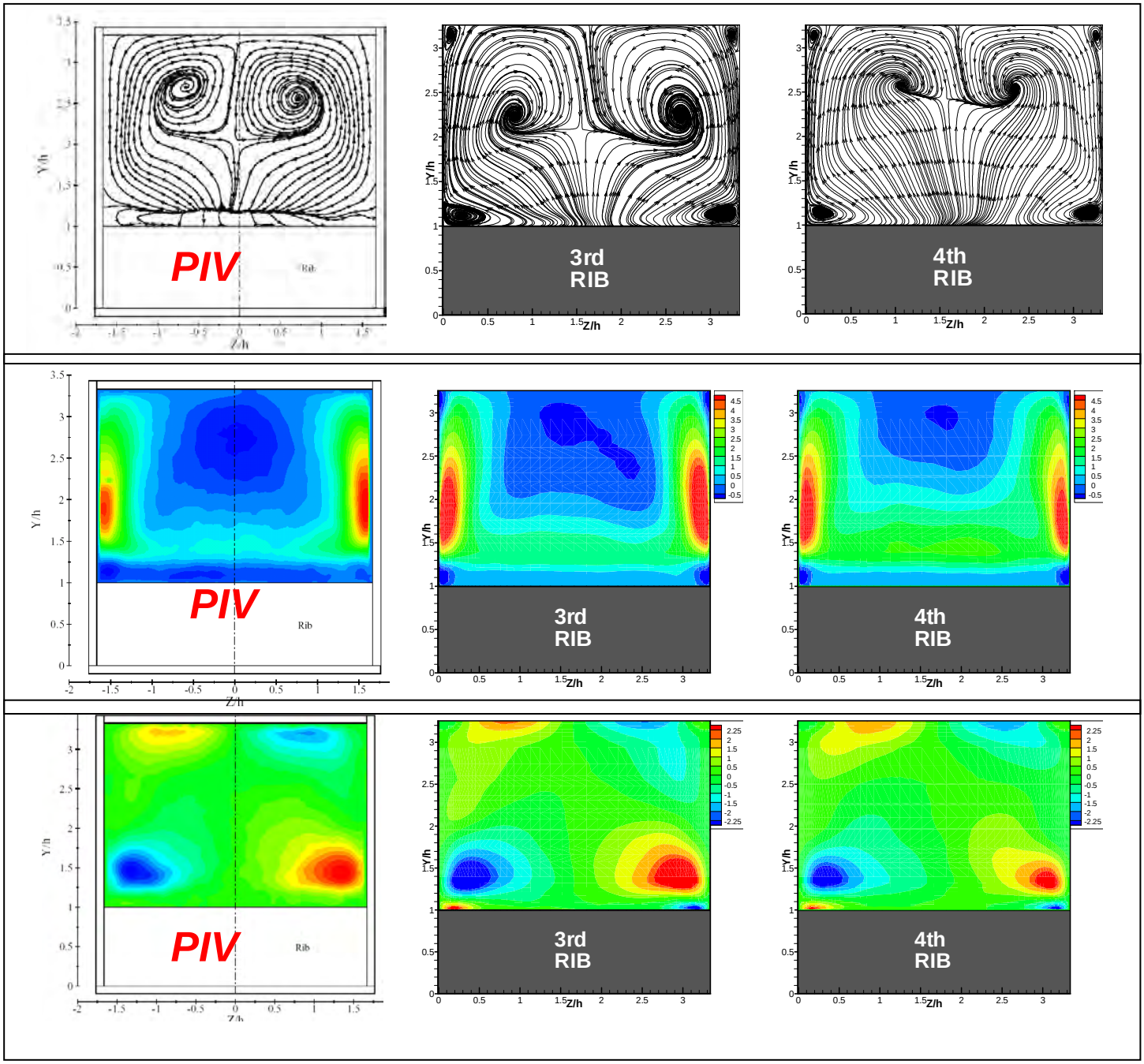

*Figure 7.28 Streamstraces, mean Normal and span-wise velocity in 1YZ*

However, LES results above the third and fourth ribs show that the pattern and location of the core of the vortices are well reproduced.
The distribution of the time averaged vertical velocity component <V> shows that the regions of high velocity inducted by the vortex are well reproduced in size and location, while the contours of the transversal component <W> of the average velocity present a comparable agreement.

### *7.7.2 Results in the plane 2YZ (X/h=4.3)*

*Figure 7.29* presents shows the stream traces and the velocity contours in the plane 2YZ, which corresponds to the location of the reattachment downstream of the main downstream separation. The stream traces show how the flow is dominated by longitudinal vortex. In the simulation the core of the vortex appears located lower than the experiment. The contours of <V> show qualitative agreement between experiment and simulation. It is visible a "core" region of negative velocity counterbalanced by local regions of high positive velocities. The contours of <W> show local regions of high velocities induced by the vortex and the behavior is well reproduced by the simulation.

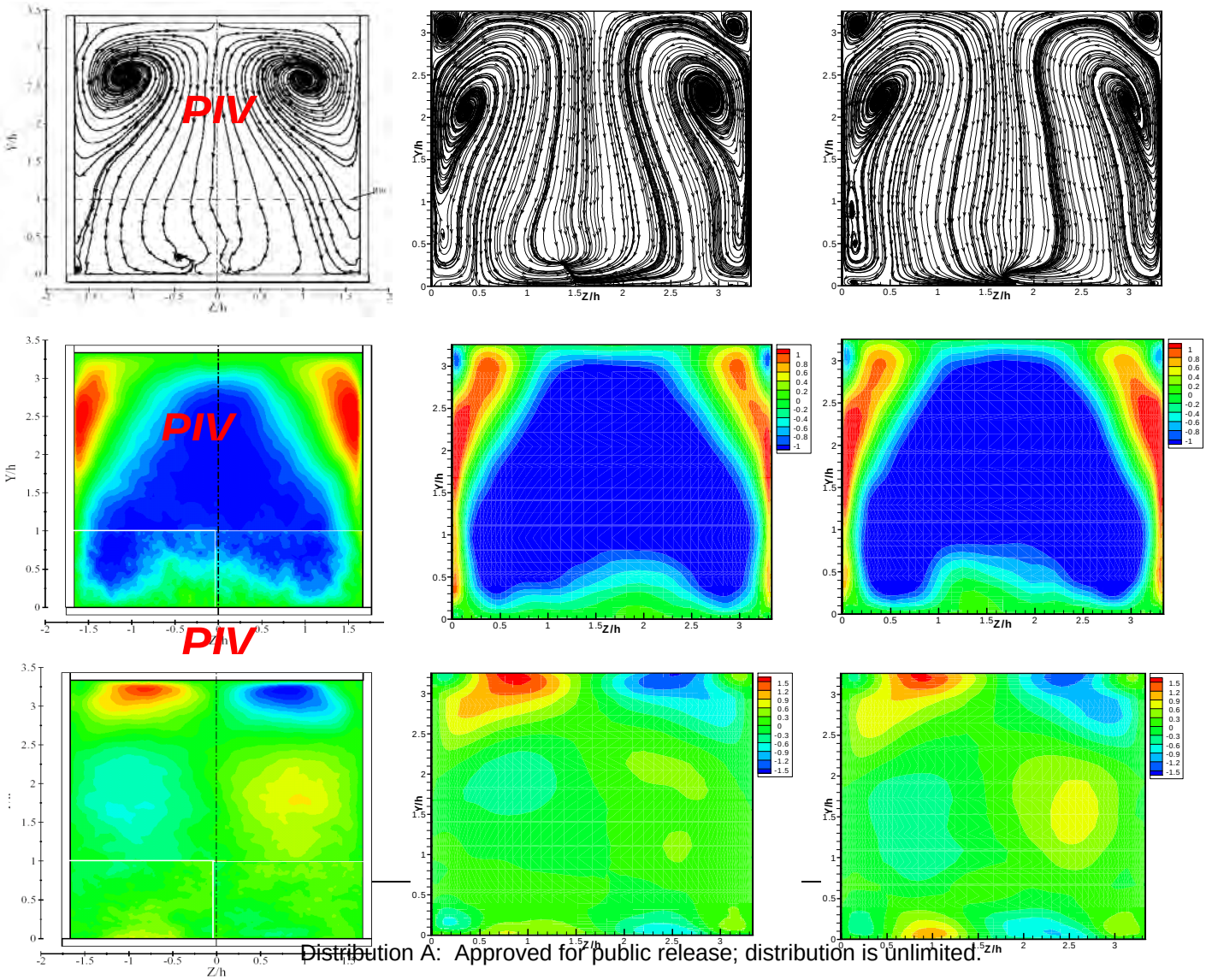

*Figure 7.29 Streamstraces; mean Normal and span-wise velocity in 2YZ*

### *7.7.3 Results in the plane 3YZ (X/h=8.3)*

Plane 3YZ corresponds to the region perturbed by the separation upstream to the rib.
PIV data are available only for the lower part of the duct and *figure 7.30* has been readjusted accordingly. Stream traces put in evidence the motion of the flow moving away the centreline toward the side walls.

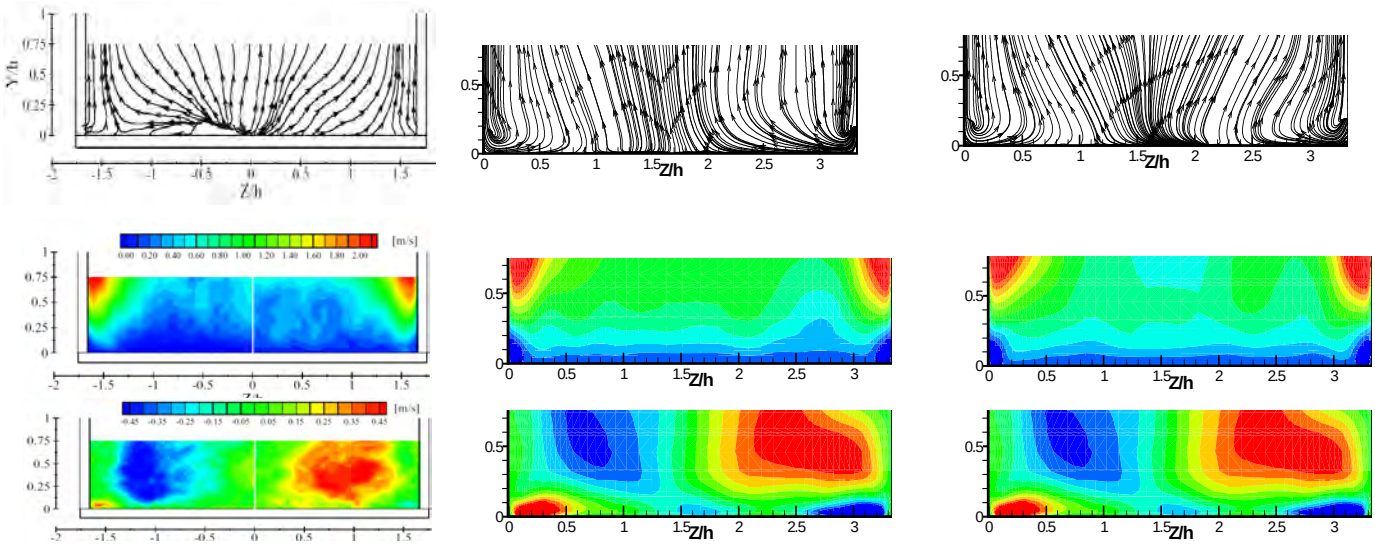


*Figure 7.30 Streamstraces; mean Normal and spanwise velocity in 3YZ*

## *7.8 Conclusions for the investigation of the flow field*

The present results allow concluding that flow stabilizes itself only downstream of the 3rd rib. The need for this long establishing length is shown by the biggest differences in $U/U_b$ profiles are at X/h=-2. Otherwise, it was already remarked that differences in turbulent quantities, given by the simulation and the experiment might be caused by insufficient convergence. The worst discrepancies are on the plane 3XY because the presence of the side wall creates a more complex flow which the grid does not fully resolve or because a better wall Boundary Condition would needed. Finally one can note that over the ribs, **L**arge **E**ddy **S**imulation

seems to reproduce the trends of the PIV (at least for planes1XY and 2XY), even if actual values are slightly different; this could be improved by using a grid refinement.

However, that the present simulation presents an acceptable matching with geometry and the previous available experimental results [8, 9] and describes the flow with acceptable accuracy to be useful for the next step which the investigation of the thermal field and its coupling with the flow field.

# *Part III Simulation of thermal field*

# CHAPTER 8 Thermal Results and Discussion

## *8.0 Introduction*

The aims of the investigation of the thermal field are:
-under the fundamental point of view, to increase the understanding of physics of heat transfer and turbulent scalar transport in complex flows
-under the engineering point of view, to assess the efficiency of ribbed ducts as cooling tool for the internal cooling of the turbine blades as expressed by the Enhancement Factor. It is of major importance to put in evidence (and possibly to predict at design stage) the zones of possible local overheating in the solid region, which is, usually, the reason for the initial cause of the damage in the turbine blades. Therefore this chapter is dedicated to analyze the temperature and the heat transfer within the ribbed channel.

## *8.1 Thermal field investigation*

In order to study the effect of the turbulent field on the mean thermal quantities (mean static temperature, mean heat flux), the aerodynamic field needs to be well resolved because, in the case of incompressible flow, the temperature is a passive scalar and it is transported by the turbulent velocity field without influencing it. This requirement justifies the detailed investigation of the flow field which has been presented in Chapter 7.

### *8.1.1 Mean Static Temperature T*

The iso-contours of the mean static temperature (in K degrees) are shown in the *figure 8.1* for the planes 1XY and 1XZ. The examination of plane 1XY shows that, contrary of the aerodynamic field, which becomes periodic after the 3$^{rd}$ rib, the stabilization of the thermal field on the bottom wall needs a longer transitional length and its behavior becomes periodic only downstream of the 4$^{th}$ rib. Therefore, only numerical results on the 3$^{rd}$, 4$^{th}$ and 5$^{th}$ rib are illustrated in this chapter, while most detailed comparisons were performed for the 4$^{th}$ rib.

In general terms, the distribution of temperature well puts in evidence strong local effects of the ribs locally enhancing the heat transfer.
The iso-contours of the mean static temperature in the 1XZ plane put in evidence the behavior of flow and heat transfer in the small secondary recirculation region located downstream the rib. The flow is trapped within this region and the momentum exchange is smaller than anywhere else in the duct. Consequently, the convection is negligible in comparison to the conduction inside these bubbles. Outside of these recirculation zones, the transport of the temperature scalar by the flow becomes more important, and, hence, the temperature on the bottom wall decreases to reach its minimum value near the reattachment point.

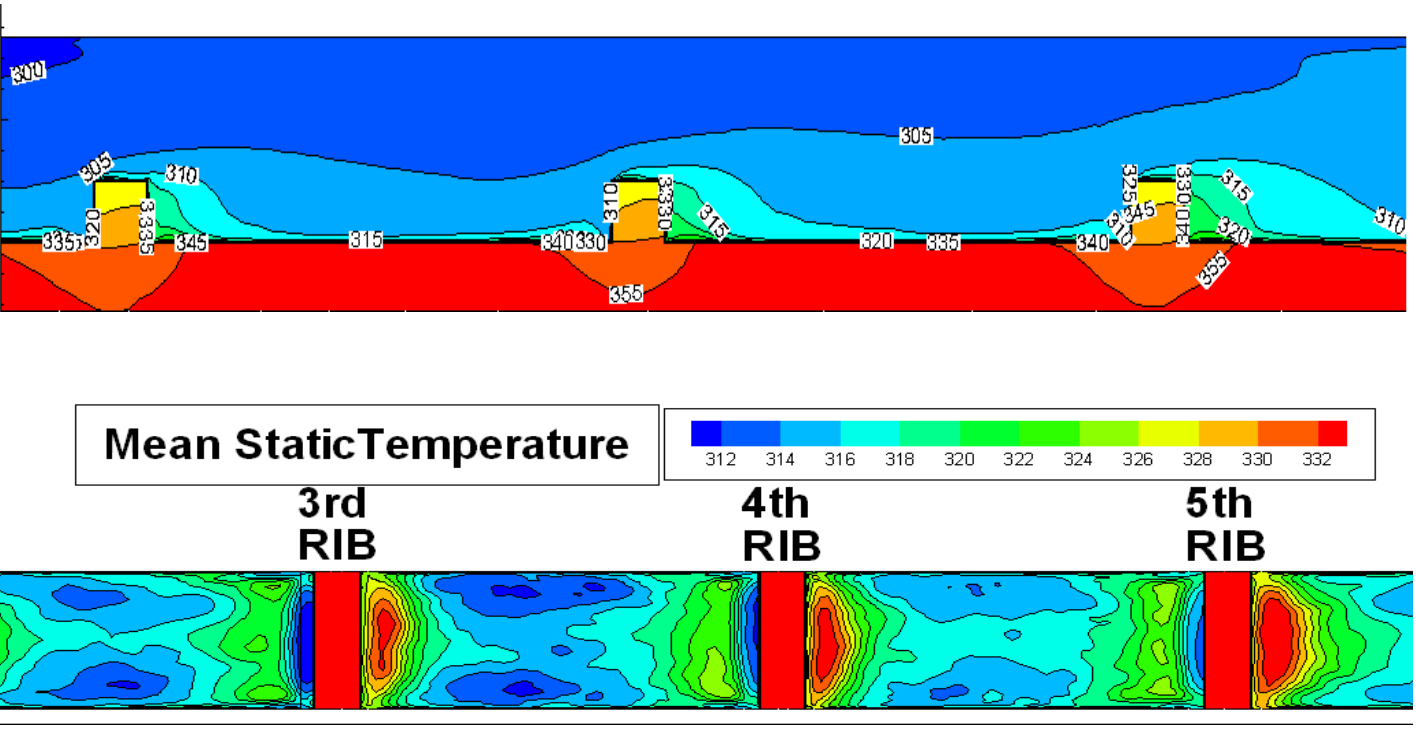


*Figure 8.1 Mean static temperature field (K) in vertical plane 1XY (top) and horizontal 1XZ plane (bottom)*

The profiles of the mean static temperature on plane 1XY are presented in *figure 8.2*.
It must be remarked that the temperature in the bulk flow increases in the stream-wise direction in consequence of the constant heath flux coming from the bottom wall. All the profiles show that the maximum of the mean static temperature is located at the bottom wall and, moving away of the wall the temperature rapidly decreases through the boundary layer over wall. Profiles at X/*h*=+1 and +2 show an inflection point which indicates the presence of non dissipated big thermal structures, which begin to disappear downstream the reattachment point. This behavior has been already remarked for the mean stream-wise velocity in the Chapter 7. The minimum heat transfer rate is found in the X/*h*=+1, position where the gradient of temperature through the wall region is lower; this behavior is related to the presence of the secondary separated region.

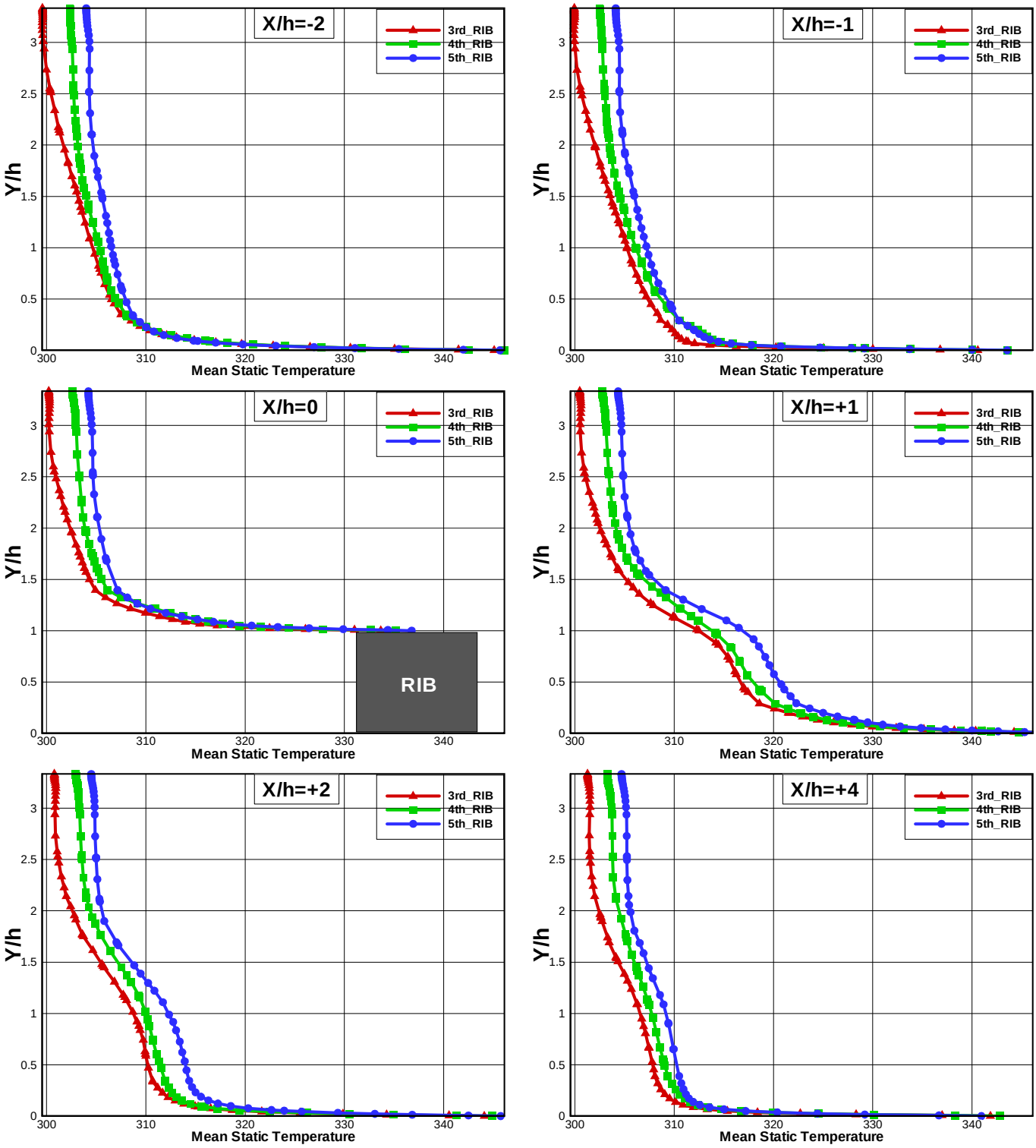


*Figure 8.2 Profiles of Mean static temperature field (K) in the 1XY plane*

.

### *8.1.2 RMS Static Temperature ($<T'^2>^{.5}$)*

The iso-contours of the standard deviation $<T'^2>^{.5}$ of the static temperature (RMS) for planes 1XY and plane 1XZ are shown in *figure 8.3*. The iso-contours for plane 1XY show the presence of that region of high $<T'^2>^{.5}$ above the rib. This region is created at the separation on the leading edge corner of the rib and transported in the shear layer, born from this singular point, develops itself over the rib and continues downstream . It can be interesting to remark that the pattern of this quantity is similar to one encountered for the mixing layer wave in a combustion chamber. The highest values of this quantity are found close to the bottom ribbed wall, in correspondence to the separation and reattachment point of the primary recirculation zone. It can be remarked that the pattern of $<T'^2>^{.5}$ begins to repeat itself after the 4th rib.

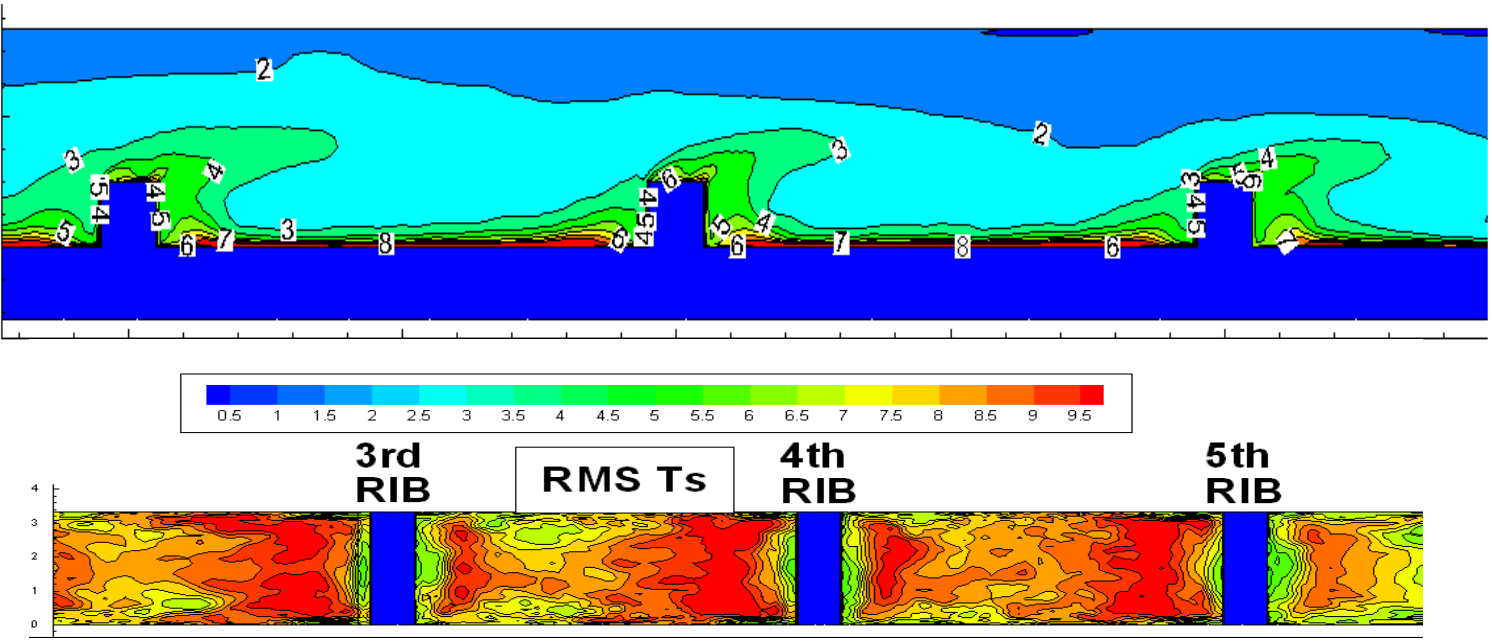


*Figure 8.3 RMS T' (K) in vertical plane 1XY (top) and horizontal 1XZ plane (bottom)*

The profiles of $<T'^2>^{.5}$ in plane 1XY are presented in *figure 8.4*. An acceptable agreement is between the different profiles, confirming the conclusions that the results for the 4th pitch are representative of established conditions. The peak close to the bottom wall is evident at all locations, while second region of high value is visible for the profiles for locations X/*h*=+2 and +4, in correspondence of the shear layer present in the wake region downstream of the rib. These high values are due to the presence of large scale thermal structures not yet dissipated by turbulent mixing.

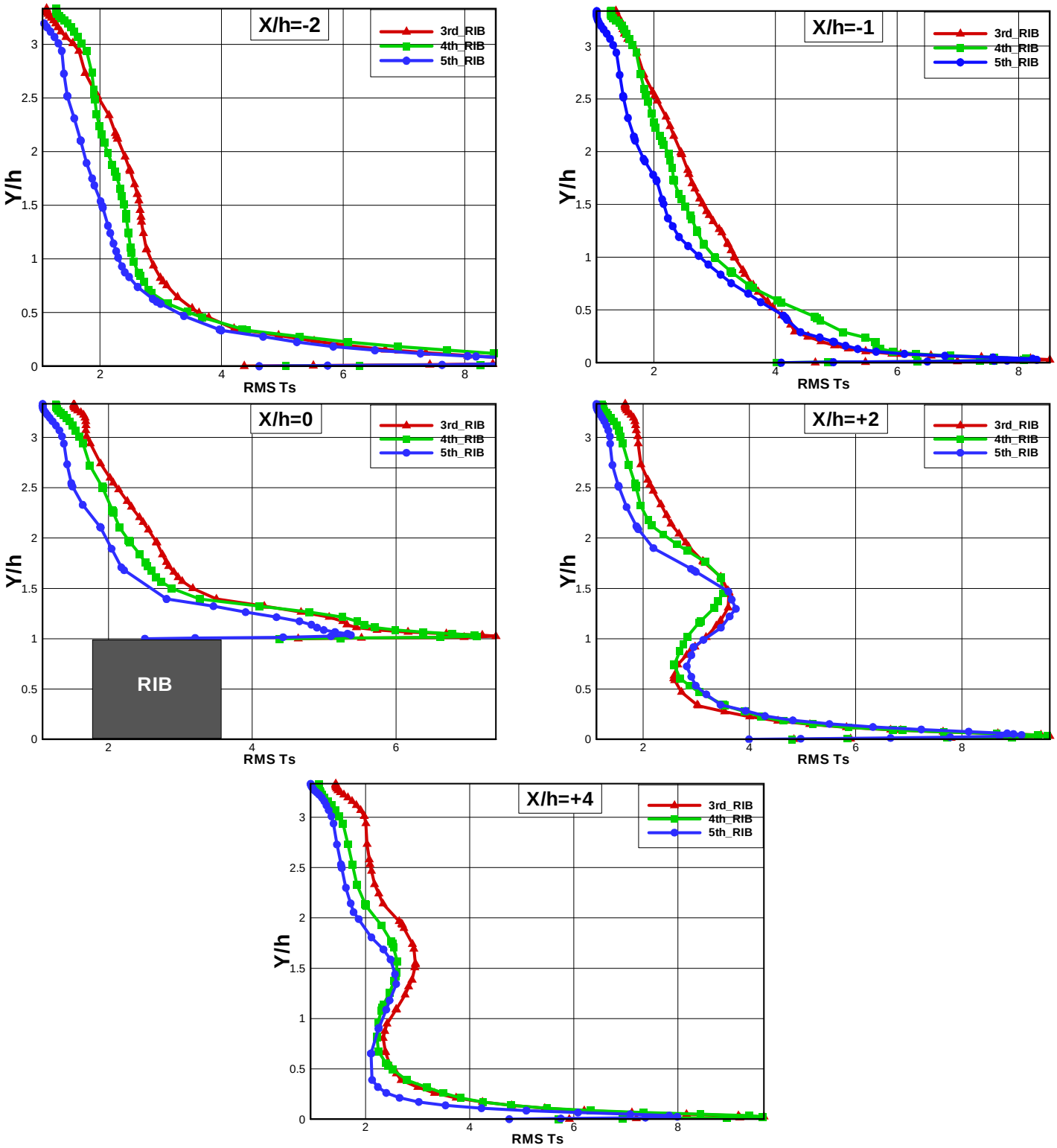


*Figure 8.4 Profiles plot of RMS static temperature (K) in the 1XY plane*

### *8.1.3 Resolved turbulent correlations between velocity and temperature*

The turbulent correlation between velocity and temperature for the longitudinal direction < *u'T'*> and direction < *v'T'*> are presented in *figure 8.5* and *figure 8.6*. The 2 quantities show patterns similar to ones observed for *RMS Ts*. Local maxima of both longitudinal and normal turbulent heat fluxes are localized at:

- In the shear layer created over the ribs.
- On the bottom wall, in correspondence of the region of separation region between main and secondary bubbles.
- On the bottom wall region, in the region close to the reattachment point of the main separated region.

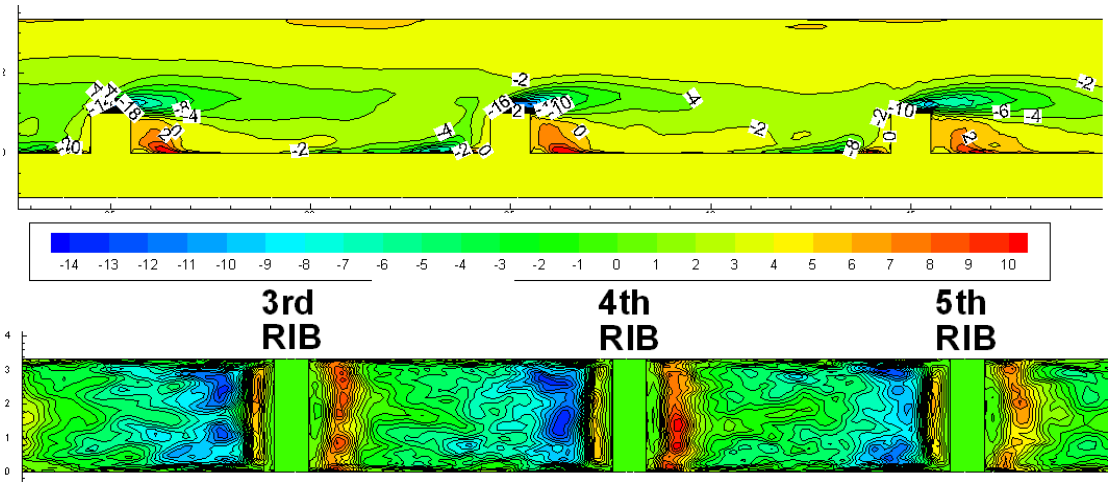


*Figure 8.5 Resolved longitudinal turbulent heat flux< u'T'> (m/sK) in vertical plane 1XY (top) and horizontal 1XZ plane (bottom)*

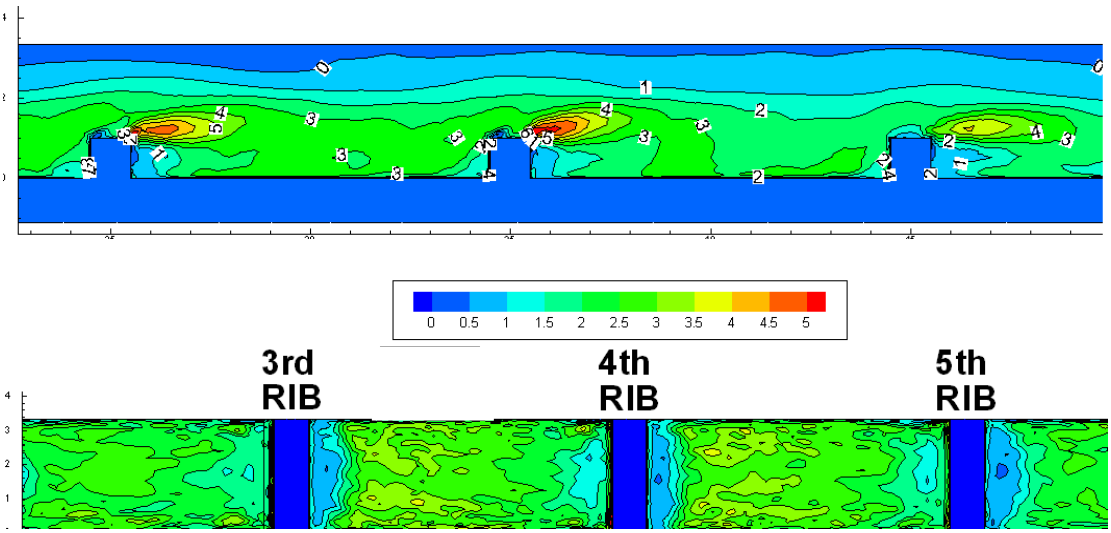


*Figure 8.6 Resolved normal turbulent heat flux <v'T'> (m/sK) in vertical plane 1XY (top) horizontal 1XZ plane (bottom)*

## *8.2 Heat transfer and Enhancement Factor EF*

The heat transfer from the heated wall to the cooling fluid is determined by a heat transfer coefficient, defined as follows:

• $\Gamma(x, y)$ convective heat transfer coefficient of the fluid where it is determined by the Newton law formula shown below:

$$\Gamma(x, y) = \frac{\|\phi\|}{\left(T_w - T_{ref}\right)}$$

- $\|\varphi\|$ : Mean wall heat transfer
- $T_w$ : Mean wall temperature
- $T_{ref}$ : Reference temperature

The quantity $T_{ref}$ should, of course, be representative of the gradient of temperature driving the heat transfer from the solid to the fluid. For a first investigation, a fixed value $T_{ref}$=*288.16 K* was applied and the corresponding distribution of $\Gamma(x,y)$ on the bottom wall and on the top faces of 2 ribs of interest are shown is presented in the following *figure 8.7*.

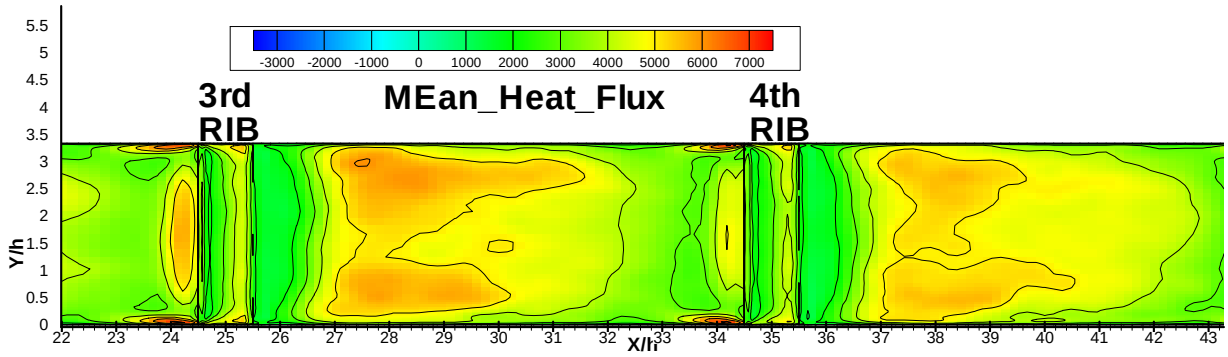


*Figure 8.7 Mean Heat Transfer at the ribbed wall*

Of course, the actual value of $\Gamma(x,y)$ depends on the choice of the reference temperature $T_{ref}$, which makes it a non-absolute reference. However, this quantity is necessary to estimate the Enhancement Factor (EF), which is the standard parameter used to evaluate the efficiency of the promoters of conjugate heat transfer.

The Enhancement Factor (EF) is defined as the ratio between the average Nusselt number for the actual geometry and the Nusselt number for a hydraulically smooth duct with fully developed flow field.

$$EF = \frac{\overline{Nu(x,y)}}{Nu_0}$$

The average Nusselt number for the actual geometry is defined as:

$$\overline{Nu(x,y)} = \frac{\Gamma(x,y)D_h}{\lambda_f}$$

Where $\lambda_f$ is the conduction heat transfer coefficient of the fluid

The Nusselt number for a hydraulically smooth duct with fully developed is given by the formula of DITTUS and BOELTER for 0.7<Pr<120:

$$Nu_0 = 0.023 * (Re)^{0.8} (Pr)^{0.4}$$

EF allows recasting the conjugate heat transfer in non-dimensional terms and evaluating the efficiency of the present rib set-up.
The resulting EF distribution is presented in *figure 8.8* which, evidently, presents patterns similar to the ones visible in *figure 8.7*.

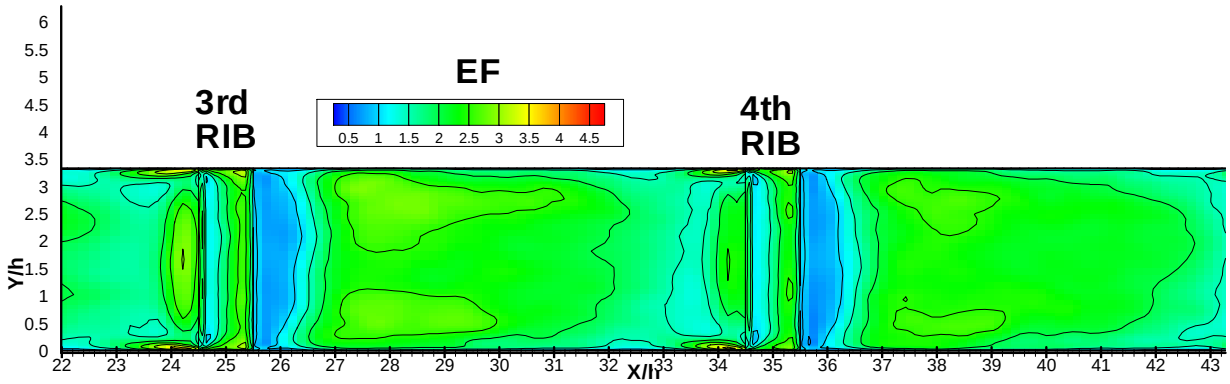


*Figure 8.8 Mean EF at the ribbed wall*
*Figure 8.8* shows that the minimum value of EF is reached within the small secondary corner bubble zone downstream the rib where the fluid is “trapped” within recirculation motion and

the convective heat transfer outside it is minimal. These regions represent hot points in the blade material and could be a reason for a catastrophic failure.
On the rib itself, on the top face of rib, it can be remarked the effect of the separate region downstream of the corner, which creates a region of relatively low EF and high EF on the reattached regions. The 3D effects on the distribution of EF will be examined in the following Chapter 10. An experimental distribution of EF, obtained in the previous campaign of tests, is presented in *figure 8.9*. It can be remarked that it presents similar patterns (the scale of colors is different), which is a first qualitative validation of the present simulation.

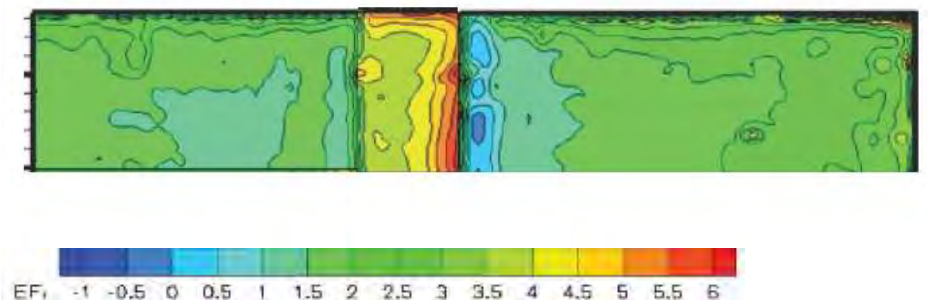


*Figure 8.9 Experimental distribution of mean EF at the ribbed wall* [4]

The separated regions downstream of the rib are put in better evidence by a zoom on the 4$^{th}$ pitch length in the following *figure 8.10*.

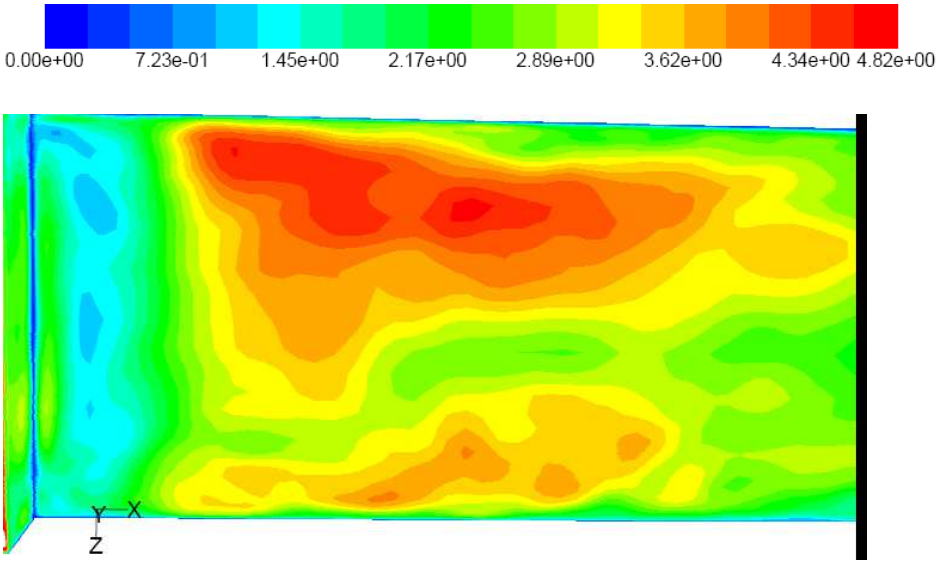


*Figure 8.10 Contours of the mean EF magnitude on the ribbed wall. Zoom of bottom wall, downstream of the 4$^{th}$ rib.*

One of the most important things to remark is that these contours are not completely symmetric, as it could have been expected and required. This imperfect result must be

attributed to the fact that thermal inertia of the solid part is very high and the convergence of the thermal variables within the solid is much slower than the convergence of aerodynamic ones. This problem surfaced again in the final part of the research and will be reviewed in chapter 17 and Annexes K and I.

More details of the distribution of EF can be remarked in *figure 8.11*, which shows two views of the distribution of EF over the ribbed wall. The downstream looking view *a* puts in evidence the high EF on the upstream face of the rib and its maximum on the upstream corner itself; the upstream looking view *b* shows that the separation downstream of the rib causes low EF values on the downstream face of the rib, with the minimum at the bottom corner. Both the views put in evidence the strong 3 D behavior of the heat transfer and the strong effect of the side walls.

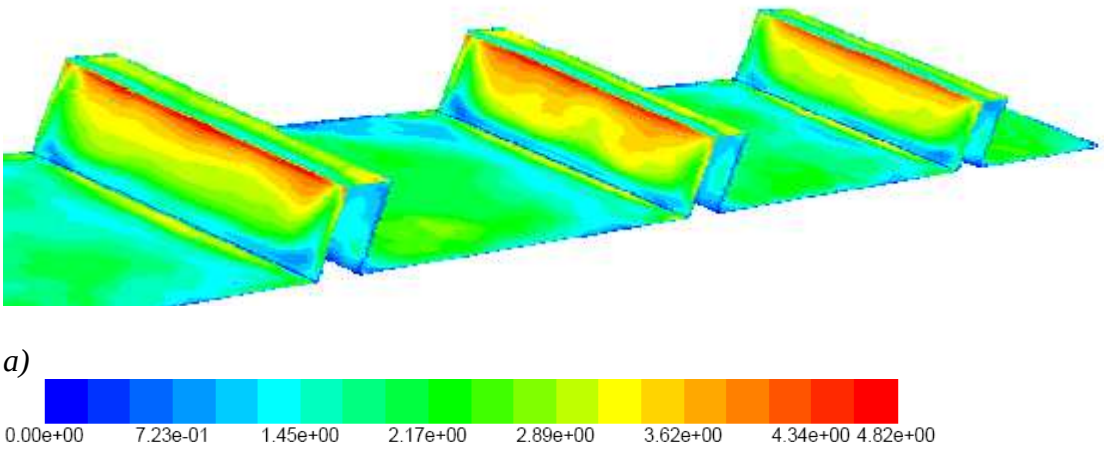


*a)*

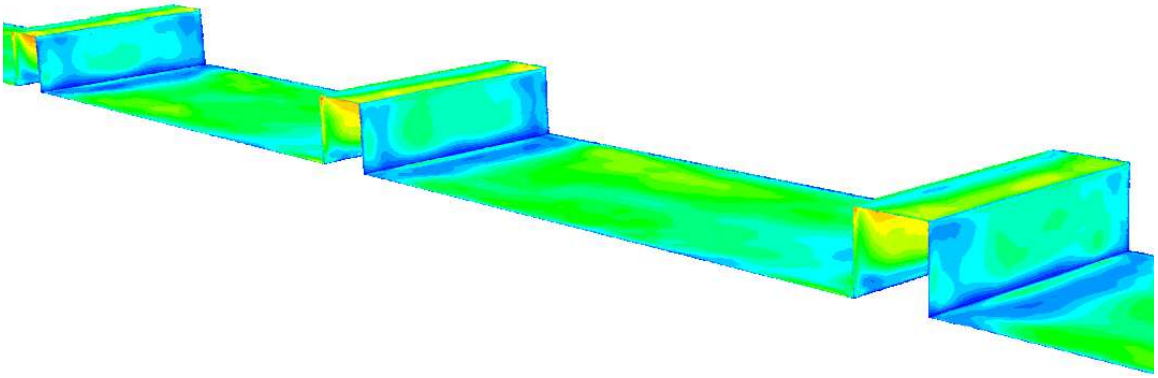

*b)*

*Figure 8.11 Contours of EF for the last 3 ribs; a) downstream looking view, b) upstream looking view*

In order to have a better understanding of the effect of the rib and of the maximum and minimum magnitude values location around the ribs, the profile of EF for the symmetry line is plotted in the *figure 8.12* below. The results on the 3rd and 4th rib are zoomed and analyzed in detail. These graphs confirm and precise the previous observations.
It is obviously to see that the profile of the EF is almost similar over both 3rd and 4th rib which allows concluding that this result is representative of the behavior of established conjugate heat transfer. In this choice of $T_{ref}$ the maximum value found lies about 4.5 and it is reached at the leading edge corner of the rib (see *figure 8.11 a*, the "spike" shape of the trace being due to the limit of resolution of the grid). The other local maxima are located values on the top face of the rib and downstream the rib in correspondence of the position of the reattachment points of the recirculation bubbles. On the bottom wall the maximum of EF is located around the symmetry line between the interval 2 < X/h < 8

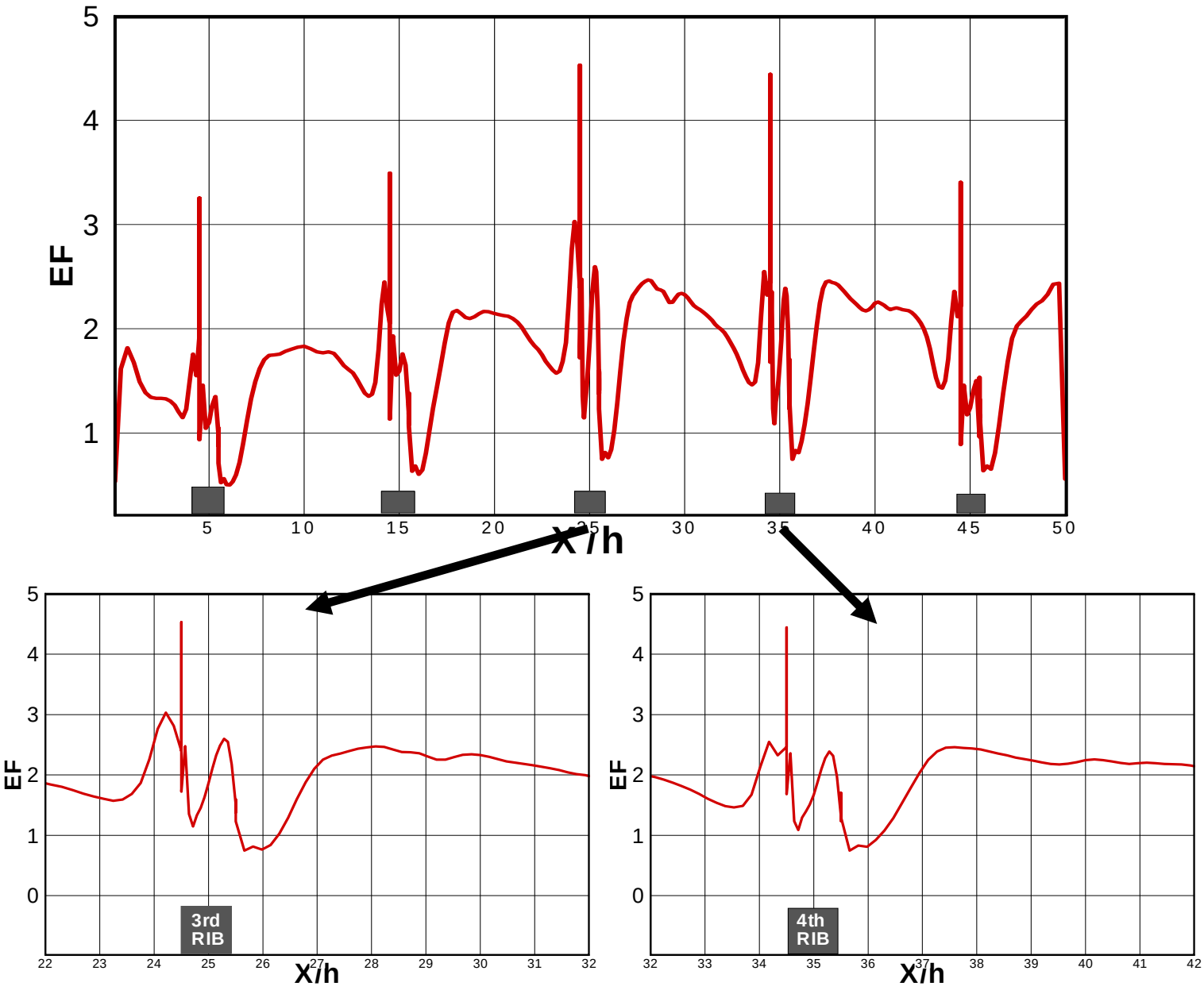

*Figure 8.12 EF profiles over the 3rd and the 4th rib.*

*Figure 8.13* presents the EF on the symmetry line of the 4th rib against the result of the Infrared Camera and the previous LES simulation [4]. The present definition of *symmetry line* corresponds to the *perimeter* of the interface of the symmetry 1XY plane; therefore represents, on one single line (from the left to right) the upstream bottom wall, the upstream face of the rib, the top face of the rib, the downstream face of rib and downstream bottom. The zero position corresponds to the centre of the rib. Therefore, the locations +/- 0.01125 correspond to the upstream and downstream corners, respectively, while the locations +/- 0.03375 correspond to the concave corner bottom wall-rib.

From *figure 8.13* it can be remarked that the two available simulations present the same patterns even if the absolute values are different. This difference is due to different definitions of $T_{ref}$ , issue which will be addressed later on. It can be remarked that present results do not contain negative EF values, which had been presented a major question mark for the previous simulation [11]. This result can be attributed to the better quality of the grid and enhances the confidence of the present simulation.

The present simulation reproduces the experimental trends, although the uncertainty concerning the choice of $T_{ref}$ makes difficult to compare the actual value. The present choice $T_{ref}$ =288.16 K yields maximal values (~ 4.5) LES comparable to the ones obtained from Infrared Camera measurements. The most important discrepancy (marked as an ellipse in the figure) is that the simulations both predict a high EF in correspondence of the upstream recirculation region. This is probably due to the fact the size of this region is quite different in PIV and in simulations, which leads to a different rates of heat transfer.

The qualitative agreement between the 2 different independent LES simulations leads to think the present discrepancy with the experimental patterns could be related to the sub-grid model or the wall condition instead to be attributed to the resolution of the grid.

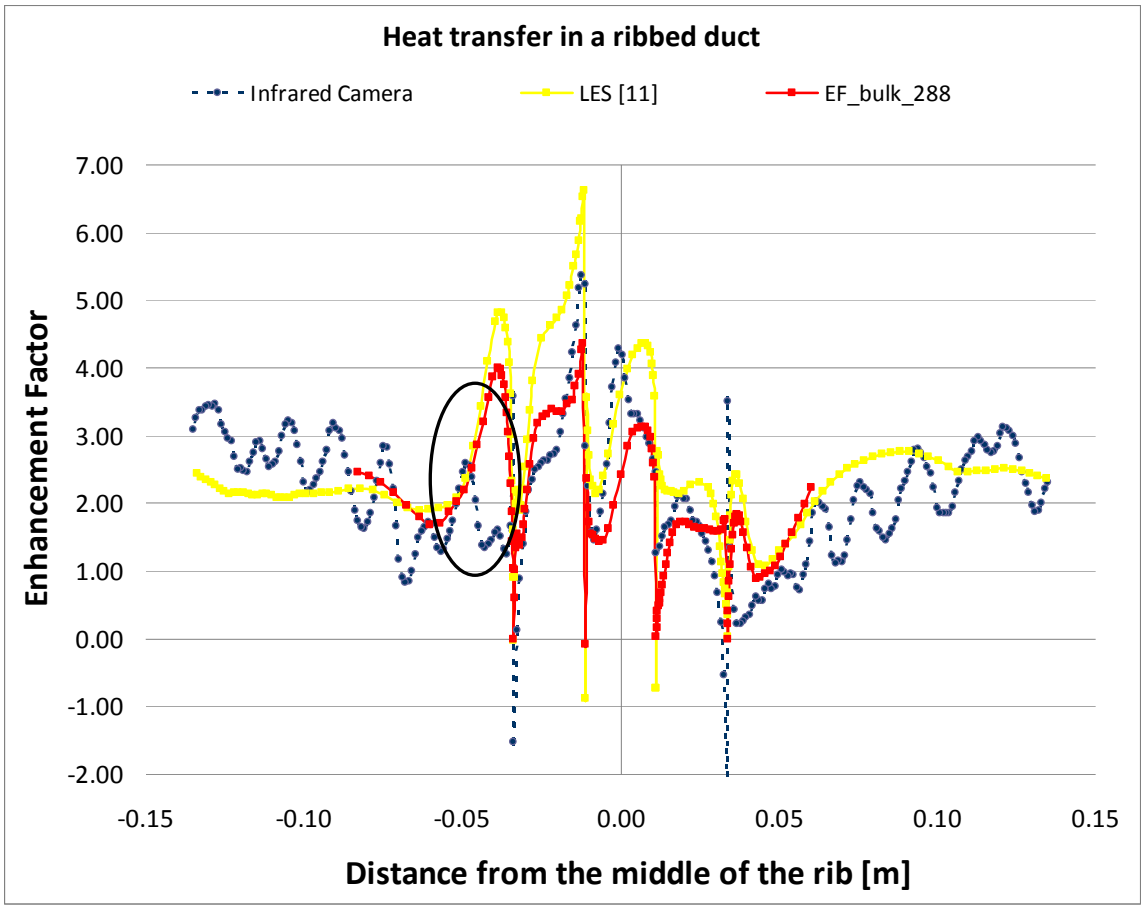


*Figure 8.13. Comparison of the symmetry line EF profiles over the 4$^{th}$ rib.*

## *8.3 Evaluation of the definition of Enhancement Factor EF*

The uncertainty present in the definition of the EF has led to investigation of the sensibility to this parameter and the search of the most consistent definition.

This investigation must begin from the straightforward approach for the determination of the heat transfer coefficient, which can be obtained applying the well known Newton formula:

$$\Gamma = \frac{q_{s,ave}(x,y)}{(T_w - T_b)}$$

where $q_{s,ave}$ is the time averaged heat flux at the surface, $T_w$ is the time averaged wall temperature and $T_b$ is the bulk temperature. The local values of $q_{s,ave}$, $T_w$ and $T_{ref}$ are available from the numerical simulations, using the standard capabilities of the FLUENT® postprocessor. However, as already remarked, different choices can be adopted for the determination of the temperatures $T_w$ and $T_{ref}$ leading to different values of *Nu* and, thus, EF.

The need of a unique definition of the heat transfer coefficient has motivated an attempt to identify the most suited approach for the calculations of the enhancement factor (EF), also taking into account the procedures adopted in the experimental campaign carried out in parallel with the numerical simulations.

Specifically, the following definitions of $T_w$ and $T_{ref}$ have been tested and compared:
*Definition I:* $T_w$ determined as the area-weighted average of the time-averaged wall temperature, $T_{ref}$ calculated as the volume-average of the time-averaged fluid temperature.
*Definition II:* $T_w$ determined as the area-weighted average of the time-averaged wall temperature, $T_{ref}$ calculated as the mass-weighted average of the time-averaged fluid temperature at the inlet section.
*Definition III:* $T_w$ determined as the area-weighted average of the time-averaged wall temperature, $T_b$ taken as a reference temperature, i.e. 288K.
*Definition IV:* $T_w$(x,y) taken as the local temperature at the duct wall. $T_{ref}$ (x) is extracted from the experimental campaign. Due to numerical reasons, it is advisable to extract the local time-averaged wall temperature from the cell centroid adjacent to the face defining the wall boundary conditions, on the solid domain side. This procedure ensures that the extracted temperature is a *true* wall temperature, unbiased by the heat exchange on the fluid side. This is further confirmed by the solid and fluid temperature profiles at the 4$^{th}$ rib (*figure 8.14*), x=0.76125 m and z=0.0375 m.
*Definition V:* $T_w$(x,y) taken as the local temperature at the duct wall. $T_{ref}$(x) is extracted from the numerical simulations. The fluid bulk temperature is extracted from the numerical simulations, outside the region interested by the heat exchange between the fluid and the hot surface. With reference to Figure *8.14*, it is clear how the fluid temperature profile over the vertical coordinate y=0.03 m is almost flat and constant up to the upper wall of the duct. Such procedure ensures that only the actual driving force for the heat transfer at the walls is taken into account for the determination of the heat transfer coefficient.

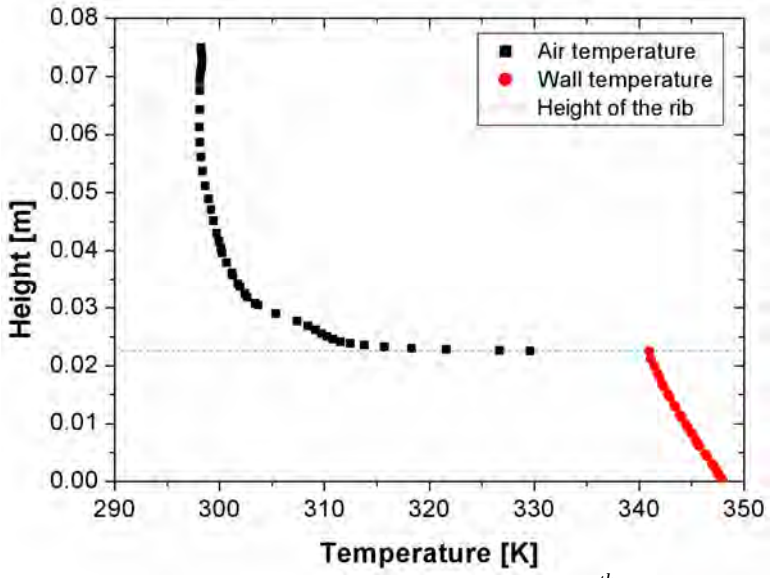


*Figure 8.14 – Temperature profile inside the 4$^{th}$ rib and in the fluid region up to the duct wall along the center-line, z=0.0375 m, at an axial distance x=0.76125 m.*

Finally, another possible definition of the heat transfer coefficient has been tested. Specifically, from the global heat transfer equation:

$$Q_{heat} = \Theta \cdot A \cdot \Delta T_{\ln}$$

it is possible to define a *global* heat transfer coefficient as

$$\Theta = \frac{Q_{heat}(x,y)}{A \cdot \Delta T_{\ln}} = \frac{q(x,y)}{\Delta T_{\ln}}.$$

The above description naturally leads to the last definition of the temperatures $T_w$ and $T_{ref}$.

*Definition VI:* The time-averaged fluid temperature is mass-averaged upstream and downstream the selected rib, to obtain an inlet and outlet value, $T_{ref,1}$ and $T_{ref,,2}$. Similarly, two temperature levels are extracted for the wall temperature, $T_{w,1}$ and $T_{w,2}$, averaging over two lines drawn upstream and downstream the rib. Then, a logarithmic mean temperature is calculated and the Newton formula is retrieved to obtain an estimate of the heat transfer coefficient.

*Figure 8.15* shows the EF values at the centre-line, z=0.0375 m, along a curvilinear coordinate centered at the rib mid-plane, obtained using the different definitions provided above. *Figure 8.15* clearly indicates that definitions I-III and VI results in a global over-prediction of the EF values, especially moving away from the rib mid-plane. This can be probably ascribed to the averaging of the wall temperature, $T_w$, which results in an under prediction of the temperature levels upstream and downstream the rib. Definition IV and, in particular, V, provide a better level of agreement between experimental data and numerical simulations. This could be expected, since definitions IV and V are similar to the procedure followed in the experimental campaign for the acquisition of the measurements. In particular, definition V appears the one providing the most solid conceptual basis for an effective comparison with experiments. In conclusion, it should be underlined that the EF values obtained from the numerical simulations are significantly higher than the measured ones in the regions adjacent to the rib vertical walls. This appears to be independent of the definition used to calculate EF, the over prediction being observed in all cases, and it is probably due to discrepancies in the prediction of the flow fields between numerical simulations and experiments. In particular, the existence of low velocity recirculation zone near the wall, which is not fully captured by the numerical simulations, could explain the low EF values indicated by the experimental campaign and the higher ones provided by the numerical simulations.

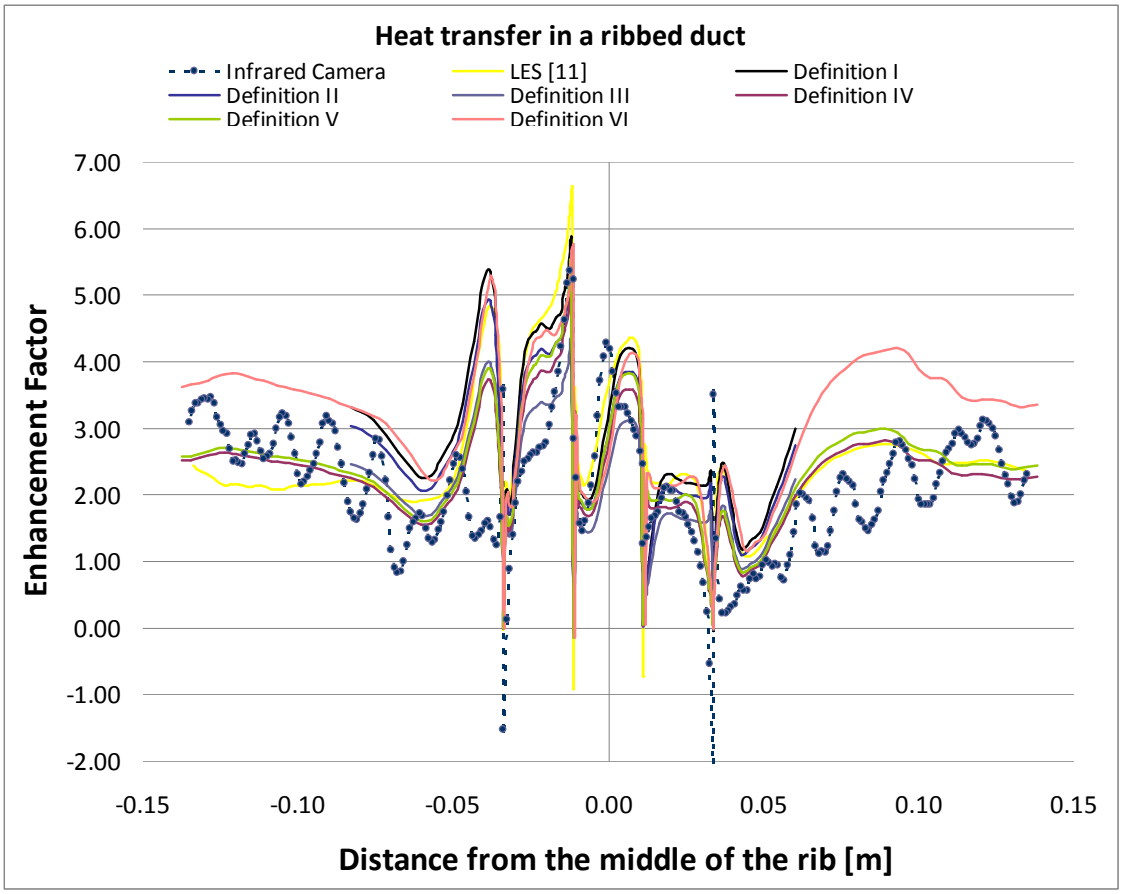


*Figure 8.15 – EF values at the center-line, z=0.0375 m, along a curvilinear coordinate centered at the rib mid-plane.*

To conclude: on one side, the choice of $T_{ref}$ for estimation of EF does not influence the investigation of the correlation between flow field and heat transfer to be presented in Chapter 9, because the analysis there presented is qualitatively and independent of the actual absolute value of EF; on the other side, it can be concluded that the definition V appears the one most suitable for quantitative comparison with the experimental data.

# CHAPTER 9 Aero-Thermal Investigation

## *9.0 Introduction*

The main aim of this chapter is to find out the correlations which might exist between the aerodynamic and the thermal fields and which might lead to a better comprehension of the present coupled (fluid-solid) problem, in order to identify the mechanisms which drive the Heat Transfer enhancement on the ribbed wall. Therefore, the correlation between EF and respectively the wall shear stress, the turbulent kinetic energy, the turbulent shear stress, while the possible role of the coherent structures will be taken investigated.

## *9.1 Wall shear stress vs. EF correlation*

A comparison between the $C_f$ and 3 EF profiles extracted from the ribbed wall is shown in the *figure 9.1* below. It can be remarked that the 3 profiles present the same trends and that the mean skin friction coefficient and the EF appear to be correlated in all the vertical XY planes; roughly the maxima of EF correspond to minima of $C_f$. Examining the profiles in detail, it can be remarked the presence of negative $C_f$ values, which represent regions of recirculation and that EF reaches its highest values in these regions; the positions of minima of $C_f$ correspond to the centre of the recirculation motions: upstream, on and downstream of the rib and. A local maximum of EF appears around the reattachment point where ($C_f$ =0). This effect is due to the fact that the sheared layer created by the rib impacts the bottom wall in this area causing an increase in the heat transfer at this region (*figure 8.8, 8.10*) is observed.

It can be remarked that the same trends can be observed in all the 3 XY planes, which justifies limiting the following analysis to the symmetry plane.

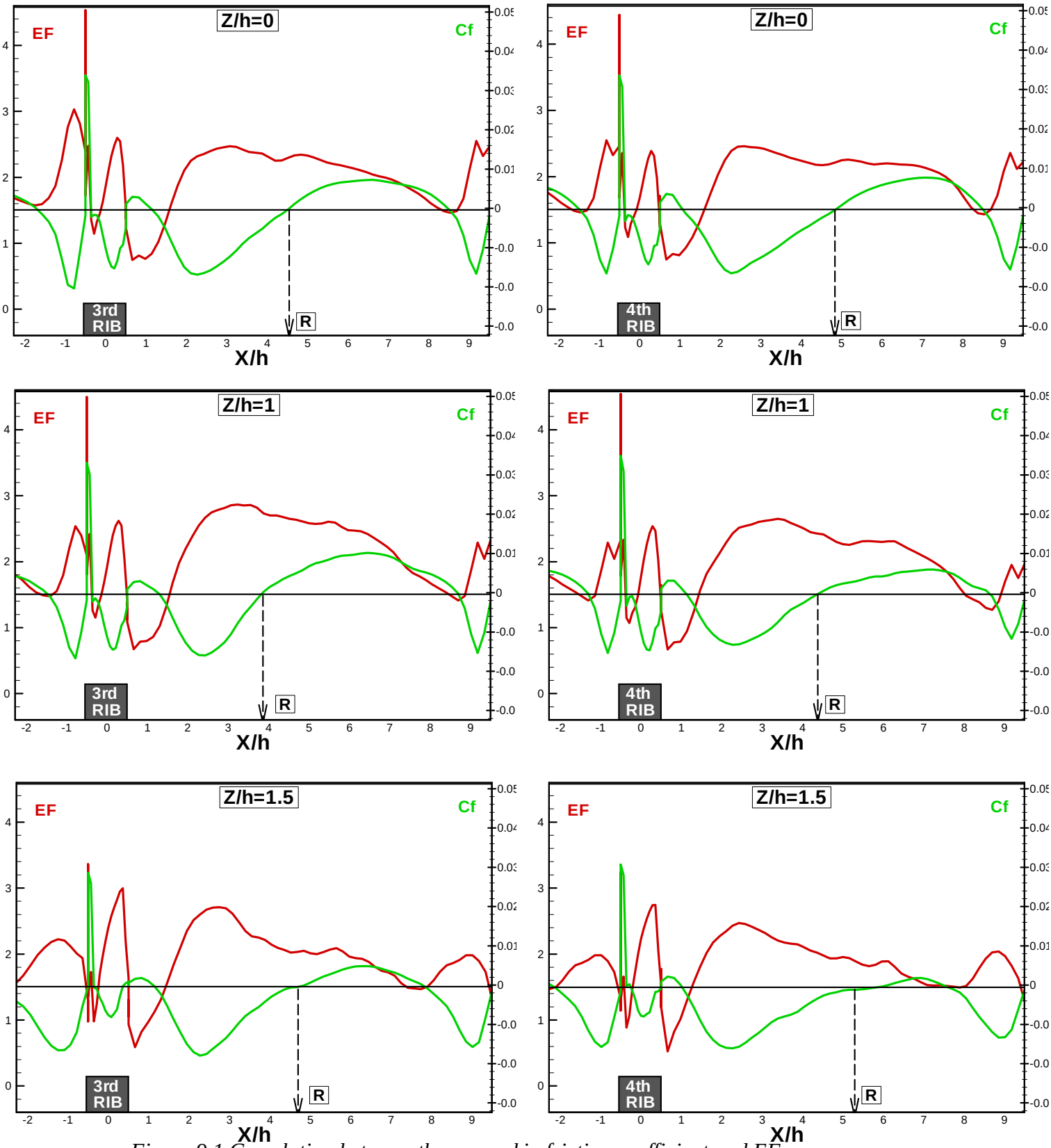


*Figure 9.1 Correlation between the mean skin friction coefficient and EF*

## *9.2 Turbulent shear stress vs. EF correlation*

The previous observations concerning the correlation between $C_f$ and EF were verified focusing on the resolved turbulent shear stresses which represent the most important contribution to the wall shear stress. *Figure 9.2* presents the distribution of stream-wise/vertical $\langle u'v' \rangle$, stream-wise/span-wise $\langle u'w' \rangle$ and vertical/span-wise $\langle v'w' \rangle$, for the line $Y/h$=0.05 ($y$+~30 away from the wall) of the symmetry plane. This line lies within the wall layer. The EF is estimated on the bottom wall A correlation between $\langle u'v' \rangle$ and EF can be remarked, which is similar to the one between $C_f$ and EF, while the others components of shear stresses instead fluctuate around zero. Therefore, it appears that, in the wall layer the shear stresses defined by the stream-wise/vertical velocity fluctuations $\langle u'v' \rangle$ seems to be the single one affecting most the heat transfer enhancement. It is obvious that maximum negative values are related to an increased EF.

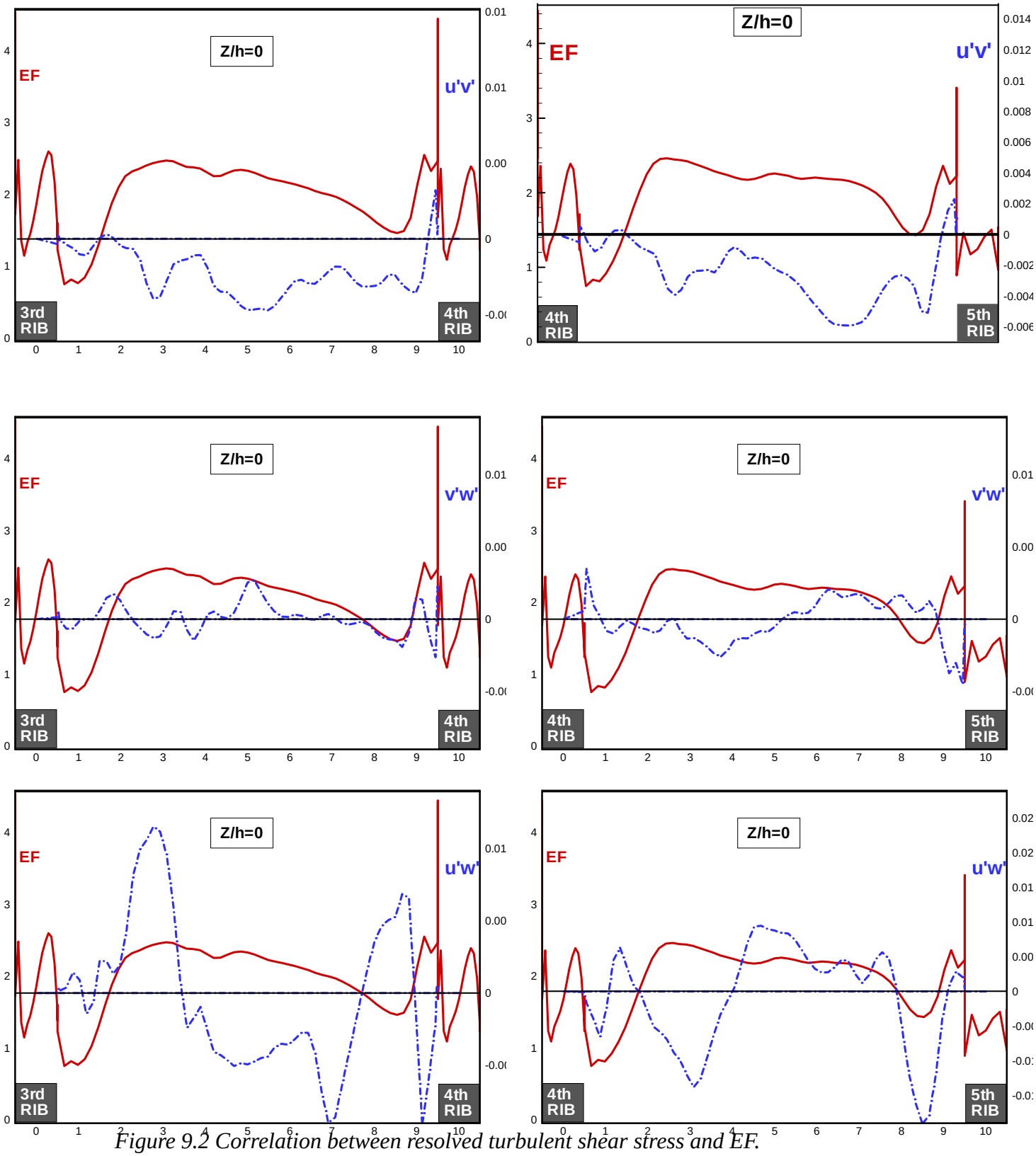


*Figure 9.2 Correlation between resolved turbulent shear stress and EF.*

## *9.3 Turbulent kinetic energy k vs. EF correlation*

It is attempted to put in evidence the effect of the turbulent velocity fluctuations on EF. The most suitable global parameter to be associated the turbulent field is the intensity of the turbulence *k* which corresponds to the square root of the resolved Turbulent Kinetic Energy (TKE), sum of the variances of the three normal stresses Tensor resolved stresses. ***k*** is defined as:

$$k = .5(<(u'u')^2> + <(v'v')^2> + <(w'w')^2>)$$

The comparison is presented in *figure 9.3* for Y*/h=0.05* line of the symmetry plane. A very good correlation between the two quantities is found in the entire domain, even on the rib itself, as it is put in evidence by the zoom on the 3rd and 4th rib.
This conclusion was verified comparing the EF on the bottom wall with the individual resolved normal stresses <*u'u'*>, <*vv'*>, <*w'v'*> for the same line (*figure 9.4*). The trends are comparable, but the correlation is weaker than the previous case, which confirm that *k* (or TKE) is the best suitable macroscopic parameter to understand the interaction between EF and the turbulent field.
The tentative conclusion is the turbulent mixing (which is directly related to the turbulent intensity) is the physical process driving the coupling the conjugated heat exchange.

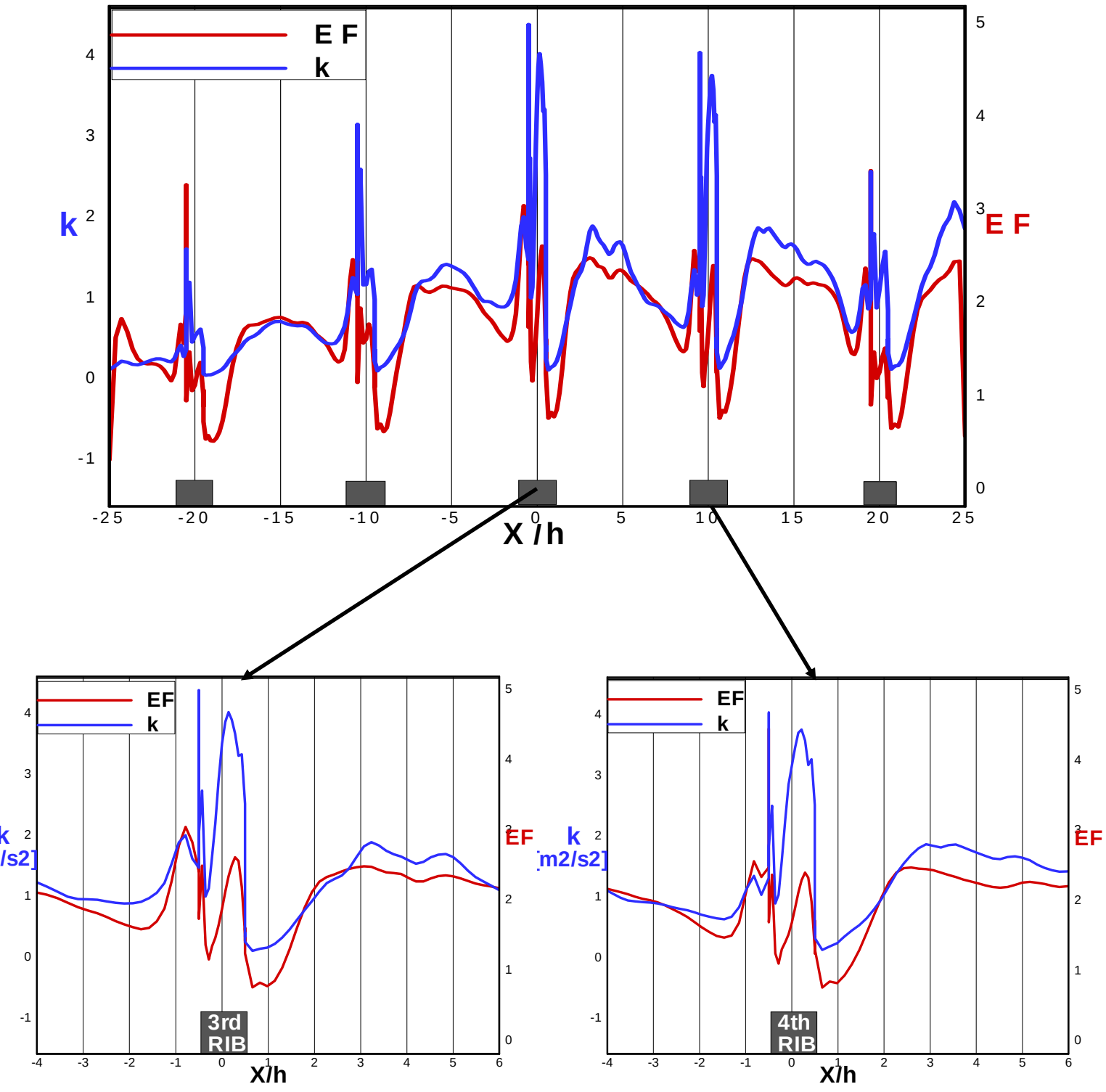


*Figure 9.3 Correlation between resolved turbulent kinetic energy k and EF*

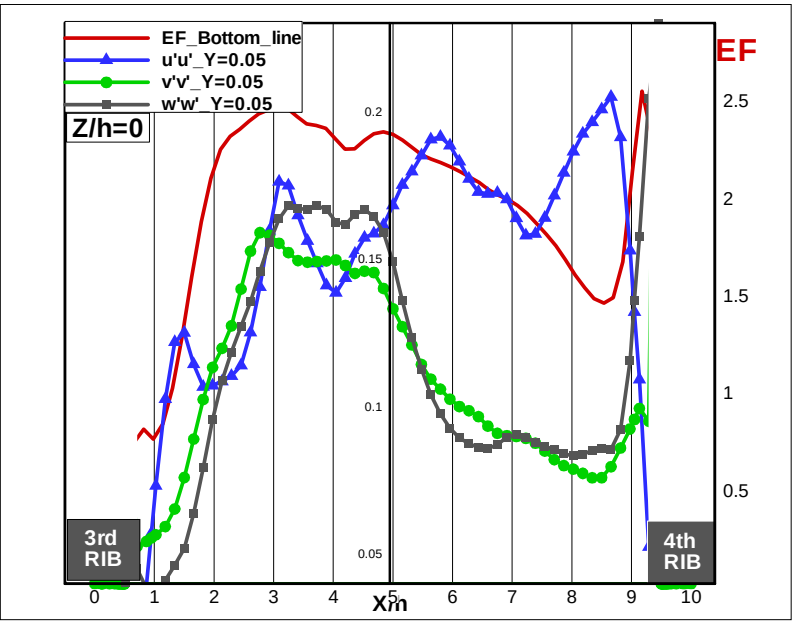


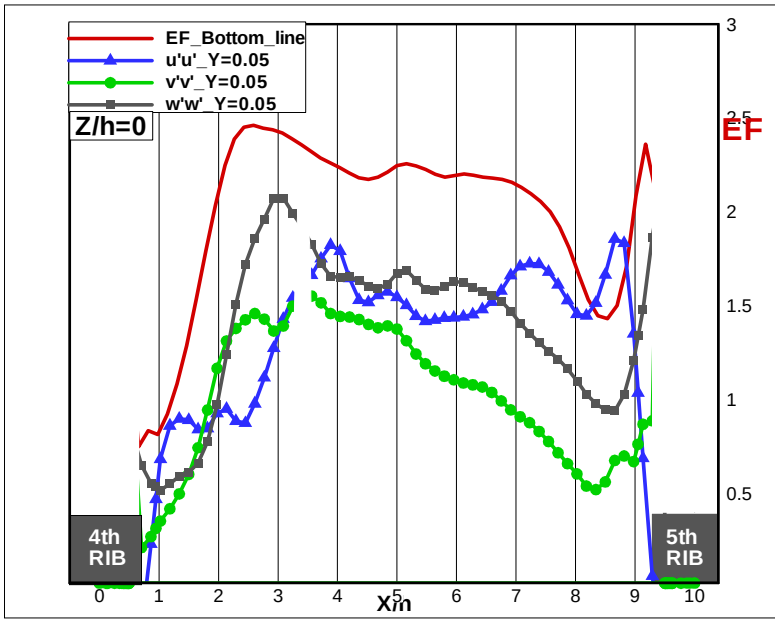


*Figure 9.4 Correlation between resolved turbulent normal stresses and EF*

## *9.4 vorticity vs. EF correlation*

One main aim of the present investigation is to highlight the role of the coherent structures [17] in conjugate heat transfer. As the vorticity $\left|\vec{\Omega}\right|$ is the main dynamic parameter characterizing the coherent structures [19], a preliminary step is to investigate the interaction between EF and the module of the vorticity $\left|\Omega\right|$.

*Figure 9.5* shows the correlation between the average module of the vorticity at the wall and EF and puts in evidence the strong correlation between the 2 parameters.

To gain a better understanding of this interaction $\left|\Omega\right|$ has been made non dimensional against $D_h / U_{bulk}$ and re-plotted for the single 4th rip span in *figure 9.6*.

*Figure 9.6* highlights that the patterns of $\left|\Omega\right|$ / [$U_b/D_h$] fully match the one of EF, which could be expected as they depend, respectively, of the gradient of velocity and of the temperature at the wall.

This trend supports two tentative conclusions:

an accurate representation of flow-field close to the wall (*i.e. gradients at the wall*) is of paramount importance for the understanding of the conjugated heat exchange and fully justifies further effort to improve the simulation

the vorticity could an important effect on the physical process driving the conjugated heat exchange the, justifying the further effort in the investigation of the effect of coherent structures (*which transport the organized part of the vorticity*) on this process.

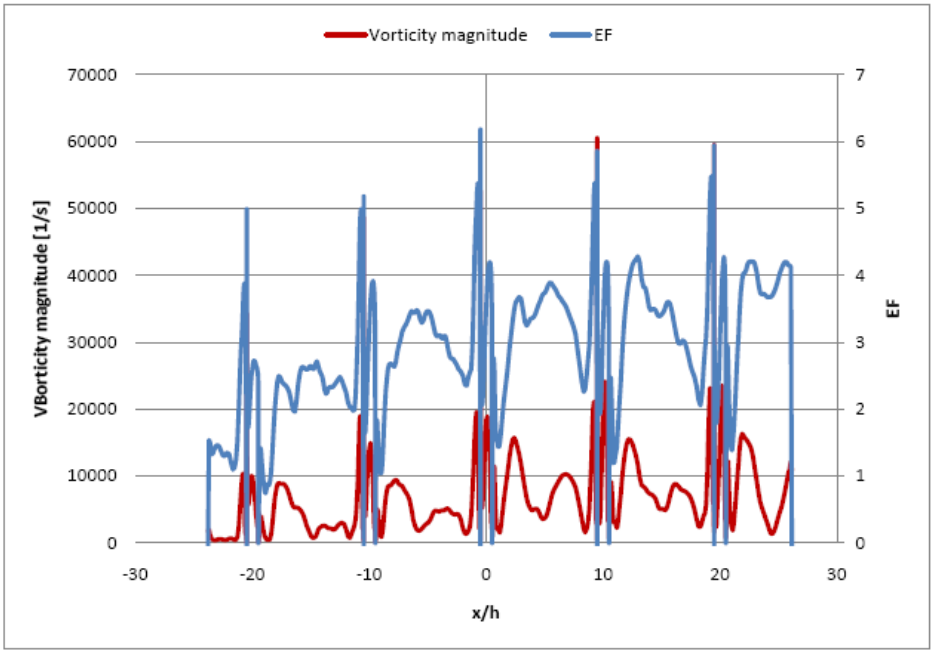


*Figure 9.5 Correlation the average module of the vorticity at the wall and EF*

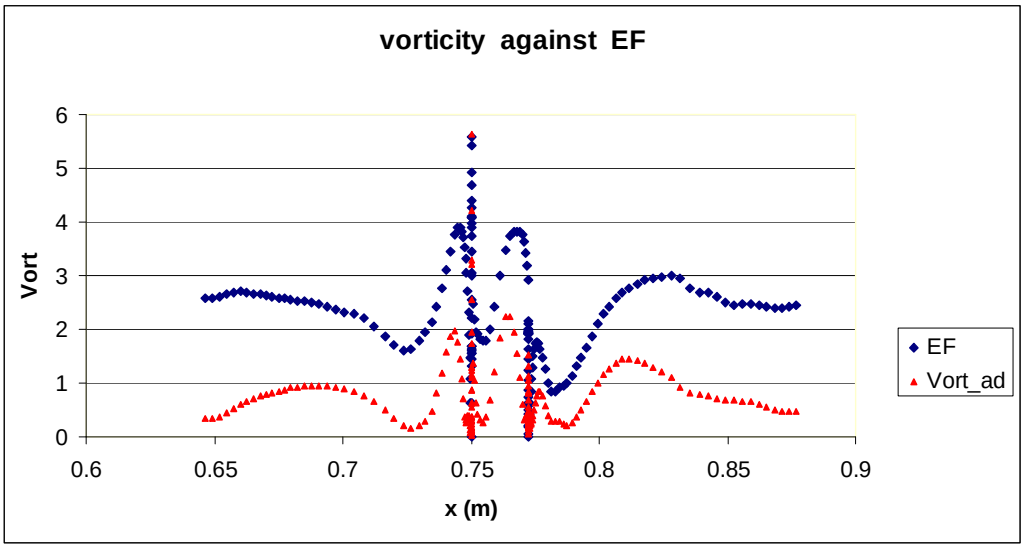


*Figure 9.6 Correlation the average module of the non dimensional vorticity at the wall and EF over the 4$^{th}$ pitch*

## *9.5 Conclusion for the investigation of the aerothermal field*

The thermal field obtained in the present simulation was been post-processed in the attempt to put in evidence the interaction between heat transfer and flow field. Close matching was found between EF and the resolved turbulent kinetic energy **k** in the wall layer and between EF and the vorticity at wall. Further simulations and further post-processing will be performed in the frame of the following Work Package to understand the mechanics of this interaction and quantify this effect.

# *Part IV Investigation of the role of the Coherent Structures*

# CHAPTER 10 Coherent Structures and Heat Transfer

## *10.1 Rotating structures (Q-criterion)*

If one refers to the comment of Professor P. Moin (Stanford University) on the nature of the turbulence:

***"Frustration results largely from the mixture of chaos and order and the wide range of length and time scales that turbulent flows possess."***

It is then likely that the "***order***" part of the mixture can be associated with the presence in the flow of Coherent Structures (CS), for which the most common definition can be:

> ***"3-D region of the flow over which at least a fundamental flow variable exhibits significant correlation with itself or another one over a range of space and/or time significantly larger than the smallest local scales of the flows"***

It is possible to make some interesting observations on the aero-thermal flow behavior combining the heat transfer data shown in the chapter 8 and the coherent structures extracted from the LES [13].

Different methods are available for the detection of rotating structures (vortices) in wall bounded flow [18], but the most widely used is the *Q-criterion* developed by Hunt et al. [19], which works locating the regions where rotation dominates strain in the main flow. This concept is implemented defining a scalar $Q$ on the flow, where rotating structures correspond to a certain value of this scalar. $Q$ can be also defined as the second invariant of $\vec{\nabla}\vec{U} = \overrightarrow{\overrightarrow{grad}U}$, given for incompressible flow by:

$$Q = \frac{1}{2}\left(\Omega_{ij}\Omega_{ji} - S_{ij}S_{ji}\right)$$

$S_{ij}$ is the strain tensor which represents the deformation (symmetric part of $\vec{\nabla}\vec{U}$)

$\Omega_{ij}$ is the asymmetric part of $\vec{\nabla}\vec{U}$ and it is related to the rotation of the fluid As we can see from its definition the scalar $Q$ is a balance between the squared rotation rate $\Omega^2 = \Omega_{ij}\Omega_{ji}$ and the squared strain rate $S^2 = S_{ij}S_{ji}$. Isosurfaces with positive values of $Q$, show sub-flows with rotation rates bigger than strain ones and this is what are defined as coherent structures. The mathematical definitions of $S_{ij}$ and $\Omega_{ij}$ are:

$$S_{ij} = \frac{1}{2}\left(\frac{\partial U_i}{\partial x_j} + \frac{\partial U_j}{\partial x_i}\right) \qquad \Omega_{ij} = \frac{1}{2}\left(\frac{\partial U_i}{\partial x_j} - \frac{\partial U_j}{\partial x_i}\right)$$

And for Cartesian coordinates we obtain:

$$S_{ij}=\begin{pmatrix} \frac{\partial u}{\partial x} & \frac{1}{2}\left(\frac{\partial u}{\partial y}+\frac{\partial v}{\partial x}\right) & \frac{1}{2}\left(\frac{\partial u}{\partial z}+\frac{\partial w}{\partial x}\right) \\ \frac{1}{2}\left(\frac{\partial u}{\partial y}+\frac{\partial v}{\partial x}\right) & \frac{\partial v}{\partial x} & \frac{1}{2}\left(\frac{\partial v}{\partial z}+\frac{\partial w}{\partial y}\right) \\ \frac{1}{2}\left(\frac{\partial u}{\partial z}+\frac{\partial w}{\partial x}\right) & \frac{1}{2}\left(\frac{\partial v}{\partial z}+\frac{\partial w}{\partial y}\right) & \frac{\partial w}{\partial x} \end{pmatrix} \qquad \Omega_{ij}=\begin{pmatrix} \frac{\partial u}{\partial x} & \frac{1}{2}\left(\frac{\partial u}{\partial y}-\frac{\partial v}{\partial x}\right) & \frac{1}{2}\left(\frac{\partial u}{\partial z}-\frac{\partial w}{\partial x}\right) \\ \frac{1}{2}\left(\frac{\partial u}{\partial y}-\frac{\partial v}{\partial x}\right) & \frac{\partial v}{\partial x} & \frac{1}{2}\left(\frac{\partial v}{\partial z}-\frac{\partial w}{\partial y}\right) \\ \frac{1}{2}\left(\frac{\partial u}{\partial z}-\frac{\partial w}{\partial x}\right) & \frac{1}{2}\left(\frac{\partial v}{\partial z}-\frac{\partial w}{\partial y}\right) & \frac{\partial w}{\partial x} \end{pmatrix}$$

$$\Omega_{ij}\Omega_{ji}=0+0+0+\frac{1}{2}\left(\frac{\partial u}{\partial y}-\frac{\partial v}{\partial x}\right)^2+\frac{1}{2}\left(\frac{\partial u}{\partial z}-\frac{\partial w}{\partial x}\right)^2+\frac{1}{2}\left(\frac{\partial v}{\partial z}-\frac{\partial w}{\partial y}\right)^2$$

$$S_{ij}S_{ji}=\left(\frac{\partial u}{\partial x}\right)^2+\left(\frac{\partial v}{\partial y}\right)^2+\left(\frac{\partial w}{\partial z}\right)^2+\frac{1}{2}\left(\frac{\partial u}{\partial y}+\frac{\partial v}{\partial x}\right)^2+\frac{1}{2}\left(\frac{\partial u}{\partial z}+\frac{\partial w}{\partial x}\right)^2+\frac{1}{2}\left(\frac{\partial v}{\partial z}+\frac{\partial w}{\partial y}\right)^2$$

$$Q=\frac{1}{2}\left(\Omega_{ij}\Omega_{ji}-S_{ij}S_{ji}\right)=-\left[\left(\frac{\partial u}{\partial x}\right)^2+\left(\frac{\partial v}{\partial y}\right)^2+\left(\frac{\partial w}{\partial z}\right)^2+\left(\frac{\partial u}{\partial y}\frac{\partial v}{\partial x}\right)+\left(\frac{\partial u}{\partial z}\frac{\partial w}{\partial x}\right)+\left(\frac{\partial v}{\partial z}\frac{\partial w}{\partial y}\right)\right]$$

The principal investigators previously applied the *Q* criterion average field (<*Q*>) to obtain a complete view of the permanent vortex region in the domain [4, 20 and 21], which represent the footprint of the CS in the average domain. A complete conceptual model of the average flow was proposed and is presented in *figure 10.1*. This model will guide the following investigation.

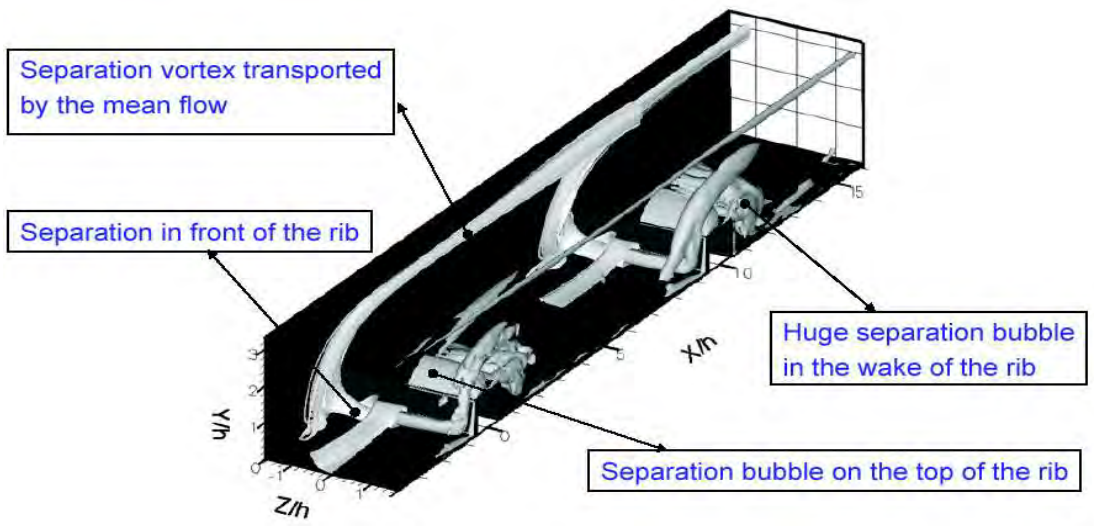


*Figure 10.1 Streamtraces (Z negative) and coherent structures extracted from the mean flow (Z positive) [4]*

The composite *figure 10.1* presents two views, showing, for the average flow field, the *Q* iso-surface and the stream surface emitted from a line (X/*h*=-1.08; Y/*h*=0.05; -1.6<Z/*h*<0). Both representations underline the importance of the structure resulting from the upstream separation on the ribbed wall, which is lifted up close to the sidewall by the upward motion and which arches over the rib.
This conceptual model of the flow will be applied to help in the understanding of the thermal field.

This model allows a better understanding of trends visible in *figures 8.8 and 8.11*. Looking to the region of the primary recirculation zone, it is possible to see the effect of impact of the fluid displaced by the rib and the trace of this topology: the flow which arches over the rib (*figure10.1*) impacts the wall near the reattachment point and causes an increase of heat transfer. A part of the hot fluid is trapped within the primary recirculation bubble and the remaining part is transported and evacuated by the main flow. It can be remarked 2 regions, grossly symmetric, of high of heat transfer (*figures 8.8 and 8.10*) which correspond to the imprint of the vortex created at the lateral corner upstream the ribs (*figure10.1*).

Moving to consider the instantaneous field, the interpretation of the present results are based on the previous work of the present principal investigators, who found that different types of coherent structures can be found in the present flow cases [2 to 4]. These structures are presented in *figure 10.2*.

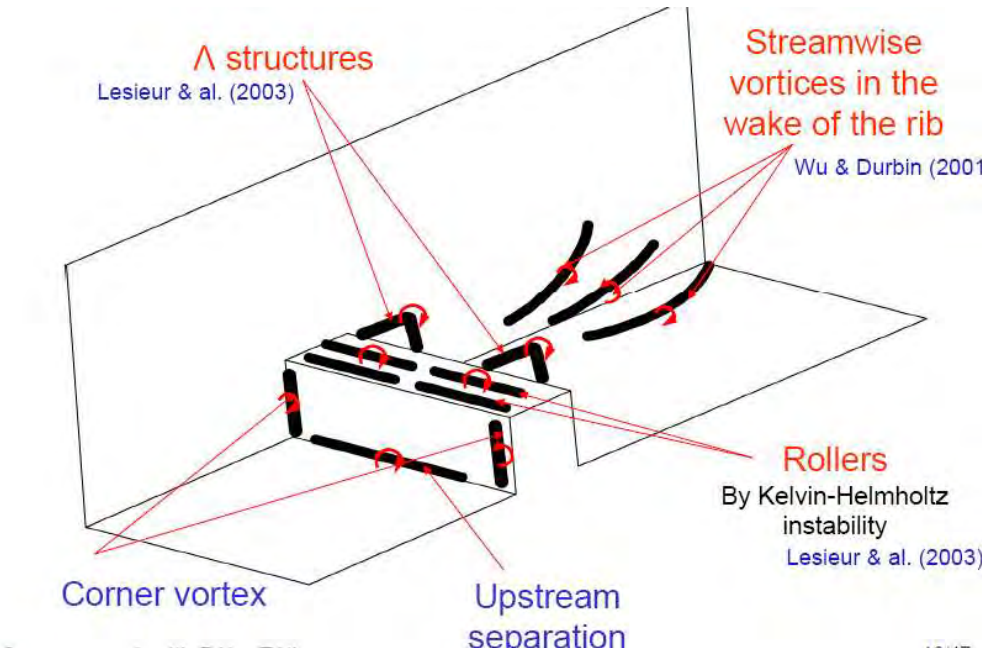


*Figure 10.2 Coherent structures identified in the present flow-field [2, 3]*

*Figure 10.3* presents a general view of the instantaneous *Q* field. It can be seen that the vortices are localized in the corner upstream the rib, over the rib and downstream the rib above the bottom wall in the region the flow re-attached itself downstream of the main separated region. It can also be observed the absence of these structures in the corner downstream the ribs, zone where the secondary clockwise recirculation zones are located.

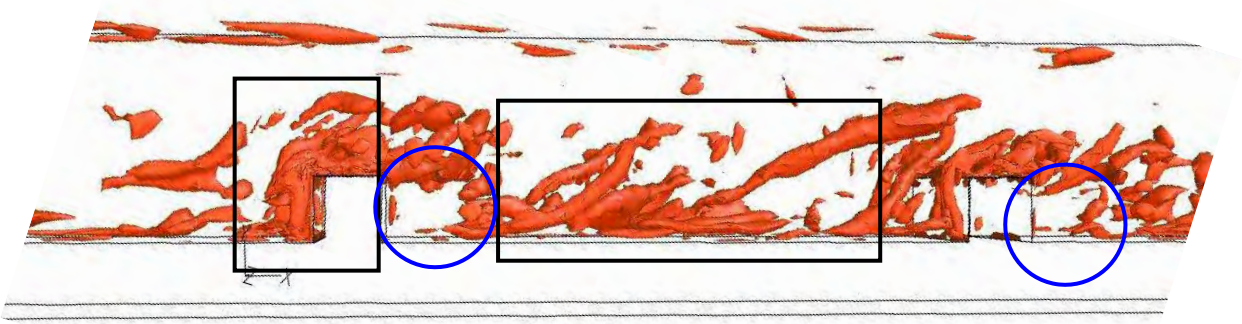

*Figure.10.3 Q=40*[$U_b^2/D_h^2$] *iso-values extracted from the instantaneous flow field. Black rectangular regions underline regions of strong presence of coherent structures; blue circles correspond to absence of structures.*

Plotting isosurfaces corresponding to higher values of *Q* (*figures 10.4*, *10.5*), it can be observed that the strongest rotating structures are situated upstream in the corner and on the top of the rib, where maximum heat transfer area can be expected

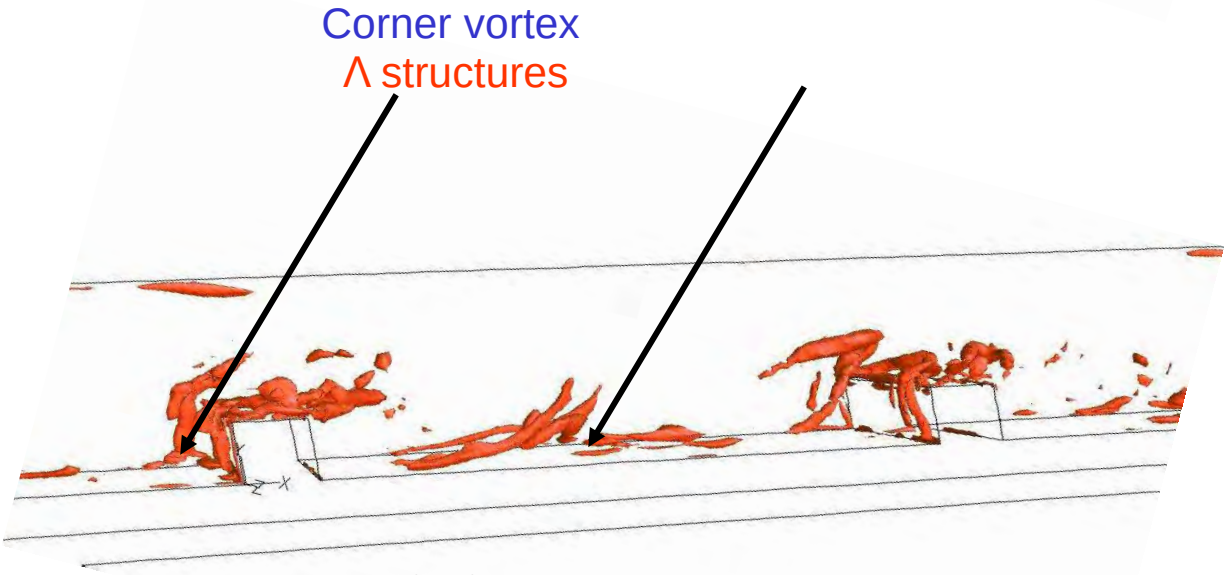


*Figure.10.4 Q=70*[$U_b^2/D_h^2$] *iso-values extracted from the instantaneous flow field*

*Figure 10.4* shows that the strongest structures are the "Corner vortex" created by the upstream separation and the Λ vortex, typical of wall layers, which develop themselves inside the boundary layer which redeveloped itself on the wall bottom downstream of the main separated region.

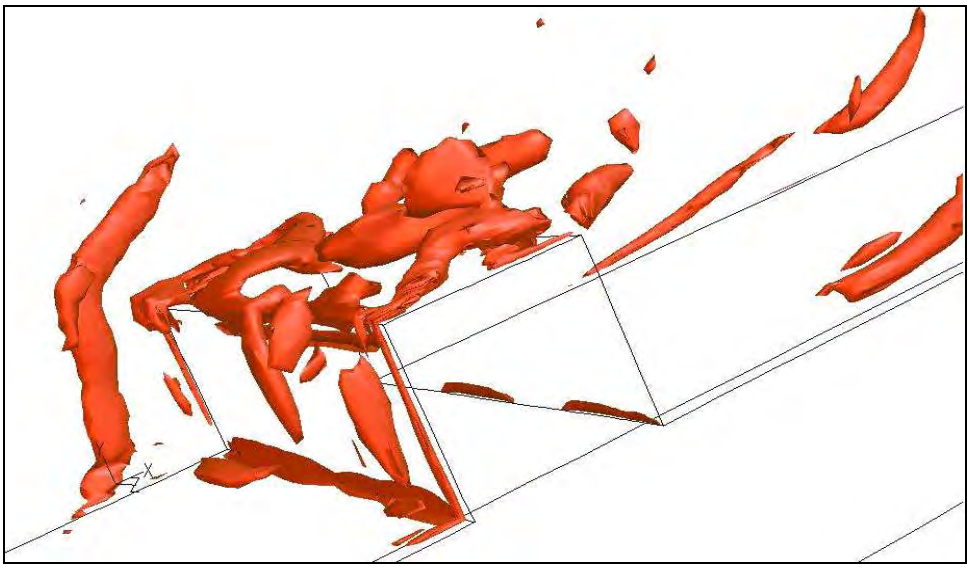

*Figure 10.5 Q=150* $[U_b^2/D_h^2]$ *iso-values extracted from the instantaneous flow field*

*Figure 10.5* presents the isosurface for the highest value of *Q* and shows the details of the organization of the structures close to the rib and confirm that they are the strongest organized structures within the domain.

## *10.2 Preliminary investigation of interaction between EF and CS*

To attempt to highlight the interaction between coherent structures and heat transfer, *figure 10.6* shows a zoom of the contours of EF on the horizontal surfaces for one a pitch interval; with comparison with *figure 8.8* the peak EF at the upstream corner has been filtered out to improve the resolution of the distribution of EF on the bottom wall and the bar of colors adjusted. Taking in account *figures 10.1* to *10.5* the trace of the effect of the coherent structures can be remarked. Upstream of the rib, the heat transfer increases in the regions where the corner vortices form themselves ("Corner vortex") on the sides and in the central region of the bottom wall where a Z-vorticity structure ("Upstream Separation) is located (*figures 10.2 and figures 10.5*). For the rib itself, a high level of EF can be seen on the top surface downstream after the centre of the recirculation bubble and in the region where flow had reattached in the wall; this process is associated with the "Rollers" vortex created by the separation on the upstream corner of the rib (*figures 10.2 and figures 10.4*). The values of EF found in this region are found to be the highest inside the entire domain, fact which can be associated by the abundant presence of the rotating structures at this region and their intensity (f*igure 10.5* and *figure 10.1*). Downstream of the rib, the lowest values of the EF are found in

correspondence of the secondary separated region, where the vortices are absent (*figure 10.3*); EF values increase moving downstream of the centre of the main recirculation zone to reach high values in the region where the attached boundary layer reforms itself on the wall and the Λ vortex are present (*figure 10.4*).
The association between the presence of coherent structures and high EF appears evident. The presence of coherent structures close a heated wall enhance heat transfer and, on the contrary their absence is associated to a minimum of EF.

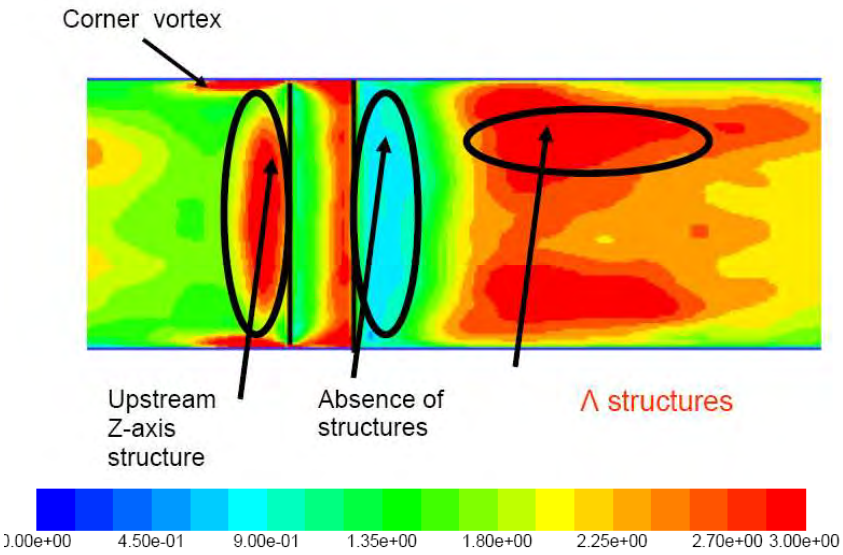


*Figure 10.6 Effect of coherent structures on EF. Bottom wall*

Focusing on the rib itself, the trace of the vortex structures is visible on the upstream face (*figure 10.7*):

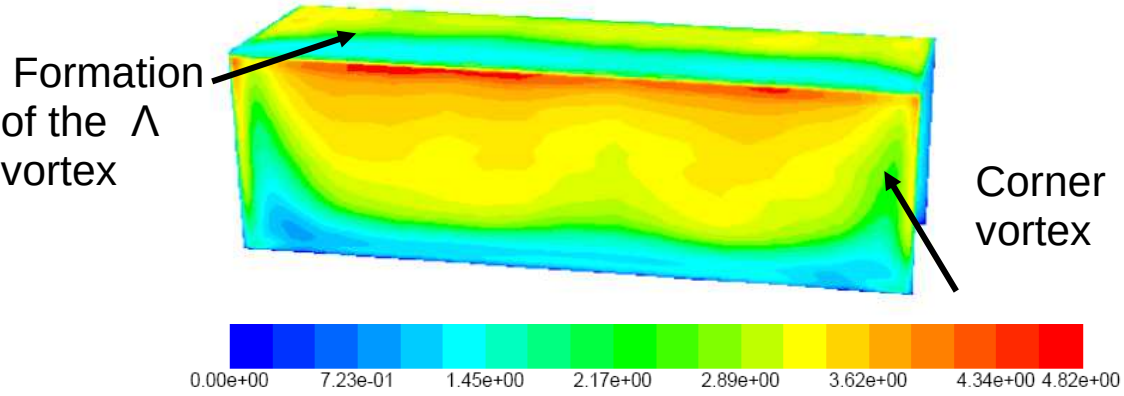


*Figure 10.7 Effect of coherent structures on EF. Upstream face of the rib*

Comparing with *figure 10.5*, the effect of the corner vortex can be remarked, as well the zone of formation of the Λ vortex (*figures 10.2 and 10.4*) on the top face. Both processes create regions of high HF.

The downstream face of the rib (*figure 10.8*) is, on the contrary, a region of low EF, coherent with the absence of organized structures (*figure 10.3*)

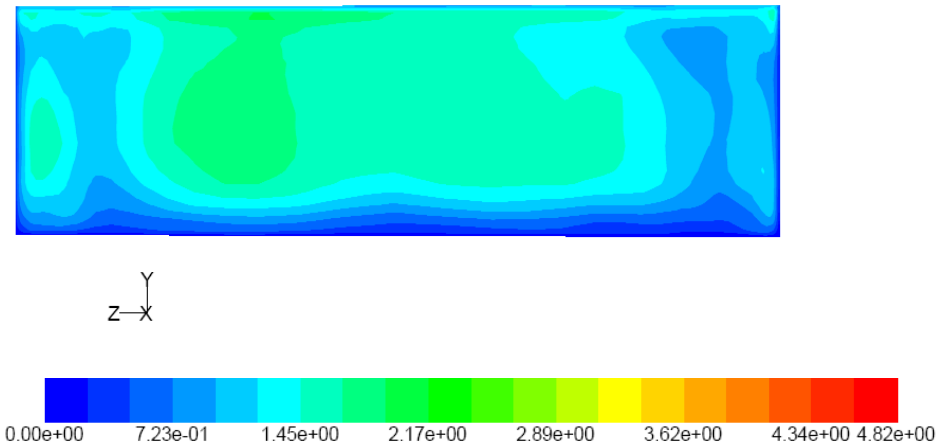


*Figure 10.8 Effect of coherent structures on EF. Downstream face of the rib*

To conclude: the interaction between coherent structures in evident. This result justifies further investigation to put in evident the mechanism of this process and quantify it effect.

A very preliminary step in this direction could be the comparison of EF with a quantity related to the averaged <*Q*>. This aim is achieved plotting difference between module of the average vorticity and average strain:

$$< Q >=< \Omega >^2 - < S >^2$$

For the different lines of the symmetry plane.

*Figure 10.9* shows $< Q > / [U_b^2/D_h^2]$ for the 4th rib span and on the line *y/h=0.5* which corresponds to the impact of the flow on the rib and the corresponding downstream separation. The logarithmic scale was used for <*Q*> *to* visualize the entire range of possible values of <*Q*>. It can be remarked that minima of EF correspond to the ones of <*Q*> and to the absence of instantaneous structures (*figure 10.3*) in these regions. EF increases after the reattachment in correspondence with the formation of the Λ vortex in wall layer (*figure 10.4*). This result allows supposing a strong connection between organized vorticity and heat transfer in the wall region. All these conclusions are resumed in the interpretative model presented in Annex B.

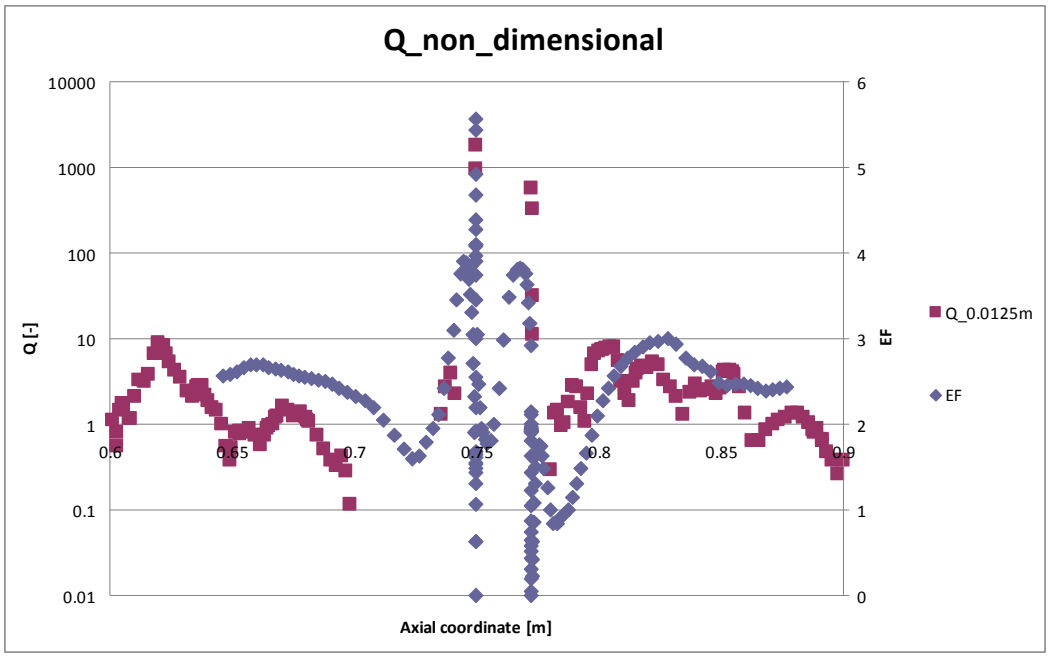


*Figure 10.9* $\langle Q \rangle / [U_b^2/D_h^2]$ *on the line Y /h=0.5 for the averaged flow field*

*Figure 10.10* presents $\langle Q \rangle / [U_b^2/D_h^2]$ at lines Y/*h= 1.20* and Y/*h=1.667*, lines whose distance from the wall is higher than the height of the rib.
Line Y/*h= 1.20* passes through the wall layer above rib and cuts the region of high activity visible in *figures 10.3* and *10.5*. The correspondence between high $\langle Q \rangle$ and EF is evident. Downstream of the rib, the level of $\langle Q \rangle$ decreases till it becomes comparable to the one of the core flow (*Y/h=1.667*).

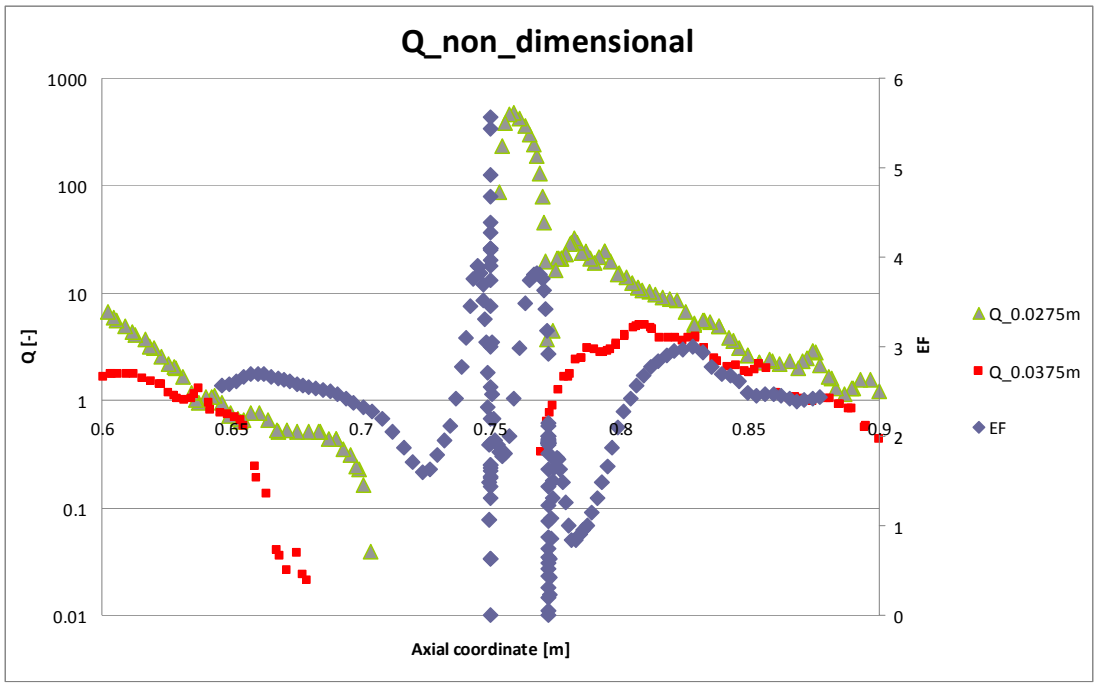


*Figure 10.10* $\langle Q \rangle / [U_b^2/D_h^2]$ *on the lines Y/h= 1.20 and Y/h=1.667 for the averaged flow field*

Comparing *figures 10.3*, *10.9* and *10.10*, it can be concluded that the level EF is associated to the presence of coherent structures within the wall layer.

# CHAPTER 11 Tools for the investigation of presence and effect of coherent structures

## *11.0 Tasks*

As the chapter 10 and the Annex B have qualitatively put in evidence the interaction between EF and CS(s) (and permanent rotation-dominated regions), the next task of the investigation is, therefore, the choice and development of the tools for the qualitative and quantitative study of the effect of CS on the flow and thermal fields.

## *11.1 Visualization*

The most direct and most intuitive approach is, of course, the visualization of the CS(s) as iso-surfaces of *Q* (*figure 11.1*). *Q* is set in non-dimensional form by the bulk velocity and height of the rib. Supplementary information can be obtained coloring the iso-surface by the local value of a chosen flow/thermal quantity (average temperature in *figure 11.1*). As it was remarked in previous chapter, the application of *Q* criterion to the instantaneous field allows to visualize the CS(s) actually present in the flow; the application of *Q* criterion to the average

field allows to visualize the permanent regions of strong rotation (high value of average <*Q*>*)*, which could be considered the footprint of the presence of CS(s) in the average field.

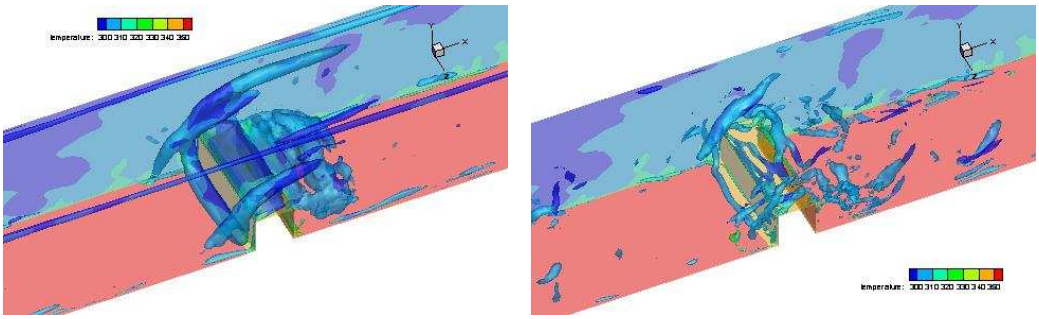

*Figure 11.1 Iso-surfaces Q/( $U_b^2/D_h^2$) =24. The Q iso-surfaces are colored by mean temperature T; right: average field; left: instantaneous field*

In order to understand the behavior of the CS(s), it is necessary to separate the effect of the CS from the un-coherent background. A suitable tool for this task is to refer to a composite figure which compares the *Q* iso-surfaces, colored by the local values of a chosen physical parameter, to a relevant iso-surface of the same parameter. The following *figure 11.2* illustrates this procedure: on the right side CS(s) (identified as iso-surfaces of *Q)* are presented, the structures being colored by the local value of the turbulent kinetic energy ***Tke***; on the left side, a relevant iso-surface ***Tke*** is shown. The possible differences between the 2 states can be, therefore, put in evidence.

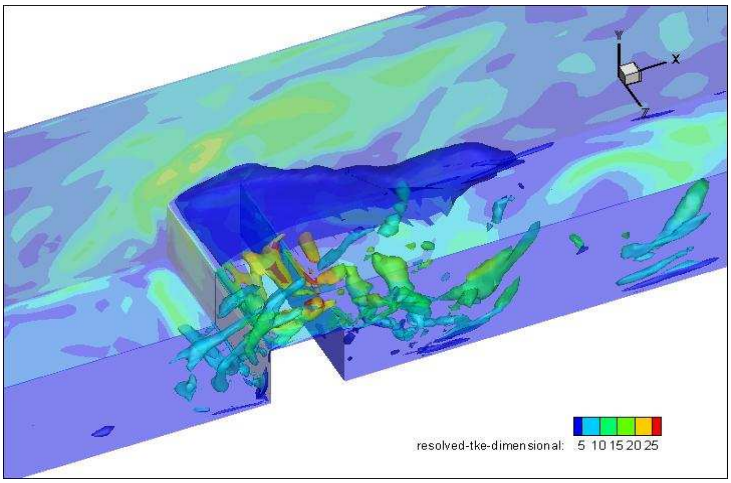


*Figure 11.2 Comparison iso-surfaces Q and iso-surface of Tke*
*Left: iso-surface Tke= 5 (see bar colors). Right: iso-surfaces Q/( $U_b^2/D_h^2$) =24. Q iso-surfaces colored by turbulent kinetic energy*

This image suggests that level of ***Tke*** within the CS (s)in the region around the rib might higher than the surrounding background level (***Tke*****=** 5)

## *11.2 Principal Component Analysis (PCA)*

A major problem of this investigation lies in the large number of parameters which affect the conjugate heat transfer problem. A first step toward the evaluation of the relative importance and the interaction of the different parameters can be undertaken examining the covariance matrix associated to the full set of low, turbulence and heat exchange parameters.
To introduce the concept of covariance matrix, one can consider 2 variables x and y defining a sample of n observations $\{x_1, x_2,\ldots\}$, $\{y_1, y_2,\ldots\}$. Assuming that the vectors x,y are centered, i.e. they have zero mean, the variance of the two variables can be defined as:

$$\sigma_x^2 \doteq \frac{1}{n}\sum_i x_i^2 \;;\; \sigma_y^2 \doteq \frac{1}{n}\sum_i y_i^2$$

Moreover, the covariance can be expressed as:

$$\sigma_{xy}^2 \doteq \frac{1}{n}\sum_i x_i y_i$$

or, in non-dimensional form, as:

$$corr(x,y) = \frac{\sigma_{xy}^2}{\sigma_x \cdot \sigma_y}$$

The result of this operation is a NUMBER which indicates the level of correlation between variables. Values close to 1 indicate that these quantities are strongly correlated (***redundancy***). If the result is close to 0, the variables are uncorrelated.
This operation can be generalized to obtain the covariance matrix ***CX*** for a matrix ***X*** data made of *m* rows and *n* columns of data.

$$CX = XX^T$$

For example, let's consider the parameters defining the average field for the 3 grid planes corresponding to the first inner node of fluid domain around the 4th rib (*figure 11.3*)

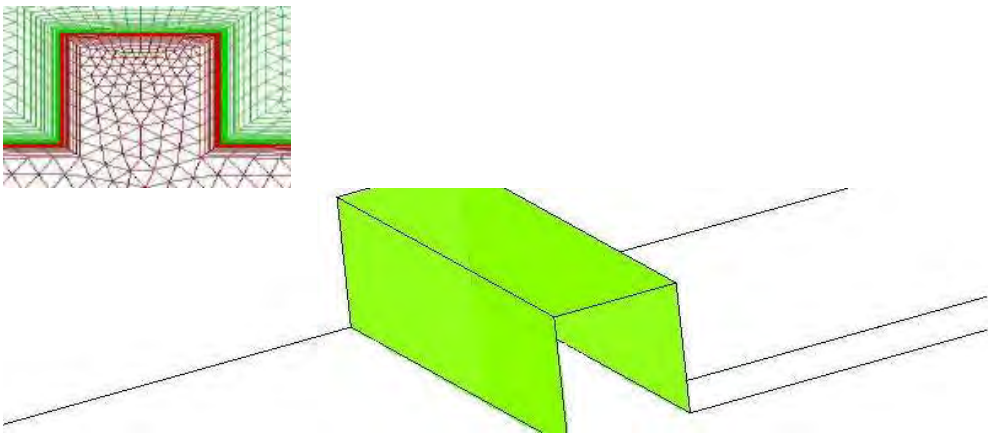

*Figure 11.3 Grid planes over the analysis performed*

The correlation matrix calculated considering mean velocity components, turbulent kinetic energy and mean temperature is summarized in table 1:

| | Tke | U_mean | V_mean | W_mean | T_mean |
|---|---|---|---|---|---|
| Tke | 1.00 | 0.24 | 0.94 | 0.00 | -0.48 |
| U_mean | 0.24 | 1.00 | 0.31 | 0.01 | 0.05 |
| V_mean | 0.94 | 0.31 | 1.00 | 0.00 | -0.47 |
| W_mean | 0.00 | 0.01 | 0.00 | 1.00 | 0.01 |
| T_mean | -0.48 | 0.05 | -0.47 | 0.01 | 1.00 |

*Table 11.1 Correlation matrix: turbulent kinetic energy against the quantities of the mean field*

The strong correlation between turbulent kinetic energy *Tke* and wall normal component of the velocity (**V_mean)** is evident**.**

The following step is the application of the ***Principal Component Analysis (PCA***) [22, 23] to identify the most important parameters of the domain.

PCA is a statistical technique which transforms a set of possibly correlated variables into a smaller number of ***uncorrelated*** variables called ***principal components***. The components are determined to successively maximize the amount of variance contained in the original sample. This approach can be thought of as revealing the internal structure of a set of data in the way which better explains its variance.

It must be remarked, that a scaling operation must be performed before performing PCA. Scaling operation is necessary when the elements of the matrix of data have different units or when they have different variances [24]. There are different methods to scale the variables:

*Standard deviation, (STD):* gives the same relevance to all the variables.
*Range:* takes a range between the minimum and maximum value of a variable.
*Variables stability (VAST):* focuses on stable variable with low variance.
Examples of the influence of the choice of scaling operation on the results will be presented later on.

Starting from the covariance matrix ***CX*** the aim is to minimize the redundancy (*covariance*) of the data and maximize the variance. The derivation of Principal Components (PC(s)) represents an eigenvalue problem applied to the covariance matrix of the original data set.

$$CX = \mathrm{X}^{\mathrm{T}}\mathrm{X} = \mathrm{ALA}^{\mathrm{T}} \quad \mathrm{A} = \begin{pmatrix} a_{11} & \cdots & a_{p1} \\ \vdots & \cdots & \vdots \\ a_{p1} & \cdots & a_{pp} \end{pmatrix} \quad \mathrm{L} = \begin{pmatrix} l_1 & \cdots & 0 \\ \vdots & \cdots & \vdots \\ 0 & \cdots & l_p \end{pmatrix} \quad l_1 > \ldots > l_p$$

*A* : orthogonal matrix (*p x p*) whose columns are the eigenvectors of ***CX***
*L*: diagonal matrix (*p x p*) containing the eigenvalues of ***CX*** in decreasing order $l_1 > ... > l_p$

The PC(s) are determined by the linear transformation:

$$\boldsymbol{Z=XA} \qquad \boldsymbol{(X=ZA^T)}$$

This operation recast **Xs** in a set of uncorrelated variables, whose coordinates are described by the columns ***A***:

The variance characterizing the original sample is concentrated in the first few PC(s), those associated to the largest eigenvalues of the covariance matrix. It is then feasible to work on a sub-set of *q* variables, smaller than the original set of *p* variables:

$$\boldsymbol{Z_q=XA_q} \qquad \boldsymbol{(X_q=ZA_q^T)} \quad \boldsymbol{q < p}$$

The size reduction process performed through PCA can be schematized using the 2D example in Flow chart 1. In practical terms, PCA performs a rotation which transforms the original variables to a set of principal components, orthogonal and oriented in the direction of maximal variance in the data. Once the PC(s) have been identified and the data have passed to the rotated space, it is possible to proceed to remove the directions associated with the smallest eigenvalue. So, for example, a 1d approximation of the original data is obtained by removing $a_2$ which is associated with an eigenvalue, $l_2$, much smaller than $l_1$.

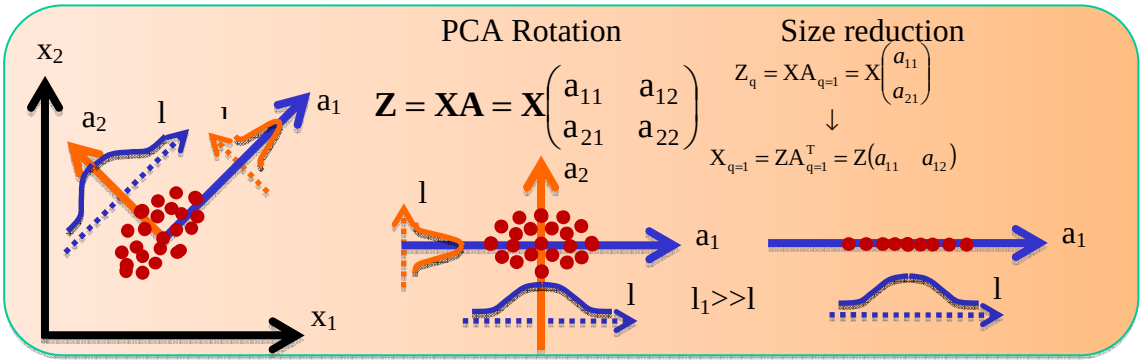


*Flow chart 1 2D example showing the PCA reduction process.*

*Figure 11.4* shows the application of PCA to the set of data collected around the fourth rib (mean velocity and temperature field).The left side of the figure shows the magnitude of the eigenvalue associated with each mode, while the right side shows the contribution of each PC to the total amount of variance accounted for by the reduced set of variables. It can be observed how the amount of variance expressed by each PC decrease with the number of the modes. In particular, the size of the 5th eigenvalue is close to zero and, thus, the associated eigenvector can be neglected.

To resume, if two variables are strongly correlated, its correlation coefficient of the covariance matrix is close to 1 and the eigenvalue of one of these variables is close to 0. Thus, it is feasible to remove the variables with very low eigenvalue, maintaining the most part of the initial information of the data range.

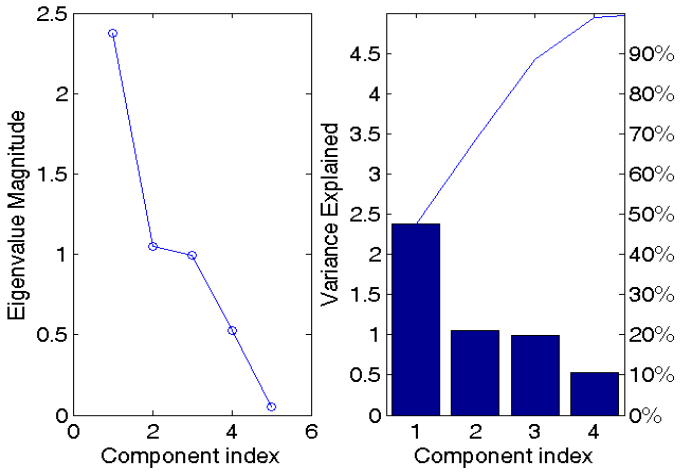


*Figure 11.4 Results of PCA: identification of relevant components*

The PCA reduction was performed by mean of a in-house MATLAB code [24].

## *11.3 Conditional Averaging*

A more complete assessment of the role of the CS(s) can be obtained comparing the global statistics of flow and thermal field with the ones conditioned by the presence of a CS [21].
Beginning from the global statistics, the average of the resolved quantities can be directly obtained from a LES simulation performed over *n* time-steps:

$$<\varphi>\doteq\frac{1}{T}\sum_{n}\varphi\Delta t$$

Where $\varphi$ is a generic resolved quantity and $\boldsymbol{T}$ ($T=n\Delta t$) is time over the average is performed (total time of the simulation).
The variance of the fluctuating part of the field can be defined as:

$$<\varphi'^{2}>=<\varphi^{2}>-<\varphi><\varphi>$$

The correlations between different fluctuations are defined as:

$$<u_i'u_j'>=<U_iU_j>-<U_i><U_j>$$

The first step towards the definition of the ***conditional average*** of variable is to define a switch *I* which will identify the appurtenance of a node of the grid to a CS:

***I= 1*** if $Q>Q_{trigger}$ ; 0 otherwise

Note that a trigger ($Q_{trigger} > 0$) must be chosen to avoid the numerical noise caused by values close to 0.

***Conditional average*** of $\varphi$ is then defined as:

$$<\varphi>^{(c)} \doteq \frac{<\varphi I>}{<I>}$$

Where the supercript © indicates a conditional quantity

The following quantities can be directly extracted from the running simulation:

$$<I>, <U_i>^{(c)}, <U_iU_j>^{(c)}, <P>^{(c)}, <P^2>^{(c)}, <S_{ij}S_{ij}>^{(c)}, <\Omega_{ij}\Omega_{ij}>^{(c)}, <T>$$

The procedure to be followed to obtain these conditional averages from the time marching process is, at the end of each time-step *i*, to add the instantaneous result to a store matrix and perform the average at the end numerical run:

Therefore, the procedure to be followed would be:
1) at the end of each time-step *i*, (in the following the superscript *i* indicates the time-step *i*) the instantaneous value of *I* and $\varphi$ at for each node of the grid are found:

$I^i = 0$ or 1

the value of the conditioned quantity is found:

$$\varphi^{(i,c)} \doteq \varphi^i I^i$$

$$(UV)^{(i,c)} = (UV)^i \; I^i$$

2) These values are added to a store matrix:

$$Store(I) = Store(I) + I^c$$

$$Store(\varphi) = Store(\varphi) + \varphi^{(i,c)}$$

$$Store(UV) = Store(UV) + (UV)^{(i,c)}$$

3) At the end of the simulation of *N* time-steps the average is performed:

$$< I >= Store(I) / N$$
$$< \varphi >^{(c)} = Store(\varphi) /(N \cdot < I >)$$
$$< UV >^{(c)} = Store(UV) /(N \cdot < I >)$$

The remaining final next step is to find the variance of the correlations and the resolved conditional turbulence:

$$< u_i u_j >^{(c)} = \left( < U_i U_j >^{(c)} - < U_i >^{(c)} < U_j >^{(c)} \right)$$

The deviation from global statistics can be found as:

$$\Delta\varphi = < \varphi >^{(c)} - < \varphi >$$
$$\Delta(UV) >= < UV >^{(c)} - < UV >$$

These algorithms are implemented by means of User Defined Subroutines (UDFG) within FLUENT.

The analysis can be refined sub-dividing the $Q$ field in different classes of different values of $Q_\alpha$ to better define the effects of the coherent structures. On the basis of the range of values of $Q$ find in the present simulation, five different classes have been defined. The two first classes separate the domains where CS(s) are present or not. The other classes allow separating the effects in the flow of CS(s) of different strength. $Q$ has been set in not-dimensional form against: $Q / \left( U_b{}^2 / D_h^2 \right)$

$$I_\alpha = \begin{cases} 1 & Q(x,t) \in Q_\alpha \\ 0 & Q(x,t) \notin Q_\alpha \end{cases} \alpha \in \{I, II, III, IV, V\}$$

$$Q_I = \{x; x \in \Re \wedge x > 0\}$$

$$Q_{II} = \{x; x \in \Re \wedge x < 0\}$$

$$Q_{III} / \left( U_{bulk}{}^2 / D_h^2 \right) = \{x; x \in \Re \wedge 0 < x < 12\}$$

$$Q_{IV} / \left( U_{bulk}{}^2 / D_h^2 \right) = \{x; x \in \Re \wedge 12 < x < 24\}$$

$$Q_V / \left( U_{bulk}{}^2 / D_h^2 \right) = \{x; x \in \Re \wedge x > 24\}$$

The previous definition of conditional average can be extended to the present sub-division as:

$$<u'_i u'_j>_\alpha = <U_i U_j>_\alpha - <U_i>_\alpha <U_j>_\alpha$$

$$<\varphi'^2>_\alpha = <\varphi^2>_\alpha - <\varphi>_\alpha <\varphi>_\alpha$$

# CHAPTER 12 Results of the Visualizations

## *12.1 Visualizations*

The first step of the investigation is the interpretation of the visualization of the structures present in instantaneous field and mean field.

### *12.1.1 Visualization of CS*

A first step the concept of composite images is applied to the instantaneous field (*figure 12.1*). In *figure 12.1* the organization of the images is the following: 2 iso-surfaces of instantaneous *Q* (colored by the local value of the turbulent kinetic energy *Tke*) and 2 iso-surfaces of *Tke* are shown. The bottom wall is colored by value of EF.
Therefore, the effect of the level of *Q* and its interaction with heat transfer is put in evidence.

*Figure 12.1* then attempts to put in evidence the relation between CS(s) and turbulent kinetic energy. The most relevant feature which can be remarked from the image is the elongated CS created at the upstream side corner and arching over the rib. This structure is associated to a low level of average kinetic energy, comparable the one of the background in the same region. In consequence, the value *Tke* on the surface of the structure changes with distance from the wall. It can be noted that transversal rolls are created above the top face of the rib, downstream of the upstream corner separation. These CS(s) correspond to a high level of average kinetic energy, comparable by the global region of high turbulence intensity created above the corner separation (deep green region in the image). Downstream of the rib, the break-down of the rolls creates CS(s) elongated in the longitudinal axis. The phenomenology is similar to the one noted by previous investigators [3,4, 20].
The twin *figure 12.2* attempts to put in evidence the relation between CS and mean the temperature. The organization of the figure is similar to *figure 12.1*: 2 iso-surfaces of instantaneous *Q* (colored by the local value of the mean temperature <*T*>) are presented and 2 iso-surfaces of <*T*> are shown.

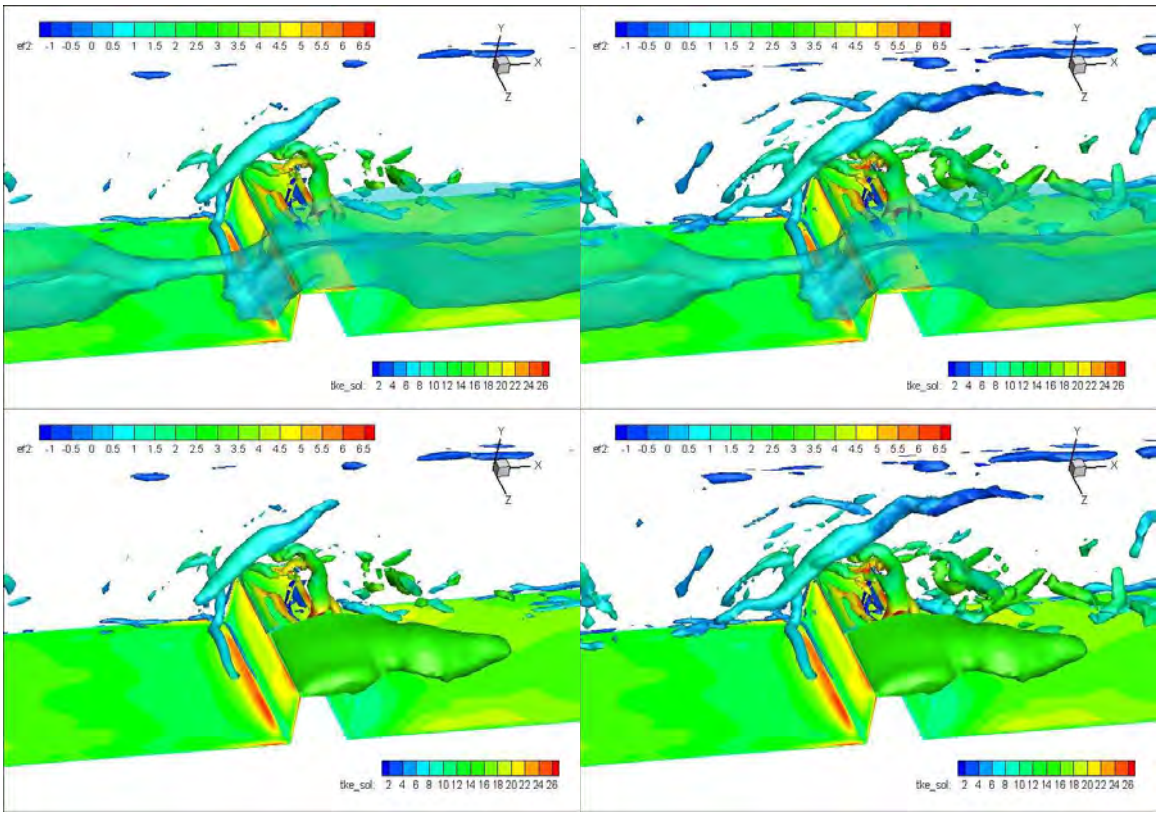

*Figure 12.1 Instantaneous Q colored by average Tke; range of colors : average Tke*
*Left Q/ ( $U_b^2/D_h^2$ ) =2 Right Q/( $U_b^2/D_h^2$)=12*
*Left top : Iso-surface Tke=8 Right top: Iso-surface Tke= 8,*
*Left bottom: Iso-surface Tke=16 Right bottom Iso-surface Tke= 16,*

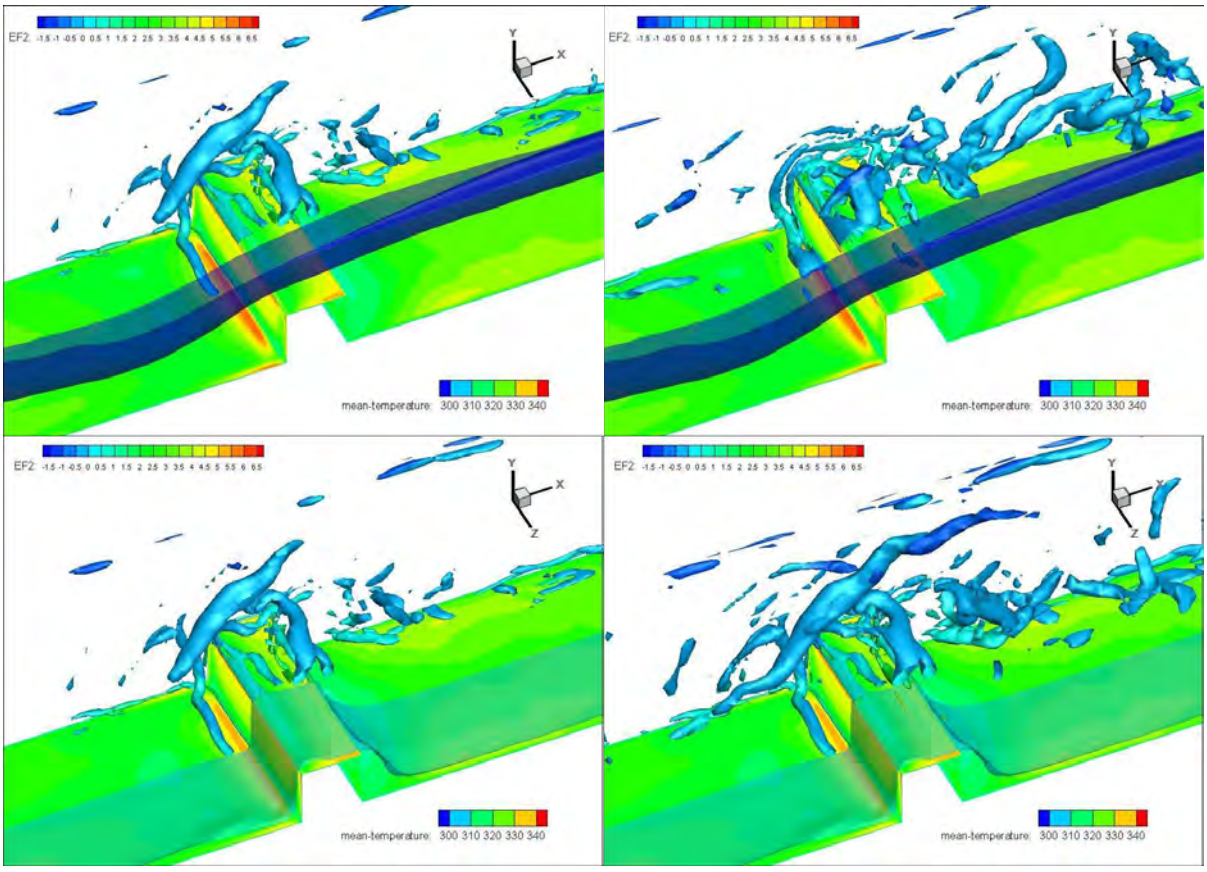


*Figure 12.2 Instantaneous Q colored by average Temperature range of colors: average Temperature*
*Left: $Q/(U_b^2/D_h^2)=24$ Right: $Q/(U_b^2/D_h^2)=12$*
*Left top: Iso-surface $<T>=300\ K^o$, Right top: Iso-surface $<T>=300\ K^o$,*
*Left bottom: Iso-surface $<T>=310\ K^o$, Right bottom: Iso-surface $<T>=310\ K^o$*

*Figure 12.2* shows that the value of $<T>$ within the main corner structures is in the same order of magnitude as the corresponding background temperature and it changes with the distance from the wall. At the bottom wall, the separation upstream of the rib is associated to a span-wise vortex at low, which is responsible of a region of high EF. Overall, the CS seems characterized by low $<T>$, which could be a first indication of the effect of the vortex structures on heat transfer.

### *12.1.2 Visualization of rotating structures in the mean domain*

Equivalent images were created of the average $<Q>$ field. *Figure 12.3* investigates the effect of the average turbulent kinetic energy. Similar to *figure 12.1*, the organization of the image: 2 iso-surfaces of $<Q>$ (colored by the local value of the turbulent kinetic energy *Tke*) and 2 iso-surfaces of *Tke* are shown.

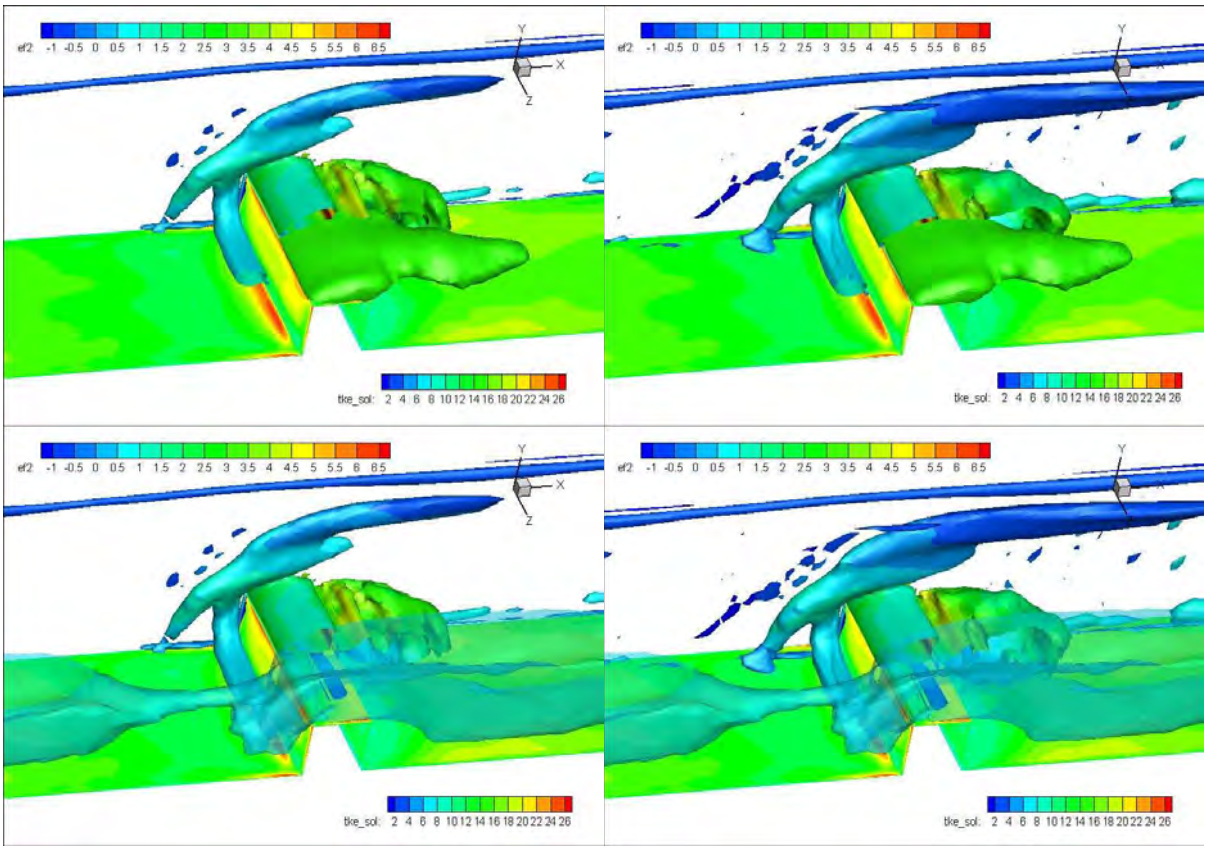

*Figure 12.3 <Q> colored by average Tke*
*Left <Q >/( $U_b^2/D_h^2$ )=24 Right <Q >/( $U_b^2/D_h^2$)=12 range of colors : average Tke*
*Left top: Iso-surface Tke=16 Right top: Iso-surface Tke= 16,*
*Left bottom: Iso-surface Tke=8 Right bottom: Iso-surface Tke= 8*

*Figure 12.3* confirms the indications of *figure 12.1*, showing that the levels of average kinetic energy associated with the vortex regions are comparable the values of the background *Tke* in the same region. This is well shown by the fact that the values of *Tke* in the main corner structures change with distance from the wall. The regions of high <*Q*> and high *Tke* downstream of rib (top row of *figure 12.3*, dark green regions) are of similar size. A tentative conclusion is that a more sophisticated approach (such as the conditional averaging) would be needed to put in evidence the possible effects of the CS(s) and of the permanent rotation dominated regions.

The corresponding *figure 12.4* attempts to put in evidence the relation between <*Q*> and mean temperature <*T*>. The organization of the image is similar to the one of *figure 12.2*: 2 iso-surfaces of average <*Q*> (colored by the local value of <*T*>) and 2 iso-surfaces of <*T*> are shown.

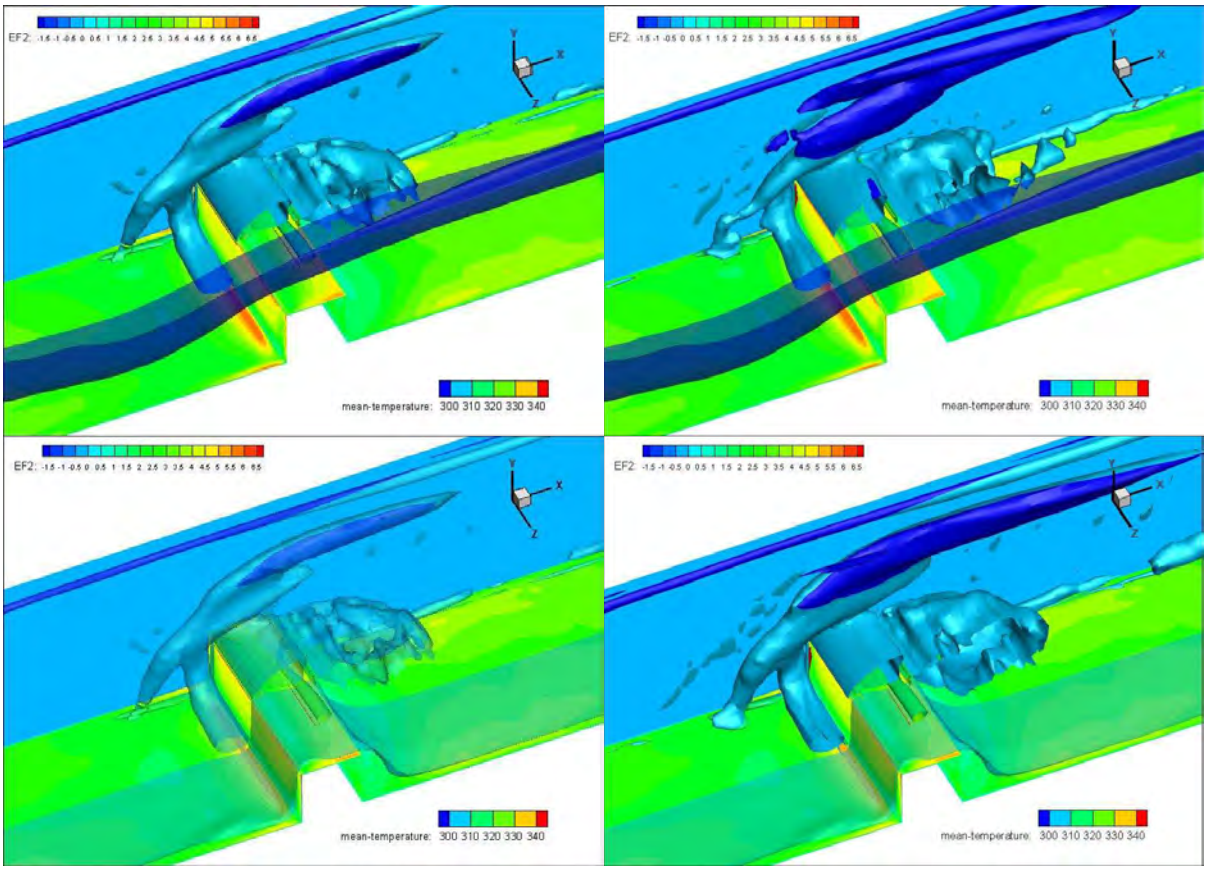


*Figure 12.4: Average Q colored by average Temperature; range of colors: average Temperature*
*Left* $<Q>/(U_b^2/D_h^2) = 24$ *Right* $<Q>/(U_b^2/D_h^2) = 12$
*Left top: Iso-surface* $<T> = 300\ K^o$, *Right top: Iso-surface* $<T> = 300\ K^o$,
*Left bottom: Iso-surface* $<T> = 310\ K^o$, *Right bottom: Iso-surface* $<T> = 310\ K^o$

*Figure 12.4* shows that the value of $<T>$ within the main corner structures is similar to the corresponding background value and its values change with distance from the wall. The upstream separation at the bottom wall the region of high value of EF appears to be associated to a ***permanent*** span-wise vortex at low $<T>$. Above and downstream the rib, the region of high $<Q>$ corresponds to a low value of $<T>$. Therefore, the effect of the vortex structures on heat transfer is made evident.

## *12.2 Results of the Principal Component Analysis*

### *12.2.0 Principal Component Analysis*

The PCA was applied to assess its capability for the present investigation.
As it was already remarked, the difficulty of the present study lies in the wide range of physical parameters which could, potentially, affect the process under investigation.

A first tentative list would include, obviously, the average enhancement factor (EF), the instantaneous *Q*, the average <*Q*>; the main parameters of the average field: the mean velocity (<*U*>,<*V*>,<*W*>), average temperature <*T*>; the main parameters of the turbulent field: the turbulent kinetic energy (*Tke*) and the time averaged correlations <*TT*>, , <*uT*>, <*vT*>, <*wT*>, <*uv*>, <*uw*>, <*vw*>.

### *12.2.1 Investigation of the covariance matrix for flow and thermal field around the 4th rib*

As already indicated, the procedure is to extract the covariance matrix for the grid planes of interest. As the focus is the heat exchange between the heated wall and the flow, the first inner grid plane for 4th pitch length was the first target of the analysis. However, the previous visualizations have well shown that the presence and behavior of the CS(s) close on the wall are quite different for the rib region and above the bottom plane, as again shown in *figure 12.5:*

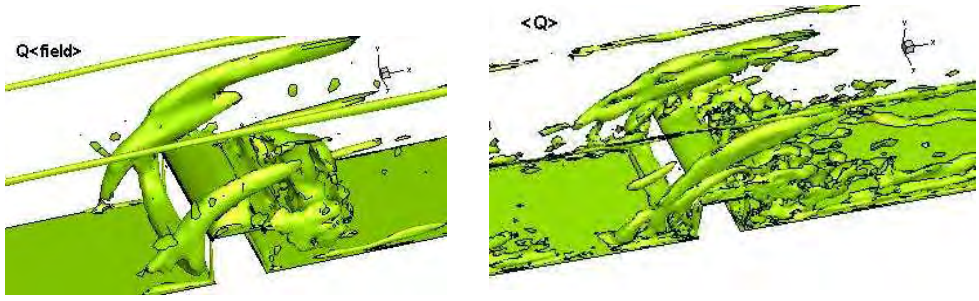


*Figure 12.5 Left: visualization of <Q>: <Q>/( $U_b^2/D_h^2$)=24. Right: <Q>/( $U_b^2/D_h^2$)=8*

Therefore, it would be logical to separate the domain in different sub-domains to put in evidence the different behaviors.
The first attempt to sub-division of the domain (sub-division 1, in the following) was to separate the set of data as:
Plane 1: upstream bottom wall and upstream vertical face of the rib.
Plane 2: top face of the rib
Plane 3: downstream bottom wall and downstream vertical face of the rib.
The resulting set-up is presented in *figure 12.6.*

This sub-division represents an attempt to put in evidence the effect of the separation on the top of the rib and the CS(s) so created. The 3 complete covariance matrixes for the 3 planes are reported in Annex C**.**

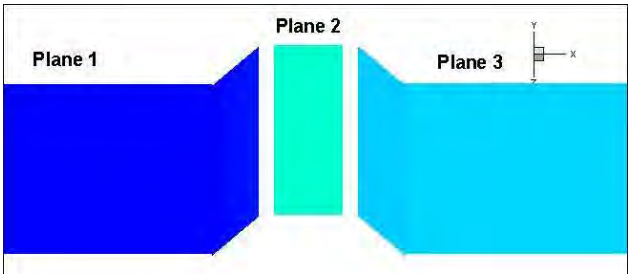


*Figure 12.6 Sub-division 1*

However, and before attempting a full analysis, a first preliminary analysis was performed on a sub-set which puts in evidence the correlations among the quantities of paramount interest, namely EF and instantaneous and average *Q*. The results are resumed in the following *table 12.1*:

| | PLANE1 | | |
|---|---|---|---|
| | EF | Q | <Q> |
| EF | 1.00 | -0.29 | -0.21 |
| Q | -0.29 | 1.00 | 0.55 |
| <Q> | -0.21 | 0.55 | 1.00 |

| | PLANE2 | | |
|---|---|---|---|
| | EF | Q | <Q> |
| EF | 1.00 | 0.03 | 0.31 |
| Q | 0.03 | 1.00 | 0.46 |
| <Q> | 0.31 | 0.46 | 1.00 |

| | PLANE3 | | |
|---|---|---|---|
| | EF | Q | <Q> |
| EF | 1.00 | -0.41 | -0.41 |
| Q | -0.41 | 1.00 | 0.41 |
| <Q> | -0.41 | 0.41 | 1.00 |

*Table 12.1 Covariance matrix for EF and Q for the planes 1, 2, 3 (sub-division 1)*

*Table 12.1* shows that instantaneous *Q* and average <*Q*> are always well correlated, which could confirm that existence of a correlation between CS(s) and the permanent vortex structures identified in the average field. However, the values remain well below of 1, which leads to suspect that field <*Q*> contains contribution other than the "true" CS, namely the effect of the vorticity due to re-circulating separated regions. On planes 1 and 3 EF is well correlated with both instantaneous *Q* and average <*Q*>. On plan 2 EF seems uncorrelated of the instantaneous *Q*, in spite of the presence of CS(s) in the region (*figure 12.5*). This result suggests a different mechanism. A tentative explanation can be found from *figure 12.7*, which attempts to relate the covariance matrix to the visualizations.

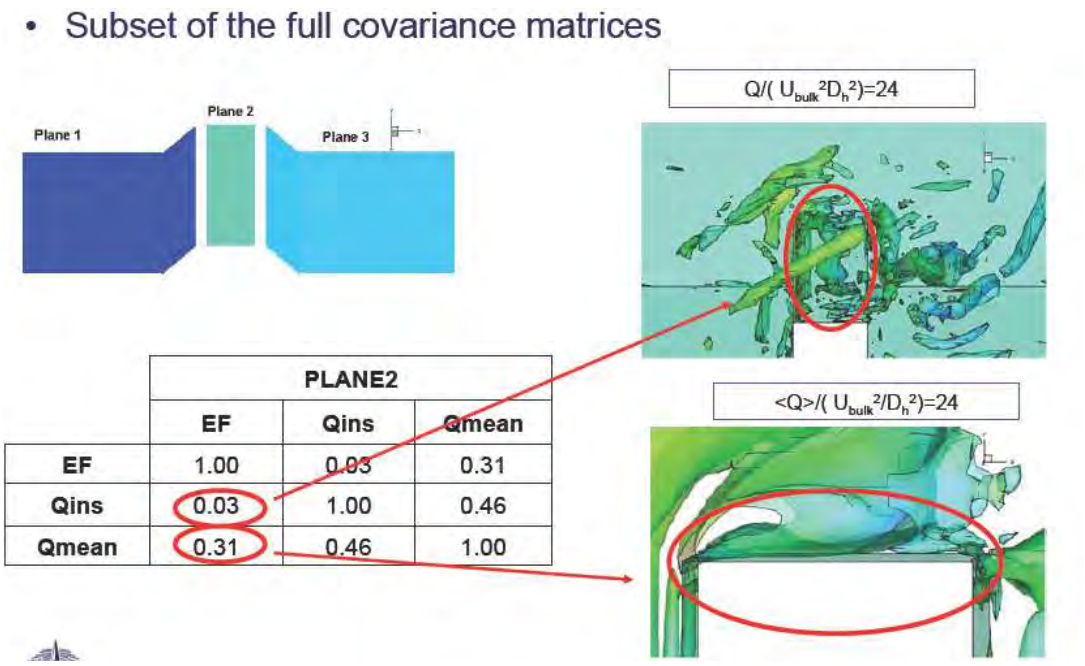


| | PLANE2 | | |
|---|---|---|---|
| | EF | Qins | Qmean |
| EF | 1.00 | 0.03 | 0.31 |
| Qins | 0.03 | 1.00 | 0.46 |
| Qmean | 0.31 | 0.46 | 1.00 |

*Figure 12.7 Interaction between EF and Q for the plane 2 (sub-division 1)*

It can be remarked is that important CS(s) are localized well above (and separated) of the top face of the rib, which explains the low correlation between EF and *Q*, while a permanent sheet of high vorticity on the top of the rib is created by the corner separation and contributes to <*Q*>. It would appear this structure is the one driving the interaction between heat transfer and flow and it is, in this region, much more important than the presence of classically defined CS(s) above the rib.
In order to verify this hypothesis, the effect of the different sub-division (sub-division 2, in the following) of the domain in 3 elements was investigated. The above procedure was repeated, the set of data being sub-separated as:
Plane 1: upstream bottom wall.
Plane 2: 3 faces of the rib
Plane 3: downstream bottom wall.
The resulting set-up is presented in *figure 12.8*.
The purpose is to fully separate the effect of the rib from the bottom plane.

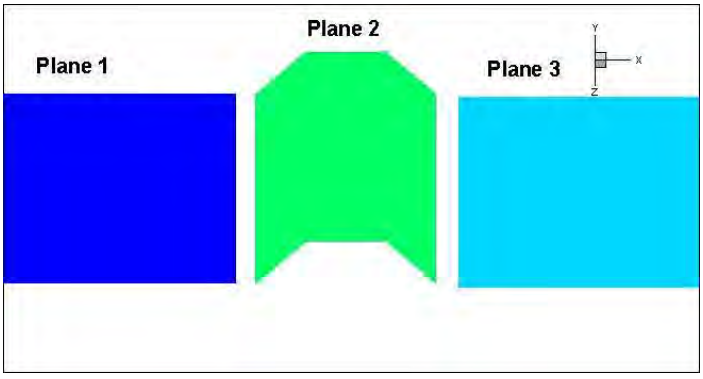


*Figure 12.8 Sub-division 2*

The corresponding results are presented in following *table 12.2:*

| | PLANE1 | | |
|---|---|---|---|
| | EF | Q | <Q> |
| EF | 1.00 | -0.32 | -0.41 |
| Q | -0.32 | 1.00 | 0.33 |
| <Q> | -0.41 | 0.33 | 1.00 |

| | PLANE2 | | |
|---|---|---|---|
| | EF | Qins | Qmean |
| EF | 1.00 | -0.02 | -0.03 |
| Q | -0.02 | 1.00 | 0.72 |
| <Q> | -0.03 | 0.72 | 1.00 |

| | PLANE3 | | |
|---|---|---|---|
| | EF | Q | <Q> |
| EF | 1.00 | -0.29 | -0.29 |
| Q | -0.29 | 1.00 | 0.19 |
| <Q> | -0.29 | 0.19 | 1.00 |

*Table 12.2 Covariance matrix for EF and Q for the planes 1, 2, 3 (sub-division 2)*

A surprising result is evident: EF is well correlated with instantaneous *Q* and average <*Q*> (and by a comparable level of correlation) on Planes 1 and 3, namely the bottom wall upstream and downstream of the rib, but it appears to be uncorrelated to them on the rib itself. The possible explanation could be found in *figure 12.9* which shows that the permanent vortex structures are well separated of the rib itself.

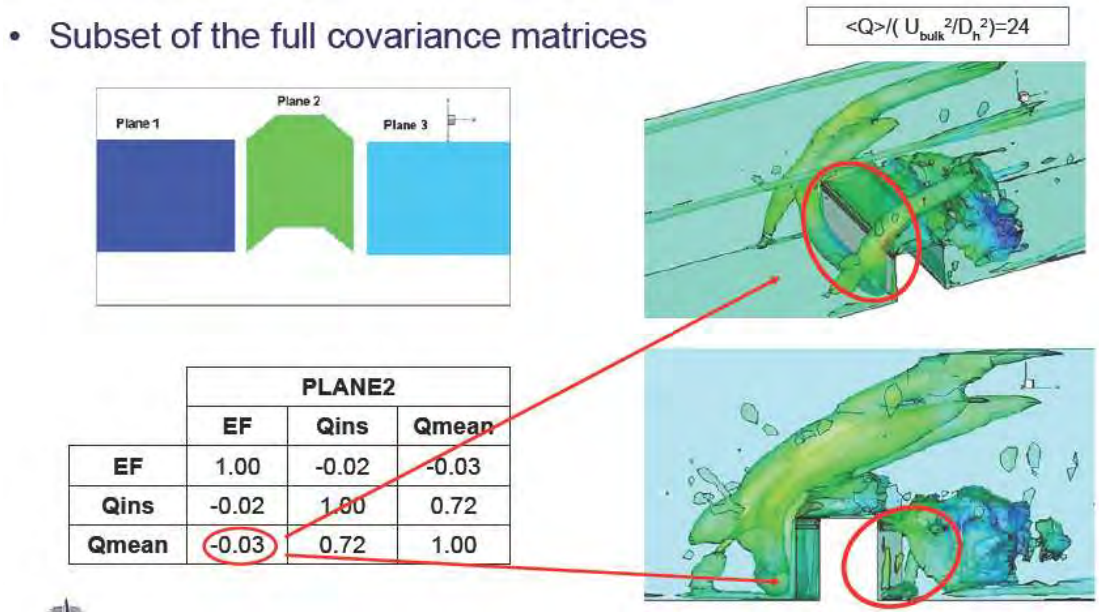


*Figure 12.9 Interaction between EF and Q for the plane 2 (sub-division 2)*

In fact, it can be sees that there are no coherent structure interacting with the two planes which form the rib sides, thus the interaction between the averaged <*Q*> and EF is insignificant. Therefore, the planes which form the sides of the ribs are not important in this heat transfer analysis. A tentative conclusion is that the CS(s) interact with heat transfer only over the plane surfaces where flow is attached and CS(s) are present in wall layer. The correlation between *Q* and <*Q*> is quite high, which confirms that the large corner regions of high <*Q*> (see *figure 10.6* and following) really represent the "footprint" of the CS in the average field.

### *12.2.2 PCA to flow and thermal field around the 4th rib*

Following this preliminary analysis, the next step is to perform the PCA on these full sets of data. Data were centered and scaled using the standard deviation (STD) scaling method. *Figure 12.10* presents the results of the principal components analysis and the contribution of different modes to the total variance of the data for the sub-division 1 (Annex 3).

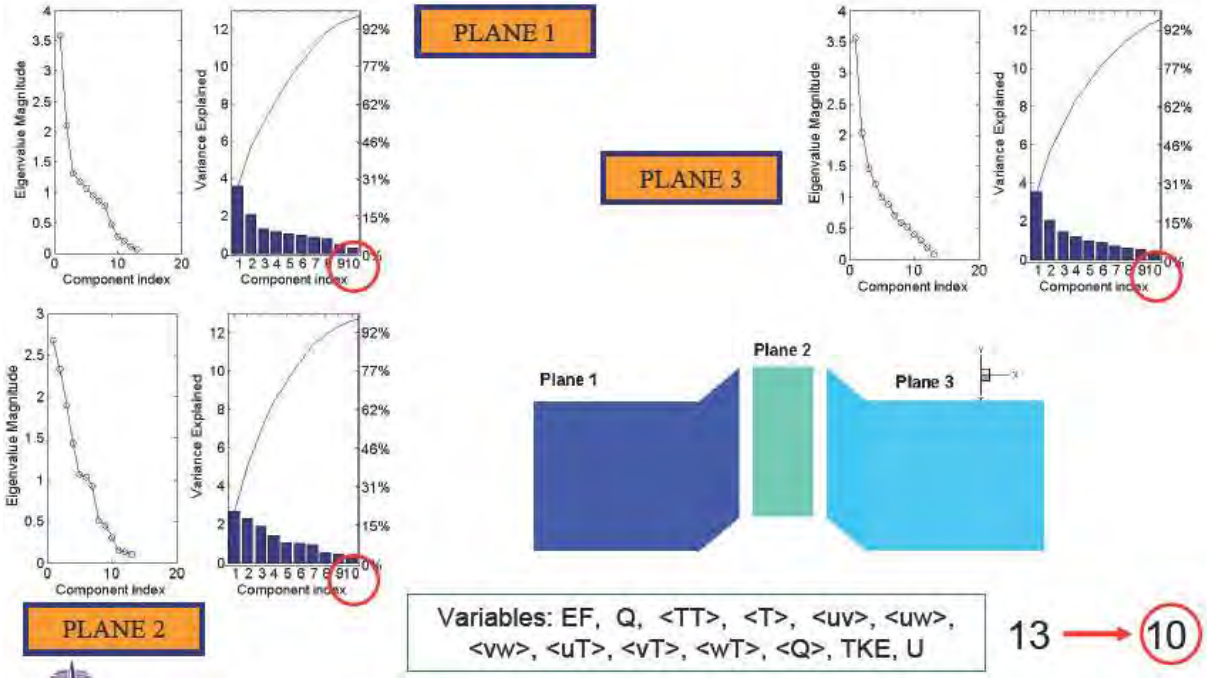


*Figure 12.10 Principal Components Analysis for EF and Q for the planes 1, 2, 3 (sub-division 1)*

*Figure 12.10* shows that the first component is dominant for planes 1 and 3, while a more uniform distribution can be remarked for plane 2, corresponding to a more isotropic behavior of the flow and the turbulence in the separated region. It can be remarked that 10 modes are necessary to recover more than the 90% of the initial information contained in the13 original parameters, which indicates the complexity of the phenomenon.

The map of first component is presented in *figure 12.11* and a qualitative comparison with EF is attempted. The similarity between the maps of the 2 parameters is evident. This first result indicates that PCA has the potentiality to represent the entire complex process of heat transfer and it can be applied to identify the parameters driving it.

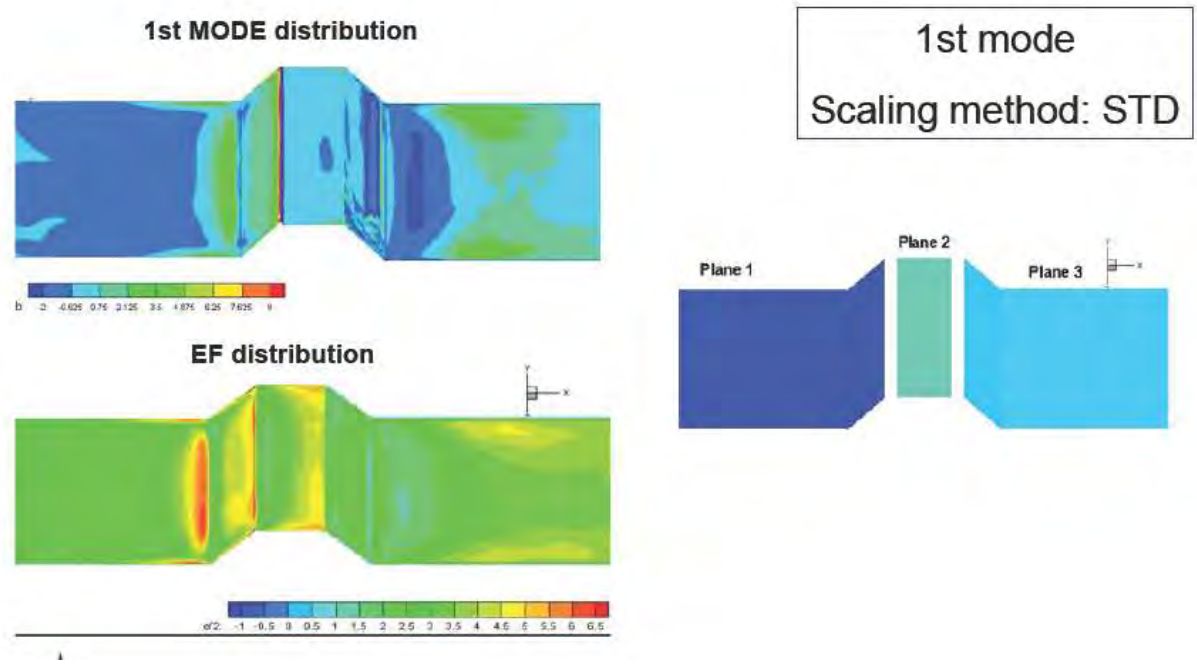


*Figure 12.11 Comparison of the First Principal Component for planes 1, 2, 3 with EF (sub-division 1)*

The distribution of the other different modes is shown in *figure 12.12*, which assembles the 4 first modes. It can be remarked that the distribution of the 2nd mode over the top of the rib is very similar to the one of EF and puts in evidence the effect of the corners, completing the information provided by the 1st mode. The need to of the 2nd mode to fully reproduce the process over the top face of the rib is also indicated by figure *12.10* which shows that, for Plane 2, the variance associate with 2nd mode is of the same order of magnitude of the one associated with 1st mode.

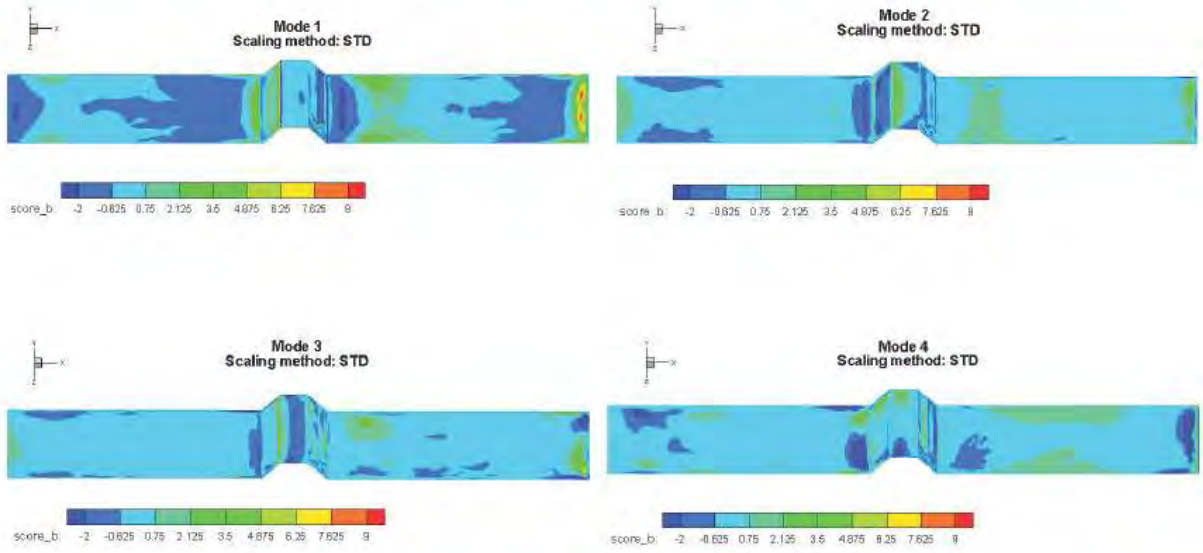


*Figure 12.12 Distribution of the first 4 Principal Component for planes 1, 2, 3 (sub-division 1)*

Corresponding distributions obtained with RANGE averaging are presented in Annex D.

These results were compared with the ones yielded by sub-division 2. The following *figure 12.13* presents the results of PCA and the contribution of different modes to the total variance of the data. Comparing with *figure 12.10*, it can be remarked that relative weight of the 1st mode is now higher for all the 3 regions, which suggests that sub-division 2 is a more efficient way to treat the present set of data. This indication is confirmed by the fact that 9 modes (against the previous 10) are necessary to recover more than 90% of the initial information.

The map of first component is presented in *figure 12.14*. A good qualitative agreement with EF is again found. With respect of the previous case (*figure 12.11*) a better matching between the two parameter is visible over the rib itself, further proves of the efficiency of the sub-division 2

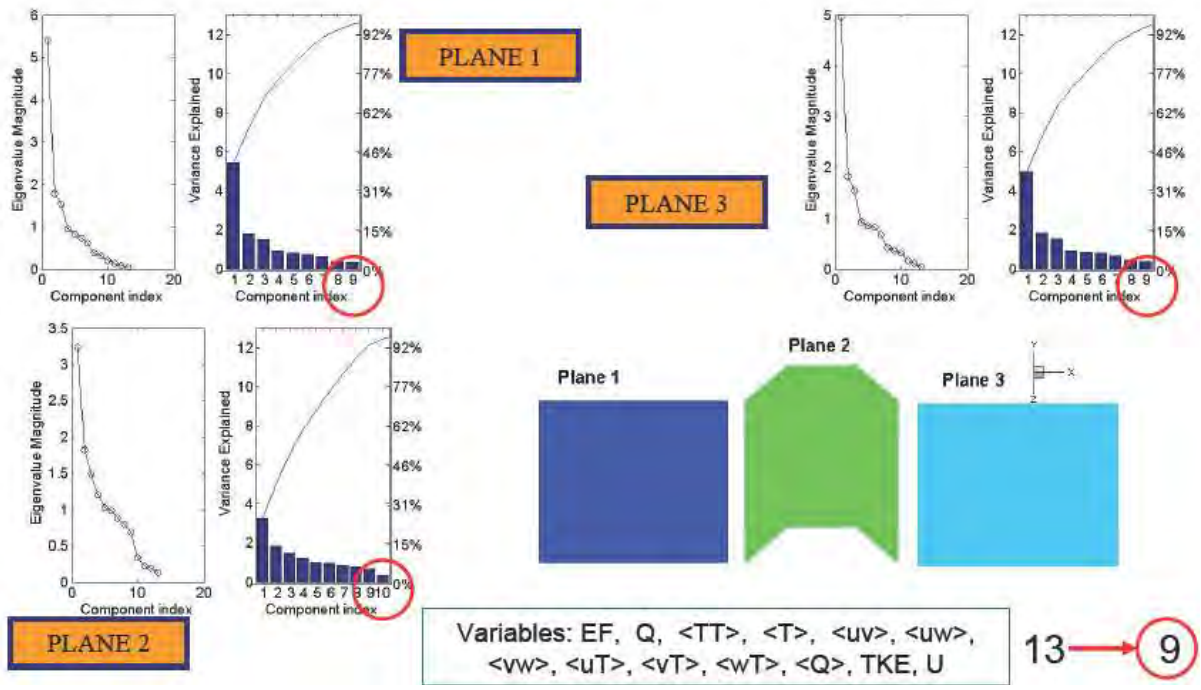


*Figure 12.13 Principal Components Analysis for EF and Q for the planes 1, 2, 3 (sub-division 2)*

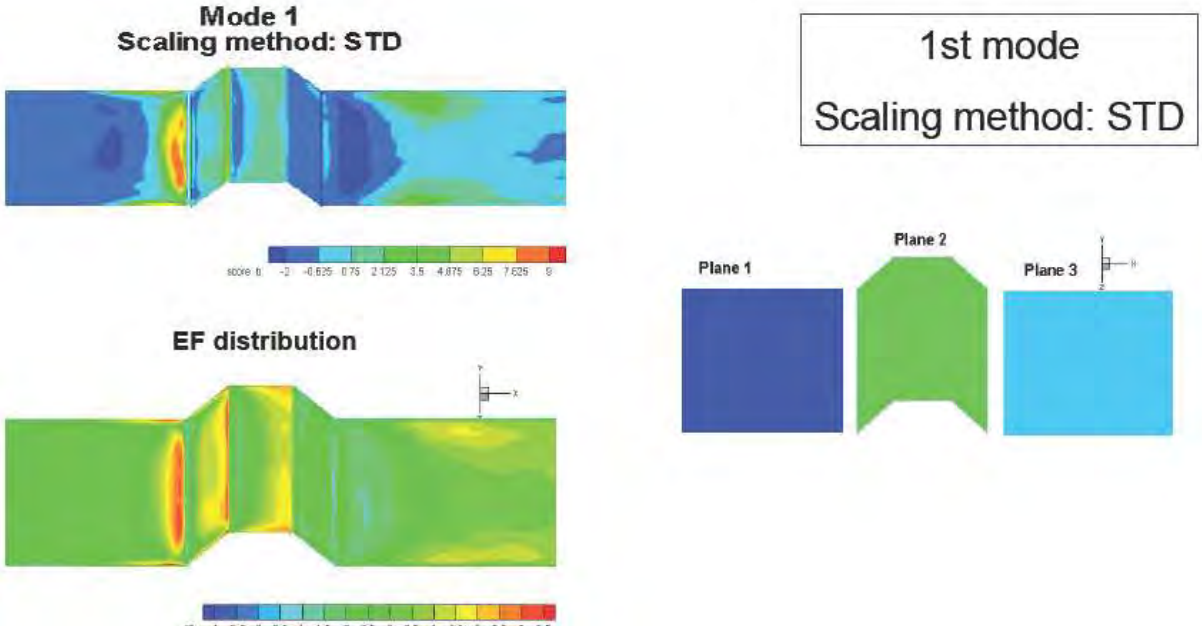


*Figure 12.14 Comparison of the First Principal Component for planes 1, 2, 3 with EF (sub-division 2)*

#### *Conclusions*

The present results indicate that the covariance matrix is a powerful tool to put in evidence the most important parameters in a complex process.
The different interaction between CS(s) and EF at the wall plane and over the rib has been highlighted. In particular, for the rib itself, no direct interaction between CS(s) and EF was found.
The capability of PCA to reproduce the behavior of the present heat transfer process with lower number of independent parameters had been demonstrated.

## *12.3 Correlation Analysis*

### *12.3.1 Principle of correlation analysis*

The previous section was demonstrated the capability to identify the most important physical parameters controlling the interactions of CS(s) and EF studying the matrix of correlation. However, these results could be criticized remaking that choice of the elements of the covariance matrix used for this investigation was, in some limits, arbitrary. Therefore, it was attempted to individuate all the physical parameters which could affect the process and to extend and complete the covariance matrix with additional variables.
The individuated variables are:

Enhancement factor of the mean and instantaneous field (EF_mean, EF_ins).

*Q* of the instantaneous field and <*Q*> of the averaged field.

Instantaneous flow variables: x-velocity (*U*), y-velocity (*V*), z-velocity (*W*), temperature (*T*), pressure (*P*), velocity-magnitude (*Vel-mag*), turbulent kinetic energy (*Tke*).

Time averaged variables: x-mean-velocity (<*U*>), y-mean-velocity (<*V*>), z-mean-velocity (<*W*>), mean temperature (<*T*>), mean pressure (<*P*>), mean velocity-magnitude (<*Vel-mag*>).

Instantaneous and time averaged correlations: *TT, PP, UU, UV, VV, VW, WW, UT, VT, WT,* <*TT*>, <*uT*>, <*vT*>, <*wT*>, <*uv*>, <*uw*>, <*vw*>.

The complexity of the resulting matrix can be appreciated comparing an example of matrix (E) with the corresponding one applied for the previous section (Annex C).

The resulting matrix of 34 elements is analyzed to individuate the physical parameters strongly correlated to EF_mean, EF_ins.

### *12.3.2 Investigation of bottom wall*

The first step of the new investigation was to repeat the investigation of the first inner grid plane around the 4th rib using the new matrix. Following the conclusions of the previous section, the sub-division 2 (*figure 12.14*) was investigated and the quantities most strongly correlated to EF and *Q* were identified. The results and the value of the correlation coefficients are presented in the following *tables 12.3, 12.4, 12.5* for the 3 corresponding sub-domains.

| | Plane 1(upstream of the rib ) | | | |
|---|---|---|---|---|
| | EF_mean | EF_ins | *Q* | <*Q*> |
| Q | -0.41 | -0.65 | 1.00 | 0.47 |
| <Q> | -0.56 | -0.42 | 0.47 | 1.00 |
| *Tke* | 0.81 | 0.58 | -0.42 | -0.41 |
| VV | 0.30 | 0.49 | -0.77 | -0.41 |
| <Vel_mag> | 0.68 | 0.55 | -0.41 | -0.39 |
| <V> | -0.49 | -0.34 | 0.32 | 0.80 |
| <*T*> | -0.85 | -0.57 | 0.52 | 0.78 |

*Table 12.3 Subset of correlation matrix in Plane 1*

| | Plane 2 (RIB) | | |
|---|---|---|---|
| | EF_mean | *Q* | <*Q*> |
| <*Q*> | 0.01 | 0.26 | 1.00 |
| UU | -0.03 | -0.57 | -0.30 |
| <UV> | 0.06 | -0.63 | -0.31 |
| <VV> | 0.23 | -0.50 | -0.14 |
| <Vel_mag> | 0.61 | -0.54 | -0.11 |
| <U> | 0.02 | 0.33 | 0.17 |
| <V> | 0.45 | -0.46 | -0.12 |

*Table 12.4 Subset of correlation matrix in Plane 2*

| | Plane 3 (downstream of the rib) | | | |
|---|---|---|---|---|
| | EF_mean | EF_ins | *Q* | <*Q*> |
| *Q* | -0.36 | -0.62 | 1.00 | 0.26 |
| <*Q*> | -0.50 | -0.27 | 0.26 | 1.00 |
| *Tke* | 0.80 | 0.44 | -0.24 | -0.34 |
| VV | 0.28 | 0.49 | -0.81 | -0.30 |
| <Vel_mag> | 0.65 | 0.37 | -0.36 | -0.33 |
| <V> | -0.46 | -0.24 | 0.23 | 0.77 |
| <*T*> | -0.83 | -0.46 | 0.36 | 0.76 |

*Table 12.5 Subset of correlation matrix in plane Plan 3*

These results confirm the different behaviour between the rib and the bottom plane remarked in the previous section.
In the case of the rib (Plane 2, *table 12.4*): EF_mean is not correlated to <*Q*>, while is strongly correlated to the mean velocity field (<*Vel_mag*>, <*V*>), suggesting that the advection associated with the increase of velocity over the restriction would be the dominant parameter; the instantaneous *Q* is also strongly correlated to both instantaneous and mean velocity field. The situation is very different for Plane 1 (*table 12.3*) and Plane 3 (*table 12.5*) where EF_mean is always strongly correlated with <*Q*>. A similar level of correlation is found between EF_ins and *Q* in two planes. Moreover, a strong correlation is remarked between EF_mean and *Tke*, which confirms the previous conclusions (chapter 9).
Concerning CS(s), < *Q* > is is always well correlated with <*T*> and <*V*>, suggesting the importance of the large structures arching over the rib (*figure 12.5*). The correlation between *Q* and *VV* indicates the role of the rib as promoter of turbulence and CS(s).

### *12.3.3 Investigation of a CS*

The capability of the present technique to put in evidence the interaction of CS and heat transfer is demonstrated investigating the correlation between *Q* and some flow variables in a plane which cuts through an instantaneous CS (*figure 12.15)*.

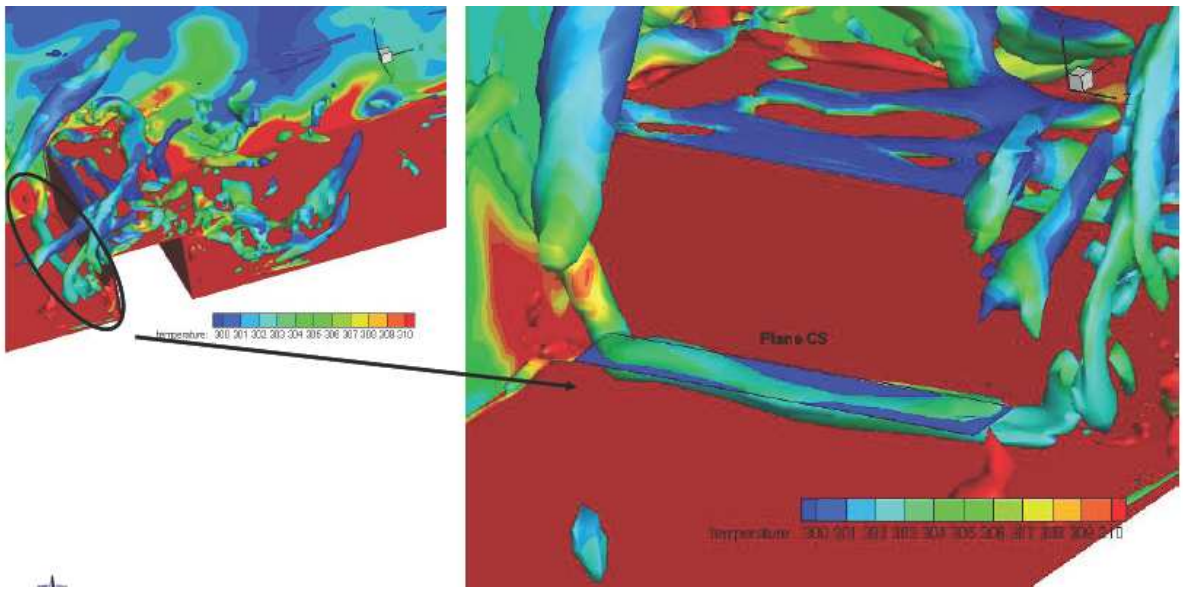


*Figure 12.15 Plane in coherent structure*

The result of the procedure is presented in *table 12.6*:

| | PLANE CS | |
|---|---|---|
| | *Q* | <*Q*> |
| PP | 0.88 | 0.03 |
| VV | -0.78 | -0.08 |
| P | -0.91 | -0.01 |
| <V> | 0.44 | -0.83 |
| <*T*> | 0.48 | -0.71 |

*Table 12.6 Subset of correlation matrix in Plane CS*

The instantaneous coherent structure is highly correlated with the pressure and the instantaneous correlations of pressure and y-velocity (*P, PP, VV*). On the other hand, the permanent vortex t structures of the averaged field are highly correlated with mean temperature and velocity (*<T>, <V>).*

To support the quantitative correlation analysis, a qualitative analysis of the previous results is presented in the following picture (*figure 12.16*), which shows the contours of *Q* instantaneous, *VV, PP* and *P*.

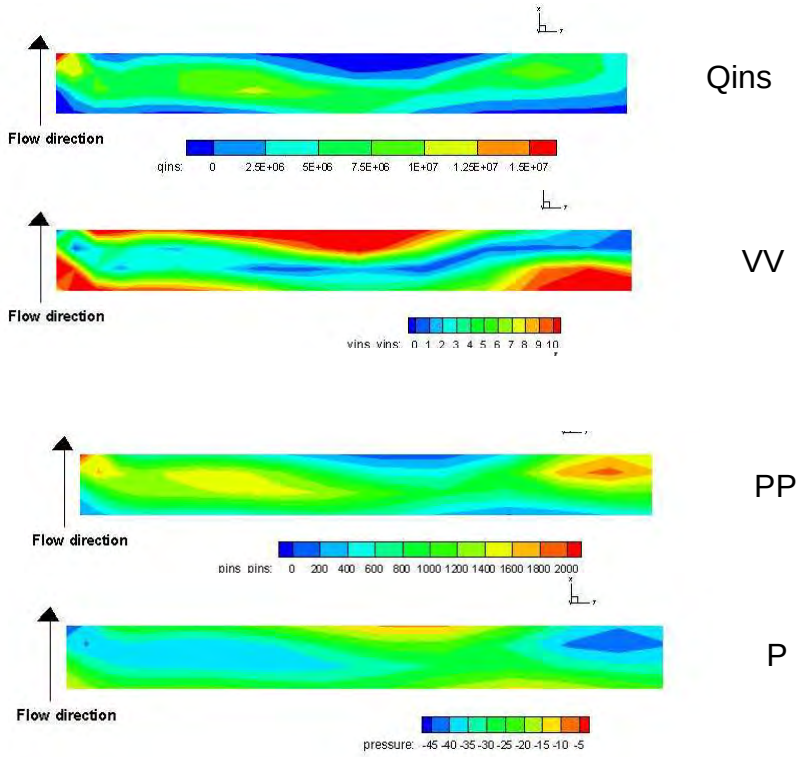


*Figure 12.16 Contours of Q, VV, PP and P in plane CS*

As it can be seen, these variables are correlated with *Q*, as qualitatively indicated by the fact that they reproduce the shape of the CS(s) (*Q*). In addition, it can be seen the presence of a

region of minimum velocity and pressure in the mid part of the coherent structure. This pattern is due to the action of two vortices which interact creating a large region of low pressure and made up compose the CS.
A similar visualization for the average field is presented in *figure 12.17*.

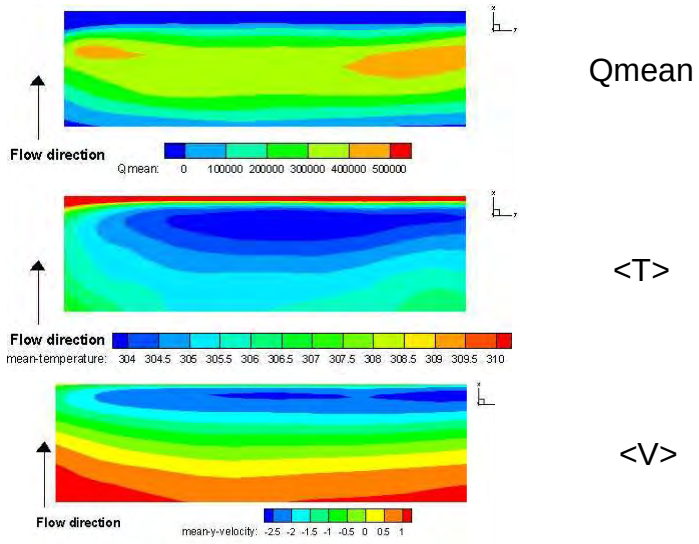


*Figure 12.17 Contours of< Q> , <T> and <V> in Plane CS*

It can be remarked in *figure 12.17* that the contours of <*Q*> qualitatively resemble those of mean temperature and velocity putting in evidence the trends already indicated by the correlation analysis. Moreover, it can be seen that the value of temperature is minimum in the regions where the velocity is negative. It can be concluded that the CS interacts with the region of bottom wall of minimum temperature (*figure 12.4*) and its own temperature reaches a comparable minimum, increasing moving away from the wall, mixing up with the rest of the fluid.

### *12.3.4 Other planes of the investigation*

The investigation of the region near to the heated wall was completed by the investigation of different horizontal and vertical planes within the domain around the 4$^{th}$ rib.
*Figures 12.18 and 12.19* show the planes selected for the study:

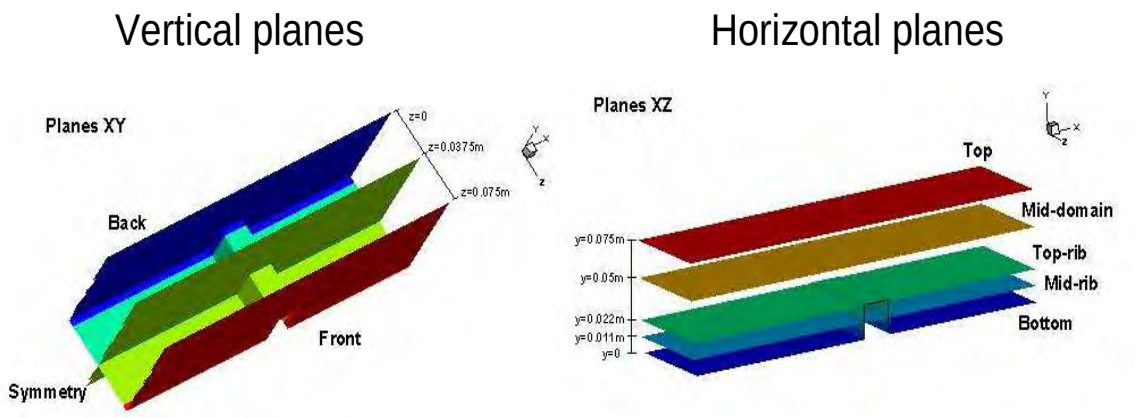


*Figure 12.18 Planes of correlation analysis*

The length of these sub-domains is equal to the distance between two ribs, 0.428 m, and they cantered on the 4$^{th}$ rib. The height of the planes is equal to the height of the channel.

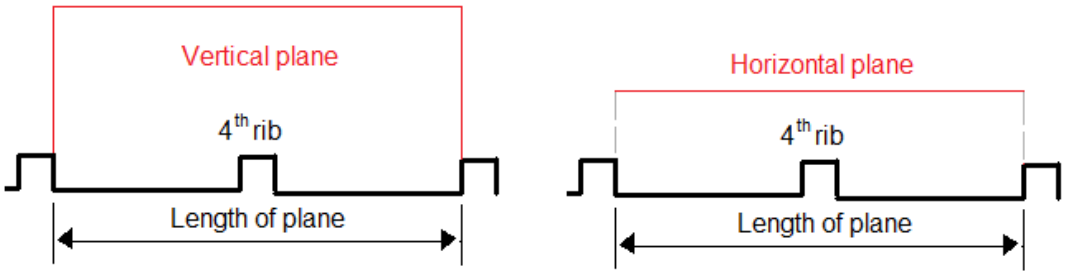


*Figure 12.19 Domain of plane for correlation analysis*

The three vertical planes are named as *Front* and *Back* with respect to the symmetry plane (*Symmetry*) of the domain. The horizontal planes are named as: *Top* is located the top part of the domain; *Mid-domain* located at a distance of 0.025m of the top of the domain; *Top-rib* is located in correspondence of the top face of the 4$^{th}$ rib; *Mid-rib* cuts in half the 4$^{th}$ rib. Each one of these planes has been studied individually and the corresponding results are resumed n the following *Tables 12.7* and 1*2.8*.

| | VERTICAL PLANES | | | | | |
|---|---|---|---|---|---|---|
| | BACK | | SYMMETRY | | FRONT | |
| | *Q* | <*Q*> | *Q* | <*Q*> | *Q* | <*Q*> |
| *TT* | 0.04 | 0.02 | 0.02 | 0.00 | 0.07 | 0.01 |
| *T* | 0.04 | 0.02 | 0.03 | 0.01 | 0.08 | 0.01 |
| <*T*> | 0.02 | 0.02 | 0.02 | 0.01 | 0.05 | 0.02 |

*Table 12.7 Subset of correlation matrix in vertical planes*

| | HORIZONTAL PLANES | | | | | | | |
|---|---|---|---|---|---|---|---|---|
| | TOP | | MID DOMAIN | | TOP RIB | | MID RIB | |
| | *Q* | <*Q*> | *Q* | <*Q*> | *Q* | <*Q*> | *Q* | <*Q*> |
| *TT* | -0.25 | 0.05 | -0.01 | -0.02 | -0.02 | 0.13 | -0.02 | -0.03 |
| *T* | -0.24 | 0.05 | 0.00 | -0.02 | 0.00 | 0.12 | 0.00 | -0.02 |
| <*T*> | -0.20 | -0.03 | -0.23 | -0.13 | -0.04 | 0.12 | -0.03 | -0.02 |

*Table 12.8 Subset of correlation matrix in horizontal planes*

On the opposite of what was remarked for the analysis of the bottom plane, the correlation between *Q* and temperature is very low for most of these planes. It can be assumed that the presence of CS(s) or the interaction of between CS and heat transfer with these planes are very small.

Important interactions are present only for the horizontal plane '*Top'* and the horizontal plane '*Top rib*'. In the case of plane '*Top'* a strong correlation is found for the instantaneous Q and temperature; this can be attributed to the CS(s) present in the attached boundary layer on the top wall; non the contrary the correlation between <*Q*> and temperature is low, confirming that permanent vortex regions and separated regions (when present) are dominant in heat transfer. In the case of plane '*Top rib*', the not negligible correlation between <*Q*> and temperature is due to the separated region on the top face of the rib (see previous section). However, the size of plane of investigation is large compared with one where the CS are present (see *figures 12.5* and *12.5*) and, therefore, the absolute value of correlation with temperature is small. This allows concluding that future analysis should be performed on smaller sub-domains to investigate homogenous regions.

### *12.3.5 Conclusions: correlation in bottom and rib planes*:

To resume the present investigation the following *figure 12.20* presents the correlation between <*Q*>, <*T*> and EF_mean between the downstream face of the 3rd rib and the downstream surface of the 4th rib. These graphs are a good reference to describe and resume the interaction of CS(s) and/or permanent vortex regions in the heat transfer process.
In both graphs it can be seen that the value of the correlation between <*Q*> with <*T*> or the correlation between <*Q*> and EF_mean increases in the regions where the regions of high vorticity. Both parameters reach a maximum in the corner upstream the rib, in correspondence of the strong corner vortex. On the top plane of the rib, the correlation number is also high, in correspondence of the separate region and the maximum downstream of the reattachment where CS(s) develop themselves at the wall.

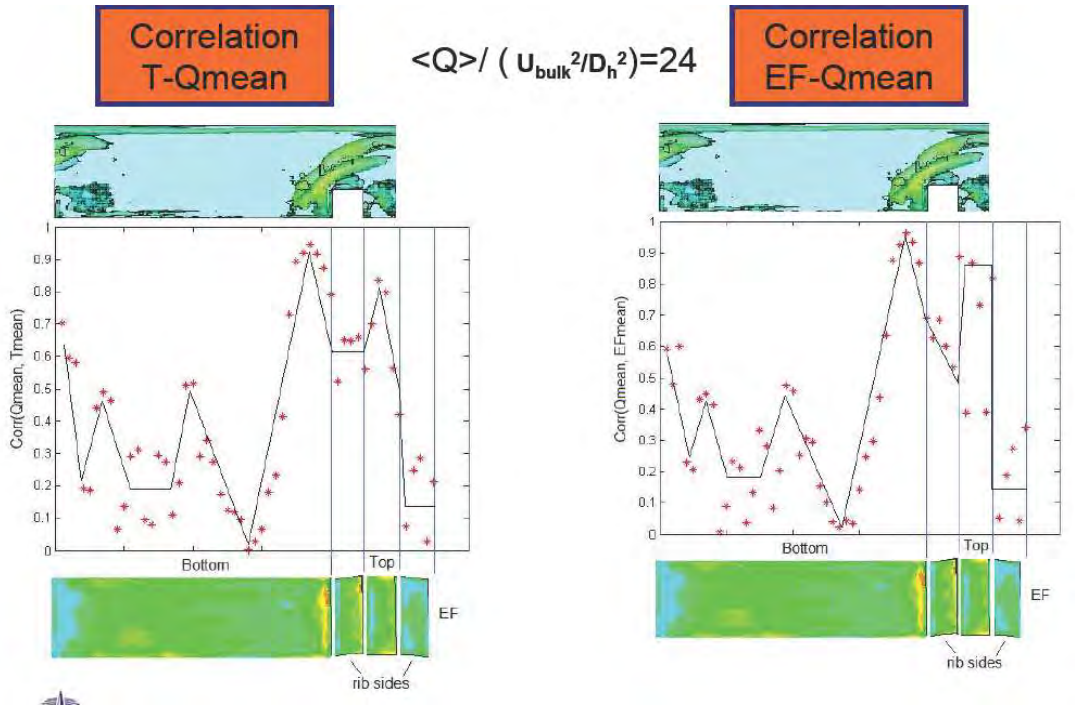


*Figure 12.20 Left: Correlation <Q> -<T> on the bottom and 4th rib surface. Right: Correlation <Q>-EF_mean on the bottom and 4th rib surface*

**Conclusion**:

It has been demonstrated that correlation analysis represents a very powerful tool to investigate a complex process such as conjugated heat transfer. It is possible to individuate the parameters driving the phenomenon and differentiate the different interactions in different regions of a flow field.

It has been verified that CS(s) and the regions of permanent high vorticity are strongly correlated with the heat transfer process. Moreover, the present results show that these structures are also strongly correlated with the temperature and they are a mechanism of the changes of temperature of the fluid in function of the temperature of the heated surface. Section 5.2.4 shows how a CS interacts with the region of minimum temperature at bottom surface: fluid within the CS reaches the same low temperature as the wall and its temperature changes moving away of the wall and mixing up with the rest of the fluid. Therefore, the increase of the presence of CS(s) in the flow enhances the heat transfer process.

On the other hand, the CS(s) seem to be strongly correlated with the component of the velocity normal to the bottom surface. To corroborate this hypothesis, it would be necessary to perform a more detailed study changing the velocity direction within the duct. Different options could be, in principle, feasible: to insert additional ribs on the bottom surface, to change the bottom ribs geometry… To assess the effect of the presence of CS, the next step would to find the optimum rate between the heat transfer process due to their presence and the minimum pressure drop.

# CHAPTER 13 Results of the Conditional Averaging

## *13.1 Application of conditional averaging to flow and thermal field*

This section presents the results of the application of the Conditional Averaging method explained in section 11.3.

To the long term, it is planned to apply this approach to all the most important parameters identified by the Correlation Analysis (Chapter 11) to reach a complete assessment of the phenomenon, but for this year, a first proof of feasibility and verification of the procedure is presented, applying it to the most relevant quantities characterizing the average field, namely, <*V_mag*>,<*Tke*>, <*T*>.

The *Q* field is sub-divided in the 5 classes introduced in section 11.3.

The first step is to visualize the time average of I (<*I*>) indicator, which shows the statistical presence of CS(s) (or of these sub- classes) in the space. *Figure 13.1* shows the distribution of <*I*> for the first two global classes (I when the vorticity rate is dominant, *Q*>0; II when the strain rate is dominant *Q*<0) for the symmetry plane of the 4$^{th}$ pitch:.

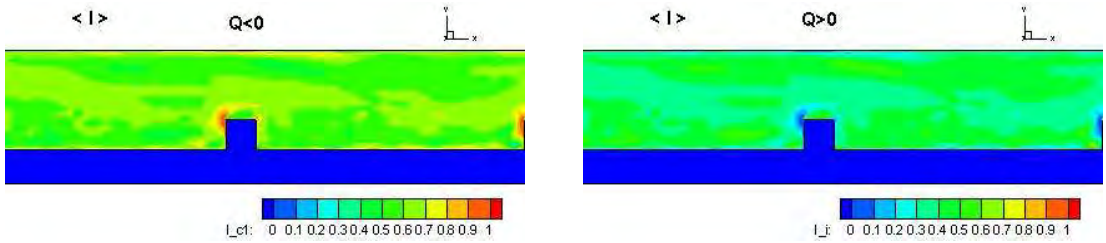


*Figure 13.1 Contours of <I> in symmetry plane. Left: class II. Right: class I*

These two images are complementary; thus, the sum of the two variables is equal to 1. When <*I*>=1 there is no perturbation in the field and the initial condition (fluid not conditioned) is recovered.

The right side image shows that the value of <*I*> for class *I* (*Q*>0, statistical presence of CS(s)) reaches a minimum at the upper corner upstream the rib. This result is explained by the distribution of <*Q*> presented in the following *figure 13.2*. It can be seen that, on the symmetry plane, there is no presence of CS(s) around this location, which explains the existence of this minimum.

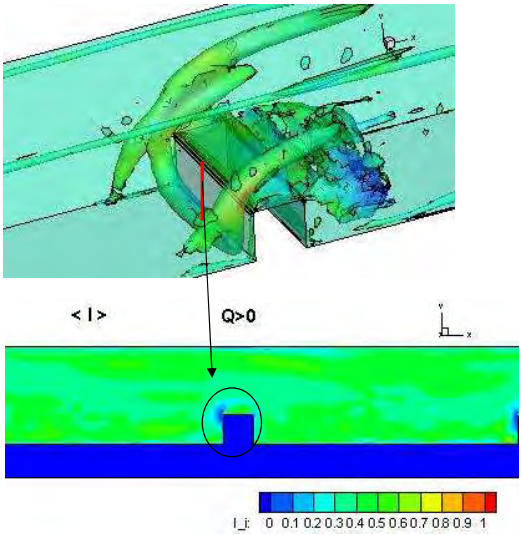


*Figure 13.2 Comparison of Q average with contour distribution of <I> in class I*

*Figure 13.3* shows the complete sub-division of <*I*> in the different sub-classes. The bottom right image presents a verification of the present routine through the sum: $\sum = < I >^{III} + < I >^{IV} + < I >^{V}$ is indeed equal to $< I >^{I}$ and adding this sum to $< I >^{II}$ the value of 1 is recovered, as it should.

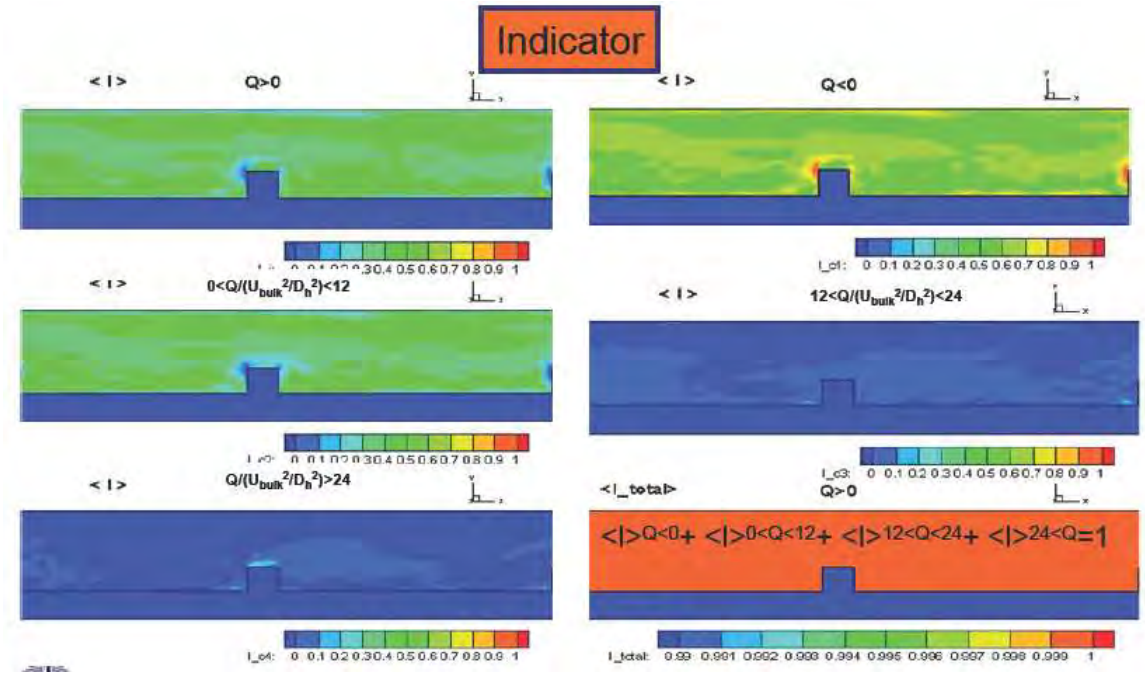


*Figure 13.3 Contours of <I> in symmetry plane in classes I, II, III, IV, V and <I> sum of classes II, III, IV and V*

Figure 29 shows that the statistical presence of vortex structures is around 50% in the regions of developed turbulence above bottom and top wall (CS(s) in the logarithmic layer) and is

lower in the core of the flow (about 20%), where the presence of CS(s) is usually low. Overall the presence of the strongest structures (classes IV and V) is statistically low. In fact, classes I and III present similar distributions, which allows concluding that most of the population of CS(s) lies within the range between 0 and 12 $U_b^2/D_h^2$. The exception is the region above the top face of the rib, where the value of $<I>$ for class V ($Q>24\ U_b^2/D_h^2$) corresponds to a statistical presence of the order of 20-30%, roughly half of the CS(s) present in this behavior is due to the vortex sheet of vorticity generated by the separation at the corner and the consequent formation of transversal rollers by Kelvin-Helmholtz instability (*figures 10.2*, *10.3* and [20]).

Further insight can be gained from *figure 13.4*, which offers a 3D view of the instantaneous field $Q$ colored by $<I>$. It can be remarked that the main structures correspond to values of $<I>$ higher of 50%, confirming the connection between $Q$ and the permanent vortex structures and the previous conclusion that most of the population of CS(s) lies within the range between 0 and 12 $U_b^2/D_h^2$. On the other hand, above rib a large contribution of the strongest structures is observed.

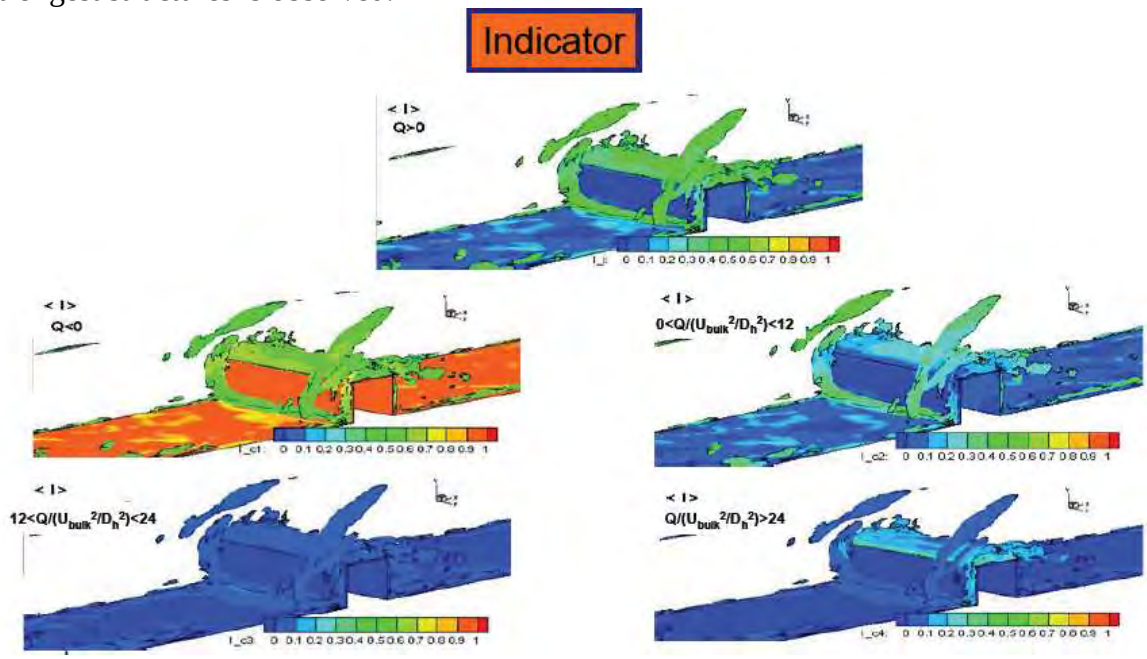


*Figure 13.4 Contours of CS coloured by of <I> in rib region: classes I, II, III, IV, V*

For what concerns the examination of the conditioned quantities, it is important to keep in mind that the sum of all variables conditioned into classes I and II is equal to the original variable, as pointed out by the following relationship and verified in *figure 13.5* for $<T>$:

$$< T >^{Q>0} + < T >^{Q<0} = \frac{\sum T \cdot I^c}{N} + \frac{\sum T\left(1 - I^c\right)}{N} \approx \frac{\sum T}{N}\left(< I >^c + 1 - < I >^c\right) = \frac{\sum T}{N}$$

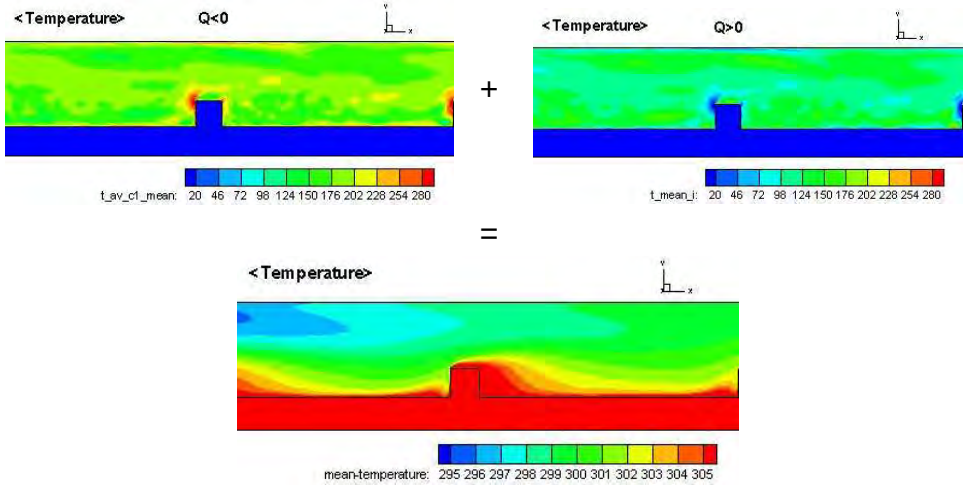


*Figure 13.5 Temperature in symmetry plane. Top: Class I and II averaged in time. Bottom: global temperature distribution*

The following *figures 13.6, 13.7, 13.8* respectively present the conditional averaged results for the velocity magnitude, the turbulent kinetic energy (*Tke*) and the temperature field conditioned by $I$ and averaged in time$(N)$. In each figure, the first image (top right) corresponds to the global average of the variable, while the successive images correspond to the previously defined sub-classes. The deviation from the initial field is not strong for the three first conditions. Relevant deviations can be remarked for classes IV, V but, as already remarked, the statistical presence of these classes is low, apart of the region above the top face of the rib.

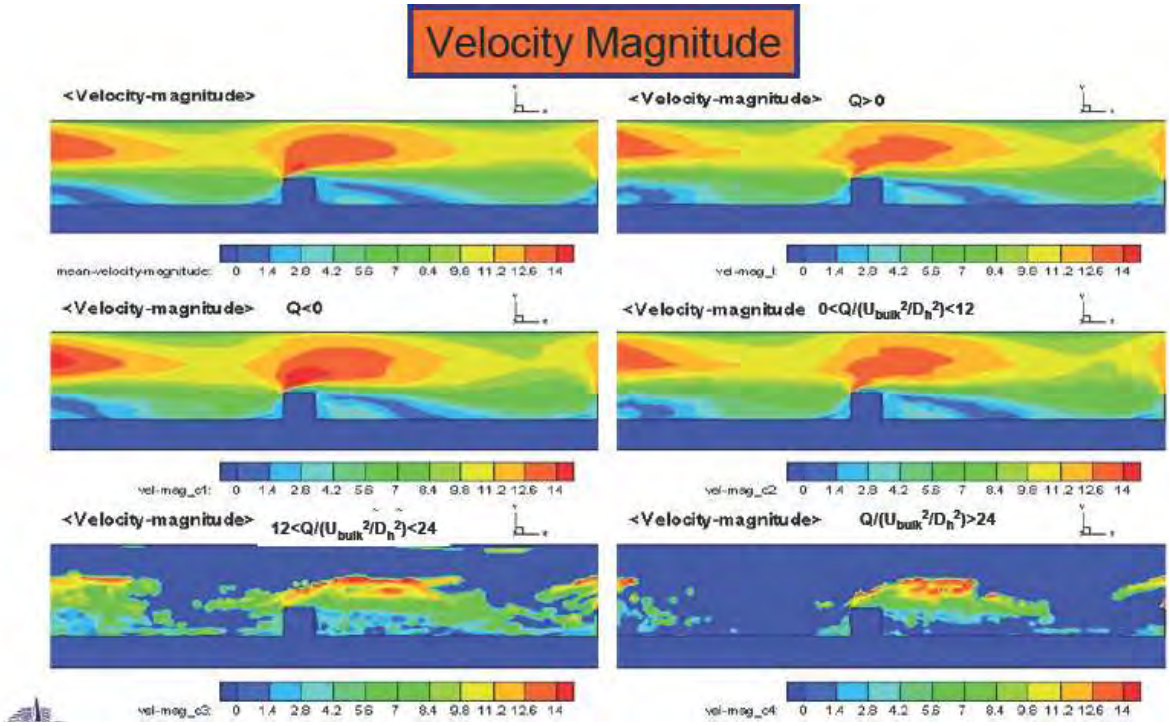


*Figure 13.6 Velocity magnitude in symmetry plane. Initial value and conditioned value in classes I, II, III, IV and V*

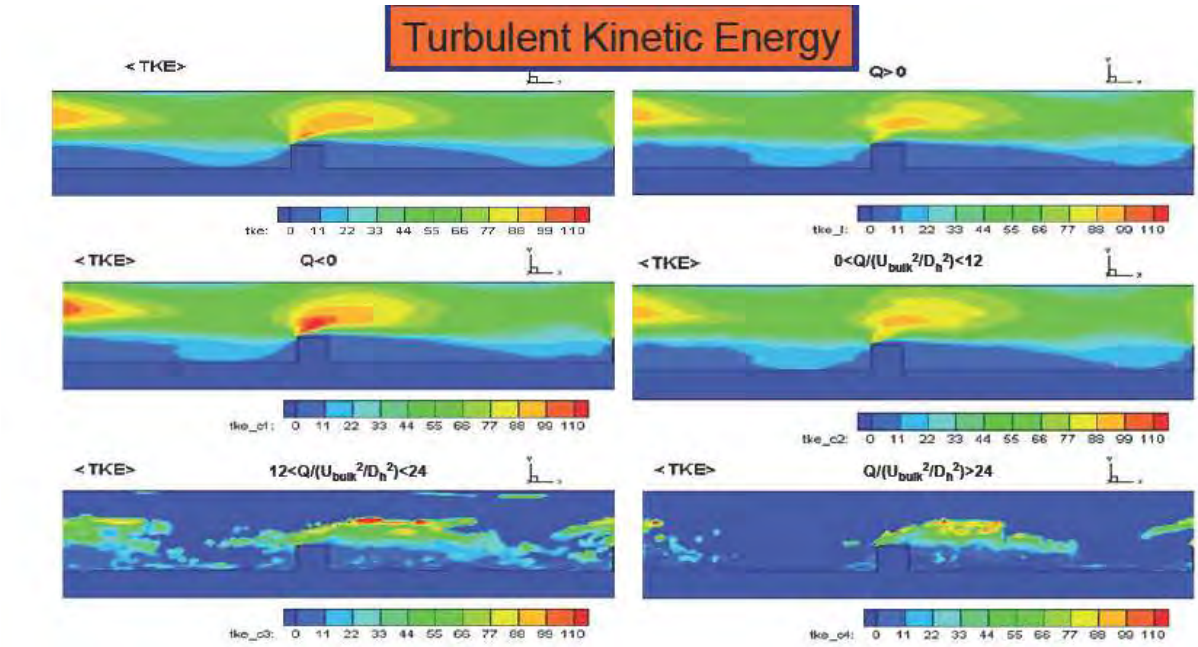


*Figure 13.7 Turbulent kinetic energy in symmetry plane. Initial value and conditioned value in classes I, II, III, IV and V*

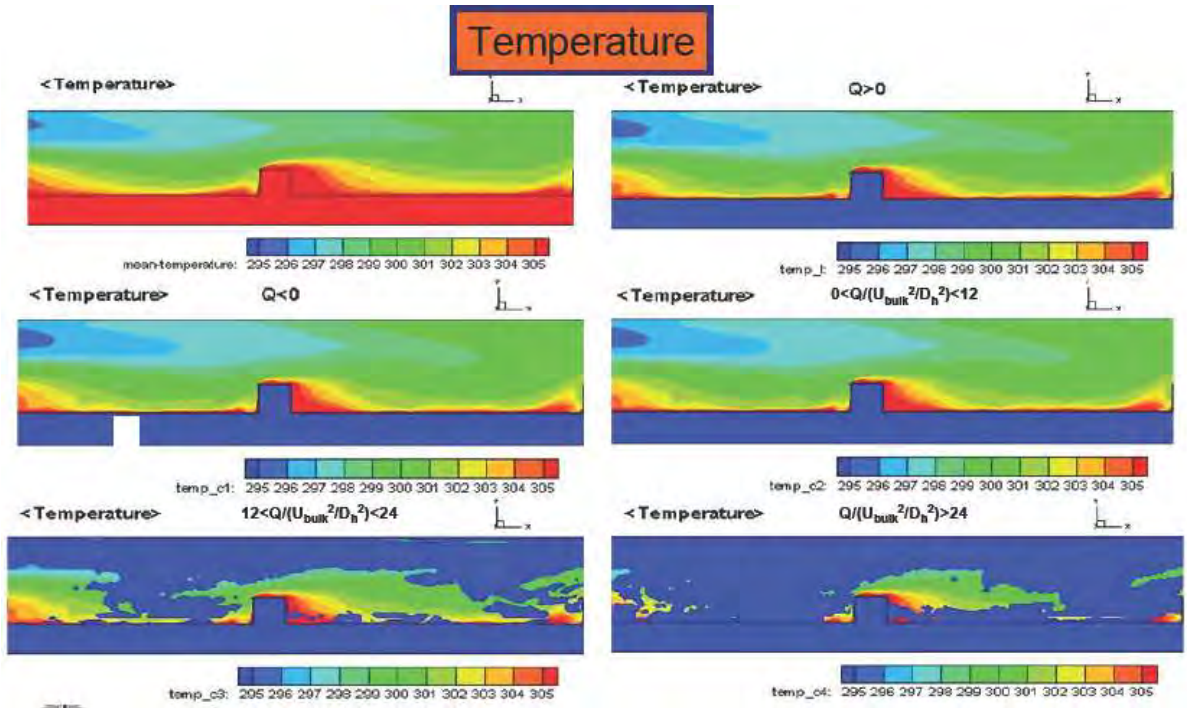


*Figure 13.8 Temperature in symmetry plane. Initial value and conditioned value in classes I, II, III, IV and V*

Concerning *figures 13.6 and 13.7,* it can be remarked that the values of velocity magnitude and *Tke* in class II (strain dominated regions) are higher than the corresponding ones observed for the original variables and for the class I (rotation dominated regions); This effect is due to the contribution of the strongest structures, which appear to correspond to lower velocity and kinetic energy, in particular above the rib, as confirmed by *figure 13.9.* This behavior will be further investigated in the following year

The distributions of values of velocity magnitude and *Tke* are very similar for classes I and III, confirming that most of the structures and their effects lie in the 12 $U_b^2/D_h^2$ class. The effect of conditioning becomes visible for classes IV and V, which indicates the different behavior of the strongest structures on the background flow, due to the presence of the rib.

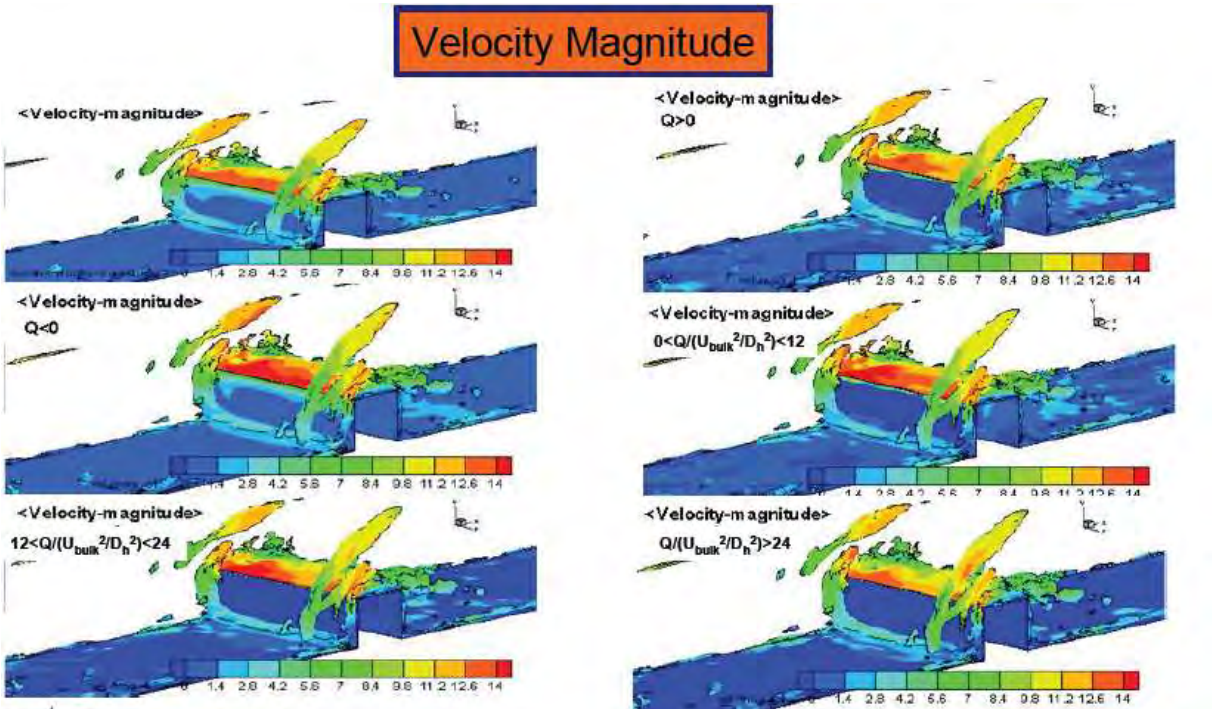


*Figure 13.9 Contours of CS coloured by of average velocity magnitude in rib region: classes I, II, III, IV, V*

## *13.2 Conditioned Enhancement Factor*

This section presents the Enhancement Factor for the different sub-classes. The objective is to compare, globally, the differences in heat enhancement due to the presence or the absence of CS(s).

The first step toward the understanding of the role of CS(s) on the heat transfer process at the heated surface is to identify the CS(s) which interact with that plane. The distribution of $<I>$ in bottom and ribs planes is presented in *figure 13.9.*

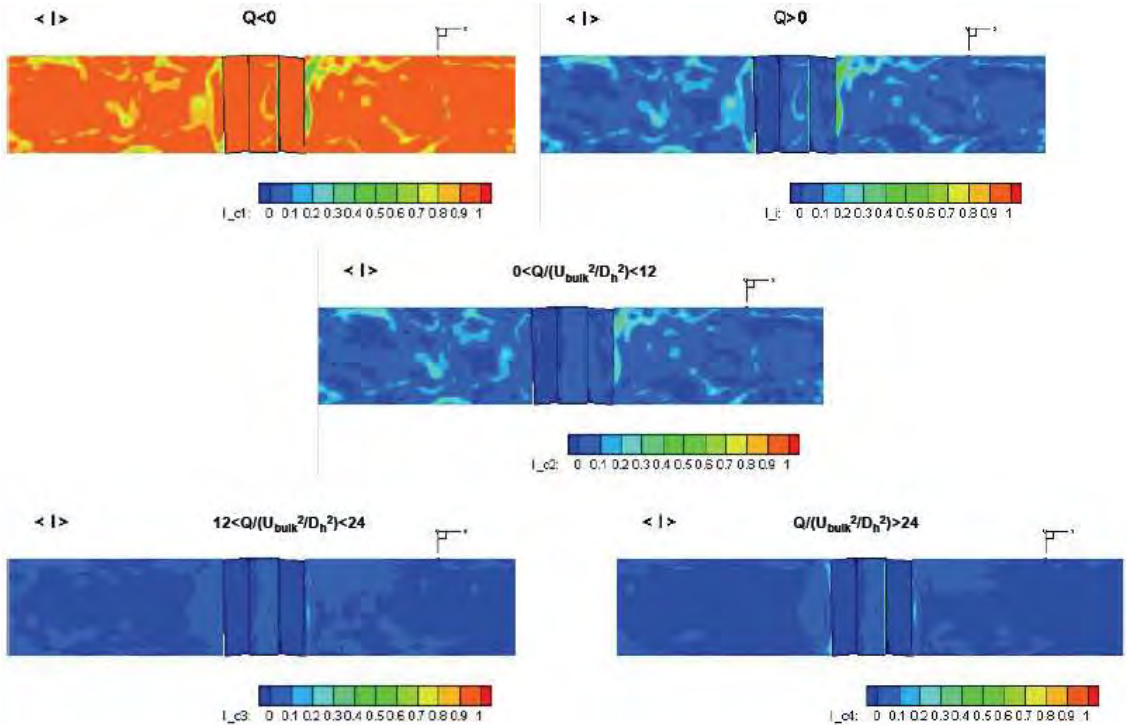


*Figure 13.10 <I> distribution in bottom planes. Conditioned value in classes I, II, III, IV and V*

Considering the distribution of $<I>$ for $Q>0$, it can be seen that the statistical presence of CS(s) which interact with this plane is globally small (0-10%) and most of these structures belong to the class $0<Q/(U_b^2/h^2)<12$. Only the trace of the upstream corner vortex is visible as small regions $Q/(U_b^2/h^2)>24$. However, the presence of the structures increases by 20-30% at some locations, namely at the upstream and downstream bottom corners, due to the permanent rotation in the separate region. In particular, at the downstream bottom corner (secondary separation and counter-rotating vortex) downstream of the rib a small region exists where this presence is close to 50%. On the other hand, in both vertical faces of the rib, no presence of CS(s) is visible and there is no effect.

Figure 37 compares the averaged Enhancement Factor with the ones conditioned. As it could be expected, in the regions where the presence of structures is low, the EF distribution is very similar to the original one; therefore, it could be tentatively concluded that the ***direct*** action of the CS(s) on the conjugated heat transfer is small in most of the domain. However, the influence of CS on the EF is visible on the top plane of the rib and at the bottom upstream corner which correspond to the presence of a permanent transversal vortex (bottom image of *figure 13.10*).

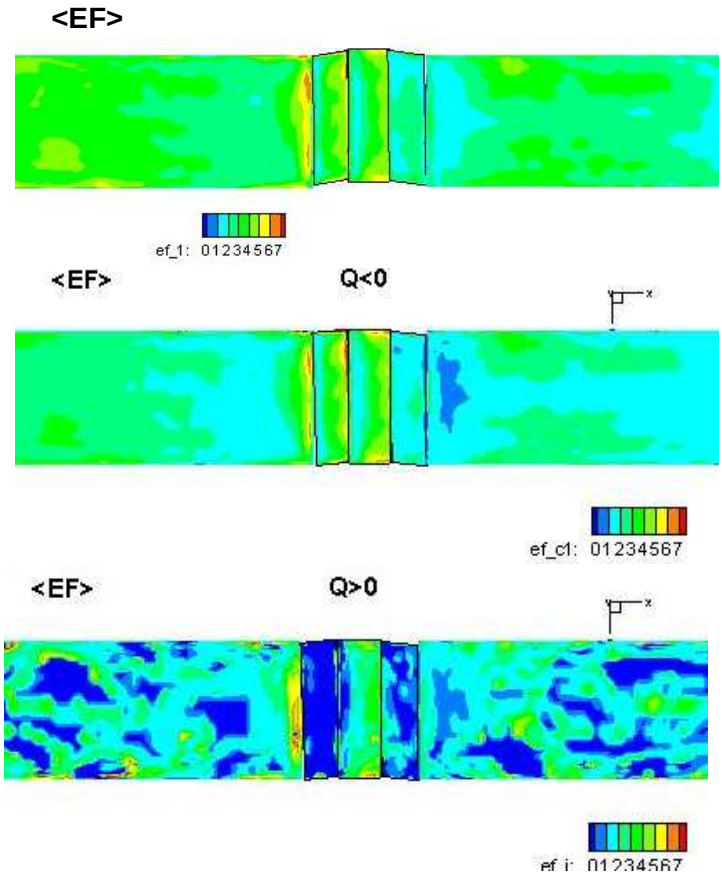


*Figure 13.11 Enhancement Factor. Original field, class II and class I*

**t**hey contribute the shaping the overall flow and strongly contribute to the generation of turbulence, but they do no interact directly with the conjugate exchange at the heated wall. Further verification and investigation of this point will be performed in the next year of this program. It should be remarked, in fact, that such preliminary conclusion could be biased by the choice of the region where the data for the conditioned analysis has been extracted, namely, the first cell above the ribbed wall. A sensitivity analysis will be performed to assess the sensitivity of the results on the size of such sampling region.

## *Conclusions for Part IV*

The present work has developed and demonstrated an integrated approach to study the role of CS(s) in a complex flow field. In the specific investigation, the effects of CS(s) have been evidenced and quantified for the thermal field in a ribbed duct of square cross section where the ribbed wall is heated.

The tools of this approach are:

-The visualization of the CS, defined as iso-surfaces of *Q* criterion for both the mean and instantaneous field, is applied for a qualitative analysis. Colouring of the iso-surfaces by different turbulent variables makes it is possible to have a first indication of the possible correlation among coherent turbulent motion, flow background and heat transfer process.

-The study of the matrix of correlation between flow and turbulent variables in different planes of the domain is applied to quantify the interaction between the CS on the thermal field. The capability of the Principal Component Analysis to reproduce the conjugate heat transfer process has been demonstrated. This approach has been applied to identify the most relevant turbulent variables in the heat transfer.
The results of this approach show that the vortex structures are strongly correlated with the wall temperature and they are a mechanism of heat transfer from the heated surface to the fluid. It can be suggested the increasing the presence and/or strength of the structures which interact with the heated surfaces would enhance the heat transfer process. The present results also indicate that vortex structures are strongly correlated with velocity in perpendicular direction to the ribbed surface. A somewhat surprising conclusion of Chapter 12 is that the permanent vortex regions and separated regions seem much more important than the classically-defined instantaneous CS(s). This tentative preliminary conclusion will be verified in the next year of investigation.

-The application of the Conditional Averaging approach is applied to assess the effects of the CS(s) in the flow field. In this approach, turbulence variables and their correlations are considered and averaged only if a specific prescribed condition on the local *Q* value is satisfied. Such condition is called a "class". In this application, sub-division in five different classes, defined on the basis of the *Q* value, has been proposed. The two first broad classes ($Q> 0$ and $Q< 0$) separate the flow coherent structures and turbulent background. The other classes separate the effects of the CS(s) in function of its intensity.

The first application of this technique has been the investigation of the symmetry plane. It is found that the statistical presence was in the order of 50% of the time of observation and most of the structures belong to the class $0 < Q < 12$ $(U_b^2/D_h^2) < 12$. At the heated surface the Enhancement Factor has been conditioned. The original distribution of EF is very similar to the one for the first class ($Q<0$), suggesting that the ***direct*** presence and effects of CS(s) is very small on heat transfer on most of the heated (bottom) surface. On the other hand, it is remarkable the correlation between of $<I>$ and EF the top of the rib: the minimum value of EF in the original field matches up with a region where there are no coherent structures.
The tentative conclusion of a weak direct effect of CS(s) on EF would appear surprising with respect of the conclusions drawn from the correlation analysis, which seemed to indicate a strong interaction between *Q* and temperature and EF. Therefore, it must be kept in mind that correlation analysis deals with non dimensional quantities and identifies the flow and heat transport quantities which are most strongly correlated with the CS(s), but does not quantify this effect in physical units. Therefore, the correlation analysis offers an insight on the physics of the process but it does not quantify its effect in absolute units.

# *Part V Comparison with the final test section*

# CHAPTER 14 Simulation of cooling holes

## *14.1 Computational domain*

The present simulation aim to reproduce the test section developed by the TUP department in the execution of the experimental part of the present study; this installation is made of a slab containing 5 consecutive ribs inserted in a duct of square cross-section (*figure 14.1*). The initial planned set-up was for 4 consecutive equal suction orifice bleeding fluid from the main flow in the duct to simulate the effect of impinging cooling system [25].

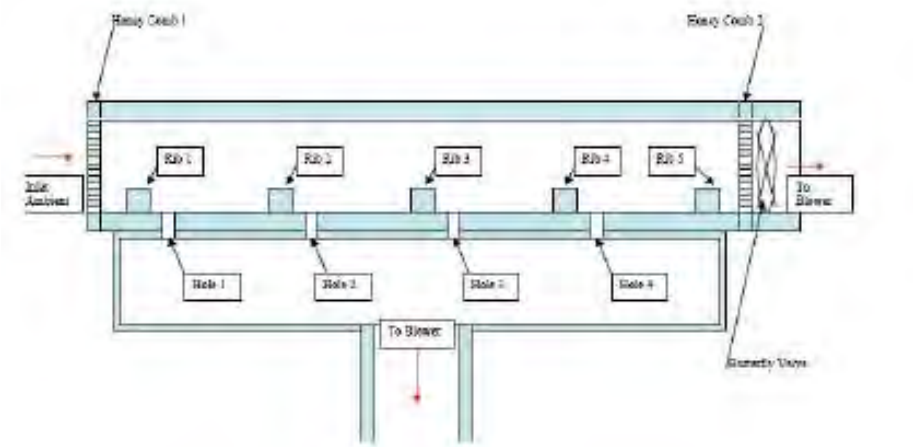

*Figure 14.1 Planned test section [25]*.

The numerical domain here investigated is a modification of the one studied during the two previous years of the present study (see Parts I, II). It is made of a duct of square cross-section. Five consecutive ribs of square cross-section extruded from the bottom wall, which is made of a solid slab (*figure 14.2*). The choice to retain this set-up is motivated by the need to compare with the previous results and past experience, which leads to expect that the simulated flow recovers from the inlet perturbation along the first three pitch lengths (pitch= distance between two successive ribs) and reaches equilibrium between the third and fourth rib, while the thermal field reaches equilibrium between the fourth and the firth rib [3]. Therefore, the $4^{th}$ rib was selected as the focus of the investigation and as comparison with the experimental data.
The bottom face of the solid slab is subjected a uniform heat flux, which is transferred to the fluid through the slab creating a conjugate heat transfer situation. The primary investigation is performed for the input heat flux q=2200 w/$m^2$ to allow the comparison with the results already obtained during the research (see Part I).
.

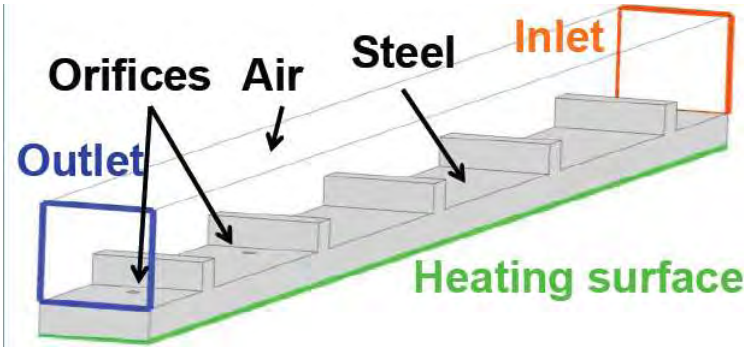


*Figure 14.2 Computational domain*

The hole is located at the centre of the passage, 26.25 mm from the downstream face of each rib

- The diameter is $d$ = 0.75 cm

The working fluid is air and the flow is assumed to be incompressible. The Reynolds number in the duct is Re = 40,000 in terms of bulk velocity (defined upstream of the first active orifice) and hydraulic diameter.

## *14.2 Preliminary Simulations*

A first difference between the present simulations and the previous ones (Part I) concerns the inlet boundary condition. In the past work, the simulation aimed to reproduce an infinite succession of consecutive ribs (Part I and [3, 20]); therefore, the flow conditions at the inlet boundary should have been the same as at the outlet boundary. Practically, this was achieved imposing at the inlet the distribution of velocity and turbulent kinetic energy obtained by a preliminary RANS simulation, performed imposing periodic boundary condition along the longitudinal direction. Differently, the present simulation should reproduce the test section developed by the TUP department in the execution of the experimental part of the present study; this test section [25] is made of a slab containing 5 consecutive ribs inserted in a duct of square cross-section (*figure 14.1*), where a honeycomb is used to uniform the flow upstream of the first rib.

Therefore, the flow conditions upstream of the first rib correspond to developed flow in a duct; due to the high Re of the flow, the inlet boundary conditions can be simplified imposing an uniform flow corresponding to the average of the experimental data [25]; the profiles of longitudinal velocity and kinetic energy at the symmetry line for the old and new simulations are shown in *figure 14.3*.

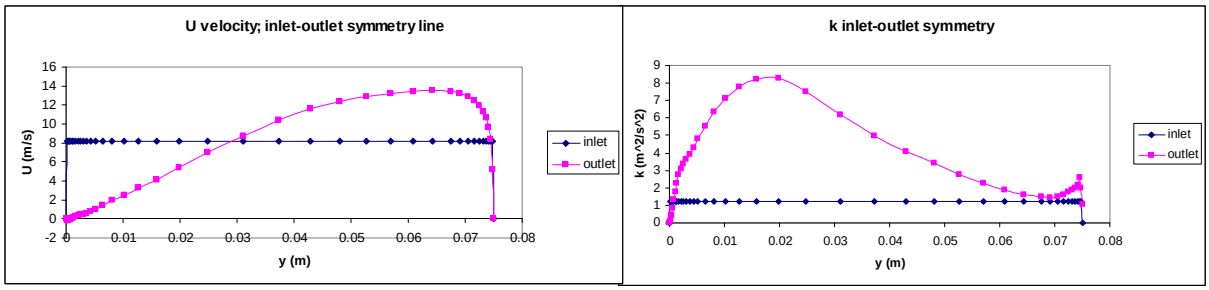


*Figure 14.3 Inlet-outlet BC. Center-line. Left: velocity; right: turbulent kinetic energy. Blue: new inlet condition; magenta: old inlet condition.*

A first preliminary steady state RANS simulation was performed applying the realizable energy-dissipation model. The resulting distribution of EF is presented in *figure 14.4*: the iso-contours (left) show that, for the last 3 ribs, the distribution of EF is similar to the one found in the previous investigation; the evolution of EF along the centre-line (right) shows the equilibrium condition is attained and the data for the 4$^{th}$ rib can be considered to represent the equilibrium state.

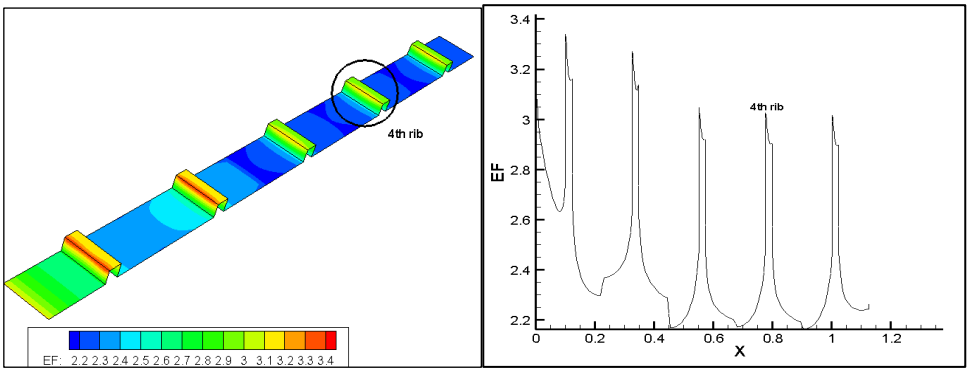


*Figure 14.4 EF. Left: map of iso-contours; right: evolution along the centre-line*

In parallel, a preliminary LES simulation was performed with uniform inlet boundary conditions [26]. *Figure 14.5* presents results of this simulation, namely: the average longitudinal velocity <U>; the variance of the resolved fluctuation <u'u'> and the resolved in-plane turbulent shear stress <u'v'>, for 2 locations on the symmetry plane at: the centre location of the 4$^{th}$ rib (X/*h*=0) and a location within the main downstream separated region (X/$H_{rib}$ =1). The present result is comparable to the previous ones (Part II) and maintains an acceptable (or better) agreement with the experiment [8], which indicates that the conclusions and conceptual models proposed on the basis of the previous simulations [4, 20] applied Part IV can be exported to the present task.

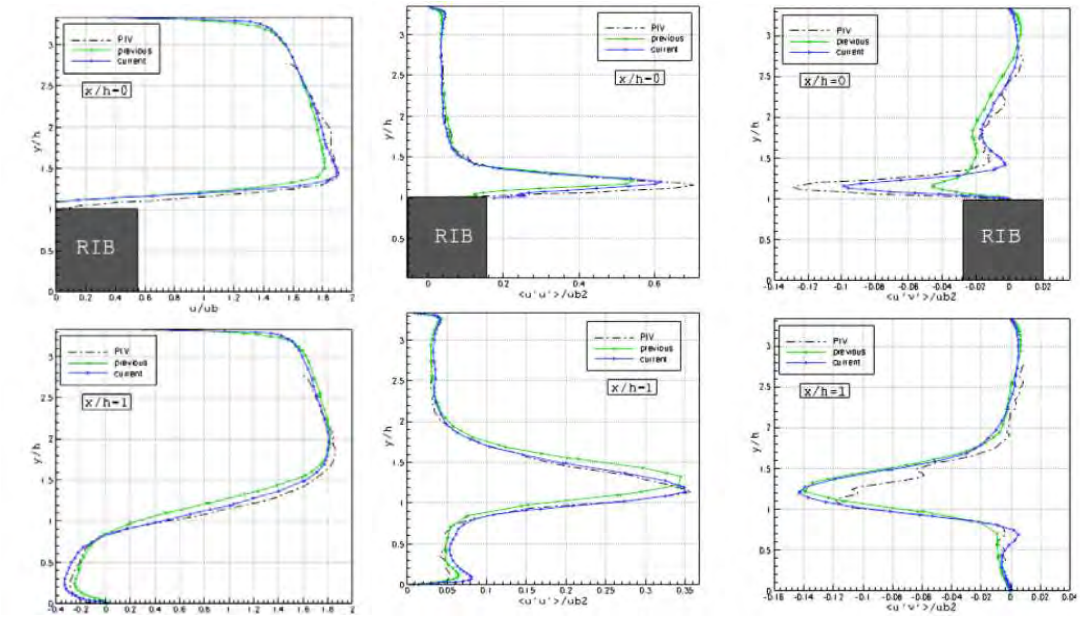


*Figure 14.5 Left column: average longitudinal velocity <U>; centre column: variance of the resolved fluctuation <u'u'> ; right column resolved in-plane turbulent shear stress <u'v'>.*

## *14.3 Building of the grid*

Gambit commercial code was applied to build a suitable grid, which was used for both RANS and LES simulations.
Due to the presence of the orifice, symmetry in the transversal direction is lost, and mesh generation cannot any longer performed generating a longitudinal section and extruding it along the transversal direction (chapter 4), procedure, which is resumed in *figure 14.6.*

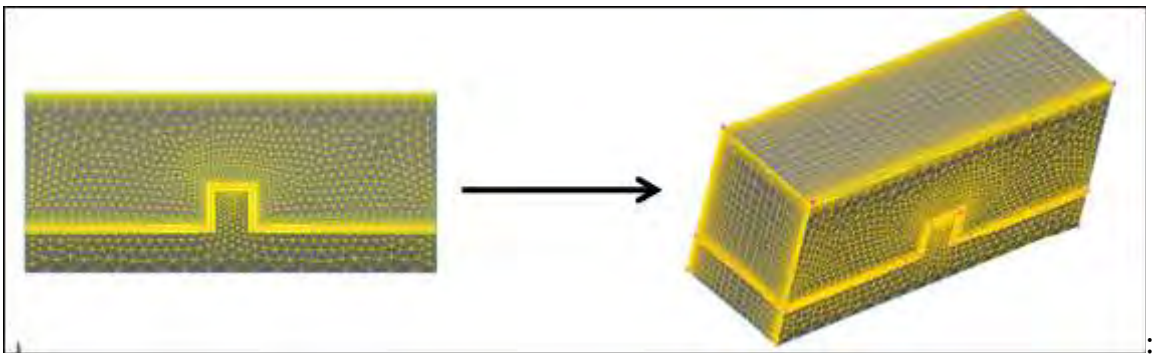

*Figure 14.6 Transversal extrusion method of mesh generation*

Therefore, mesh generation was carried out creating of separated grid blocks, which are connected at posterior. An example of this procedure is presented *figure 14.7*, which shows the union of the grid blocks describing the orifice and the rib.

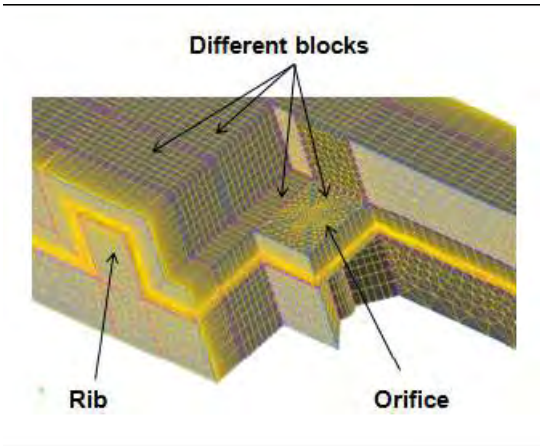


*Figure 14.7 Building of grid by combination of different block: orifice and rib region*

This approach results in a hybrid grid, made of different structured and unstructured blocks. Most of the blocks are created with Cooper Scheme, which generates structured blocks extruding an unstructured block face made of triangular prisms. A block generated with such technique is shown in *figure 14.8.*

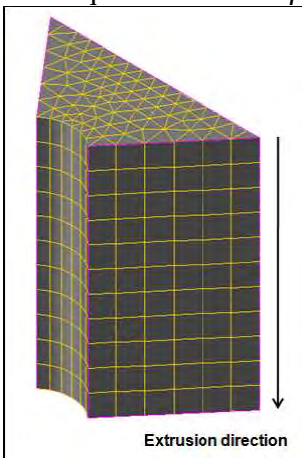


*Figure 14.8 Example of a block generated by Cooper technique*

Tetrahedral elements are introduced in the block close to cooling orifice. This region is the one where the quality of the mesh is worst. A slice of this zone is shown in *figure14.9*, the elements being colored in terms of iso-skewness.

A maximum skewness of 0.78 is found in such zone. In the rest of the mesh, skewness has an acceptable maximum value of 0.34.

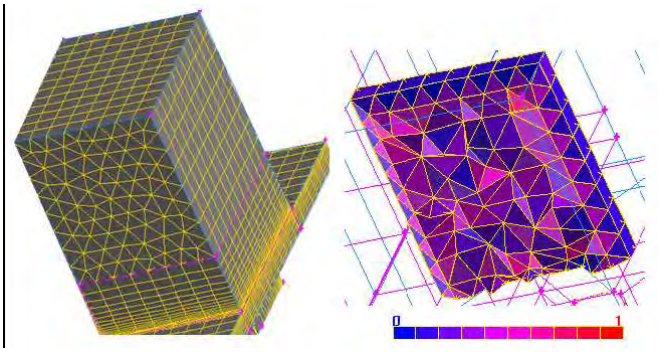


*Figure 14.9 Detail of the mesh block formed by tetrahedral elements*

Reason to introduce this unstructured mesh lies on the need of encasing the region near to the orifice within an ad hoc block to minimize the number of nodes necessary to grid this region, as shown in *figure 14.10.*

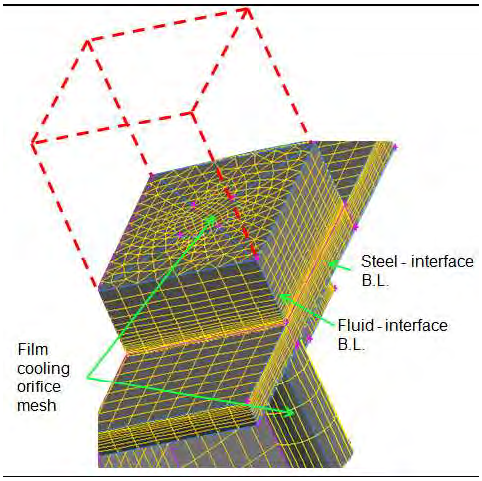


*Figure 14.10: Detail of grid of the orifice; interface with fluid and solid parts.*

An overview of the mesh layout for the symmetry plane is shown in *figure 14.11*. The region of the slab is meshed with cubic elements corresponds to the surroundings of the orifice.

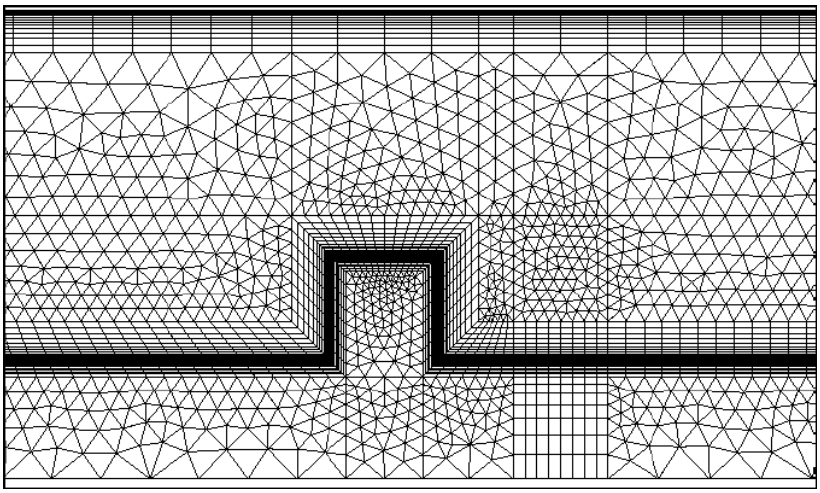

*Figure 14.11 Mesh at symmetry plane*

Boundary layer regions are inserted at the wall and at the interface steel –fluid (*figure 14.12*) to improve the accuracy of the simulation.

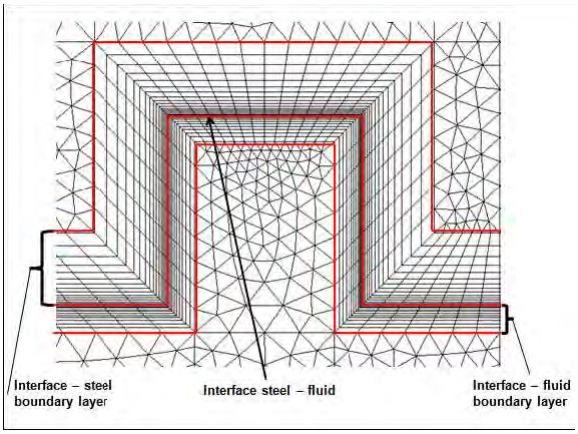


*Figure 14.12 Boundary layer grid at the steel-fluid interface*

A detail of the interface steel-fluid at the bottom wall is shown in *figure 14.13*.

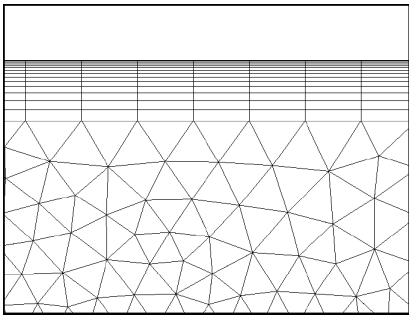

*Figure 14.13 Detail of the interface steel-fluid at the bottom wall*

The numerical parameters of the boundary layer regions are resumed in the following table:

| Boundary Layer | Growing factor | Number of rows | First row height (mm) |
|---|---|---|---|
| Top wall fluid | 1.2 | 14 | 0.15 |
| Interface - fluid | 1.1 | 22 | 0.02688 |
| Interface - steel | 1.2 | 16 | 0.03 |

*Table 14.1: Numerical parameters of the boundary layer regions*

Within these boundary layers, distances from the wall of the nodes are small enough (in wall coordinate $y^+ = \frac{u_\tau y}{\nu}$), to allow resolving the flow down to the wall and avoiding the recourse to wall functions. Namely, at least the first cell center height falls within the viscous laminar sub-layer. The map of $y^+$ obtained from a RANS simulation is presented in *figure 14.14.*

Although zones with $y^+$ higher than unity exist, those correspond to zones of separated flow, where shear stress at wall is close to zero and do not affect the accuracy of the simulation.
.
A similar order of magnitude for $y^+$ was obtained for the LES simulation.

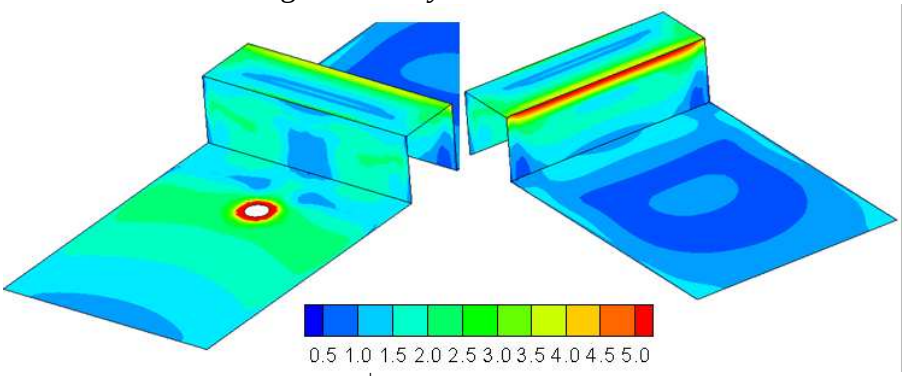


*Figure 14.14: Contours of $y^+$ at first cell centers*

The complete grid is made of 1.353 million nodes.

# CHAPTER 15 Preliminary RANS tests

## *15.1 Setting the boundary conditions for the suction*

A preliminary steady simulation was performed, applying the κ-ε RANS model, in order to define the boundary conditions suitable for the simulation of the action of the orifice. Under this point of view, the main task is to set the boundary conditions for the orifice itself, because it is unfeasible to include in the simulation the entire aspiration set-up used for the experimental set-up (*figure 14.1*). For reasons of feasibility, the boundary condition must be

applied to outlet of the orifice itself. This boundary condition must be set to attain the mass flow expected at the orifice for the test section at design condition. This value was chosen to correspond to the blowing ratio (BR) between bulk velocity at the orifice $V_b$ and at inlet of the duct $U_b$ to 4.5, or : $V_b$=4.5 $U_b$ .
As Fluent does not support both "outlet velocity" and "pressure outlet" in the same simulation it was necessary pass through an intermediate step:
-In the intermediate simulation, the outlet of the duct is simulated as "outlet velocity" ($2^{nd}$ derivate along the direction normal to the boundary is imposed to 0); at the outlet of the orifice the requested nominal $V_b$ is imposed.
This simulation provides the average pressures at the outlet of the duct and outlet of the orifices. These values were applied as pressure boundary condition ("pressure outlet") at the respective boundaries.

This first simulation was performed requiring the same mass flow through all the holes. This definition represents a strong simplification of reality, because the mass flow through the different orifices can be expected to change with the local pressure in the main duct, but it allowed testing the procedure waiting for the final operational data for the test section.
A posteriori, it was verified that the target mass flow is maintained with minimal difference of exit pressures for different holes, as shown in the *Table 15.1* below.

| Boundary | kg/s | P (Pa) |
|---|---|---|
| Inlet | 0.055125 | 99.6 |
| Hole 1 | -0.001948 | -1651.6 |
| Hole 2 | -0.001948 | -1646.1 |
| Hole 3 | -0.001948 | -1638.6 |
| Hole 4 | -0.001948 | -1629.9 |
| Hole 5 | -0.001948 | -1614.1 |
| Outlet | -0.045383 | -0.000387 |

| Boundary | kg/s | P (Pa) |
|---|---|---|
| Inlet | 0.055125 | 100.1 |
| Hole 1 | -0.001925 | -1610.4 |
| Hole 2 | -0.001925 | -1604.7 |
| Hole 3 | -0.001925 | -1597.1 |
| Hole 4 | -0.001925 | -1588.2 |
| Hole 5 | -0.001925 | -1572.4 |
| Outlet | -0.045498 | -0.000397 |

*Table 15.1: Mass flow and pressure for imposed velocity boundary condition at the outlet of the hole (left). Mass flow and pressure for pressure outlet and mass flow target at the outlet of the hole (right)*

*Figure 15.1* and *15.2* respectively present the iso-contours of pressure and temperature in the symmetry plane of the orifice of the $4^{th}$ pitch, for the two boundary conditions.

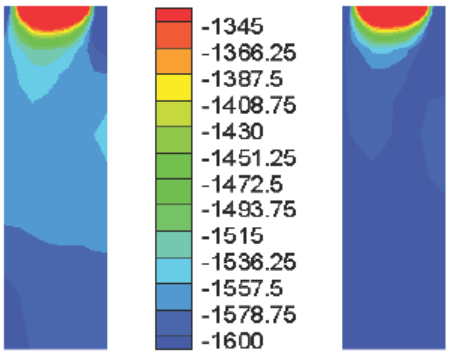


*Figure 15.1 Symmetry plane of the 4th orifice. Distribution of pressure: imposed velocity boundary condition at the outlet of the hole (left); pressure outlet and mass flow target at the outlet of the hole (right).*

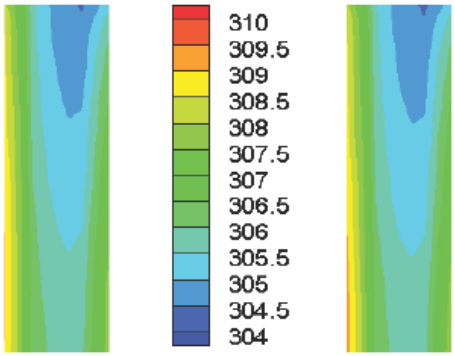


*Figure 15.2 Symmetry plane of the 4th orifice. Distribution of temperature: imposed velocity boundary condition at the outlet of the hole (left); pressure outlet and mass flow target at the outlet of the hole (right).*

The flow and thermal fields so obtained were compared with the one with closed orifices for the same conditions.
The effect of the suction at the wall is visible in *figure 15.3*, which presents the wall shear stress with and without action of the orifice. This image assembles: the upstream bottom wall, the three faces of the rib and the downstream bottom wall. It can be remarked that effect of the suction is confined to downstream face of the rib and to the downstream bottom wall; the other regions of the domain appear not to be affected by the action of the orifice. The action of the suction is visible through the local maxima and minima on the downstream face of the rib, which are related to the high level of transversal velocity (flow moving toward the hole) and on the bottom wall, where the negative values of shear stress in the separated region are higher than it is the case for the unperturbed duct.

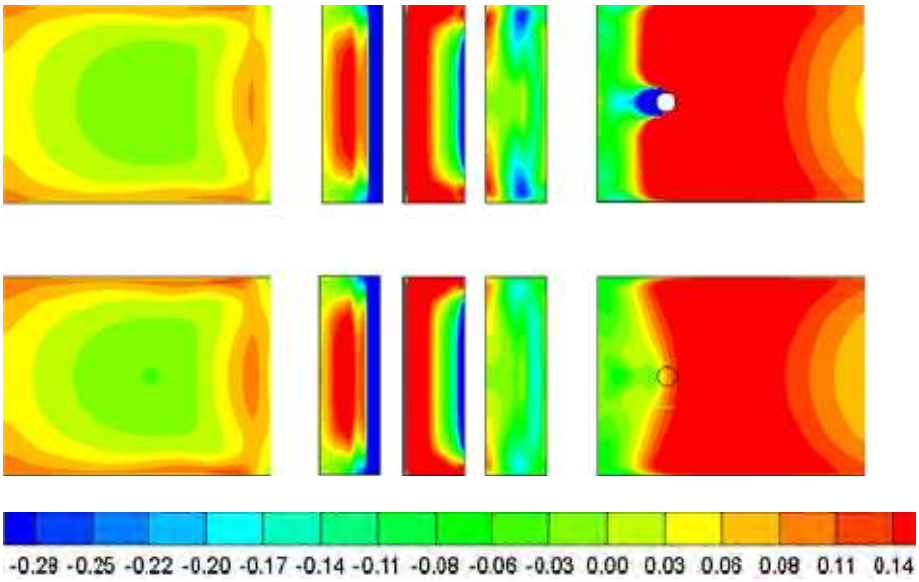


*Figure 15.3 Wall shear stress. Left to right: upstream bottom wall, upstream face of the rib, top face of the rib, downstream face of the rib and the downstream bottom wall. Top: active orifice. Bottom: no active orifice.*

Similar trends can be seen for the distribution of EF, presented in *figure 14.4*. The effect of the suction is confined to downstream face of the rib and bottom wall, where EF higher than it is the case for the unperturbed duct.

.

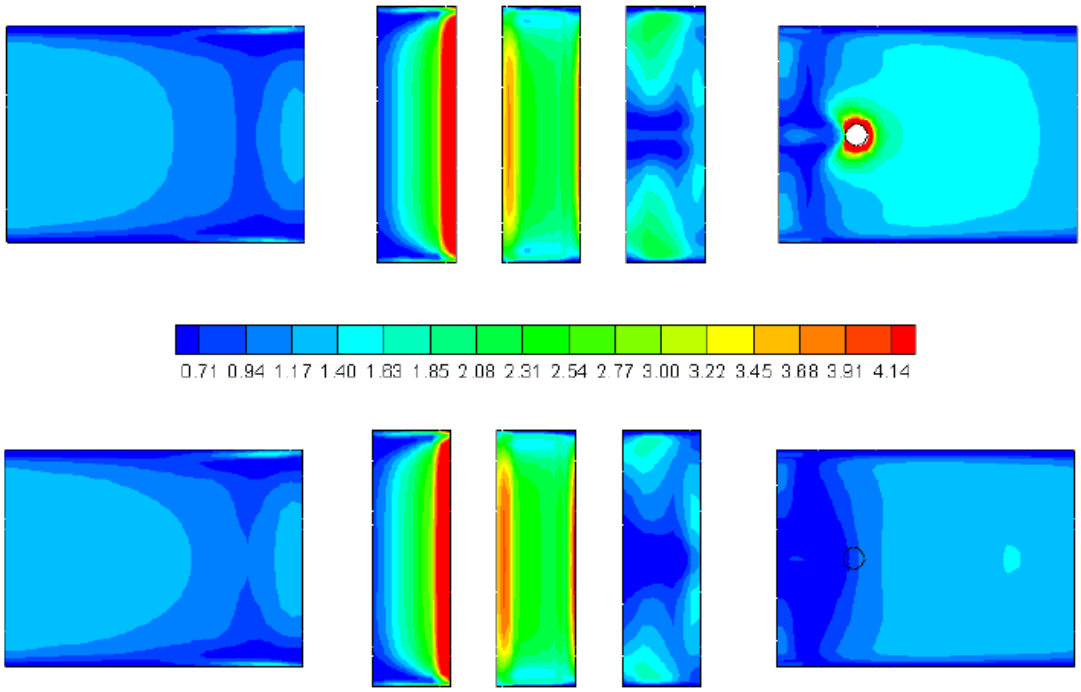


*Figure 15.4 Enhancement Factor. Left to right: upstream bottom wall, upstream face of the rib, top face of the rib, downstream face of the rib and the downstream bottom wall. Top: active orifice. Bottom: no active orifice.*

These preliminary results are coherent with the previous analysis and allow progressing to the successive step.

## 15.2 *Final set-up for the simulation*

The above set-up for the simulation was modified to adapt it to the changed operation condition of the test section. In fact, the experimenters decided to plug all the orifices upstream of the 4th rib (*figure 15.5*) to maintain a constant Re upstream of 4th rib of interest. Therefore, the boundary conditions of the simulation were modified accordingly.
The pressure at the exit of the 4th hole was fixed to here obtain the requested nominal $V_b$ and the same pressure was applied at the exit of the 5th hole, simulating the experimental set-up. Successive testing has shown that the change of configuration has no visible modification of the simulated flow and thermal field on the 4th rib: the corresponding distribution of wall shear stress and EF are similar to the ones presented in *figures 15.3* and *15.4*.

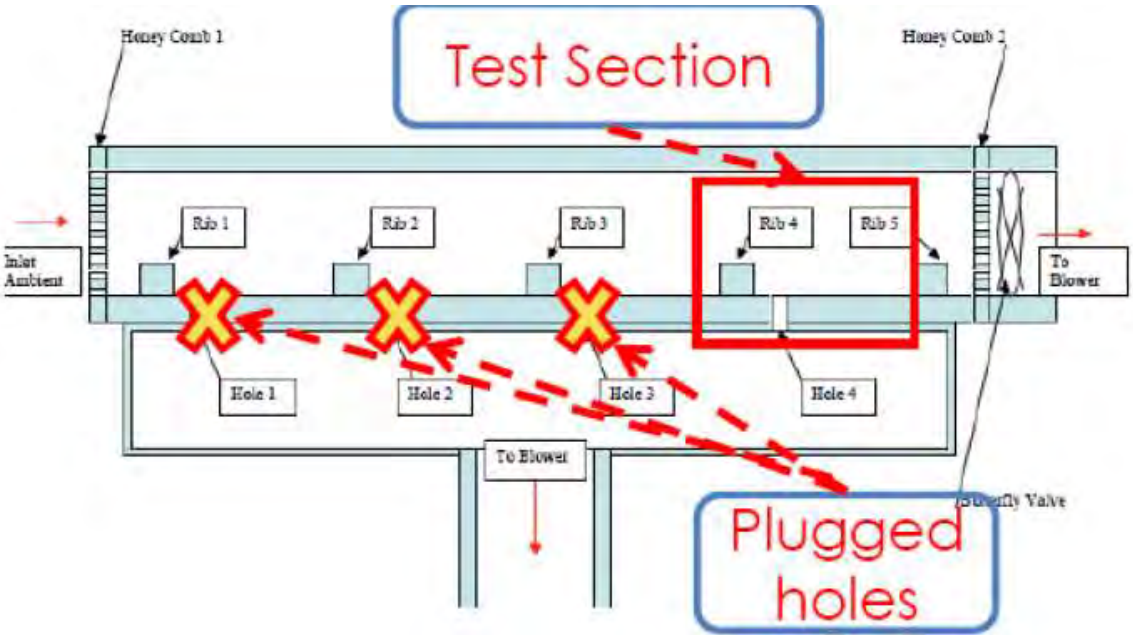


*Figure 15.5 Final set-up for the experimental investigation*

The EF for the bottom wall is compared with the experimental result (for convective heating i.e, no conjugate heat transfer) (*figure 15.6*) and a qualitative agreement is found with the exception of the region of upstream separation, where the simulation presents a lower EF.

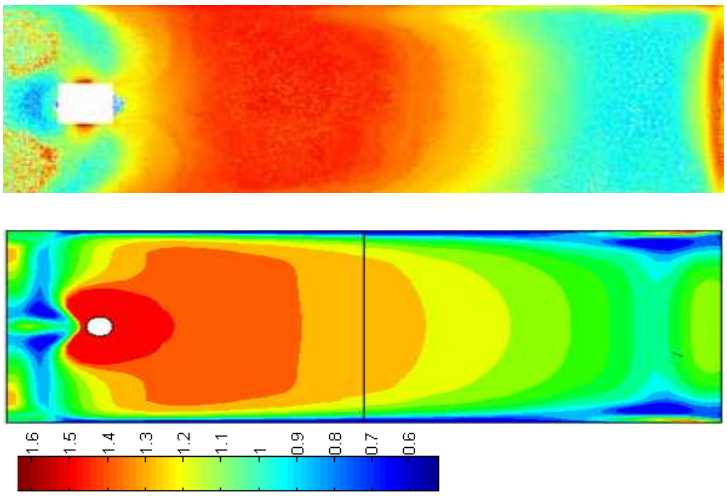


*Figure 15.6 EF for the downstream wall: top: exp. (LC); bottom: RANS*

Therefore, this configuration was applied for the final LES simulations whose results are discussed in the following.

# CHAPTER 16 Investigation of the flow-field

## *16.0 LES simulations*

The simulations were performed following the procedure described in (chapter 5) to the reader is referred, while the planes from the following results are defined in chapter 7 (*figures 7.1, 7.2* and *7.3*). Annex G shows that the Eulerian statistics of the fluid phase reach stationary state after 5 flow-through.

## *16.1 Topology of the flow*

### *16.1.1 Overall Structure of flow*

The topology of the flow without effect of suction, as such deduced from the previous simulations, has been discussed in detail in [3, 3, 20] and has been resumed in Part II. However, at the light of the results of Part II, it is useful to review the fundamental aspects useful to compare and assess the effect of suction. This topology is presented in *figure 16.1*, which shows that the flow is dominated by the combined influence of the rib and lateral walls.

The presence of the rib flow induces multiple separations and reattachments, which correspond to rotation dominated areas. In such regions the flow follows circular a motion around a vortex core, moving through helical trajectories, which depend on the strength of three dimensional effects. The interaction between the lateral walls and the deflection of the

flow by the rib causes secondary flows which imprint a strong three dimensional behavior to the main flow.

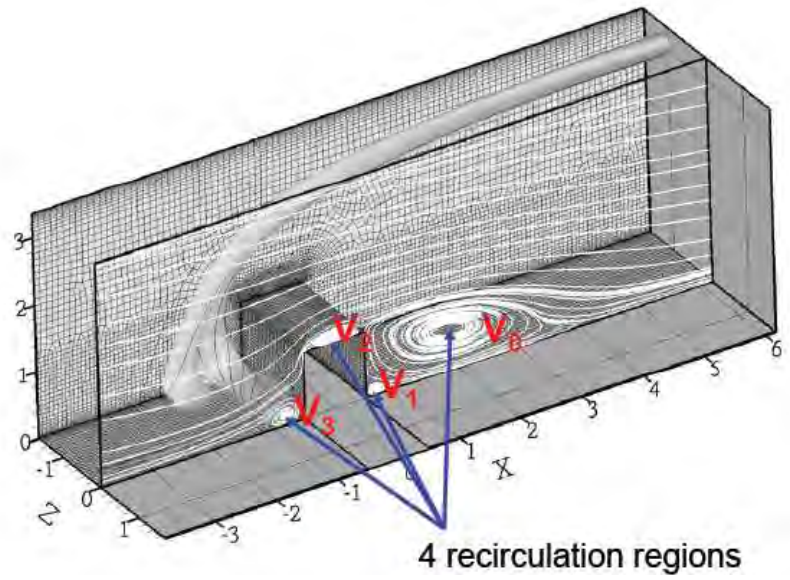


*Figure 16.1 Topology of the flow with closed hole [3, 2]*

It can be seen from *figure 16.1* that the flow contains 4 separated regions, namely:
-$V_0$: the main separation downstream of the rib
-$V_1$: the secondary counter rotating vortex at the bottom downstream corner, located within the main separation $V_0$
-$V_2$: the separation on the top face of the rib, born of the separation of the flow at the top corner of the rib
-$V_3$: the separation on the upstream bottom wall of the duct

$V_0$ recirculation, as permanent separated region, does not really exist in the instantaneous flow, as it represents the average of the behavior of the different transient vortices present in this zone [8]. The other regions: $V_1$, $V_2$ and $V_3$ have sizes of the same order of the instantaneous largest vortex present in these zones, especially $V_1$and $V_3$, which correspond to a permanent rotating motion in the transversal direction; therefore their time averaged features do not differ much from those of the corresponding transient vortices. $V_1$, $V_2$ and $V_3$ are caused by local flow separation and, with the exception of $V_2$, show a strongly three dimensional behavior, actually being helical shaped structures where flow is displaced in the direction perpendicular to the rotation. This behavior is visible in *figure 16.1*, which shows that the upstream separation $V_3$ is associated with a transversal vortex, which fundamental role in heat transfer was underlined in Part IV. At the side corners, the fluid captured in this vortex feeds corner rotating structures, which arch over the rib to feed the secondary flow pattern shown in the following *figure 16.2*. *Figure 16.2* shows that the transversal plane is dominated by a couple of counter rotating vortex, whose action covers the upper part of the flow field.

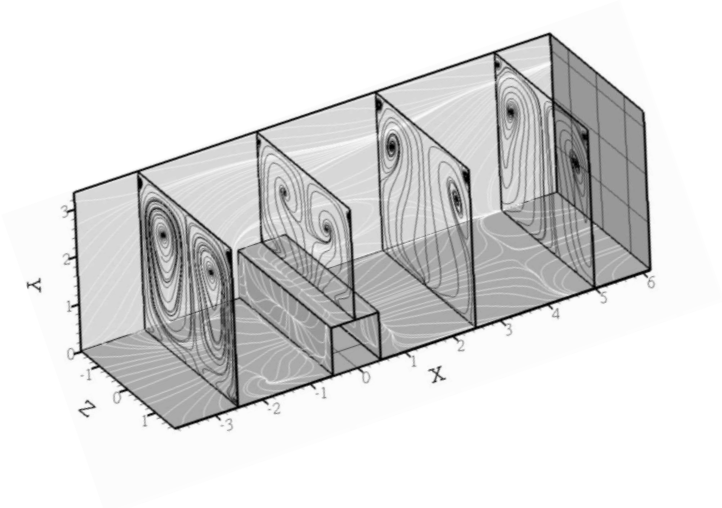


*Figure 16.2 Topology of the flow with closed hole; secondary flow [3, 20]*

The purpose of the following sections is to investigate how this phenomenology is modified by the effect of the suction by mean of comparison of corresponding visualizations with active and closed orifice**.**

### *16.1.2 Structure of downstream recirculation regions*

The next two figures compare the mean streamlines along the entire 4$^{th}$ pitch of 2 X-Z planes for the respective cases of active and inactive orifice: the symmetry plane (figure 5.3.1) and the intermediate plane located half-way between the side wall and the symmetry plane itself (*figure 16.3.2*). A first observation is that, upstream of the rib and on the rib itself, the main patterns of separation and reattachment are similar for the two cases and the two planes; this is a first rough indication that the main effect of the orifice is mostly confined to the regions downstream of the rib. The examination of the symmetry plane (*figure 16.3.1*) shows the major effect of the suction through the orifice: the separation streamline, which separates the region $V_0$ from the main flow moving downstream, is similar for both two cases, but the behavior of the fluid trapped below it (i.e. within $V_0$) is fully different: in the case of active orifice, the main rotation in $V_0$, as well the entire secondary region $V_1$, disappear, replaced by a motion toward the orifice, which acts as a sink. On the contrary, the intermediate plane (*figure 16.3.2*) shows similar patterns for active and closed orifice, being characterized by the main rotation in $V_0$ and the counter-rotating secondary vortex in $V_1$; this observation suggest that, outside the central region of X-Z plane, of the action of orifice modifies but does not destroy the main topology.

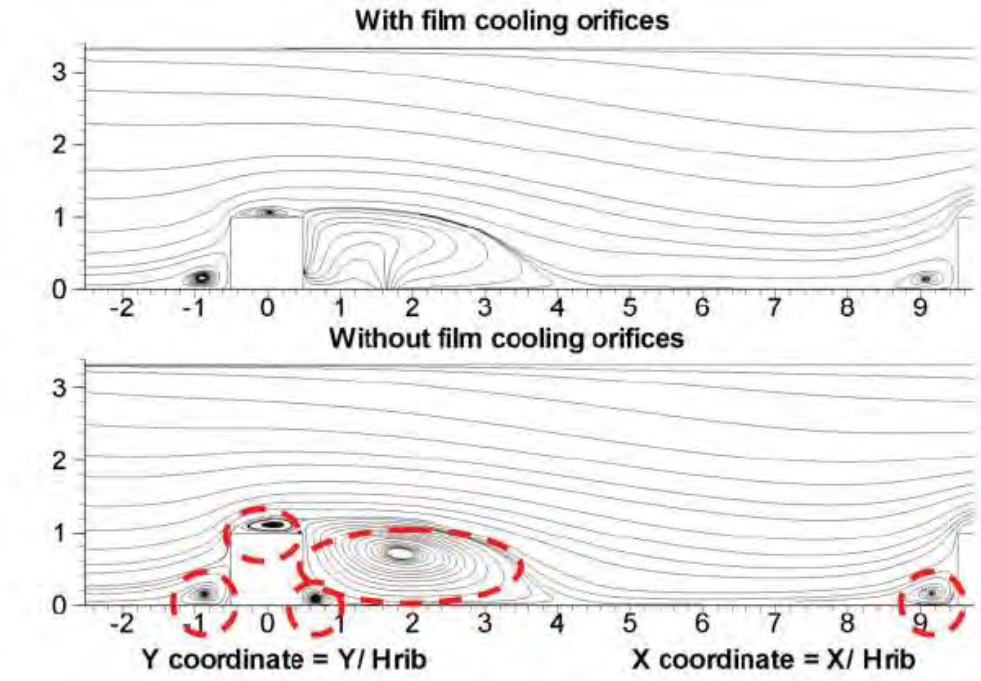


*Figure 16.3.1 Average streamlines. Symmetry plane; Top: active orifice; bottom: close orifice.*

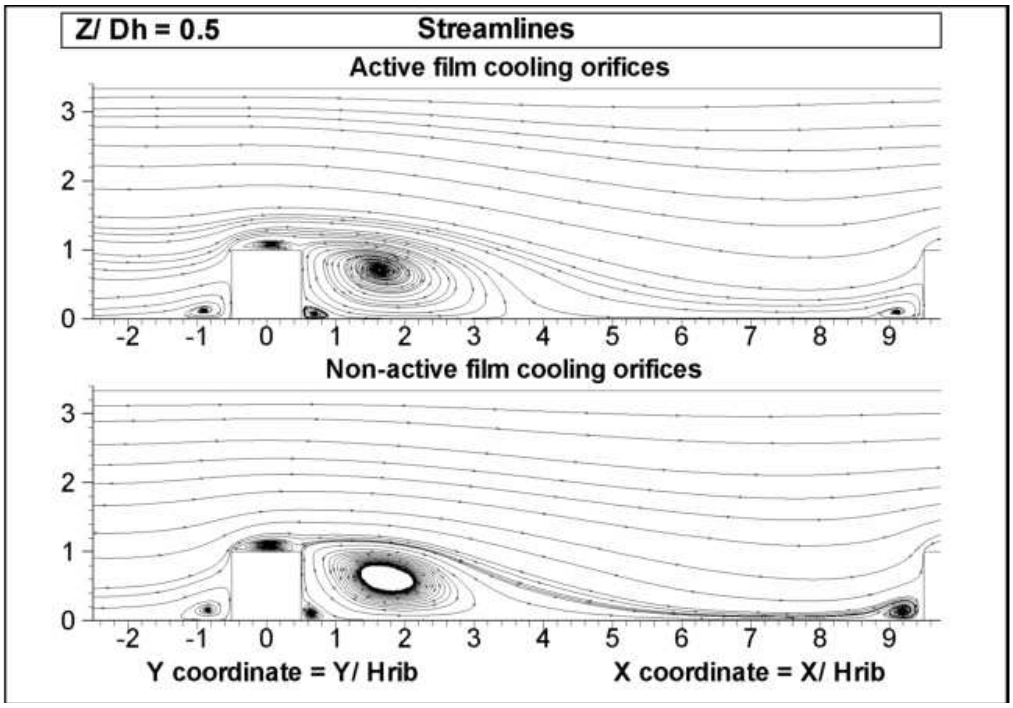


*Figure 16.3.2 Average streamlines. Intermediate plane. Top: active orifice; bottom: close orifice.*

The behavior of the flow can be highlighted examining different X-Z planes. Figure 16.4.1 presents the wall streamlines [3, 20] on bottom wall Y/*h*=0; figure 16.4.2 presents the streamlines for plane Y/*h*=0.25 and figure 5.4.3 the ones for the plane Y/*h*=0.5 (chapter 7).

The three images confirm that the topology of the flow upstream of rib is unaffected by the action of the orifice and the focus of the investigation should be on the downstream region. The suction of the orifice, acting as a sink, disrupts the downstream region and modifies the topology of $V_0$ and $V_1$ (*figure 16.1*). In consequence, the flow undergoes a strong pull toward the symmetry plane, where the orifice located. The footprint of this motion is shown by the wall streamlines in *figure 16.4.1*: in the central part of the duct, fluid trapped within $V_0$ is directly dragged toward the orifice; on the sides, flow is pulled back toward the downstream face of the rib, entering $V_1$ region on the sides to move toward the symmetry plane, where it is pulled to the orifice. In the case on the case of close orifice, motion within $V_1$ is quasi two dimensional. These different motions can be seen (underlined in red) in *figure 16.4.2* and remain visible in *figure 16.4.3*; the action of the orifice causes a significant difference with respect to the case of closed orifice: in the central part of $V_0$ fluid moves toward to the face of the rib, impacts it and then moves toward the lateral walls, to the contrary of the other case. *Figures 16.4.2 and 16.4.3* both show the separation between the part of flow which attracted toward the orifice (or trapped within $V_0$ for the case of closed orifice) and the one which reattaches downstream of $V_0$ to move further downstream; this part of this motion is similar for active and closed orifice and the corresponding separation streamline allows the identification of the borders of the regions affected by the action of the orifice.

*Figure 16.4.1* can be studied applying the theory of critical points; lines converging to a single point (node; blue) correspond to flow leaving the surface: such a node is visible at the location of the orifice and corresponds to the mechanism to be shown in *figure 16.5*; the nodes upstream of the rib correspond to the formation of the side corner structure (*figure 16.1)*; the saddle points (red) correspond to the fluid transported by these side vortex which have been drawn back to the wall (*figures 16.5 and 16.15*). The trace of these side structures is clearly visible in *figure 16.4.3.*

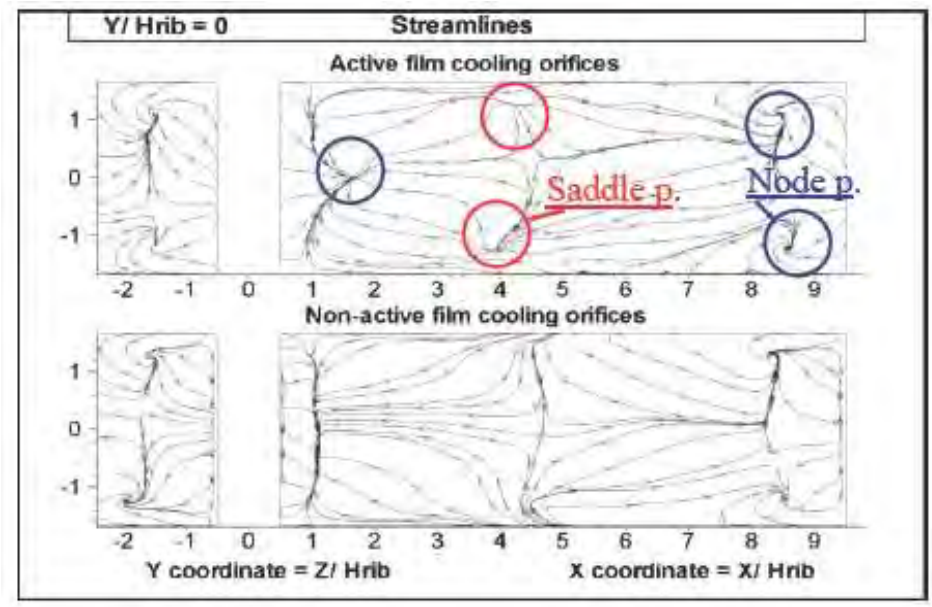


*Figure 16.4.1 Average streamlines in X-Z plane Y/h=0. Top: active orifice; bottom: closed orifice. Blue: node; red: saddle*

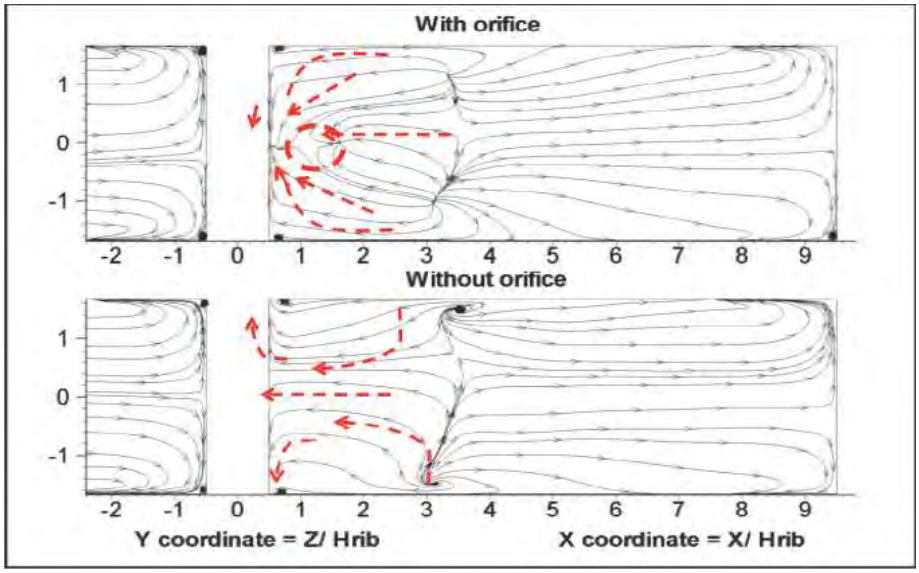


*Figure 16.4.2 Average streamlines in X-Z plane Y/h=0. 25. Top: active orifice; bottom: closed orifice*

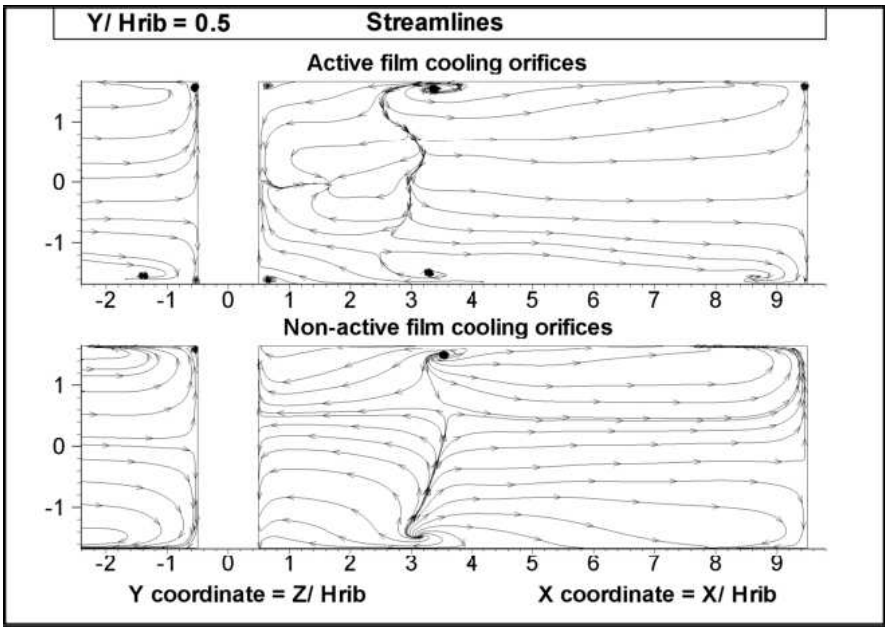


*Figure 16.4.3 Average streamlines in X-Z plane Y/h=0. 5. Top: active orifice; bottom: closed orifice*

To resume, the effect of the orifice is a massive displacement toward the symmetry plane within the whole separated region $V_0$, which results in a strong motion in the neighborhood of the symmetry plane. This process is dominated by a bifurcation mechanism at the downstream face of the rib, which will be addressed as SPB mechanism (Symmetry Plane Bifurcation mechanism) in the following, which is visible in *figure 16.3.1* and is shown in detail in *figure 16.5*.

*Figure 16.5* summarizes the process in terms of streamsurfaces. The left image shows the basic macroscopic behavior of flow at closed orifice. $V_1$ is visible as a quasi-two dimensional vortex (dark orange), where flow moves from the symmetry plane to the side walls, where it moves up joining the main rotation. In region $V_0$, low velocity flow close to the wall (brown) moves back to the rib, arching over region $V_1$ and rotates back (green surfaces). The core of region $V_0$ is dominated by a rotating motion (violet and yellows streamsurfaces) originated from the singular point on side wall visible in *figure 16.8*.

The right image shows how this mechanism is destroyed by the action of the orifice. Low velocity flow close to the wall (dark orange), now enters region $V_1$ from the sides walls and moves toward the symmetry plane, where $V_1$ itself is destroyed as flow moves up to a bifurcation (see above) located about Y/*h*=0.3 from the bottom wall: below this bifurcation flow is again drawn toward the bottom wall and toward the orifice; as it is moving closer to the orifice a small uplifting mechanism takes place: the flow arches up, before being pulled down again toward the orifice. Flow above the bifurcation, on the contrary, undertakes an uprising motion: the flow is lifted up to the top of the rib, where it interacts with the high momentum flow of the free stream (green surfaces), before being drawn again in $V_0$ region to be pulled toward the orifice where it is aspirated; the separation surface between $V_0$ and the main flow is the border confining the process. Below this surface, rotating flow from the sides (violet and yellow streamsurfaces) is dragged to the orifice (*figure 16.4.1*); in the central

part of the duct, the rotation is substituted by a direct motion toward the orifice (figure 5.3.1) and $V_1$ disappears.

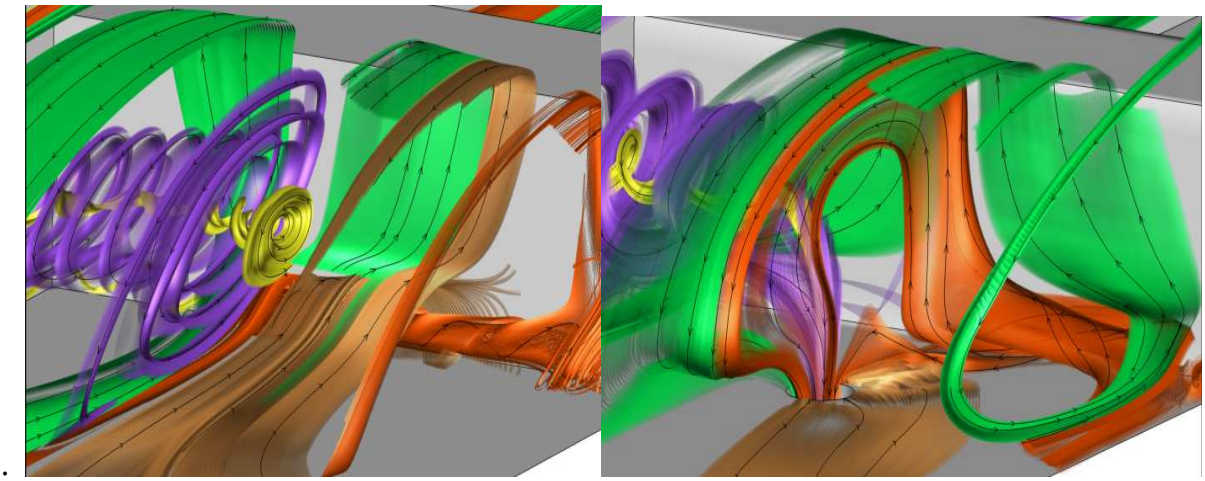

*Figure 16.5 Left side: closed orifice; right side: active orifice. Motion is visualized by stream-surfaces.*
*Green: fluid high momentum; dark orange: flow entering $V_1$; brown: flow with low momentum close the bottom; violet and yellow: rotating flow.*

An overall external view of the region $V_0$ for the case of active orifice is visualized by mean of average streamlines in *figure 16.6*. The two views allow a full understanding of *figure 16.4* showing the three dimensional extent of the perturbation of the orifice. The left view shows how the side structures confine $V_0$, pushing the rotating flow toward the central part of the duct till the action of the orifice perturbs the process. The right view shows how the fluid moved up by SPB mechanism is confined and pushed downstream by the free flow to be aspirated by the orifice, producing the two symmetric lobe-like shape surfaces.

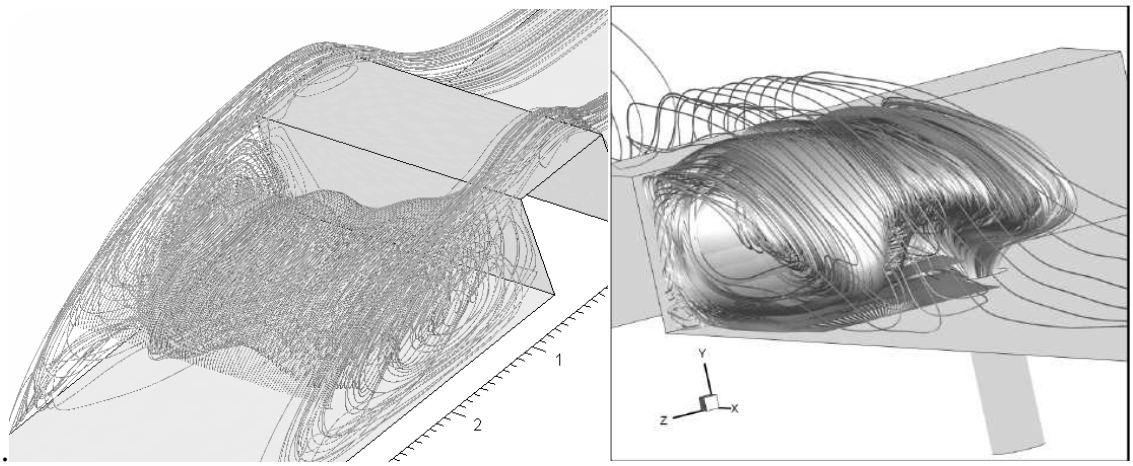


*Figure 16.6 Downstream recirculation visualized by streamlines. Left: overview; right detail of the aspiration by the orifice*

It can be concluded that the most important difference between active and closed orifice is a direct consequence of SPB mechanism. This mechanism has a drastic effect on the rotating structures $V_0$ and $V_1$, whose formation is inhibited, within the region near by the symmetry plane, where the fluid here trapped is driven to the orifice.

The effect of this mechanism is shown in *Figure 16.7*, which presents iso-contours of the longitudinal velocity at different Y-Z planes located upstream of the orifice (which is located at X/*h*=1.667). It can be seen how $V_0$ is broken, in the central part of the duct, by a region of positive longitudinal velocity. The region corresponds to flow moving toward the orifice and has a size of about -0.5<Z/*h*<0.5; it can be considered the boundary of the region of direct effect of the orifice.

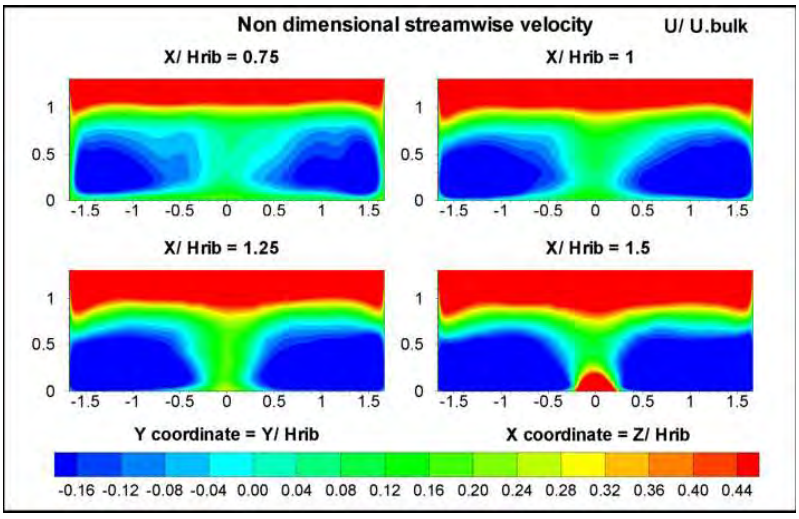


*Figure 16.7 Contours of longitudinal velocity at different X locations within $V_0$*

*Figure 16.8* complements *figure 16.3* presenting a zoom on $V_0$ and $V_1$ structures at different Z locations, for active and closed orifice. It can be seen that, at the intermediate plane, the structures are similar for both cases of active orifice and closed orifice case, which is consistent with the above estimation of the range of the direct effect of the orifice. It can be also remarked that, close to the side wall, the streamlines are similar for the two cases, indicating that the boundary layer on the side walls is the dominating effect; the node point located at the wall is the origin of the rotating motion visualized in *figure 16.5*. *Figure 16.9* shows the details of the behavior of $V_2$ for the case of active hole; it can be remarked that its size does not change in an important way along the transversal direction, apart within the region close to the side wall, where the interaction with the lateral wall boundary layer dominates the flow, causing the structure becoming bigger. *Figure 16.8* had already shown that the behavior of this region is not changed by the action of the orifice.

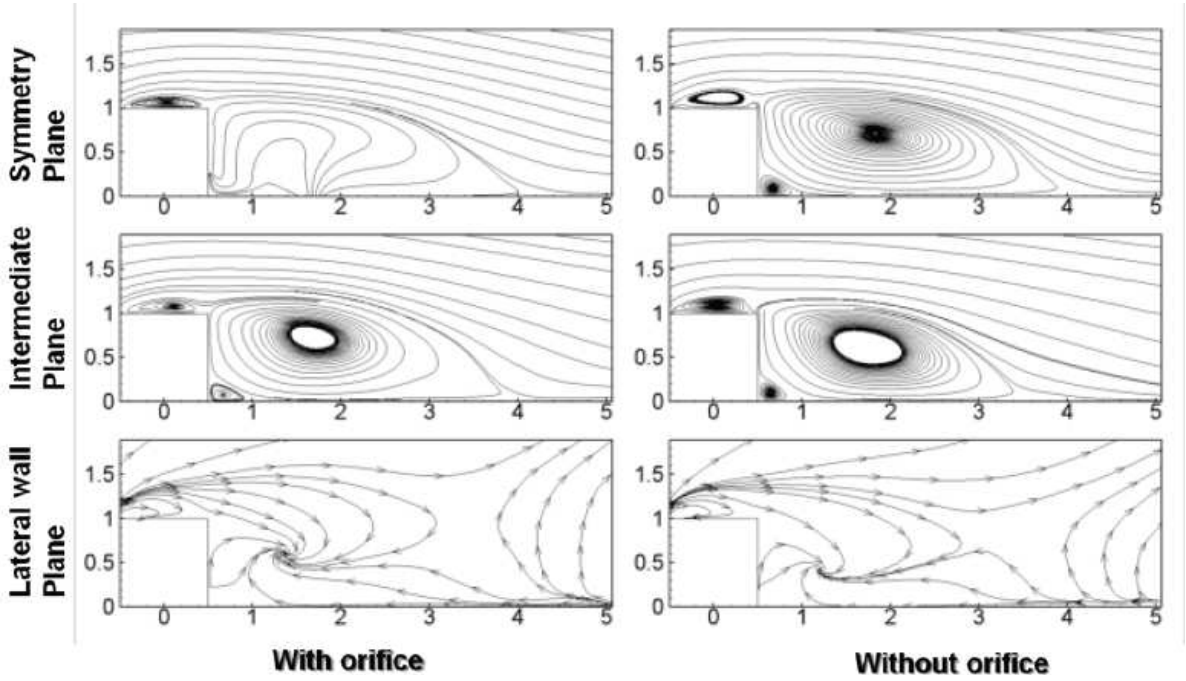


*Figure 16.8 Streamlines in $V_0$ region, for X-Y planes at different locations Z/h*

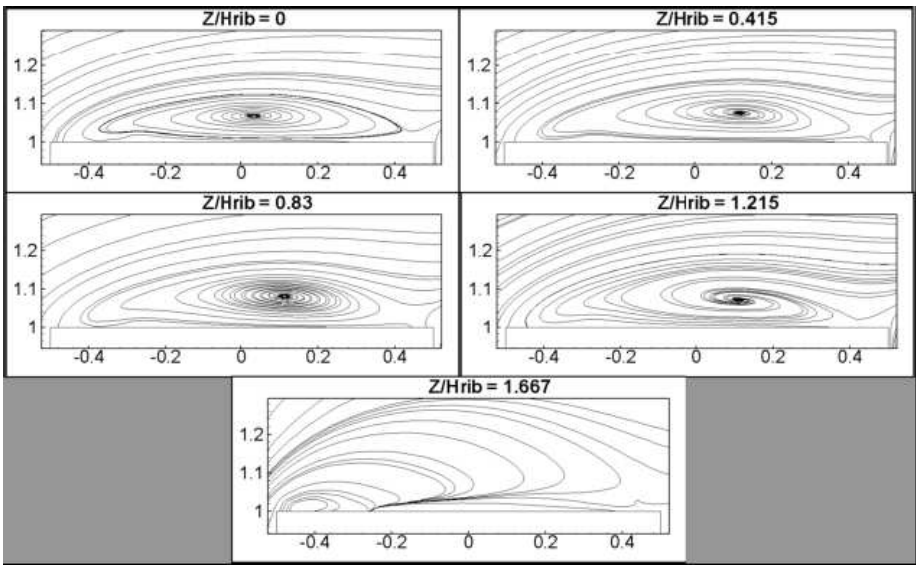


*Figure 16.9 Streamlines in $V_2$ region, for x-y planes at different locations Z/h*

It can be concluded that, although the action of the orifice drastically modifies the recirculation structures $V_0$ and $V_1$ through the SPB mechanism, the basic behavior of the flow downstream of the rib remains practically unchanged. This implies that the sink action by the orifice is not strong enough to overcome the original tendency of the flow to separate and evolve toward reattachment, downstream of the sudden expansion caused by the rib. Outside

of the -0.5<Z/*h*<0.5 region, structures $V_0$ and $V_1$ structures reform themselves and have shape and size similar to the case of closed orifice.

### *16.1.3 Secondary motion*

*Figure 16.2* had shown that the cross section of the duct is dominated by two counter-rotating vortex, which cover the entire cross section of the upper part of the flow. The effect of the orifice in shown in *figure 16.10*, which presents streamtraces for different Y-Z planes for closed orifice (left) and active orifice (right). Biggest difference between the two cases is, evidently, found at the location of the orifice (X/*h* = 1.667). At this location, in the case of closed orifice case, the separating streamtrace of the recirculation structure $V_0$ is visible in the central region of the duct, confined by the side rotations (see previous section); for the case of active orifice, the streamtraces directly enter the orifice, showing how fluid is dragged downward to be aspirated by the orifice. Downstream of the orifice, the flow structures are similar for both cases: in the upper part of the ribbed duct the twin counter rotating vortex cores are dominating in both cases, without significant difference; in the lower region, a slight difference is visible at location X/*h* =4 in the case of active orifice, where the trace of the rotating side flow, which reattaches outside $V_0$ is visible; this mechanism will be evidenced by the following *figure 16.15*.

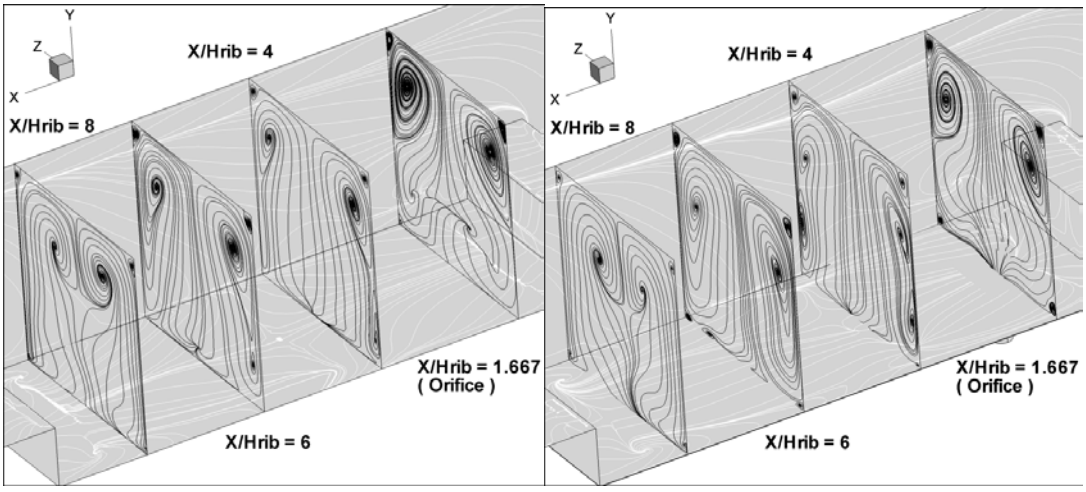


*Figure 16.10 Streamtraces for Y-Z planes at different X for active orifice (left) and closed orifice (right).*

*Figure 16.1* had shown that the flow upstream of the rib is dominated by two side counter-rotating vortex cores associated to the upwards motion of fluid ejected from the bottom wall region, at correspondence of the corner between the upstream face of the rib and lateral walls. This mechanism is not modified by the action of the orifice, as shown by *figure 16.11*, which presents the structure of the corner flow for closed (left) and active (right) orifice: it can be observed that the motion is similar, confirming the previous conclusion (from *figures 16.3* and *figure 16.4*) that the effect of the orifice is small upstream of the rib. The wall streamlines are shown as white lines; their similar pattern offers a confirmation that the behavior at the side wall is the same for both cases, it being controlled by boundary layer on this wall.

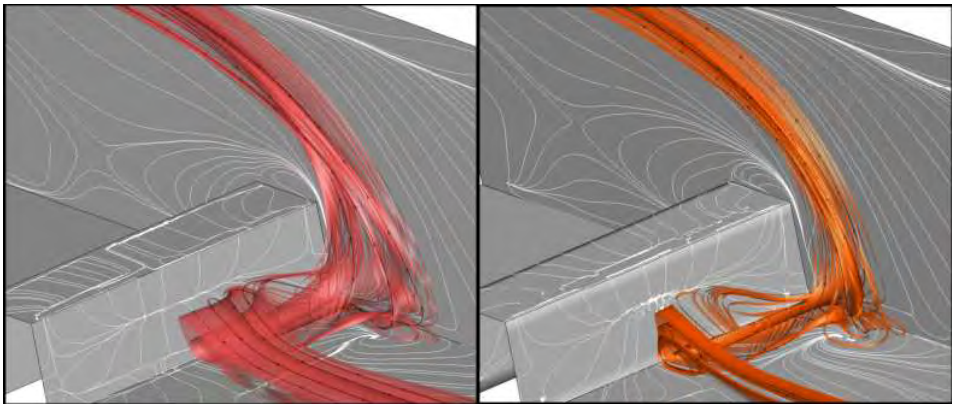

*Figure 16.11 Ejection of flow from upstream corner; streamtrace. Left side: close orifice. Right side: active orifice. Wall streamlines in white.*

The detail of the evolution of upstream transversal structure $V_3$ (*figure 16.1*) is presented in *figure 16.12* for the case of active orifice; as it was also remarked for $V_2$, the size of structure practically is constant in the core of the flow but, close to the side wall, its shape and size are modified, the structure itself disappearing in the vicinity of the wall. As it was already remarked for $V_2$ and $V_1$, close to the side wall the low momentum boundary layer on the wall is the dominant effect and, in consequence, the streamlines (*figures 16.11* and *16.12*) there show a sink-like structure. Comparison with results for the closed orifice (chapter 7) shows that the nature of this effect is not modified by the action of the orifice.

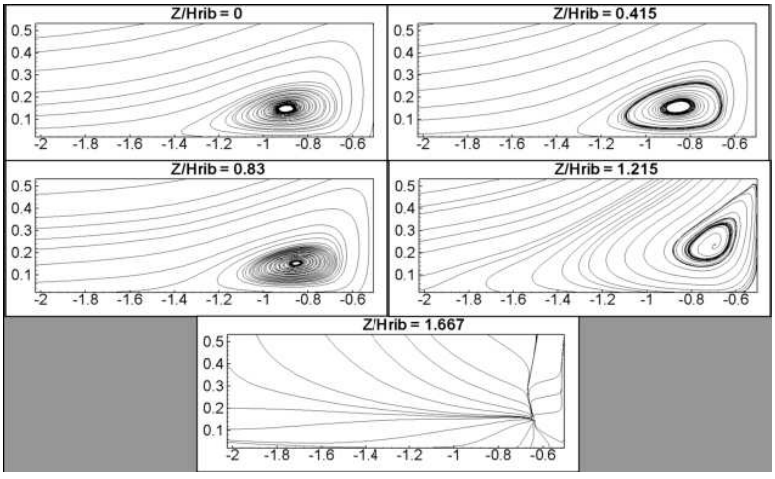


*Figure 16.12 Evolution of rotating structure $V_3$ in the transversal direction; streamlines*

*Figure 16.13* compares the contours of vertical velocity with active and closed orifice for X-Z planes at different Y locations. Upstream of the rib, the behavior is similar for both cases, the flow being dominated by two symmetrical side regions of high positive velocities; these regions are the trace of the flow arching over the rib through the side vortex (*figures 16.1, 16.11*). Downstream of the rib, two symmetry side regions of negative velocities are visible in

both cases: they are the trace of the side structures which, downstream of the rib, arch down to impact the bottom wall downstream of $V_0$ (see also the following *figure 16.15*); these regions are wider and stronger for the case of active orifice, showing how the orifice pulls flow from the sides. Close to the downstream of face of the rib, a region of positive velocities can be identified, which corresponds to the main rotation in $V_0$ visualized in *figure 16.5*: above $V_1$ flow reaches the rib and here moves upwards; this motion is weaker in the case of active orifice. This is consistent with the topology already identified: in the neighborhood of the symmetry plane, fluid trapped between the face of the rib and the orifice is pulled downstream by SPB mechanism, affecting the whole separated region $V_1$ (*figure 16.5*) and the upwards motion of flows in $V_0$.

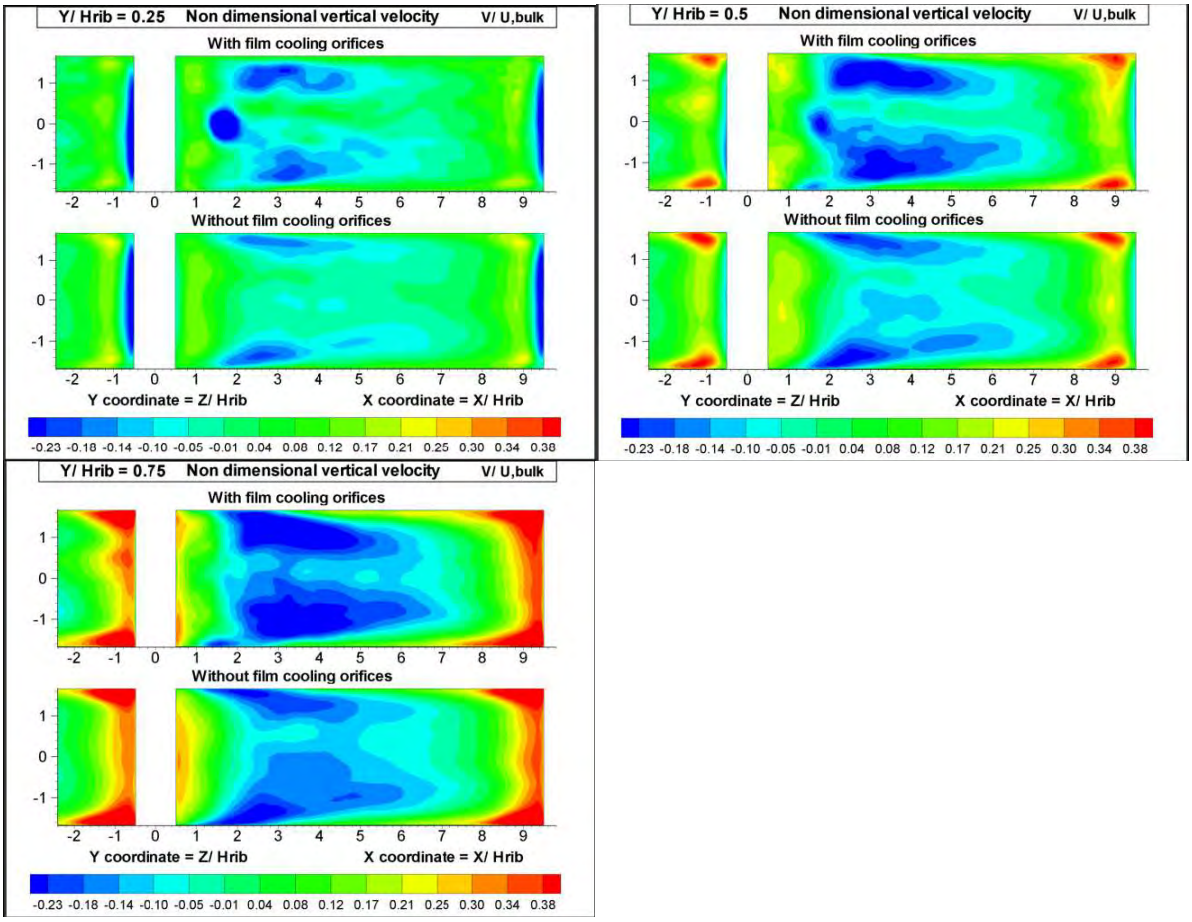


*Figure 16.13 Vertical velocity contours at different x-z planes*

*Figure 16.14* presents iso-lines of pressure at plane X-Z plane located at Y/*h* = 0.25. A small region of high pressure exists in correspondence of the location of the orifice: it corresponds to flow moving directly downstream to the orifice, but, outside this region, the SPB mechanism causes pressure values which are lower upstream of the orifice than it is the case downstream of it and on the sides. These gradients correspond to flow is moving to orifice by sink effect, this effect and, hence the descending motion, being stronger in the sides. Sink effect also appears to affect the reattachment line next to the wall, as it was also observed

from the streamtraces in figure 5.4. The action of the orifice drags flow away from the lateral walls to the central part of the flow, motion being made easier by the low longitudinal momentum of the flow in the boundary layer on the side wall.

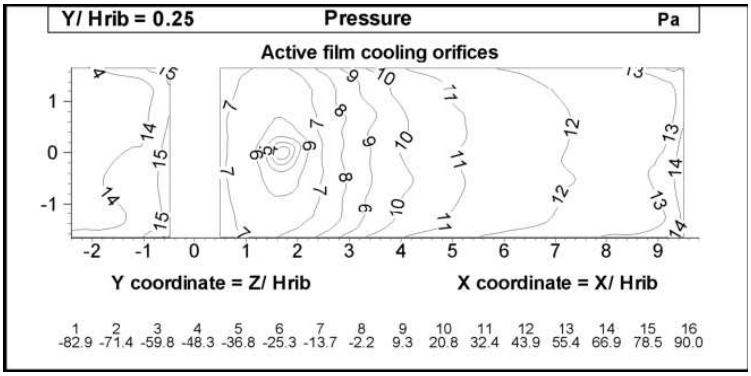


*Figure 16.14 Pressure contours for plane Y/h= 0.25*

*Figure 16.15* resumes and justifies the previous observations concerning the effect of the side corner structures. It shows how the upstream side structure (*figure 16.1*1) had arched over the rib to move back toward the bottom wall without entering $V_0$ structure. The left image shows the case of closed orifice: the flow impacts the bottom wall and part of it is pulled back toward the rib to become part of $V_0$ motion. The right image shows how this motion is perturbed by the action of the orifice, flow being directly dragged to the orifice (*figures 16.4* and *15.14*). This behavior is coherent with previous analysis, and is again discussed in detail in Annex K. The effect of this motion on the heat transfer will be put in evidence in the next chapter.

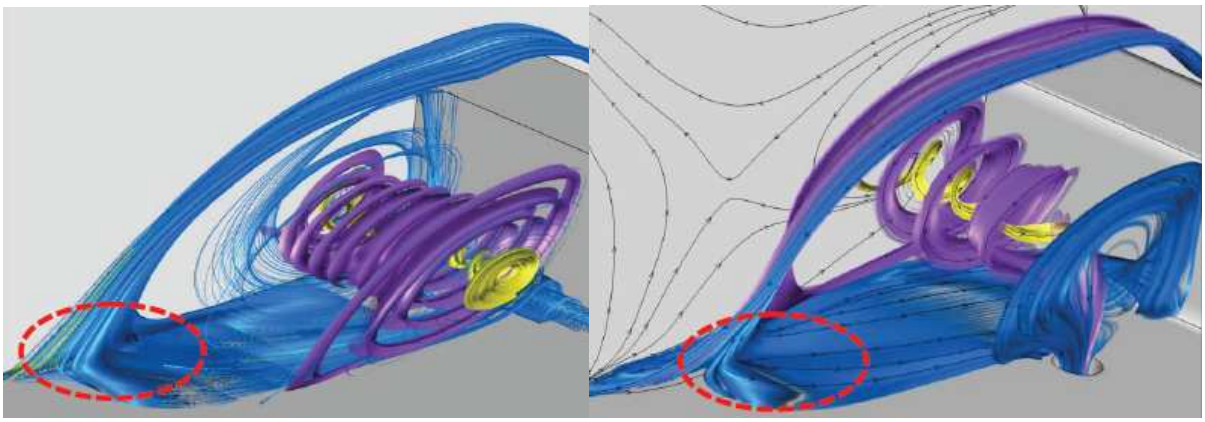

*Figure 16.15 Side flow above $V_0$ separated structure; streamsurface. Left side: closed orifice. Right side: active orifice.*

## 16.2 Average flow field

The modifications of the average flow fields are discussed in this section. Two aspects of the flow will be discussed: the friction factor and the velocity and turbulent quantities at the symmetry plane.

### 16.2.1 Friction factors

The wall shear stress is the most interesting macroscopic parameter to characterize the present flow and put in evidence the effect of the aspirating orifice, in view of both its own engineering interest and its evident analogy with heat transfer. It is here set in non-dimensional form as friction factor $Cf = \frac{\tau_{wall}}{.5\rho U_{bulk}^2}$. For an easier understanding, the ribbed wall has been projected on a two dimensional surface. The mapped area covers: the bottom wall upstream of the rib from X/*h* = -6 to X/*h* = -1.5; the 3 consecutive faces of the rib; the bottom wall downstream of rib from X/*h* = 1.5 to X/ *h* = 6. *Figure 16.16* compares the maps of friction factor for active and closed orifice, respectively. Qualitatively, few differences exist upstream of the rib: in the case of active orifice values are slightly higher in the attached region, while are slightly lower values within friction factor in $V_3$. Two significant differences can be observed in the top face of the rib. First: the thin region of very low *Cf*, present in the vicinity of the upstream corner, is stronger and better defined for the case of closed orifice. The second difference lies with the region of high *Cf* located in downstream half of this face, region, which corresponds to the reattachment of $V_2$: the values are lower for the case of active orifice; as the shape and size is similar for the two cases (as discussed above and *figure 16.8)*, this effect could be caused by different mass flow within the $V_2$ region, caused by the global by the orifice.

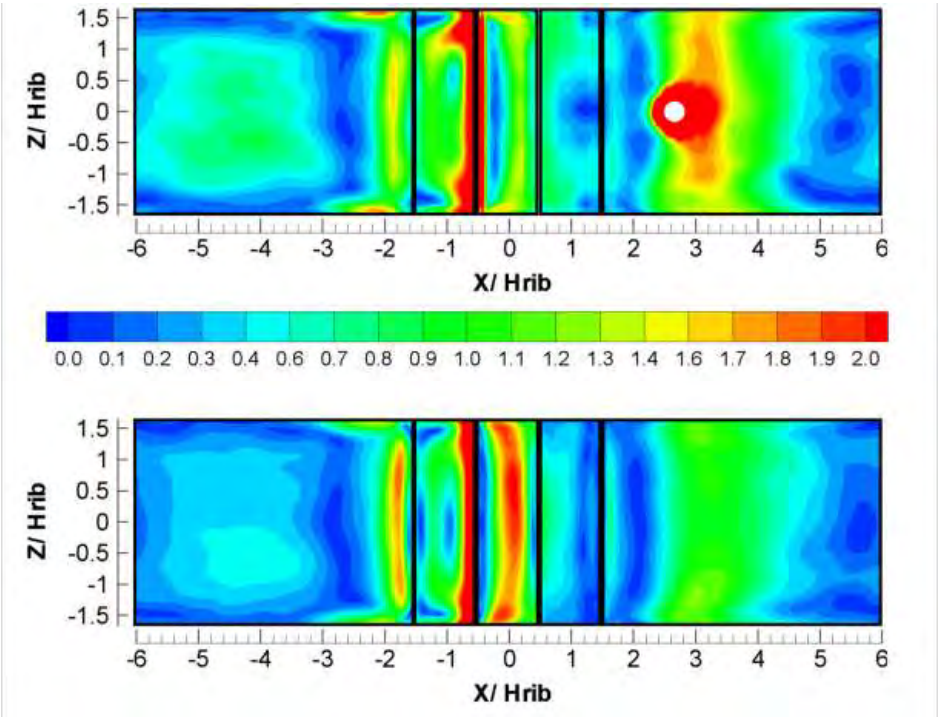


*Figure 16.16 Friction factor. Top: active orifice; bottom: close orifice*

On the downstream face of the rib, the different behavior is visible for the two cases. In the case of active orifice, friction factor decreases moving from the lateral walls to the symmetry plane. This effect is explained by the high pressure gradient caused by flow driven by the SPB mechanism. In the region affected by this mechanism, momentum is transferred from the transversal direction to the vertical one as fluid is uplifted by the SPB mechanism. The most important differences are, of course, found on the bottom wall downstream of the rib. Much stronger shear stress is observed for the region of the active orifice, as flow is directly dragged into the orifice; the effect is stronger for the region downstream of the orifice than for the one upstream of the orifice. This is caused by the lower longitudinal velocity of the flow upstream of the orifice, which is lifted by SPB mechanism. Higher friction coefficient can also be observed downstream of $V_0$, in the region of attached flow located between the reattachment line and the perturbation introduced by the presence of $V_3$. These higher values of drag for most of the entire surface are coherent with the better cooling performance found also in most of this surface, as will be shown in chapter 17.

### *16.2.2 Profiles of mean and turbulent quantities*

The capability of the present LES approach to reproduce the Eulerian statistics of the present case had been demonstrated in chapter 7. Therefore, the first part of the analysis can be confined to the symmetry plane to attempt to appreciate the effect of SPB mechanism. An overall view of the corresponding flow field can be seen in *figure 16.17*, which maps the longitudinal component of the mean velocity.

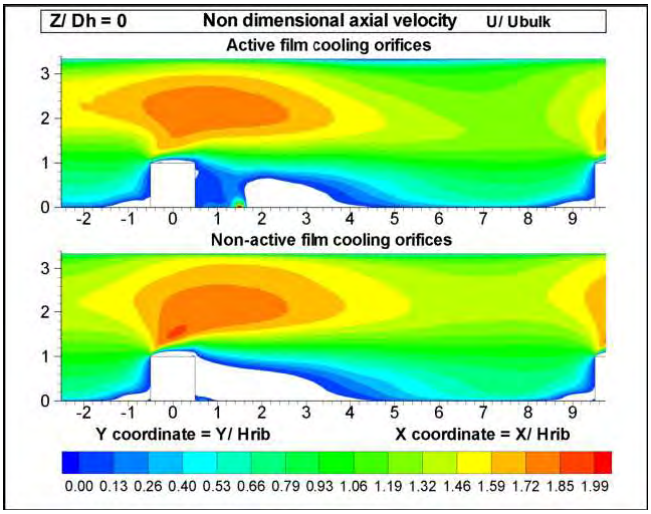


*Figure 16.17 Mean longitudinal component of the velocity; negative values are whitened out. Top: active orifice; bottom: close orifice*

The effect of the orifice is visible in the larger region of high velocity above the rib, where flow is transported by SPB, but more importantly, in the local destruction of region $V_0$ and $V_1$ by the action of the orifice; in this region, it must again be remarked the existence of a region of the positive velocity between the rib and the orifice, where fluid is dragged to the orifice.

*Figure 16.17* confirms that the flow upstream the rib is unperturbed and the analysis can be focused to the region on the rib itself and the downstream region. Therefore, profiles of average relevant quantities in this region are presented in the following figures. In the following, all quantities were made non-dimensional against the bulk velocity and the cases of closed and active orifice are compared.
*Figure 16.18* presents the longitudinal component of the mean velocity on the rib and in the region X/*h* <2 (it is reminded that the orifice itself is located at X/*h*=1.667). It can be seen that, on the rib and in the region outside $V_0$ the profiles are very similar for the two cases; close to the wall, the region of negative velocity found in the case of closed orifice is replaced by low ***positive*** velocities, where fluid is driven toward the orifice itself.

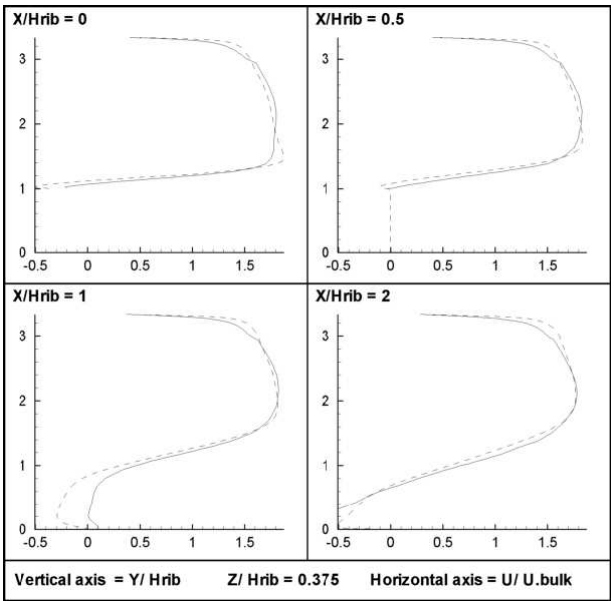


*Figure 16.18 Longitudinal component of the mean velocity. Continuous line: active orifice; broken line: closed orifice. Region X/h <2*

The evolution of the region X/*h* >2 is shown in *figure 16.19*. The effect of the orifice is visible for the higher velocities in the lower part of the plane (and the corresponding lower velocities in the upper part) in the case of active orifice. The orifice is pulling fluid toward the bottom wall, part of it entering the orifice itself, the other part feeding its boundary layer.
This effect and the corresponding higher velocities explain the higher *Cf* remarked in *figure 16.16* for these regions.

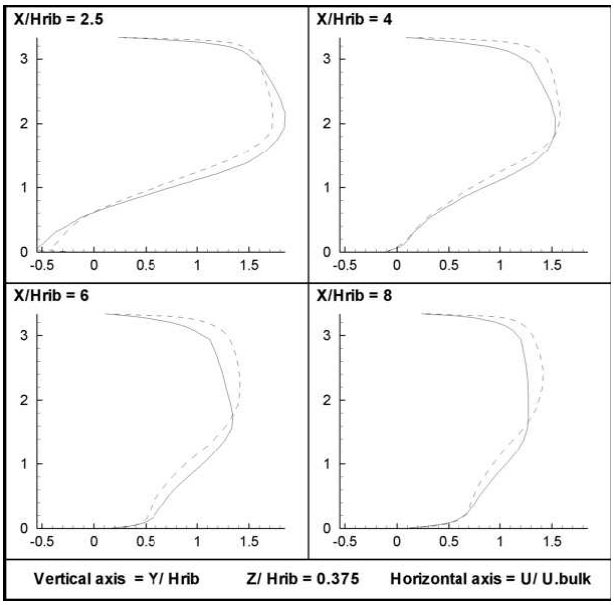


*Figure 16.19 Longitudinal component of the mean velocity. Continuous line: active orifice; broken line: closed orifice. Region X/h >2*

The effect on the turbulent field can be seen in *figures 16.20 and 16.21*, which present the rms of the fluctuation part of the longitudinal component of the velocity at the same locations.
*Figure 16.20* presents the region X/*h* <2 and shows that the SPB mechanism causes a decreased level of turbulence over the rib, without modifying the qualitative aspect of the process; downstream of the rib, the level of turbulence is comparable for the two cases, but, for the active orifice, the maximum begins to shift toward the bottom wall which be more evident in the next image. *Figure 16.21* presents the region X/*h* >2 and shows, for the active orifice, a higher level of turbulence is found in the lower part of the duct, coherent to the higher velocities remarked in *figure 16.19.*

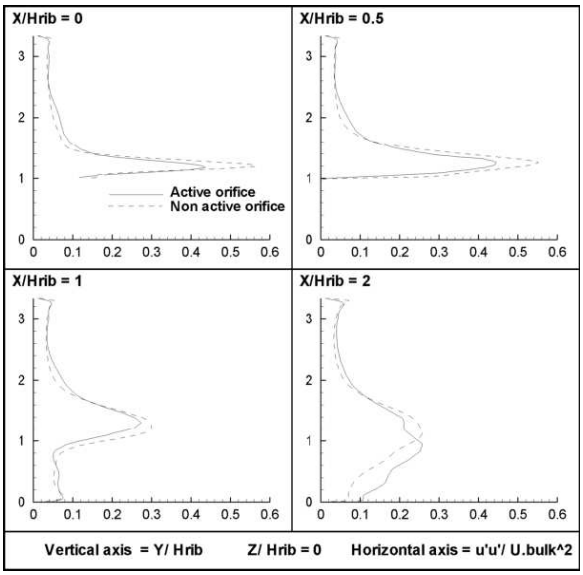


*Figure 16.20 RMS of longitudinal component of the velocity. Continuous line: active orifice; broken line: closed orifice. Region X/h<2*

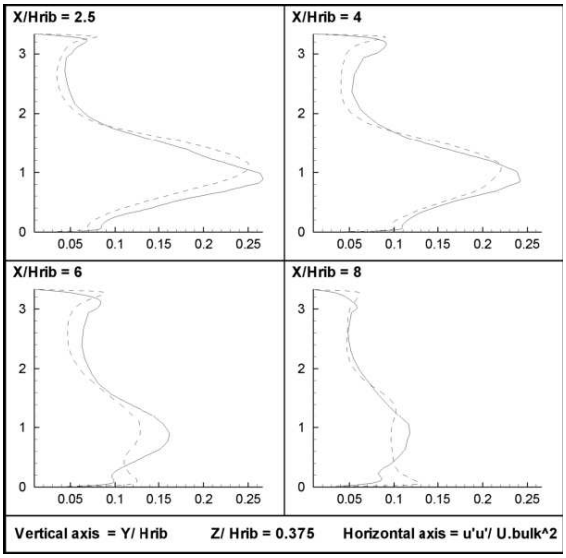


*Figure 16.21 RMS of longitudinal component of the velocity. Continuous line: active orifice; broken line: closed orifice. Region X/h>2*

The effect of the orifice on the transversal velocity is presented in *figure 16.22* and *16.23*, which present the mean component at the intermediate X-Y plane located half-way between and the side wall (*figure 7.1*). The most important effect is, obviously, located in the region upstream of the orifice, where flow is pulled toward the orifice (*figure 16.5*). Downstream of the separation and in the entire upper part of the domain, the two results are similar, being an indication that the direct effect of the orifice is limited to $Y/h \leq 1.5$.

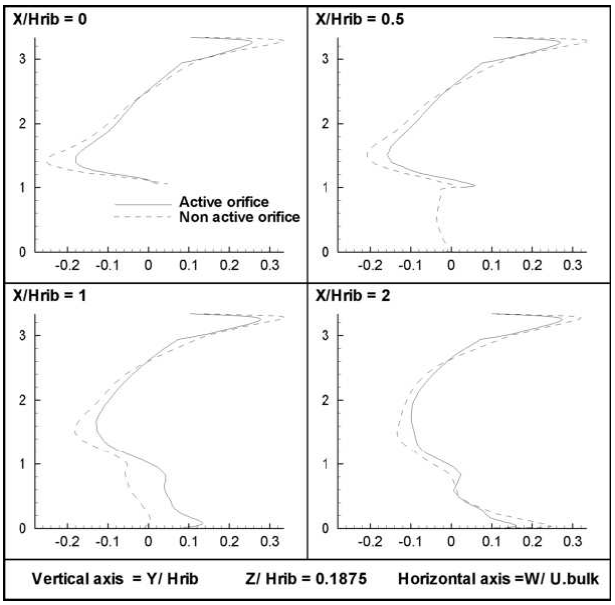


*Figure 16.22 Transversal component of the mean velocity. Continuous line: active orifice; broken line: closed orifice. Region X/h <2*

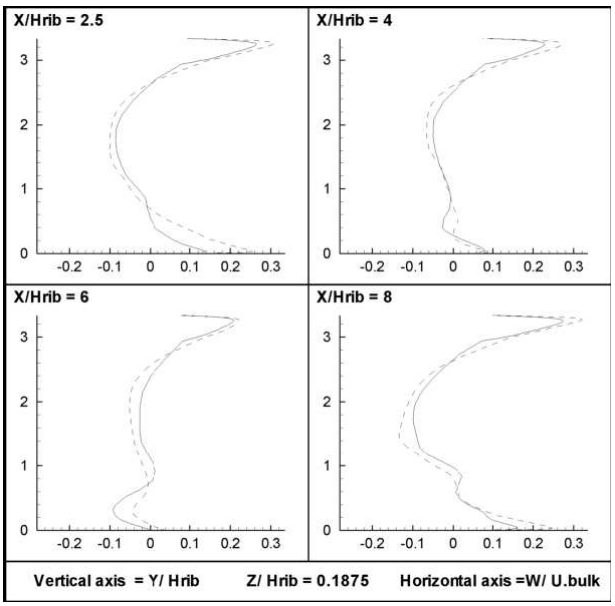


*Figure 16.23 Transversal component of the mean velocity. Continuous line: active orifice; broken line: closed orifice. Region X/h >2*

### *16.2.3 Effect of active orifice on the coherent structures*

Limits of available time for the research made it impossible to perform an in-depth analysis of the action of Coherent Structures (CS(s)) comparable to the one presented in Part IV.

However, some two-dimensional preliminary visualization was performed applying *Q* criterion (part IV [19]).

*Figure 16.24* presents a typical instantaneous *Q* fields for different X-Y planes for the region downstream of the rib for the both case of active (left) and closed (right) orifice. Vortex born on the downstream corner and transported downstream are visible in both cases, but a surprising behavior can be remarked, namely the strong decrease of the level of Q for the case of active orifice. It appears that the perturbation of region $V_0$ has a strong effect on the organization of flow; *figures 16.5* and *16.15* show that the rotation in $V_0$ is destroyed in the central part of the flow, substituted by a direct aspiration toward the orifice. This process is shear-dominated, leading to lower levels of *Q* over the entire flow field and to smaller effect of CS(s) in the process. Further investigation of the process must being left to further investigation.

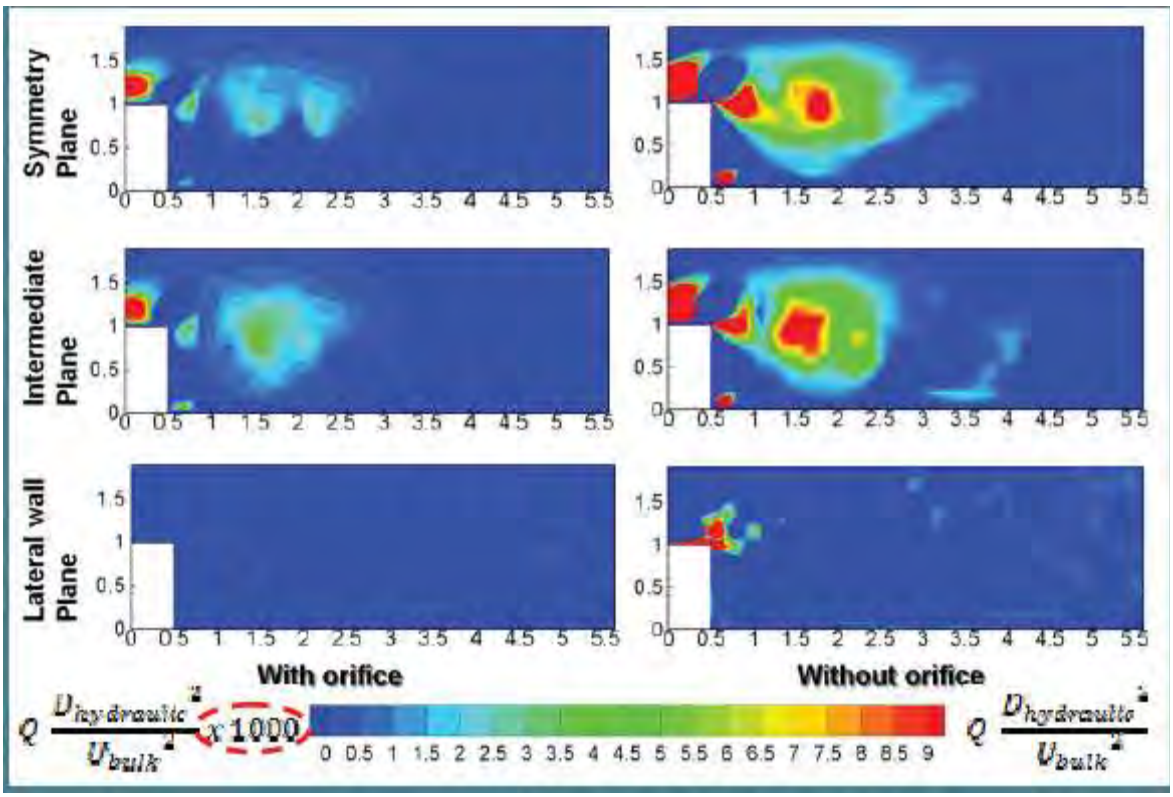


*Figure 16.24 Iso-contours of Q at different X-Y plane. Left side: active orifice; right side: closed orifice.*

# CHAPTER 17 Investigation of the thermal field

## *17.1 The temperature field*

The purpose of this chapter is to apply the findings of chapter 5 to the understanding of the effect of the orifice to the thermal field.

A comparison of the thermal field at the symmetry plane for the present case with the previous closed orifice case (chapter 8) is presented in *figure 17.1*, which allows appreciating the major effect of the aspiration through the orifice, which causes an important decrease of temperatures in the regions of the solid slab where the orifice is active.

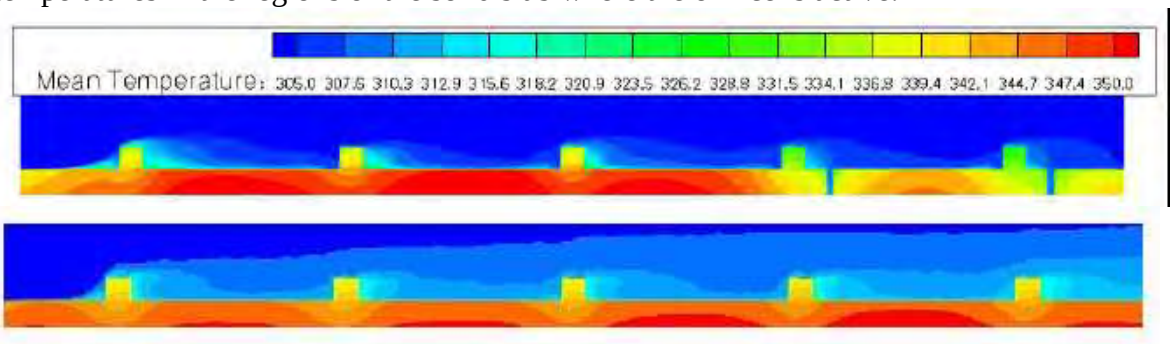


*Figure 17.1 Average temperatures at the symmetry plane. Top: active orifice; bottom: closed orifice*

Examining thermal field within the solid, it must be kept present that, due to its very high heat capacity (see *table 1.1*), the final average temperatures remained close to the corresponding ones obtained from the steady RANS (see below) initial solution.

In fact, the present investigation was unable to fully overcome a problem which had not emerged from the results discussed in Part III, namely an unbalance of the numerical unsteady heat transfer at the interface solid/fluid, caused by the very high thermal inertia of the solid phase. The problem and the assessment of its effect for the present and previous results are detailed in Annex K and Annex I, which lead to conclude that only the non-dimensional representation of the heat transport at the interface is reliable under the quantitative point of view. Therefore, the following analysis is focused on the EF parameter (section 17.2).

## *17.2 Analysis of effect of orifice on Enhancement Factor*

The available of new experimental data obtained by liquid crystals (LC) [4] allows a full comparison between simulation and experiment, to validate the first and interpret the second one. Therefore, the basic case of ribbed duct without orifice (Part III) is studied first and the differences with due to the effect of the orifice are discussed later on.

Enhancement Factor is mapped in the 2 dimensional representations introduced in the previous chapter; the mapped area covers: the bottom wall upstream of the rib from X/*h* =

-6 to X/*h* = -1.5; the 3 consecutive faces of the rib; the bottom wall downstream of rib from X/ *h* = 1.5 to X/ *h* = 6. The definition of EF (section 2.2) is coherent with the one applied in the experiments to allow a quantitative comparison. Two cases are therefore considered: closed orifice (part III): BR=0 and active orifice with the test conditions discussed in chapter 15, namely: BR=4.5.

The results area-averaged EF are presented and compared with the experimental data in *table 17.1*, to gain an overall view of the macroscopic aspects of the process. An acceptable agreement is found, apart of the case of the top face of the rib, which will be discussed later on and is further explored in Annex L. This result confirms the argument in Annex K that mean EF is not very sensible to the unbalance of heat flux in the slab and, therefore, present and past (part III)] results can be confidently to the analysis of conjugate heat transfer.

| | **EF exp BR=0** | **EF les BR=0** | **EF exp BR=4.5** | **EF les BR=4.5** |
|---|---|---|---|---|
| **Bottom wall** | **2.20** | **2.12** | **2.64** | **2.43** |
| **Rib upstream face** | **3.20** | **3.16** | **3.61** | **3.53** |
| **Rib top face** | **2.86** | **2.43** | **3.22** | **2.65** |
| **Rib downstream face** | **1.89** | **1.98** | **2.88** | **2.79** |

*Table 17.1 Experimental and LES area-average EF*

It can be remarked that both experimental and computed values of EF are higher for the case of active orifice than for the one of closed orifice, which is an indication that film cooling has a positive effect on the overall cooling system.
The detailed results of the two cases are discussed in the two next sections. In the case of the simulation, it is attempted to relate the behavior of EF to the different topological features identified in chapter 5.

### *17.2.1 Analysis of Enhancement Factor for closed orifice*

The maps of EF extracted from the simulation (top) and the experiment (bottom) for the case of close orifice are shown in *figure 17.2*, the scale of colors being equivalent.

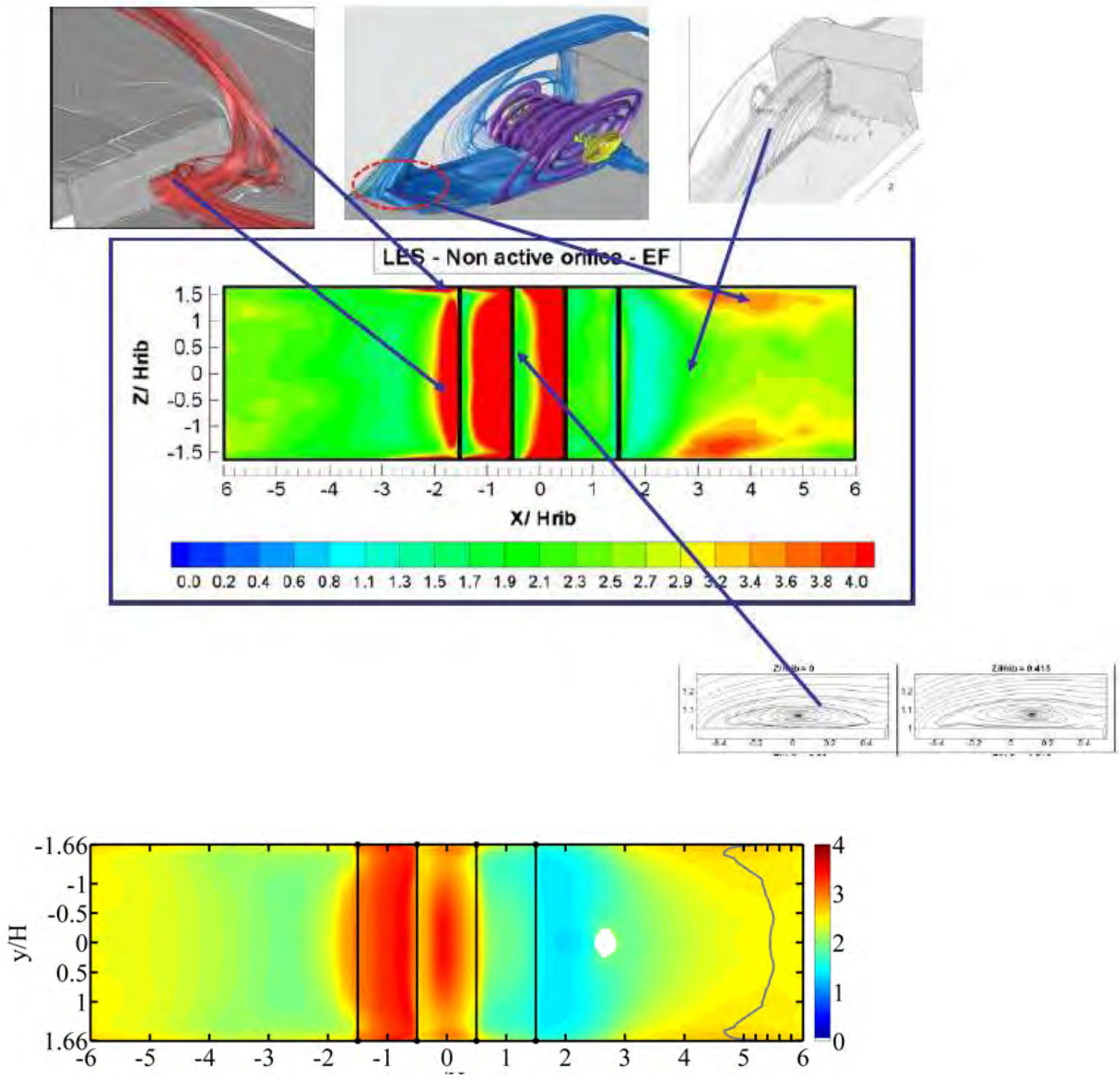





*Figure 17.2 Map of EF. Top: simulation; bottom: experiment.*

.

Both maps indicated similar trends, with the exception of the top face of the rib, as it was already remarked. On the upstream bottom wall, a region of high EF at the bottom corner is evident in both simulation and experiment; this is due to the transversal vortex (*figure 16.1*) whose effect has been discussed in part IV. The simulation shows two regions of high EF in correspondence of the two corners made by the intersection of bottom wall, side wall and rib: this corresponds to the footprint of the side vortex (discussed in section 16.2 and marked in *figure 16.2*); this effect seems stronger, or better defined, than it is the case of the experiment. Considering the upstream face of the rib, a region of high EF is found on the part of the face, which is directly exposed to the impact of the upstream flow; the lower part of this surface and the side corners are shielded by the corresponding rotating structures (see wall streamlines

in present figure) and EF is lower; the distribution is similar for both cases, but the effect is stronger for the simulation. As said, two very different behaviors are found for the top face of rib: according the experiment, a region of very high EF would be present on the central part of the plane, while the simulation presents a region of relatively low EF just downstream of the corner, followed by a region of higher EF in the downstream part of the face; it must be remarked that the same pattern is found in all the present and past simulations, whatever the system of heating [1, 2, 3 and 20], as shown in Annex K. The interpretation here proposed is that this distribution of EF is consequence of the separation of the flow on the upstream corner, which creates the separate region $V_2$ (*figure 16.1* and indicated in *figure 17.2*) covering large part of this surface, where heat exchange is weak. Downstream of its reattachment, EF increases to reach a local maximum. This interpretation is consistent with the available Particle Imaging Velocimetry (PIV) data [8], which indicates a separated region covering most of the surface, having a size comparable to the one found for the simulation. At the present time, the discrepancy with LC data remains unexplained. The downstream face the rib corresponds to a region of low EF for both representations, in correspondence of the separated region $V_0$, whose trace footprint is also visible on the bottom wall, as a region of low EF; it can be remarked that this region has its maximum length in the central part of the duct, as it is confined by the flow from the sides. The simulation shows two symmetric local regions of high EF, downstream of the reattachment; their presence can be explained by the impact of the flow external to $V_0$, discussed in section 16.2.2 (*figure 16.15*) and indicated above in *figure 17.2*.

### *17.2.2 Analysis of Enhancement Factor for active orifice*

The maps of EF for the case of active orifice, extracted from the simulation (top) and the experiment (bottom) are shown in *figure 17.3,* the scale of colors being equivalent. Again, for the simulation, it is attempted to show directly, in the figure, the connection between topological features of the flow field and EF. Experiment and simulation both confirm (chapter 16) that the effect of the orifice is mostly limited to the downstream face of the rib and the downstream bottom wall; upstream, the distribution of EF is substantially unchanged with respect to the previous case. On the contrary, the situation is different for the downstream face of the rib; the motion toward the symmetry plane (section 16.5.2 and indicated in *figure 17.3*) causes two areas of high EF on the sides. This increase can be explained by the totally different behavior of $V_1$ and $V_0$. In the present case, the sink effect of the orifice drags the fluid trapped in the wall layer toward the orifice, this effect being stronger for the central part of the duct (*figures 16.4, 16.7 and 16.10*). The part of the fluid which is not be directly dragged into the orifice reaches back to the downstream face of the rib entering $V_1$ by the side (*figure 16.5* and *figure 17.3* below), causing the strong gradient of EF within this zone. EF decreases approaching the symmetry plane, due to the low local velocity caused by the SPB mechanism. Looking to the bottom wall, it is visible that the effect of the orifice is to decrease the size of the region of low EF caused by $V_0$. The orifice itself causes a local region for very high EF, corresponding to flow entering the orifice at high velocity, while the destruction of $V_0$ in the central part of the duct causes an overall higher EF. The side regions of high EF caused by the impact of the side flow external to$V_0$ (section 16.2.2 and *figure 16.15*) are more important than in the previous case, showing the importance of the SBP mechanism modifying the flow field. Downstream of the main reattachment, the EF(s) are higher than in

the previous case; this result is consistent to the higher velocities and level of turbulence above the bottom wall remarked in section 16.3.

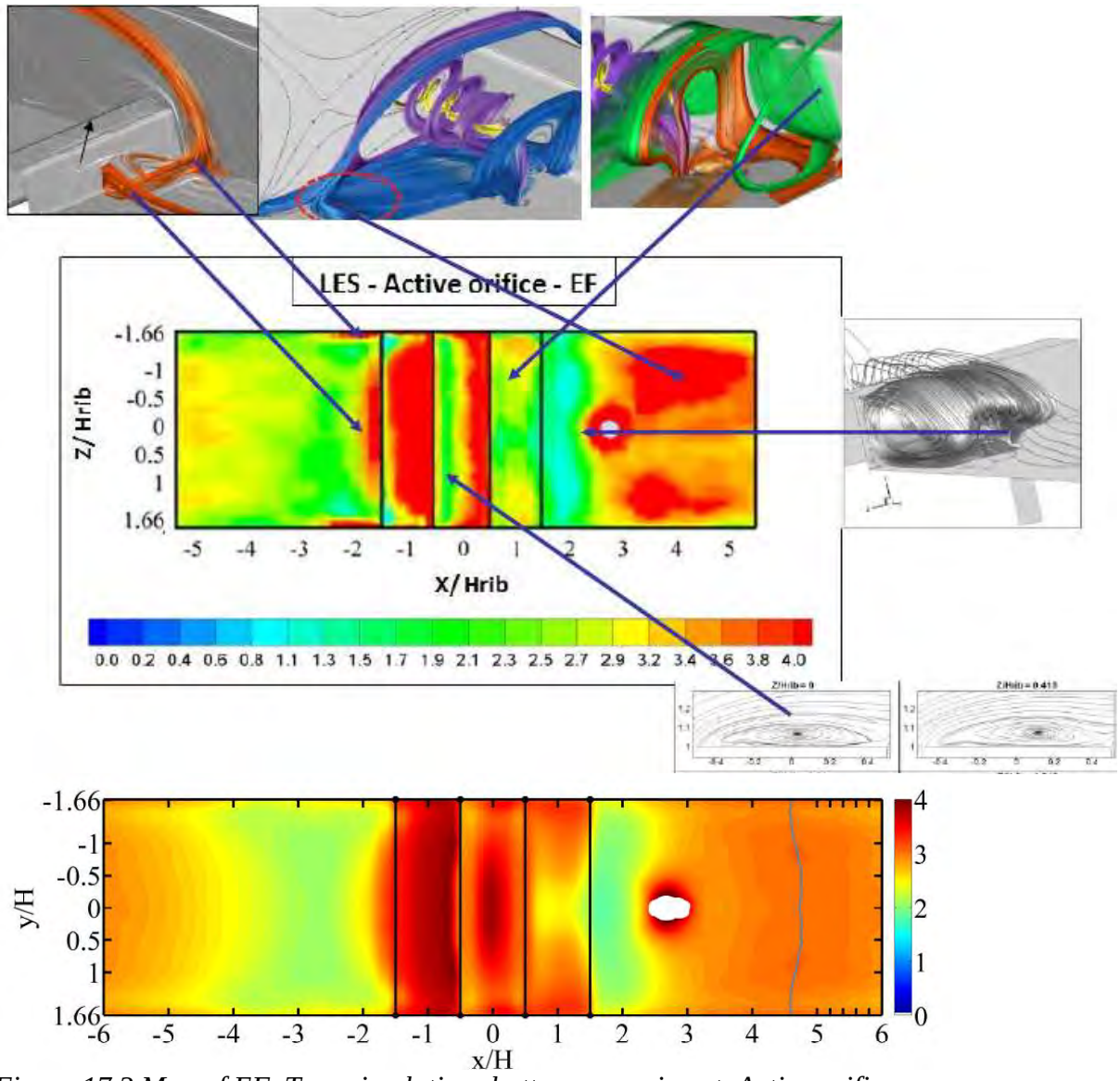


*Figure 17.3 Map of EF. Top: simulation; bottom: experiment. Active orifice.*

*Figure 17.4* compares the values of EF on the centerline for the simulation (left) and experiments (right). Comparing with the experimental data, globally, an acceptable quantitative agreement is found, as it could have expected from *Table 17.1*. Locally, the simulations present a higher local EF on the upstream corner than the experiment; it could be, partially, caused by the numerical error inherent to the estimation of local gradient on a sharp corner; the discrepancy of behavior in the central part of the top face, was already remarked and discussed in Annex K and L: in absence of experimental data concerning the flow in the present test section this discrepancy remains unexplained.

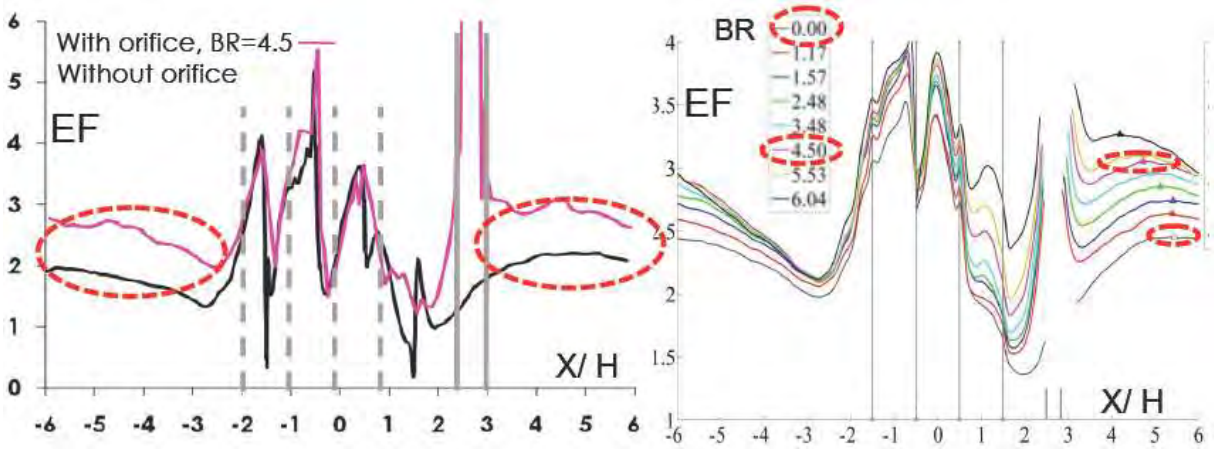


*Figure 17.4 EF on the centerline. Left: simulation; right experiment.*

Concerning the results of the simulation, the values for the closed orifice are compared with ones for the active orifice with ratio BR=4.5. It must be taken in account that the limitations of the available time and CPU power made impossible to simulate the closed orifice case on the present grid and inlet condition (chapter 7, 8, 9), therefore, the previous data (part III) have been here plotted for comparison. On the rib itself, the values for the upstream and top faces of the rib are similar for the cases (with the exception of the concave corners, where the worse quality of the older grid causes very low local values); this confirms the indication of chapter 16 that the action of the orifice does not change by a substantial way the action of the rib on the flow and the heat transfer; only on the downstream face, the SPB effect causes higher EF(s), as already remarked. On the bottom wall, the EF is higher for the case of active orifice; this effect can be partially attributed higher velocities in the attached flow, put in evidence in section 16.3, which cause higher *Cf* and EF (Annex M), but the increase of EF can be also originated by the totally different topology in the separated flow region. In fact, cooling performance is strongly improved by the removal of high temperature fluid which is dragged into the orifice through the SPB mechanism, as visualized in f*igure 16.5*. A completely opposite behavior occurs in closed orifice. In this case, low EF(s) are caused by high temperature fluid close at the bottom wall, which is trapped in $V_0$ and $V_1$. This mechanism is shown in *figure 17.5*. Green stream traces represent structure $V_1$. Blue stream traces represent rotating flow in $V_0$ (see also *figure 16.5*) moving from the lateral wall toward the symmetry plane. Orange stream traces represent flow confined within $V_0$, which moves back toward the face of the rib, impinging on it above $V_1$, moving upward, but remaining trapped in $V_0$. As it is shown by the blue stream traces entangled with the green ones, it is possible to have a recirculation loop between $V_0$ and $V_1$, but high temperature fluid close to the bottom wall remains part of $V_0$. As a result, this fluid flows again over the heated bottom wall, while being displaced by the helical motion of $V_0$ and it is redirected to high temperature areas. This absence of macroscopic exchange with fluid outside of $V_0$ explains the low EF(s) in this region.

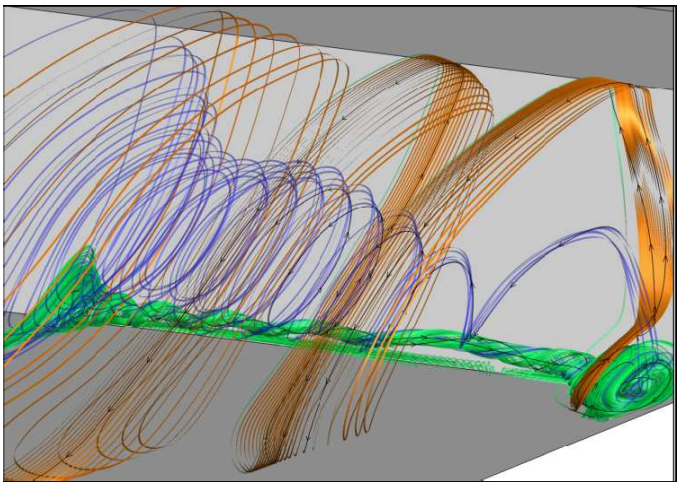

*Figure 17.5 Behavior of flow trapped in $V_0$ recirculation structure. Closed orifice*

### *17.2.3 Comparison with convective heating*

A final simulation was performed to check the possible effect of unbalance of the unsteady heat flux on the present investigation. The computational domain was modified to mimic the convective heat system of the test section [25] (*figure 17.6*). With this approach, the interface is directly heated and the conjugate problem does not rise. The heat transfer becomes similar to the one investigated in [25]. A heat flux of q=1443 w/m$^2$ was applied to match the experimental value.

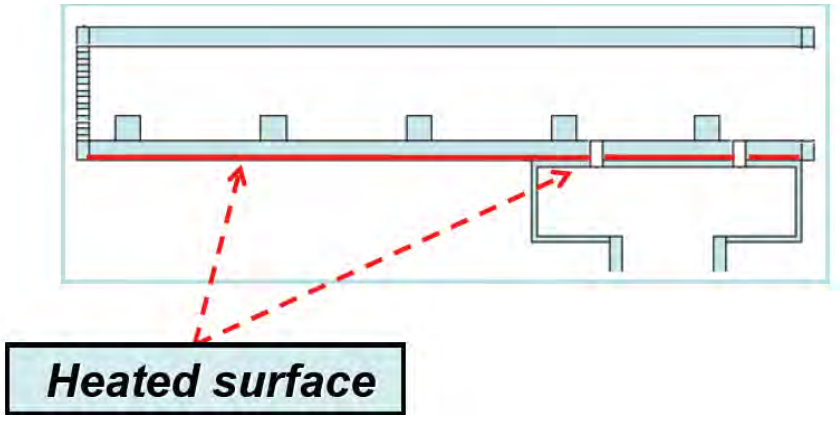


*Figure 17.6 Convective heating set-up*

The area-average EF for the present simulation is compared with the experimental data in *table 17.2*. It can be remarked that the simulation well matches the experimental results, with the exception for the downstream face of the rib, where a sensibly lower EF is found. Apart of this surface, the comparison with *table 6.1* shows that the difference between the two simulations remains within the order of 10% and does not invalidate the general conclusions here drawn. The timeframe of the investigation made impossible to further investigate the discrepancy.

| | EF exp BR=4.5 | EF les (conv.) BR=4.5 |
|---|---|---|
| **Bottom wall** | **2.64** | **2.54** |
| **Rib upstream face** | **3.61** | **3.65** |
| **Rib top face** | **3.22** | **2.96** |
| **Rib downstream face** | **2.88** | **2.17** |

*Table 17.2 Experimental and LES area-average EF; convective heating*

The two-dimensional map of EF is presented in *figure 17.7*. It can be seen that main patterns are qualitatively similar to *figure 17.3*. In the former case, the local maxima are stronger and wider, effect which might be attributed to the imprecision on unsteady heat exchange, but the fundamental interpretation proposed in the previous section is not invalidated. In particular, qualitatively, the distribution of EF on the top face of the rib is unchanged, result which may support the hypothesis it might be related to the flow-field itself. It can also be remarked is the side maxima on the downstream bottom wall are still present.

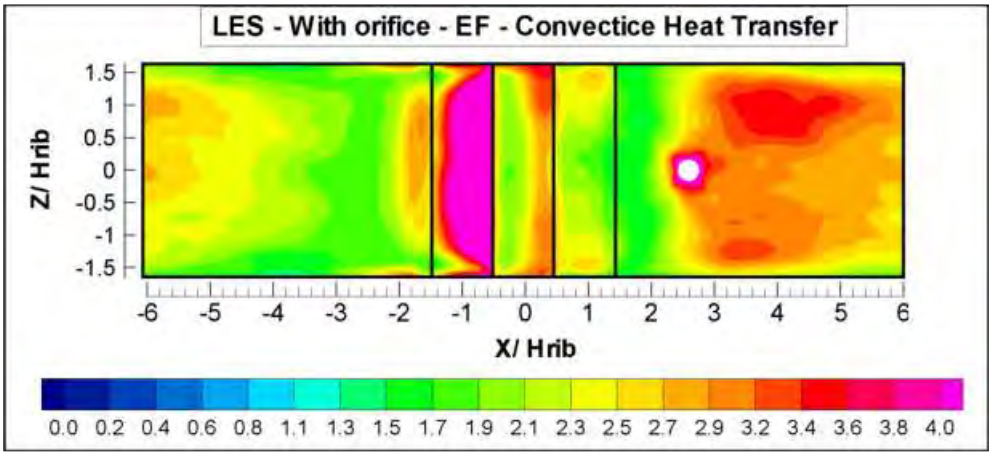


*Figure 17.7 Map of EF. Convective heating. Active orifice. LES*

# Conclusions for Part V

The effect of the action of bleeding orifices on flow field and conjugate heat transfer in ribbed duct was investigated by LES, with the purpose to assess the efficiency of the system for the film cooling of turbine blades.

The simulations allowed understanding the complex topology of the flow which results of the effect of the aspiration at the orifice and its effect on the heat flux at the interface solid/cooling fluid. The present results indicate that the resulting flow is shear dominated and

the effect of organized rotation (CS) is inhibited, even if further investigation would be necessary to fully confirm this tentative conclusion.
It was found that, on the contrary to LES, eddy-viscosity RANS solvers are unable to fully reproduce the topology of the flow and heat transfer (Annex J) and cannot be recommended for application in the field.
A satisfactory agreement was found between measurements and LES simulation for what concerns the non-dimensional heat flux, apart of the top face of the rib, whose respective (measurements and simulation) results must be evaluated and re-assessed (Annex L).

# General Conclusions

The fundamental aspects of the internal cooling of turbine blades by flow in ribbed ducts have been investigated simulating flow and thermal fields in a ribbed square rib and through the solid ribbed wall. The LES approach is applied for the fluid phase. The investigated set-up reproduces the test section developed in the companion experimental program [25 and 27].
The LES approach has been validated against available experimental data (Part II and Part III) and it was demonstrated that this approach is capable (at difference to RANS) to reproduce flow and thermal fields with satisfactory accuracy.

The presence of Coherent Structures in the flow field and its interaction with wall heat transfer have put in evidence (Part IV); moreover, it was confirmed and put in evidence the dominant effect of rotation dominated permanent regions in the average flow and heat transfer. Advanced post-processing by Principal Component Analysis has been applied to identify the physical quantities more important in heat transfer. It was attempted to quantify the effect of Coherent Structures applying Conditional Average (Part IV), but it was found that conditioned and unconditioned were not different by a important amount, leading to conclude that the importance of Coherent Structures (and the corresponding permanent structures in the average field) lie with way they shape the overall flow, more than fundamental differences between organized and un-organized background turbulent field.
The effect of orifices for film cooling in the duct was investigated and very complex resulting topology was identified and studied. It was found that action of the orifices drastically reduces the effect of organized rotation. The improvement of heat transfer by the cooling holes was put in evidence.

The present investigation, as well previous results [1, 2, 3 and 20] put in evidence the strong correlation between and flow and thermal field, indicating that good simulation of the former is necessary at the stage of design to estimate the expected heat transfer. Under this point of view, LES approach is capable to assess the working of the internal cooling of turbine blade and can offer a solid support to its design.
The remaining problems, concerning the determination of the actual temperatures within the blade, were identified and possible solutions investigated, even if the time limits of the research made impossible to complete this part of the work. Successive follow-up of this work is recommended to accelerated the convergence of conjugated heat transfer (Annex K, I) make LES a full reliable design tool in this class of problem.

# References

[1] M.M.Lohász ; P. Rambaud; C.Benocci (2003). LES simulation of ribbed square duct flow with Fluent and comparison with PIV data. *Conference on Modeling Fluid Flow CMFF'03 The 12th International Conference on Fluid Flow Technologies, Budapest, Hungary*

[2] M.M.Lohász ; P. Rambaud; C.Benocci (2004). MILES flow inside a square section ribbed duct. RTO. *Meeting, AVT-120 Workshop on "Urban Dispersion Modeling" April 1-2., Rhode-Saint-Genèse, Belgium*

[3] M.M.Lohász ; P. Rambaud; C.Benocci (2005). Flow features in a fully developed ribbed duct flow as a result of LES. *Engineering Turbulence Modeling and Experiments 6 – Proceedings of ERCOFTAC ETMM6, 23-25May, Sardinia, Italy, 267-276*

[4] P. Vass; P. Rambaud; T. Arts; C. Benocci (2007) Numerical investigation in flow and heat transfer in a ribbed square duct applying LES. *7TH ETC Conference Athenes, 4March; Greece*

[5] S.B Pope (2000). Chapter 13: Large-eddy simulation. *Turbulent Flows, Cambridge University Press.*

[6] U. Piomelli (2006). Large eddy simulation and related techniques; theory and applications. *Large Eddy Simulation of Turbulent Flows, VKI Lecture Series 2006-04*

[7] J.P. Boris; F.F. Grinstein; S.S Oran; R.L. Kolbe, (1992). New insight into large eddy simulation. *Fluid dynamics research.* **10.** 199-228.

[8] L. Casarsa; M. Çakan; T. Arts. (2002). Characterization of the velocity and heat transfer fields in an internal cooling channel with high blockage ratio. *Proceedings of ASME TURBO EXPO 2002 June 3-6, 2002 Amsterdam, The Netherlands*

[9] L. Casarsa (2003). Aerodynamic performance investigation of a fixed rib-roughened internal cooling passage. PhD Thesis, Universita degli Studi di Udine, Von Karman Institute for Fluid Dynamics

[10] F. Agostini and T. Arts, (2005). Conjugate heat transfer investigation of rib-roughened cooling channels. *Proceedings of ASME Turbo Expo*, June 6-9, Reno-Tahoe, Nevada, USA

[11]W. Rodi, J.H. Ferziger; M. Breuer and M. Pourquie (1997). Status of Large Eddy Simulation: Results of a Workshop. *J. Fluids Eng.*", 119, 248--262

[12] J. Cui; V.C.Patel and C.-L Lin (2003). Large-eddy simulation of turbulent flow in a channel with rib roughness. *International Journal of Heat and Fluid Flow,* **24**, 372-388.

[13] Y. Dubief and F. Delcayre. (2000). On coherent-vortex identification in turbulence. *Journal of Turbulence,* **1,** 011

[14] FLUENT 6.3 User's Guide, Fluent Inc

[15] A. Smirnov; S. Shi.; I. Celik (2001). Random flow generation technique for large eddy simulations and particle-dynamics modeling. *Journal of Fluids Engineering,* **123,** 359-371.

[16] B. Fighiera (September 2008). Investigation of turbulent flow and heat transfer in a ribbed square duct applying Large Eddy Simulation." VKI internship report. Supervisors Profs. C. Benocci & P. Rambaud. Report also registered in University Pierre et Marie-Curie (France).

[17] H. Choi and P. Moin (1994). Effects of the Computational Time Step on Numerical Solutions of Turbulent Flow, *Journal of Computational Physics*, **133,** 1-4.

[18] H. Hornung,and A. E.Perry, (1984). Some aspect of three dimensional separation Part I.: Streamsurface bifurcations. *Zeitschrift für Flugwissenschaften und Weltraumforschung,* **8,** 77-87.
[19] J. C. R. Hunt; A. A Wray, and P Moin,. (1988). Eddies, Streams, and Convergence Zones in Turbulent Flows. *Center for Turbulence research, Proceedings of the summer Program*
[20] M.M.Lohász; P. Rambaud ; C. Benocci (2007). Flow features in a fully developed ribbed duct flow as a result of LES. *J. of flow, turbulence and combustion. Vol. 77,* pp. 59-76
**[21]** M.M.Lohász ; P. Rambaud; C. Benocci (2005). Conditional averaging of the fully developed stationary ribbed duct flow using Q criteria. *ITI Conference on Turbulence, September 25-28, 2005, Bad Zwischenahn, Germany, Progress in Turbulence 2, Proceedings of the iTi Conference in Turbulence 2005, Springer Proceedings in Physics , Oberlack, M.; Guenther, S.; Weller, T.; Khujadze, G.; Osman, A.; Frewer, M.; Peinke, J. (Eds.) , Vol. 109.*
**[22]** Principal Component Analisys. *Wikipedia, free enciclopedia*
**[23]** J. Sheins (2009) A tutorial on Principal Component Analisys. *Center for neural Science. NY University*
**[24]** A. Parente (2008). Experimental and Numerical Investigation of Advanced Systems for Hydrogen-based Fuel Combustion. *Doctoral Thesis, University of Pisa (I)*
[25] B. Cukerel and T. Arts (2010). Experimental and numerical investigation of conjugate transfer in rib roughened channel. Experimental activity. Year 2,**Grant 083048 Work Package 2000.** *Von Karman Institute, Contract Report*
[26] L. Hasalova (2010). LES simulation of flow an heat transfer in ribbed duct. Von Karman Institute, Stager Report 31
[27] B. Cukerel and T. Arts (2011). Experimental and numerical investigation of conjugate transfer in rib roughened channel. Experimental activity. Year 3**Grant 083048 Work**

# Annex A Convergence of the statistics

The convergence and the sensibility of the LES simulation was verified restarting the calculation from the previous results, but applying the Dynamic Smagorinsky SGS model and the wall boundary condition proposed by Werner & Wengle [6, 14]:

$$y^+ \le 11.65 \qquad y^+ > 11.65$$
$$\overline{U}_1^+ = y^+ \qquad \overline{U}_1^+ = A(y^+)^B \; ; \qquad A = 8.3, B = 1/7$$

Following the literature, this definition would be more accurate in the separated regions than the classical logarithm law.

The available results are resumed in the following table:

| | |
|---|---|
| Smagorinsky, Cs=. 1; log. wall law; | 7.5 flow-through |
| Dynamic; W-W wall law; restart; | + 3.75 flow-through |
| Dynamic; W-W wall law; restart; | + 7.5 flow-through |

Results are here presented for 3 representative locations:
*X/h*= 0 at the centre of the rib
*X/h*= 1 with the main separated region downstream of the rib
*X/h*= 5 in the re-attached boundary layer downstream of the main separation

As it is shown in the following figures, the results for average field and resolved turbulent fields are practically identical, leading to conclude the simulation is converged and stable.
It can be, therefore, used as basis of the study of CS field.

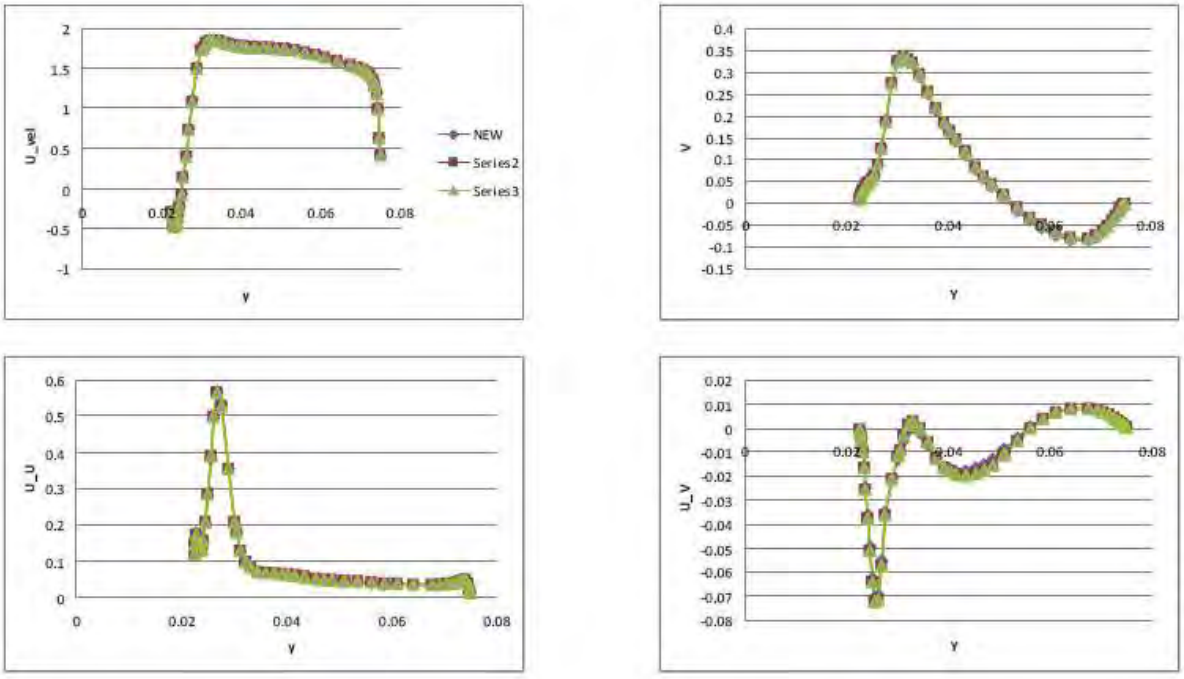


*Figure A 1 Profiles of for location X/h=0*

Original Smagorinsky simulation

1st restart Dynamic

2sd restart Dynamic

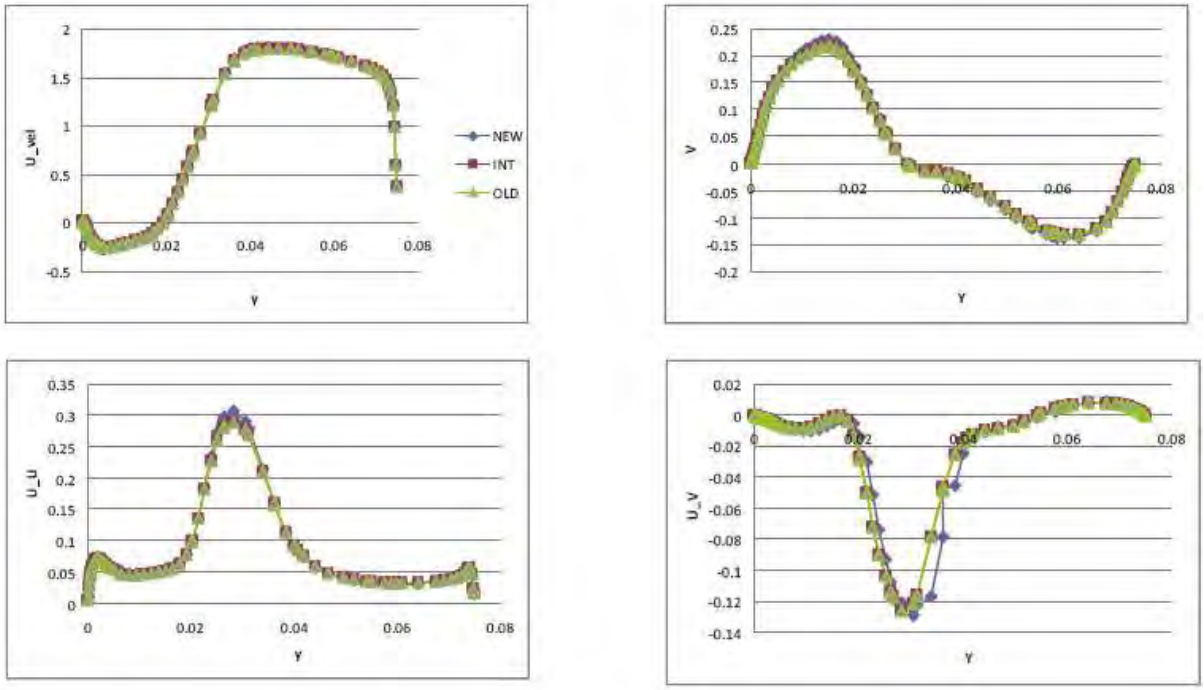


*Figure A.2 Profiles of for location X/h=1*

Original Smagorinsky simulation

1st restart Dynamic

2sd restart Dynamic

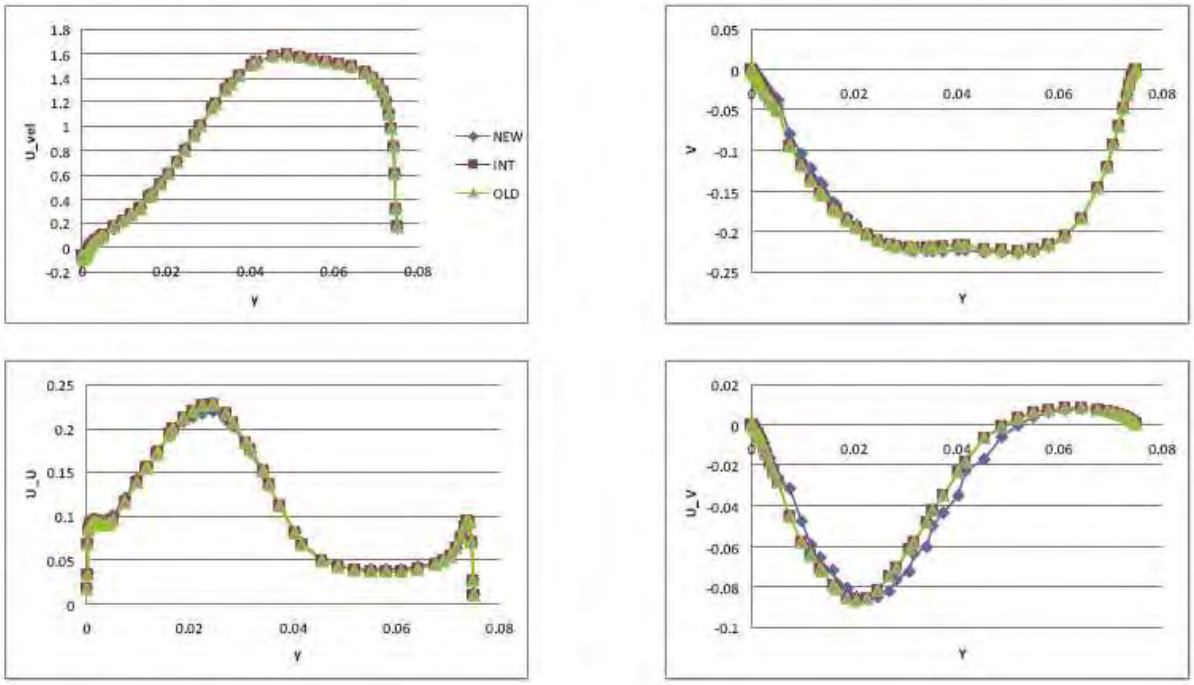


*Figure A 3 Profiles of for location X/h=5*

Original Smagorinsky simulation

1st restart Dynamic

2sd restart Dynamic

# Annex B Interpretation of thermal data

Following the observations in chapter 8 and 10, the interpretation of thermal data was checked and summarized.
The topological model proposed by the previous investigators [3, 4 and 20] was applied (*figure B 1*) to attempt to relate heat transfer to the flow patterns. The composed *figure B* 1 puts together: vortex regions, re-circulating regions and wall streamlines in an attempt to identify their respective roles. A strong correlation was remarked between heat transfer and large scales flow structures identified and underlined in *figure B 1*.

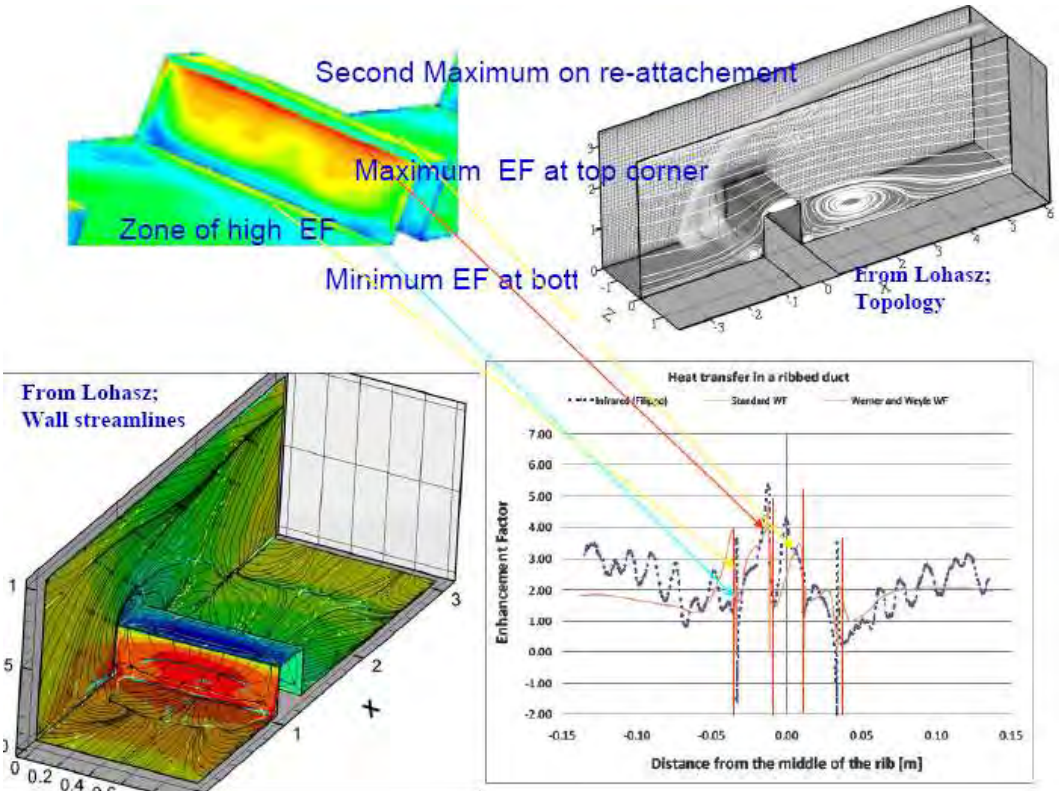


*Figure B 1 EF against the present conceptual model of the flow topology.*

The present interpretation is that the heat transfer on the rib is driven by the permanent rotating- dominated structures (*figure B 2*).

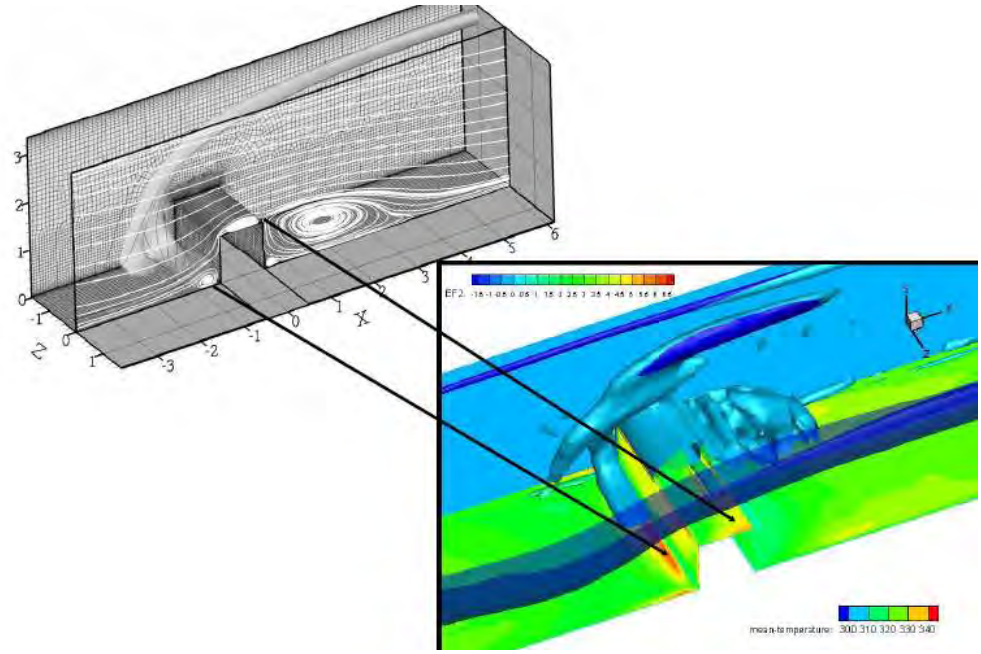

*Figure B 2 Identification of regions of high EF versus presence of permanent rotation dominated structures in the flow field*

This model of interpretation was found coherent with the successive LES results.

# Annex C Example of Covariance Matrix

PCA has been applied the first grid plane above the bottom wall and around the rib (*figure C 1*)

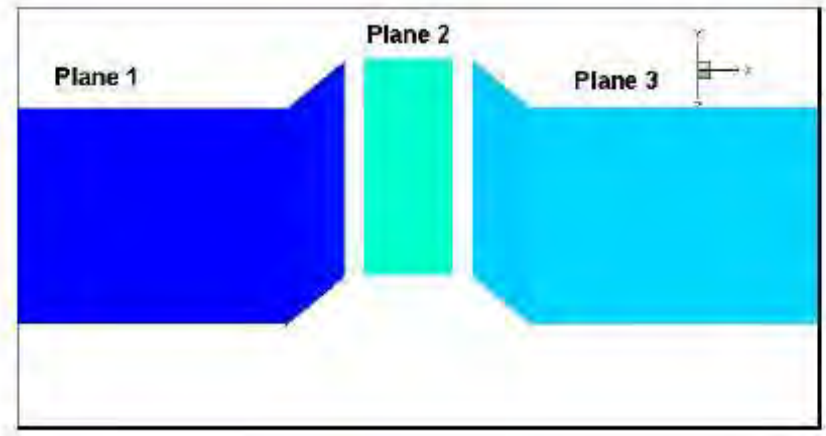


*Figure C 1 Planes where the covariance matrix is extracted.*

The correlation matrix is extracted for planes 1, 2 3 and presented here.

| | PLANE1 | | | | | | | | | | | | |
|---|---|---|---|---|---|---|---|---|---|---|---|---|---|
| | EF | Qins | <TT> | T | <uv> | <uw> | <vw> | <uT> | <vT> | <wT> | Qmean | tke | U |
| EF | 1.00 | -0.29 | -0.81 | -0.77 | 0.28 | 0.01 | -0.02 | 0.25 | 0.26 | -0.03 | -0.21 | 0.25 | 0.54 |
| Qins | -0.29 | 1.00 | 0.50 | 0.50 | -0.16 | -0.01 | 0.09 | -0.01 | 0.11 | 0.07 | 0.55 | -0.44 | -0.58 |
| <TT> | -0.81 | 0.50 | 1.00 | 0.99 | -0.20 | -0.02 | 0.03 | -0.10 | -0.30 | 0.03 | 0.43 | -0.41 | -0.72 |
| T | -0.77 | 0.50 | 0.99 | 1.00 | -0.21 | -0.03 | 0.03 | -0.06 | -0.29 | 0.03 | 0.44 | -0.43 | -0.72 |
| <uv> | 0.28 | -0.16 | -0.20 | -0.21 | 1.00 | 0.02 | 0.00 | 0.22 | -0.23 | -0.03 | 0.01 | 0.10 | 0.16 |
| <uw> | 0.01 | -0.01 | -0.02 | -0.03 | 0.02 | 1.00 | 0.05 | -0.06 | 0.01 | 0.12 | 0.00 | 0.00 | -0.01 |
| <vw> | -0.02 | 0.09 | 0.03 | 0.03 | 0.00 | 0.05 | 1.00 | 0.00 | -0.05 | 0.01 | -0.02 | -0.01 | -0.01 |
| <uT> | 0.25 | -0.01 | -0.10 | -0.06 | 0.22 | -0.06 | 0.00 | 1.00 | 0.01 | -0.04 | 0.05 | -0.05 | 0.20 |
| <vT> | 0.26 | 0.11 | -0.30 | -0.29 | -0.23 | 0.01 | -0.05 | 0.01 | 1.00 | 0.00 | -0.05 | -0.09 | 0.00 |
| <wT> | -0.03 | 0.07 | 0.03 | 0.03 | -0.03 | 0.12 | 0.01 | -0.04 | 0.00 | 1.00 | 0.01 | 0.00 | -0.01 |
| Qmean | -0.21 | 0.55 | 0.43 | 0.44 | 0.01 | 0.00 | -0.02 | 0.05 | -0.05 | 0.01 | 1.00 | -0.75 | -0.70 |
| tke | 0.25 | -0.44 | -0.41 | -0.43 | 0.10 | 0.00 | -0.01 | -0.05 | -0.09 | 0.00 | -0.75 | 1.00 | 0.79 |
| U | 0.54 | -0.58 | -0.72 | -0.72 | 0.16 | -0.01 | -0.01 | 0.20 | 0.00 | -0.01 | -0.70 | 0.79 | 1.00 |

*Table C 1 Correlation matrix Plane 1*

| | PLANE 2 | | | | | | | | | | | | |
|---|---|---|---|---|---|---|---|---|---|---|---|---|---|
| | EF | Qins | <TT> | T | <uv> | <uw> | <vw> | <uT> | <vT> | <wT> | Qmean | tke | U |
| EF | 1.00 | 0.03 | -0.72 | -0.75 | 0.20 | -0.03 | 0.05 | -0.27 | 0.66 | 0.03 | 0.31 | 0.36 | 0.21 |
| Qins | 0.03 | 1.00 | 0.28 | 0.30 | 0.01 | -0.12 | 0.04 | 0.20 | 0.32 | -0.01 | 0.46 | -0.07 | -0.34 |
| <TT> | -0.72 | 0.28 | 1.00 | 0.97 | 0.03 | 0.03 | -0.04 | 0.53 | -0.27 | -0.03 | 0.27 | -0.28 | -0.32 |
| T | -0.75 | 0.30 | 0.97 | 1.00 | 0.01 | 0.03 | -0.06 | 0.54 | -0.31 | -0.03 | 0.23 | -0.27 | -0.32 |
| <uv> | 0.20 | 0.01 | 0.03 | 0.01 | 1.00 | 0.01 | 0.03 | 0.30 | -0.22 | -0.01 | -0.21 | 0.42 | 0.47 |
| <uw> | -0.03 | -0.12 | 0.03 | 0.03 | 0.01 | 1.00 | -0.06 | 0.05 | -0.01 | 0.38 | 0.00 | -0.03 | -0.02 |
| <vw> | 0.05 | 0.04 | -0.04 | -0.06 | 0.03 | -0.06 | 1.00 | -0.03 | 0.06 | 0.40 | 0.00 | 0.02 | 0.02 |
| <uT> | -0.27 | 0.20 | 0.53 | 0.54 | 0.30 | 0.05 | -0.03 | 1.00 | -0.09 | -0.01 | 0.18 | 0.43 | 0.23 |
| <vT> | 0.66 | 0.32 | -0.27 | -0.31 | -0.22 | -0.01 | 0.06 | -0.09 | 1.00 | 0.02 | 0.75 | 0.00 | -0.28 |
| <wT> | 0.03 | -0.01 | -0.03 | -0.03 | -0.01 | 0.38 | 0.40 | -0.01 | 0.02 | 1.00 | 0.00 | 0.00 | 0.00 |
| Qmean | 0.31 | 0.46 | 0.27 | 0.23 | -0.21 | 0.00 | 0.00 | 0.18 | 0.75 | 0.00 | 1.00 | -0.14 | -0.48 |
| tke | 0.36 | -0.07 | -0.28 | -0.27 | 0.42 | -0.03 | 0.02 | 0.43 | 0.00 | 0.00 | -0.14 | 1.00 | 0.83 |
| U | 0.21 | -0.34 | -0.32 | -0.32 | 0.47 | -0.02 | 0.02 | 0.23 | -0.28 | 0.00 | -0.48 | 0.83 | 1.00 |

*Table C 2 Correlation matrix. Plane 2*

| | PLANE3 | | | | | | | | | | | | |
|---|---|---|---|---|---|---|---|---|---|---|---|---|---|
| | EF | Qins | <TT> | T | <uv> | <uw> | <vw> | <uT> | <vT> | <wT> | Qmean | tke | U |
| EF | 1.00 | -0.41 | -0.91 | -0.85 | 0.39 | 0.01 | -0.04 | 0.38 | 0.68 | -0.04 | -0.41 | 0.61 | 0.68 |
| Qins | -0.41 | 1.00 | 0.50 | 0.52 | -0.30 | 0.02 | -0.04 | -0.30 | -0.41 | -0.06 | 0.41 | -0.48 | -0.41 |
| <TT> | -0.91 | 0.50 | 1.00 | 0.98 | -0.41 | -0.02 | 0.04 | -0.39 | -0.77 | 0.06 | 0.58 | -0.66 | -0.70 |
| T | -0.85 | 0.52 | 0.98 | 1.00 | -0.42 | -0.03 | 0.04 | -0.37 | -0.81 | 0.07 | 0.66 | -0.66 | -0.68 |
| <uv> | 0.39 | -0.30 | -0.41 | -0.42 | 1.00 | 0.03 | -0.04 | 0.40 | 0.35 | -0.06 | -0.25 | 0.36 | 0.39 |
| <uw> | 0.01 | 0.02 | -0.02 | -0.03 | 0.03 | 1.00 | 0.16 | -0.07 | 0.04 | 0.26 | -0.04 | -0.05 | -0.03 |
| <vw> | -0.04 | -0.04 | 0.04 | 0.04 | -0.04 | 0.16 | 1.00 | -0.05 | -0.07 | 0.59 | 0.05 | -0.07 | -0.04 |
| <uT> | 0.38 | -0.30 | -0.39 | -0.37 | 0.40 | -0.07 | -0.05 | 1.00 | 0.15 | -0.06 | -0.11 | 0.71 | 0.74 |
| <vT> | 0.68 | -0.41 | -0.77 | -0.81 | 0.35 | 0.04 | -0.07 | 0.15 | 1.00 | -0.06 | -0.61 | 0.33 | 0.37 |
| <wT> | -0.04 | -0.06 | 0.06 | 0.07 | -0.06 | 0.26 | 0.59 | -0.06 | -0.06 | 1.00 | 0.06 | -0.10 | -0.07 |
| Qmean | -0.41 | 0.41 | 0.58 | 0.66 | -0.25 | -0.04 | 0.05 | -0.11 | -0.61 | 0.06 | 1.00 | -0.35 | -0.35 |
| tke | 0.61 | -0.48 | -0.66 | -0.66 | 0.36 | -0.05 | -0.07 | 0.71 | 0.33 | -0.10 | -0.35 | 1.00 | 0.81 |
| U | 0.68 | -0.41 | -0.70 | -0.68 | 0.39 | -0.03 | -0.04 | 0.74 | 0.37 | -0.07 | -0.35 | 0.81 | 1.00 |

*Table C 3 Correlation matrix. Plane 3*

# Annex D Principal Components obtained through RANGE approach

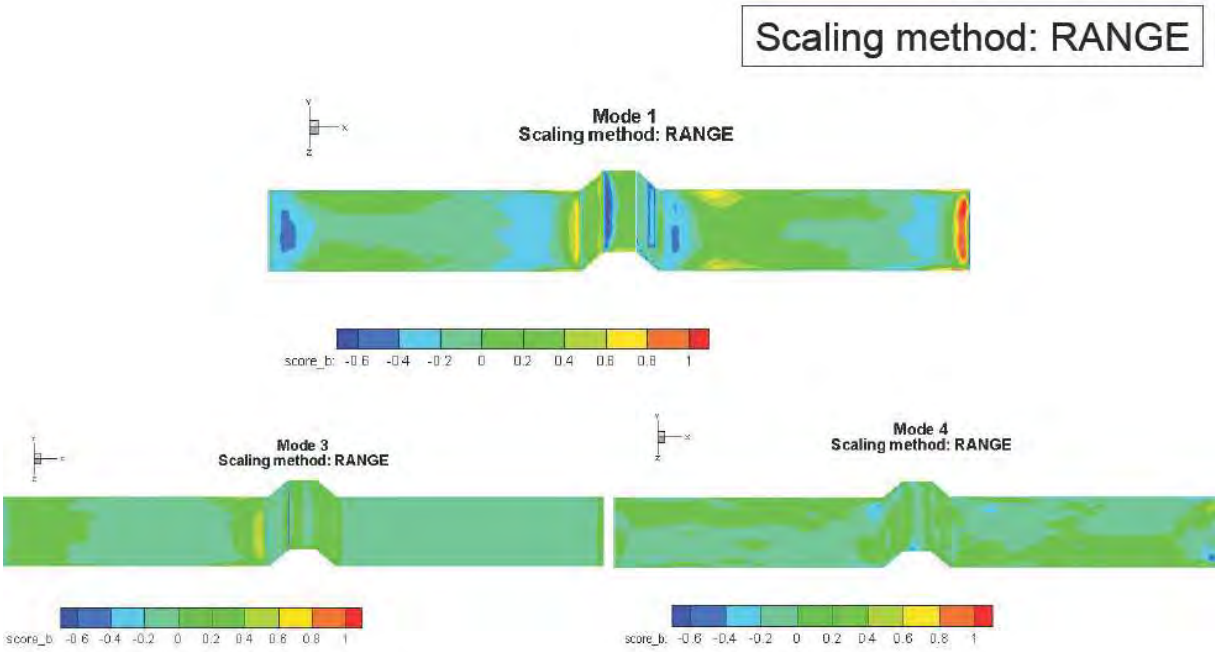


*Figure D 1 Distribution of different modes obtained applying RANGE scaling*

# Annex E final covariance matrix

The covariance matrix of the correlation analysis is presented in the top plane of the rib (*TOP*):

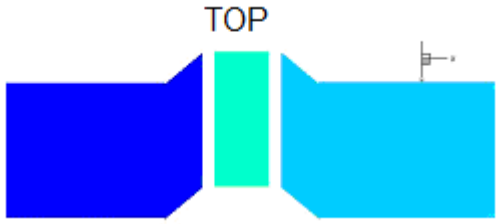


*E 1 Top plane of the rib*

| | EF_mean | EF_ins | Qins | Qmean | TT | PP | TKE | UU | UV | VV | UW |
|---|---|---|---|---|---|---|---|---|---|---|---|
| EF_mean | 1.00 | 0.69 | 0.03 | 0.32 | -0.44 | -0.28 | 0.53 | 0.42 | -0.29 | -0.32 | -0.21 |
| Qins | 0.03 | -0.20 | 1.00 | 0.45 | 0.36 | -0.24 | 0.12 | 0.10 | -0.41 | -0.53 | -0.03 |
| Qmean | 0.32 | 0.15 | 0.45 | 1.00 | 0.27 | -0.03 | 0.18 | 0.04 | -0.81 | -0.94 | -0.10 |
| TT | -0.44 | -0.83 | 0.36 | 0.27 | 1.00 | 0.21 | -0.12 | -0.45 | -0.18 | -0.26 | 0.37 |
| PP | -0.28 | -0.17 | -0.24 | -0.03 | 0.21 | 1.00 | -0.11 | -0.28 | 0.11 | 0.08 | 0.14 |
| TKE | 0.53 | 0.28 | 0.12 | 0.18 | -0.12 | -0.11 | 1.00 | 0.28 | -0.18 | -0.16 | -0.28 |
| UU | 0.42 | 0.35 | 0.10 | 0.04 | -0.45 | -0.28 | 0.28 | 1.00 | -0.17 | -0.06 | -0.60 |
| UV | -0.29 | -0.20 | -0.41 | -0.81 | -0.18 | 0.11 | -0.18 | -0.17 | 1.00 | 0.86 | 0.22 |
| VV | -0.32 | -0.16 | -0.53 | -0.94 | -0.26 | 0.08 | -0.16 | -0.06 | 0.86 | 1.00 | 0.12 |
| UW | -0.21 | -0.38 | -0.03 | -0.10 | 0.37 | 0.14 | -0.28 | -0.60 | 0.22 | 0.12 | 1.00 |
| WW | 0.14 | 0.39 | -0.13 | -0.01 | -0.34 | 0.29 | 0.32 | 0.16 | 0.00 | 0.00 | -0.60 |
| VW | -0.08 | -0.01 | -0.15 | -0.24 | -0.14 | 0.13 | -0.04 | 0.05 | 0.33 | 0.34 | 0.07 |
| UT | 0.39 | 0.31 | 0.06 | -0.02 | -0.41 | -0.30 | 0.25 | 0.85 | -0.11 | 0.00 | -0.54 |
| VT | -0.38 | -0.29 | -0.54 | -0.90 | -0.11 | 0.16 | -0.14 | -0.12 | 0.80 | 0.95 | 0.15 |
| WT | -0.09 | -0.26 | -0.06 | -0.06 | 0.23 | 0.18 | -0.25 | -0.39 | 0.16 | 0.09 | 0.64 |
| P | 0.30 | 0.17 | 0.29 | 0.17 | -0.14 | -0.97 | 0.14 | 0.26 | -0.26 | -0.23 | -0.14 |
| Vel_magn | 0.39 | 0.52 | -0.24 | -0.06 | -0.54 | 0.15 | 0.41 | 0.61 | 0.00 | 0.06 | -0.59 |

*Table E 1 Subset covariance matrix, Top plane of the rib*

| | EF_mean | EF_ins | Qins | Qmean | TT | PP | TKE | UU | UV | VV | UW |
|---|---|---|---|---|---|---|---|---|---|---|---|
| U | 0.36 | 0.24 | 0.16 | 0.10 | -0.26 | -0.27 | 0.28 | 0.75 | -0.21 | -0.11 | -0.48 |
| V | -0.38 | -0.34 | -0.36 | -0.84 | -0.06 | 0.13 | -0.06 | -0.07 | 0.82 | 0.89 | 0.12 |
| W | -0.05 | -0.24 | -0.08 | -0.07 | 0.20 | 0.11 | -0.22 | -0.32 | 0.16 | 0.09 | 0.59 |
| T | -0.44 | -0.88 | 0.38 | 0.20 | 0.93 | 0.13 | -0.14 | -0.31 | -0.13 | -0.19 | 0.30 |
| <P> | 0.71 | 0.44 | 0.10 | 0.28 | -0.36 | -0.34 | 0.32 | 0.47 | -0.30 | -0.26 | -0.16 |
| <Vel_magn> | 0.14 | 0.21 | -0.39 | -0.48 | -0.33 | -0.03 | 0.35 | 0.10 | 0.36 | 0.44 | -0.11 |
| <U> | 0.07 | 0.02 | 0.09 | -0.03 | -0.13 | -0.04 | -0.13 | 0.25 | -0.04 | 0.03 | 0.03 |
| <V> | -0.41 | -0.24 | -0.34 | -0.96 | -0.17 | 0.04 | -0.07 | -0.05 | 0.77 | 0.92 | 0.08 |
| <W> | -0.01 | -0.19 | -0.06 | 0.00 | 0.25 | 0.16 | -0.01 | -0.49 | 0.15 | 0.03 | 0.50 |
| <T> | -0.75 | -0.57 | 0.30 | 0.25 | 0.66 | 0.29 | -0.37 | -0.43 | -0.14 | -0.22 | 0.13 |
| <uv> | 0.20 | 0.17 | 0.01 | -0.12 | -0.04 | 0.00 | -0.06 | -0.17 | 0.22 | 0.08 | 0.01 |
| <uw> | -0.03 | 0.03 | -0.12 | 0.00 | 0.08 | 0.48 | -0.03 | -0.32 | 0.05 | 0.01 | 0.29 |
| <vw> | 0.05 | 0.06 | 0.04 | 0.00 | -0.16 | -0.13 | 0.02 | 0.28 | 0.16 | 0.03 | -0.11 |
| <uT> | -0.27 | -0.22 | 0.20 | 0.20 | 0.44 | 0.16 | 0.21 | -0.34 | -0.11 | -0.18 | 0.07 |
| <vT> | 0.66 | 0.48 | 0.32 | 0.73 | -0.18 | -0.23 | 0.32 | 0.34 | -0.65 | -0.69 | -0.20 |
| <wT> | 0.03 | 0.19 | -0.01 | 0.00 | -0.21 | 0.18 | 0.02 | 0.39 | -0.09 | 0.00 | -0.33 |
| EF_ins | 0.69 | 1.00 | -0.20 | 0.15 | -0.83 | -0.17 | 0.28 | 0.35 | -0.20 | -0.16 | -0.38 |

*Table E 2 Subset covariance matrix, Top plane of the rib*

# Annex F Example of UDF routine of conditional averaging

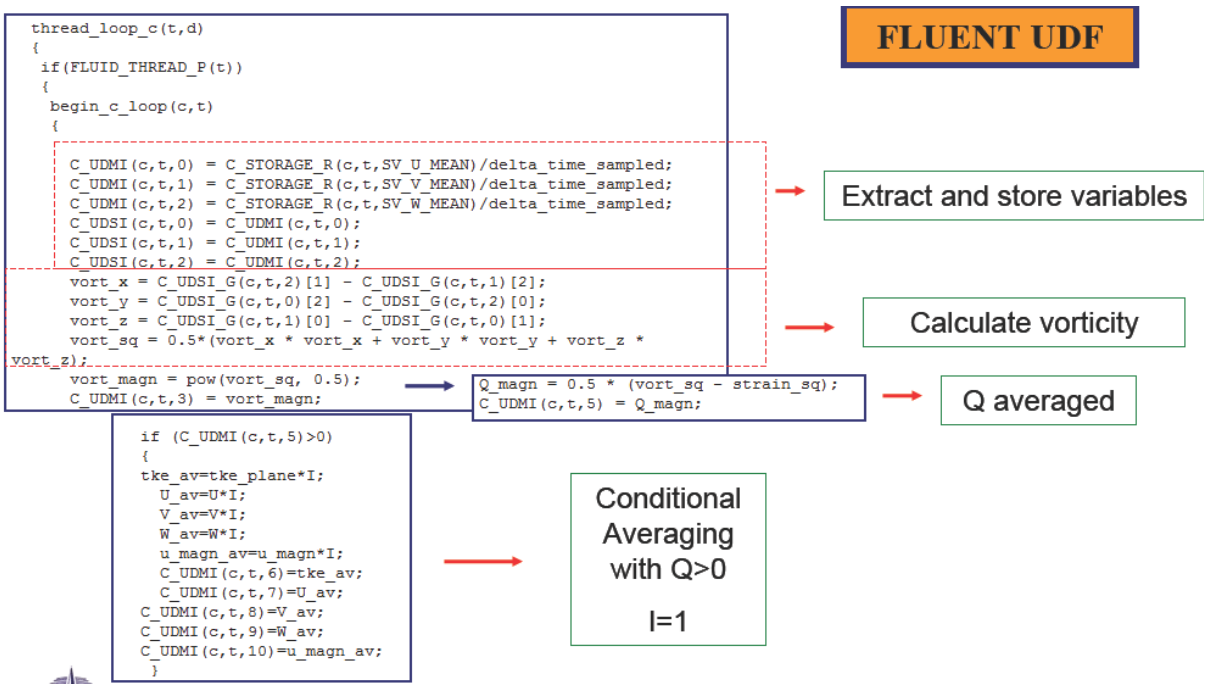

# Annex G Convergence of the Eulerian statistics

Profiles of mean quantities and resolved turbulent shear stress in the symmetry surface are presented in *figure G 1* and *2*, respectively. It can be concluded that the Eulerian statistics have reached convergence after 5 flow-through; this result is similar to one found in [26].

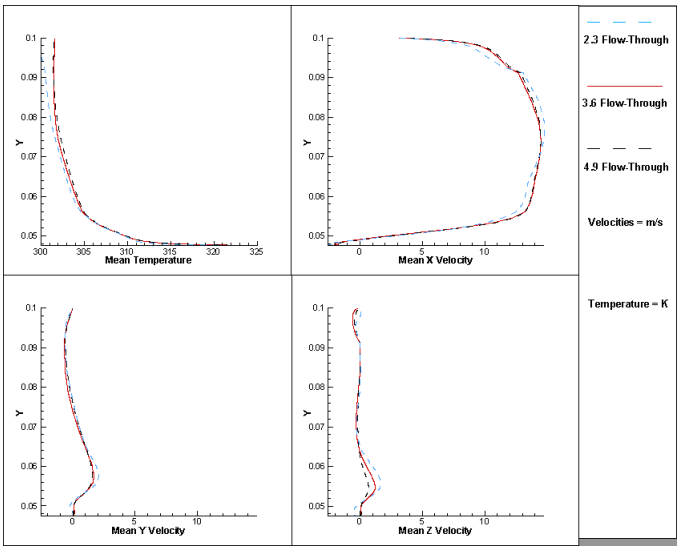


*Figure G1 Convergence history for the average flow*

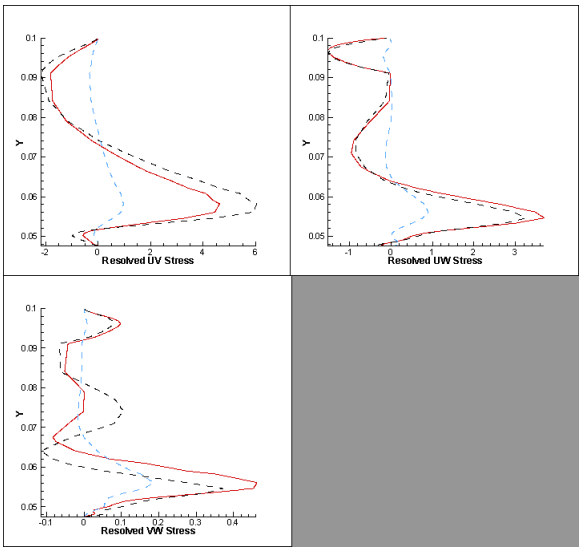


*Figure G 2: Convergence history for the average flow*

# Annex H Role of corner flow

The importance of the corner flow was put in evidence in [8] and the topological model presented in *figure H 1* was proposed on the basis of the interpretation of those experimental results.

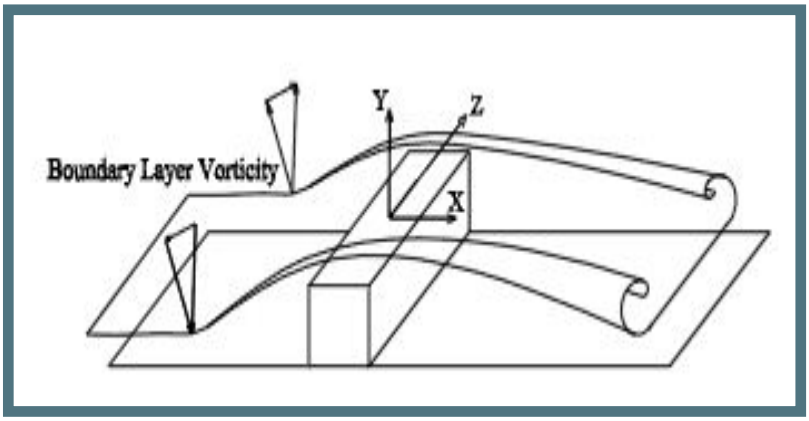


*Figure H 1: Topological model of corner flow over the rib [8]*

This corner flow was also put in evidence by the simulation (*figure H 2*), in the frame of the present investigation.

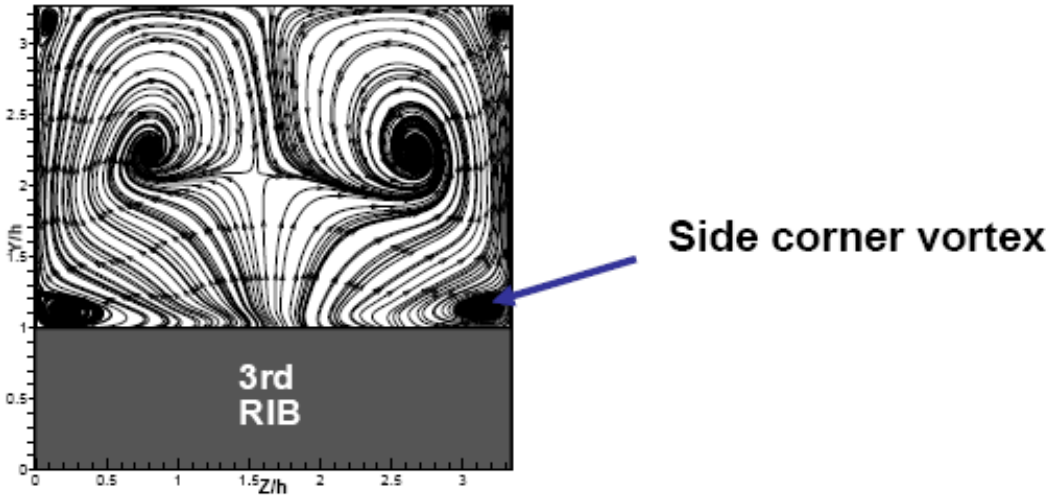


*Figure H 2 Corner flow over rib; streamlines in Y-Z plane. LES*

The composed *figure H 3* (see also chapter 16) resumes the topology of this flow. It can be seen how the corner flow arches over the rib to move back toward the bottom wall remaining

outside of $V_0$ region. The flow then impact the bottom wall creating a local region of strong exchange, whose effect on the heat transfer is discussed in chapter 17.

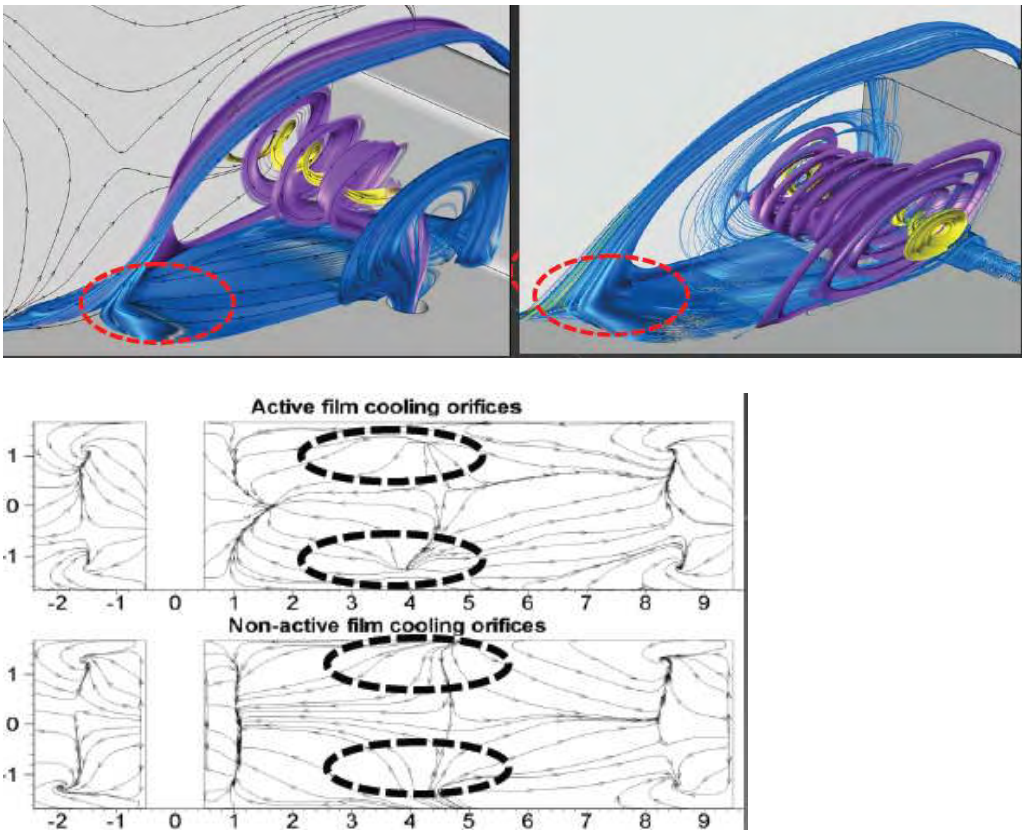


*Figure H 3 Impact of the corner flow on the bottom wall.*

# Annex K: Balance of unsteady heat transfer in LES

The investigation has put in evidence a major problem which was not fully taken in account in previous analysis [4], namely the consequence of the different time-scales associated with fluid and steel phase with calculation of the heat transfer. This difference of scale causes the thermal field in the solid to react only after a much longer lag time than the fluid, introducing a spurious unsteady effect on the budget of the energy equation. In practical terms: as already stated (chapter 5), LES simulation is initiated from a steady state RANS simulation and the effect of this initial perturbation, including the one in the thermal field, would be washed away from the computational domain before a *true* stationary state being attained. The consequence of this difference of time-scales is that the solid phase reacts to any change in temperature in the fluid only with a time lag several orders of magnitude bigger than the time scale of the fluctuation itself; therefore, impractical simulation times would be needed before a full stationary state would be reached. In the present case, the time-scale associated to a temperature fluctuation within the fluid would be in the order of one flow-through or: 0.15 time-units. On the other hand, the thermal time-scale of the steel slab can be estimated as:

$$\text{Steel thermal timescale} = \frac{1}{\alpha_{steel} \times \text{Minimum slab thickness}} = 148.81$$

Therefore, the two time-scales differ by almost three orders of magnitude, meaning that the temperature field within the slab would need a relaxation time three orders of magnitude longer than the velocity field to dissipate the initial solution. Due this difference between fluid and steel time-scales, an instantaneous balance is impossible to achieve in the course of an unsteady simulation and, more, such instantaneous balance would not be physical, because the thermal capacity of the slab and its lower response are such that, at each step time step of the simulation, it expels/absorbs significant amounts of energy. Proof of this effect is the existence of an oscillation for the total heat flux at the coupling interface fluid/steel, shown in *figure K 1*.

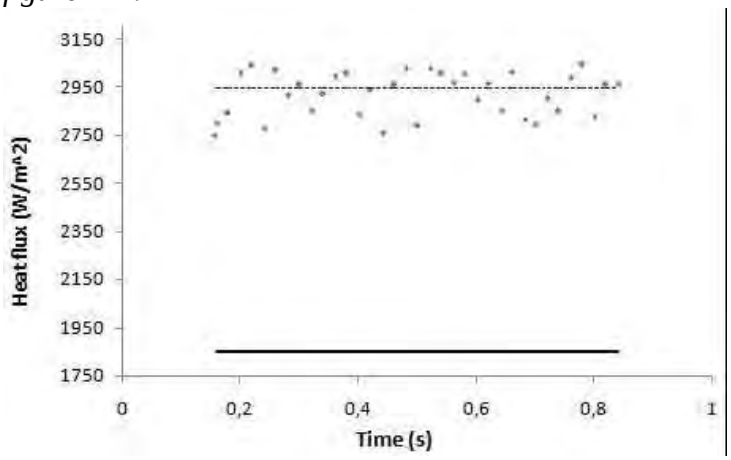


*Figure K 1 Area-averaged heat flux at the interface solid/fluid. Dashed line: time average LES result (closed orifice); continuous line: input heat flux at the bottom face of the slab*

Present and previous simulations have shown that the time needed by the flow field to adapt itself to the initial RANS solution is about one flow-through and the successive time needed to reach convergence on the velocity field is of five flow-through(s). This short time necessary to dissipate the effects of the initial solution is a consequence of the small time-scale of the fluid phase. Therefore, much larger times would be needed for the steel phase. Therefore, the mean value of heat transfer at interface undertakes a long time transient, which prevented the temperature field in the slab from reaching the ***true*** new equilibrium within the resources and time constraints of the present investigation. In fact, it was feasible to run the simulations utilized in this project for 16 flow-through(s) for the case of closed orifice and for 5 for the case of active orifice, respectively.

The practical consequence is that the temperatures within the slab and at its interface fluid/steel remain close to the initial RANS solution during the simulations, as it can be seen in the *table K 1*. The resulting temperatures remain, of course, realistic, because they correspond to the conductive solution of the converged RANS simulation, but the differences between RANS and LES for the gradients at the interface are such that the balance between the flux heat at the heated bottom wall of the slab and the one at the interface fluid/steel, (which had been attained in the RANS) not are maintained in the LES simulation. *Figure K 2* illustrates this situation, presenting an example of profiles of average velocity and temperature for, respectively, RANS and LES.

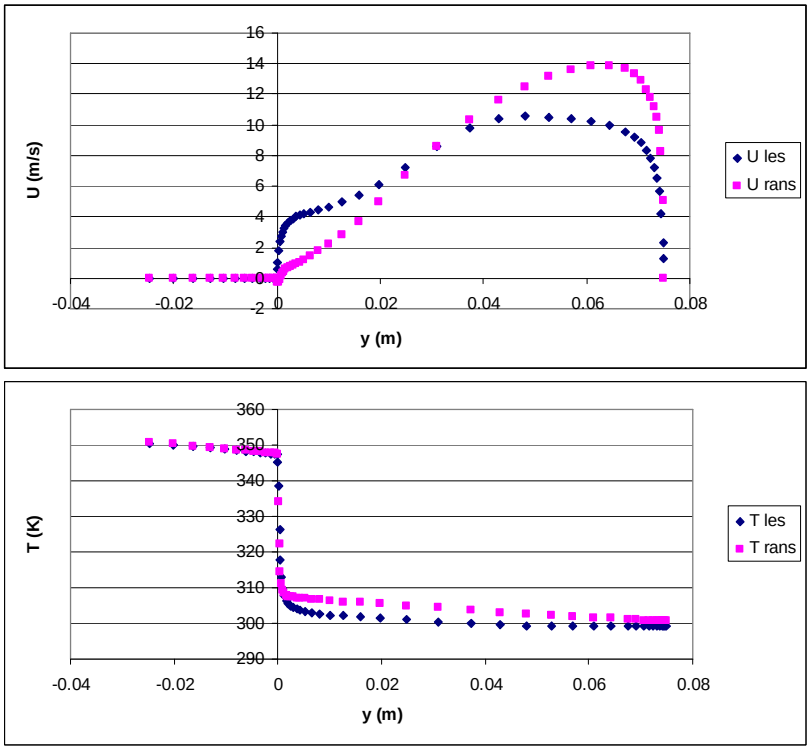


*Figure K 2 Comparison RANS and LES. Typical profile of average velocity (top) and temperature (bottom) across phase and fluid phases*

The consequence of the difference was already shown in *figure K 1*; that the heat flux at the interface fluid/steel reaches a quasi-stationary state, fluctuating around its numerical average value with a quasi-period in the order 0.15 time units, undergoing a fluctuation with amplitude of 8% around the average, but the ***numerical average*** of this heat flux (estimated within fluent code itself from the local temperature gradient) is in the order of 265 Watts against the 185 Watts imposed as input at the heated face of the slab. This must be attributed to the differences between the initial flow field (obtained by RANS) and the converged average field flow field from LES (the energy in the fluid phase being a passive scalar mirroring the convection in the flow field); other words, the differences of gradients at the wall are large enough to originate a ***numerical*** imbalance, corresponding more than half the total heating power.

To conclude, the unsteady calculation causes a decoupling of the 2 thermal fields, the one in the fluid phase corresponding to a quasi-stationary heat flux from the interface (different of the one theoretically imposed at the bottom face of the slab); therefore, the distributions of the of temperature provided in chapter 8 and 17 correspond to this numerical flux. However, in the present case of established turbulent state, the temperature directly reacts to the flow field and, therefore, these corresponding data can be utilized, in non-dimensional terms, for the qualitative analysis of the correlation of the turbulence and of the CS(s) with thermal field.

Temperature

| Static Temperature | (k) | (k) | (k) |
|---|---|---|---|
| default-interior:001.1.1 | 348.50174 | 348.54596 | 348.5368 |
| default-interior:001.1.1.1 | 348.34601 | 348.35016 | 348.33502 |
| default-interior:001.1.1.1.1 | 348.10379 | 348.08633 | 348.09937 |
| heating_surface | 341.52139 | 341.5213 | 341.52127 |
| heating_surface.1 | 345.04175 | 345.04166 | 345.04163 |
| heating_surface.1.1 | 351.92487 | 351.92487 | 351.92487 |
| heating_surface.1.1.1 | 351.32156 | 351.32156 | 351.32156 |
| heating_surface.1.1.1.1 | 348.16687 | 348.16687 | 348.16687 |
| hole_outlet.1.1 | 351.28177 | 351.28177 | 351.28177 |
| hole_outlet.1.1.1 | 351.19797 | 351.19797 | 351.19797 |
| hole_outlet.1.1.1.1 | 350.62128 | 350.62128 | 350.62128 |
| hole_wall-shadow | 333.42783 | 333.31866 | 333.17731 |
| hole_wall-shadow.1.1 | 349.77307 | 335.5343 | 335.38297 |
| interace_upstream-shadow | 341.24124 | 341.29572 | 341.33328 |
| interace_upstream-shadow.1 | 345.29803 | 345.35922 | 345.40024 |
| interace_upstream-shadow.1.1 | 349.5845 | 349.64267 | 349.69193 |
| interace_upstream-shadow.1.1.1 | 347.69006 | 347.74435 | 347.78726 |
| interace_upstream-shadow.1.1.1.1 | 341.80215 | 341.8078 | 341.8147 |
| interface_downstream-shadow | 336.13718 | 336.19635 | 336.23657 |
| interface_downstream-shadow.1 | 339.15552 | 339.21732 | 339.25583 |
| interface_downstream-shadow.1.1 | 348.34039 | 348.41156 | 348.44083 |
| interface_downstream-shadow.1.1.1 | 348.95047 | 349.00409 | 349.02798 |
| interface_downstream-shadow.1.1.1.1 | 348.36075 | 348.35965 | 348.35629 |
| slab_face_downstream | 331.04544 | 331.07141 | 331.0896 |
| slab_face_downstream.1 | 333.02206 | 333.0437 | 333.05881 |
| slab_face_downstream.1.1 | 340.07416 | 340.09695 | 340.10446 |
| slab_face_downstream.1.1.1 | 339.29721 | 339.29984 | 339.30566 |
| slab_face_downstream.1.1.1.1 | 338.78702 | 338.76248 | 338.75885 |
| slab_face_top | 328.84174 | 328.85345 | 328.85461 |
| slab_face_top.1 | 330.62628 | 330.64136 | 330.64883 |
| slab_face_top.1.1 | 336.75262 | 336.76443 | 336.76935 |
| slab_face_top.1.1.1 | 335.90601 | 335.92725 | 335.95493 |
| slab_face_top.1.1.1.1 | 335.84558 | 335.81335 | 335.79599 |
| slab_face_upstream | 330.67001 | 330.72345 | 330.75629 |
| slab_face_upstream.1 | 332.63895 | 332.68283 | 332.72195 |
| slab_face_upstream.1.1 | 338.9285 | 338.98239 | 339.03668 |
| slab_face_upstream.1.1.1 | 338.13266 | 338.18713 | 338.23291 |
| slab_face_upstream.1.1.1.1 | 337.25711 | 337.30002 | 337.3201 |

2 flow-through | 1 flow-through | 0 flow-through

Default interior:

Closed hole interface

*Table K 1 Interface temperature. RANS versus LES*

In particular, for what concerns the heat transfer the available results can be used, in spite of the lack of stabilization in the slab, through a careful non-dimensional analysis. The empirical proof of this argument lies on the fact that the order of magnitude of the non dimensional parameters, notably the EF, was always found comparable to the experimental ones [1, 2, 3, 20 and 25] independent of the heat flux was introduced at the wall. This is a consequence of the fact that the non-dimensional variables, such as Nusselt number, are not sensible to the actual values of the different parameters, ***but only to their respective ratios***: the short time-scale of the fluid causes its temperatures to be at equilibrium at the interface, here determining a ***numerical*** heat flux which maintains a pseudo-stationary behavior during the time of averaging, as it was shown in *figure K 1*; therefore, the difference of temperature $T_w$-$T_{ref}$ entering the definition of the Nusselt number is in equilibrium with this heat flux and the corresponding ratio is not invalidated, as can be deduced from the discussion concerning the definition of EF in chapter 8. An empirical proof is offered by previous results for the case of closed orifice. *Figure K 3* shows the distribution of EF of the case of convective heating (heat

directly introduced at the walls of the duct) [3, 20], while *figure K 4* shows the corresponding result for conjugate heat; the same numerical and modeling approaches have been applied.

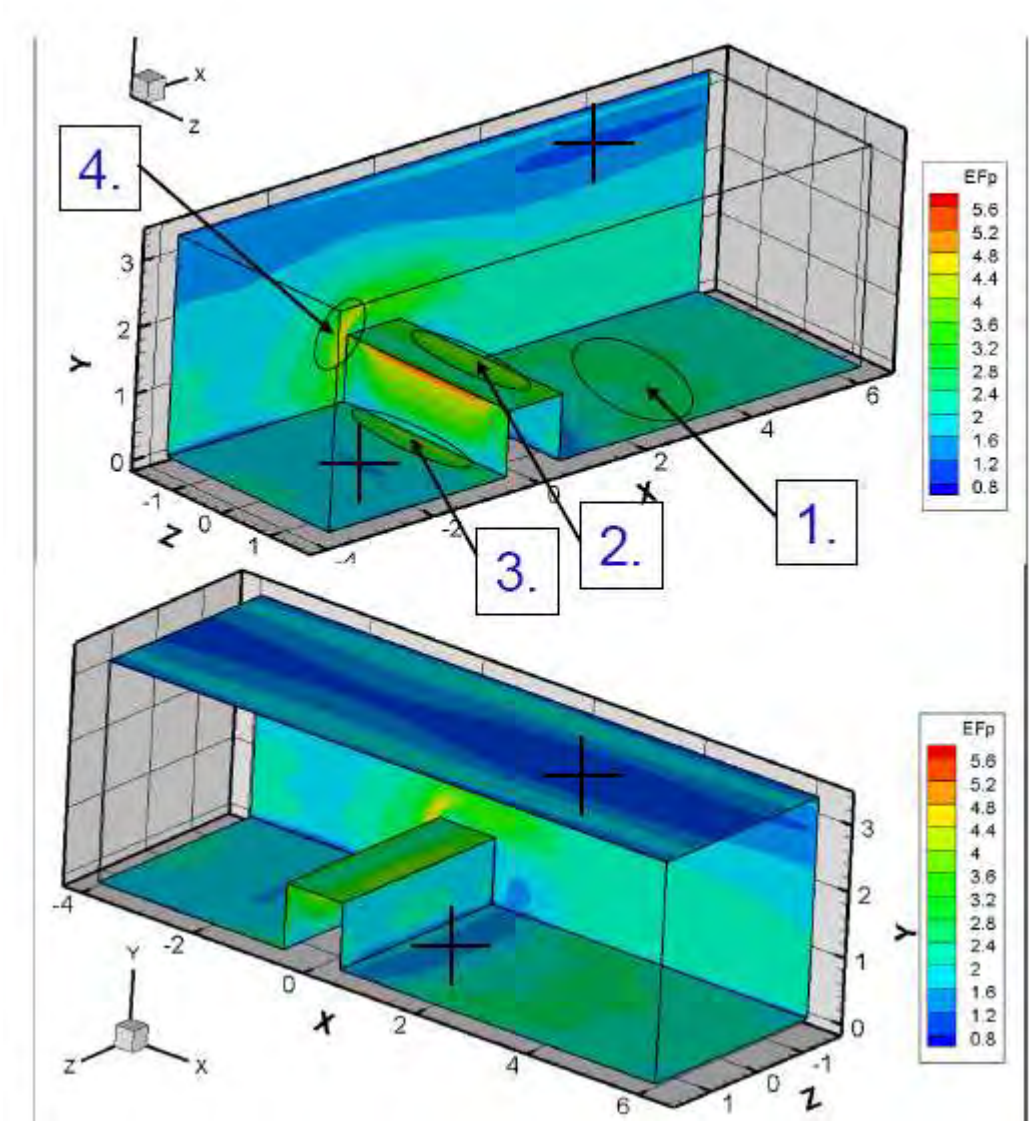


*Figure K 3 EF map; convective heating [20] :upstream and downstream view. Local maxima are indicated as a circles, local minima as a crosses*

The comparison between *figure K 3* and *K4* suggested that, in spite of different system of heating and different definition of the reference quantities selected for the definition of EF, the order of magnitude of EF is comparable, and, more important, its distribution on the rib and in its immediate neigh borough is comparable for the two cases. The differences which can be remarked on the downstream bottom wall could be caused by fact, in the case of convective heating, the side walls are heated, while they are assumed adiabatic in the present case.

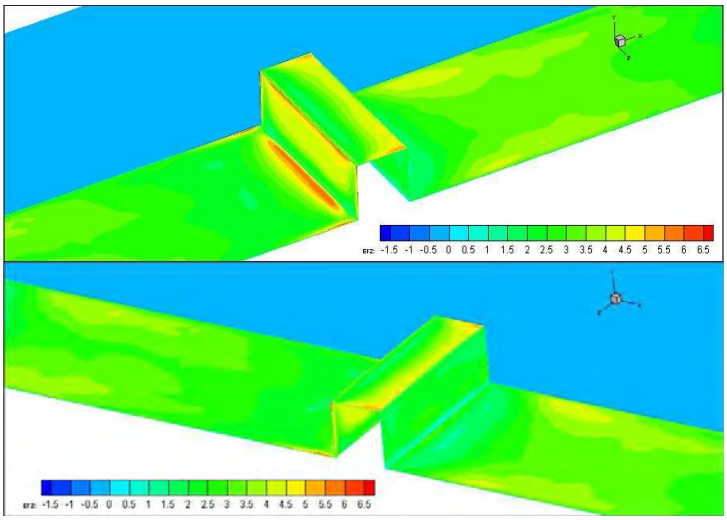

*Figure K 4 EF map; conjugate heating (present) :upstream and downstream view*

A further confirmation of this assessment can be found in the comparison of EF(s) extracted, respectively from RANS and LES solution, presented in *figure K 5*, which show comparable order of magnitude and behavior on the rib and for its immediate neigh borough.

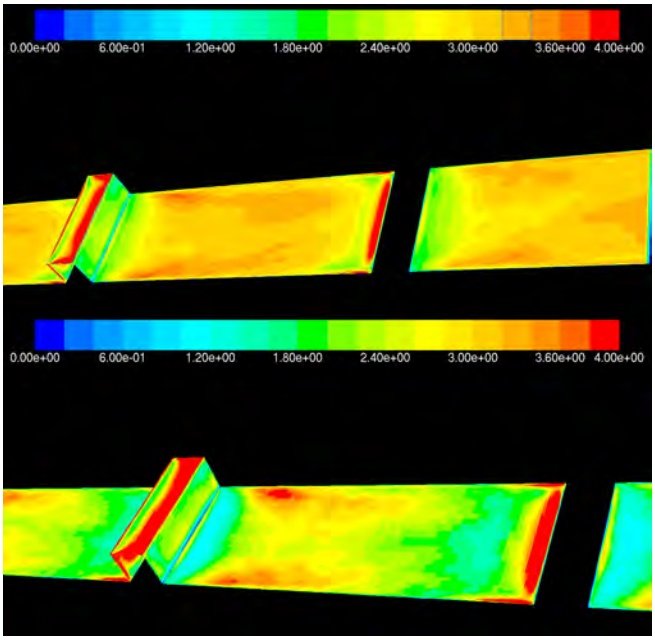


*Figure K 5 EF map. Top: RANS; bottom LES*

It can then be assumed that the EF results obtained from LES can be reliably utilized to assess the effects of the rib and the orifice and for the interpretation of the action of the flow on the heat transfer. However, the temperature field in the solid phase is basically the result of RANS simulation and subject to the lower accuracy of the reproduction of the flow field.

# Annex I: Acceleration of convergence of conjugate unsteady heat transfer in LES

An attempt was made to solve the problem of the non stabilization of the temperatures in solid phase. The explored approach requires freezing the flow field and solving the single energy equation with a steady state solver. This leads to a steady state temperature field in the steel which is at equilibrium with the frozen flow field. A critical point in this procedure that the thermal field in the slab develops itself in function of this frozen flow field; any unbalance of the latter will be reflected on the former. Therefore, the flow field must be well converged.
This led to an iterative procedure of three steps.
-First: LES flow field must reach stationary state and mean flow field be extracted.
-Second: the flow is frozen. For this, temperatures at the interface solid/fluid are extracted and applied as boundary condition at the steel surface. The fluid cells are deactivated and a steady solver is applied for the energy equation in the solid.
-Third: the fluid cells are reactivated and a new LES run from the temperature field in the solid obtained from step two. Once a new flow field has reached equilibrium the procedure can be repeated.
The entire procedure is resumed in *figure I 1*

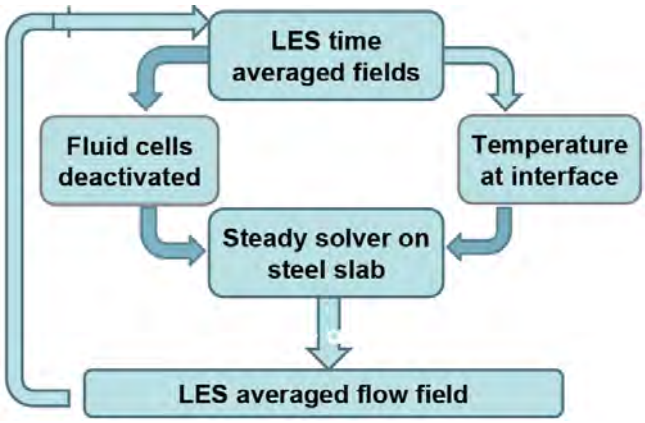


*Figure I 1 Procedure for the stabilization of the temperatures in the solid part*

This method was applied to the LES simulation starting from the flow field averaged for five flow-through(s). Once applied this procedure, a new LES simulation was run till heat flux had stabilized itself again. The new heat flux showed a decrease of unbalance of approximately 16%, respect to the heating power applied to the slab, as shown in *figure I 2*. Red dashed line corresponds to the result of the acceleration method, while the grey dashed line corresponds to numerical heat flux without acceleration. The time interval corresponds to one flow-through: 0.15 time units. LES simulation was not run for longer time because the fluid had stabilized itself.

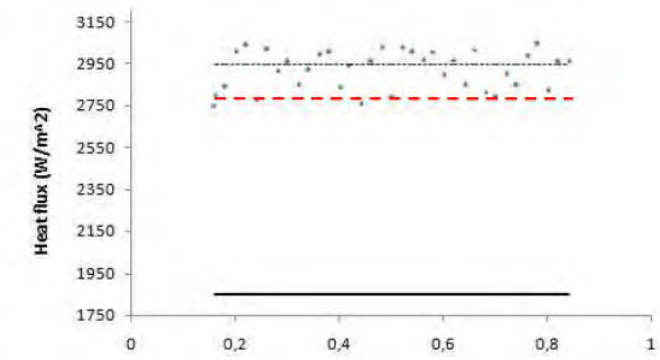


*Figure I 2 Area-averaged heat flux at the interface solid/fluid. Dashed red line: result of one iteration; dashed grey line: uncorrected flux; continuous line: input heat flux*

Despite this improvement, the need to bring to stationary state the fluid phase is such there was not enough time, during the realization of this project, to continue this iteration process to obtain a full stabilization.

# Annex J: RANS versus LES

The present investigation has put in evidence that eddy-viscosity models are unable to fully reproduce the complex topology associated with aspiration at the orifice. *Figure J 1* shows how the initial solution obtained applying the approach RANS κ-ε is dominated, downstream of the rib, by a pair of X-Z vortex which does not appears in final LES solution.

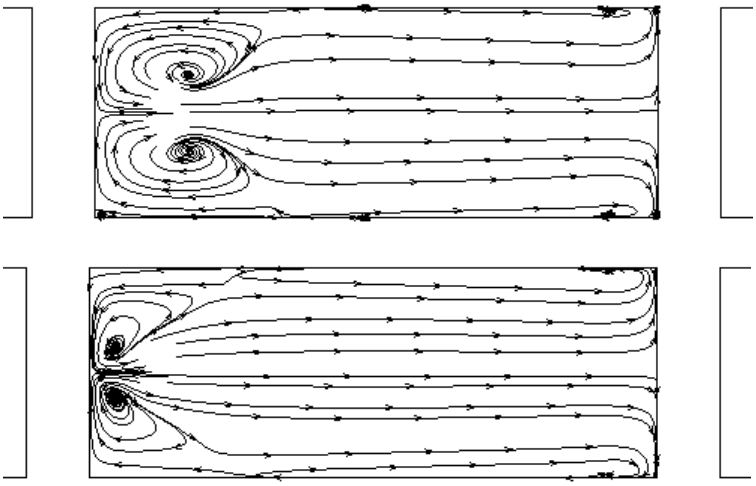

*Figure J 1 Streamlines, X-Z plane Y/h=.0.5. Top: active orifice; bottom: closed orifice RANS*

In consequence, heat flux on the heat flux at the bottom wall is strongly different, as shown in *figure J 2*.

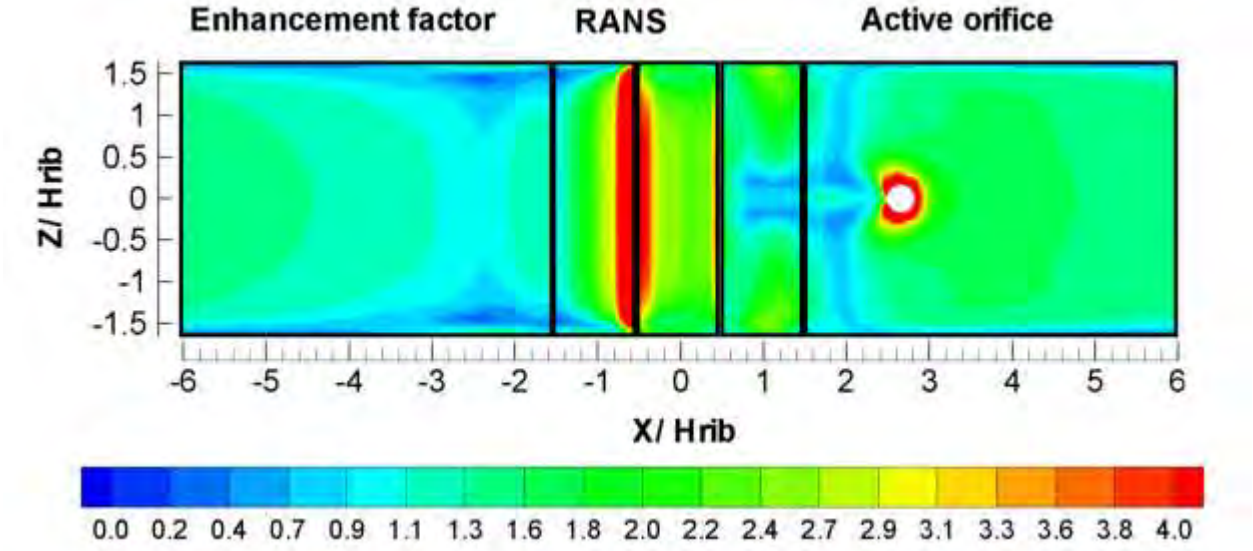


*Figure J 2 EF active orifice; RANS*

A prove of the paramount influence of the flow field is offered by *figure J 3*, which presents the EF field obtained applying the final average flow field of the LES as fixed flow field for a steady state RANS solution of the thermal domain. It can be remarked that resulting EF map is, qualitatively, similar to the one presented in *figure 17.3*.

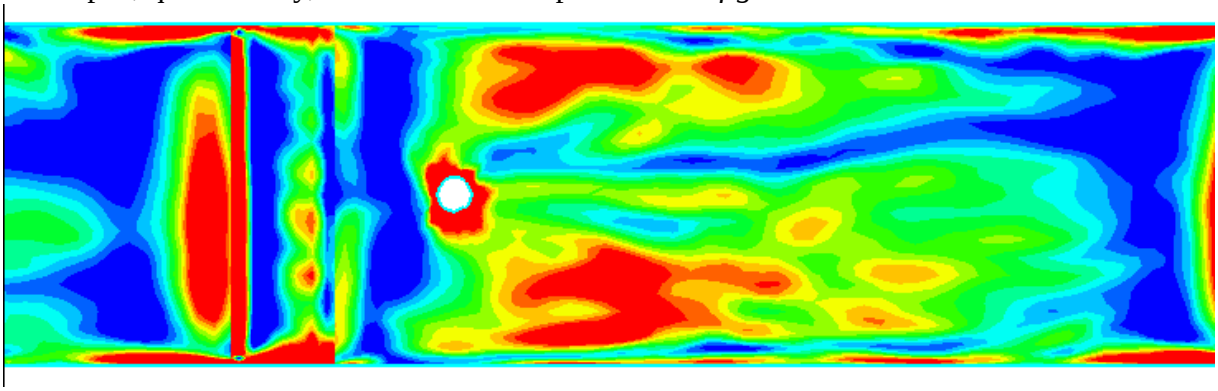

*Figure J 3 EF active orifice; frozen flow field from LES; RANS on thermal field*

# Annex L: Interpretation of the results for the heat flux at the top face of the rib

As indicated in chapter 17, the most important discrepancy between the experimental data and the present simulation concerns the EF(s) on the top face of the rib. The result from Liquid Crystal (LC) presents a maximum in the central part of this surface, while the simulation locates the highest EF(s) in the downstream region of this surface. It must be remarked that previous measurement by Infrared camera (IRC) [9], presented an EF map qualitatively similar to the simulation. All the available results are assembled in *figure L 1.*

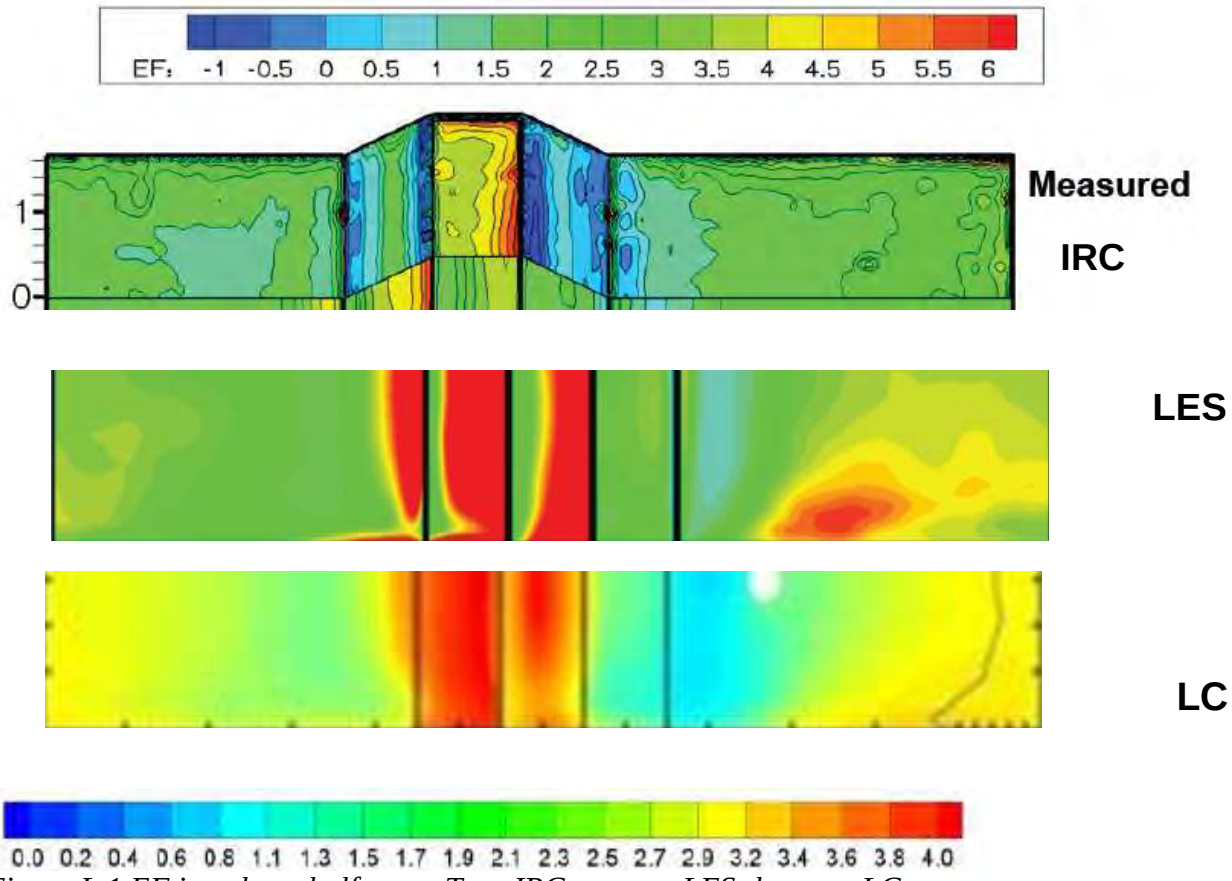


*Figure L 1 EF is-colors; half-span. Top: IRC; center: LES; bottom: LC*

At the present time, the discrepancy is not explained and further investigations are recommended, particularly for what concerns the qualification of the flow field in the present test section. The opinion of the present authors is that LES and IRC results are coherent with the presence of large separated region on this face, identified by the previous investigators [3,4 and 20], shown in *figure L 2.* It is to be remarked that simulations performed with convective heating (*figure K 2)* show a similar pattern, which seems indicate that this behavior is independent of the heating system itself.

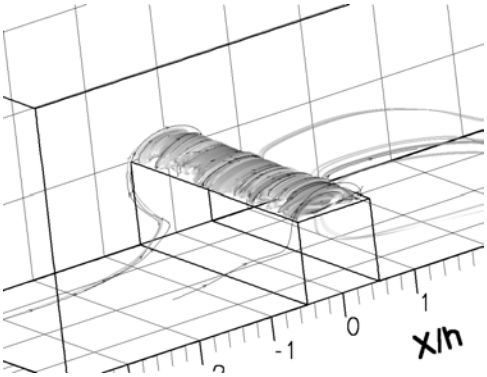


*Figure L 2 topology of top face recirculation [3, 20]*

# Annex M: Correlation *Cf*-EF

The connection between flow field and heat flux was identified in the previous parts of the investigation (chapters 7, 16 18). Here the correspondence between Friction factor *Cf* and EF is presented in *figure M 1* to prove that this analogy holds also for the case of active orifice. Regions of similar behavior are marked as black for the case of closed orifice and as red for the case of active orifice; a full correspondence is visible for the main topological features, confirming the strong correlation between flow and thermal field and that, therefore, a correct representation of the flow field is indispensable for the understanding and prediction of the latter.

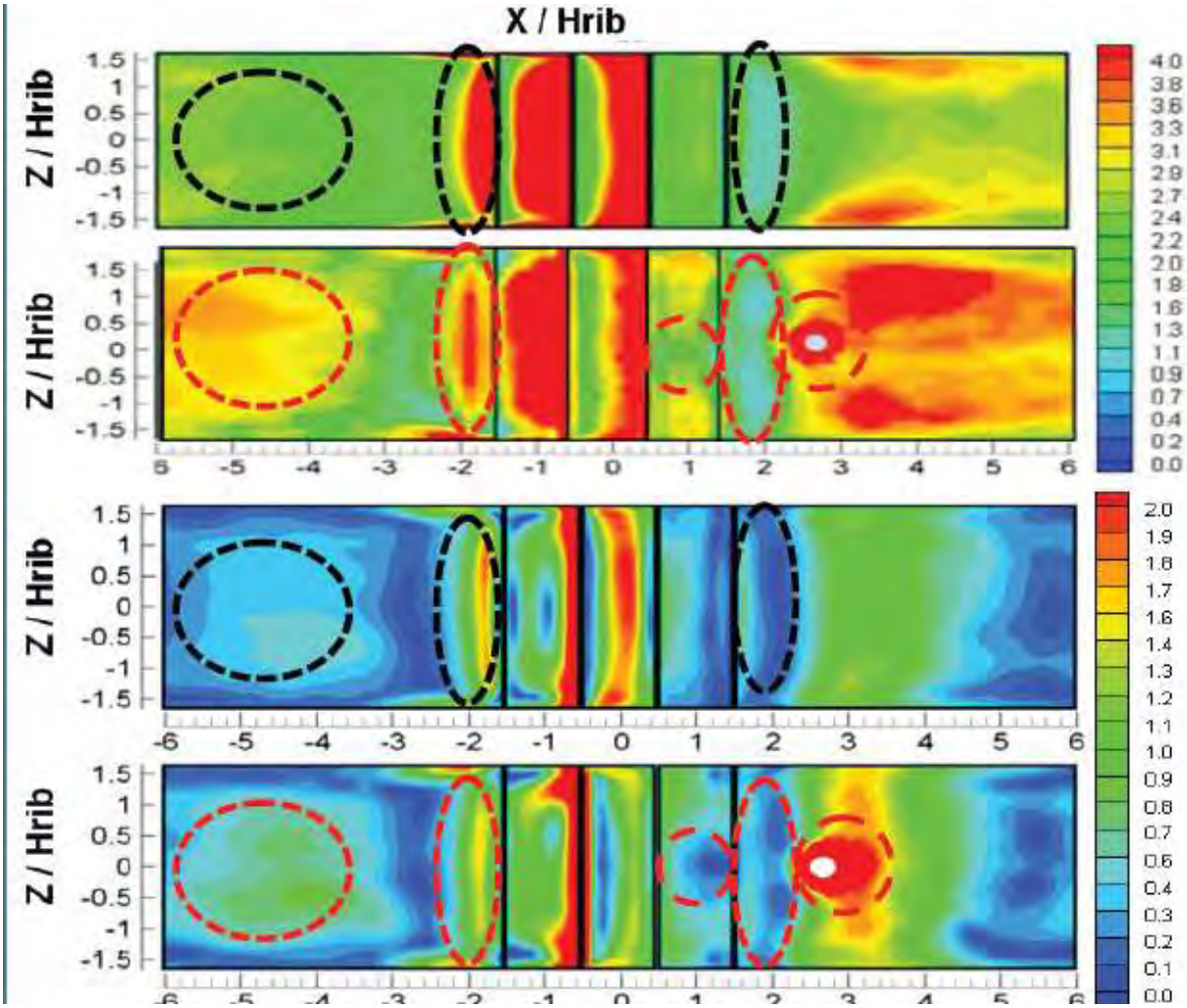


*Figure M 1 EF (top images) and Cf (bottom mages) iso-color maps. Regions of concordance marked as black for case of closed orifice and red for case of active orifice*

# EXPERIMENTAL AND NUMERICAL INVESTIGATION OF CONJUGATE HEAT TRANSFER IN RIB-ROUGHENED DUCT

*Experimental Activity*


**B. Cukurel, T. Arts**

Turbomachinery & Propulsion Department
von Karman Institute
B1640 – Rhode Saint Genèse, Belgium

# 1. Introduction

In order to increase the thermal efficiency of a turbine, it is needed to have an inlet temperature as high as possible. In order to guarantee a prolonged blade life, the first two stages have most of the time to be cooled, due to the temperature of the air (after the combustion chamber) exceeding the melting point of the metal.

There are two categories of cooling techniques, liquid and air cooling. As far as aircraft applications are concerned, only the second one is used; liquid cooling techniques are preferred for land-based applications. In air cooling, four techniques are commonly preferred: internal forced convection, impingement cooling, film cooling and transpiration cooling. It is important to note that the first three techniques can be used together. Even though the focus of this work is primarily the internal forced convection, a part of the experiments are to be conducted with a slab that couples ribbed forced convection with the film cooling holes, investigating the interaction.

Internal forced convection is used as a means of cooling the turbine blade for which a part of the air bled from one of the stages of the compressor is channeled via serpentine passages located internally within the airfoil. Aerodynamicists have lined these passages with repeated ribs called turbulence promoters (turbulators). The effect of such turbulators is not only the increase in effective heat exchange area but at the same time enhancing the global heat transfer rate. The heat is extracted by forced convection.

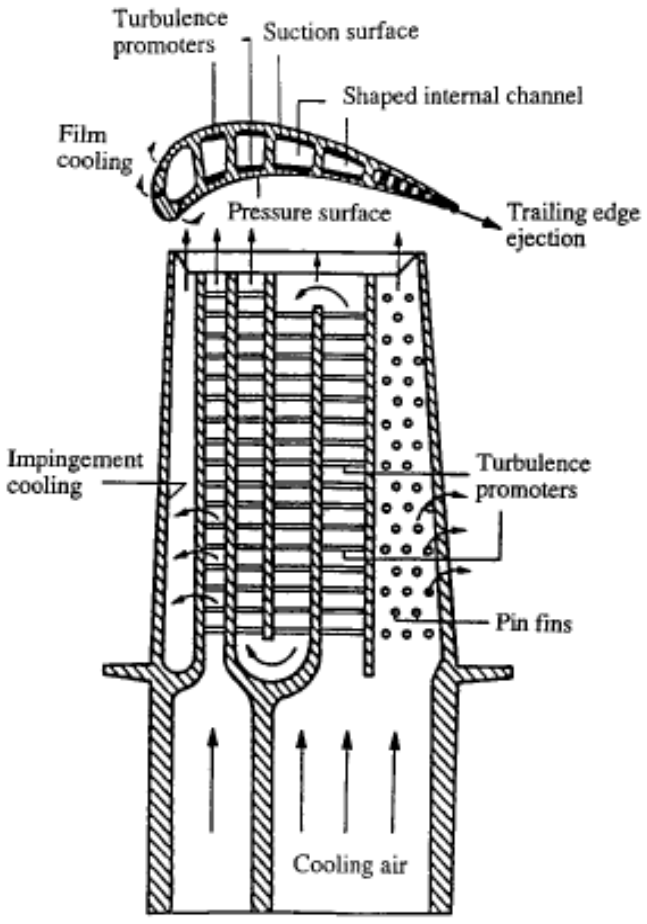


Figure 1: Turbine Blade Schematic

Figure 1 demonstrates the different cooling techniques that can be applied on a turbine blade. Focusing on the internal forced convection, the air is introduced from the hub, and follows a serpentine composed by four passages downstream. The passages are ribbed in order to promote the heat exchange. The angle of attack is 90° as the investigated case. The cooling air is discharged from both the trailing edge and the tip of the blade.

The technology of cooling gas turbine components via internal convective flows of single-phase gases

has developed over the years from simple smooth cooling passages to very complex geometries involving many different surfaces.

The fundamental aim of this technology is to obtain the highest overall cooling effectiveness with the lowest possible penalty on the thermodynamic cycle performance in terms of pressure losses. In all practicality, this yields to the goal of highest achievable internal convective heat transfer coefficients with the lowest achievable friction coefficient or pressure loss. In common literature, there have been many investigations with convective turbine blade models with constant heat flux on the cooling channel surface. Even though this is a good initial approximation of the physical phenomenon, it doesn't model the real physics. The complex interaction of the fluid-solid convection-conduction coupling phenomena (conjugate heat transfer) plays a major role on the local heat flux.

The level of the heat fluxes, in reference to the first stages of a gas turbine, is in the order of $1MW/m^2$. In order to minimize the cooling mass flow, it is fundamental to maximize the heat exchange and this can only be achieved through a deeper understanding of the mechanisms driving the aerodynamic and heat transfer performance.

# 2. Scope of Work

The purpose of this project is to have a deeper understanding of the conjugate heat transfer phenomenon by conducting experiments for the fundamental understanding, as well as creating a baseline database for numerical investigations. The targeted application is the ribbed internal cooling channels used in turbine blades. A test section is built to model the underlying physics of the conjugate heat transfer phenomena in a turbine blade. The investigation focuses on measurements conducive to turbulence characterization of the channel by means of a hotwire, and local heat flux calculations over flat, ribbed and ribbed/film cooled slab configurations through local temperature measurements made by Infrared Thermography. The turbulence characterization of the channel is not only important for the interpretation of the experimental based local heat flux calculations, but also crucial for the conjugate numerical models that predict the cooling performance in parallel to the experimental work conducted.

# 3. Experimental set-up

The channel built is the simplified model of an internal cooling blade channel that is scaled up by a factor of 15. It consists of three pieces such as the inlet, test and exit sections and each section has a cross-sectional dimension of 75x75mm, with longitudinal dimension of 1400mm, 1260mm, 800mm respectively.

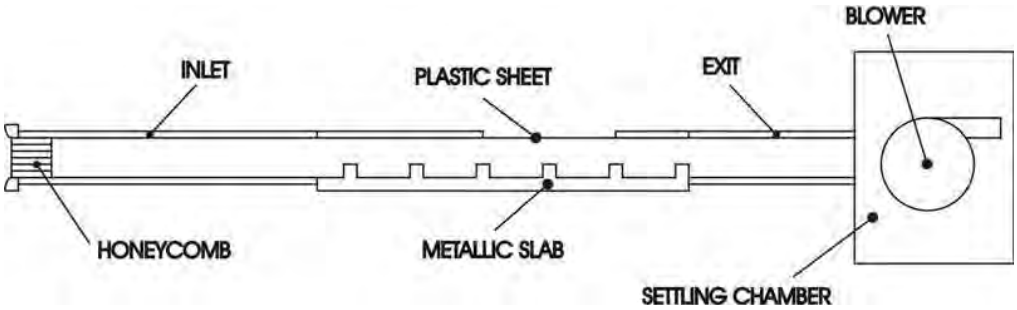


Figure 2: Schematic of the Experimental Setup

At the inlet section, made of Plexiglas, a honeycomb with 3mm cell size is used along with a NACA bellmouth to provide flow conditioning. A honeycomb effectively reduces the lateral components of mean velocity and of the larger turbulent eddies, as well as producing some turbulence of its own, which decays very slowly, creating a high turbulence intensity region in the test section. [Ref. D-2] This setup is beneficial for damping out the inlet disturbances, as well as for maintaining a closer resemblance to the physical flow in a turbine blade.

The flow in the channel is expected to be fully turbulent, considering the fact that experiments are conducted at Reynolds number based on hydraulic diameter, $D_h$, equal to 40,000 which is much larger than the laminar threshold imposed by the Moody chart (Re > 3000) . There doesn't seem to be a well established entry length for turbulent channels, and the inconsistency in the literature is evident. The entry length for turbulent duct flows seems to vary from $10x/D_h$, to $50x/D_h$ and to $100x/D_h$ even in well established literature. [Ref. A-3, A-4, A-5]. These approximations on the entry length are further diluted by the fact that a fully developed velocity field does not necessarily guarantee an invariance of local turbulence in the flow direction; the development length for a "fully developed" turbulence field is known to be much larger [Ref. A-5]. For the test setup, at the inlet of the test section, even though the flow isn't believed to be fully developed, neither from a velocity profile nor from a turbulence intensity perspective, neither is the flow at the actual serpentine passages. Thus, a greater similarity between the model and a real turbine blade is established.

The exit section, made of Plexiglas, is connected to a settling chamber that has 3 layers of honeycomb structures to damp out the fluctuations created by the blower downstream. The setup operates below atmospheric pressure and special attention is given to acquire a good seal between the parts. Note that the wind tunnel is in aspiration because the flow is more uniform at the inlet than with the opposite configuration.

Immediate upstream and downstream of the test section, static pressure measurements, along with temperature, are made at three faces of the channel (averaged pneumatically and numerically). Also, the inlet and exit sections are modified for an access hole to introduce a hotwire and Kiel-head total pressure probe at each end of the test section.

In the current proposed plan there are three different test sections. The first configuration is a rectangular channel (slab without ribs) made of Steel AISI304. The thickness of the slab

has been chosen respecting the geometric similarity with to the real section of an internal cooling blade channel. In this case, the thickness has been chosen to equal to 25mm, in agreement with the prior purely convective studies conducted in VKI. [Ref. A-6] One of the primary uses of the flat test section is to measure the turbulence intensity at the inlet and the exit of the duct. These values will be used as input parameters for the CFD code that predicts the conjugate heat transfer over both the flat plate, as well as other test section configurations. It is important to understand the behavior of the flow, even without ribs, because there is strong correlation between the heat transfer and the turbulent characterization of the flow. In this configuration, Infrared Thermography measurements for heat transfer are also to be made as a validation tool for the CFD results.

The second test section is a ribbed channel made of Steel AISI304. The rib configuration has an angle of attack of 90°, the rib height being 22.5mm, which gives a blockage ratio of 0.33. The inter-rib space is 225mm, in accord with the set up of Çakan [Ref. A-7] and Casarsa [Ref. A-8]. Similar to the first test section, hotwire measurements along with Infrared Thermography are to be made for the ribbed test section. The last test section is a ribbed/film cooled slab that is to be used for the conjugate heat transfer investigation of a film cooling hole on the serpentine passages.

During heat transfer measurements, the lateral walls of the test sections are made of thick glass. In this case, the adjacent walls are glued to the metallic slab, which is heated by means of thin Inconel sheet (glued beneath the ribbed wall over the entire width). The entire measurement section, and parts of the inlet and discharging channels, are then placed on a wooden box, surrounded by insulation all around.

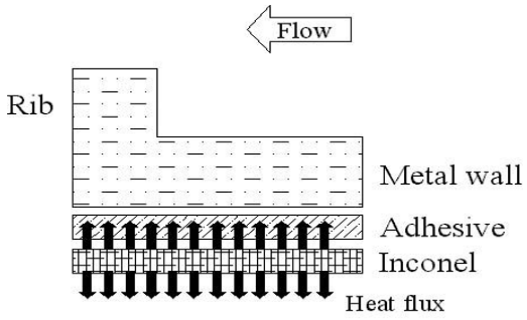


Figure 3: Metal Slab Heating Configuration

The Inconel sheet, 25μm thick, is powered by a 16V-150A DC power supply and the current is dissipated as thermal energy by the Joule effect. This thermal energy is conducted away by the parts in contact. Since the thermal insulator has a conductivity of 0.024W/m-K and the AISI 304 metal slab has thermal conductivity of 16.3 W/m-K, considering the conservation of energy across the Inconel $q''_{gen} - k_{steel}\left(\frac{dT}{dx}\right)_{x=0^+} - k_{ins}\left(\frac{dT}{dx}\right)_{x=0^-} = 0$, and as an order of magnitude approximation assuming equal thicknesses and a temperature difference of 60°K from the insulator to Incolnel and 15°K from the metal slab to Inconel, the heat flux losses into the insulator can be estimated to be in the order of 0.5%. It clearly appears that the main direction of the heat flux will be towards the metallic slab where the heat flux encounters a minor thermal resistance.

Lastly, it is important to note that, in the Infrared Thermography experiments, plexiglass or glass could not be used in the construction of the top wall of the channel, due to their opaqueness to the infrared radiation, instead a polyethylene film is preferred.

# 4. Channel Heat Transfer Considerations

The conjugate heat transfer is dominated by the Nusselts number which, by Buckingham Pi, is a function of $Nu = f\left(\mathrm{Re}, \mathrm{Pr}, \frac{T_b}{\Delta T}, Ec\right)$, where $\mathrm{Re} = \frac{\rho V D_h}{\mu}$ ($D_h$ being the hydraulic diameter), $\mathrm{Pr} = \frac{c_p \mu}{k}$, $T_b/\Delta T$ and $Ec = \frac{V^2}{C_p \Delta T}$ are Reynolds number, Prandtl number, scaled relative bulk flow temperature and Eckert number respectively. Influence of the relative bulk flow temperature is found experimentally to have a small influence on the Nusselts number. Also, especially for low speed applications, the relative importance of the kinetic energy with respect to the enthalpy is found to be very small, which largely reduces the influence of the Eckert number as well.

For this application and under the assumptions above, $Nu \approx f(\mathrm{Re}, \mathrm{Pr})$; the variation of Pr in the temperature range of the experiment is very small, thus in order to respect similarity, it suffices to maintain the same Reynolds number.

Another consideration is the relative weight of forced convection with respect to natural convection: $\frac{Gr}{\mathrm{Re}_L^2}$, where the Grashof number, $Gr = \frac{g\beta(T_w - T_b)}{\mu^2}$ , $\beta \simeq -\frac{1}{\rho}\frac{\rho - \rho_{film}}{T - T_{film}}$ and $T_{film} = \frac{\overline{T_w} + \overline{T_b}}{2}$. For this setup, $\frac{Gr}{\mathrm{Re}_L^2} \sim o(10^{-3})$, clearly making the forced convection the dominant phenomena.

# 5. Instrumentation

## 5.1 Pressure Transducers / Kiel-Head Total Pressure Probe

Two Validyne Model Dp10 pressure transducers are used for pressure measurements at the inlet and exit sections of the experimental setup. They are equipped with diaphragms with a maximum differential pressure of 22.5mm $H_20$. The calibration of the pressure transducers are done by means of a water monometer with an increment of 0.1mm $H_20$ in parallel with a DPI 610 Portable Pressure Calibrator with a 70mbar range and provide an accuracy of 0.05% FS. The linear calibration curve of the pressure transducers resulted in a $R^2$ value of about 0.9999 and in the operating range. the maximum and mean deviations from linearity was shown to be in the order of 0.35Pa and 0.15Pa.

At both the inlet and exit cross-sections, the static pressure is pneumatically averaged and recorded along with the total pressure measured by a Kiel head total pressure probe experimentally tested to be less than 1% sensitive to flow angle variations up to ±25º for the velocity range observed in this experiment.

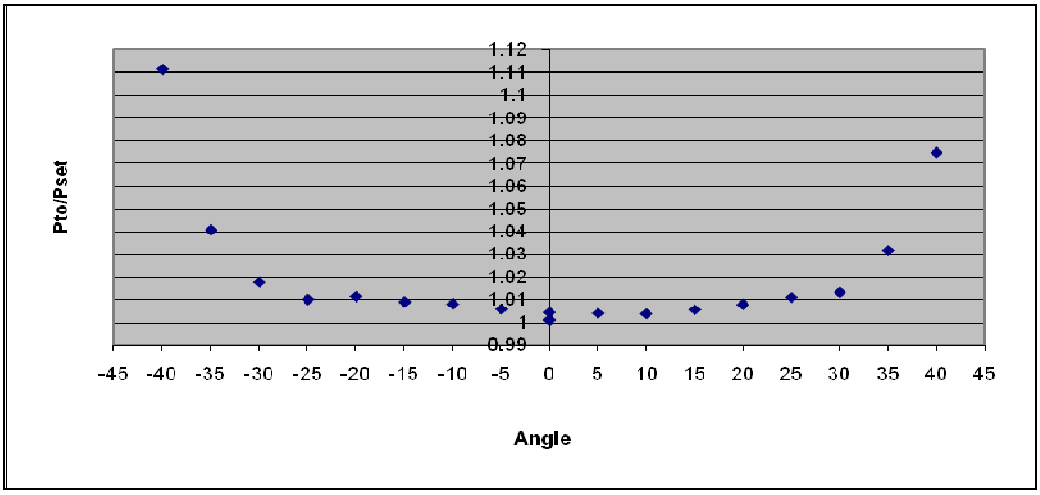


Figure 4: Kiel-head Total Pressure Probe Angle Sensitivity

## 5.2 Thermocouples

For the temperature measurements, 6 T-type (Copper–Constantan) thermocouples, which have a nominal operating range of −185°C to +300°C, are built and installed at the inlet and exit sections of the test setup. They are calibrated in an oil bath along with a thermometer that has an increment of 0.1°K. The calibration curve showed that the voltage-temperature linearity results in an $R^2$ value of about 0.9998 which implies a maximum and mean deviation in temperature of 0.75ºK and 0.37°K respectively. These thermocouples are used for setting the operating condition of the channel, as well as for estimating the heating losses of the system by means of computing the average enthalpy increase of the bulk flow.

## 5.3 Hotwire Anemometry

For turbulence intensity measurements, Dantec Dynamics Hotwire Anemometry System along with an in-house built hotwire probe, equipped with a PT coated Tungsten wire, is used. The hotwire is calibrated in a fully turbulent jet for mean velocities observed in the channel and the requency response was measured to be around 13kHz. The raw hotwire signal is filtered through a 30kHz low-pass filter and the values of the offset and span are adjusted such that 0-11 m/s velocity range corresponds to a voltage differential of 10V. Considering that the

data acquisition board is 16 bits, and under the operation mode of ±5V, the uncertainty in data acquisition due to discretization is 0.15mV.

One of the considerations when calibrating the hotwire is the non-linear (in the log scale) characteristic of the wire voltage in the low velocity range. The King's Law: $E^2 = A + B(U)^n$ doesn't provide sufficient accuracy in this range, which is why a polynomial fit is preferred. For ambient and test conditions the n-value in the King's law is around 0.5 yielding to a velocity voltage dependency of the fourth order, which makes the fourth order polynomial fit, considering the Taylor series expansion, an obvious choice for the characteristic calibration curve.

It is also important to quantify the limits of the hotwire measurement capabilities where eventually, as the velocities are lessened, the natural convection over the wire starts dominating the convection imposed by the flow. Two conditions have to be satisfied to ensure the proper operation of the hot wire [Ref. A-9], $\frac{l}{D}\sqrt{Gr} < 1$, $\mathrm{Re}_D > Gr^{\frac{1}{3}}$ with $Gr = \frac{g(T_w - T_a)D^3}{T_m \nu^2}$, $T_m = \frac{T_w + T_a}{2}$ and $\mathrm{Re}_D = \frac{VD}{\nu}$, where $T_w$, $T_a$, $T_m$, D, L are wire temperature, air temperature, mean temperature, wire diameter (8.89μm) and active length of the wire (950μm). The overheat ratio, defined as $OV = b_1(T_w - T_a)$ with $b_1 = 3.2E^{-3} / {}^oK$ (property of PT coated Tungsten wire), is chosen to be 0.8. The high overheat ratio ensures a much greater sensitivity to flow unsteadiness.

Using the formulas described above, the Grashof number can be calculated to be $Gr = 1.667\ 10^{-5}$, satisfying the first condition $\frac{l}{D}\sqrt{Gr} = 0.4376 < 1$. The second condition imposes a lower limit on the minimum resolved velocity due to natural convection over the wire, which is found to be $V > 0.0451\ m/s$.

Hot wire uncertainty can be divided into two parts such that the uncertainty in the mean and perturbation velocities can be treated as independent quantities. The mean velocity deviation from the 4th order polynomial voltage vs. velocity fit is in the order of 1% for the lower end of the velocity range (0-3 m/s) and is in the order of 0.2% for the upper end of the velocity range (3-8 m/s). The signal to noise ratio, SNR, of the hotwire on the perturbation quantities can be estimated from the standard deviation of the voltage acquired at a nominal operating point and at conditions where there is no flow over the wire. For the case where there is no flow, the fluctuations on the voltage are merely a result of the vortex shedding over the wire due to natural convection coupled with the electrical noise that most commonly emerges as a Gaussian distribution. For this setup, the hot wire signal to noise ratio on the velocity perturbations can be estimated as $SNR = \frac{\sigma_{V_{noflow}^{hotwire}}}{\sigma_{V_{measurements}^{hotwire}}} = 1.4\%$ This is an upper limit, considering that most measurements are done at velocities where $\frac{Gr_{D_{wire}}}{\mathrm{Re}_{D_{wire}}} = 7.46E^{-7} \ll 1$,

indicating that the natural convection over the wire is negligible. Also it should be considered that due to the logarithmic growth nature of the hotwire voltage vs. velocity characteristic curve, the effect of variation in voltage at higher mean velocities results in much larger velocity variation than those measured at the lower mean velocities. These considerations indicate a lower statistical signal to noise ratio on the perturbation velocity, with high mean values, than the one calculated above.

### 5.4 Infrared Thermography Measurements

It is a non-intrusive technique for wall temperature measurement. The idea behind IR Thermography is to convert the invisible electromagnetic radiation in an electric signal that can be treated to observe the body's temperature since all bodies at a temperature above absolute zero emit infrared radiation. The temperature distribution over the slabs are to be measured through a a FLIR SC3000 camera with a 240x340 pixels resolution. Each pixel is like a single IR detector. The data acquisition system, ThermaCam Researcher 2001, is provided with the camera.

A uniform heat flux is to be applied on the bottom face of the slab by means of the Inconel sheet. The surfaces of the channel end walls are to be insulated. The metal temperature distribution is close to periodic (axial direction) due to the effect of the ribs. Finally, the surface temperature distribution is acquired by means of an Infrared Camera (calibrated through surface thermocouples). Any commercial code can be used to solve the energy equation with boundary conditions:

- Uniform heat flux along the bottom surface of the slab.
- Measured temperature distribution on the wetted surface.
- Adiabatic wall condition along the end walls.
- Periodicity condition along the walls parallel to the rib.

The information provided suffices to acquire a 3D temperature distribution in the slab, yielding to the heat flux distribution on the surface.

## 6. Operating point

Operating Reynolds number of the channel is set by means of temperature, static and total pressure measurements in the channel. The total to static differential pressure and the static gage pressure are measured, along with temperature at the inlet and/or the exit of the test section. Through compressible flow relations and ideal gas law, $\frac{P_s}{P_t}=\left(1+\frac{\gamma-1}{2}M^2\right)^{\frac{-\gamma}{\gamma-1}}$, $\frac{T_s}{T_t}=\left(1+\frac{\gamma-1}{2}M^2\right)^{-1}$, $P=\rho RT$, $M=\frac{V}{\sqrt{\gamma RT_s}}$, velocity, density and static temperature can

be calculated. By Sutherland's correlation [Ref. A-10], $\frac{\mu}{\mu_o} = \left(\frac{T}{T_o}\right)^{\frac{3}{2}} \frac{T_o + S}{T + S}$, where $\mu_o$= 17.16E$^{-6}$ Pa-s, $T_o$= 273.15 ºK and S=110.4 ºK; and the definition of Reynolds number, $\mathrm{Re} = \frac{\rho V D_h}{\mu}$, the operating point, Re=40000 based on centerline total pressure measurements, can be set. Prior to data acquisition the Reynolds number of the channel is monitored over a period of time of 10 minutes. Analyzing this data statically, it is possible to acquire a sense of operating point variation and for the hot wire measurements in the rectangular channel, it was calculated to be Re = 39988.50 ± 1.0 % with the 95% confidence interval.

# 7. Flow characterization at the Test Section Inlet over the Rectangular Test Section

The 75x75mm rectangular flat test section is divided into 3348 grid points such that 85% of the vertical direction (y-direction) and 100% of the horizontal direction (x-direction) has been resolved by a grid size of 1mm$^2$. The loss of 15% in the measurement plane in the vertical direction, distributed as 13% and 2% at the top and bottom of the channel respectively, do not create a significant handicap from the perspective of conjugate heat transfer. Considering that the measurement points towards the top of the channel are far away from the heated slab, the effect of the turbulence level do not contribute significantly to the flow close to the solid-gas interface. Towards the bottom of the channel, considering the ribbed channel configuration, the flow fields created by the ribs dominate and significantly alter the local flow field, locally de-emphasizing the value of the rectangular frame boundary layer measurements. Hotwire anemometry data is acquired at 100kHz for one second duration at each grid point. The L-shaped hotwire is translated for the vertical and rotated for the motion in the horizontal direction; the data acquired is then transformed into the 2-D plane, imposing the origin at the channel centerline. The data point location resolution is limited by the wire diameter (8.89μm) and the active length of the hot wire (950μm) in the horizontal, and the vertical directions respectively.

## 7.1 Basic Boundary Layer Concepts

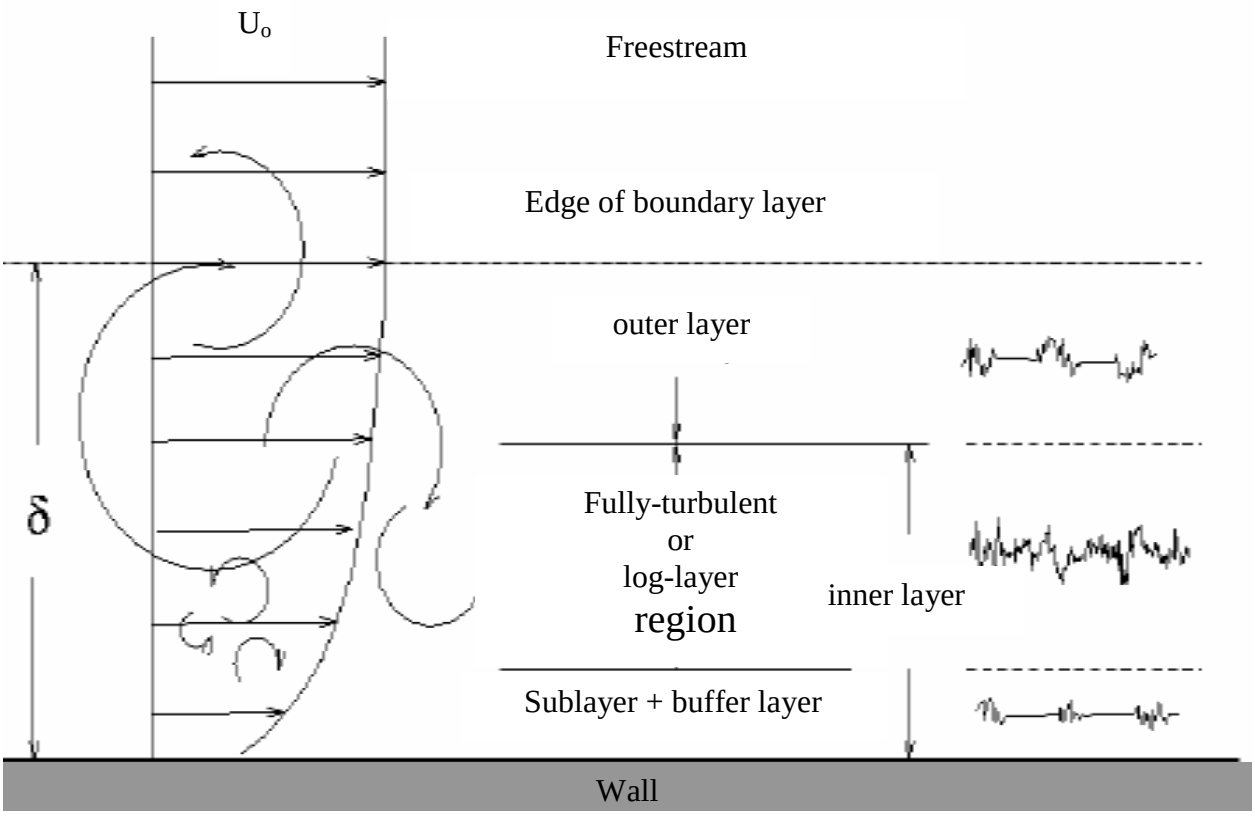


Figure 5: Boundary Layer Sub-regions

The typical turbulent boundary layer over a flat plate consists of several regions such as the linear sublayer, the buffer layer, the logarithmic law region and the outer layer. These regions each have their own characteristic regarding the relative importance of local inertial effects with respect to the eddy shear and viscous shear stresses. Focusing on the flow features and examining from the surface of the wall where the viscous shear stresses are very large (in the proximity of the laminar-sublayer), there is a clear trend such that the viscous shear stresses gradually looses importance further away from the wall (towards the buffer layer), and eventually the larger turbulent eddies are the dominant flow features (log-layer). Towards the edge of the boundary layer (outer-layer), even the eddy shear stresses are suppressed by the inertial forces of the mainstream flow. [Ref. A-11]

## 7.2 Velocity Profile

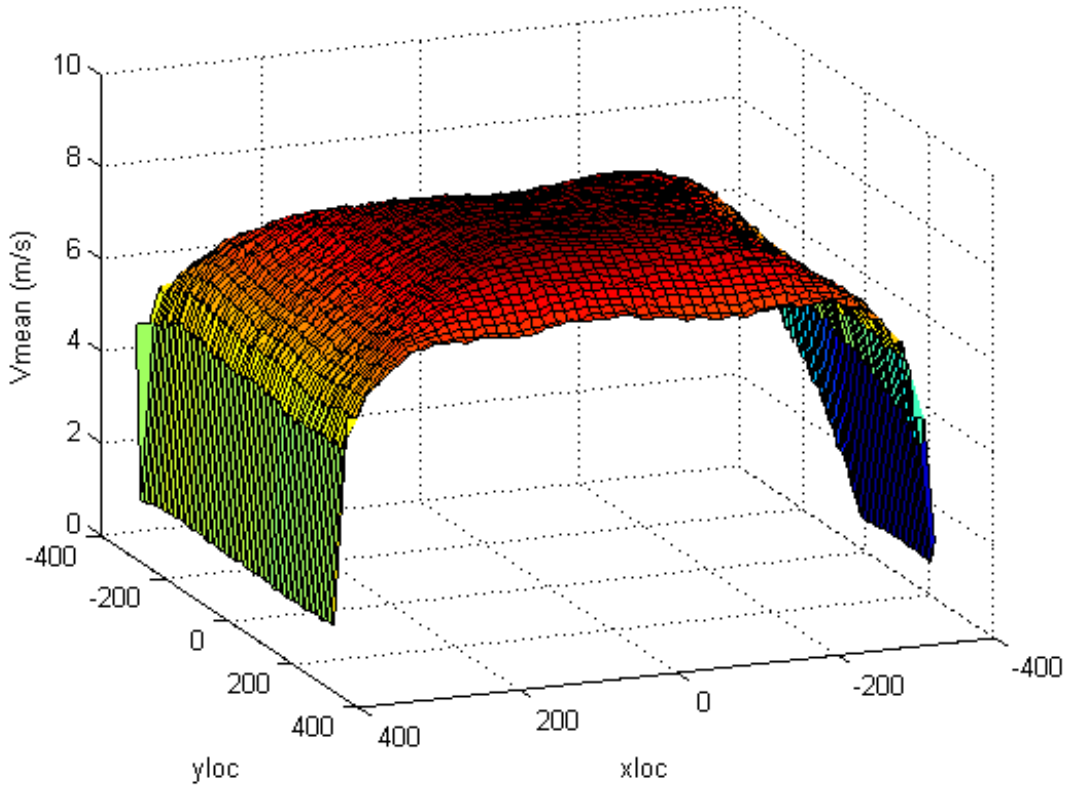


Figure 6: Velocity Distribution at the Test Section Inlet

The velocity profile is acquired by means of averaging the unsteady hotwire anemometry data at each grid point of the test section inlet. It possible to see the decrease in mean velocity towards the wall of the channel due to the effect of the boundary layer, even though the particular regions of the boundary layer can not be identified from this figure. The bulk velocity in the channel centerline is calculated to be 8.3 m/s.

## 7.3 Turbulence Intensity

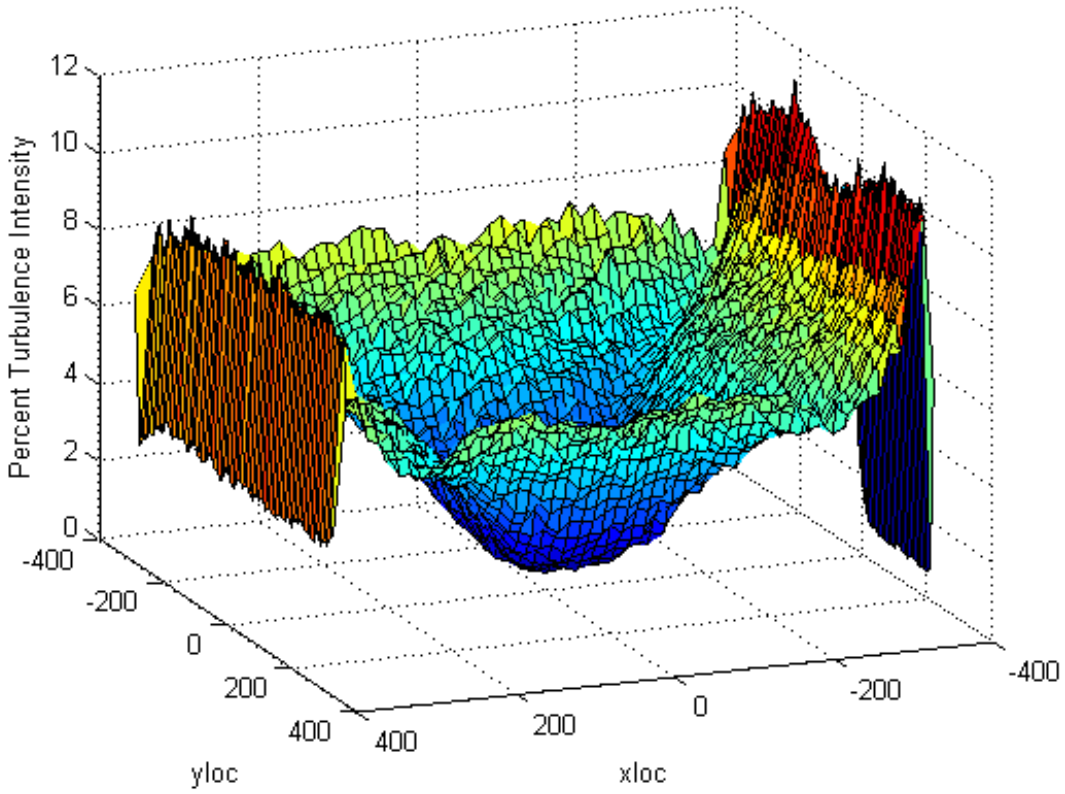


Figure 7: Turbulence Intensity Distribution at the Test Section Inlet

The hotwire time resolved velocity data, allows the computation of turbulence intensity. The turbulence intensity is defined as the ratio of the root-mean-square of the perturbation velocities at a particular location over a specified period of time and the mean velocity at the channel centerline, $TI = \frac{\sqrt{\overline{u'^2}}}{U_{bulk}}$. Across the channel the mean turbulence intensity is calculated to be 5.2%, where as towards the channel centerline turbulence intensity drops to 1.5 %.

In Figure 7, the distribution of turbulence intensity across the channel can be explained by the existence of the different regions in the turbulent boundary layer. The main force driving the turbulence, in the absence of the ribs, is the eddy shear stresses. Towards the edges of the channel around sub and buffer layers the sharp decrease of TI is due to the fact that the eddy shear stresses in these regions are relatively small in comparison. Around the log-layer a steep increase in TI can be explained by the fact that this is the region where the eddy shear forces are the greatest (eddy generation). Focusing towards the outer layer, as the inertial forces become more and more dominant, a gradual transition to freestream can be observed. At the

channel centerline, where TI is the lowest, the inertial forces are the dominant flow features in the local flow field.

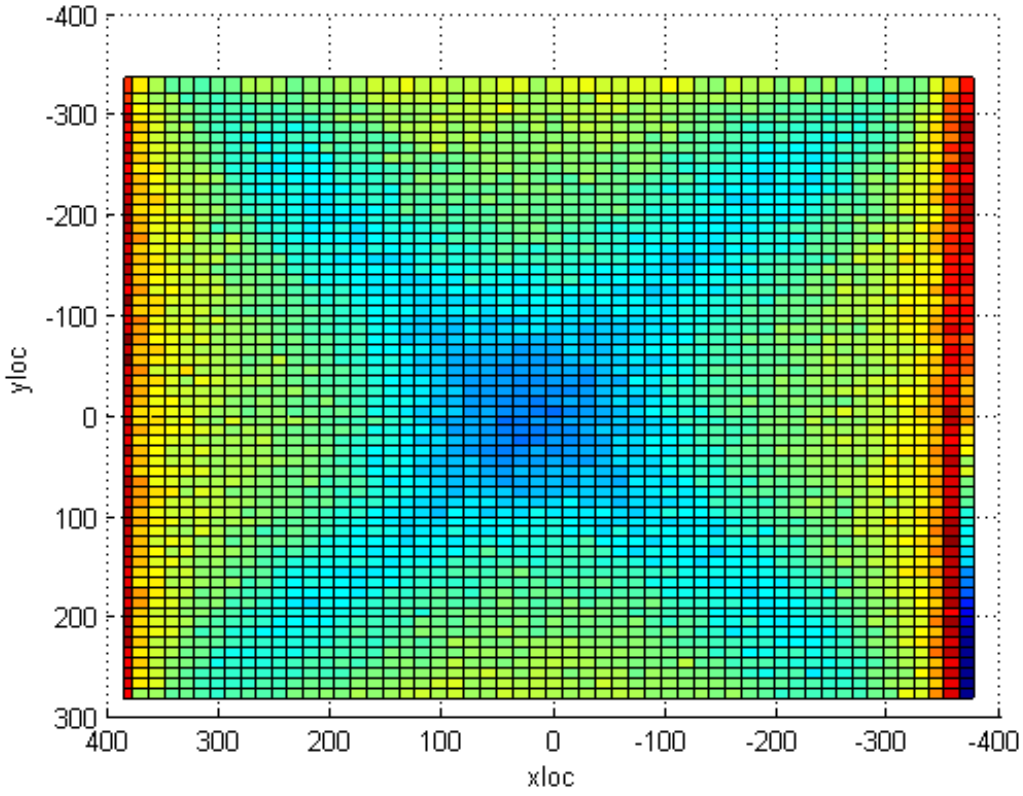


Figure 8: 2-D Turbulence Intensity Distribution

Analyzing the turbulence intensity distribution from another perspective on the x-y plane, Figure 8, the clear quadrant symmetry can be observed. The regions where the boundary layers from adjacent walls merge are seen as lower turbulence intensity regions. This trend of symmetry is observed in all velocity related measurements to a large extent.

## 7.4 Integral Time Scales

The integral time scale describes the time scale of the mean eddy perturbation weighted by the energy content of the eddies. Since more energy is maintained in the large eddy scales of the turbulent field but not necessarily in the largest, the averaging indicates an order approximation for the large eddy time scales. [Ref. A-12] It is based on the Taylor's frozen turbulence assumption, $\frac{\partial}{\partial x} = -\frac{1}{u}\frac{\partial}{\partial t}$, where a spatial change is related to a change in time related by the propagation velocity.

To be able to calculate the time scales, the first step is to compute the autocorrelation coefficient function, $\rho_u(\tau) = \frac{\overline{u'(t)u'(t+\tau)}}{\overline{u'^2}}$, where u' is the perturbation velocity, from which the time scale can be computed as the indefinite integral of $T_1 = \int_0^\infty \rho_u(\tau) d\tau$. [Ref. A-13]

The autocorrelation quantifies the similarity of the velocity perturbations at two separate points in space or in this case at different instances in time. Analytically the numerator of the auto-correlation function is computed as the cross correlation function defined by $R_{uu}(\tau) = \lim_{T\to\infty} \frac{1}{T}\int_0^T u'(t+\tau)u'(t)\,dt$. By the discretization of this integral, $R_{uuf}(j) = \lim_{N\to\infty} \frac{1}{N}\sum_{n=0}^{N-1} u'_n u'_{n+j}$, the auto-correlation function can be estimated for a finite number of data points. Since the autocorrelation function is an indefinite integral from zero till infinity and the data length is finite, to reduce the propagation of the edge effects on the autocorrelation values in the entire time domain, the signal is elongated by adding the signal end to end $2^4$ times (at which point the autocorrelation values showed convergence) and by this way data corruption due to finite summation approximation is prevented.

Another measure to protect data integrity was to apply the autocorrelation function to perturbation velocities rather than absolute instantaneous velocity data. Since the length scale, or the related time scale, phenomena can be related to the size of the structures being shed from a point in space, the mean velocity only affects the propagation velocity of these structures rather than the size or local pertubrative time scales.
Since the time scale calculation is based on the Taylor's frozen turbulence assumption, which is not necessarily the exact representation of the physical flow, the analyzed noisy data needs further processing to ensure a more accurate time scale representation of the channel. The autocorrelation function computed by the perturbation velocities is fitted with a third order exponential function, $R_{uuf-f} = C_1 e^{\lambda_1 \tau} + C_2 e^{\lambda_2 \tau} + C_3 e^{\lambda_3 \tau}$.

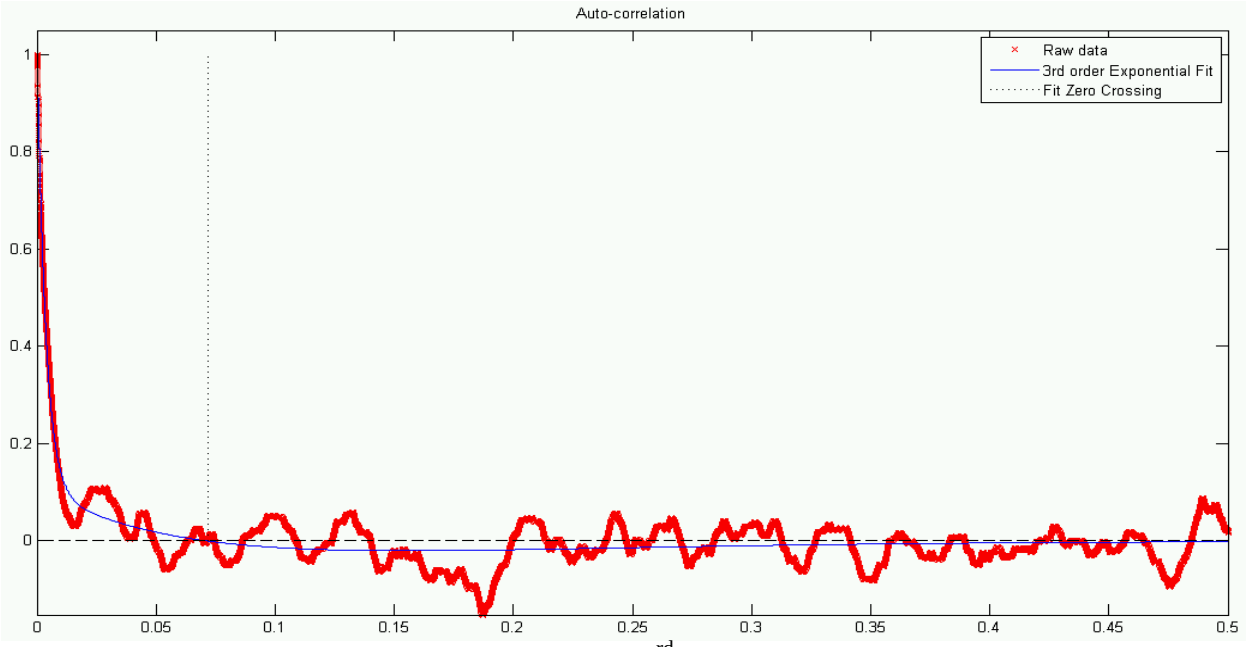


Figure 9: Autocorrelation and 3rd Order Exponential Fit

Figure 9 clearly shows that the fit is a reasonable approximation to the noisy auto-correlation data. Finally, to calculate the time scale value, the curve fit is to integrated until the first zero crossing $\tau_o$, $T_1 = \int_0^{R_{uuf-f}(\tau_o)} R_{uuf-f}(\tau) d\tau$.

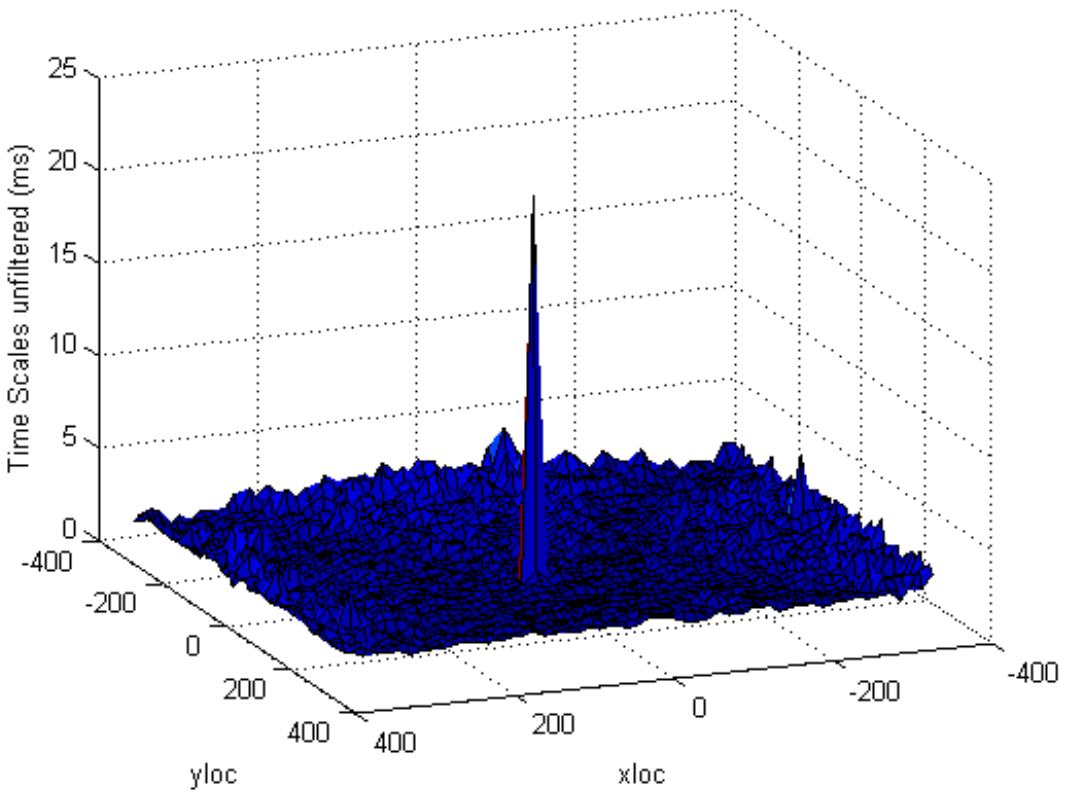


Figure 10: Raw Time Scales Distribution

Finally, the raw time scale distribution, Figure 10, is post-processed by means of a two stage filter, where the first stage compares the mean time scale of the channel with the individual grid points and filters the points where the value is larger than the global threshold. The second stage of the filter is a neighborhood validation of each individual point where the mean of the neighboring points is compared with the grid point of interest and the values above a certain threshold are filtered. At these measurements specifically, the 1st stage and 2nd stages of the filter thresholds were set to be 200% and 30 % respectively; the number of data points that were below the predefined thresholds were respectively 0.3% and 4.1% of the total number of data points. The time scale distributions resulting from the 1st and 2nd stages of the filtering can be seen in Figures 11 and 12.

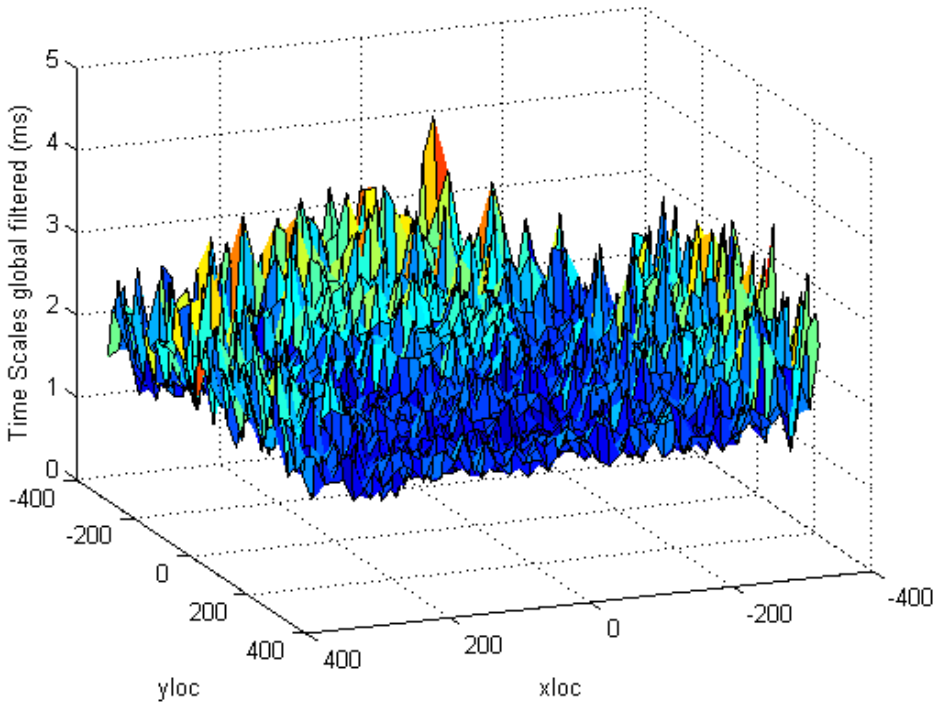


Figure 11: 1st Stage Time Scales Filter

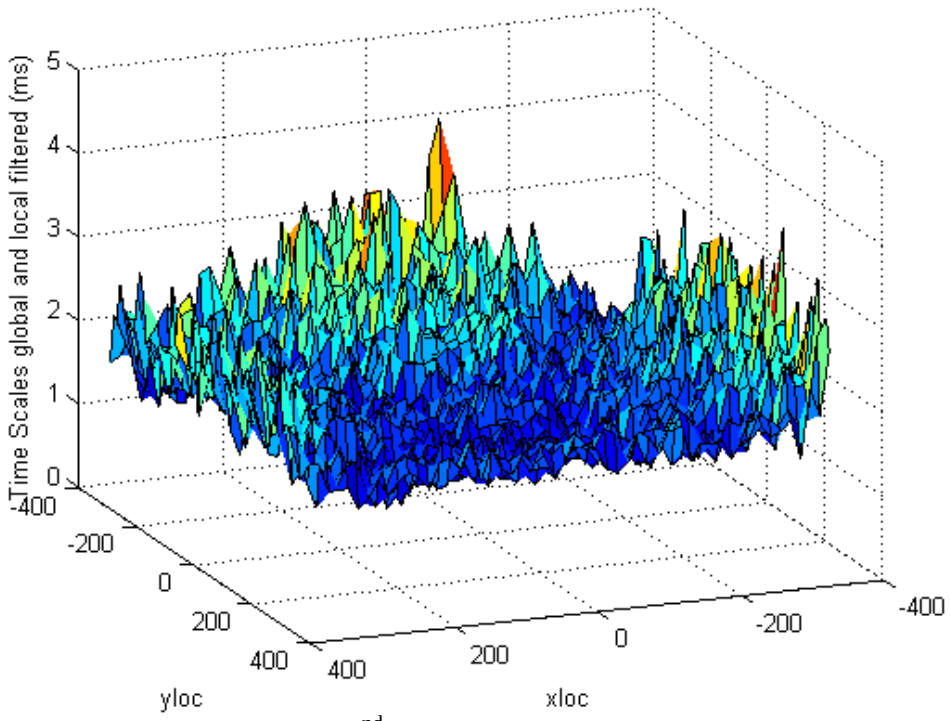


Figure 12: 2nd Stage Time Scales Filter

From this time scale distribution, the mean time scale across the channel is computed to be 1.8 ms.

## 7.5 Integral Length Scales

For the computations of integral engths scales, Taylor micro scales, Epsilon dissipation rate and the Kolomogrov scales, the local mean velocities are used as the propagation quantities. Even though it is known that the eddies formed in the boundary layer do not necessarily propagate with the local mean velocities, the propagation rate is a function of the local mean velocity, where as a scaling with bulk velocities would result in an even less physical representation.

The integral length scale can be estimated by applying the frozen-turbulence-pattern hypothesis (Taylor hypothesis) to the integral time scales, and calculated in discrete form as, $L = \bar{u}\, T_1$, where u is the local flow velocity. Integral length scales are those that correspond to the mean scales of the most energy containing eddies, which also are maintained in the large scales of the turbulent field but not necessarily at the largest scales. The idea of length scales is not of numerical precision but is rather of qualitative significance. [Ref. A-12] From the calculations above, the mean length scale across the channel is found to be in the order of 12 mm.

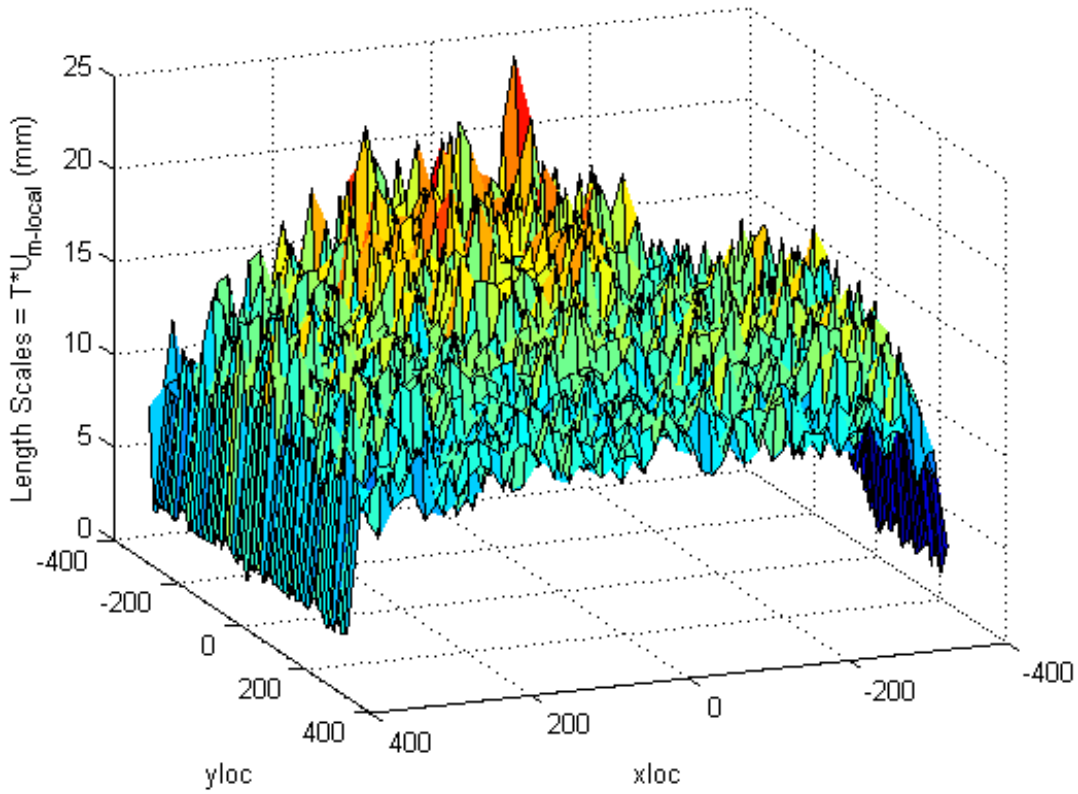


Figure 13: Length Scale Distribution

## 7.6 Taylor Micro-scales

Even though Taylor's micro-scale, defined as $\lambda = \bar{u}\left(\frac{\overline{u'^2}}{\left(\frac{\partial u'}{\partial t}\right)^2}\right)^{0.5}$ and calculated by the local velocities, is not a direct measure of either the large, energy-containing, eddies nor of the smallest dissipating eddies, it is a measure of the eddies where the dissipation phenomenon starts (in the inertial outer sublayer) and it can be used to correlate with the ε dissipation rate and the Kolomogrov scales. [Ref. A-14] The mean λ across the channel is computed to be 2.3 mm.

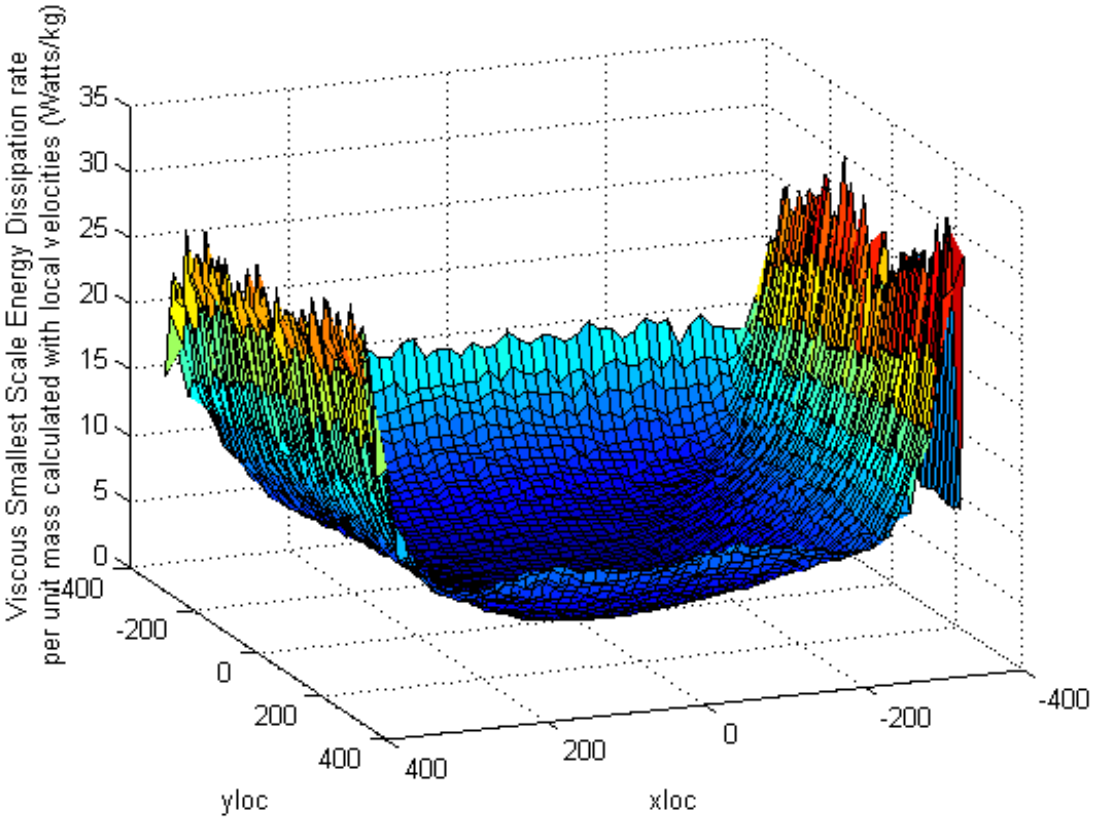


Figure 14: Taylor Microscales Distribution

## 7.7 Epsilon Dissipation Rate

The ε dissipation rate, defined as $\varepsilon = \frac{15\nu\overline{u'^2}}{\lambda^2}$, quantifies the conversion rate of kinetic energy to internal energy at the small eddy scales. It is observed that the dissipation per unit mass gradually increases towards the boundary layer, with a channel averaged mean ε value of 8.5 Watts/kg.

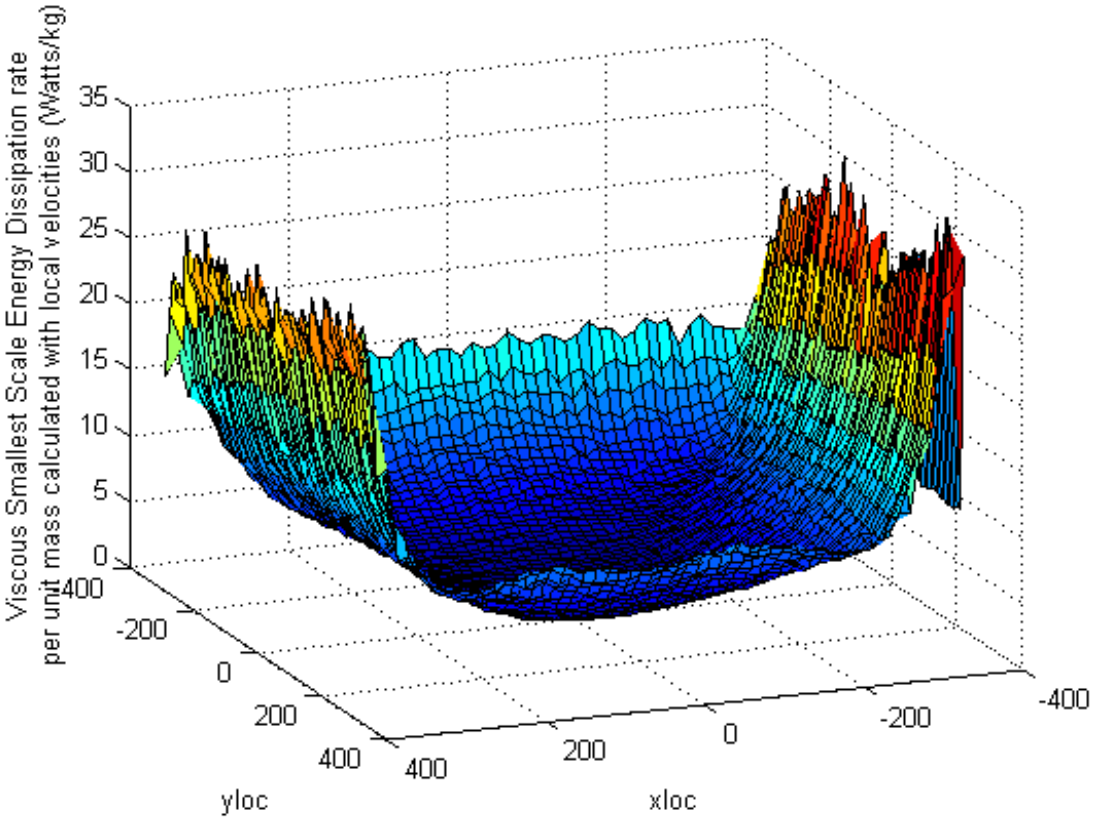


Figure 15: Epsilon Dissipation Rate

## 7.8 Kolmogrov Scales

The geometry and anisotropy of a flow-field will influence only the large scales of turbulent flow. The small scales will be less affected by the gross features of the flow and more influenced by the interaction between the turbulent eddies in the field, which is through the dissipation rate, ε, and viscosity, υ. Turbulent energy is created at relatively large eddy scales and is transferred, through a process of eddies breaking into other eddies, to smaller and smaller scales till the dissipation effects, which increase at decreasing scales with respect to inertial effects, predominate and the kinetic energy is consumed into internal energy. [Ref. A-12] Kolmogorov Scales, defined as $\eta = \left(\frac{\upsilon^3}{\varepsilon}\right)^{1/4}$, quantifies size of the small eddies where the kinetic to internal energy transfer occurs. As seen from Figure 16, the channel averaged Kolmogrov Scale equals to 0.15 mm, distribution indicating a trend of gradual decrease in scale size towards the boundary layer.

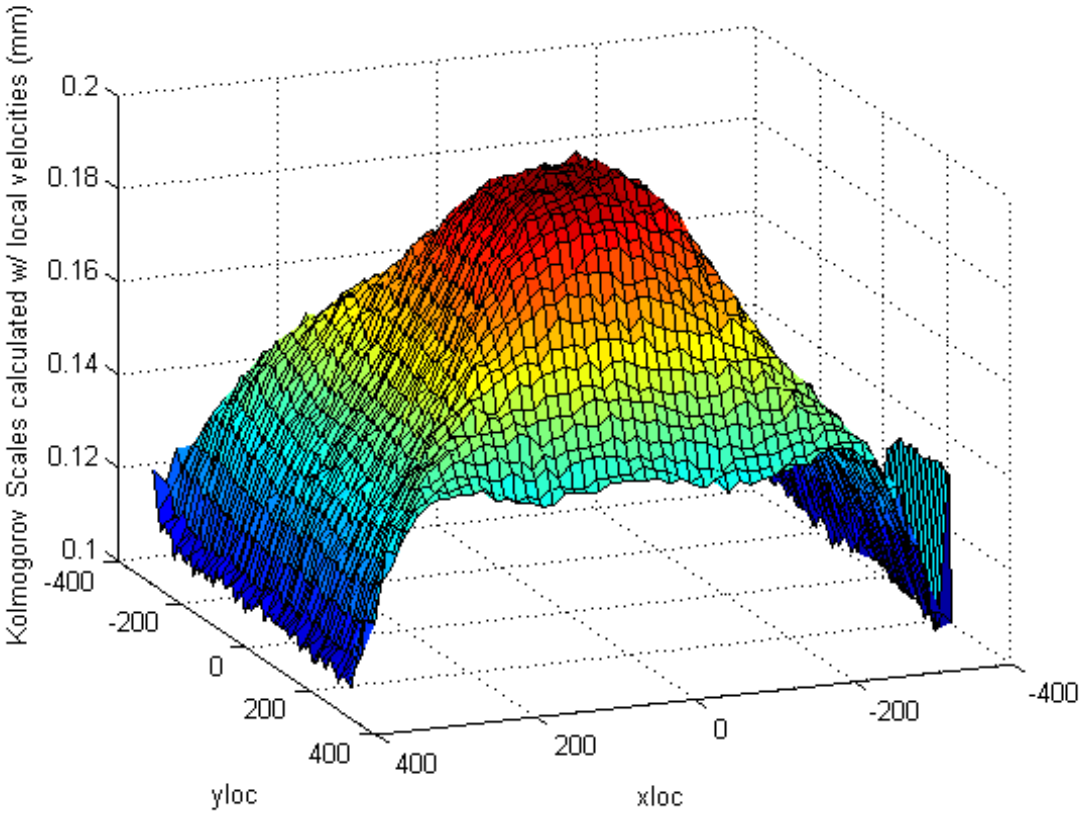


Figure 16: Kolomogrov Length Sclaes

# 8. Conclusions of the Aerodynamic Characterization

The flow in the rectangular channel is characterized in terms of turbulence. The mean turbulence intensity is found to be 5.2% and 1.5% averaged across the channel and channel centerline respectively. Mean ε dissipation scales across the channel are computed to be 8.5 Watts/kg and the related channel averaged Kolmogrov Scales are 0.15mm. These ε energy dissipation and turbulence intensity distributions will be inputs for the CFD code predicting the heat transfer rate in parallel with the experimental investigations. The acquired data is not only invaluable for the numerical investigation, but also gives the experimental investigators, for the sake of completeness of the baseline database, the opportunity to establish turbulence characterization of the channel in priori to experimental heat transfer measurements.

# 9. References for the aerodynamic investigation

A-1 Nirmalan N.V., Bunker R.S., Hedlund C.R. “The measurement of full-surface internal heat transfer coefficients for turbine airfoils using a non-destructive thermal inertia technique” GE R&D centre, Technical information series, 2002GRC010, February 2002

A-2. SCHEIMAN, J.; BROOKS, J.D., "Comparison of experimental and theoretical turbulence reduction from screens, honeycomb and honeycomb-screen combinations" J. Aircraft 18, 638 and NASA TP 1958

A-3. Bejan, A., Kraus, A.D., "Heat Transfer Handbook" John Wiley & Sons, 2003

A-4. Fox, R.W., McDonald, A.T., Pritchard, P.J., "Introduction to Fluid Mechanics" John Wiley & Sons, 2003

A-5. Panton, R.L, "Incompressible Flow" Wiley-Interscience, 1996

A-6. Fedrizzi, R., "Aero-thermal investigation of rib-roughened internal cooling channels" VKI, Project report 2003-10, June 2003

A-7. Çakan, M., "Aero-thermal investigation of rib-roughened internal cooling passages" VKI, Phd Thesis, July 2000

A-8. Casarsa, L., "Aerodynamic performance investigation of a fixed rib-roughened internal cooling passage" VKI, Phd Thesis, July 2003

A-9. Arts, T., Riethmuller, M.L, Boerrigter, H.L., Carbonaro, M., Van Den Braembussche, R.A., Buchlin, J.M., Olivari, D., Degrez, G., Fletcher, D., Denos, R., Olivari, D., "Measurement Techniques in Fluid Dynamics" VKI, 2001

A-10. White, F.M., "Viscous Fluid Flow" New York: McGraw-Hill, 1974

A-11. Kiock, R., "Boundary Layers on Turbomachinery Blades" VKI, 1983

A-12. Biswas, G., Eswaran, V., "Turbulent Flows: Fundamentals, Experiments and Modeling" Narosa, 2002

A-13. Bruun, H.H., "Hot-wire Anemometry: Principles and Signal Analysis" OUP Oxford, 1995

A-14. Hinze, J.O., "Turbulence", McGraw-Hill Companies, 1975

# 10. Fundamentals of Radiative Heat Transfer

There are several factors involved in the surface thermal emission. The basic concept involved is the concept of energy conservation. However, the energy can be distributed differently among viewing angles and also among different wavelength of radiation. The "black body" is a conceptual ideal surface that absorbs completely any incoming radiation regardless of angle of incidence. The inherently omni-directional definition coupled with imaginary thermal equilibrium condition eventually leads to the conclusion that a black body is also a perfect emitter that emits the same intensity of radiation in all direction. Thus the directional radiance of a black body in any direction is proportional to the total amount of energy emitted per unit surface area per unit time. The blackbody serves as standard for all surface emission of radiation in the sense that it is the best emitter in the temperature specified. Some real surfaces like the Sun and some blackened paints have surface emission properties very close to those of an ideal blackbody. Other surfaces are like blackbodies only in certain wavelength ranges. To describe this variation from the ideal black body, the ratio of the actual energy emitted compared to the ideal quantity is defined to be "emissivity" ε. In general, since ideal bodies behave wavelength independent, for all wavelengths, Blackbody ε=1, Greybody $\varepsilon < 1$, [Ref. B-9, Ref. B-10].

It is important to note that real surface emission properties not only differ from the ideal blackbody in terms of wavelength dependence but also on the directional distribution pattern. The directional spectral emissivity of a surface has different values at different directions and wavelengths. For mere simplification, commonly, an average quantity is used for all directions and wavelengths. Except for some special phenomena all surfaces interact with incident radiation in the following ways: reflection, ρ, absorption, α, and transmission, τ; and from conservation of energy, ρ+α+ τ=1. For opaque surfaces, transmissivity, τ, is equal to 0 and since Kirchoff's law states that emissivity, ε, and absorptance, α, are equal for any material for a given temperature and wavelength, under the wavelength independence generalization (grey body assumption), the conservation of energy simplifies to ε+ρ=1. If a given smooth surface is to be coated by a uniform highly emissive layer, the heat conducted to the upper layer is merely dissipated by omni-directional wavelength independent radiative emission due to grey body like behavior. Then, assuming a two surface enclosure where both surfaces are to behave as grey bodies, the net radiation exchange by the two surfaces can be approximated as,

$$Q = \sigma(T_{surf}^4 - T_{cam}^4) / \left[ \left(1-\varepsilon_{surf}\right) / \left(\varepsilon_{surf} S_{surf}\right) + \left(1 / F_{surf-to-cam} S_{surf}\right) + \left(1-\varepsilon_{cam}\right) / \left(\varepsilon_{cam} S_{cam}\right) \right],$$

where σ and S are Stephan Boltzman's constant and surface area respectively, [Ref. B-11].

# 11. Channel Aero-thermal Considerations

The conjugate heat transfer is dominated by the Nusselts number which, by Buckingham Pi, is a function of $Nu = f\left(\mathrm{Re}, \mathrm{Pr}, \frac{T_b}{\Delta T}, Ec\right)$, where $\mathrm{Re} = \frac{\rho V D_h}{\mu}$ ($D_h$ being the hydraulic diameter), $\mathrm{Pr} = \frac{c_p \mu}{k}$, $T_b/\Delta T$ and $Ec = \frac{V^2}{C_p \Delta T}$ are Reynolds number, Prandtl number, scaled relative bulk flow temperature and Eckert number respectively. Influence of the relative bulk flow temperature is found experimentally to have a small influence on the Nusselts number. Also, especially for low speed applications, the relative importance of the kinetic energy with respect to the enthalpy is found to be very small, which largely reduces the influence of the Eckert number as well.

For this application and under the assumptions above, $Nu \approx f(\mathrm{Re}, \mathrm{Pr})$; the variation of Pr in the temperature range of the experiment is very small, thus in order to respect similarity, it suffices to maintain the same Reynolds number.

Another consideration is the relative weight of forced convection with respect to natural convection: $\frac{Gr}{\mathrm{Re}_L^2}$, where the Grashof number, $Gr = \frac{g\beta(T_w - T_b)}{\mu^2}$ , $\beta \simeq -\frac{1}{\rho}\frac{\rho - \rho_{film}}{T - T_{film}}$ and $T_{film} = \frac{\overline{T_w} + \overline{T_b}}{2}$. For this setup, $\frac{Gr}{\mathrm{Re}_L^2} \sim o(10^{-3})$, clearly making the forced convection the dominant phenomena

# 12. Instrumentations for Operating Point Selection

## *c. Pressure Transducers / Kiel-Head Total Pressure Probe*

Two Validyne Model Dp10 pressure transducers are used for pressure measurements at the inlet and exit sections of the experimental setup. They are equipped with diaphragms with a maximum differential pressure of 22.5mm $H_20$. The calibration of the pressure transducers are done by means of a water monometer with an increment of 0.1mm $H_20$ in parallel with a DPI 610 Portable Pressure Calibrator with a 70mbar range and provide an accuracy of 0.05% FS. The linear calibration curve of the pressure transducers resulted in a $R^2$ value of about 0.9999 and in the operating range. the maximum and mean deviations from linearity was shown to be in the order of 0.35Pa and 0.15Pa.

At both the inlet and exit cross-sections, the static pressure is pneumatically averaged and recorded along with the total pressure measured by a Kiel head total pressure probe experimentally tested to be less than 1% sensitive to flow angle variations up to ±25º for the velocity range observed in this experiment.

### *d. Thermocouples*

For the temperature measurements, 6 T-type (Copper–Constantan) thermocouples, which have a nominal operating range of −185°C to +300°C, are built and installed at the inlet and exit sections of the test setup. They are calibrated in an oil bath along with a thermometer that has an increment of 0.1°K. The calibration curve showed that the voltage-temperature linearity results in an $R^2$ value of about 0.9998 which implies a maximum and mean deviation in temperature of 0.75ºK and 0.37°K respectively. These thermocouples are used for setting the operating condition of the channel, as well as for estimating the heating losses of the system by means of computing the average enthalpy increase of the bulk flow.

## 13. Operating point Selection

Operating Reynolds number of the channel is set by means of temperature, static and total pressure measurements in the channel. The total to static differential pressure and the static gage pressure are measured, along with temperature at the inlet and/or the exit of the test section. Through compressible flow relations and ideal gas law, $\frac{P_s}{P_t}=\left(1+\frac{\gamma-1}{2}M^2\right)^{\frac{-\gamma}{\gamma-1}}$, $\frac{T_s}{T_t}=\left(1+\frac{\gamma-1}{2}M^2\right)^{-1}$, $P=\rho RT$, $M=\frac{V}{\sqrt{\gamma RT_s}}$, velocity, density and static temperature can be calculated. By Sutherland's correlation [Ref. B-12], $\frac{\mu}{\mu_o}=\left(\frac{T}{T_o}\right)^{\frac{3}{2}}\frac{T_o+S}{T+S}$, where $\mu_o$= 17.16E$^{-6}$ Pa-s, $T_o$= 273.15 ºK and S=110.4 ºK; and the definition of Reynolds number, $\mathrm{Re}=\frac{\rho V D_h}{\mu}$, the operating point, Re=40000 based on centerline total pressure measurements, can be set. Prior to data acquisition the Reynolds number of the channel is monitored over a period of time of 10 minutes. Analyzing this data statically, it is possible to acquire a sense of operating point variation and for the hot wire measurements in the rectangular channel, it was calculated to be Re = 39988.50 ± 1.0 % with the 95% confidence interval.

## 14. Flat Plate Test Section Modifications for Heat Transfer

The test section of the experimental rig, which is 1260mm long with an internal cross-section of 75x75mm², has been modified for heat transfer measurements, while the inlet and exit sections remained the same. The new test section is made of several components, where at the base of the channel a flat slab made of Steel AISI304 rests. The thickness of the slab,

25mm, has been chosen such that it respects the similarity with the serpentine channels of a turbine blade where the Biot number, which is the ratio between the conductive resistance to the advective term, is approximately equal to 1. The steel slab is painted black with uniform highly emissive layers of Nextel Primer 5523 and Nextel Suede Coating 428-26, by means of an airbrush. The black coating is mat, soft and due to diffuse reflection the surface is non-dazzling. The end finish is found to be suitable for infrared measurements due to its black-body like behavior, albeit the camera is calibrated for the specific setup and the performance of the black paint is merely a matter of measurement quality.

The lateral and top walls around the slab are built with 10mm, and 15mm thick glass respectively. Plexiglas could not be used since during the experiments the temperature of the metal slab exceeds the melting point of the material. As the glass is opaque to infrared wavelength, an optical access window is designed on the top wall of the channel, centered on the test section, which spans across the whole width and is 300mm in length, Figure 17. For measurements done in the infrared spectrum, the commonly used materials are Sapphire, Germanium, Zinc Selenide and simple salts, which are transparent to the broadband infrared spectrum but are significantly more expensive than other common materials used in this setup. For this experiment, the optical access window is covered with a thin polyethylene film which is sufficiently transparent to the infrared spectrum, in the order of 80-85% transparency, allowing the measurements to be conducted. Since the plastic film transmits a suitable fraction of the infrared radiation, through an adequate calibration of the infrared camera, it can be used as the optical medium.

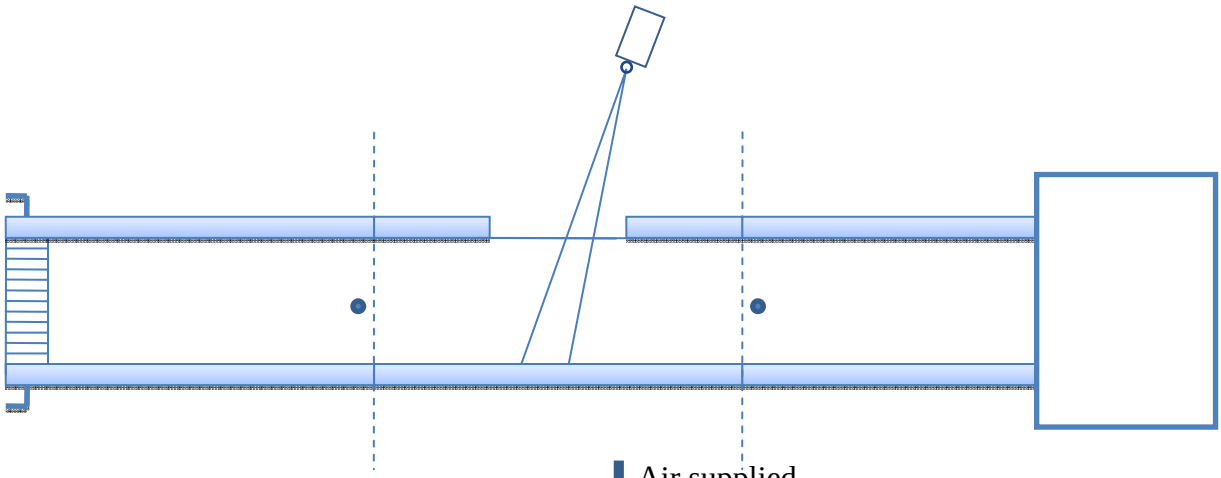

Figure 17: Experimental Test channel

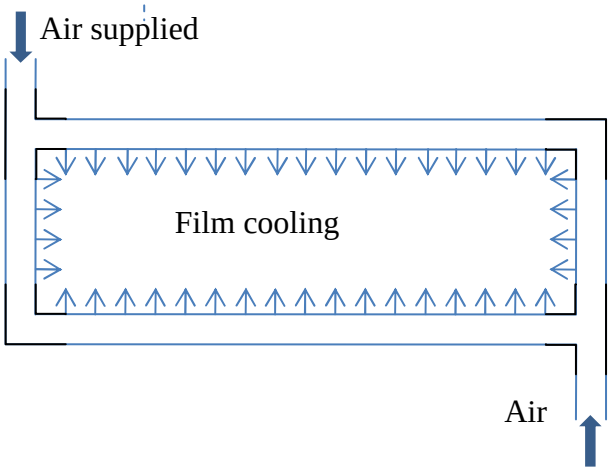


Figure 18: The optical film cooling aparatus

Even though the polyethylene film is *relatively* transparent to the infrared spectrum, the air temperature during the Infrared Thermography calibration procedure and measurement conditions are shown to vary significantly, in the order of 30° K; and through the convective process, this has a significant effect on the optical film temperature, which in return changes, though slight, the radiation emitted by the film itself to the infrared camera. To prevent an error, a bias shift favoring lower slab temperatures caused by the change in film temperature, a cooling technique is used in order to maintain the film temperature at ambient conditions at all times.

A rectangular piece, fitted perfectly to the opening, made of four copper tubes (with an inner diameter of 6mm) and held together by elbow and T-type joints, is supplied with air at 4 bars from two opposite corners, and the air is bled on the film through centimeter apart holes located along the copper tubes Figure 18.

One of the other hindrances of not having a solid window is that the film has a tendency to bow towards the inside of the channel due to the pressure differential with the ambient, caused by the aspiration through the experimental rig (in the order of 40Pa). Therefore, the film is attached with two torsion springs (one on each end of the channel) in order to maintain both the structural integrity and the parallel nature of the surface with respect to the steel bottom wall Figure 19.

The slab is heated by means of a 25µm thick Inconel sheet which is powered by a 16V-150A DC power supply. The current is dissipated as thermal energy by the Joule effect and is conducted away by the parts in contact. Inconel is known to provide uniform heat flux across the applied area and retains strength over a wide range of temperatures. The Inconel folio is packed in with layers of heat resistant plastic sheet on each side such that electric contact between the Inconel and the slab is avoided, and the structural sturdiness of the folio is augmented. The Inconel assembly is attached to the test slab by means of a 3M adhesive, and the channel is sealed with the glass side and top walls and silicon paste. Finally, the flat plate test section is placed on 100 mm thick thermal insulation. The cross sectional schematic of the test section can be seen in Figure 20.

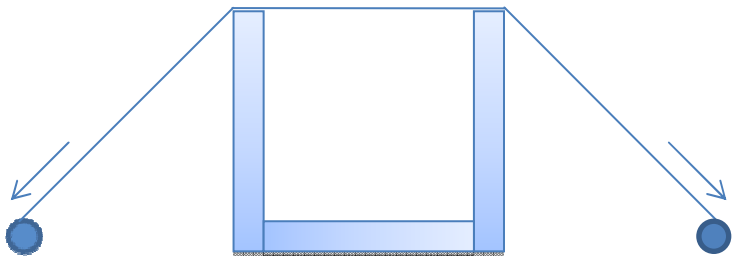

Figure 19: The optical acces window

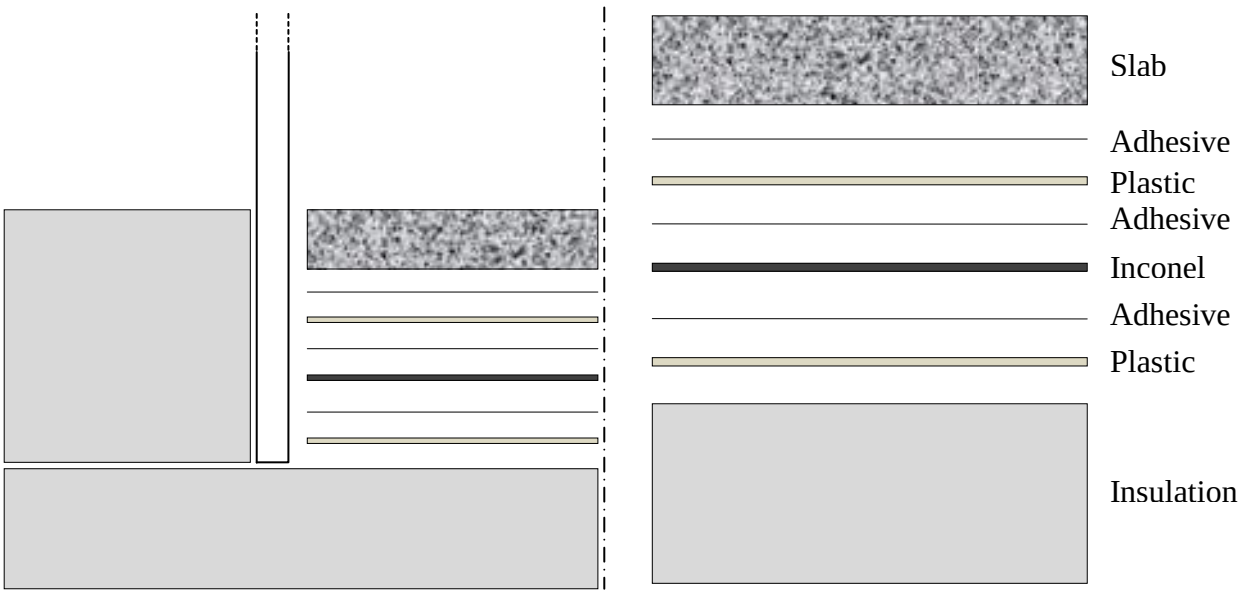


Figure 20: Cross-Sectional Schematic of the Test Section and the Slab Assembly

Since the thermal insulator has a conductivity of 0.024W/m-K and the AISI 304 metal slab has thermal conductivity of 16.2 W/m-K, considering the conservation of energy across the Inconel, $q''_{gen} - k_{steel}\left(\frac{dT}{dx}\right)_{x=0^+} - k_{ins}\left(\frac{dT}{dx}\right)_{x=0^-} = 0$, and as an order of magnitude approximation considering the thicknesses of the slab and insulation, 25mm and 100mm

respectively and a temperature difference of 30°K from the insulator to Inconel and 1.5°K from the metal slab to Inconel, the heat flux losses into the insulator can be estimated to be in the order of 0.7%. This demonstrates clearly that the main direction of the heat flux will be towards the metallic slab where the heat flux encounters a minor thermal resistance.

The final assembled test section and the experimental facility can be seen in Figures 21.1 and 21.2.

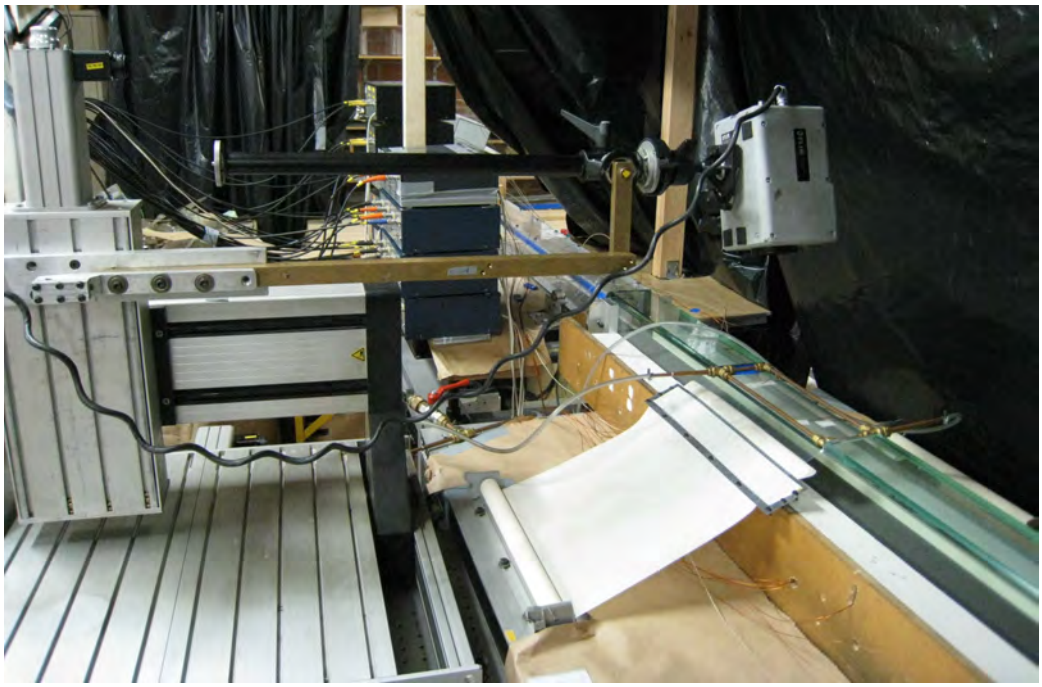

Figure 21.1: Assembled test section and the experimental facility

Figure 21.2: Test section

# 15. Instrumentations for Heat Transfer

## *a) Infrared Scan Radiometry*

An infrared thermal imager is a camera that detects electromagnetic energy radiated, near 10μm, by an object (whose temperature has to be measured) and converts it into an electronic video signal. In particular, infrared energy is radiated through a medium, passes through a lens, an aperture (or a filter) and finally impinges on a single infrared detector or a focal plane array (FPA) sensor, which transform the radiation into electrical signals. After analog-digital conversion, thermal object signal maps are post-processed with adequate temperature and geometric calibrations to relate to a 2-D temperature map, [Ref. B-13].

In this experimental campaign, a FLIR SC3000 infrared camera with long-wave Quantum Well Infrared Photo-detector has been used. The nominal response of the photo-detector peeks in the 8-9 micron wavelength range, and since each pixel relates to a single IR detector, the spatial image deformation due to the optical system aberration is negligible. The total resolution of the camera is 240x320 pixels, and thermal sensitivity is 0.02ºK.

## *b) Metallic Slab Thermocouple Temperature Measurements*

The slab is instrumented with 14 T-type thermocouples, held in place by Omega OB-101 thermally conductive, electrically insulating paste, applied to 3mm holes drilled in the metallic slab at several locations along the slab shown in Figure 22. The thermocouples are located 0.5 mm away from the surface of the slab, and considering the Biot number, approximately $10^{-3}$, for this characteristic length, it is observed that the temperatures measured at the thermocouple bead locations are equivalent to surface measurements.

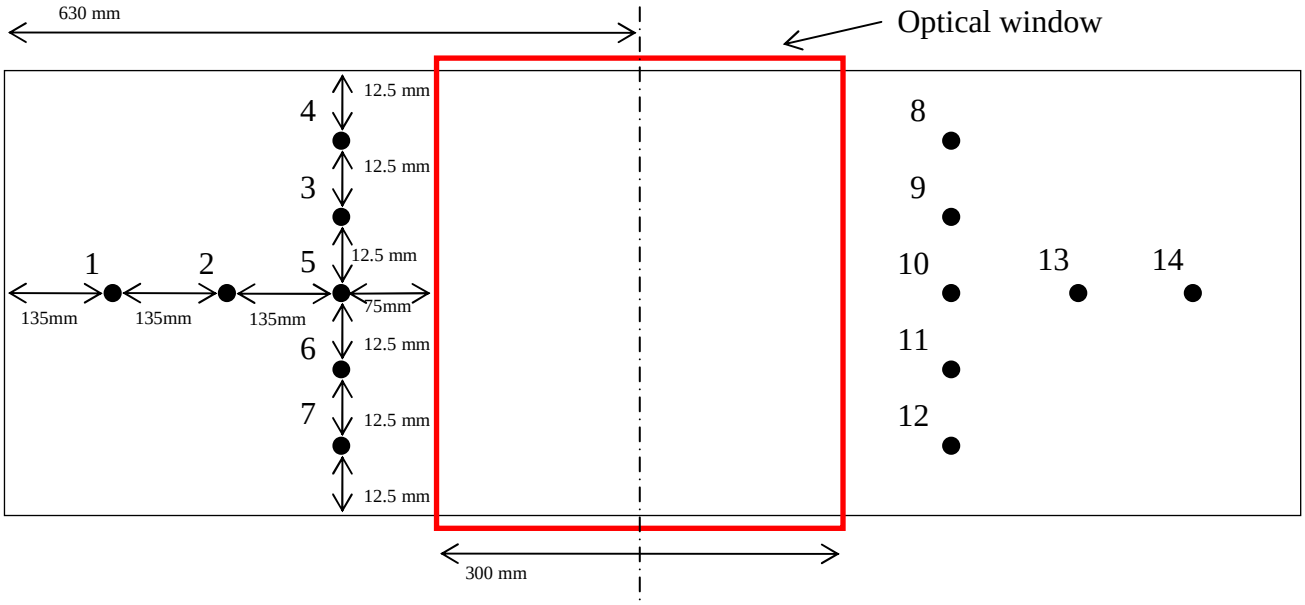


Figure 22: Slab Thermocouple Locations

The locations of the thermocouples along the slab have been chosen such that the temperature across the channel centerline (TC1, TC2, TC5, TC10, TC13, TC14), as well as the distribution/uniformity over the width of the channel (TC3, TC4, TC5, TC6, TC7 and TC8, TC9, TC10, TC11, TC12), can be observed.

In addition to thermocouples placed in the slab, the Inconel foil temperature underneath the slab, as well as the temperature on the polyethylene film placed over the optical window is monitored by means of 2 and 4 thermocouples respectively.

### *c) Heat flux Measurements*

Heat flux measurements on the inconel have been conducted by applying energy balance over a control volume drawn over the entire heating element, $q''_{tot} = \frac{q}{A} = \frac{V_{INC} I_{INC}}{A}$. The Inconel foil has been cut very carefully to fit the dimensions of the slab in the width-wise direction and the voltage applied across the foil is measured at 2 edges in the length-wise direction. It has been found that the accuracy of the current measurements are significantly improved by calculating the current with a calibration curve for a known resistance shunt placed in series with the foil resistance, Figure 23. Since the Inconel is known to produce uniform heat flux due to the Joule effect, the simple calculation of the foil area, in this case 0.1176m$^2$, along with the measured voltage and calculated current, suffice to calculate heat

flux under the slab at any given point and time. The computed heat flux is then compensated for the estimated losses through the insulation.

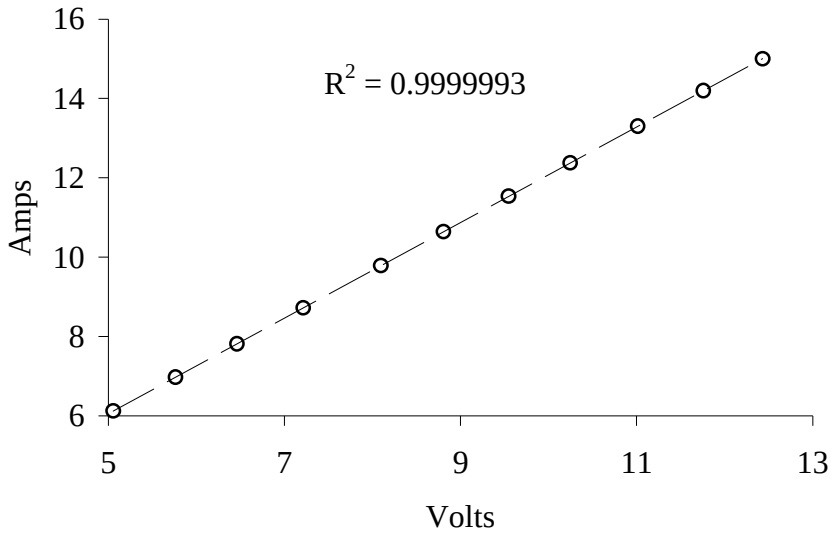


Figure 23: Inconel Voltage-Current Calibration Curve

# 16. Infrared Thermography Data Acquisition and Post-Processing

## *a) Infrared Thermography Data Acquisition*

A Labview code is generated to interface the data acquisition cards with the computer as well as for online monitoring of the measurement samples. This program manages the data acquisition and synchronization of various components during the initial experimental setup, calibration procedure of the infrared camera and the measurements campaigns.

There are two 16-bit multiplexed data acquisition boards that are in use, Keithley 2700, and NI-6251. The voltages of the 2 pressure transducers (static pressure at the inlet and total pressure at the exit) and the 6 air (3 at the inlet, 3 at the exit) and 4 optical film thermocouples are read with the NI board, where as the voltage across the Inconel foil and voltages of the 14 thermocouples used to measure the slab temperature and the 2 thermocouples in between the Inconel sheet and the insulation are read with the Keithley board.

With the Keithley 2700, the acquisition is done at a sampling rate of 2kHz, for a span of 10V, and by use of the integrating voltmeter, the values acquired are averaged over 5 power line cycles, 0.1 seconds. From both discretization error estimation and parts per million (ppm) based estimation scheme given by the supplier, the accuracy of the integrating voltmeter is approximately ±150μV. The data acquired by the NI-6251 board is sampled at a rate of 50kHz for 25000 samples for an input range of 10V and 1V for pressure transducer and

thermocouple amplifier readouts respectively. The discretization error of this unit is in the order of ±150μV and ±15μV for the selected input ranges.

Even though the thermocouples have been calibrated a priori, since there is no way to recalibrate them after they are placed in the slab and there can be zero drifts (in the order of 0.3K) due to the electronic cold junction compensators in the amplifiers; the slab thermocouple calibration zeros are readjusted before each measurement campaign by imposing the average value of all slab thermocouples as the cold metal slab temperature. Similarly, the thermocouples that read the air temperature and optical film temperature during the test have been corrected by a "soft-zero", imposing the air temperature read by a mercury thermometer with an accuracy of 0.1K.

All the conditions of the test setup are monitored periodically during the operation of the experimental rig, and at the imposed instances of infrared acquisition. For the moments where infrared thermography measurements are conducted, an analog trigger is sent from the NI-6251 board to the ThermaCam Researcher Pro software, which manages infrared camera, through the serial port of the computer; consecutive thermal images are recorded with the infrared camera at 3Hz for 10 seconds. The basic flow of information among various electronic devices present in the setup can be seen in Figure 24.

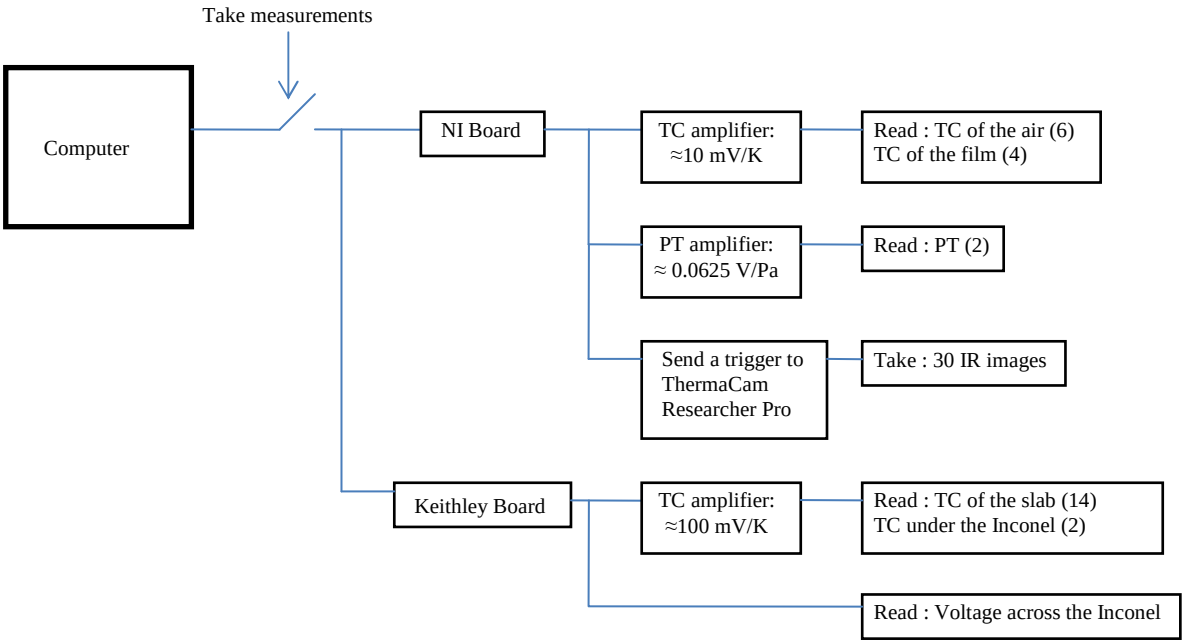


Figure 24 : Data Acquisition Flow Chart

## *b) Infrared Camera Image Domain Transformation*

The infrared camera is placed above the optical window 30 degrees from the vertical and perpendicular in the two other axes with respect to the reference frame of the channel, Figure 25. The angle chosen is a compromise among the out of focus effect of the lens, the resolution and the area observed in the image. It is of special importance to prevent the reflections to the camera, of the glass on the slab, as well as the copper film cooling system and the film.

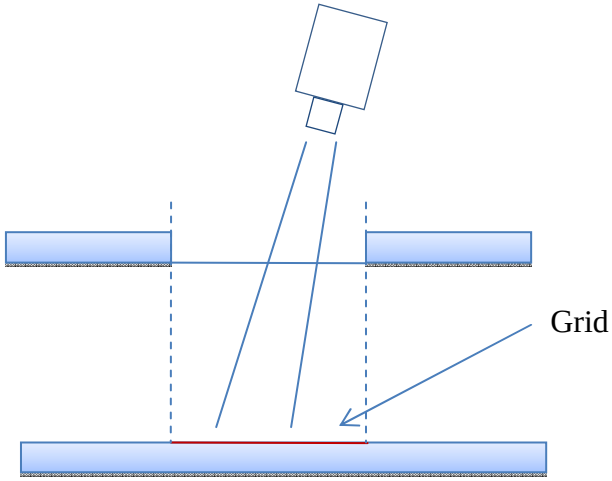


Figure 25: Camera Orientation

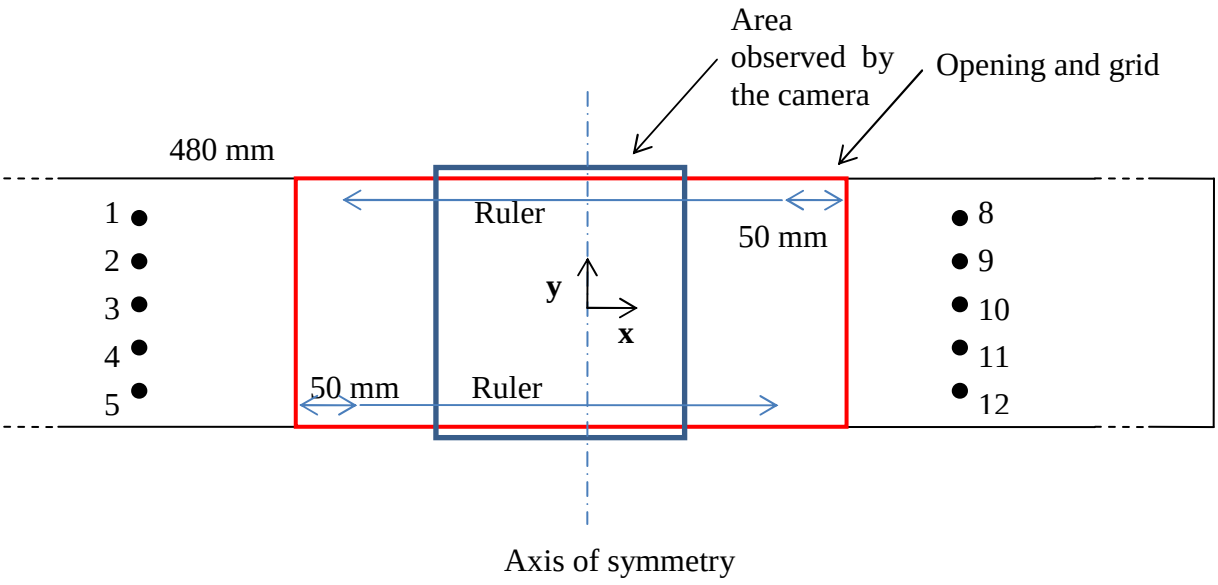


Figure 26: Test Slab Schematic for Image Domain Transformantion

In order to precisely transform the image observed by the camera to the surface in the physical domain, a thin grid (~1mm thick, 300mm long, 75mm wide, and with 10x10 mm lead squares) is introduced into the measurement section of the channel. The grid, which fits perfectly to the opening, along with two metallic rulers, which are flush to the edges of the channel and each one 50mm from the end of the opening, are used to transform the image from the perspective of the camera to the physical domain, Figure 26.

The grid is created by lead lines drawn on a piece of paper that become visible in the infrared spectrum when simulated by heat due to the difference of reflectivity between lead

and paper, Figure 27.1. The image transformation is done through a bicubic interpolation scheme, and the resolution of the transformed image is superficially augmented in each dimension through sub-pixel interpolation, Figure 27.2. The mean scale factors corresponding to the original image acquired by the camera, and the transformed interpolated image are 2.64 pixels/mm, and 5.21 pixels/mm respectively. The images are then cropped to fit the width of the metallic slab, Figure 27.3.

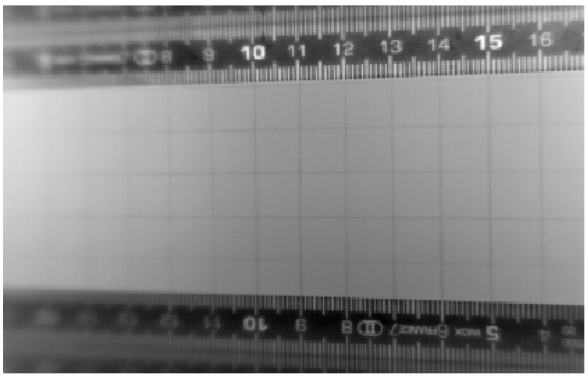

Figure 27.1: Raw Image of Calibration Grid

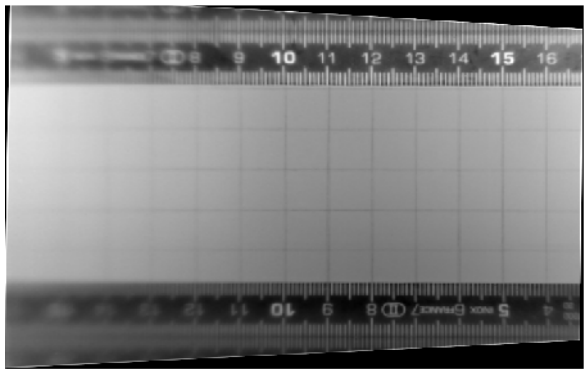

Figure 27.2: Transformed Image of Calibration Grid

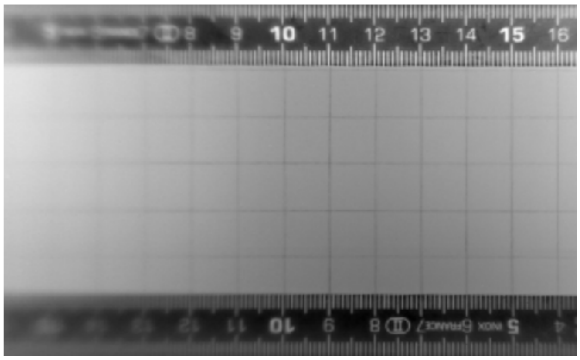

Figure 27.3 : Cropped and Transformed Image of Calibration Grid

## *c) Infared Camera Pixel by Pixel Temperature Calibration*

The infrared radiation, emitted by the model and its surroundings, is absorbed by the photon-detectors of the infrared camera and for which the intensity is a function of slab area and temperature, and relative orientation of the surfaces. The irradiation is then converted into electrical signals, ”object signal”, at each pixel. To get an accurate representation of temperature from the acquired object signal at each pixel, and avoid uncertainties that might arise from the camera out of focus effect, the existence of the optical film, reflections, and influence of the surroundings, an experimental pixel-by-pixel calibration methodology is employed, where each pixel is calibrated with its own sensitivity to test section temperature.

To calibrate each pixel's object signal with a known temperature of the corresponding area in the physical domain of the slab, a uniform slab temperature is ensured by means of a heat exchanger placed upstream of the inlet section and the blower operating downstream, Figure 28. The slab is heated for an extended amount of time, in the order of 3 hours, until, through convection, a uniform slab temperature of about 340K is reached. The slab is then cooled gradually, while the heat exchanger is detached, and the object signal from the infrared camera, along with the slab thermocouple voltages, are recorded periodically through out the cooling process. The objective is to attain a width-wise spatially uniform temperature distribution that can be used to calibrate the infrared camera, and through experimentation with the setup, it has been observed that natural convection cooling does not satisfy this criteria, and there exist an optimum cooling Reynolds number for which the width-wise slab temperatures seem to be the most uniform. In the mean time, the film over optical window is cooled to ambient temperature with the film cooling apparatus to sustain a consistent uniform temperature with the data acquisition conditions.

Figure 28: Upstream Heat Exchanger

More specifically, in this calibration, 30 different slab temperatures, varying from 297K to 340K, are considered; and for the data acquired at each temperature, 30 infrared images are recorded at 3Hz and averaged to result in a single mean infrared image for that particular slab temperature. This mean image is then spatially transformed by the methodology outlined in the Infrared Camera Image Domain Transformation Section. At each temperature calibration point, instead of averaging all slab temperatures and imposing an assumed uniform temperature through out the slab for all pixels observed by the camera, the means of the five upstream (TC3, TC 4, TC 5, TC6, TC 7) and downstream ( TC8, TC9, TC10, TC11) width-wise placed thermocouples are linearly distributed over the length-wise direction. The imposed temperature values on the infrared images are the interpolated values of this linear fit, and are increasing in the length-wise but uniform in the width-wise directions, Figure 29.

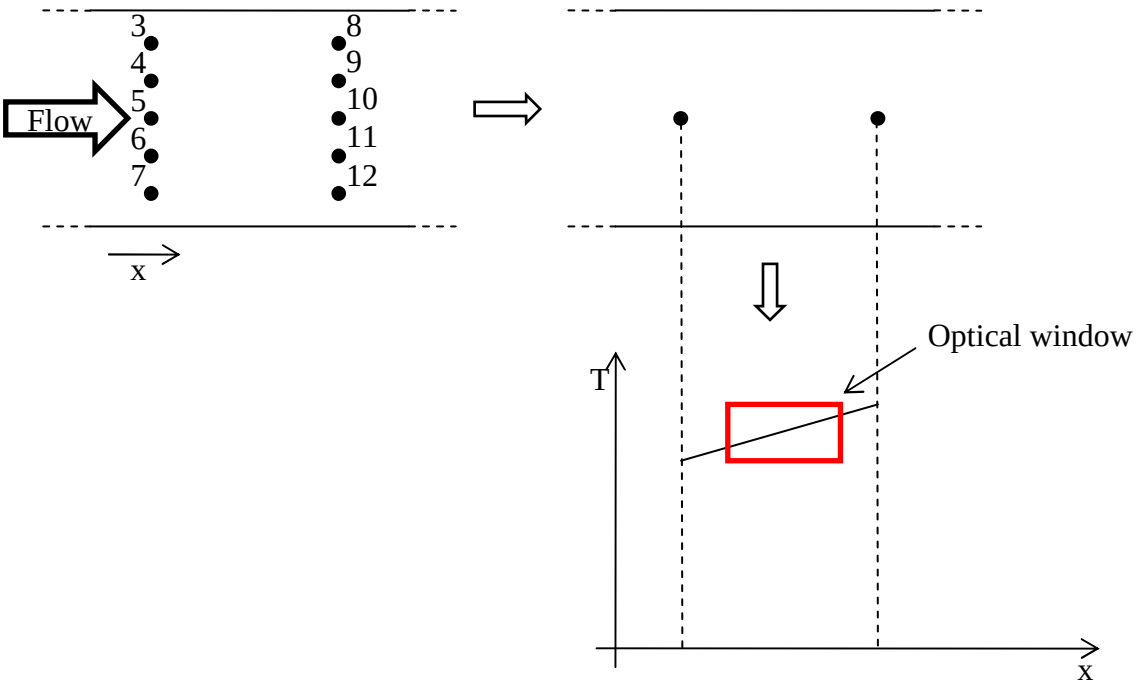


Figure 29: Imposed Slab Temperature Distribution

Finally, the object signal data at each pixel is fitted with a second order polynomial with respect to the imposed temperatures and for a given imposed temperature, if the spatially averaged deviation from the polyfit is more than 0.1K, then that temperature calibration point is omitted from the fit. The average deviation for all temperature calibration points over the spatial mean is calculated to be 0.056K, and 28 out of the 30 temperature calibration point we found to be suitable for the criteria. As an example, the calibration curve for the pixel at the center of the infrared image can be found in Figure 30.

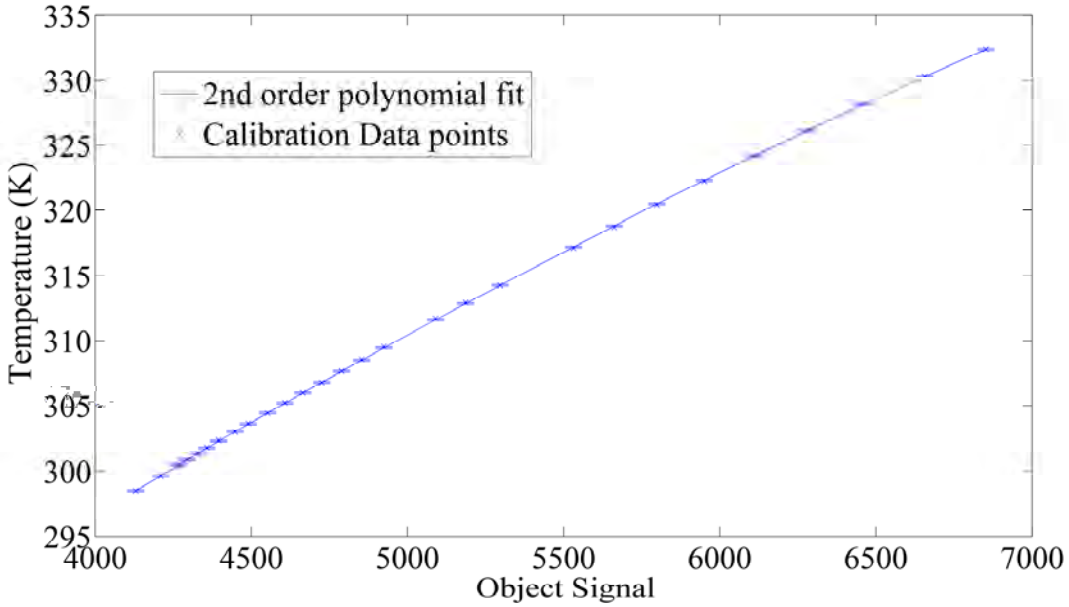


Figure 30: Camera Center Pixel Object Signal versus Temperature Calibration Fit

# 17. Infrared Thermography Results

## a) Temperature Distribution

The Reynolds number during the Infrared Thermography measurement campaigns, based on centerline total pressure at the exit is set to a nominal value of 40000. While the blower supplies the experimental rig with ambient temperature air for convection over the slab, the power supply connected to the Inconel foil is turned on, and the heat flux under the slab is gradually increased to 1167 W/m². Until steady-state conditions are reached, all temperatures along and under the slab, over the optical film and in the test section are monitored online and periodically. Once the test-section is believed to have reached steady conditions, for this case the temperature history of the slab thermocouples can be seen in Figure 31, 30 infrared images are acquired.

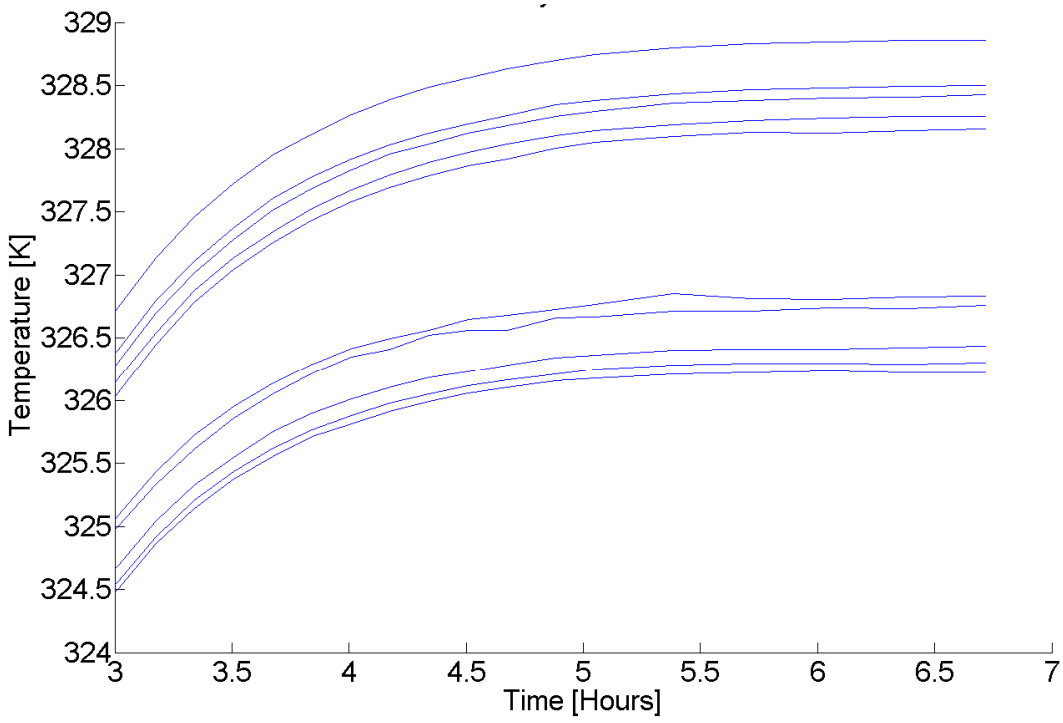


Figure 31 : Slab Thermocouple Temperature Time History

The acquired infrared images are averaged, resulting in the mean object signal distribution over the slab, which is then transformed into the physical domain. The subsequent object signal distribution can be seen in Figure 32, where the origin of the reference frame is set at the center point of the slab from both length and width wise directions represented as y and x direction in the figures respectively. The row temperature at each pixel is then calculated by applying the polynomial fits, which are calculated with by the calibration procedure and vary pixel by pixel, Figure 33. The directly measured temperature data seems to be fairly noisy and is further post-processed by a series of filters that first compare the spatially averaged temperature with the temperature at each pixel and filters the pixels where the difference is larger than 4K, replacing them by the average of their neighboring cells; the second stage of the filter is a neighborhood validation of each individual pixel where the mean of the neighboring pixels is compared with the pixel of interest and the values above 0.1K are replaced by the mean temperature of the surrounding cells. The applied filters still proved to be ineffective to reduce the noise in the temperature distribution. For a configuration such as used in this setup, and considering that geometric and aerodynamic singularities do not exist, it is not expected to observe large pixel by pixel variations, such as the ones observed. Thus, to be able to capture the global change in temperature across the entire interrogation region and impose it as a boundary condition while solving for the heat flux on the surface, a 10th order surface bipolynomial is fitted over the temperature distribution, Figure 34. The spatially averaged absolute error caused by this estimation is approximately 0.15K, and its distribution over the measurement surface is presented in Figure 34. The larger peaks are clearly isolated

regions which result in non-uniformities due to reasons like the surface finish of the slab as a consequence of the machining process and the quality of the applied paint.

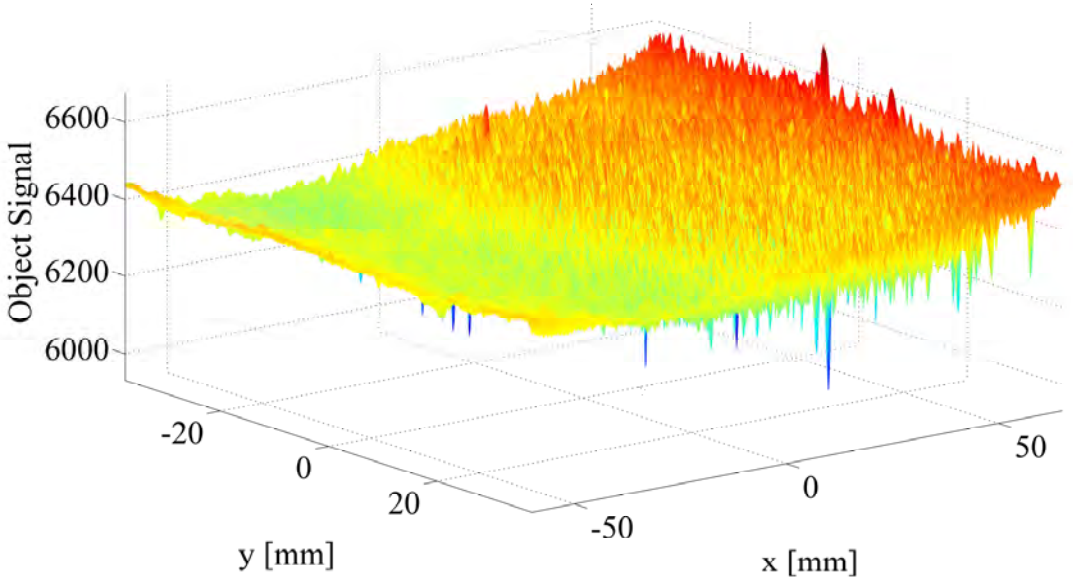


Figure 32 : Raw Infrared Camera Object Signal Distribution

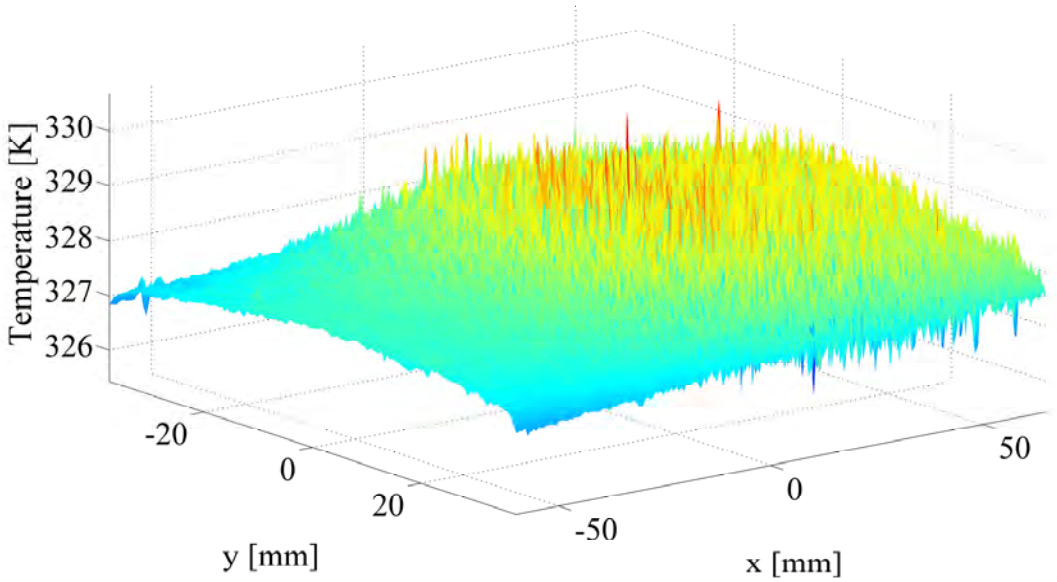


Figure 33 : Raw Infrared Thermography Temperature Distribution

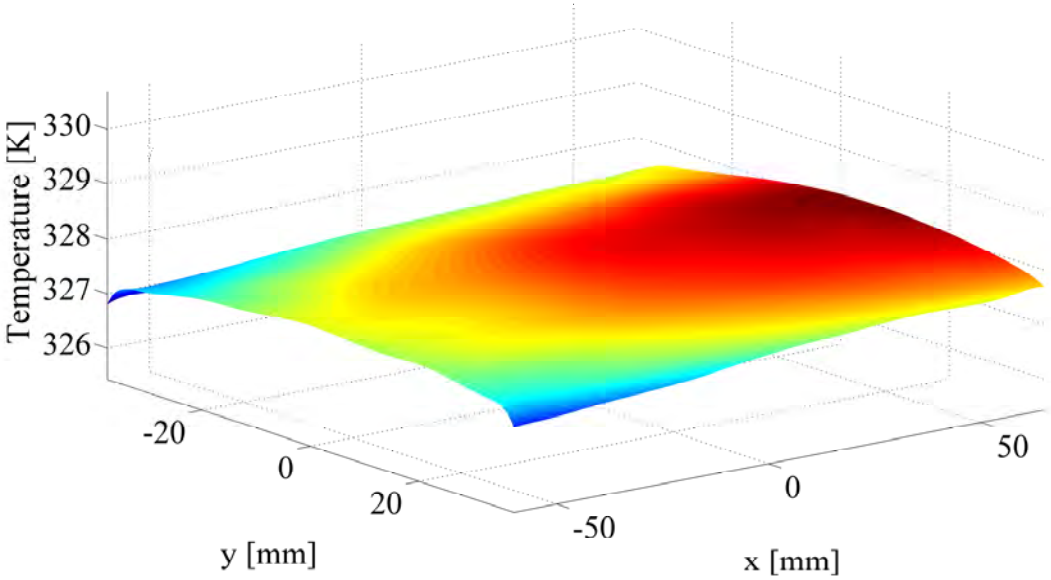


Figure 34 : 10th order Temperature Surface BiPolynomial Fit

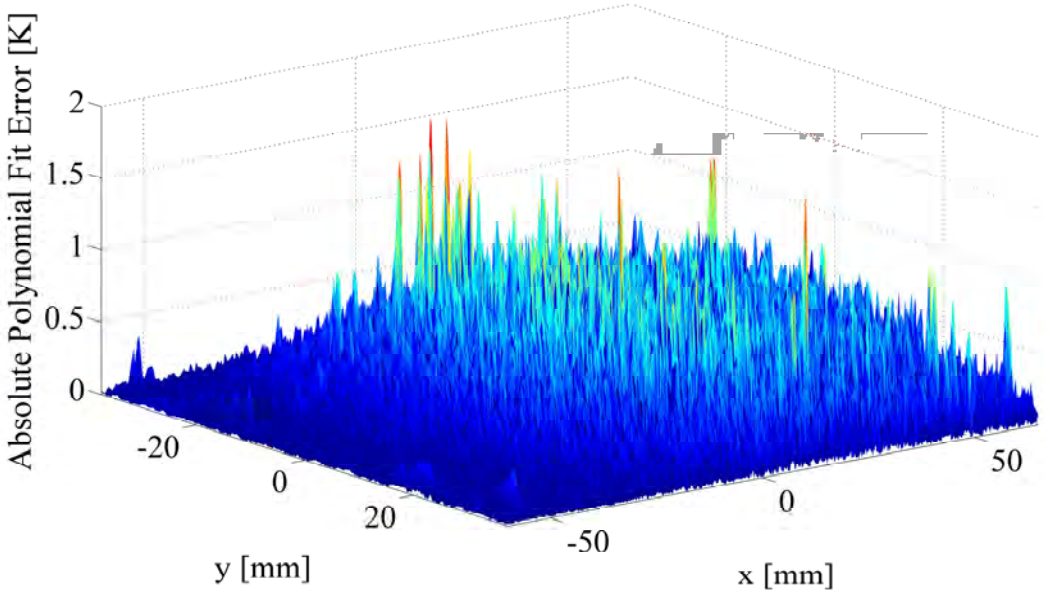


Figure 35 : Absolute Error due to Surface BiPolynomial Fit

Examining the temperature distribution along the centerline length-wise direction, it can be observed that the temperature in this region increases almost linearly towards the exit within the uncertainty limits, Figure 36. When this distribution is compared with the thermocouple measurements made along the slab, upstream (TC1, TC2, TC5) and downstream (TC10, TC13, TC14), along with a $4^{th}$ order polynomial fit through the thermocouple data, the Infrared Thermography data show good consistency Figure 37. The relative decrease in temperature observed by the last two downstream thermocouples is shown to be consistent through out the experimentation process and is believed to be due to the

length-wise edge effects of the channel Figure 37. At the very ends of the test section, since the metallic slab is in contact with the plexiglass inlet and exit sections, it is possible to have local heat sinks. This effect may have been further amplified by the excess Inconel foil sticking out from each side of the metallic slab, done intentionally to apply voltage in a uniform manner, acting as a local low temperature region on the uniform assumed imposed heat flux.

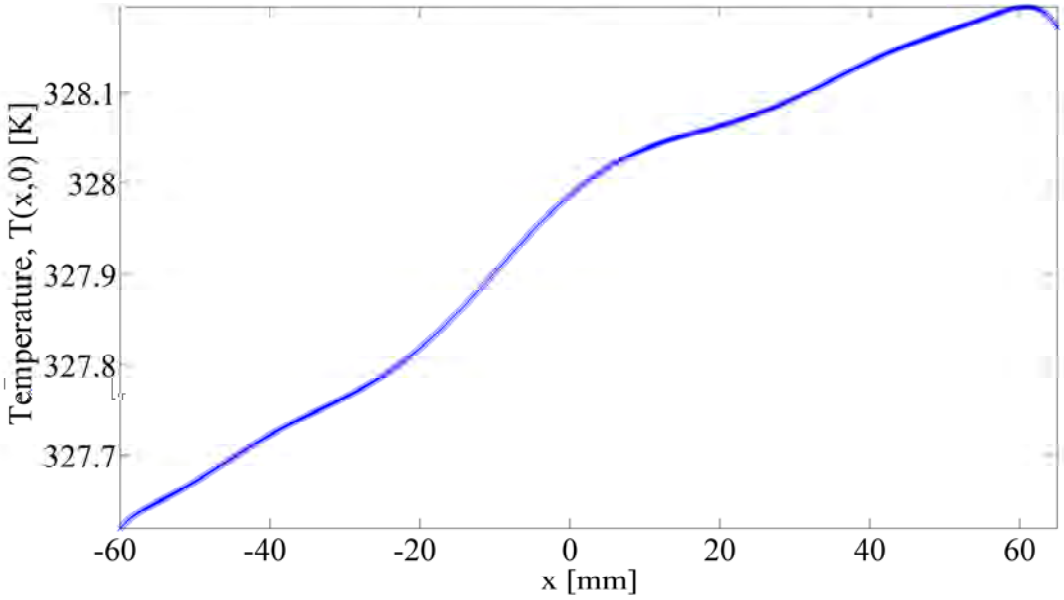


Figure 36 : The Longitudinal Temperature Distribution through the Slab center

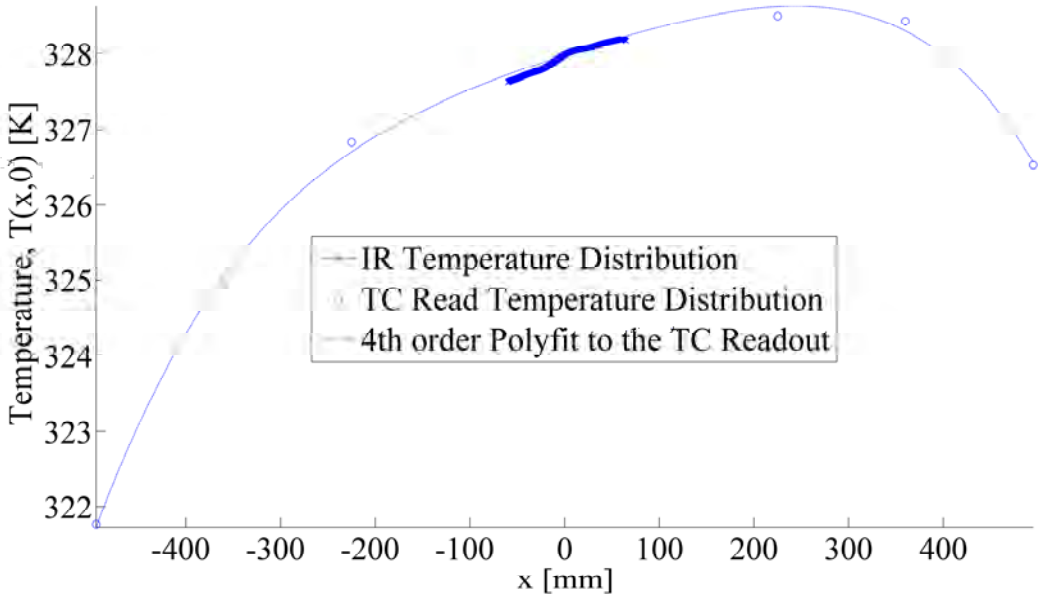


Figure 37 : The Longitudinal Temperature Distribution along the Centerline comparison with the 4$^{th}$ order Thermocouple Polynomial fit

Investigating the temperature differences in the width wise direction across the slab center point, T(0,y), and comparing the experimental data with the thermocouples placed equidistantly upstream (TC3, TC4, TC5, TC6, TC7) and downstream (TC8, TC9, TC10, TC11, TC12), temperatures measured by the infrared camera lie almost at the half way but closer to the downstream thermocouple measured temperatures, Figure 38. This is rational since the cooling effectiveness decreases as the thermal boundary layer develops and the local freestream temperature rises, resulting in higher temperatures, also observed in Figure 37. While the maximum temperatures are observed for the test section centerline, followed by a gradual decrease towards the side-walls, there exists a sudden drop in temperature at each edge of the channel, in the order of 0.7K with respect to the local mean. This plunge in temperature is believed to be due to the corner vortices formed at the edges of the channel, locally enhancing heat transfer.

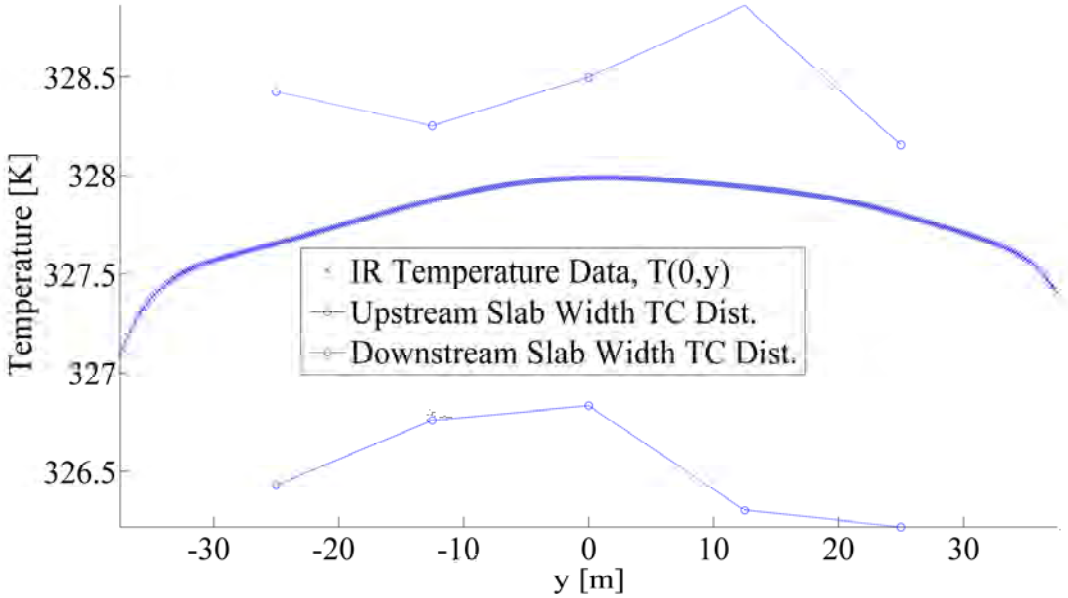


Figure 38 : The Widthwise Temperature Distribution along the center, T(0,y), compared with the upstream and downstream thermocouple data

The temperature profile in the width-wise direction is further investigated at 18 different length wise values, equidistant slices in the width-wise direction across the entire length observed by the camera, $T(x_i,y)$, Figure 39. When these temperatures are normalized by the local centerline temperature and multiplied by a global reference temperature, which in this case is the channel center point temperature, $T^{"}(x_i,y)=T(x_i,y)/T(x_i,0)\cdot T(0,0)$, it is observed that all the width-wise temperature profiles measured at different length-wise points collapse on one and another. This normalized temperature data is fitted with a $4^{th}$ order polynomial and the maximum deviation in the width wise direction is averaged across all location length-wise slices Figure 40. The average maximum deviation in this fitting procedure is 0.078K, and is believed to be due to the precision of the infrared measurements; the precision of infrared thermograph temperature measurements is calculated to be 0.18K.

This fitting procedure is non-error producing and results in a global temperature shape factor that can be utilized at a point where the channel centerline temperature is known.

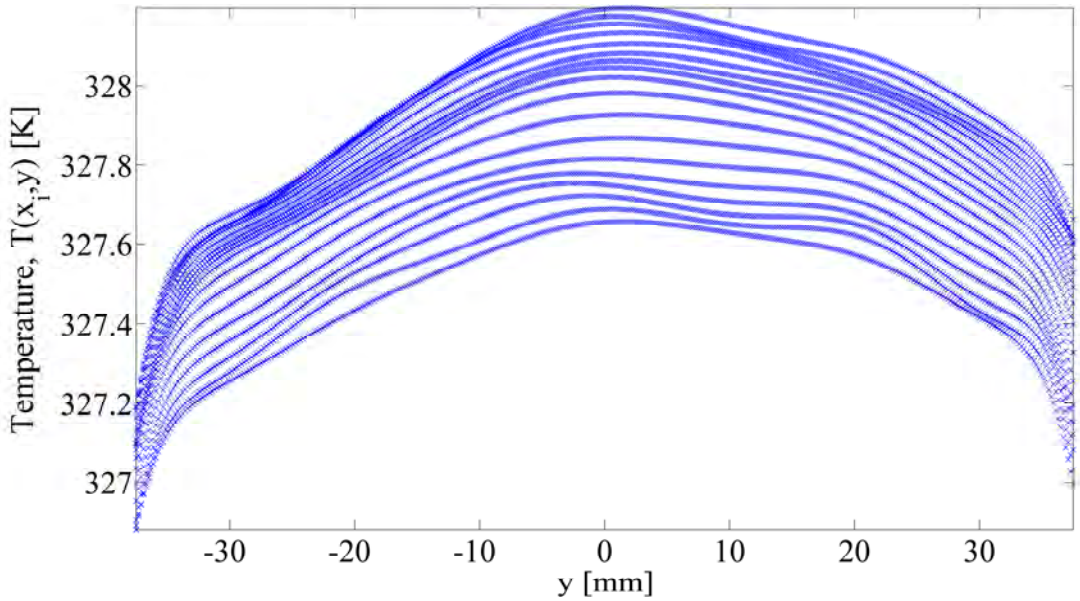


Figure 39: Width-wise Infrared Thermography Temperature Measurements at equidistant longitudinal slices, $T(x_i,y)$

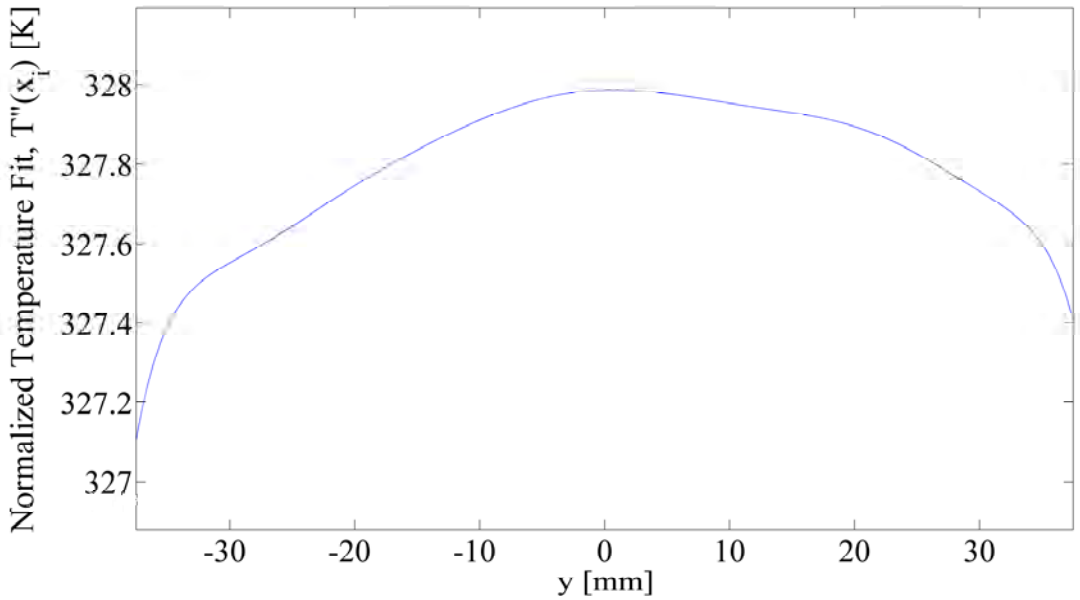


Figure 40: Normalized Width-wise Infrared Thermography Temperature Measurements for all Longitudinal points, $T^{*}(x_i, y)$

***b) Conjugate Temperature Distribution Comparison with Theoretical Convective Correlations***

For parallel turbulent flow over a flat plate, the local Nusselt number is a function of local Reynolds and the Prandtl numbers [Ref. B-11], $Nu_x = St \cdot \mathrm{Re}_x \cdot \mathrm{Pr} = 0.0308 \cdot \mathrm{Re}_x^{0.8} \cdot \mathrm{Pr}^{0.333}$ for 0.6< Pr <60. This correlation is derived for a uniform surface heat flux imposed over a flat plate, where there is convection over the top surface by parallel fully turbulent flow with no pressure gradients. As outlined in [Ref. B-14], this correlation is a consequence of assumed thermal and aero boundary layer shapes and computed through the use of integral boundary layer and energy balance solutions. There are several limitations to the applicability of this solution, one being the fact that under test conditions, the flow starts developing aerodynamically further upstream in the non-heated inlet section. Fortunately, this effect on Nusselt number can be corrected by an unheated length correlation, [Ref. B-11], $Nu_{x\xi} = Nu_x / \left(1 - \left(\xi / x\right)^{3/4}\right)^{1/3}$ ,where $\xi$ is the inlet unheated section length, 1400mm and x is calculated locally from the beginning of the inlet section. In this correlation, the unheated starting section, where x < $\xi$, is assumed to be at the same temperature as the air passing over it. Since the aero boundary layer starts developing prior to its thermal counter-part, such an effect augmenting Nusselt number on the surface is crucial for a descent comparison.

Some of the other assumptions imposed in the derivation of this correlation deviates from the test conditions, and they are harder to compensate for. As assumed for this correlation, under the test conditions, the flow over the slab is not fully turbulent, Reynolds number is out of the domain of $\mathrm{Re}<10^3$ or $\mathrm{Re}>10^6$, there is a favorable pressure gradient in the length wise direction due to classical Poiseuille flow, and all these have a significant effect on the thermal and aero boundary layer profile and thicknesses. To acquire more accurate relations, the equations may have to be re-derived for different aero and thermal boundary layer profiles. Also, the theoretical relations are derived for convection only, and it is important to note that the conjugate effects, thus the coupling with conduction is ignored. Thus, the theoretical surface temperature computed by the correlations is comparable with the data, only if it is to be assumed that the conduction through the slab is absolutely 1-D and the fact the channel is a square duct plays no role on the local aerodynamical phenomena. It is none-the-less still believed that the correlations are reasonable for purposes of comparison.

By using these theoretical correlations, the local temperature distribution can be estimated by use of the following equations, $\mathrm{Re}_{D_H} = 40000$, $\mathrm{Re}_x = \frac{\mathrm{Re}_{D_H}}{D_H} * x$, $h(x) = Nu_{xzeta_{UH}} * k_f / x$, $T_s(x) = T_\infty(x) + q_s^{"} / h(x)$, where $D_H$ = 75mm, $q_s^{"}$=1167W/m$^2$, $k_f$ [W/m-K] is the thermal conductivity of the fluid and is computed by the mean air temperature, $k_f$ = 1.5207E$^{-11}$*$\overline{T_\infty}^3$-4.8574E$^{-8}$*$\overline{T_\infty}^2$+1.0184E$^{-4}$*$\overline{T_\infty}$- 3.9333E$^{-4}$ , and $T_\infty(x)$ is estimated to be the air temperature calculated by the linear distribution of the mean test section inlet and exit temperatures, applied locally in the length-wise direction, $T_\infty(x) = \overline{T_{\infty_{inlet}}} + \frac{\overline{T_{\infty_{exit}}} - \overline{T_{\infty_{inlet}}}}{L_{slab}} * \left(x - \xi\right)$, $L_{slab} = 1260mm$.

Figure 41, illustrates the comparison between the centerline Infrared Thermography temperature data and the theoretical correlation. There seems to be good consistency between

the theoretical and empirical values, for the region where the data is acquired. For the theoretical correlation, as expected, the cooling effectiveness decreases in the length-wise direction due to the augmentation in thermal boundary layer thickness and the local freestream temperature.

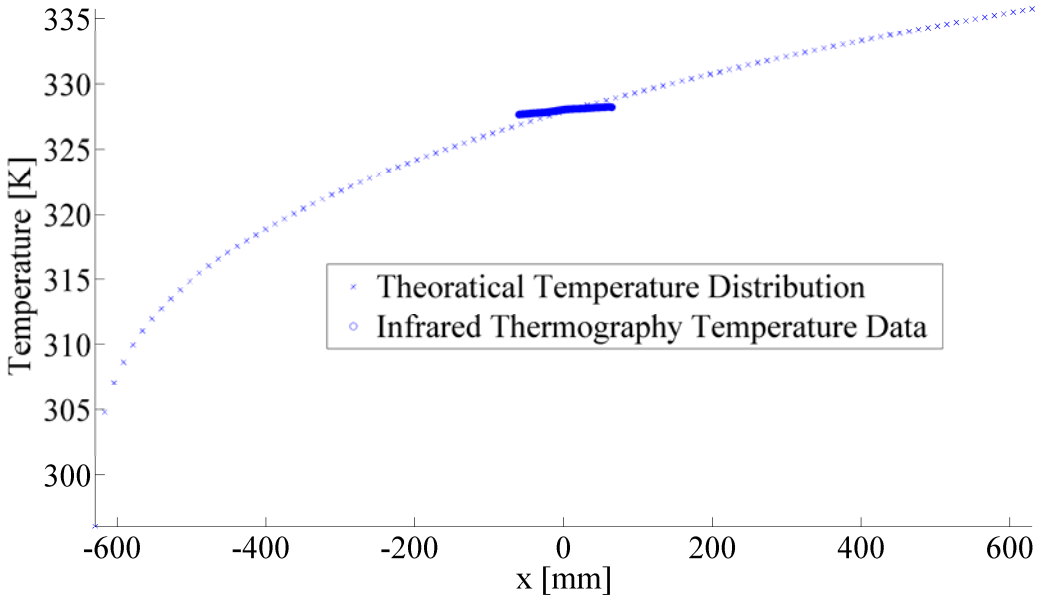


Figure 41: Theoratical and Experimental Temperature Distribution Comparison

### *c) Heat Transfer Rate Computation*

The boundary conditions for the numerical problem are uniform heat flux along the bottom surface of the slab, measured temperature distribution on the wetted surface, and adiabatic side walls. In the numerical model, the only modeled portion of the slab volume is where surface Infrared Thermography temperature measurements exist, Figure 42.

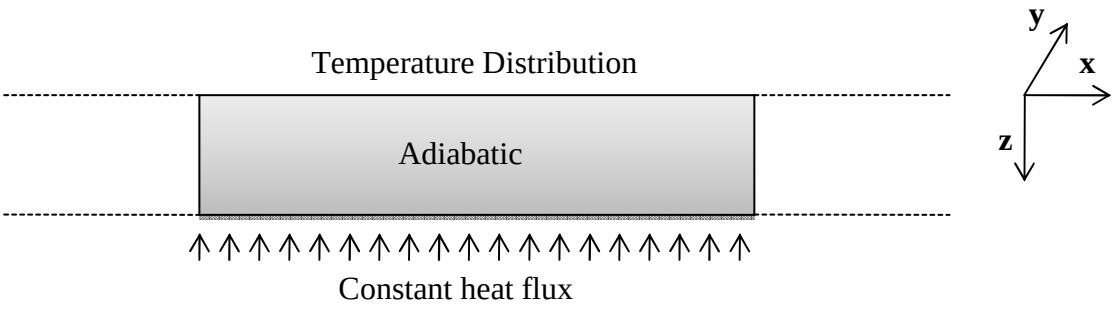


Figure 42 : COMSOL Model Schematic

The modeled portion of the slab is meshed with over 1.5million tetrahedral elements, which results in a maximum element size of 1.5mm and the edges are further refined to consist of nodes that maximum 0.1mm apart. The refinement of the edges is of special importance due to error propagation in the heat flux balance. The commercial code Comsol solves the 3-D Fourier equation through out the model to compute the temperature distribution at all directions, and for this case the convergence criteria is set to $10^{-10}$ for the relative pre-conditioned residuals. It has been shown that further grid refinement does not significantly affect the solution computed in the model.

Figure 43 shows the imposed heat flux at the bottom of the slab after the COMSOL iterations, which presents an opportunity to estimate the model's convergence. When the solution computed by the heat balance is compared with the imposed boundary condition at the bottom of the slab, the maximum deviation across the bottom surface is 0.01%.

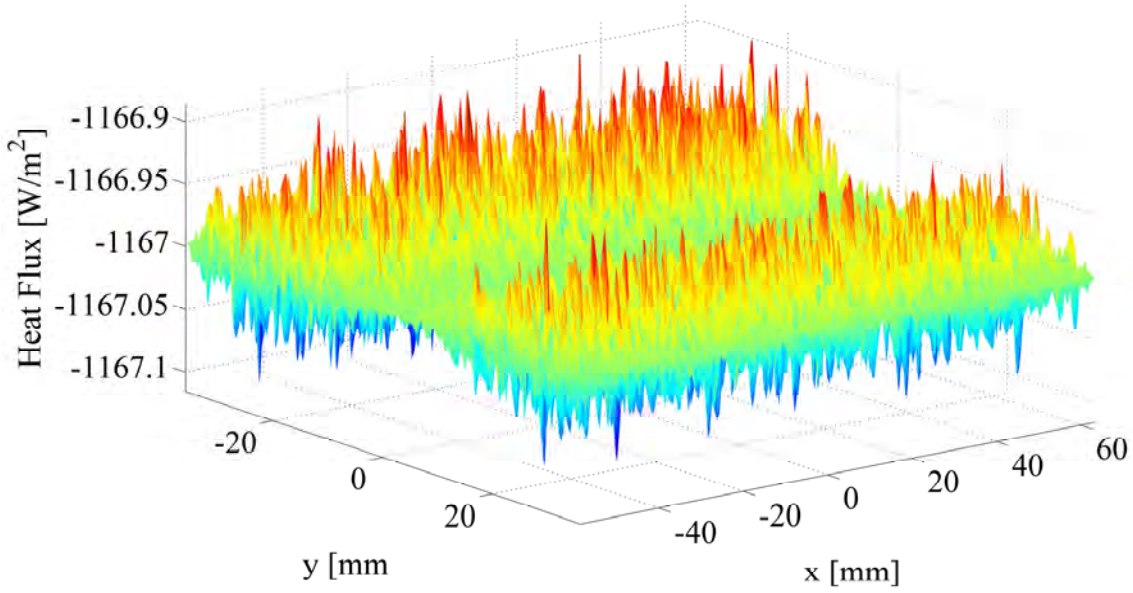


Figure 43: COMSOL Slab Bottom Heat Flux Distribution

Figure 44 is the distribution of heat-flux across the surface of the slab, where Infrared Thermography measurements are conducted, normalized by subtracting the bottom heat flux, $\left(q''_{top} - q''_{bottom}\right) / q''_{bottom}$. This parameterization allows the quantification of one dimensionality of the flow. It is observed that there are significant non-1D conduction effects even in a simple geometry such as this one, indicated by significant surplus of heat flux at the edges of the channel with respect to that expected if the conduction in the slab was assumed to be 1-D. Even though around the around the channel edges, the heat flux seems to be significantly higher locally, the deficit of heat flux is not concentrated specifically on a region but distributed across the rest of the slab.

The width (0,y) and length (0,x) wise normalized heat flux distributions can be seen in Figures 45 and 46 respectively. It is observed that the heat, through conduction in the slab, diffuses towards the edges and the local surface heat flux shows that the conduction from

bottom to top of the slab is not 1-D, and the error associated with such an assumption can be as high as 60% locally in the edges and in the order of 20% around the channel centerline. It is clear that the conjugate effects, conduction convection coupling, should not be ignored even for simple geometries such as the one experiments conducted upon.

From the results acquired from COMSOL, the heat transfer coefficient on the top surface is then computed by, $h(x,y) = q''_{top}(x,y)/\left(T(x,y) - T_\infty(x)\right)$, where $T_\infty(x)$ is estimated to be the air temperature calculated by the linear distribution of the mean test section inlet and exit temperatures, applied locally in the length-wise direction. In this experiment, the mean heat transfer coefficient is found to be 38.31 W/m$^2$-K.

By the known local heat transfer coefficient, h(x,y), Nusselt number distribution across the top surface can be computed as, $Nu = h(x,y) * D_h / k_f$, where $k_f$ is the thermal conductivity of air taken to be 0.026 [W/m-K] and $D_h$ =75mm is the hydraulic diameter of the channel. Figure 47 shows the local Nusselt number distribution across the slab and the mean value corresponds to $Nu_{mean}$=102.4±3.8.

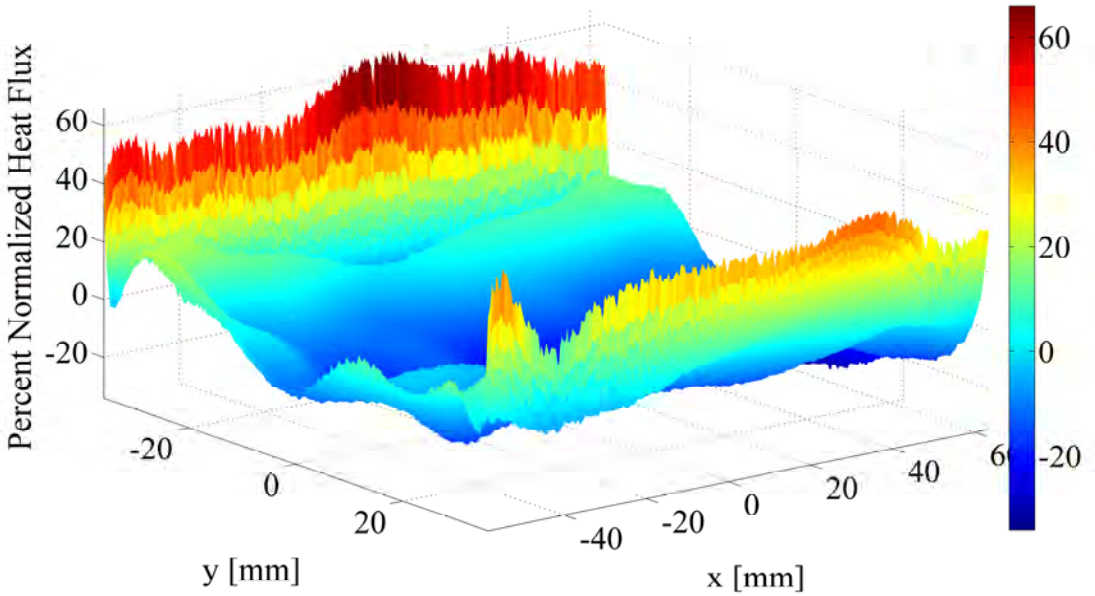


Figure 44: COMSOL Slab Top Heat Flux Distribution

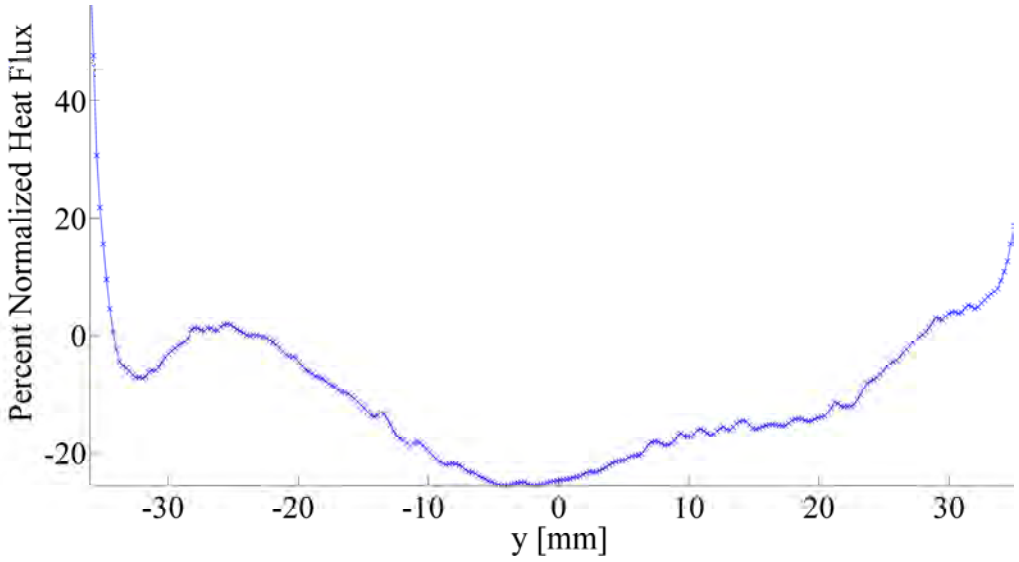


Figure 45: COMSOL Slab Top Heat Flux Distribution

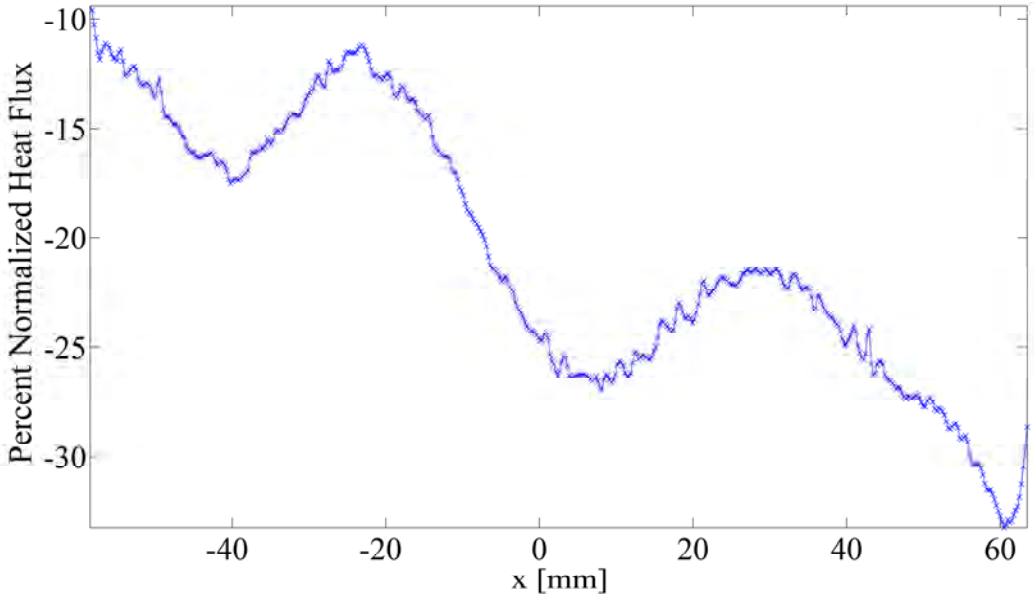


Figure 46: COMSOL Slab Top Heat Flux Distribution

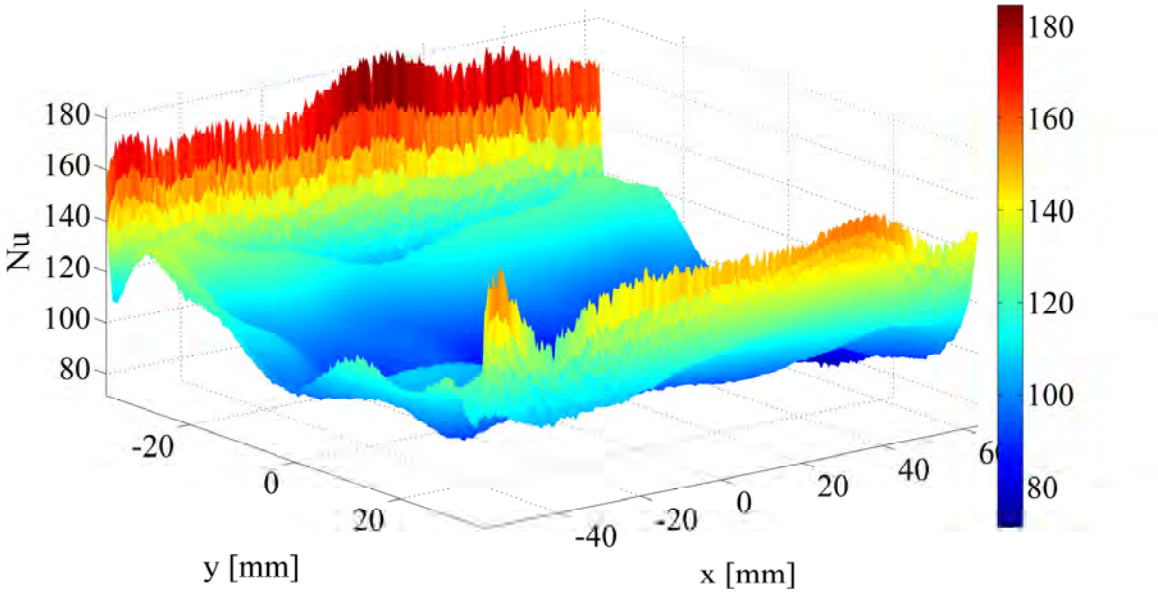


Figure 47: Distribution of Nusselt Number

It is of importance to compare the mean experimental Nusselt number with some preceding theoretical convective heat transfer correlations. The Dittus-Boelter Nusselt number correlation given in [Ref. B-11], which is validated by experiments conducted in circular tubes under fully developed turbulent forced convection, states that $Nu_D = 0.0243 \mathrm{Re}_D^{0.8} \mathrm{Pr}^{0.4}$, confirmed for $0.7 \le \mathrm{Pr} \le 160, \mathrm{Re}_D \ge 10000, L/D \ge 10$. For the test conditions, Pr is equal to 0.71, Re is equal to 40000 and the length to diameter ratio is much larger than 10, allowing the equation above to be used for comparison. The resulting Nusselt number is $\mathrm{Nu}_{theo}$=101.8 in good agreement with the measurements and well within the uncertainty of the experimental results, $\mathrm{Nu}_{mean}$=102.4±3.8.

# 18. . Conclusions for the Heat Transfer measurements on the Flat Plate

An experimental setup conducive to conducting transient and steady heat transfer measurements through Infrared Thermography has been developed. The experimental campaign successfully developed reliable means of Nusselt number characterization in shoeboxes. Conjugate heat transfer experiments have been over a flat plate.

The temperature measurements on the top portion of the slab indicated that the width-wise temperature distribution can be normalized by the local centerline temperature, and all temperature profiles collapse into a single curve within the uncertainty of the measurements. In the length-wise direction, the temperature data appeared to be close to linear within the error bounds and the infrared measured temperatures are shown to be in good agreement with

both the convective theoretical calculations as well as the thermocouple temperature readout acquired along the channel.

It is observed that the surface heat flux, through conduction in the slab, diffuses towards the edges and that the conduction from bottom to top of the slab is not 1-D, and the error associated with such an assumption can be as high as 60% locally in the edges and in the order of 20% around the channel centerline. It is clear that the local conjugate effects, conduction convection coupling, should not be ignored even for simple geometries such as the one experiments conducted upon. The experimental Nusselt number distribution is estimated within an uncertainty of 3.7% and the mean value is in good agreement with the theoretical correlations.

In the experiments conducted for the flat plate, the local heat transfer phenomena (the distribution of surface heatflux and Nusselt number) seems to be highly influenced by the existence of the slab and thus the effects of conduction, but the mean heat transfer does not seem to be as susceptible to the conjugate phenomena for this configuration, indicated clearly by the close agreement with convective correlations.

# 19. References for the Flat Plate Heat Transfer

B-1 Nirmalan N.V., Bunker R.S., Hedlund C.R. "The measurement of full-surface internal heat transfer coefficients for turbine airfoils using a non-destructive thermal inertia technique" GE R&D centre, Technical information series, 2002GRC010, February 2002

B-2. SCHEIMAN, J.; BROOKS, J.D., "Comparison of experimental and theoretical turbulence reduction from screens, honeycomb and honeycomb-screen combinations" J. Aircraft 18, 638 and NASA TP 1958

B-3. Bejan, A., Kraus, A.D., "Heat Transfer Handbook" John Wiley & Sons, 2003

B-4. Fox, R.W., McDonald, A.T., Pritchard, P.J., "Introduction to Fluid Mechanics" John Wiley & Sons, 2003

B-5. Panton, R.L, "Incompressible Flow" Wiley-Interscience, 1996

B-6. Fedrizzi, R., "Aero-thermal investigation of rib-roughened internal cooling channels" VKI, Project report 2003-10, June 2003

B-7. Çakan, M., "Aero-thermal investigation of rib-roughened internal cooling passages" VKI, Phd Thesis, July 2000

B-8. Casarsa, L., "Aerodynamic performance investigation of a fixed rib-roughened internal cooling passage" VKI, Phd Thesis, July 2003

B-9. Lin, S.S, "Review: extending visible band computer vision techniques to infrared band Images," Technical Report MS-CIS-01-04, GRASP Laboratory, Pennsylvania

B-10. Schulz, A., "Infrared Thermography as applied to film cooling of gas turbine components"
Measurement Science Technology, 2000, vol. 11, n$^{o}$ 7, pp. 948-956

B-11. Incropera, F.P., DeWitt, D.P, "Fundamentals of Heat and Mass Transfer", John Wiley & Sons, 2007.

B-12. White, F.M., "Viscous Fluid Flow" New York: McGraw-Hill, 1974.

B-13. Carlomagno, G.M., de Luca, L., "Infrared Thermography for Flow Visualization and Heat Transfer Measurements," presented at the International Conference on Engineering Education, 1998.

B-14. Kays, W., Crawford, M., Weigand, B., "Convective Heat and Mass Transfer," McGraw-Hill, 2005

B-15. Rabin Y., "A general model for the propagation of uncertainty in measurements into heat transfer simulations and its application to cryosurgery," Cryobiology, 2003, vol. 46, n$^{o}$2, pp. 109-120

# 20. Uncertainty Analysis

The precision and accuracy of the measurements are two separate issues. Precision is based on measurement repeatability and is affected mostly by the data processing and handling. On the other hand, the degree to which the data represent the actual physics of the process is determined by the accuracy. Measurement uncertainty is a function of both precision and accuracy. For a three parameter model, an uncertainty estimate can be given by,

$$\delta V = \left[ \left( \frac{\partial V}{\partial x_1} \delta x_1 \right)^2 + \left( \frac{\partial V}{\partial x_2} \delta x_2 \right)^2 + \left( \frac{\partial V}{\partial x_3} \delta x_3 \right)^2 \right]^{1/2}$$ ,where $x_1$, $x_2$, $x_3$ are the independent variables.

### *a) Uncertainty of Pressure Measurements*

The pressure is measured by means of a Validyne Model Dp10 pressure transducer that is capable of measuring a maximum pressure differential of 22.5 [mm H2O] = 220.7 Pa. The calibration is done by means of a water monometer with an increment of 0.1 [mm H2O] = 9.8 Pa. The calibration curve of the pressure transducer is calculated to be $P = (\Delta P / \Delta V) V + P_0 = 16.06V - 1.23Pa$. The pressure measurements have three sources of uncertainty,

$$\delta P = \left[ \left( \frac{\partial P}{\partial \left( \frac{\partial P}{\partial V} \right)} \right)^2 \left( \delta \left( \frac{\partial P}{\partial V} \right) \right)^2 + \left( \frac{\partial P}{\partial V} \right)^2 (\delta V)^2 + \left( \frac{\partial P}{\partial P_0} \right)^2 (\delta P_0)^2 \right]^{0.5}$$ , which simplifies to, $\delta P = \left[ V^2 \left( \delta \left( \frac{\partial P}{\partial V} \right) \right)^2 + \left( \frac{\partial P}{\partial V} \right)^2 (\delta V)^2 + (\delta P_0)^2 \right]^{0.5}$. The error on the slope, $\delta \frac{\Delta P}{\Delta V}$, can be derived as,

$$\delta \frac{\Delta P}{\Delta V} = \left[ \left( \frac{\partial \frac{\Delta P}{\Delta V}}{\partial \Delta P} \right)^2 \delta (\Delta P)^2 + \left( \frac{\partial \frac{\Delta P}{\Delta V}}{\partial \Delta V} \right)^2 \delta (\Delta V)^2 \right]^{0.5},$$

$$\delta \frac{\Delta P}{\Delta V} = \left[ \left( \frac{1}{\Delta V} \right)^2 \delta (\Delta P)^2 + \left( \frac{-\Delta P}{(\Delta V)^2} \right)^2 \delta (\Delta V)^2 \right]^{0.5}$$. In the experiments, the nominal differential pressure is in the order of 40.4 Pa, $\Delta P = 40.4Pa$. Given the calibration curve, this value corresponds to a voltage of $V = \Delta V = 2.59$. Considering that the maximum uncertainty on the reading from the water monometer is 0.1mm $H_2O$, thus $\delta(\Delta P) = \delta P_0 = 0.1mm\ H_2O = 0.97Pa$,

and the discretization error associated with the 16-bit A/D board, NI 6251, over a span of 10 V is , then the total uncertainty of pressure can be estimated as $\delta P = 1.40 Pa$ , or $\frac{\delta P}{P} = 3.47\%$.

In this uncertainty computation, it can be seen that the discretization error contribution is two orders of magnitude smaller than the other contributors. Note that the mean deviation from linearity from the calibration curve is 0.35Pa. That empirically calculated uncertainty for pressure is within the theoretically calculated bounds. Comparing the uncertainty values found empirically and theoretically, the theoretical error estimation seems to be an upper bound on estimated error but is none the less used for consistency.

### *b) Uncertainty of Thermocouple Temperature Measurements*

The temperature is measured by means of T-type thermocouples. The calibration is done in an oil bath by means of a thermometer with an increment of 0.1 K. An exemplary calibration curve is $T = \frac{\Delta T}{\Delta V} V + T_0 = 9.50V + 272.73K$ . The temperature measurements have three sources of uncertainty,

$$\delta T = \left[ \left( \frac{\partial T}{\partial \left( \frac{\partial T}{\partial V} \right)} \right)^2 \left( \delta \left( \frac{\partial T}{\partial V} \right) \right)^2 + \left( \frac{\partial T}{\partial V} \right)^2 (\delta V)^2 + \left( \frac{\partial T}{\partial T_0} \right)^2 + (\delta T_0)^2 \right]^{0.5}$$ , which simplifies as

$$\delta T = \left[ V^2 \left( \delta \left( \frac{\partial T}{\partial V} \right) \right)^2 + \left( \frac{\partial T}{\partial V} \right)^2 (\delta V)^2 + (\delta T_0)^2 \right]^{0.5}$$ . The error on the slope, $\delta \frac{\Delta T}{\Delta V}$ can be derived as,

$$\delta \frac{\Delta T}{\Delta V} = \left[ \left( \frac{\partial \frac{\Delta T}{\Delta V}}{\partial \Delta T} \right)^2 \delta (\Delta T)^2 + \left( \frac{\partial \frac{\Delta T}{\Delta V}}{\partial \Delta V} \right)^2 \delta (\Delta V)^2 \right]^{0.5},$$

$$\delta \frac{\Delta T}{\Delta V} = \left[ \left( \frac{1}{\Delta V} \right)^2 \delta (\Delta T)^2 + \left( \frac{-\Delta T}{(\Delta V)^2} \right)^2 \delta (\Delta V)^2 \right]^{0.5}$$ . An estimate of the thermocouple temperature uncertainty can be done with the following quantities; the maximum uncertainty on the thermometer reading is 0.1K, $\delta(\Delta T) = \delta T_0 = 0.1K$ ; and the discretization error associated with the 16-bit A/D board, NI 6251, over a span of 10 V is $\delta V = \delta(\Delta V) = 0.000150V$.

***For Thermocouples Located in the Slab:***

The nominal temperature reading in the slab throughout the experiments is approximately 330K. This corresponds to a nominal voltage of V = 6.04, temperature differential of $\Delta T = 40K$ and voltage differential of $\Delta V = 3.86$ and from which the uncertainty can be computed to be $\delta T = 0.18K$ .

***For Thermocouples Located at the Inlet and Exit Sections Measuring Air Temperature:***

The temperature of the air during the experiments is approximately 297K. Applying the same procedure, it is found that the uncertainty is in the order of $\delta T = 0.19K$ .

In this uncertainty computation, it can be seen that the discretization error contribution is two orders of magnitude smaller than the other contributors. Note that the mean deviation from linearity from the calibration curve is 0.15K. The empirically calculated uncertainty for temperature is within the theoretically calculated bounds described above.

## *c) Uncertainty of Reynolds number*

The Reynolds number is defined by, $\mathrm{Re} = \frac{\rho u D_h}{\mu}$. Thus the uncertainty on Reynolds number can be estimated,

$$\delta \mathrm{Re} = \left[ \left( \frac{\partial \mathrm{Re}}{\partial \rho} \right)^2 (\delta\rho)^2 + \left( \frac{\partial \mathrm{Re}}{\partial u} \right)^2 (\delta u)^2 + \left( \frac{\partial \mathrm{Re}}{\partial D_h} \right)^2 (\delta D_h)^2 + \left( \frac{\partial \mathrm{Re}}{\partial \mu} \right)^2 (\delta\mu)^2 \right]^{0.5}$$ , which simplifies as $\delta \mathrm{Re} = \mathrm{Re} \left[ \left( \frac{\delta\rho}{\rho} \right)^2 + \left( \frac{\delta u}{u} \right)^2 + \left( \frac{\delta D_h}{D_h} \right)^2 + \left( \frac{-\delta\mu}{\mu} \right)^2 \right]^{0.5}$ .

***Uncertainty of Density:***

The density is computed with the ambient pressure and temperature, $\rho = \frac{P_{amb}}{RT_{amb}}$. Thus the uncertainty on density can be estimated as,

$$\delta\rho = \left[ \left( \frac{\partial\rho}{\partial P_{amb}} \right)^2 (\delta P_{amb})^2 + \left( \frac{\partial\rho}{\partial T_{amb}} \right)^2 (\delta T_{amb})^2 \right]^{0.5}$$ , which simplifies to

$$\delta\rho = \left[ \left( \frac{\delta P_{amb}}{RT_{amb}} \right)^2 + \left( \frac{-P_{amb}}{RT_{amb}} \delta T_{amb} \right)^2 \right]^{0.5}$$ . The nominal pressure, nominal temperature, and nominal density values are, $P_{amb} = 101000\ [Pa]$, $T_{amb} = 293.45[K]$, $\rho = 1.199\ [kg/m^3]$ respectively. An estimate of the uncertainty can be done considering the maximum uncertainty on the thermometer reading is $\delta T_{amb} = 0.1K$ , and the reading of the atmospheric pressure is done by a reference pressure transducer and the maximum uncertainty provided by the manufacturer is P = 10 [Pa]. These result in a cumulative uncertainty of $\delta\rho = 0.00414[kg/m^3]$, or $\frac{\delta\rho}{\rho} = 0.35\%$.

***Uncertainty of Mean Channel Velocity Based on Total Pressure:***

Using Bernouilli's equation, the velocity can be computed as, $u = \left[2\frac{P_{tot}}{\rho}\right]^{0.5}$. Thus the velocity uncertainty can be estimated as, $\delta u = \left[\left(\frac{\partial u}{\partial P_{tot}}\right)^2 (\delta P_{tot})^2 + \left(\frac{\partial \rho}{\partial \rho}\right)^2 (\delta \rho)^2\right]^{0.5}$,

$\delta u = \left[\left(\frac{1}{(2P_{tot}\rho)^{0.5}}\right)^2 (\delta P_{tot})^2 + \left(-\left(\frac{P_{tot}}{2\rho^2}\right)^{0.5}\right)^2 (\delta \rho)^2\right]^{0.5}$. The nominal velocity, total pressure and density are, $u = 8.21 m/s$, $P_{tot} = 40.4[Pa]$, $\rho = 1.199[kg/m^3]$ respectively. An estimate of the uncertainty can be done with the computed quantities such as the uncertainty of the total pressure, $\delta P_{tot} = 1.40[Pa]$ and uncertainty of the density, $\delta \rho = 0.00414[kg/m^3]$. Using the parameters, the mean channel velocity uncertainty can be estimated as $\delta u = 0.14[m/s]$, or $\frac{\delta u}{u} = 1.75\%$.

***Uncertainty of Hydraulic Diameter:***

The hydraulic diameter is defined as the following, $D_h = \frac{4S}{P}$, where P and S are the cross-sectional perimeter and area respectively. The cross-section of the channel is a square with each side of length x, $S = x^2$, and $P = 4x$. Thus the uncertainty on the hydraulic diameter can be estimated as $\delta D_h = \left[\left(\frac{\partial D_h}{\partial S}\right)^2 (\delta S)^2 + \left(\frac{\partial D_h}{\partial P}\right)^2 (\delta P)^2\right]^{0.5}$, which simplifies to

$\delta D_h = \left[\left(\frac{4}{P}\delta P\right)^2 + \left(-\frac{4S}{P^2}\delta P\right)^2\right]^{0.5}$. The uncertainties on the area and the perimeter can be derived such as , $\delta S = \left[\left(\frac{\partial S}{\partial x}\right)^2 \delta x^2\right]^{0.5}$, $\delta S = 2x\delta x$, and $\delta P = \left[\left(\frac{\partial P}{\partial x}\right)^2 \delta x^2\right]^{0.5}$, $\delta P = 4\delta x$. Considering the fact that the length of each side is equal to x = 75 [mm] and, uncertainty associated with the ruler reading is $\delta x = 0.5[mm]$, the total uncertainty on the hydraulic diameter is $\delta D_h = 1.12[mm]$, or , $\frac{\delta D_h}{D_h} = 1.49\%$.

***Uncertainty of Dynamic Viscosity:***

The dynamic viscosity is computed with the Sutherland's correlation, $\mu = \mu_0 \left( \frac{T}{T_0} \right)^{3/2} \frac{T_0 + S}{T + S}$, where $\mu_0 = 17.16\ 10^{-6} [Pa\ s]$, $T_0 = 273.15[K]$, $S = 110.4[K]$. The uncertainty on the dynamic viscosity can be estimated as, $\delta\mu = \frac{\partial \mu}{\partial T} \delta T$,

$\delta\mu = \frac{\mu_0 (T_0 + S)}{T_0^{3/2}} \left( \frac{1.5 T^{1/2} (T + S) - T^{3/2}}{(T + S)^2} \right) \delta T$. With the following nominal values, T = 293.35 [K] and an uncertainty of the thermometer reading of $\delta(\Delta T) = 0.1K$, the dynamic viscosity uncertainty is computed to be $\delta\mu = 1.81E^{-5} [Pa\ s]$

***Computation of Reynolds Number Uncertainty:***

The uncertainty on the Reynolds number can be approximated as ,

$$\delta \mathrm{Re} = \mathrm{Re} \left[ \left( \frac{\delta\rho}{\rho} \right)^2 + \left( \frac{\delta u}{u} \right)^2 + \left( \frac{\delta D_h}{D_h} \right)^2 + \left( \frac{-\delta\mu}{\mu} \right)^2 \right]^{0.5}$$ , $\delta \mathrm{Re} = 928.6$, or $\frac{\delta \mathrm{Re}}{\mathrm{Re}} = 2.3\%$.

The major contributors to the uncertainty on the Reynolds number are velocity and the hydraulic diameter. Note that the mean deviation of the Reynolds number during measurements is 230. The empirically calculated uncertainty for Re is within the theoretically calculated bounds described above. Comparing the uncertainty values found empirically and theoretically, the theoretical error estimation seems to be an upper bound on estimated error but is none the less used for consistency.

## *d) Uncertainty of Slab Surface Temperature Measured by Infrared Thermography*

The uncertainty of slab surface IR Thermography temperature measurements, $T_{wall}$, is mainly affected by 6 factors: the presence and the temperature of the optical film, $T_{wall,film}$, the assumption of width-wise temperature uniformity during IR camera calibration, $T_{wall,calib}$, the uncertainty of the slab thermocouples, $T_{wall,TC}$, the error introduced by the deviation of data points from the second order polynomial, $T_{wall,fit}$, the variation of object signal among the 30 images taken during measurements, $T_{wall,OS}$, and the error introduced by the 10th order bipolynomial fit on the $T_{wall}$ measurements, $T_{wall,10thorderfit}$. The uncertainty on $T_{wall}$ can be estimated as, $\delta T_{wall} = \left[ \delta T_{wall,\,film}^2 + \delta T_{wall,calib}^2 + \delta T_{wall,TC}^2 + \delta T_{wall,\,fit}^2 + \delta T_{wall,OS}^2 + \delta T_{wall,10tharderfit}^2 \right]^{0.5}$. The ambient temperature is approximately $T_{amb}$ = 20.3 C = 293.45 K and the nominal test slab temperature is $T_{operating}$ = 328 K.

***Due to Film Temperature Variation, $T_{wall,film}$***

The temperature difference of the film during the calibration and the data acquisition is measured to be approximately 1 K. Through experimentation, it is observed that the resulting variation of object signal corresponds to a apparent slab temperature deviation of 0.2 K, thus uncertainty due film temperature variation can be estimated as, $\delta T_{wall,\,film} = 0.2K$.

***Due to Width-wise temperature non- uniformity during the IR camera calibration $T_{wall,calib}$***

At a given calibration point, the uncertainty is the mean absolute difference between the linear fit used as the imposed temperature gradient across the slab and the temperatures measured by the 5 x 2 width-wise distributed thermocouples. This width-wise non-uniformity error is further averaged among all temperature calibration points and is estimated to be $\delta T_{wall,calib} = 0.10K$ .

***Due to Uncertainty of the Thermocouple measurements, $T_{wall,TC}$***

The uncertainty on the thermocouple measurements has been previously determined for the nominal ambient and operating temperatures as $\delta T_{wall,TC} = 0.18K$ .

***Due to Fitting of the calibration curve, $T_{wall,fit}$***

This uncertainty can be quantified as the average of the absolute difference between the calibration points and the calibration curve. The maximum allowed spatially averaged deviation from the polynomial fit is $\delta T_{wall,fit} = 0.10K$ .

***Due to Variation of Object Signal, $T_{wall,OS}$***

The object signal is a function of $OS = f(x, y, T, n)$, where (x,y) is the spatial location, T is the temperature of the surface, n is the image number from 1 to 30 out of the 30 images acquired at each data set point. The uncertainty quantified is the variation of the object signal among the 30 images. For each pixel (i.e. (x,y) = constant) at a given temperature (i.e. T is constant), the object signal is a function of n only, $OS = f(n)$,

$$\Delta OS = \frac{\sum_{i=1}^{n_0=30} abs\left( OS(i) - \frac{\sum_{j=1}^{n_0=30} OS(j)}{n_0} \right)}{n_0}$$

. This value is then spatially averaged for each temperature, and finally, meaned over all acquired temperatures. The resulting OS variation is $\Delta OS = 3.2$ . The second order component of the calibration curve is 5 orders of magnitude smaller than the first order component. Thus, it can be ignored for the purpose of the uncertainty analysis. A representative first order value of the polynomial fit is 0.018 K/OS. And the uncertainty on $T_{wall,OS}$ is $\delta T_{wall,OS} = 0.058K$ .

***Due to the 10th order bipolynomial fitting, $T_{wall,10thorderfit}$***

The contribution of $T_{wall;10thorderfit}$ results from the spatially averaged absolute deviation in slab temperature from the 10th order bipolynomial surface fit and is in the order of $\delta T_{wall,10tharderfit} = 0.15K$ .

***Computation of the uncertainty on $T_{wall}$***

The total uncertainty of $T_{wall}$ is computed to be $\delta T_{wall} = 0.34K$ . Note that the five sources of uncertainty that compose the cumulative uncertainty over $T_{wall}$ are all in the same order of magnitude.

***Relative Uncertainty of temperature from one pixel to another***

The relative uncertainty of temperature from one pixel to another is a matter of the precision of the wall temperature measurements, which can also be interpreted as the relative accuracy from one pixel to another. The two sources of uncertainty on the wall temperature measurements are the 10th order bipolynomial fit, and the width-wise averaging applied to the linear temperature profile for the calibration of the IR camera. And it can be estimated as, $\delta T_{wall,relative} = 0.18$ K.

## *e) Uncertainty of Heat Flux Imposed at the Bottom of the Slab*

The bottom heat flux is computed as $q = \frac{VI}{A}$. The uncertainty of the slab bottom heat flux is

$$\delta q = \left[ \left( \frac{\partial q}{\partial V} \right)^2 (\delta V)^2 + \left( \frac{\partial q}{\partial I} \right)^2 (\delta I)^2 + \left( \frac{\partial q}{\partial A} \right)^2 (\delta A)^2 + \left( \frac{\partial q}{\partial q_{loss}} \right)^2 (\delta q_{loss})^2 \right]^{0.5},$$

$$\delta q = \left[ \left( \frac{I}{A} \right)^2 (\delta V)^2 + \left( \frac{V}{A} \right)^2 (\delta I)^2 + \left( \frac{-VI}{A^2} \right)^2 (\delta A)^2 \right]^{0.5}$$ . The nominal voltage, current and area values are $V = 10.70[V]$, $I = 12.92[A]$, $A = 0.1176$ $[m^2]$ respectively; resulting in a nominal heat flux of $q = 1175.16$ [W/m$^2$]. An estimate of the uncertainty can be done with the following quantities:

The discretization error associated with the 16-bit A/D board, NI 6251, over a span of 10 V is $\delta V = \delta(\Delta V) = 0.000150V$ . The current is evaluated with the current-voltage calibration curve experimentally determined by a shunt. The mean deviation of the current is $\delta I = 0.002A$ . The uncertainty of the area can be determined as $A = LW$ , $\delta A = \left[ \left( \frac{\partial A}{\partial L} \right)^2 (\delta L)^2 + \left( \frac{\partial A}{\partial W} \right)^2 (\delta W)^2 \right]^{0.5}$ ,

$\delta A = \left[ (W)^2 (\delta L)^2 + (L)^2 (\delta W)^2 \right]^{0.5}$ .The nominal length and width values are W = 75 [mm], L = 1568 [mm] respectively. And the uncertainty of the ruler reading is $\delta W = \delta L = 0.5[mm]$. Thus, the uncertainty of the heat flux imposed at the bottom of the slab is computed to be $\delta q = 0.006676$ $W/m^2$ , or $\frac{\delta q}{q} = 0.6671\%$ .

## *f) Uncertainty of the heat transfer coefficient*

The heat transfer coefficient is defined by $h = \frac{q_{top}}{T_{wall} - T_{bulk}}$, where $q_{top}$ is the heat flux at the top surface. The bulk temperature increases toward the exit and is approximated by a

linear fit, $T_{bulk} = \frac{T_e - T_i}{L} x + T_i$, where $T_i$ and $T_e$ are the mean inlet and mean exit air temperatures respectively . With this approximation, the heat transfer coefficient definition reduces to $h = \frac{q_{top}}{T_{wall} - \left( \frac{T_e - T_i}{L} x + T_i \right)}$, resulting in an uncertainty equation such as

$\delta h = \left[ \left( \frac{\partial h}{\partial q_{top}} \right)^2 (\delta q_{top})^2 + \left( \frac{\partial h}{\partial T_{wall}} \right)^2 (\delta T_{wall})^2 + \left( \frac{\partial h}{\partial T_i} \right)^2 (\delta T_i)^2 + \left( \frac{\partial q}{\partial T_e} \right)^2 (\delta T_e)^2 \right]^{0.5}$. The nominal quantities for heat flux imposed at the bottom of the slab, temperature of the slab, temperature of the air at the inlet cross section, temperature of the air at the exit cross section, the distance between the inlet and exit thermocouple measurement locations, and the relative position of the center point of the slab are $q_{top} = 1178\ W/m^2$, $T_{wall} = 330K$, $T_i = 296.09K$, $T_e = 297.91K$, $L = 1260\ mm$, $x = 632.5\ mm$ respectively.

***Evaluation of*** $\frac{\partial h}{\partial q_{top}} \delta q_{top}$

Considering this partial derivative, $\frac{\partial h}{\partial q_{top}} \delta q_{top} = \delta q_{top} / \left( T_{wall} - \left( \frac{T_e - T_i}{L} x + T_i \right) \right)$, the only unknown is $\delta q_{top}$. The heat flux at the top surface results from a numerical computation which is performed using quantities directly measured, the wall temperature and the heat flux at the bottom of the slab. A way to estimate the propagation of measurement uncertainty into a mathematical solution is outlined in [Ref. 15]. Rabin indicates that three elements are required in order to simulate heat transfer in a specific problem, which consists of a thermal model of heat transfer, most commonly presented in the form a differential equation, a numerical technique for translating the thermal model into a numerical scheme and a list of numerical values for all the thermal model parameters. Translating the physical model into a numerical solution is also associated with some level of uncertainty. This uncertainty results from numerical discretization of the mathematical model, stability and convergence of the solution and round off errors in computer calculations. Following the method presented by Rabin [Ref. 15], and considering a solution at a given location in space depends on parameters ($p_i$), $q_0 \equiv q(x, y, z) = q(p_1, p_2, ..., p_i, ... p_n)$, let another solution obtained at the same location, using the same values for all parameters with the exception of a perturbed parameter, $p_i = p_i + \delta p_i$, $q_0^{'} \equiv q(x, y, z) = q(p_1, p_2, ..., p_i + \delta p_i, ... p_n)$. The last equation represents a series of n solutions, each with the variation of a different model parameter and the difference with the original unperturbed equations gives an estimate on the sensitivity of the model to each of the variables. The partial derivatives can readily be obtained as

$\frac{\partial q}{\partial p_i}\delta p_i \approx \frac{q_i - q_0}{\Delta p_i}\delta p_i = \left[q_i - q_0\right]_{\Delta p_i = \delta p_i} \equiv \Delta q_i$. In this case, $\Delta q_i$ represents the uncertainty in the heat flux due to the uncertainty in model parameter i. This mathematical formulation proposed by Rabin [Ref. 15], is suitable for estimation propagation of experimental uncertainties into computer simulations, when the functional behavior of each model parameter is known. The fundamental characteristic of this model is that it does not depend on a specific numeric technique. In this case, q is the result of a numerical solution of the energy equation, with the variable boundary conditions $q_{bottom}$, $T_{wall}$; $\delta q_{top} = f\left(q_{bottom}, T_{wall}\right)$,

$\delta q = \left[\left(\frac{\partial q}{\partial q_{bottom}}\delta q_{bottom}\right)^2 + \left(\frac{\partial q}{\partial T_{wall}}\delta T_{wall}\right)^2\right]^{0.5}$. Following the methodology outlined,

$\frac{\partial q}{\partial q_{bottom}}\delta q_{bottom} \approx \frac{q_i - q_0}{\Delta q_{bottom}}\delta q_{bottom} = \left[q_i - q_0\right]_{\Delta q_{bottom} = \delta q_{bottom}} \equiv \Delta q\big|_{q_{bottom}} = 7.85\ W/m^2$,

$\frac{\partial q}{\partial T_{wall}}\delta T_{wall} \approx \frac{q_i - q_0}{\Delta T_{wall}}\delta T_{wall} = \left[q_i - q_0\right]_{\Delta T_{wall} = \delta T_{wall}} \equiv \Delta q\big|_{T_{wall}} = 2.84\ W/m^2$,

and $\delta q = \left[\left(\frac{\partial q}{\partial q_{bottom}}\delta q_{bottom}\right)^2 + \left(\frac{\partial q}{\partial T_{wall}}\delta T_{wall}\right)^2\right]^{0.5} = 8.35\ W/m^2$, the total uncertainty can be estimated as $\frac{\partial h}{\partial q_{top}}\delta q_{top} = 0.36\ W/m^2$.

***Evaluation of*** $\left(\frac{\partial h}{\partial T_{wall}}\right)^2 (\delta T_{wall})^2$

For the $\left(\frac{\partial h}{\partial T_{wall}}\right)^2 (\delta T_{wall})^2$ term, the uncertainty can be estimated as

$\frac{\partial h}{\partial T_{wall}}\delta T_{wall} = \left(\frac{\partial q_{top}}{\partial T_{wall}}\frac{1}{T_{wall} - \left(\frac{T_e - T_i}{L}x + T_i\right)}\right)\delta T_{wall} + \left(\frac{q}{\left(T_{wall} - \left(\frac{T_e - T_i}{L}x + T_i\right)\right)^2}\right)\delta T_{wall}$, and

the $\frac{\partial q}{\partial T_{wall}}$ and $T_{wall}$ have been previously computed.

***Evaluation of*** $\frac{\partial h}{\partial T_e}\delta T_e$

The dependency of heat transfer coefficient on exit temperature can be estimated as $\frac{\partial h}{\partial T_e}\delta T_e = \left( \frac{q}{\left( T_{wall} - \left( \frac{T_e - T_i}{L} x + T_i \right) \right)^2} \frac{x}{L} \right) \delta T_e$; the only term that needs to be determined is $\delta T_e$.

There are two sources of uncertainty for $\delta T_e$, the accuracy of the thermocouple readings and the fact that exit temperature is determined as the average of 3 thermocouples located at the exit of the test section, $\delta T_e = \left[ \delta T_{e,TC}^2 + \delta T_{e,average}^2 \right]^{0.5}$. $\delta T_{e,TC}$ has previously be determined as $\delta T_{e,TC} = 0.19K$, and $\delta T_{e,average}$ is estimated as the mean deviation of the 3 exit thermocouples from one and other, $\delta T_{e,average} = 0.52K$. This results in $\frac{\partial h}{\partial T_e}\delta T_e = 0.61\ W/m^2$.

***Evaluation of*** $\frac{\partial h}{\partial T_i}\delta T_i$

Similarly, the dependency of heat transfer coefficient on inlet temperature can be estimated as $\frac{\partial h}{\partial T_i}\delta T_i = \left( \frac{q}{\left( T_{wall} - \left( \frac{T_e - T_i}{L} x + T_i \right) \right)^2} \left( 1 - \frac{x}{L} \right) \right) \delta T_i$, where the only undetermined variable is $\delta T_i$. With a similar methodology as the dependence on the exit thermocouples, the following quantities can be computed, $\delta T_i = \left[ \delta T_{i,TC}^2 + \delta T_{i,average}^2 \right]^{0.5}$, $\delta T_{i,TC} = 0.19K$, $\delta T_{i,average} = 0.41K$; and the resulting total uncertainty is $\frac{\partial h}{\partial T_i}\delta T_i = 0.46\ W/m^2$.

***Computation of*** $\delta h$

Given the above calculated relative uncertainties, the cumulative uncertainty of heat transfer coefficient can be estimated as,

$$\delta h = \left[ \left( \frac{\partial h}{\partial q_{top}} \right)^2 \left( \delta q_{top} \right)^2 + \left( \frac{\partial h}{\partial T_{wall}} \right)^2 \left( \delta T_{wall} \right)^2 + \left( \frac{\partial h}{\partial T_i} \right)^2 \left( \delta T_i \right)^2 + \left( \frac{\partial q}{\partial T_e} \right)^2 \left( \delta T_e \right)^2 \right]^{0.5} = 1.25\ W/m^2, \text{ or}$$

$\frac{\delta h}{h} = 3.4\%$.

### *g) Uncertainty of the Nusselt number*

The Nusselt number is defined as, $Nu = \frac{hD_h}{k}$, thus, $\delta Nu = \left[ \left( \frac{\partial Nu}{\partial h} \right)^2 (\delta h)^2 + \left( \frac{\partial Nu}{\partial D_h} \right)^2 (\delta D_h)^2 + \left( \frac{\partial Nu}{\partial k} \right)^2 (\delta k)^2 \right]^{0.5}$, which simplifies to $\delta Nu = \left[ \left( \frac{D_h}{k} \right)^2 (\delta h)^2 + \left( \frac{h}{k} \right)^2 (\delta D_h)^2 + \left( \frac{-hD_h}{k^2} \right)^2 (\delta k)^2 \right]^{0.5}$. From previous computations, the only remaining unknown is $\delta k$, the uncertainty on the thermal conductivity can be estimated as 0.1 W/ (mK) while the mean value is $k = 16.2 \ W/(mK)$. Then, the total cumulative uncertainty

# 21. Conjugate Heat Transfer

Usually in a general heat transfer problem more than one form of heat transfer takes place at the same time. Conjugate heat transfer (CHT) is the term used for the case where both conduction and convection occur. An example is shown in Fig. 48, where a fluid flows with velocity V over a plate with thickness L. Convection takes place in the thermal boundary layer close to the solid wall, whereas conduction occurs in the solid.

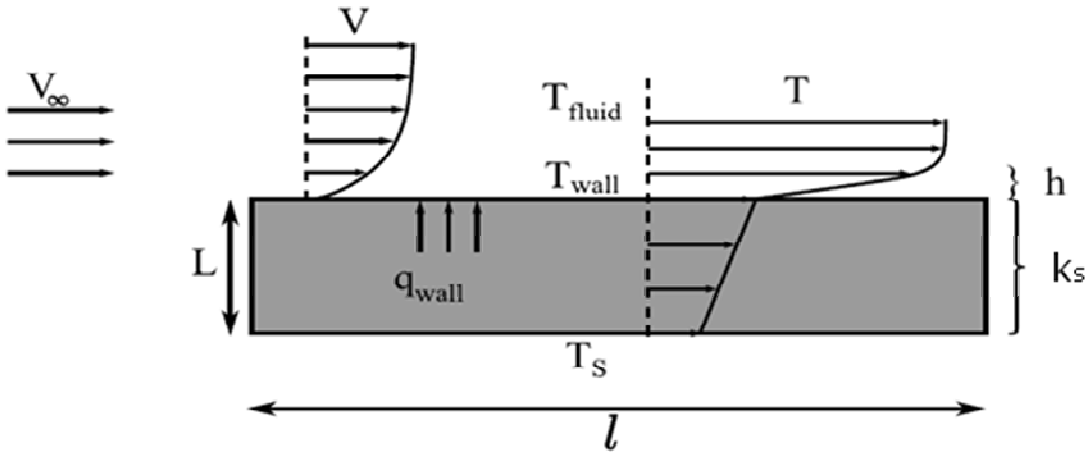


Figure 48: 1D conjugate heat transfer problem

In a convective problem the heat transfer levels depend not only on the velocity field and on the fluid properties, but also on the thermal boundary conditions, as extensively discussed by Dorfman [Ref C-3]. When the conduction through the wall is not negligible, the conductive and convective heat transfer modes are fully coupled: the convective fluid motion will affect the heat extraction from the wall, hence influencing the conduction pattern; in turn, the conduction through the wall will influence the wall temperature distribution, hence the convective heat transfer coefficient. The key parameter is the temperature distribution at the solid-fluid interface: indeed, the properties of a conjugate problem are the same as those of a convective problem where an identical temperature field is imposed along the wall surface.

When devising and investigating a model of a real internal cooling channel (numerically or experimentally) the reproduced thermal boundary conditions should resemble the engine environment. If this is not the case, the modeling of the heat transfer process can be inaccurate in the first place. In purely convective experimental and numerical simulations, where uniform temperature or uniform heat flux is usually imposed along the wet surface, the thermal boundary conditions are clearly not realistic. The implicit assumption of most studies in the literature of internal cooling channels is that the influence of the thermal boundary condition is negligible. This is sometimes a fair assumption; however, in case of large spatial thermal gradients and/or geometrical asperities, the impact of the wall temperature

distribution can be much greater. Such situations are common in internal blade cooling, since large use of jet impingements, bleeding holes and vortex generators i.e. turbulators are made. In conjugate mode no constraint is forced at the solid-fluid interface, except thermal equilibrium and heat flux continuity.

Two characteristic non-dimensional numbers have to be considered as important quantities in conjugate heat transfer: Biot number and Nusselt Number. Neglecting radiation, the equations governing the simple one dimensional problem of Fig. 48 are:

$$q = \frac{K_s}{L(T_s - T_{wall})} \qquad \text{Eq. 1.1}$$

$$q = h(T_{wall} - T_{fluid}) \qquad \text{Eq. 1.2}$$

with $T_s$ the temperature at the lower solid wall and $K_s$ the conduction coefficient of the solid.

A characteristic number for the conjugate heat transfer is the Biot number defined as:

$$Bi = \frac{hL}{K_s} \qquad \text{Eq. 1.3}$$

The latest adimensional number characterizes the thermal boundary layer. The fluid velocity on the wall is zero and heat is only transferred by conduction:

$$q = -K_f \left.\frac{dT}{dn}\right|_{wall} \qquad \text{Eq.1.4}$$

Considering the continuity of heat flux at the fluid solid interface, one can thus write:

$$h \cdot \left(T_{wall} - T_{fluid}\right) = -K_f \left.\frac{dT}{dn}\right|_{wall} \qquad \text{Eq.1.5}$$

or by making the temperature gradient at the wall non-dimensional, the Nusselt number, which is proportional to the ratio of the conductive resistance of the non-moving fluid over the convective thermal resistance, can be obtained.

$$Nu = \frac{h \cdot l}{K_f} \qquad \text{Eq.1.6}$$

where l is the characteristic length.

Note the important difference between Biot and Nusselt number. The Nusselt number is related to convective heat transfer and compares the convective resistance with the conductive resistance of the fluid, whereas the Biot number is of importance for conjugate heat transfer and compares the convective resistance of the fluid with the conductive resistance of the solid. [Ref C-4]

# 22. Similarity analysis for heat transfer in cooling channels

Similarity considerations in fluid dynamics and turbomachinery, are consulted when a mathematically deductive solution statement is not able to succeed with regard to a given problem. In this case modeling approaches are utilized to attain a solution; however these models have to satisfy the problem at hand to ensure its transferability.

A distinct problem is defined unique by the entity of primary variables it is comprised of. By means of dimensional analysis, two problems are regarded to be similar if the characteristic numbers formed upon the innate primary variables of these systems coincide.

The problem of conjugate heat transfer is governed by Eq. 1.1 and 1.2. When further considering the fluid flow along a non adiabatic passage, it is most likely to assume the heat flux density q between the solid and the fluid to depend on the driving temperature difference $\Delta T$, the characteristic length scales d and $D_h$ representing the hydraulic diameter of the duct and the wall thickness respectively; the bulk flow velocity $U_b$ and temperature $T_b$, as well as the physical fluid properties $\mu$, $\rho$, $C_p$ and $\kappa_f$, respectively dynamic viscosity, density, specific heat and thermal conductivity; $\kappa_w$ being the thermal conductivity of the wall. Making explicit use of the Buckingham $\Pi$ theorem, the relation of these primary variables among each another can by reduced to a relation between the base quantities of the International System of Units, length, time, mass and temperature in this case. The power functions of the primary variables eventually yield dimensionless groups or characteristic numbers which clearly define the problem, hence are consulted for similarity considerations.

The primary variables governing conjugate heat transfer can therefore be written as follows:

$$f\left(D_h, \quad d, \quad U_b, \frac{Tb}{\Delta T}, \Delta T, \quad \mu, \rho, C_p, k_f, k_w, q\right) = 0 \qquad \text{Eq.1.7}$$

With the definition of the heat transfer coefficient between the solid and the fluid:

$$h = \frac{q}{\Delta T} \qquad \text{Eq. 1.8}$$

Dimensional analysis by Buckingham $\Pi$ theorem yields the dimensionless expression of Eq. 1.7:

$$f\left(Re, Pr, Ec, \Theta, K, \frac{T_b}{\Delta T}\right) = 0 \qquad \text{Eq. 1.9}$$

Where

$$Re = \frac{\rho V D_h}{\mu} \qquad \text{Eq. 1.10}$$

$$\mathrm{Pr} = \frac{C_p \mu}{\kappa} \qquad \text{Eq. 1.11}$$

$$Ec = \frac{V^2}{C_p \Delta T} \qquad \text{Eq. 1.12}$$

$$\frac{T_b}{\Delta T} \qquad \text{Eq. 1.13}$$

are Reynolds number, Prandtl number, Eckert number and scaled relative bulk flow temperature respectively.

$$\Theta = \frac{k_f \Delta T}{q D_h} \qquad \text{Eq. 1.14}$$

$$K = \frac{k_w}{k_f} \qquad \text{Eq. 1.15}$$

Θ and K are the non-dimensional wall temperature and the solid-fluid thermal conductivity ratio, respectively.

The relative bulk flow temperature is experimentally found to have only a small influence; the sixth term in Eq. 1.9 is therefore neglected. This is a fair assumption when the physical properties of the fluid do not vary significantly with respect to temperature and small temperature differences. [Ref C-5] The Eckert number is a measure of the viscous dissipation of the flow arising in high-speed heat transfer problems. Especially for low speed applications, the relative importance of the kinetic energy with respect to the enthalpy is found to be very small, which largely reduces the influence of this dimensionless group as well. For this reason, also the third term in Eq. 1.9 is omitted.

In the final relation the adimensional wall temperature can be expressed as a function of the remaining terms:

$$\Theta = f(Re, Pr, K) \qquad \text{Eq. 1.16}$$

Therefore one can infer that a non-dimensional temperature distribution in a scaled test facility and in a geometrically similar internal cooling cavity proof to be in the same line, when Re, Pr and K coincide each other under the conditions of engine and laboratory environment. The conjugate character of the problem and thus the thermal boundary conditions are initially included in this reasoning.

Similarly, when referring to the definition of the heat transfer coefficient h and non-dimensional wall temperature Θ in Eq. 1.8 and Eq. 1.14 respectively, Θ can be substituted by the Nusselt number Nu which can in turn be interpreted as a non-dimensional heat transfer coefficient.

$$Nu = f(Re, Pr, K) \qquad \text{Eq. 1.17}$$

With the Nusselt number defined as:

$$Nu = \frac{hD_h}{k_f}$$ Eq. 1.18

The Nusselt number, as the ratio of convective to conductive heat transfer, clearly expresses the absolute level of heat transfer rate from the heated wall to the cold fluid. However it can not be consulted for effectiveness considerations by comparing the heat transfer rate acquired from the ribbed cooling passage to the one from the smooth channel wall. In order to quantitatively assess the impact of artificial roughness elements on internal cooling channels and thus determine the relative heat transfer enhancement, the Nusselt number is written in a normalized form:

$$\frac{Nu(x,y)}{Nu_0} = \frac{\frac{h(x,y)D_h}{k_f}}{0.0243Re^{0.8}Pr^{n}}$$ Eq. 1.19

This normalized Nusselt number is introduced as the "enhancement factor" EF.

The denominator in this fraction is the *Dittus-Boelter equation*, a empirical correlation for computing the local Nusselt number for fully developed (hydrodynamically and thermally) turbulent flow in smooth circular tubes.

$$Nu = 0.024Re^{0.8}Pr^{n}$$ Eq. 1.20

n = 0.4 is chosen for heating ($T_{Wall} > T_{Fluid}$) and n = 0.3 for cooling ($T_{Wall} < T_{Fluid}$).

[$0.7 \leq Pr \leq 160$; $Re_D \geq 10.000$; $\frac{L}{D} \geq 10$]

Although it has become a common practice to refer to

$$Nu = 0.023Re^{0.8}Pr^{n}$$ Eq. 1.21

as the *Dittus-Boelter equation*, the original Dittus-Boelter equations are actually of the form

$$Nu = 0.024Re^{0.8}Pr^{0.4}$$ *(Heating)* Eq. 1.22

$$Nu = 0.0265Re^{0.8}Pr^{0.3}$$ *(Cooling)* Eq.1.23

The historical origins of Eq. 1.21 are discussed by Winterton. [Refs C-6, C-7]

The consideration of the conjugate heat transfer case regarding the two different length and conductivity scales, for the fluid and the solid respectively, yields the Biot number Bi, representing the counterpart to the Nusselt number. Defined as:

$$Bi = \frac{hd}{k_w}$$ Eq. 1.24

It gives the ratio of the conductive ($L/K_s$) over the convective (1/h) thermal resistance: a low Biot number corresponds to a high convective thermal resistance and thus a high temperature gradient in the fluid. In the case of a high Biot number the largest temperature gradient will be in the solid and the wall temperature will be close to the fluid temperature. It is used as a criterion to estimate whether it is valid to handle a conjugate heat transfer problem as purely convective (neglecting conduction) or not.

In addition to the Nusselt number, the dimensional analysis using the Buckingham Π theorem yields a characteristic number that, instead of Nu, is sometimes referred to in heat transfer considerations in forced convection. The Stanton number St is a dimensionless number to measure the ratio of heat transferred into the fluid to the thermal capacity of the fluid.

$$St = \frac{h}{C_p \rho V} \qquad \text{Eq. 1.25}$$

It can also be represented in terms of the characteristic numbers mentioned afore:

$$St = \frac{Nu}{Re\,Pr} \qquad \text{Eq. 1.26}$$

The variation of Prandtl number in the temperature range of the experiment carried out in this study is very small, thus in order to respect similarity, it suffices to maintain the same Reynolds number in the scaled geometrical model.

Another issue that has to be taken into account in this section is the relative weight of natural or free convection with respect to forced convection:

$$\frac{Gr}{Re_L^2} \qquad \text{Eq. 1.27}$$

For this purpose the Grashof number, a dimensionless measure which approximates the ratio of the buoyancy to viscous force acting on a fluid, is addressed:

$$Gr = \frac{g\beta(T_w - T_b)}{\mu^2} \qquad \text{Eq. 1.28}$$

$$\beta = -\frac{1}{\rho}\frac{\rho - \rho_f}{T - T_f} \qquad \text{Eq. 1.29}$$

$$T_f = \frac{T_w + T_b}{2} \qquad \text{Eq. 1.30}$$

Considering the magnitude of the fraction and its deviation from unity:

| | |
| --- | --- |
| $\frac{Gr}{Re_L^2} \ll 1$ | Free convection is regarded negligible. |
| $\frac{Gr}{Re_L^2} \gg 1$ | Forced convection is regarded negligible. |
| $\frac{Gr}{Re_L^2} \approx 1$ | Combination of forced convection and free convection. |

In the setup of the present study the weight ratio of natural and forced convection is in the order of:

$$\frac{Gr}{Re_L^2} = o(10^{-3})$$

This clearly demonstrates that forced convection is the dominant phenomenon and thus natural convection is negligible in this study.

# 23. Literature Review for ribbed cooling channels

## 23.1 Introduction

The quest of improved performance and energy efficiency of heat exchangers in general is of profound importance in various industrial systems and processes. The prevailing desire forming the basis of investigations in this field is the augmentation of heat transfer rate between the flowing fluid medium and the passage walls.

It is generally accepted that the introduction of turbulence to the flow is of major avail in the sense of convective heat transfer enhancement. Based on this beneficial effect of turbulent flow structures, the concepts used in internal cooling passages of gas turbines in principle depend on the promotion of phenomena like increased mixing and generation of secondary flows by means of vortex inducing geometrical elements. Deliberately designed to significantly interfere with the mean flow, obstacles like ribs, pin fins and other turbulators are applied, in order to literally create an artificial surface roughness of the respective cooling channel. In this sense, the impact of roughening devices in cooling channels on the coolant flow can essentially be interpreted as raised surface roughness.

The effect of wall surface roughness on pressure drop and heat transfer in circular tubes has been extensively studied in historical literature. [Refs C-8 – C-10] The pioneering work of Nikuradse [16] established the sand grain roughness or relative roughness λ/d (ratio of the obstacle height over the hydraulic diameter of the tube) as a major parameter in defining the friction factor during laminar and turbulent flows. Continuing this tradition, the correlations concerning heat transfer and friction aspects of roughness devices used in internal

forced convection today, also rely on the geometrical obstacle dimensions. Initially based on the analogy laws between heat and momentum transfer by Reynolds and Prandtl, Webb et al. [Ref C-11], and Han et al. [Refs C-12, C-13] extended the friction similarity functions to geometrically non-similar roughness conditions in ribbed channels of gas turbine cooling applications.

The geometric scales featuring fundamental importance for the development of the flow inside the rib roughened rectilinear or squared channel are represented by:

- Aspect ratio of the channel, $\frac{W}{H}$
- Blockage factor $\frac{h}{D_h}$ where h is the rib height and $D_h$ the hydraulic diameter of the channel
- Rib pitch to height ratio, $\frac{P}{h}$
- Rib angle of attack, $\alpha$
- Rib shape and profile
- Number of ribbed channel walls

In the present work, the selection of the test section geometrical dimensions reflects the research line of the former studies carried out in this field at the VKI. The channel geometry parameters are chosen as follows:

- A rectilinear channel of a squared cross section
- A blockage ratio of: $\frac{h}{D_h} = 0{,}3$
- A rib pitch to height ratio of: $P/h = 10$
- An angle of attack with respect to the mean flow direction of: $\alpha = 90°$

This configuration was chosen for the experiment, since it combines the settings of a standard reference case like squared cross section with a high blockage ratio of the channel. The pitch to height ratio of $P/h = 10$ lies within the optimal range which has been experimentally determined by many authors to yield the highest enhancement of heat transfer rate in the respective geometrical arrangement. It results in a particularly involved flow behavior with high levels of turbulence and a substantially three-dimensional character; therefore it shows great promise to be suitable for a fundamental analysis of the rib-roughened channel flow.

## 23.2 Geometrical similarity parameters

Effect of blockage ratio $\frac{h}{D_h}$

The blockage ratio is of major importance for the flow behavior in a rib-roughened channel. By controlling the magnitude of the local reduction in cross sections it significantly influences the acceleration of the flow when passing the rib and the subsequent expansion directly after the obstacle. Thus the impingement of the flow on the front of the rib and the recirculation zone spreading in its wake are affected.

The majority of studies on heat transfer enhancement in the literature involve configurations characterized by noteworthy small blockage- or rib height to hydraulic diameter ratios with $h/D_h$ = [0.02-0.08]. [Refs C-12 – C-22] Slightly higher values were used by Liou. et al. [Ref C-23] and Taslim et al. [Ref C-24], while Rau et al. [Ref C-25] and Çakan [Ref C-26] perform measurements on a squared channel with higher blockage ratios up to $h/D_h$ = 0.3.

Effect of rib pitch-to-height ratio P/h

The rib pitch-to-height ratio represents another significant parameter, for it indicates the channels' wall roughness effects on the flow field and thus on heat transfer and pressure drop.

In a square cross sectioned channel with small blockage ratios, Han et al. [Ref C-19] indicate that a P/h of 10 yields the optimal performance. In turn Taslim et al. [Ref C-24] and Ichimiya et al. [Ref C-27] for high blockage ratio and Zhang et al. [Ref C-20] for very small blockage ratio tell the optimal rib-to-height ratio to be around 8.

Effect of rib angle of attack α

The general impact of rib shaped obstacles with an angle of attack to the mean flow direction generally yields both, a significant increase in the heat transfer rate and the pressure drop.

From experiments regarding a rib pitch-to-height ratio of 10 to 20, Han et al. [Ref C-19] determined the most desirable angle of attack for maximal heat transfer and the accordant pressure penalty at 75°. Measurements contrasting both, angle of attack and the channel aspect ratio W/H which were also carried out by Han et al. [Ref C-15] and Çakan [Ref C-26] who found the optimal angle at 45°. Park et al. [Ref C-28] reported a 45-60° angle for narrow channels (W/H < 1) and 30-45° inclination for shallow channels (W/H > 1) to provide best performance. Lau et al. [Ref C-29] told a parallel arrangement of ribs on two opposite walls to be more effective than the use of crossed angled ribs.

Effect of channel aspect ratio W/H

In gas turbine applications the internal cooling channels can be estimated as rectangular and the respective aspect ratios vary with the position in the blade where the channel is located. While the mid-chord regions of the airfoil usually exhibits nearly squared cooling passages, the aspect ratio increases with the blade thickness decreasing towards the trailing edge. In general, the channel aspect ratio is reported to be significant for the heat transfer rate enhancement, in particular when inclined ribs are used. [Ref C-19]

On the one hand, Han et al. [Ref C-15] determined square cross sectioned channels to be more favorable than rectangular ones, using various rib inclination angles. On the other hand, small aspect ratio channels are reported to yield higher heat transfer enhancement at the ribbed wall than achieved in narrow channels (W/H < 1). [Ref C-14]

Effect of rib shape and profile

An alternative to usual rib arrangements is the use of V-shaped ribs as turbulators in cooling channels which result in the generation of oblique secondary flows forming in a region downstream of the leading edge. V-shaped ribs aligned with or opposed to the mean flow direction yields the augmentation of the channels cooling effectiveness. [Ref C-26]

With a configuration of downstream facing V-shaped ribs with an angle of 45°, the heat transfer rate can be raised more to a higher extent than with upstream facing ribs. [Ref C-29] A comprehensive study by Han et al. [Ref C-18], comparing V-shaped ribs of a 60° angle with parallel and crossed ribs of the same angle of attack, determined V-shaped ribs to be more effective in general, independent of heat flux ratio and Reynolds number.

Concerning the rib profile, Han et al. [Ref C-31] performed measurements with wedge- and delta-shaped profiles instead of the usual rectangular profiles. While delta-shaped ribs proofed more advantageous than wedge-shaped ribs, in particular configurations with a not consistent cross section orthogonal to the flow direction performed better than on full length. It is a fact that the gradual wear of friction of roughness elements in cooling channels alters the initially sharp edges of rib turbulators during the life-cycle. Investigating the impact of this phenomenon on heat transfer, Taslim et al. [Ref C-24] carried out experiments on the effect of cross section variation, contrasting the performance of sharp to round rib edges.

Effect of number of ribbed channel walls

In general, the need for rib roughened cooling channels in gas turbine applications arises from the fact that smooth channel walls alone are not capable to achieve convective heat transfer rates of the magnitude required to balance the significant thermal load externally exerted on the airfoil. With respect to the potential of flow perturbing obstacles to noticeably enhance heat transfer rates, in the majority of cases both, the channel walls facing suction and pressure side are roughened. This is in consequence of the major heat fluxes entering the turbine blade from these directions. However, similarly to the experimental configuration in

the present work, under certain conditions it is justified to rib roughen one channel wall only, for it suffices to provide necessary cooling performance.

Comprehensive studies dedicated to the effect of number of ribbed channel walls investigated arrangements of one, two and four walls respectively. [Ref C-32] Sparrow and Tao [Refs C-33, C-34] contrasted the heat transfer enhancement of symmetrically to asymmetrically roughened channels, reporting that asymmetrical configuration induce periodic structures to the flow that result in enhanced heat transfer rates.

## 23.3 Former investigations conducted at VKI

In the wake of a more detailed investigation on the heat transfer enhancement of rib-roughened cooling channels in gas turbine blades, the present work continues the research line developed at the VKI before.

Previous contributions towards this subject matter were brought by Çakan [Ref C-26] who carried out an extensive experimental study, however only addressing the purely convective nature of this phenomenon. By means of liquid crystal measurements he derived heat transfer coefficient distributions from the wall temperature distributions obtained in a scaled cooling passage model. The parameters used encompassed various geometrical configurations of blockage ratios, pitch-to-height ratios, rib angles of attack and total number of ribbed walls at a Reynolds number of 30,000. The arrangements included the case of traverse rectangular ribs of an pitch-to-height ratio of 10 and a 0.3 blockage ratio in a square cross sectioned channel, used in the experimental campaign in the work at hand.

Agostini et al. [Ref C-35] performed measurements in a cooling channel geometry assuming more realistic boundary conditions, i.e. regarding the clearly conjugate nature of this problem essentially coupling convective and conductive heat transfer modes. Similar to the experimental approach in the present study, carried out at a Reynolds number of 40,000, the test section comprised of a metallic slab that was exerted to uniform heat flux by means of an Inconel sheet at the bottom side and employed with metallic ribs on the top side. Facing the coolant flow, the temperature distribution at the metal surface was determined by an infrared camera, which ultimately yielded the distribution of the heat transfer coefficient.

Apart from heat transfer measurements, Casarsa [Ref C-36] focused on the aerodynamic aspect of the problem, carrying out profound investigations of the flow field of the fluid by utilizing PIV measurement techniques. The high spatial resolution associated with this technique was used to obtain insight into the involved flow patterns and structures characterizing the flow in rib-roughened internal cooling passage geometries. The sequent chapter of this survey discusses the results and outcome of the research effort in detail, thereby indicating the correlation between the thermal and aerodynamic character of the problem at hand.

# 24. Rib-roughened Internal Cooling Passage Flow Field Model

## 24.1 Motivation

Generally speaking, a detailed description of the mean flow patterns of the stream inside rib-roughened internal cooling passages of gas turbine blades is of major importance for an analysis of the conjugate heat transfer problem. For this purpose, the chapter at hand is devoted to the mean flow model by Casarsa [Ref C-36], which has been conducted at the VKI before. Throughout the investigation which addressed the aerodynamic aspects of the conjugate case, a representative, 3-dimensional model of the mean stream inside the channel cavity has been developed. In order to achieve deeper insight in the involved coupling between the flow behavior on the one hand side and the heat transfer coefficient distribution on the other hand side, it will further be referred to this flow model in the present work.

Since the analysis of the distinct flow features and structures occurring in the stream is considered to be essential to contrast the respective mean flow model and the results yielded by heat transfer measurements.

## 24.2 Experimental Arrangement

In the study, the rib-roughened channel flow has been experimentally determined by means of optical measurements, making explicit use of the PIV technique. Based on the former research line at VKI, a geometric arrangement of a square cross sectioned passage employed with rectangular traverse ribs on one wall was chosen for the large scale model. With respect to the similarity parameters introduced before, the configuration exhibited a channel blockage ratio of 0.3 complemented with an obstacle pitch-to-height ratio of 10. Considering the fact that this configuration coincides with the geometry chosen for the test section of the present research effort, one can infer that the acquired results concerning the flow structures can be directly adopted.

## 24.3 Mean Flow Field

Formed upon the complex geometry of internal cooling passages, the consecutively employed disturbance elements inside the cavity introduce a number of secondary flow features into the mean stream. These secondary flow structures are considered to be of major importance for the heat transfer enhancement in the cooling passage and will therefore be discussed more in detail when regarding the main flow model.

Figure 49 illustrates the mean velocity distribution by means of stream traces in the channel symmetry plane. Approaching from the left hand side of the figure the fluid enters the test section and encounters the rib. The stream experiences a strong deviation imposed by the obstacle, forcing it to adapt to the decreased channel cross section. It is accelerated in order to

pass the rib and subsequently experiences an expansion further downstream as the cross section is abruptly increased again by the backward-facing step. This is also notified by fluctuations of the wall static pressure, where the largest pressure drop is located in the proximity of the rib. The periodic behavior of consecutive acceleration in the vicinity of the obstacle and deceleration of the fluid in the inter-rib spacing is one most remarkable aspects of the flow field in rib-roughened channels.

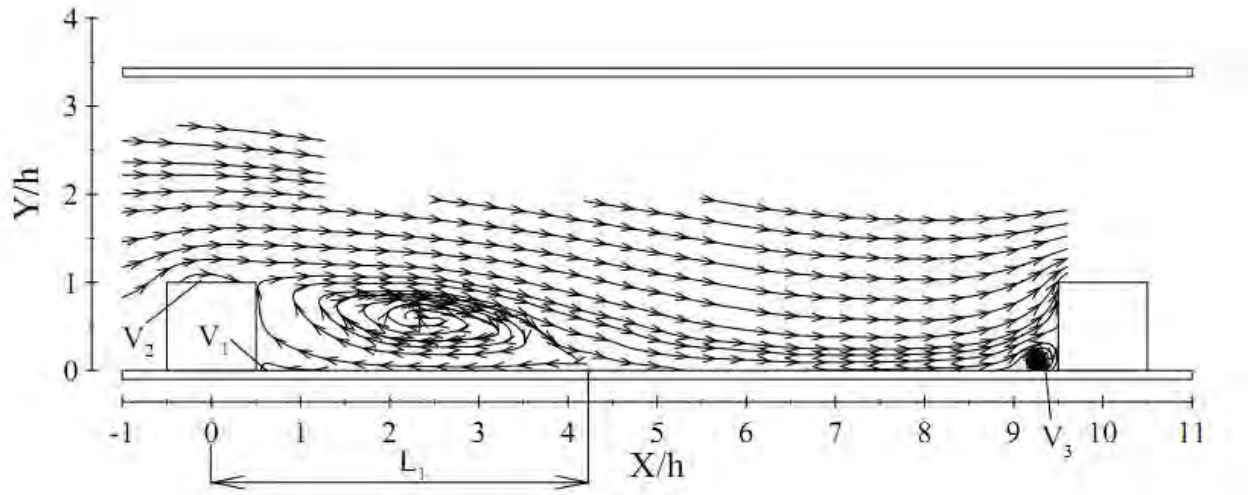


Figure 49 Visualization of the mean velocity field in the symmetry plane [Ref C-36]

Since the fluid flow is not able to follow sharp turns in the surface contour, it is the sudden enlargement of the channel after passing the perturbator which causes the flow to separate from the surface. A free shear layer is formed upon the interaction between the separated flow and the reverse flow in the recirculation region downstream of the rib. It is important to denote that even though, this recirculation region or separation bubble gives the impression to be a distinct vortex cell, it clearly is not. Being more of an artificial character rather than existing in the instantaneous velocity field, the general trend of the flow in this region is emphasized by the principle of illustrating time averaged flow field data, innate to the PIV technique when determining the velocity field. Apart from this recirculation region, the flow field exhibits a separated flow region $V_2$ on top of the perturbator as well as a small vortex $V_1$ in the downstream corner between the rib and the channel bottom, as indicated by Rau et al. [Ref C-38]. While $V_2$ rotates in the clockwise direction, $V_1$ exhibits a counter-clockwise rotation. Unlike the large recirculation region in the wake of the obstacle, these two vortex cells not only statistically represent the mean flow model, but also exist in the instantaneous velocity field.

A detailed visualization of $V_2$ and its appearance on top of the obstacle are given in figure 50. From the three illustrations it can clearly be seen that the recirculation structure extends along the entire top rib surface and increases in size when approaching the lateral channel walls. With respect to the front edge of the rib, its extension increases from $\Delta X_{V2}/h$ = 0.9 in the centerplane to $\Delta X_{V2}/h$ = 0.97 in the plane directly adjacent to the wall. Its dimension

in the vertical direction increases similarly. The change in appearance of the bubble, from flattened to spherical, is attributed to high momentum flow in the symmetry plane and low momentum flow in the region of the lateral wall boundary layer. Therefore being less energetic in the proximity of the wall, the flow separates earlier and reattaches later. In addition, the shape is affected by a downward directed secondary flow present above the rib.

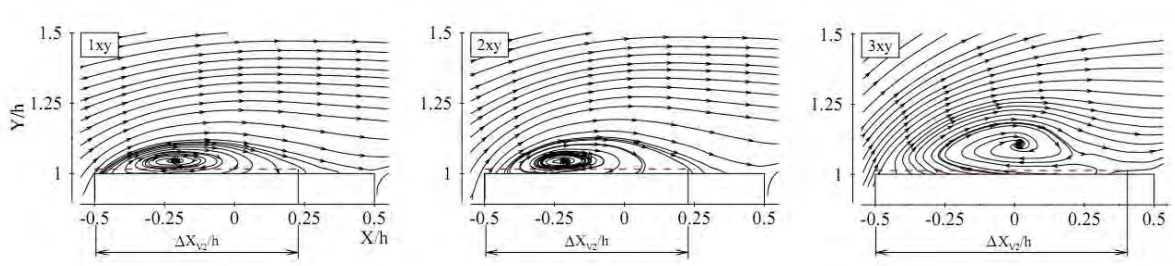


Figure 50 Cross section of the vortex structure $V_2$ along the lateral direction: symmetry plane (left), intermediate (center), lateral wall (right)

Since the small vortex cell $V_1$ exhibits a counter-clockwise rotary motion, this recirculation region in the downstream corner of the rib and the large separated flow region in its wake rotate in the opposite directions. Their stream traces coincide when approaching the obstacle, so that the flow impinges onto the rear surface of the rib in this region. Similar to $V_2$, this recirculation region develops over the entire spanwise channel direction, as depicted in figure 50 However, unlike the change in size of $V_2$, the dimension of $V_1$ appears to be of substantially the same extent along the rib length.

After the mean flow passes the rib and the sequent recirculation region, it turns downward and impinges on the channel bottom. This downwash responds to the again increased cross section of the passage. The reattachment region of the stream to the channel bottom, indicated by $L_1$ in figure 49, will be addressed more in detail later on. When the flow aligns with the wall and reattaches, the boundary layer redevelops and grows within the inter-rib spacing, until it approaches the next turbulator. The stream strongly impinges on the front of the rib so that its vorticity and the repeatedly induced separation of the boundary layer give rise to the vortex structure $V_3$. Rotating in the clockwise direction, this flow feature is substantially different from the vortex cells $V_1$ and $V_2$ mentioned afore. As can be inferred from figure 51, $V_3$ essentially does not extend along the entire spanwise direction of the ribbed wall. While its size slightly increases towards the lateral channel walls, the structure is not present in the vicinity of the wall any more. Instead, a remarkable upwash of the fluid and an abrupt separation from the bottom surface at around X/h = 8 can be noticed in this region. This is induced by the influence of secondary flow features.

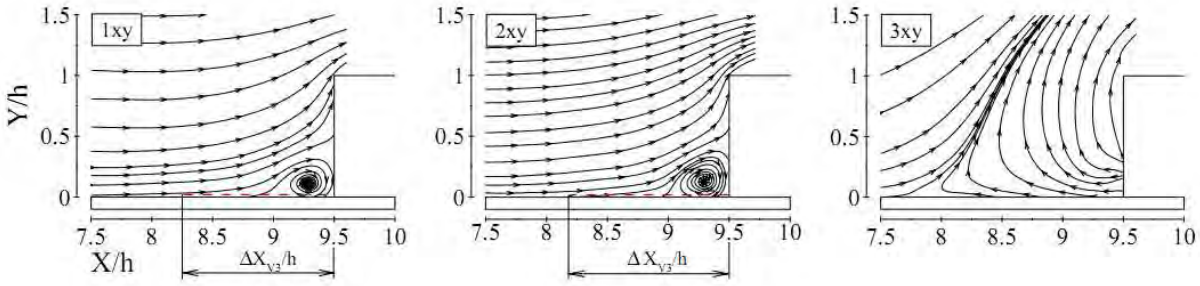


Figure 51: Cross section of the vortex structure $V_3$ along the lateral direction: symmetry plane (left), intermediate (center), lateral wall (right)

From the secondary flow features present in the mean stream field, the vertical motion of the fluid, in the vicinity of the obstacle, is mainly affected by the flow structure given in figure 52. However, since these two counter rotating vortex cells propagate along the entire channel axis they also affect the velocity field of the flow within the inter-rib spacing. On the one hand, their downward facing streamlines coincide in the channel symmetry axis and thus induce a broad downwash in center of the passage. On the other hand, the rotary motion generates a significant upwash at the channel lateral walls which in turn evokes the unique behavior of the stream near to the rib.

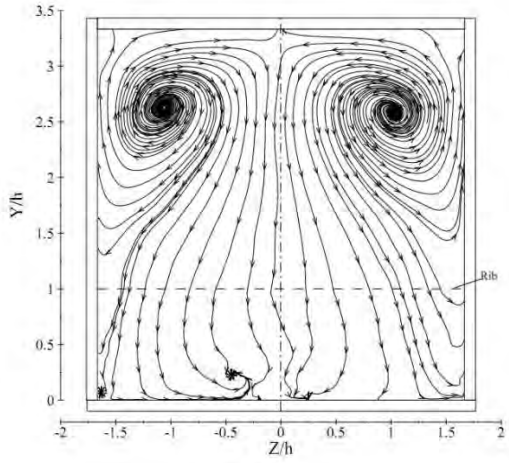


Figure 52 Illustration of the secondary flow in a plane orthogonal to the channel axis at the location of $L_1$

As the mean flow approaches the rib, it strongly impinges onto the front surface of the obstacle which results in the sudden spanwise deflection of the fluid. This deflection is indicated by the abrupt transverse flow motion directly upstream of the rib, clearly visualized by the stream traces given in figure 53. The abrupt turn of the flow towards the lateral walls essentially is a pressure driven acceleration and induces a region of high momentum $S_2$ in the corner between the rib and the wall. Captured by the considerable upward facing rotation of

the secondary flow vortex cells at the walls, this high momentum region is effectively lifted upward and shed away downstream by the mean flow. On the contrary, a region of low horizontal velocity, with respect to the surrounding, $S_1$ is generated directly downstream of the rib. Initially emerging from the channel bottom, this low momentum region is highly susceptible to the entrainment of the secondary flow vortex. Similar to $S_2$, it is lifted upward and gradually shed away downstream by the bulk flow.

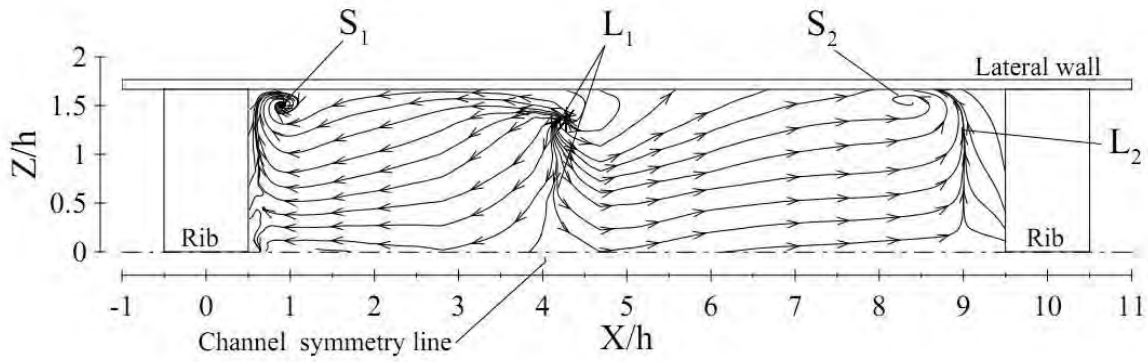


Figure 53: Demonstration of the secondary flow structures $S_1$ and $S_2$ at the channel bottom plane

Ultimately, in order to give a telling and consistent overview on the mean flow field inside the rib-roughened cooling passage, figures 54 and 55 demonstrate the overall flow behavior and illustrate the distinct structures that occur in this regard. From the direction of the stream traces, representing the mean velocity field, one can clearly locate the main and secondary flow features pointed out before. The higher magnitude of the streamwise velocity indicates the general acceleration of the flow when passing the rib. While the vortex structures $V_3$ upstream and $V_1$ downstream of the rib are clearly visible by their rotary motion, the stream line direction highlights the presence of the recirculation bubble $V_2$ on top of the rib and the large recirculation region in its wake. Moreover the upward motion of the flow demonstrates the lift of the high momentum region $S_2$ upstream of the turbulator. For sake of completeness, the simplified mean flow model is drawn in figure 56, emphasizing its substantial 3-dimensional character. Exemplified by line 3 in the figure 56, downstream of the reattachment point the fluid impinges onto the rib and is deviated by the pressure-driven transverse flow motion. The evoked region of high momentum at the lateral wall is entrained and convected upward by the rotary motion of the secondary flow, corresponding to line 4.

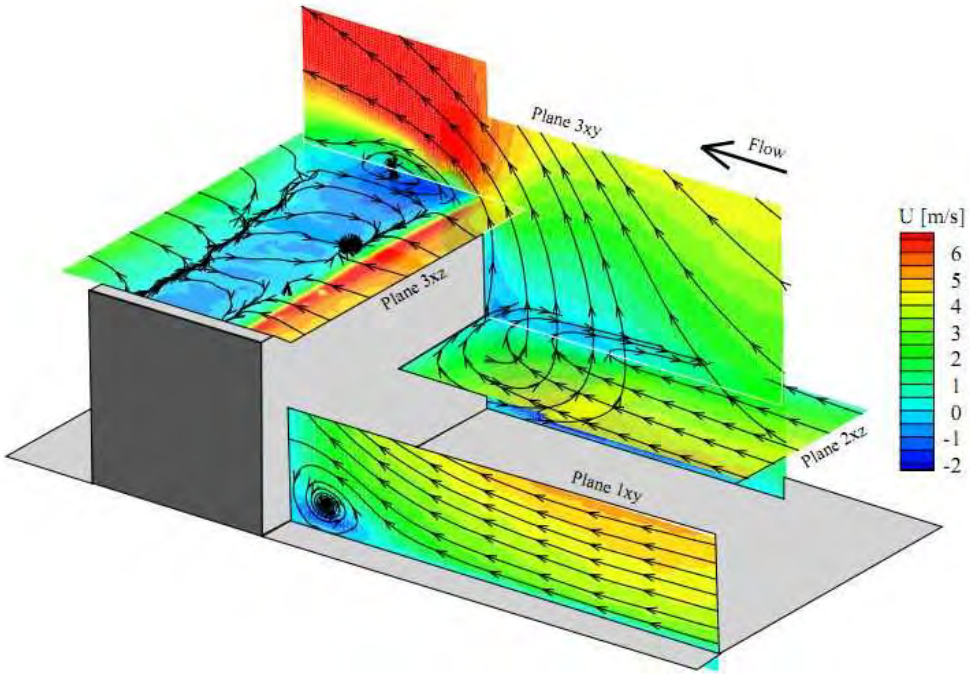


Figure 54 Visualization of the main flow field around the rib perturbator

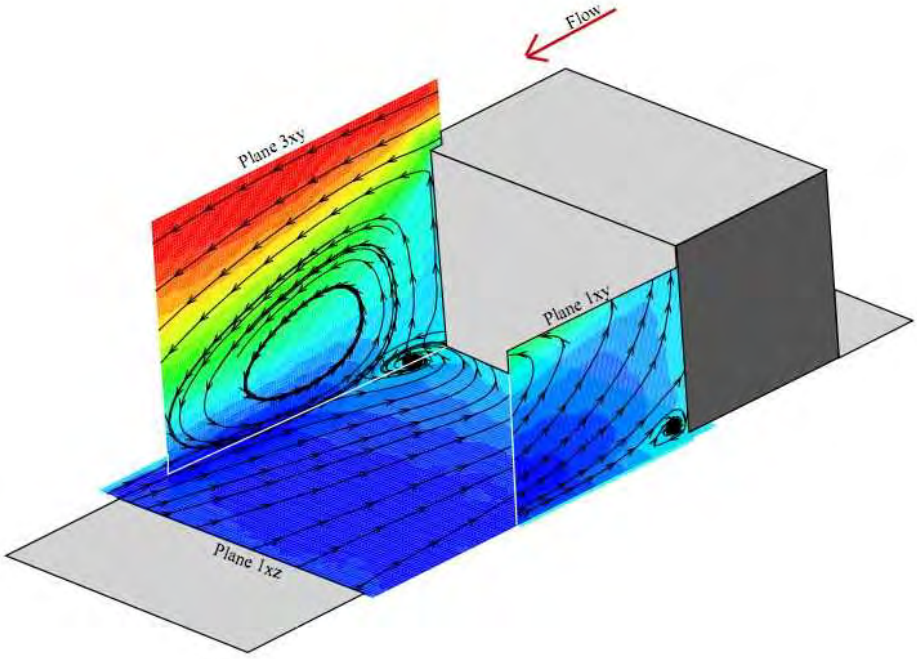


Figure 55: Visualization of the main flow field around the rib perturbator

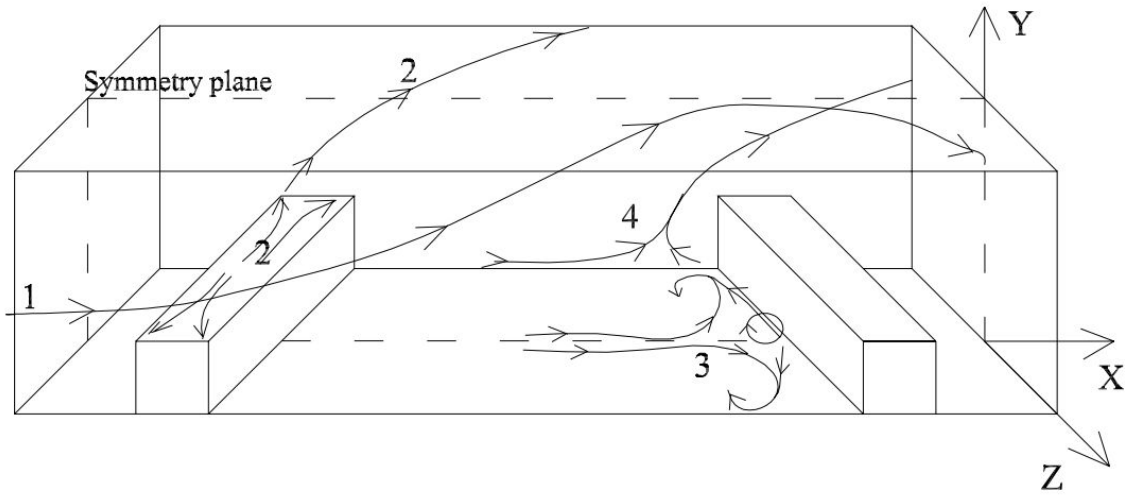


Figure 56: Illustration of the mean flow model inside the rib-roughened cooling passage

## 24.4 Reattachment

As pointed out in the previous section, the flow field inside a rib-roughened channel arrangement is characterized by a consecutive progression of separation of the flow from the passage walls followed by its reattachment. The major importance of analyzing flows with separation regions is due to their significance for numerous engineering applications. Flow reattachment and redevelopment of the boundary layer, involving heat transfer, are generally considered disadvantageous, since they are associated with large variations of the local heat transfer coefficients. The resulting overall heat transfer peaks greatly enhances the risk of affected engine components to suffer from thermal fatigue and thus is sought to be avoided. On the contrary, in the scope of cooling applications, an increase in the heat transfer coefficient is explicitly desired. The extensive use of flow perturbators and turbulators is mainly based on the intent of introducing separation and recirculation zones, encompassing regions of reattachment and redevelopment of boundary layers to the flow.

The working fluid is not able to follow the sharp turns in the surface contour when the channel cross section is abruptly enlarged again behind the rib, the flow behavior in internal cooling channels is essentially similar to the one induced by a backward-facing step. Contrasting its simple geometry, the turbulent flow downstream a backward-facing step encompasses distinctly different flow regions, including: reversal and recovery in the presence of a strong adverse pressure gradient, mixing, regions of reattachment as well as redeveloping velocity and thermal boundary layers. In this regard, the backward-facing step has been considered an excellent choice for a study of heat transfer phenomena associated with flow separation and reattachment.

When the flow passes the rib obstacle, a free shear layer is formed upon the interaction between the separated mainstream flow and the reverse flow in the recirculation region

downstream of the rib, fig. 57. Based on the generated turbulence, the free shear layer gradually increases in size with increasing distance from the rib [Ref C-46]. In terms of near wall flows, the determining factors for flow reattachment are the growth of the shear layer and its entrainment by the mainstream towards the bottom wall. In this region, the shear layer is substantially split into two distinct fractions. Since the energy of the first part does not suffice to overcome the prevailing pressure gradient, it is reversed and ultimately forms the recirculating flow. A contrasting behavior is shown by the other part of the shear layer, which is carried away downstream and contributes to the redevelopment of the boundary layer [Ref C-46]. The region of separated flow in the wake of the rib, between its trailing edge and the reattachment line, is occupied by the recirculation region. With the length confined by the point of reattachment, its size is substantially dependent on the state of separation. Considering this brief background, the location of reattachment is regarded as a key parameter for the separated flow. The relaxation of the flow field downstream of the reattachment point is affected by the high level of free stream turbulence behind the rib and a highly deformed average velocity field [Ref C-39].

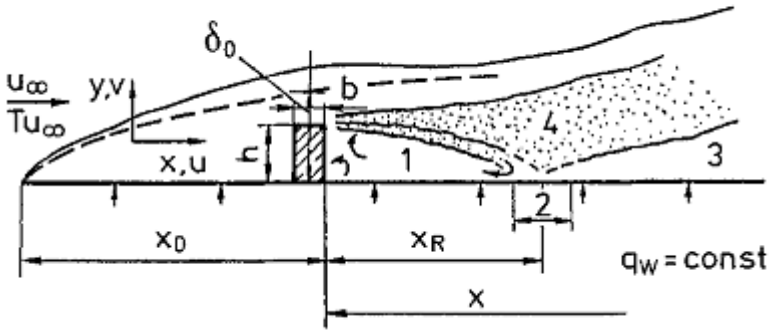


Figure 57: Visualization of the flow field behind a rib turbulator: 1- recirculation region; 2- point of reattachment; 3- redeveloping boundary layer; 4-separated shear layer

The location of the reattachment, where the wall near flow initially begins to realign with the surface again, is given by the reattachment length $x_R$, defined as the distance between the rib trailing edge and the point of reattachment. The determining factors for $x_R$ may be written as follows:

$$\frac{x_R}{h} = f\left(Re_{\delta'}, \frac{h}{\delta_o}, Tu, H\right) \qquad \text{Eq. 1.31}$$

The first two terms represent the flow regime, where $\delta'$ and $\delta_o$ are the momentum thickness over the rib and the boundary layer thickness in the case of a smooth wall respectively. Moreover the free-stream turbulence, Tu, and rib relative height ratio, H, are also relevant determining factors.

The dependency of reattachment length $x_R$ on $Re_h$ is highly complex; a consequence of the transition from a predominantly laminar state of separation $Re_h < 10^2$ to a fully developed turbulent separation state at $Re_h > 10^3$. In the turbulent flow regime, the perturbations of the

near-wall layers are generally lower, mainly caused by the considerably larger shadow effects and scale of the reattaching eddies. [Ref C-39]

Having a wide variety of applications and of academic importance, the reattachment region in the wake of a backward facing step, including heat transfer in the channel walls, has been extensively studied in literature. Substantial differences in turbulent kinetic energy, skin-friction coefficient, heat transfer coefficient and velocity profiles are reported. Early studies focusing on the fluid dynamic character of the problem have been reviewed by Eaton et al. [Ref C-40] and Watkins et al. [Ref C-41], but could not provide quantitative data on the flow behavior.

Streamwise distribution of the local heat transfer coefficient provides indications regarding the state of the reattachment. It is typically characterized by an initial increase within the separation bubble, followed by a peak in the vicinity of the reattachment point. In literature, there appears to be a high scatter in the predicted locations of maximum Nusselt number with respect to the reattachment length, $x_R$. Heat and mass transfer investigations carried out by Armaly et al. [Ref C-42] found that the maximum Sherwood number is upstream of the reattachment point for turbulent flows, yet both, Sherwood and Nusselt number exhibited a double peak for laminar flows. While it is generally assumed that the locations of maximum heat transfer, $x_{max}$, and reattachment, $x_R$, coincide, there is conclusive evidence that $x_{max} = x_R$ is, at best, an exceptional case [Ref C-47]. Laminar flows typically exhibit $x_{max} > x_R$ [Ref C-43], while studies on turbulent flows yield to more controversial results. [Refs C-44, C-45] Nonetheless, the reattachment is shown to greatly enhance the local heat transfer coefficient, maximum corresponding to the location of the turbulence intensity peak. [Refs C-46, C-47]

Giovannini et al. [Ref C-37] observed that the reattachment point positions defined at maximum of heat transfer, maximum of the velocity or pressure fluctuations or change in sign of the mean streamwise velocity are different. In particular, the definition using the sign of the mean velocity provides the biggest value (reattachment more downstream), while the use of the pressure fluctuations gives the smallest one (reattachment more upstream).

As the separation region behind the backwards facing step becomes relatively large or elongated, in the order of 6H, the flow incidence angle towards the bottom wall grows smaller. Thus, downstream of the reattachment point, a region of less impingement type of behavior, due to smaller velocity component in the vertical direction, is created. In this case, the location of the maximum heat transfer $x_{max}$ is highly dependent on local shear stress fluctuations [Ref C-45], which are shown to be prior to the reattachment point. In the case of the relatively smaller or narrower separation zones, the flow incidence angle appears much larger, creating an impingement zone which ultimately dominates the local heat transfer distribution. Therefore, the relation between $x_{max}$ and $x_R$ is believed to depend on the separation bubble aspect ratio. With $x_{max} < x_R$ for relatively long bubbles and $x_{max} > x_R$ for short bubbles. [Ref C-47]

As previously mentioned, the Stanton number within the reattachment zone is controlled by the turbulence level near the wall. The fluctuating skin friction is substantially

increased compared to an ordinary boundary layer. This is attributed to the very energetic free shear layer eddies that are impinging on the wall. The RMS level of the skin-friction fluctuations is determined by the structure of the impinging shear layer. When the upstream layer is thin, the shear-layer turbulence is more energetic and the skin-friction fluctuations are large relative to a thick boundary layer case. The larger skin-friction fluctuations in turn result in a proportionally larger Stanton number. [Ref C-45] Further downstream, the steady decrease in the Stanton number coincides with the growth of the thermal boundary layer following reattachment. [Ref C-46]

It is reasonable to expect that apart from the vertical velocity component, the magnitude of the streamwise velocity adjacent to the wall affects the local heat transfer coefficient and region of reattachment. In this regard, the magnitude and the maximum of the reverse flow within the separation region have to be considered, which is done by determining the profiles of the skin-friction coefficient. As the ratio between the upstream boundary layer thickness to the rib height increases, there is a decrease in the levels of skin-friction fluctuations throughout the recirculation, reattachment, and recovery regions. An increasing upstream boundary layer thickness was found to lead to a decrease in the turbulence level in the reattachment zone. Since skin-friction fluctuations are a measure of the limiting value of u'/U as the wall is approached, $C_f$' is expected to decline within the reattachment zone as $\delta/h$ is increased. When the flow is turbulent (large boundary layer thickness), the peak in fluctuating wall shear component is observed to present a maximum downstream of the reattachment point. [Ref C-48]

# 25. Experimental Facilities

The channel built is the simplified model of an internal cooling blade channel that is scaled up by a factor of 15. It consists of three pieces such as the inlet, test and exit sections and each section has a cross-sectional dimension of 75x75mm, with longitudinal dimension of 1400mm, 1260mm, 800mm respectively. The basic schematic of the test section can be found in Figure 2.1.

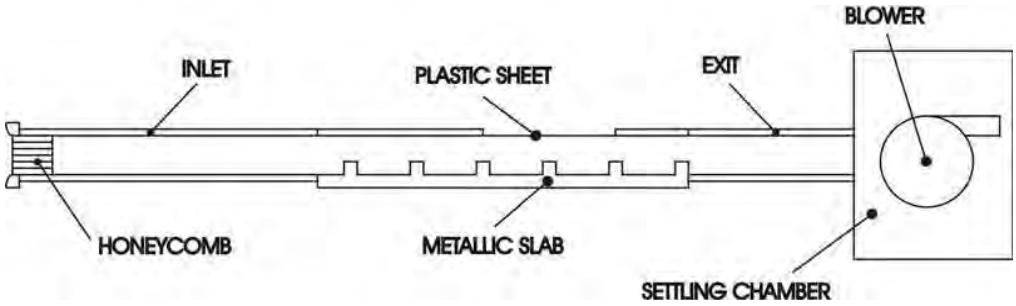


Figure 58: Schematic of the Experimental Setup

At the inlet section, made of Plexiglas, a honeycomb with 3mm cell size is used along with a NACA bellmouth to provide flow conditioning. The honeycomb effectively reduces the lateral components of mean velocity and of the larger turbulent eddies, as well as producing some turbulence of its own, which decays very slowly, creating a high turbulence intensity region in the test section. [Ref C-49] This setup is beneficial for damping out the inlet disturbances, as well as for maintaining a closer resemblance to the physical flow in a turbine blade.

The flow in the channel may expected to be in the turbulent regime, considering the fact that experiments are conducted at Reynolds number based on hydraulic diameter, $D_h$, equal to 40,000 which is much larger than the laminar threshold imposed by the Moody chart (Re > 3000) . There doesn't appear to be a well established entry length for turbulent channels, and the inconsistency in the literature is evident. The entry length for turbulent duct flows seems to vary from $10x/D_h$, to $50x/D_h$ and to $100x/D_h$ even in well established literature. [Refs C-50 – C-52] These approximations on the entry length are further diluted by the fact that a fully developed velocity field does not necessarily guarantee an invariance of local turbulence in the flow direction; the development length for a "fully developed" turbulence field is known to be much larger. [Ref C-52] For the test setup, at the inlet of the test section, even though the flow isn't believed to be fully developed, neither from a velocity profile nor from a turbulence intensity perspective, neither is the flow at the actual serpentine passages. Thus, a greater similarity between the model and real turbine blade is established.

The exit section, made of Plexiglas, is connected to a settling chamber with 3 layers of honeycomb structures employed to damp out the fluctuations created by the blower downstream. The setup operates below atmospheric pressure and special attention is given to acquire a good seal between the components. Note that the wind tunnel is in aspiration because the flow is more uniform at the inlet than with the opposite configuration.

Immediate upstream and downstream of the test section, static pressure measurements, along with temperature, are made at three faces of the channel (averaged pneumatically and numerically). Also, the inlet and exit sections are modified for an access hole to introduce a hotwire and Kiel-head total pressure probe at each end of the test section.

## 25.1 Flat Plate Test Section

The test section of the experimental rig, which is 1260mm long with an internal cross-section of 75x75mm², has been modified for heat transfer measurements, while the inlet and exit sections remained the same. The new test section is made of several components, where at the base of the channel a flat slab made of Steel AISI304 rests. The thickness of the slab, 25mm, has been chosen such that it respects the similarity with the serpentine channels of a turbine blade where the Biot number, which is the ratio between the conductive resistance to the advective term, is approximately equal to 1. The steel slab is painted black with uniform highly emissive layers of Nextel Primer 5523 and Nextel Suede Coating 428-26, by means of an airbrush. The black coating is mat, soft and due to diffuse reflection the surface is non-dazzling. The end finish is found to be suitable for infrared measurements due to its black-

body like behavior, albeit the camera is calibrated for the specific setup and the performance of the black paint is merely a matter of measurement quality.

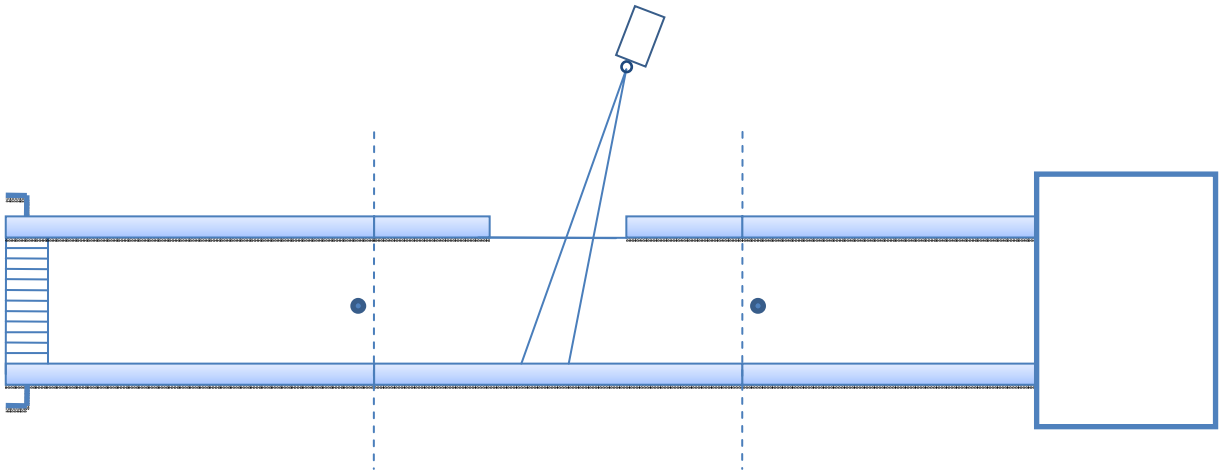

Figure 59: Schematic of the Optical Access Window utilized for IR-Thermography

The lateral and top walls around the slab are built with 10mm, and 15mm thick glass respectively. Plexiglas could not be used since during the experiments the temperature of the metal slab exceeds the melting point of the material. As the glass is opaque to infrared wavelength, an optical access window is designed on the top wall of the channel, centered on the test section, which spans across the whole width and is 300mm in length, Figure 59. For measurements done in the infrared spectrum, the commonly used materials are Sapphire, Germanium, Zinc Selenide and simple salts, which are transparent to the broadband infrared spectrum but are significantly more expensive than other common materials used in this setup. For this experiment, the optical access window is covered with a thin polyethylene film which is sufficiently transparent to the infrared spectrum, in the order of 80-85% transparency, allowing the measurements to be conducted. Since the plastic film transmits a suitable fraction of the infrared radiation, through an adequate calibration of the infrared camera, it can be used as the optical medium.

Even though the polyethylene film is *relatively* transparent to the infrared spectrum, the air temperature during the Infrared Thermography calibration procedure and measurement conditions are shown to vary significantly, in the order of 30 K; and through the convective process, this has a significant effect on the optical film temperature, which in return changes, though slightly, the radiation emitted by the film itself to the infrared camera. To prevent an error, a bias shift favoring lower slab temperatures caused by the change in film temperature, a cooling technique is used in order to maintain the film temperature at ambient conditions at all times.

A rectangular piece, fitted perfectly to the opening, made of four copper tubes (with an inner diameter of 6mm) and held together by elbow and T-type joints, is supplied with air at 4

bars from two opposite corners, and the air is bled on the film through centimeter apart holes located along the copper tubes, Figure 60.

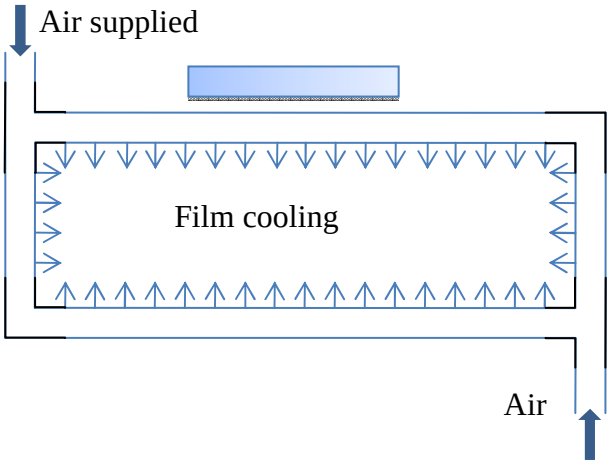


Figure 60: The optical film cooling apparatus

One of the other hindrances of not having a solid window is that the film has a tendency to bow towards the inside of the channel due to the pressure differential with the ambient, caused by the aspiration through the experimental rig (in the order of 40Pa). Therefore, the film is attached with two torsion springs (one on each end of the channel) in order to maintain both the structural integrity and the parallel nature of the surface with respect to the steel bottom wall, Figure 61.

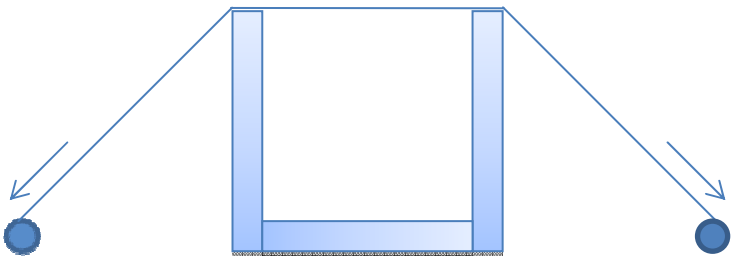

Figure 61

The slab is heated by means of a 25µm thick Inconel sheet which is powered by a 16V-150A DC power supply. The current is dissipated as thermal energy by the Joule effect and is conducted away by the parts in contact. Inconel is known to provide uniform heat flux across the applied area and retains strength over a wide range of temperatures. The Inconel folio is embedded in layers of heat resistant plastic sheet on each side such that electric contact between the Inconel and the slab is avoided, and the structural sturdiness of the folio is augmented. The Inconel assembly is attached to the test slab by means of a 3M adhesive,

and the channel is sealed with the glass side and top walls and silicon paste. Finally, the flat plate test section is placed on 100 mm thick thermal insulation. The cross sectional schematic of the test section is illustrated in Figure 62.

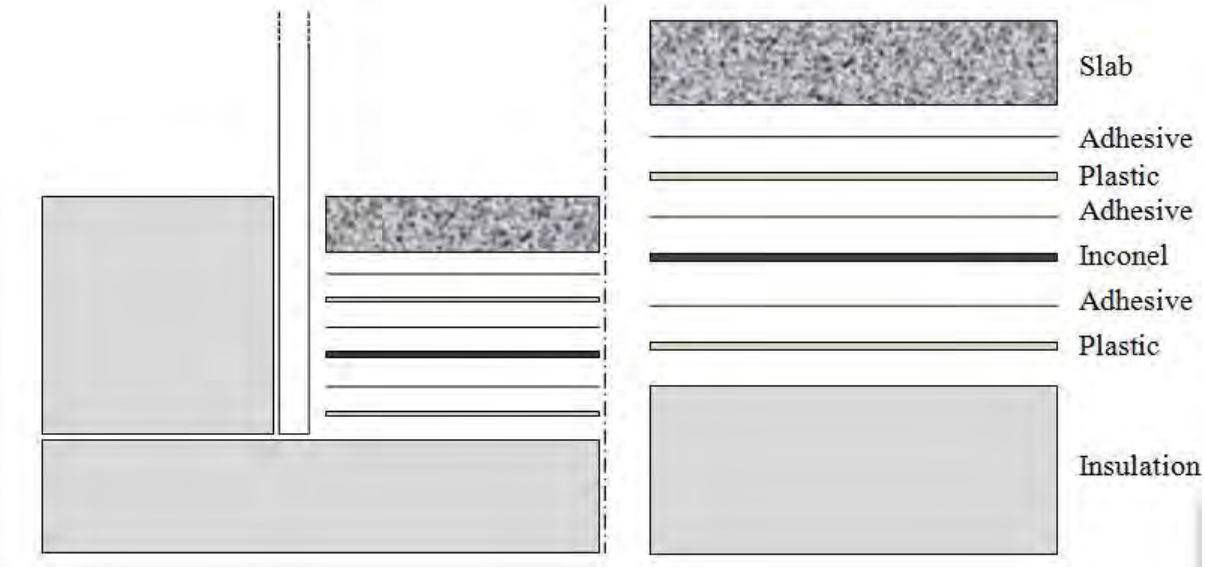


Figure 62: Cross-Sectional Schematic of the Test Section and the Slab Assembly

Since the thermal insulator has a conductivity of 0.024W/m-K and the AISI 304 metal slab has thermal conductivity of 16.2 W/m-K, considering the conservation of energy across the Inconel,

$$q''_{gen} - k_{steel}\left(\frac{dT}{dx}\right)_{x=0^+} - k_{ins}\left(\frac{dT}{dx}\right)_{x=0^-} = 0 \qquad \text{Eq. 2.1}$$

and as an order of magnitude approximation considering the thicknesses of the slab and insulation, 25mm and 100mm respectively and a temperature difference of 30°K from the insulator to Inconel and 1.5°K from the metal slab to Inconel, the heat flux losses into the insulator can be estimated to be in the order of 0.7%. This demonstrates clearly that the main direction of the heat flux will be towards the metallic slab where the heat flux encounters a minor thermal resistance. The final assembled test section and the experimental facility can be seen in Figures 63 and 64.

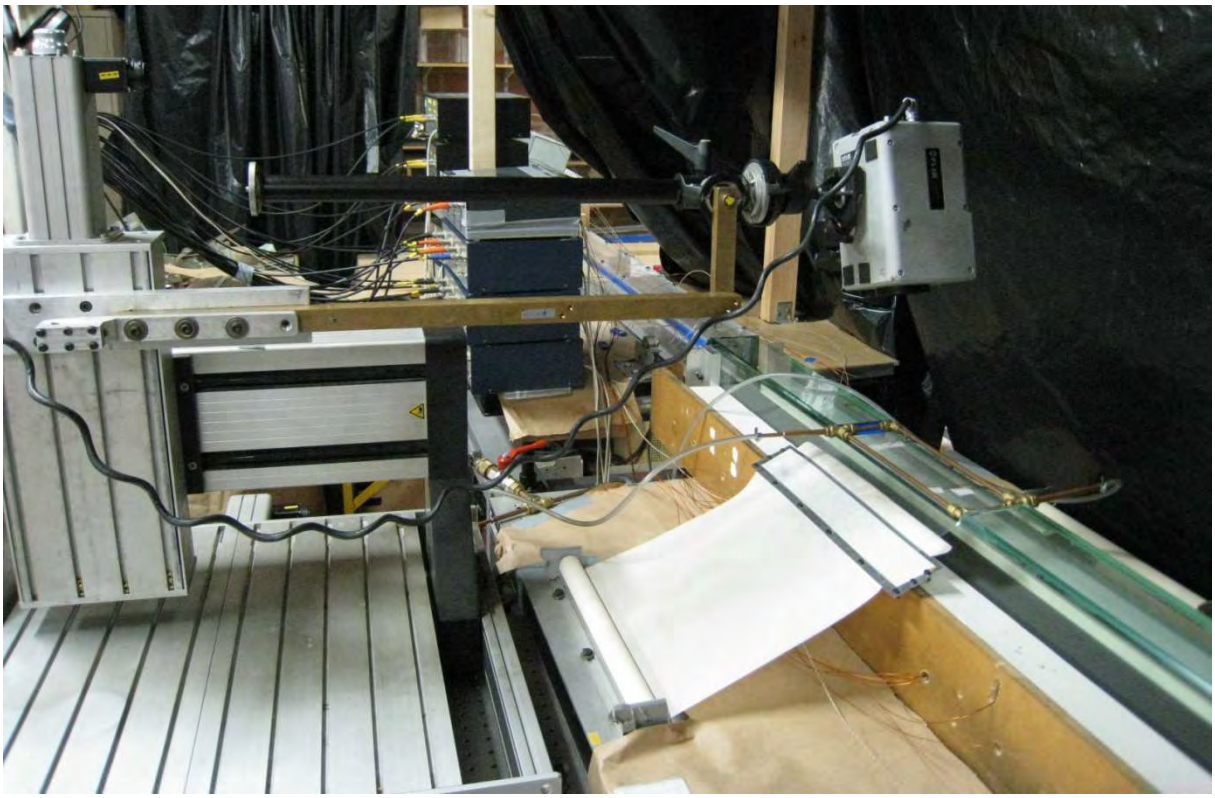

Figure 63: Assembled test section and the experimental facility

Figure 64: Assembled test section and the experimental facility

## 25.2 Ribbed Test Section Modifications

On the ribbed slab, there are 3 sets of 5 thermocouples distributed equally along the width of the slab, mounted 0.1 mm from the surface, Figure 65. Each set of thermocouples is located 108mm downstream of 1$^{st}$, 2$^{nd}$ and 4$^{th}$ rib. These thermocouples are implemented in order to monitor the development of the temperature distribution along the slab over the time, as well as for the calibration procedure of the infrared camera.

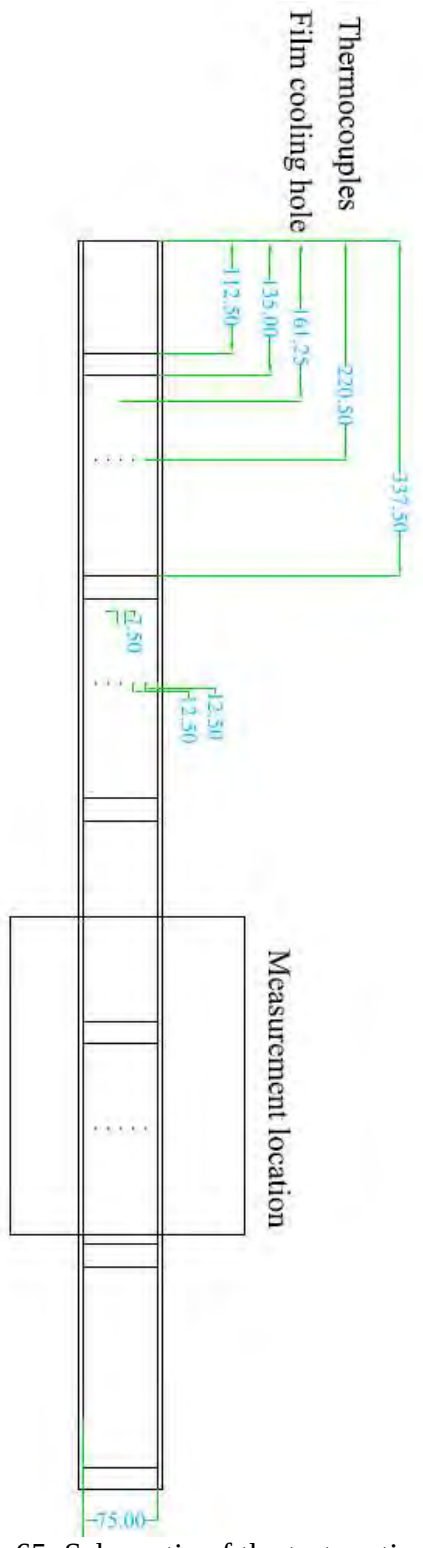


Figure 65: Schematic of the test section - Top View

In the present work, the selection of the test section geometrical dimensions reflects the research line of the former studies carried out in this field at the VKI. The channel geometry parameters are chosen as follows:

- A rectilinear channel of a squared cross section
- A blockage ratio of: $\frac{h}{D_h} = 0.3$
- A rib pitch to height ratio of: $P/h = 10$
- An angle of attack with respect to the mean flow direction of: $\alpha = 90°$

This configuration was chosen for the experiment, since it combines the settings of a standard reference case like squared cross section with a high blockage ratio of the channel and an arrangement of traverse rib perturbators. The rib height of 22.5mm providing a pitch to height ratio of $P/h = 10$ , which lies within the optimal range which has been experimentally determined by many authors to yield the highest enhancement of heat transfer rate in the respective geometrical arrangement. The inter-rib space is 225mm and has been chosen in accord with the test section previously investigated by Çakan [Ref C-26] and Casarsa [Ref C-36]. The test section is manufactured of Steel AISI304.

The basic schematic of the setup is depicted in Figure 66. The camera is located at 46.8 degrees from the vertical; since the radiation exchange of surfaces are linearly proportional with the view factor, this configuration is selected to provide a good compromise for pixels on both the vertical and horizontal surfaces. The downstream face of the rib, along with the rib-shadowed portion of the inter-rib space is observed via Newport 75K00ER.3 mirror, featuring a reflectance in the order of 95% in the 8-9 micron range of the camera.

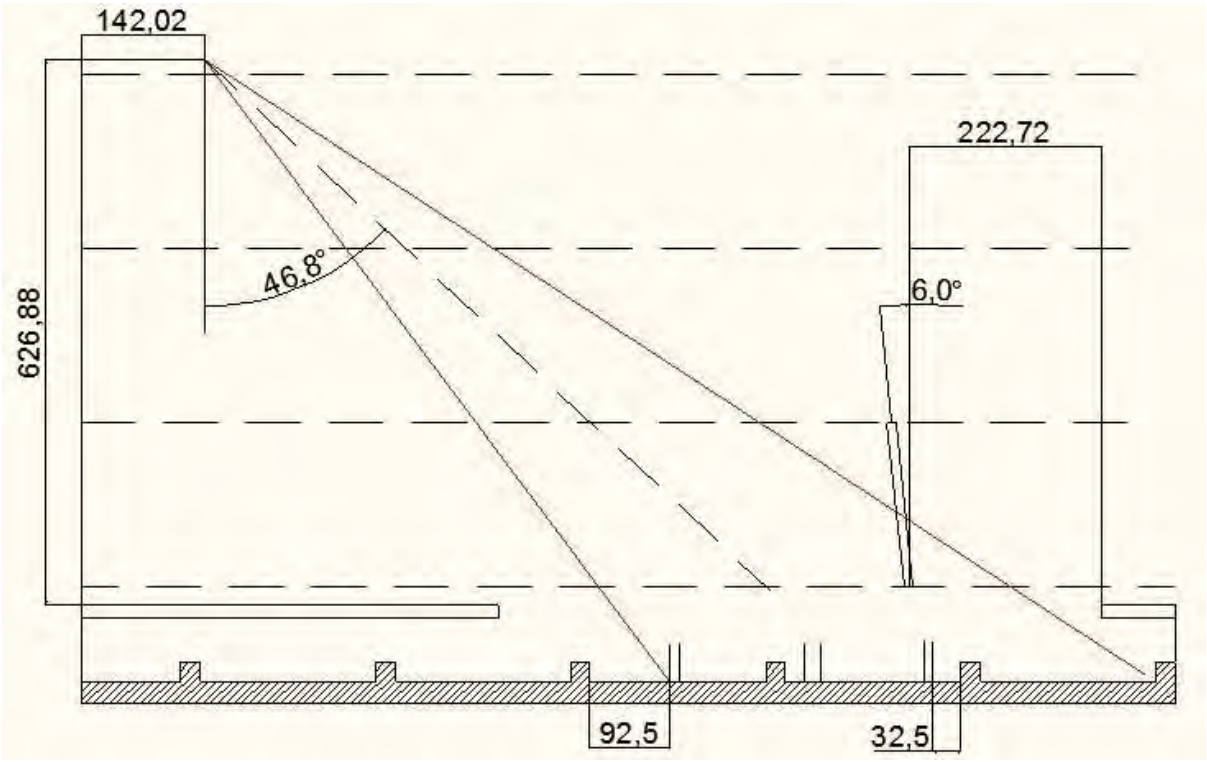


Figure 66: Illustration of the Test Section Camera and Infrared Mirror Locations

# 26. Technical Approach

## 26.1 Infrared Thermography Calibration Methodology

### Pixel by Pixel Approach

The "Pixel by pixel" technique consists in founding a calibration curve for each pixel of the image. The surface is heated up at different isothermal conditions and the corresponding thermograms are grabbed in order to link the object signal of each different pixel detected by the IR-camera with the relative uniform temperature and finally these data are fitted with a second order polynomial curve.

This technique doesn't require any assumptions and allows to consider most of the error sources as constant noise coming from the surrounding and out of focus phenomenon due to varying distance of the investigated surface. The main disadvantages can be summarized in the need of a perfect isothermal condition of the entire domain during the calibration and to maintain exactly the same position of the camera respect to the target both in calibration and measurement.

### Single point Approach

In the ribbed slab configuration the isothermal surface condition is not achievable which is why the "Single point calibration" has been preferred. It is based on the assumption that the slope of the calibration curve is constant for all the pixels of the image; this allows to use just one curve found for a reference point, the temperature of which is well known, to retrieve the complete temperature map.

### Ribbed Slab Calibration

Figure 67 presents the raw object signal image acquired by the camera. The superimposed rectangular regions (calibration reference zones) indicate the location of the thermocouples embedded into the slab, as observed directly and reflected from the mirror, from the view point of the infrared camera. In the present experimental work the calibration reference zones are bound by the center 3 thermocouples, the variation of temperature is imposed cooling down the slab in natural convection. Since this calibration methodology is based on the assumption that the slope of the calibration curve is constant for all the pixels of the image, considering the large difference in view factors of the direct and reflected portions of the image, independent calibration curves are established for the directly observed and mirror reflected portions of the image. Figure 68 and 69 presents the object signal (OS) versus temperature calibration curves for the two different domains. For the pixels outside of the calibration zone, the out of focus effects are compensated by acquiring infrared images under conditions where the slab is at uniform temperature (ambient); and the deviation of OS from the reference zone is utilized as a local bias shift, Figure 70 and 71.

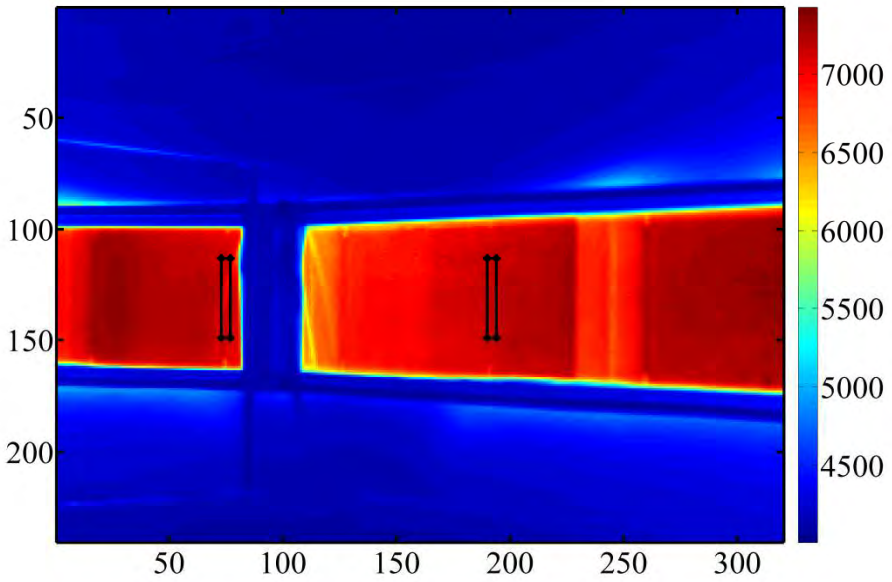


Figure 67: Raw IR Image with Thermocouples locations

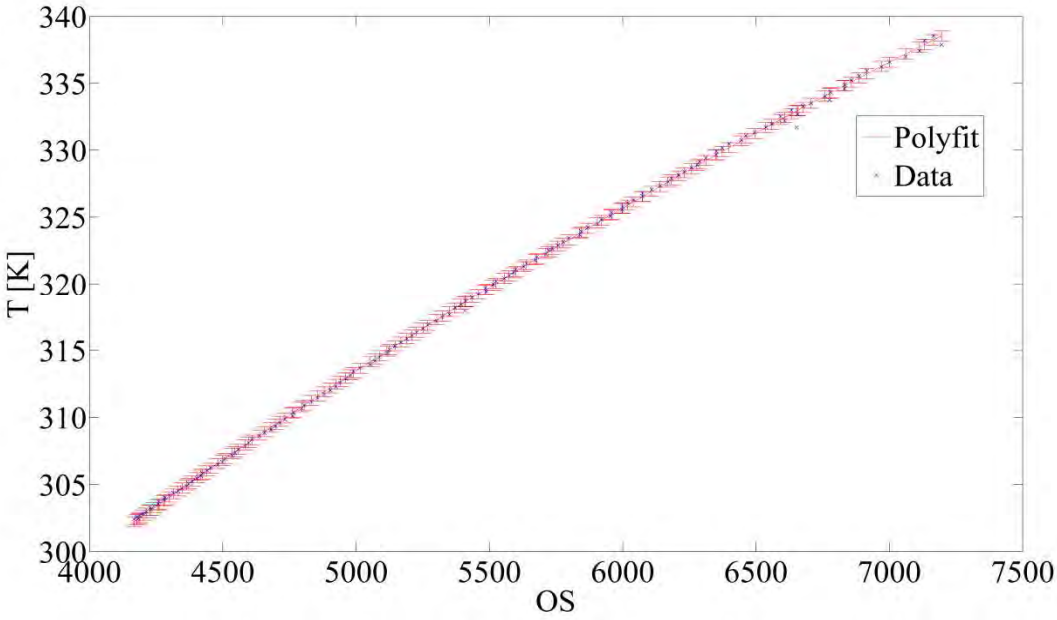


Figure 68: Object Signal versus Thermocouple Temperature - Direct View

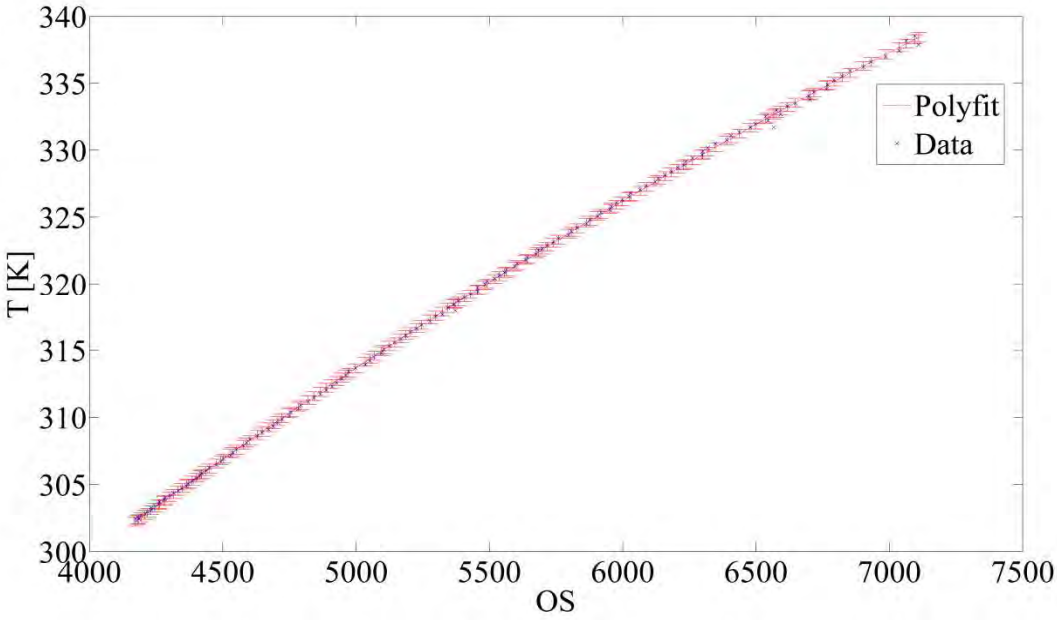


Figure 69: Object Signal versus Thermocouple Temperature – Mirror Reflected View

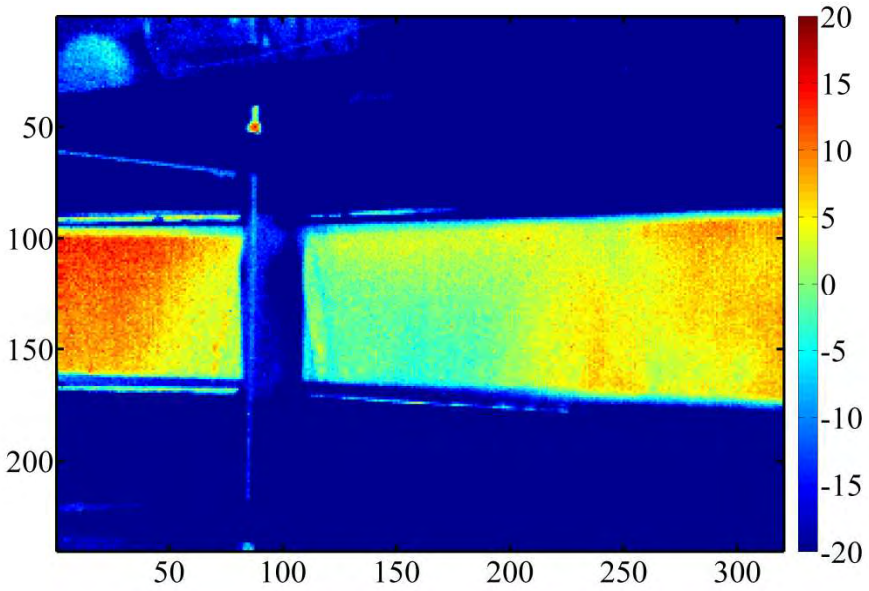


Figure 70: Ambient Object Signal Shift from Reference Zone - Direct View

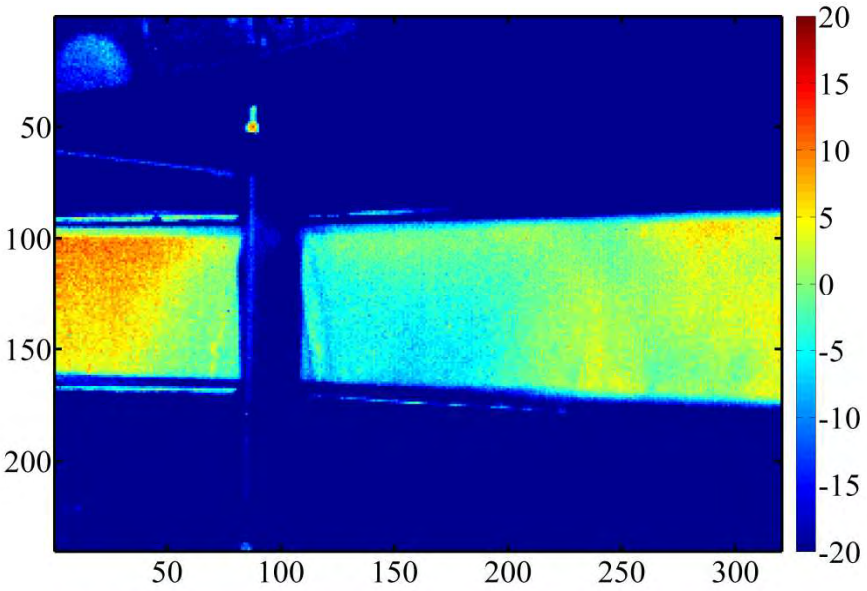


Figure 71: Ambient Object Signal Shift from Reference Zone – Mirror Reflected View

## 26.2 Ribbed Slab - Image Processing

Figure 72, presents an exemplary temperature distribution along the measurement section, while the test section is at steady state. This distribution is achieved by utilizing the two calibration curves with local out of focus compensation. The black lines superimposed on the image indicate the regions which consist of the different geometric features such as the upstream, top, downstream portions of the rib, along with the direct and reflected views of the inter-rib space.

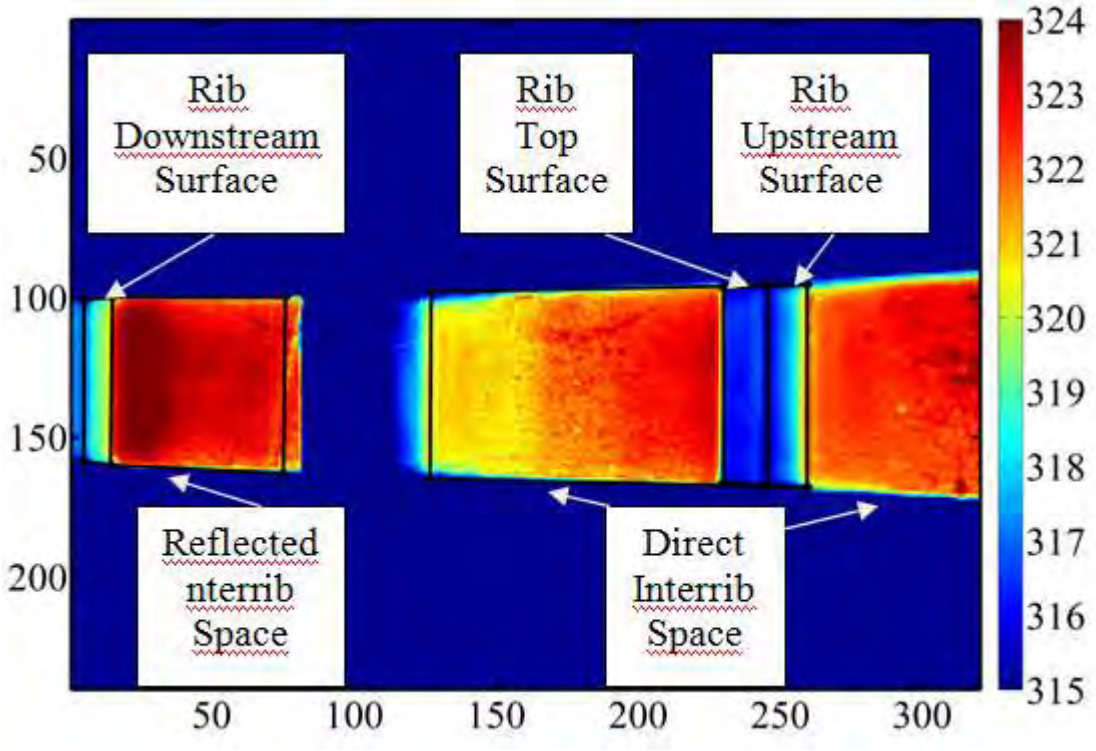


Figure 72: Temperature Distribution [K]

All portions of the image are transformed independently by a perspective transformation, which uses bicubic interpolation, and are projected onto a plane. The resolution of the transformed image is superficially augmented in each dimension through sub-pixel interpolation. Since this procedure is conducted independently on different regions of the geometry and perspective of the camera varies significantly along the image, it is not possible to define a true uniform scale factor, nonetheless, the presented temperature distribution has a scale factor of 1.7 pixels/mm, Figure 73. The different regions of the geometry, as projected on a single plane, are identified; the pre-rib portion of the data is 78mm of the domain preceding the upstream face of the rib (40% of the previous passage), and the region identified as inter-rib space is the complete space in between the 4$^{th}$ and the 5$^{th}$ ribs.

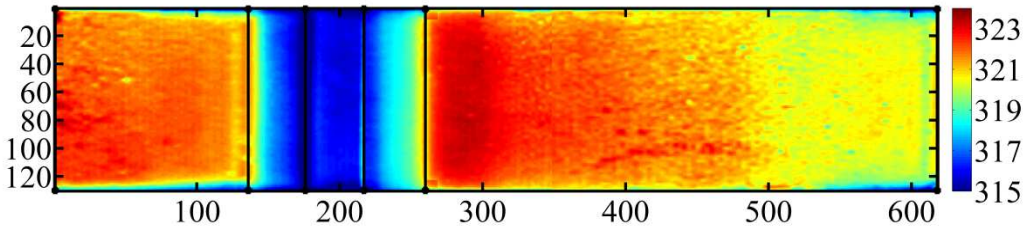


Figure 73: Temperature Distribution - Perspective Corrected [K]

The temperature data presented in Figure 73 has several limitations, one being the fact that the data, as is, clearly is not periodic in the rib domain indicated by the fact that the temperatures at the end of the pre-rib region do not coincide with the temperatures towards the end of the following domain inter-rib space. The aperiodicity is evoked by several factors, such as the edge effects, heating of the bulk flow, and the aerodynamically non fully developed flow field.

This aperiodicity would have been unproblematic if there existed surface temperature data for the entire test section, and thus the entire section could have been modeled by a FEM solver to retrieve the local surface heat flux distributions. The issue arises when there exists surface temperature data for only a portion of the test section and which boundary condition to impose on the transverse faces of the modeled geometry while retrieving heatflux. Imposing adiabatic boundary condition would be highly unrealistic considering the fact that there are large local thermal gradients within a rib passage. Furthermore, imposing periodicity boundary condition on an aperiodic temperature domain, results in superficial heat sources and sinks. Thus, one of the reasonable approximations, which also makes this data set more generic and applicable in a broader sense, is to perform a linearly weighted averaging in the overlap region (pre-rib and the overlapped inter-rib space), based on axial direction, such that the original pre-rib temperature data is more dominant in the vicinity of the rib, Figure 4.8. This doesn't only provide a smoother transition, but also creates a realistic temperature distribution for a generic ribbed channel where periodicity holds. This is as well the general philosophy of the image post-processing methodology, which is to generalize the currently studied case as much as possible. Nonetheless, the results acquired by periodicity corrected and raw temperature boundary conditions are compared within the results.

As observed in Figure 74, there exists a high degree of local temperature fluctuations on the surface of the passage, which are mainly caused by the non-uniformity of the paint layer. In order to reduce these effects a median filtering methodology is used; this is typical for applications when the goal is to simultaneously reduce peek noise and preserve edges, Figure 75. The temperature distribution across the channel is averaged with respect to the symmetry plane, Figure 4.76, followed by a Gaussian low pass filter to smooth out the local gradients of temperature induced by the averaging process, Fig. 4.77.

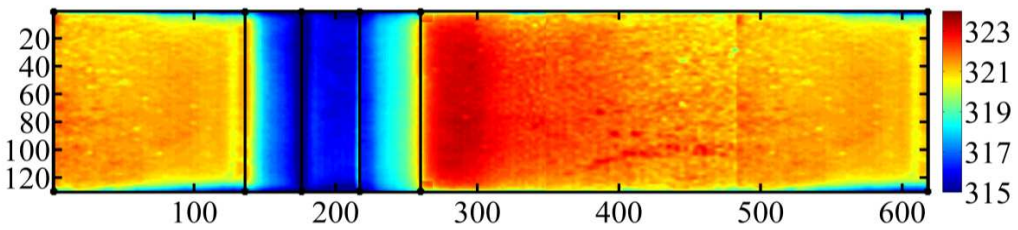


Figure 74: Temperature Distribution – Periodicity Corrected [K]

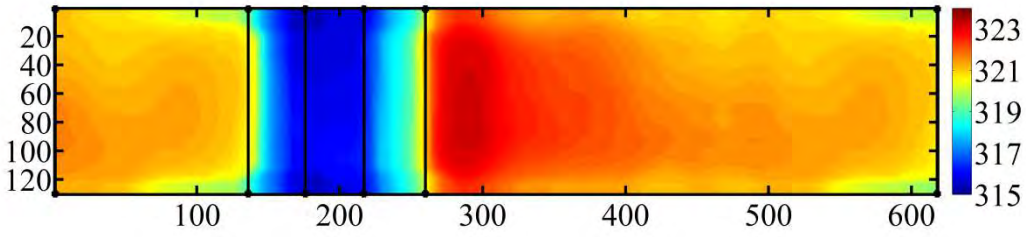


Figure 75: Temperature Distribution – Median Filtered [K]

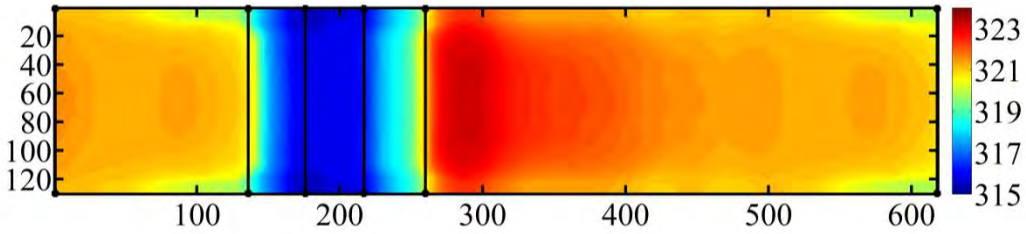


Figure 76: Temperature Distribution – Up/Down Symmetry [K]

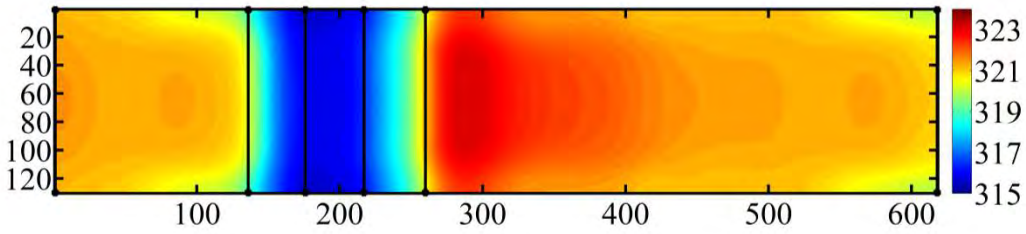


Figure 77: Temperature Distribution – Gaussian Low Pass Filter [K]

## 26.3 Ribbed Slab – Surface Heat Flux Computation

The boundary conditions for the numerical problem are uniform heat flux, in this case 1733 W/m$^2$ along the bottom surface of the slab, measured temperature distribution on the wetted surface, adiabatic side walls and periodic boundary condition on the transverse direction where the solid, in reality, is interrupted. In the numerical model, the only modeled portion of the slab volume is a single complete passage where the surface Infrared Thermography temperature measurements exist, Figure 78. The passage is modeled such that the rib is preceded by 45mm of inter-rib space and after the downstream face of the rib, the remaining 15.75mm of the inter rib space is modeled.

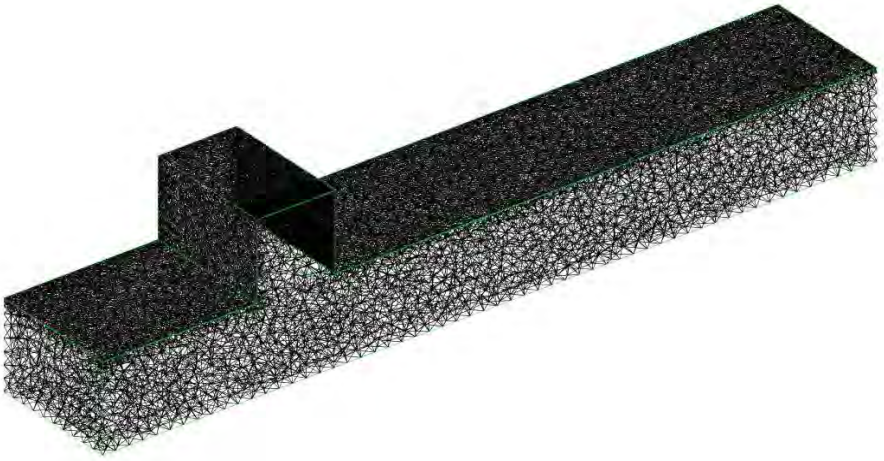

Figure 78: Comsol Mesh Characteristics

Over the surface of the ribbed passage, the 160 micron paint layer is modeled, measured a priori by the Fischer Mp20 sensor. The thermal conductivity of the paint layer is imposed as k=0.3 W/m-K based on literature [Refs C-60, C-61] and shows consistency with the heat flux distributions in the passage. There exist 85787 and 132538 mesh elements in the paint layer, and ribbed metal slab domain respectively. The convergence criterion is set to $10^{-10}$ for the relative pre-conditioned residuals. It has been shown that further grid refinement does not significantly affect the solution computed in the model.

# 27. Results

Figure 79 presents the measurement imposed projected surface boundary temperature within the passage. Since the continuity in the boundaries of the Comsol model is established via periodicity condition, the redistribution of the results, see Figure 78, in a given passage is non-error producing. In addition, all dimensions in the passage are normalized by the height of the rib, H. From the temperature distribution, lacking the heat flux information, it is only possible to point out some general trends in the passage. The lowest temperatures are observed in the vicinity of the rib. Over the rib, on the upstream facing wall, $-1.5<x/H<-0.5$, there is a continuous decrease in temperature, followed by a relatively constant temperature region on the upper surface of the rib with a slight increase towards the edge, $|x/H|<0.5$, Figure 80. On the downstream side, $0.5<x/H<1.5$, the temperature monotonously increases, and this trend continues in the beginning of the inter-rib space until x/H=2.2. It is possible to observe the existence of this hot spot, for all the width-wise location, Figure 79. Temperatures over the rest of the inter-rib surface decrease almost monotonously, from x/H 2.2 to 6 and from -6 to -1.5. The slope of this temperature reduction decreases significantly for $-6<x/H<-2$, followed by a sharp sudden decrease in $-2<x/H<-1.5$. For all lateral cross-sections, towards the side walls, there is a smooth decrease in temperature with respect to the centerline, y/H=0, more significant in the region $|y/H|>1.3$.

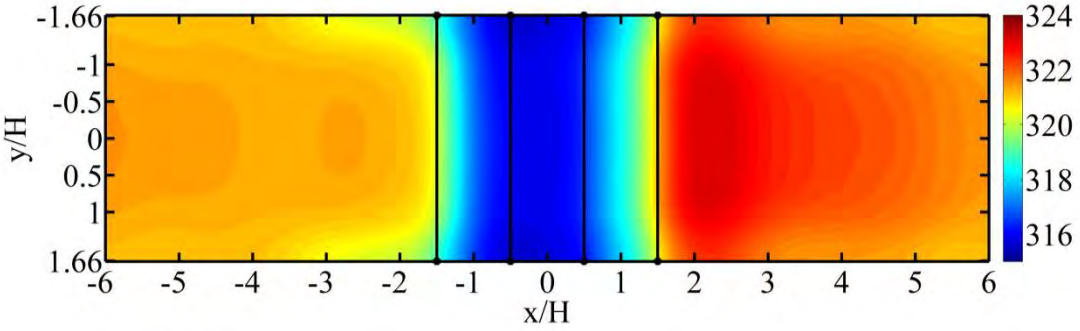


Figure 79: Comsol Temperature Distribution at the Projected Boundary [K]

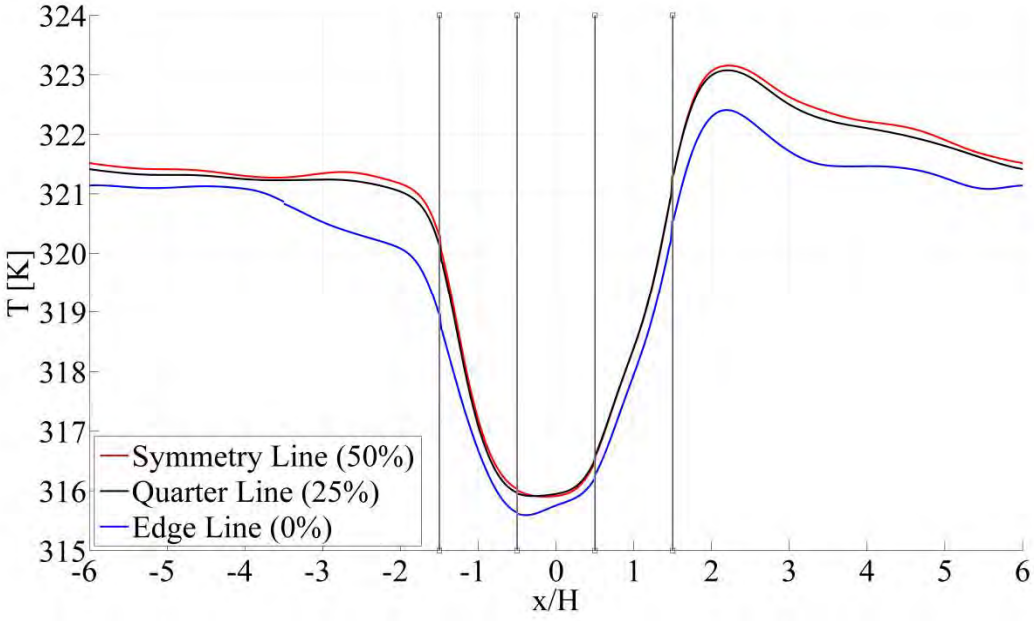


Figure 80: Comsol Temperature Distribution [K]

By applying this temperature distribution to Comsol as boundary condition, it is possible to acquire the heat flux normal to the boundary, as presented in Figure 80; where the values are normalized by the heat flux imposed on the bottom surface of the ribbed channel, in this case 1733 W/m$^2$. It is important to point out that there is a large effect of heat flux redistribution within the solid. Comparing temperature profiles, Figures 79 and 80, with the respective heat flux distributions, Figures 81 and 82, it is evident that even though the global trend of low temperature implying higher heat flux extraction from the surface of the solid is valid, in various regions of the wetted surface, these effects are amplified, suppressed, and at certain regions are completely dominated over by 3-D conduction effects.

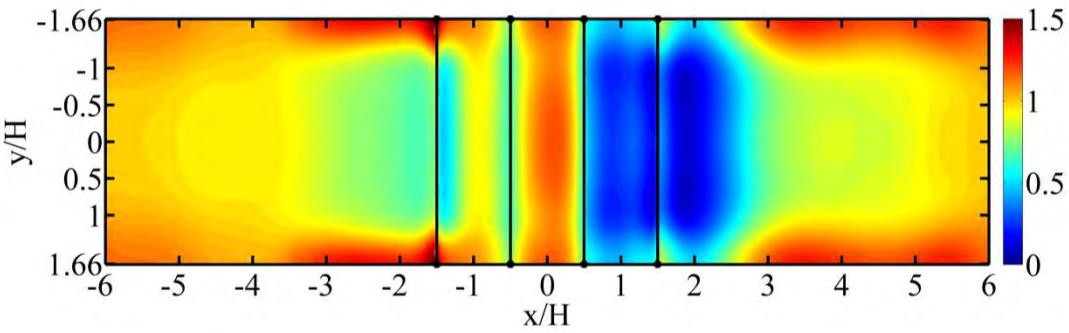


Figure 81: Comsol Normalized Heat Flux Distribution at the Projected Boundary [-]

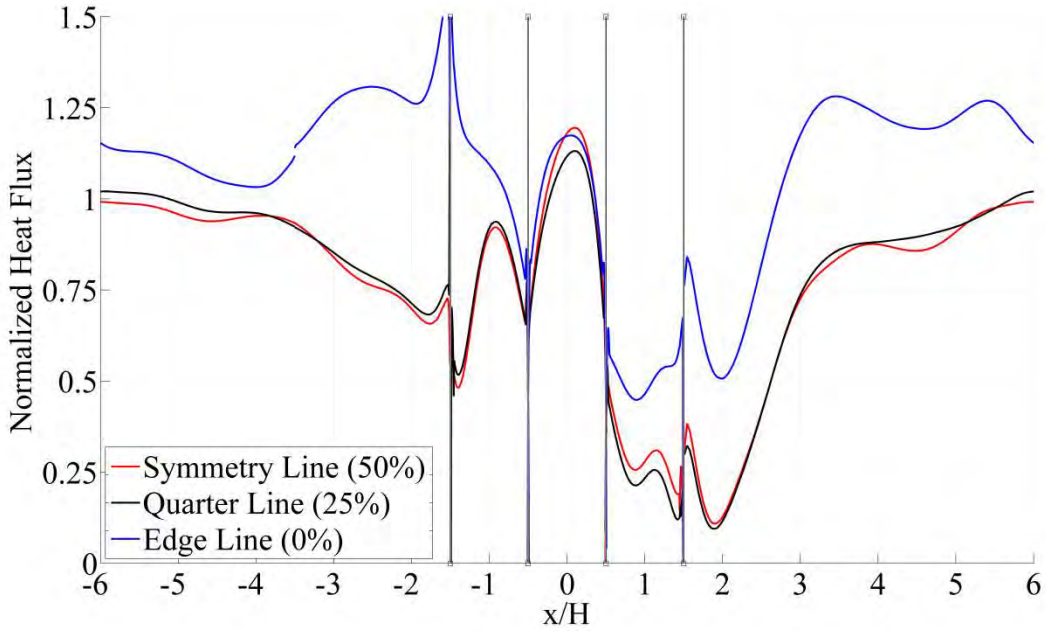


Figure 82: Comsol Normalized Heat Flux Distribution [-]

For example, in the core region prior to the rib, -3.5<x/H<-1.5 |y/H|<1.3, it is possible to observe an almost uniform decrease in heat flux, where the temperature presents an initial plateau followed by a steep decrease. Similarly on the upstream face of the rib, -1.5<x/H<-0.5 |y/H|<1.3, where the temperature presents a monotonous decrease, the heat flux is shown to decrease followed by a peel and then a gradual decrease. On the top surface of the rib, towards the center, there exists a peek in heat flux, not noted in the temperature contours. Similarly, even though the hot spot in temperature contours occurs at about x/H=2.2, the heat flux minima occurs at x/H=1.9. This aforementioned behavior is caused by the 3-D redistribution of heat flux due to the conduction within the solid. Especially in the vicinity of the rib, the heat flux pattern is dominated by the heat sink effect of the rib, clearly observed in Figure 83.

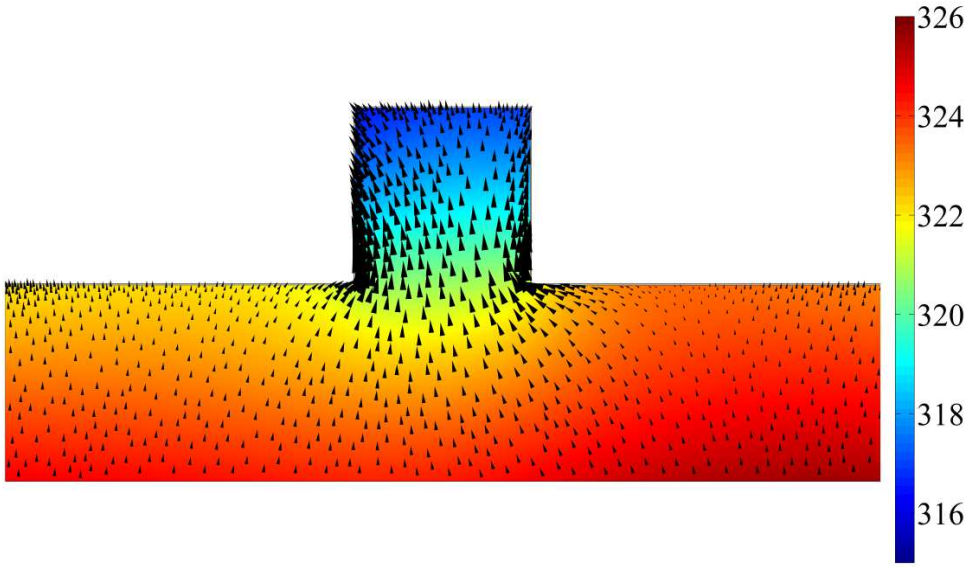


Figure 83: Comsol Temperature Distribution with Heatflux Pattern - Rib Symmetry Line [-

Having the temperature and the heat flux distributions, it is possible to calculate enhancement factor distributions over the wetted surface,

$$EF = \frac{Nu}{Nu_o} \qquad \text{Eq. 5.1}$$

where

$$Nu = \frac{hD_h}{k_f} \qquad \text{Eq. 5.2}$$

$$h = \frac{q_n''}{T - T_\infty} \qquad \text{Eq. 5.3}$$

and

$$Nu_o = 0.0243\, Re^{0.8}\, Pr^{0.4} \qquad \text{Eq. 5.4}$$

presented in Figures 84 and 85. Overall, the enhancement factor distributions are shown to follow the same trends as heat flux. The reasons behind this specific distribution are more apparent when related to the aerodynamic flow field.

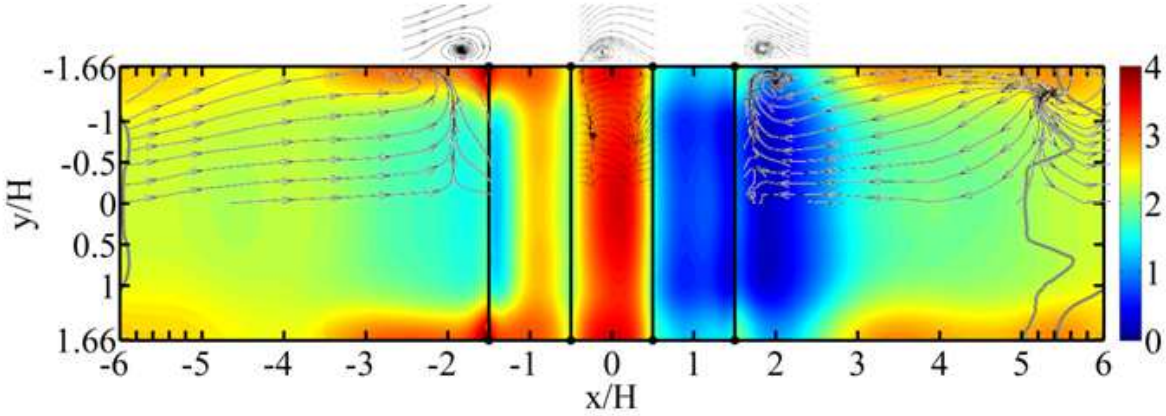


Figure 84: Comsol Enhancement Factor Distribution at the Projected Boundary [-]

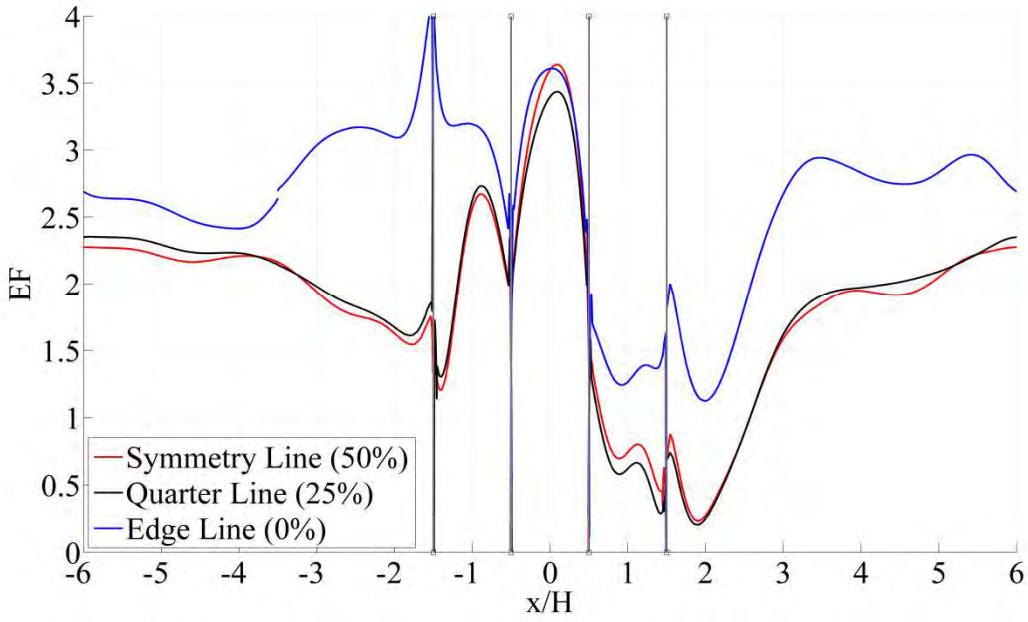


Figure 85: Comsol Enhancement Factor Distribution [-]
Periodic Boundary Condition/Modeling Paint

## 27.1 Aero-thermal Effects

Considering the insight about the flow structures which Particle Image Velocimetry experiments of Casarsa [Ref C-36] provide, it is possible to identify some unique distributions of enhancement factor associated with the nearby flow feature, on half of Figure 84 are the surface streamlines superimposed from [Ref C-36]. The schematics denoted on the side of the figure are the $V_3$, $V_2$ and $V_1$ vortex structures, located in front of, over, and behind the rib respectively, observed around the channel centerline.

The -6<x/H<-3.8 region, is the part of the ribbed channel where the flow is attached immediate downstream of a large separation region. Slight overall decrease in enhancement factor is associated with the boundary layer growth of an attached flow; this is the portion of the ribbed channel which resembles the behavior of a developing flat plate boundary layer. Due to the increase in boundary layer thickness the heat transfer decreases in the stream-wise direction. Most of the benefit associated with the high overall level of heat transfer, EF≈2.4, is caused by the increased turbulence levels and the complex flow structures associated with the flow field. The enhancement factor is observed to be higher towards the edges caused by the increased level of fresh cold fluid entrainment due to the secondary flow features.

Downstream, for the region bounded by-3.8<x/H<-1.5 |y/H|<1.3, the initial decrease in the enhancement factor, from to x/H≈-3.8 up to x/H≈-2.5 is due to the potential effect of the rib reducing the axial component of the velocity, causing an adverse effect on the boundary layer (an increase in boundary layer thickness). Further downstream, in the region -2.5<x/H<-1.5, the flow is dominated by the existence of the clockwise rotating corner vortex $V_3$. In the vicinity of the rib, -1.8<x/H<-1.5, this vortex creates a local downwash zone where the flow impinges on the bottom surface, indicated by the local peak in EF. Further away from the rib, in -2.5<x/H<-1.8, the flow direction opposes the mainstream flow due to the rotation direction of the vortex; this not only prevents the cold fluid from coming in contact with the heated surface, due to blockage created by this flow structure, but also creates a local low momentum zone, yielding to a region of low EF, especially visible in the symmetry plane where the vortex strength is much higher. For the same region, towards the lateral wall, -3.8<x/H<-1.5 |y/H|>1.3, the corner vortex $V_3$ seizes to exist and the flow field is dominated by the upwash effect, caused by the S2 flow structure; since S2 is created by the pressure driven acceleration of the rib impinging mainstream flow, this high momentum region is observed as a global increase in EF distributions.

The upstream facing of the rib is denoted in Figures 5.6 and 5.7 in the -1.5<x/H<-0.5 domain. Initially, concentrating on the core flow region, |y/H|<1.3, at first in the -1.5<x/H<-0.8 domain, due to blockage created by the $V_3$ flow structure, the mainstream flow can't come in contact with this portion of the upstream surface of the rib, indicated by a low enhancement factor region. Around x/H≈-0.8, a peak in EF can be observed; this peak is the combined effect of the downwash of the $V_3$ vortex along with the impingement of the mainstream flow to the upstream surface of the rib, the location of this peak is consistent with the PIV data. Beyond the impingement region, -0.8<x/H<-0.5, the flow deviates from the surface of the rib, creating a relative low momentum region, indicated by a decrease in EF. For the same region, in the viscinity of the side walls, -1.5<x/H<-0.5 |y/H|>1.3, the flow field is dominated by the $S_2$ flow feature being pulled up by the secondary flow vortices over on top of the passage; and since $S_2$ is a high momentum region, created at the horizontal surface of the channel, similar effects of enhancement are observed as it is convected upwards.

The top face of the rib, -0.5<x/H<0.5, is where the overall highest EFs are observed. This is caused by the reduction in effective area of the mainstream flow (due to the existence of the rib), in turn resulting in much higher momentum flow, generating a region of high heat transfer rate. Locally, the location of the peak, at x/H≈0.15, is consistent with the downwash caused by the $V_2$ vortex, which is the dominant flow feature in this portion of the passage.

Towards the lateral wall, at the edge, the EF peak is observed to be slightly wider, in agreement with the larger, more diffuse, $V_2$ vortex formation, Figure 85.

The downstream surface of the rib, $0.5<x/H<1.5$, along with the immediate downstream in the axial direction, $1.5<x/H<2$, are the regions where the lowest EF values are observed. This is caused by the large separation region behind the rib, generating a local low momentum region with reversed flow, where the heat transfer is considerably less than the rest of the passage. This is clearly observed by the sudden drop in EF for $0.5<x/H<0.9$. In addition to the global separation, there is the existence of a counter clockwise rotating vortex $V_1$, further isolating the region from the mainstream flow, $0.9<x/H<1.5$. The local peak at $x/H\approx1.2$ is caused by the downwash of the vortex impinging on the downstream surface of the surface, locally increasing EF. Towards the lateral wall, $|y/H|>1.3$, the effects of the separation are reduced by the $S_1$ flow feature, a region of low momentum fluid in the horizontal plane, being sucked upwards with relatively larger velocity due to the secondary flow features, hence increasing the heat transfer rate on the vertical face of the rib.

Immediate downstream of the rib in the inter-rib space, $1.5<x/H<2$, the flow is dominated by the existence of the rib downstream corner vortex $V_1$. There is an initial relative increase in EF, $x/H\approx1.2$, caused by the impingement of the downwash of $V_1$, followed by the gradual decrease due to the low momentum isolation zone inherent to the region.

Further downstream of the rib, $2<x/H<6$, is associated with a large separation region, until the flow reattaches at around $x/H \approx 5.5$. Due to the fact that there is increased penetration of the cool mainstream flow at increased axial position, the EF increases monotonously within $2<x/H<3.4$. At around $x/H\approx3.4$, there exists an unexpected peak in EF prior to the reattachment region suggested by [Ref C-36]. Such an occurrence has been observed in literature a priori [Ref C-42]; which can be explained by the local minima in skin friction, local maxima in fluctuating component of the shear stress, and local sharp maxima in reverse flow velocity, [Ref C-48]. In this region, the reverse flow velocity is large enough to create a local high momentum region, due to the strong recirculation created by the shear layer and its interaction with the wall, locally augmenting heat transfer characteristics; a peak in heat transfer prior to the reattachment point is well documented [Ref C-42, C-45, C-46, C-47]. At increased axial position, $x/H \approx5.5$, the flow reattaches, but the maximum EF factor is observed further downstream. For this geometry, since the created separation region is relatively narrow (~5H), the peak in heat transfer occurs after the reattachment point, [Ref C-46, C-47].

## 27.2 Reattachment and Peak Enhancement Factor

The reattachment region is estimated in Figure 84 by the gray lines drawn in between $5<x/H<6.1$. The earlier line presents the local maximum in axial derivative of enhancement factor. This line indicates a strong increase in EF in a region bordering the large separation bubble, the sudden increase in EF can only be indicative of the beginning of the reattachment zone. If a reattachment *point* is to be selected, this would be the lower limit on the reattachment region. The gray line further downstream indicates the location of the axial

maxima in EF, considering that the literature [Ref C-46, C-47], for this geometry, suggests that maxima in heat transfer occurs downstream of the reattachment, the second line is an upper limit for the reattachment point.

In reality, the reattachment point, selected aerodynamically by the change of sign in the skin friction coefficient, is suggested to lie in between. In this case, the aerodynamic investigations of Casarsa [Ref C-36] suggested that the aerodynamic reattachment occurs at around $5.3<x/H<5.7$. This is consistent with the observation of the suggested upper and lower limits of reattachment region. When compared with convective measurements conducted in literature [Ref C-36], it has been observed that the peak heat transfer occurred at $4.5<x/H<6$; the results seem to be in good agreement with the current study.

Furthermore, analyzing the shape in the spanwise direction, Figure 84, it is observed that there exists an earlier re-attachment in the channel centerline. Towards the side walls, the location of the reattachment point initially increases until $y/H = 0.8$, followed by a decrease in reattachment length towards the very edge of the channel. This type of behavior in 2-D reattachment point was also observed by [Ref C-42]

## 27.3 Comparison with literature

Comparing some of the averaged values with the liquid crystal measurements conducted by Cakan [Ref C-26] on the purely convective case study at a lower Reynolds number, the data seems to be in agreement. Table 1 presents the area averaged EFs for different portions of the ribbed channel. The average EF on the upstream face is relatively high, 2.35, due the impingement of the mainstream flow on the surface. On the top face, the EF is even further augmented, 3.02, due to the local increase of momentum by the decrease in effective area. On the downstream side of the rib, the lowest average EF is observed, 0.86, due to the large separated region behind the step. The rib, inter-rib and domain averaged EFs are 2.08, 2.01 and 2.03 respectively. When the findings are compared with the results by Cakan [Ref C-26], there seems to be a trend of redistribution of heat flux such that the enhancement factor is more distributed across the domain. This is somewhat expected since with conjugate phenomena enables the redistribution of heat flux in the entirety of the solid domain.

Figure 86 presents the comparison of the findings in the current study with respect to similar studies conducted in prior literature, investigated for the channel symmetry line. The “Convective LC” data are the results gathered by Cakan [Ref C-26] in his convective liquid crystal study conducted for Re 30,000. The “LES” data is from an internal study at VKI, based on the current test case for the conjugate problem [Ref C-2]. The “Conjugate IR” data is the result of the conjugate heat transfer infrared thermography experiments conducted by Agostini [Ref C-35]. All test cases show remarkable resemblance to the current experimental data set. The “Convective LC” dataset is difficult to compare with the current investigation, not only due to the lack of underlying physics associated with the heat transfer within the solid domain (conjugate case study), but also due to the fact that it is of much lower resolution, since the technique used in the investigation only permitted the observance of iso-temperature contour lines.

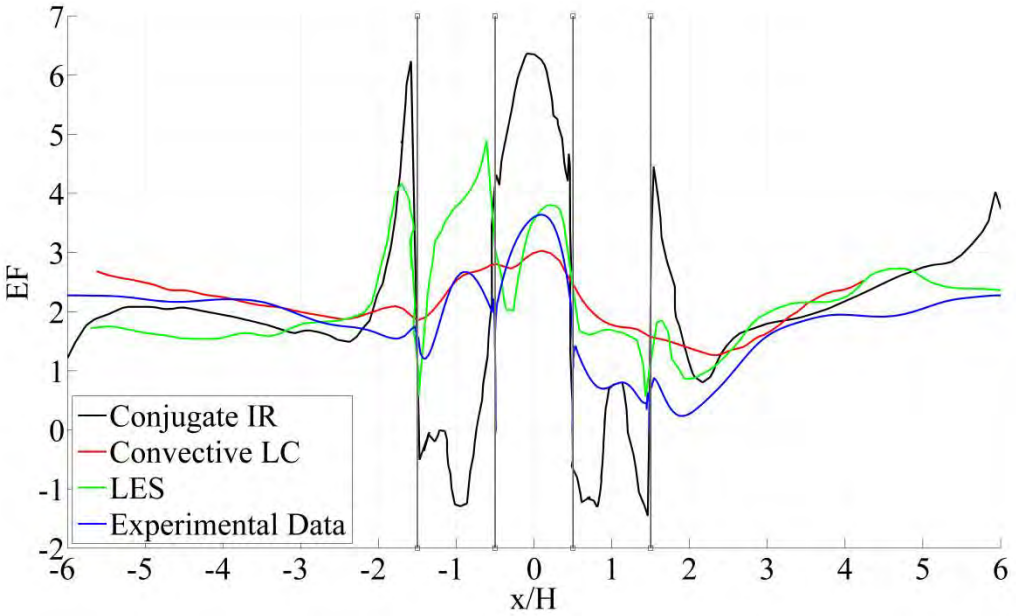


Figure 86: Enhancement Factor Comparison – Symmetry Line (50%) [-]

In the case of the "Conjugate IR" tests conducted by Agostini [Ref C-35], there are several major issues, sources of error, which prevent a descent comparison. To demonstrate the sources of these errors, a brief study is conducted to imitate and possibly explain the two major obvious problems with the Agostini data; one being the fact that there are negative enhancement factor values, and the other is the apparent aperiodicity of the data (the mismatch between the EF values at x/H=±6) even though the periodicity boundary condition was applied on the transverse walls.

To reproduce the aperiodicity error, the imposed temperature distribution on the finite element solver, which is not truly periodic under which the conditions acquired by the infrared camera, is kept in its original form; more specifically, the periodicity is not imposed artificially on the temperature distribution after the acquisition but all other processes are kept the same as the baseline case. Even though, in the FEM the periodic boundary condition is selected for the transverse walls, the results in EF factor are asymptotically divergent on the points where the solid slab is cut at x/H=3.5, Figure 87. Such a trend is also seen in the Agostini dataset; considering the imposed periodicity, even though the x/H =±6 are identical points, the observed EFs at these locations are drastically different, and similarly asymptotically divergent. These are the points which were the ends of the domain modeled by Agostini. The main reason behind the divergence is that, in the lack of imposed periodicity on the temperature boundary condition, one transverse edge of the slab acts as a source where the other one acts as a sink. This effect corrupts the heat transfer distribution within the domain, especially in the region of the solid cut, as seen by the difference between the "Baseline Data" and "W/o Peridicity" Data, Figure 87.

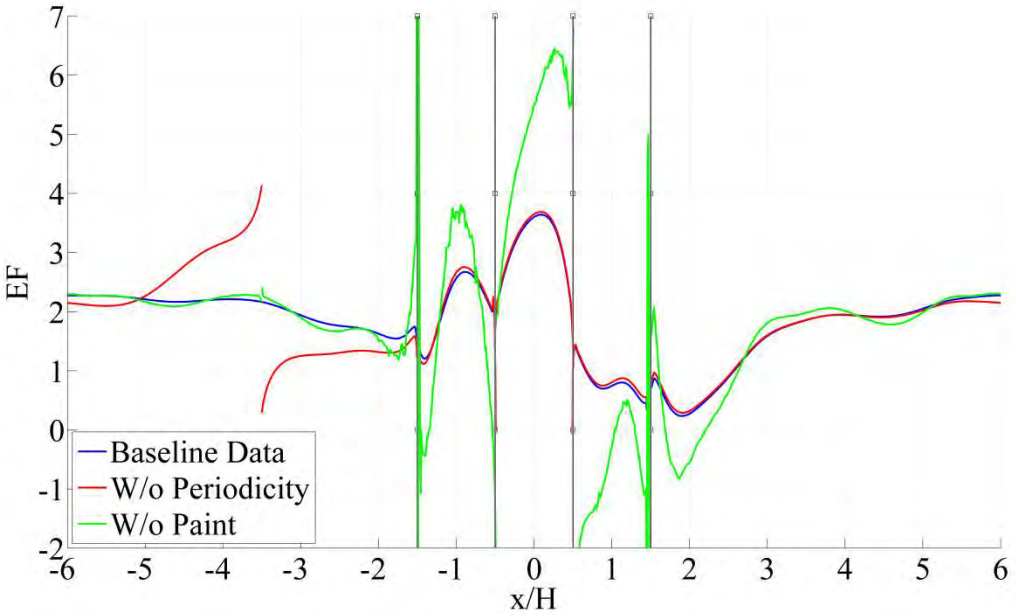


Figure 87: Comsol Enhancement Factor Distribution – Symmetry Line (50%) [-]
Modeling Configuration Comparison

The negative EF regions imply that there is heat transfer from the cold fluid to the hot solid, defying the second law of thermodynamics. This effect can easily be imitated by lack of paint layer modeling in the FEM, Figure 5.9, all other variables are kept the same as the "Baseline Data". Even though the paint layer is considerably thin, ~160 μm, if not modeled at all, then due to the false distribution of the high temperature gradients, the heat flux values at regions surrounding the lower temperatures, such as the vicinity of the top of the rib, are computed to be negative normal to the surface of the solid, Figure 5.9. This is an artifact of the large unsustainable surface temperature gradients in the absence of surface heat addition, which the FEM model resolves, in the absence of fluid domain information, by simply creating such a zone. The thermal conductivity of the paint layer is shown to be a weak parameter, not significantly affecting the solution, as long as the relative insulating behavior, when compared to the steel slab, persists. The existence of these negative EF regions highly affect the domain since the large artificial energy input from these regions create superficially augmented EF values in their vicinity, Figure 87.

| | Current Conjugate IR Experiments $Re_{D_h}$=40,000 | Convective LC Experiments [Ref C-33] $Re_{D_h}$=30,000 with $Nu_o$ correction |
|---|---|---|
| Average EF Rib Upstream Face | 2.35 | - |
| Average EF Rib Top | 3.02 | - |
| Average EF Rib Downstream Face | 0.86 | - |
| Average EF Rib | 2.08 | 2.215 |
| Average EF Inter-rib | 2.01 | 1.921 |
| Average EF Overall | 2.03 | 2.215 |

Table 1: Area Averaged Enhancement Factor

# 28. Conclusions on the Ribbed Channel

The conjugate heat transfer investigation is conducted for the ribbed roughened internal cooling channel geometry. The enhancement factor trends are compared with the basic flow features observed in prior literature and reflected excellent agreement. Basic errors in conjugate modeling, used in the evaluation of surface heat flux from experimental temperature data are identified and the effects are demonstrated.

For the attached flow immediate downstream of the large separation region, a slight overall decrease in enhancement factor is observed, associated with the boundary layer growth; this is the portion of the ribbed channel which resembles the behavior of a developing flat plate boundary layer. Approaching the rib, there is an initial decrease in the enhancement factor, from due to the potential effect of the rib reducing the axial component of the velocity, causing an adverse effect on the boundary layer (an increase in boundary layer thickness). In the direct vicinity of the rib upstream face, the flow is dominated by the existence of the clockwise rotating corner vortex $V_3$, which not only prevents the cold fluid from coming in contact with the heated surface, due to blockage created by this flow structure, but also creates a local low momentum zone, yielding to a region of low EF. The top face of the rib is where the overall highest EFs are observed. This is caused by the reduction in effective area of the mainstream flow (due to the existence of the rib), in turn resulting in much higher momentum flow, generating a region of high heat transfer rate. The downstream surface of the rib, until reattachment, is the region where the lowest EF values are observed; this is caused by the

large separation region behind the rib, generating a local low momentum region with reversed flow, where the heat transfer is considerably less than the rest of the passage. A double peak in enhancement factor is observed, the initial weaker peak is located prior to the reattachment point, where the local minima in skin friction, local maxima in fluctuating component of the shear stress, and local sharp maxima in reverse flow velocity are observed. The second global maximum in enhancement factor is observed after the reattachment point, typical considering the relatively narrower separation region.

# 29. Bibliography on the ribbed channel

[C1] Nirmalan N.V., Bunker R.S., Hedlund C.R. "The measurement of full-surface internal heat transfer coefficients for turbine airfoils using a non-destructive thermal inertia technique" GE R&D centre, Technical information series, 2002GRC010, February 2002

[C2] Nakhle, D., VKI Stagaire Report

[C3] Dorfman, A., 2009, "Conjugate Problems in Convective Heat Transfer". Taylor & Francis

[C4] Coletti, F., Arts. T., "Internal Cooling in Turbomachinery," VKI Lecture Series 2010-05

[C5] Kay, J.M., Nedderman, R.M., "Fluid Mechanics and Transfer Processes," Cambridge University Press, 1985, ISBN 0 521 30303 6

[C6] Incropera, F.P., DeWitt, D.P., "Fundamentals of Heat and Mass Transfer," John Wiley & Sons, Inc. ISBN 0-471-38650-2

[C7] Winterton, R.H.S., Int. J. Heat Mass Transfer, 41, 809, 1998

[C8] Schiller, L., „*Rohrwinderstand bei hohlen Reynoldsschen Zahlen. Vortrage aus dem Gebiete der Aerodynamik und verwandter Gebiete*," Aachen 1920, herausgegeben von A. Gilles, L. Hopf und Th. v. Karman, Berlin, J. Springer, 1930.

[C9] Nikuradse, J., "Law of Flow in rough pipes," Translation of "Strömungsgesetze in rauhen Rohren," VDI-Forschungsheft 361, 1933

[C10] Colebrook, F.C., "Turbulent flow in pipes, with particular reference to the transition region between the smooth and rough pipe laws," *J. Inst. Civ. Eng.*, Lond. 11, 133–156, 1939

[C11] Webb, R.L., Eckert, E.R.G., Goldstein, R.J., "Heat transfer and friction in tubes with repeated-rib roughness," Int. J. Heat Mass Transfer, 14, 601-617, 1971

[C12] Han, J.C., Glicksman, L.R., Rohsenow, W.M., "An investigation of heat transfer and friction of rib-roughened surfaces," Int. J. Heat Mass Transfer, 21, 1143-1156, 1978

[C13] Han, J.C. “Heat transfer and friction in channels with two opposite rib-roughened walls,” J. Heat Transfer, 106, 774-781, 1984

[C14] Han, J.C., “Heat transfer and friction characteristics in rectangular channels with rib turbulators,” J. Heat Transfer, 110, 321-328, 1988

[C15] Han, J.C., Park, J.S., “Developing heat transfer in rectangular channels with rub turbulators,” Int. J. Heat Mass Transfer, 31, 183-195, 1988

[C16] Han, J.C., Park, J.S., Lei, C.K., “Augmented heat transfer in rectangular channels of narrow aspect ratios with rib turbulators,” Int. J. Heat Mass Transfer, 32, 1619-1630, 1989

[C17] Han, J.C., Zhang, Y.M., Lee, C.P., “Augmented heat transfer in square channels with parallel, crossed and V-shaped angled ribs,” J. Heat Transfer, 113, 590-596, 1991

[C18] Han, J.C., Zhang, Y.M., Lee, C.P., “Influence of surface heat flux ratio on heat transfer augmentation in square channels with parallel, crossed and V-shaped angled ribs,” J. of Turbomachinery, 114, 872-880, 1992

[C19] Han, J.C., Park, J.S., Lei, C.K., “Heat transfer enhancement in channels with turbulence promoters,” J. Engineering for Gas Turbines and Power, 107, 628-635, 107

[C20] Zhang, Y.M., Gu, W.Z., Han, J.C., “Heat transfer and friction in rectangular channels with ribbed or ribbed-grooved walls,” J. Heat Transfer, 116, 58-65, 1994

[C21] Chandra, P.R., Niland, M.E., Han, J.C., “Turbulent flow heat transfer and friction in a rectangular channel with varying numbers of ribbed walls,” J. of Turbomachinery, 119, 374-380, 1997

[C22] Burggraf, F., “Experimental heat transfer and pressure drop with two-dimensional discrete turbulence promoters applied to two opposite walls of a square tube,” Augmentation of convective heat and mass transfer, Bergles, A.E., Webb, R.L., eds., ASME, New York, 70-79

[C23] Liou, T.M., Hwang, J.J., “Turbulent Heat Transfer Augmentation and Friction in Periodic Fully Developed Channel Flows,” J. of Heat Transfer, 114, 56-64, 1992

[C24] Taslim, M.E., Spring, S.D:, “Effects of Turbulator Profile and Spacing on Heat Transfer and Friction in a Channel,” AIAA J. of Thermophysics and Heat Transfer, 8, 555-562, 1994

[C25] Rau, G., Arts, T., “Local Interference Effect in a Straight Square Channel with Two Opposite Rib-roughened Walls as a Function of Rib Height to Hydraulic Diameter Ratio,” Experimental Heat Transfer, Fluid Mechanics and Thermodynamics1997, Vol. 3, eds., M. Giot, F. Mayinger, G.P., Celata, 1637-1647

[C26] Çakan, M., "Aero-thermal Investigation of Fixed Rib-roughened Internal Cooling Passages," PhD thesis, Université Catholique de Louvain, von Karman Institute for Fluid Dynamics, July 2000

[C27] Ichimiya, K., Yokoyama, M., Shimomura, R., "Effects of Several Roughness Elements for the Heat Transfer from a Smooth Heated Wall," Proc. ASME/JSME Thermal Engineering Joint Conference, Vol. 1, 359-364, 1983

[C28] Park, J.S., Han, J.C., Huang, Y., Ou, S., Boyle, R.J., "Heat Transfer Performance Comparison of Five Different Rectangular Channels with Parallel Angled Ribs," Int. J. Heat Mass Transfer, 35, 11, 2891-2903, 1992

[C29] Lau, S.C., McMillin, R.D., Han, J.C., "Turbulent Heat Transfer and Friction in a Square Channel with Discrete Rib Turbulators," J. of Turbomachinery, 113, 360-366, 1991

[C30] Taslim, M.E., Li, T., Kercher, D.M., „Experimental Heat Transfer and Friction in Channels Roughened with Angled, V-shaped and Discrete Ribs on Two Opposite Walls," ASME, 94-GT-163

[C31] Han, J.C., Huang, J.J., Lee, C.P., "Augmented Heat Transfer in Squared Channels with Wedge-shaped and Delta-shaped turbulence promoters," Enhanced Heat Transfer, 1, 37-52, 1993

[C32] Chandra, P.R., Niland, M.E., Han, J.C., "Turbulent Flow Heat Transfer and Friction in a Rectangular Channel with Varying Numbers of Ribbed Walls," J. of Turbomachinery, 119, 374-380, 1997

[C33] Sparrow, E.M., Tao, W.Q., "Enhanced Heat Transfer in a Flat Rectangular Duct with Streamwise-periodic Disturbances at One Principal Wall," J. of Heat Transfer, 105, 851-861, 1983

[C34] Sparrow, E.M., Tao, W.Q., "Symmetric vs. Asymmetric Periodic Disturbances at the Walls of a Heated Flow Passage," Int. J. Heat Mass Transfer, 27, 11, 2133-2144, 1984

[C35] Agostini, F., Arts. T., "Conjugate Heat Transfer Investigation of Rib-roughened Cooling Channels," Proceedings of ASME TURBO EXPO 2005

[C36] Casarsa, L., "Aerodynamic Performance Investigation of a Fix Rib-roughened Internal Cooling Passage," PhD theses, Università degli Studi di Udine, von Karman Institute for Fluid Dynamics, June 2003

[C37] Jourdain, C., Escriva, X., Giovannini, A., "Unsteady Flow Events and Mechanisms Leading to Heat Transfer Enhancement in a Ribbed Channel," In Proceeding of Eurotherm Seminar 55: Heat Transfer in single phase flow, 1997

[C38] Rau, G., Moeller, D., Çakan, M., Arts, T., „The Effect of Periodic Ribs on the Local Aerodynamic and Heat Transfer Performance of a Straight Cooling Channel," ASMEE 96-GT-541, Sept. 1996

[C39] Zukauskas, V.A., Pedisius, K.A., "Heat Transfer to Reattached Fluid Flow Downstream of a Fence," Wärme- und Stoffübertragung, 21, 125-131, 1987

[C40] Eaton, J.K., Johnston, J.P., "A Review on Subsonic Turbulent Flow Reattachment," AIAA J., 19, 9, 1093-1100, 1981

[C41] Watkins, C.M., Gooray, A.M., "Numerical Calculations of Turbulent Recirculating Heat Transfer Beyond Two-dimensional Backsteps and Sudden Pipe Expansions," Dept. of Mech. Engrg., Howard University, Washington D.C., 1982

[C42] Armaly, B.F., Durst, F., Kottke, V., „Momentum, Heat and Mass Transfer in Backward-Facing Step Flows," Proceedings of 3rd Symposium on Turbulent Shear Flows, Davis, CA, 1981

[C43] Aung, W., "An Experimental Study on Laminar Heat Transfer Downstream of Back Steps," J. Heat Transfer, 105, 823-829, 1983

[C44] Seban, R.A., Emery, A., Levy, A., "Heat Transfer to Separated and Reattached Subsonic Turbulent Flows Obtained Downstream of a Surface Step," J. Aerospace Sci., 28, 809-814, 1959

[C45] Eaton, J.K., Vogel, J.C., "Combined heat Transfer and Fluid Dynamic Measurements Downstream of a Backward-Facing Step," ASME, 107, 922, 1985

[C46] Avancha, R.V.R., Pletcher, R.H., "Large Eddy Simulation of the Turbulent Flow Past a Backward-facing Step With Heat Transfer and Property Variations," Int. J. Heat Fluid Flow, 23, 601-614, 2002

[C47] Sparrow, E.M., Kang, S.S., Chuck, W., "Relation Between the Points of Flow Reattachment and Maximum Heat Transfer for Regions of Flow Separation," Int. J. Heat Mass Transfer, 30, 7, 1237-1246, 1987

[C48] Adams, E.W., Johnston, J.P., "Effects of Separating Shear Layer on the Reattachment Flow Structure Part 2: Reattachment Length and Wall Shear Stress," Experiments in Fluids, 6, 493

[C49] SCHEIMAN, J.; BROOKS, J.D., "Comparison of experimental and theoretical turbulence reduction from screens, honeycomb and honeycomb-screen combinations" J. Aircraft 18, 638 and NASA TP 1958

[C50] Bejan, A., Kraus, A.D., "Heat Transfer Handbook" John Wiley & Sons, 2003

[C51] Fox, R.W., McDonald, A.T., Pritchard, P.J., "Introduction to Fluid Mechanics" John Wiley & Sons, 2003

[C52] Panton, R.L, "Incompressible Flow" Wiley-Interscience, 1996

[C53] White, F.M., "Viscous Fluid Flow" New York: McGraw-Hill, 1974

[C54] Schulz A., "Infrared thermography as applied to film cooling of gas turbine components", Meas. Sci. Technol. 11 (2000) 948–956.

[C55] Carlomagno G. M., de Luca L., "Infrared Thermography for Flow Visualization and Heat Transfer Measurements", INTERNATIONAL CONFERENCE ON ENGINEERING EDUCATION 1998.

[C56] Buchlin J. M., "Convective Heat Transfer and Infrared Thermography (IRTh)", Journal of Applied Fluid Mechanics, Vol. 3, No. 1, pp. 55-62, 2010.

[C57] Lin, S.S, "Review: extending visible band computer vision techniques to infrared band Images," Technical Report MS-CIS-01-04, GRASP Laboratory, Pennsylvania

[C58]Schulz, A., "Infrared Thermography as applied to film cooling of gas turbine components," Measurement Science Technology, 2000, vol. 11, n$^{o}$ 7, pp. 948-956

[C59] Carlomagno, G.M., de Luca, L., "Infrared Thermography for Flow Visualization and Heat Transfer Measurements," presented at the International Conference on Engineering Education, 1998.

[C60] Raghu, O., Philip, J., "Thermal Properties of Point Coatings on Different Backings using a Scanning Photo Acoustic Technique," Meas. Sci. Technol., 17, 2945-2949, 2006

[C61] Mori, M., Novak, Lovrenc, Sekavcnik, M., "Measurement on Rotating Blades Using IR Thermography," Experimental Thermal and Fluid Science, 32, 387-396, 2007

# 30. Rib Roughened Channel Flow with Cooling Extraction

## 30.1 Principal Flow Structures

Despite the geometric simplicity of rib roughened internal cooling passages, the employed step disturbance elements inside the channel introduce a number of complex secondary flow features into the mean stream. The examples of which can be found in a complimentary PIV investigation, absent of film cooling holes, [Ref D-1] in **Error! Reference source not found.** 88, where time-averaged streamtraces along with axial velocity contours are presented.

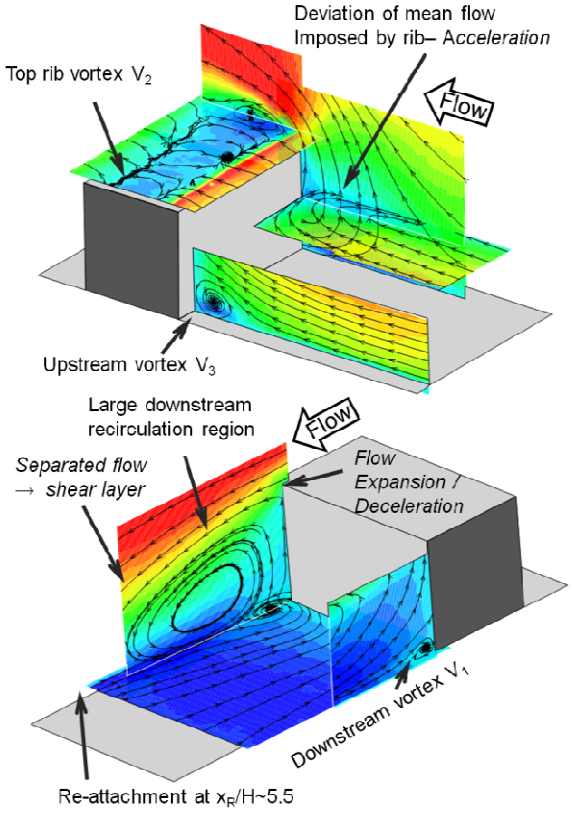


Figure 88: Visualization of the Ribbed Channel Flow Field

Starting form an unperturbed state, as the fluid encounters the rib, it experiences a strong deviation imposed by the obstacle, forcing it to adapt to the decreased channel cross section. It is accelerated in order to pass the rib and subsequently experiences an expansion further downstream, as the cross sectional area abruptly increases following the backward-facing step. The periodic behavior of consecutive acceleration in the vicinity of the obstacle and deceleration of the fluid in the inter-rib spacing is one of the most dominant aspects of the flow field. At the investigated Reynolds number, since the contribution of the inertial terms into fluid momentum balance is dominating, the fluid flow is not able to follow the abrupt changes of the surface. It is the sudden enlargement of the channel downstream of the

perturbator which causes the stream to separate from the surface. A free shear layer is formed upon the separation of the upstream boundary layer at the sharp corner due to the interaction between the mainstream flow and the reverse flow downstream of the rib.

The region beneath the separated flow in the wake of the rib is occupied by a recirculation zone, with its length confined by back face of the rib and the point of reattachment. In the region of flow reattachment, the separated shear layer curves sharply downward and impinges on the wall. When subjected to the effects of stabilizing curvature and a strong interaction with the wall, the shear layer is split into two fractions.[Ref D-2] [Ref D-3] Since the energy of the first part does not suffice to overcome the strong adverse pressure gradient, it is deflected upstream; being reversed, it forms the recirculating flow region. The second part of the shear layer is carried away downstream, and contributes to the growth of a new sub-boundary layer, as it reattaches to the wall.[Ref D-2]

In this case, defined by the change of sign in skin friction coefficient, the reattachment point is determined to be around ~5.5 rib heights downstream of the rib centerplane. The direct relation of flow reattachment region with local heat transfer distribution has been extensively studied in literature and the maximum in the streamwise local Nusselt number profile, $x_{max}$, has been considered a significant indication for the location of flow reattachment, $x_R$.[Ref D-4][Ref D-5][Ref D-2][Ref D-6] [Ref D-7][Ref D-8].

Apart from this recirculation region, the flow field exhibits a local separated flow region $V_2$ on top of the perturbator, rotating counter-clockwise, as well as a small vortex $V_1$ in the rib downstream, both spanning across the entire channel width. Within the wake of the rib, the small vortex cell $V_1$ exhibits a clockwise rotary motion. This corner vortex $V_1$ and the recirculation region exhibit opposite mean angular velocities. Towards the obstacle, their stream traces coincide, such that the flow impinges onto the backward facing surface of the rib.

Further downstream, the mean flow passes the rib and the subsequent recirculation zone, and impinges towards the channel wall at the reattachment region. Once the flow aligns with the channel wall, the boundary layer redevelops and grows within the inter-rib spacing, until it approaches the next turbulator. The stream strongly impinges on the front surface of the rib so that its vorticity and the repeatedly induced separation of the boundary layer give rise to the vortex structure $V_3$. [Ref D-1]

## 30.2 Film Cooling Hole Effects

The introduction of alternating film cooling holes to the inter-rib spacing induces major changes to the flow topology. In order to identify aerodynamic implications of purge flow on the rib-roughened flow field, results of a complementary LES investigation at purge rate of 4.5, are contrasted with the prior observations.

Qualitative analysis by means of time averaged streamline charts yield valuable insight concerning the distortions imposed by the suction effect of the film cooling hole, noticeably

affecting the regions situated downstream of the rib obstacle. A three-dimensional visualization of stream traces for configurations with and without film cooling orifice can be found in Figure 89 (Ref D-12).

In the absence of film cooling holes, comparing the LES based Figure 89A with PIV founded Figure 88, there appears to be a high degree of qualitative correlation in the observed flow structures. With the film cooling orifice located at x/H=5/3, clearly submerged entirely into the prior dominant recirculation bubble, the prevailing local suction effect can be viewed in Figure 89B. The flow in the vicinity of the hole is continuously entrained and purged out of the rib pitch, thereby inducing significant distortions to the separated flow region and successive reattachment.

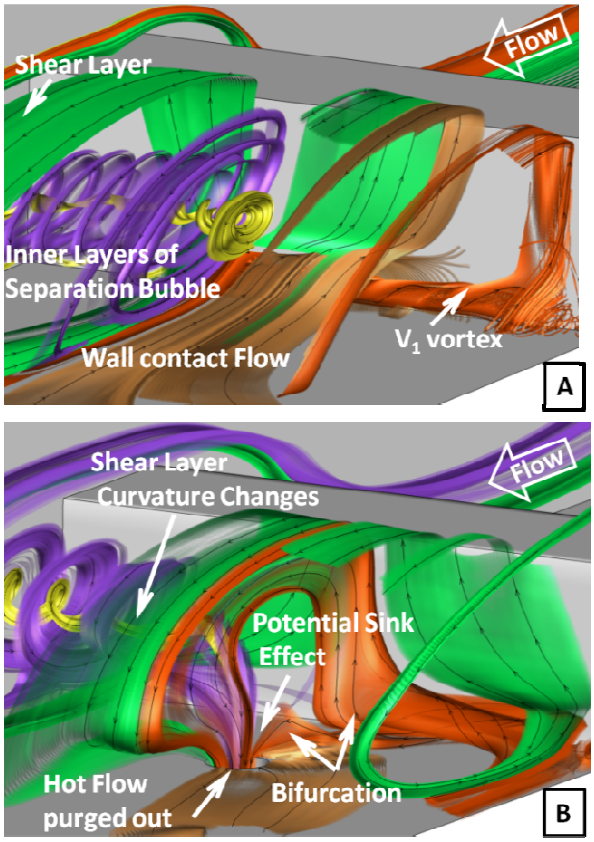


Figure 89: Rib Downstream Flow-w/o film cooling hole (B) w/ film cooling hole

For the passage with the film cooling hole, the flow field downstream of the rib is primarily dominated by a flow characteristic that can be addressed as a type of bifurcation mechanism. By splitting the fluid entrained in the prevailing recirculation region, the portion of the flow structure below 1/3H height is transported along the bottom wall and entrained by the suction of hole. The flow above this zone experiences an abrupt upward lift dominated by the shear layer driven vorticity. Being initially shed away downstream over the orifice, it exhibits a reverse flow motion while descending again behind the hole. After impinging on

the channel bottom wall, fluid is again diverted upstream due to the suction effect and thus likewise entrained by the orifice.

The green stream trace surface represents flow propagation of fluid from the downstream face of the rib. In the absence of film cooling hole, accumulated by the recirculating behavior of the separation bubble, mainstream flow near the channel lateral wall is entrained and transported to the back side of the rib. Ascending under the effect of the upward flow motion, it interacts with the channel mainstream flow, and thus forms a part of the free shear layer. It is evident that stream traces corresponding to the configuration with cooling hole exhibit a higher curvature than the case without and are bent towards the wall perpendicular. Thus, since the orifice is acting as a potential sink for the locally separated low momentum fluid, the reattachment line is deformed and shifted further upstream; this trend is expected to be amplified at increased suction rates.

Development of vortex structure $V_1$, exemplified by the orange surface of stream traces, appears to be distorted due to bifurcation in the presence of the film cooling hole. In contrast to the case in the absence of the orifice, the flow is significantly diverted towards the symmetry plane, as well as the sudden upward rise and subsequent drop of the flow attributed to the entrainment of the suction effect of the orifice.

The inner layers of the recirculation bubble, purple and yellow surfaces, exhibit the characteristic vortical motion within the separation bubble in addition to the spanwise translational motion. In the presence of film cooling suction, Figure 89B, under the potential sink effect, not only the structures seem to be purged directly from the hole located in the symmetry plane, in addition, by comparing the number of coils in helical patterns for the two cases, it could be hypothesized that the reduction in windings in the presence of film cooling holes could be indicative of weakening local vorticity field.

**Apart from aerodynamic flow topology, from a heat transfer perspective, one of the most important regions is associated with the fluid in contact with the bottom wall, depicted as the brown surface in Figure 89**

**Figure**. In the absence of film cooling hole, fluid heated at the bottom and lateral walls is observed to be entrained by the separation region and to persist in the recirculation bubble, thereby isolating the region downstream of the rib against penetration of cool mainstream flow.

In contrast, with active film cooling holes, high temperature fluid near the passage bottom wall is eventually entrained by the suction effect and purged out of the channel, whether directly or after interaction with $V_1$. It can be deduced that the removal of the overall hottest fluid layers from the passage implies a significant rise in overall cooling effectiveness.

# 31. Results

In order to investigate the aerothermal effects of film cooling holes on the internal cooling channel, experiments are conducted with a set of 1/3H diameter, 90° film cooling holes, located 5/3H downstream of the center of the rib on the symmetry plane. The holes

carry the flow out of the test section at mass flux ratios of PR= 0, 1.17, 1.57, 2.48, 3.48, 4.50, 5.53 and 6.04. **Error! Reference source not found.**90 presents enhancement factor distributions along the ribbed test section for all investigated film cooling hole purge rates , while the grey lines represent the location of the stream-wise maximum in the vicinity of the reattachment zone. Presenting a more comprehensive understanding of the separation phenomena, Figure 91 portrays the symmetry plane EF distribution charts, along with point of maximum reattachement heat transfer indicated by symbols. Furthermore, providing a more global perspective, Figure 92 depicts the spanwise averaged EF line charts of all considered film cooling conditions.

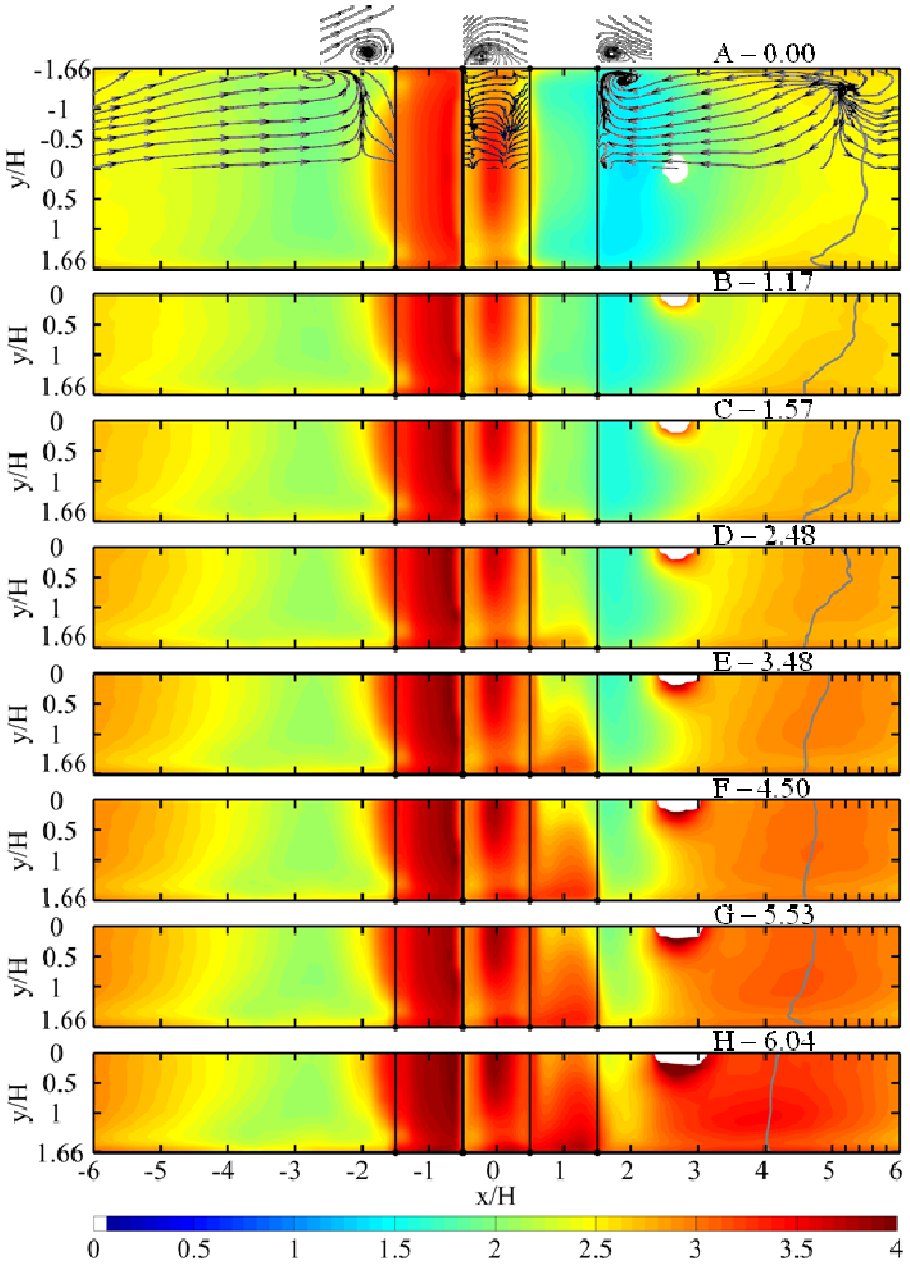


Figure 90: Effects of Purge Rate on EF distributions

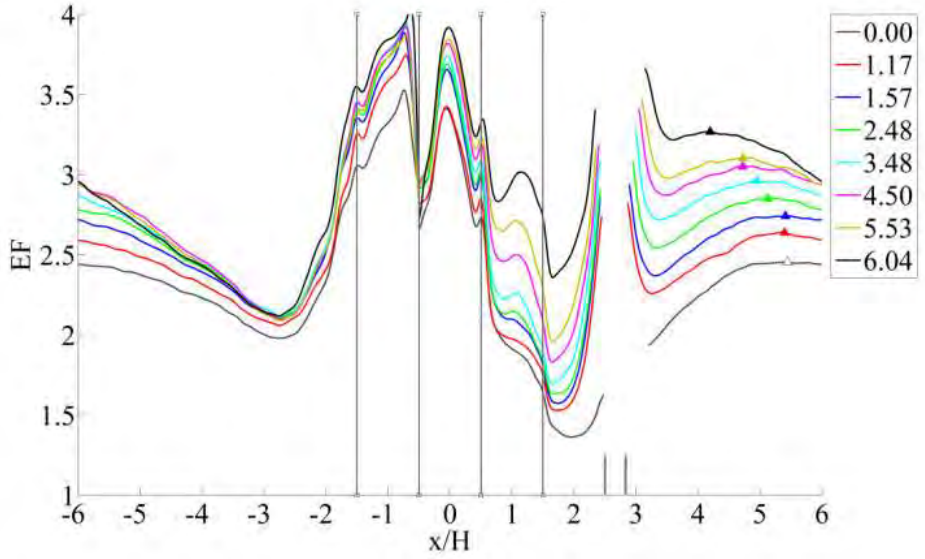


Figure 91: Symmetry Plane EF and $x_{max}$ at several PR

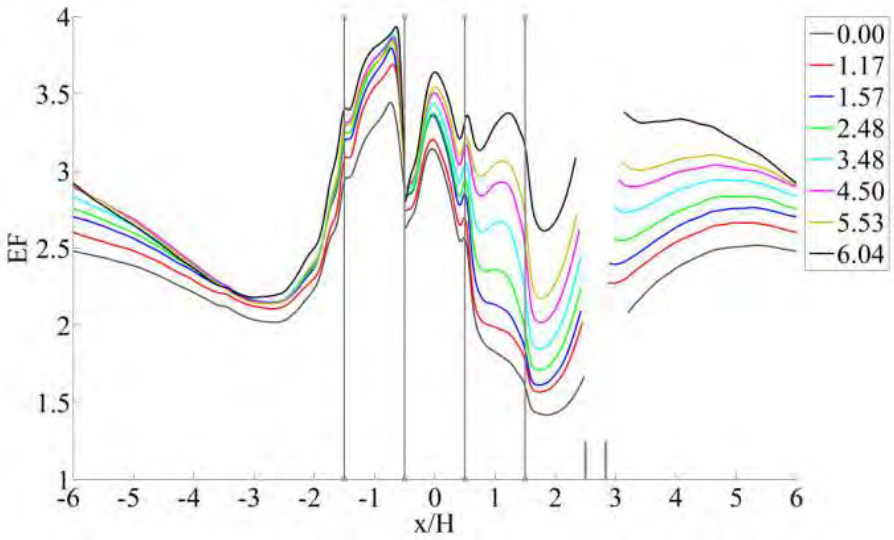


Figure 92: Spanwise Averaged EF at several PR

## 31.1 Baseline Ribbed-Roughened Flow Heat Transfer

Considering the characteristic flow patterns developing inside internal ribbed cooling channel geometries and analyzing the results obtained from the liquid crystal experiments, some distinctive heat transfer distributions can be correlated to nearby flow structures. Figure 90A presents the EF distribution in the absence of film cooling suction, PR=0; in addition, imposed on upper half of the heat transfer map are the bottom wall PIV stream traces, along with channel centerline, surface perpendicular $V_3$, $V_2$ and $V_1$ vortex structures located in front of, over, and behind the rib respectively.

The region confined by -6<x/H<-4.5, situated downstream of the large recirculation, is characterized by a zone where the attached flow exhibits gradual boundary layer development, supported by the overall slight decrease in enhancement factor in the axial direction. Within this region, even though the flow resembles a state of unperturbed boundary layer development over a flat plate, the elevated enhancement factor, EF≈2.4, is mainly due to higher than ordinary local turbulence levels typical in such geometries [Ref D-9] [Ref D-10][Ref D-5] [Ref D-11].

Further downstream, convective heat transfer is greatly affected by the potential effect of the rib element; reduction in the flow axial velocity, generally associated with boundary layer thickening, results in the initial drop in enhancement factor, -4.5<x/H<-2.5 region. This effect is less emphasized in the lateral direction due to aerodynamic wall effects, 1.2>|y/H|. The portion of the inter-rib area directly upstream of the front face of the rib, bound by -2.5<x/H<-1.5, is under the influence of the clockwise rotating corner vortex formation $V_3$. The increased entrainment of colder fluid causes a steep rise in enhancement factor of up to EF≈3 on the channel bottom surface in the direct proximity of the rib.

The upstream face of the rib, described by -1.5<x/H<-0.5, is an area characterized by globally high enhancement factors attributed to the strongly impinging mainstream flow on the front face of the obstacle. This high-momentum impinging flow, guided by the $V_3$ vortex, causes a peak in heat transfer, EF≈3.5, at x/H≈-0.8. The top surface of the perturbator, bound by -0.5<x/H<0.5, is another region where large EFs are observed attributed to the abrupt reduction in effective flow area caused by the blockage of the rib element, in turn locally augmenting the flow velocity; this is particularly true for the channel center line where the mass flux is largest. EF values, around 3.4 in the symmetry plane, diminish in widthwise direction, indicated by lower heat transfer levels of EF≈3.2 at |y/H|=0.83 and EF≈2.8 at |y/H|=1.66.Within this region, the location of the distinct peak appears to be related to $V_2$ flow structure, creating a local maxima towards the center of the rib top surface.

Regarding the EF distribution over the vertical back face of the rib, 0.5<x/H<1.5, a significant drop in EF is observed from around EF≈2.5 at the top rib edge, x/H=0.5, to EF≈1.5 at the bottom corner, x/H=1.5. Adjacent bottom surface of the inter-rib section, directly in the wake of the obstacle, 1.5<x/H<2, exhibits a similar trend. Here, the reduction in EF is even more remarkable, indicated by a local minimum of EF≈1.3 at x/H=2 for |y/H|<1.4. The entire

section of distinctively reduced heat transfer rates downstream of the flow perturbator, 0.5<x/H>2.5, is induced by the considerably separated and recirculatory flow behind the rib caused by the abrupt increase in cross sectional area. The recirculation bubble, not only prevents the entrainment of fresh fluid, but also generates a local low momentum region with reversed flow orientation and thus; consequently, the region directly downstream of the rib has particularly low levels of effective heat transfer. This trend of sharp reduction is apparent in the entire width-wise direction.

Further downstream of the rib, 2.5<x/H<6, the EF begins to increase monotonously as more and more cooler flow is entrained from the mainstream, a consequence of the diminishing effects of the recirculation region in the streamwise direction, observed along the entire passage width. At increased axial position, eventually, the effects of the wake of the rib are reduced and the mainstream flow becomes once again attached to the bottom surface, indicated by a change of direction in streamtraces at around x/H ≈5 in **Error! Reference source not found.**A. Even though the maximum heat transfer can occur downstream or upstream of the reattachment point, as a qualitative indicator, the maximum inter-rib space EF in the axial direction is indicated by the grey line. The PIV acquired stream traces and the liquid crystal heat transfer investigations seem to agree on the location of the reattachment region and this point is demonstrated to slightly vary slightly in widthwise direction, from around x/H≈5.4 in the symmetry plane to x/H≈4.8 towards the lateral walls. Downstream of the reattachment point, considering the flow structure periodicity, the cyclic behavior perpetuates.

From a more global perspective, locally averaging EF maps at various zones of the rib roughened geometry, the mean EF for rib upstream face, rib top face, rib downstream face, interrib spacing are computed to be 3.20, 2.86, 1.89, 2.20 respectively, resulting in a pitch averaged EF of 2.31. Consequently, the highest heat transfer zones are the upstream and top faces of the rib, followed by inter-rib space and the rib downstream surface.

## 31.2 Film Cooling Hole Suction Effect on Local EFs

In order to isolate the internal cooling heat transfer ramifications of film cooling holes, the “baseline case” where the cooling passage lacks any film cooling suction, **Error! Reference source not found.**A, is compared with EF distributions in the presence of an active film cooling hole at various suction rates **Error! Reference source not found.**B-H. Moreover, Table 1, summarizes the regionally averaged EFs, in addition to providing surface EF percent standard deviation from the passage mean (quantifying the non-uniformity), along with centerline reattachment associated heat transfer maximum point, $x_{max}$.

Even from qualitative inspection of the distributions presented in **Error! Reference source not found.**, it is apparent that the purge flow into the film cooling hole significantly alters the heat transfer patterns on the internal cooling passage, especially in the vicinity of the hole, **Error! Reference source not found.**. The downstream rib face and early inter-rib space, 0.5<x/H<5.5, seem to be the regions most affected by this suction affect, where EF could even locally double, comparing the PR 0 with PR 6.04 in **Error! Reference source not**

**found.**. In the absence of cooling holes, this is the region of the flow field which is dominated by the separation bubble with local reversed flow and the associated CCW rotating $V_1$ vortex, followed by gradual reattachment. With the increased suction mass flux, it is clear that the effects of the separation bubble diminish, indicated by the monotonous decrease in reattachment length, suggested by the shift in maximum heat transfer point, from 5.45x/H at PR=0 to 4.2x/H at Pr=6.04. This upstream shift is believed to be related to the hole suction effect changing the curvature of the shear layer potential sink for the locally separated low momentum fluid. In addition, at surfaces surrounding the hole, x/H=2.67 ±0.7, heat transfer peaks are generated by the local acceleration of the fluid from all directions, **Error! Reference source not found.**.

Closer to the rib downstream face, there seems to be a local spike in heat transfer with increased blowing. Though not conclusive, this could be an indication of the strengthening V1 vortex impinging on the rib side wall at a greater momentum, creating a local maxima in enhancement factor at around x/H = 1.15.

In comparison, the local effect of the film cooling hole seems to decrease at increased axial distance from the hole; specifically, for points downstream of the decreased reattachment zone, the heat transfer rates seem to gradually converge for all mass flux ratios until they roughly coincide at x/H = -2.8. This is the region of the inter-rib space where the flow is dominated by the potential effect of the rib, resulting in a mostly unchanged distribution indicated by the broad collapse of EF lines. Further downstream, -2.8<x/H<-1.5, higher mass flux ratios still result in higher EFs despite their earlier flow reattachment and thus more developed thermal boundary layer. The diminishing effects of the augmentation in thermal boundary layer thickness is contrasted by the fact that the flow in this zone is expected to have similar static pressure for all mass flux conditions, but at increased suction with the reduction in flow back pressure created by the hole, the enhacement factors still augment. This effect can also be observed on the upstream and top faces of the rib, -1.5<x/H<0.5, where there is a self-similar distribution augmentation in EF at increased suction rates. This suggests a *local* overall increase in velocity magnitude, while maintaining the same flow structures.

Focusing on the widthwise heat transfer distributions at various film cooling conditions, **Error! Reference source not found.**, there is a clear trend change in lateral enhancement factor and thus flow structure distributions; most apparent by the changes in the shape of the reattachment line. For the case without film cooling holes, towards the lateral walls, the reattachment occurs earlier due to decreased axial mainstream velocity with respect to the center plane [Ref D-1]. In the existence of film cooling suction, at increased mass flux ratio, the reattachment line seems to occur more uniform (flatter) in the widthwise direction.

Furthermore, in the absence of film cooling holes, the region close to the lateral wall on the rib downstream face, **Error! Reference source not found.**A 0.5<x/H<1.5 &1 <y/H<1.66, is a local minima in heat transfer. In contrast, in the presence of film cooling, this region is characterized by locally higher enhancement factor, with this effect being emphasized at higher mass flux ratios.

**Error! Reference source not found.** depicts the widthwise averaged line charts of the enhancement factor for various film cooling conditions. When compared with **Error! Reference source not found.**, with increased mass flux ratios, one can observe a larger change in EF. For example, at x/H=1.5, in the symmetry plane, **Error! Reference source not found.**, the EF range for different suction ratios is 1.9-3.0, in contrast to wider change in the spanwise averaged results, 1.8-3.4, **Error! Reference source not found.**. This is indicative of the hole suction non-uniformity, affecting lower axial momentum regions such as lateral wall flow field more, and thus creating a larger widthwise averaged variation than symmetry plane variation.

Table 1 summarizes the results acquired for various mass flux ratios. Considering the spatial distribution, for all operating conditions including no suction, the rib upstream and top faces have higher heat transfer rates than the interrib space. Globally, the lowest heat transfer is consistently observed for the rib downstream surface which is associated with highly separated flow.

At increased film cooling suction rates, for all regions of the ribbed passage, the enhancement factor augments, overall from 2.31 up to 2.98, and the location of the inter-rib space peak heat transfer (associated with the reattachement zone) drops, from 5.45 to 4.20 x/H. This indicates a globally earlier reattachment, reduction in separation bubble size, and higher overall heat transfer rates. The regions which are most affected by the change in mass flux ratio are primarily the rib downstream face, due to its separated low momentum flow characteristic and close proximity to the hole, and interrib space indicated by maximum EF changes of 1.38 and 0.63 throughout the operating conditions. The most basic benefit of such a film cooling hole configuration is that, it enables sucking out the low momentum recirculation region downstream of the rib perturbator and facilitates an earlier flow reattachment. In addition to flow reattachment considerations, indicated by the EF augmentation at the rib downstream face for increased mass flux ratios, there exists the complimentary benefit of low momentum fluid purge through the film cooling suction. For low suction rates up to 3.48, the inter-rib space average EF is higher than the mean rib downstream face EF. At higher hole mass fluxes, this trend reverses, and what used to be the lowest heat transfer region due to highly separated flow, rib downstream face, performs higher than average (2.88 with respect to 2.79) at suction rate 4.50, indicating significant purge of the low momentum fluid.

Within the tested operating condition limits, from a purely heat transfer perspective it seems favorable to augment the suction rate as much as possible to benefit from the monotonously higher EFs. Yet, the other consideration is the temperature uniformity of such cooling configurations to prevent thermal fatigue. In the case thermal investigations for which the boundary condition is iso-heatflux on the fluid-solid interface, such as this one, the temperature uniformity is directly proportional to the uniformity in EF.

| Purge Rate | Region Averaged EFs | | | | | | % Stand. Dev. | $x_{max}$ |
|---|---|---|---|---|---|---|---|---|
| | Rib | | | | Inter rib | Pitch ave. | | |
| | Ups. | Top | Downs. | Mean | | | | |
| 0 | 3.20 | 2.86 | 1.89 | 2.65 | 2.20 | 2.31 | 20.0% | 5.45 |
| 1.17 | 3.42 | 2.94 | 2.04 | 2.80 | 2.34 | 2.45 | 18.6% | 5.40 |
| 1.57 | 3.51 | 3.06 | 2.18 | 2.92 | 2.42 | 2.54 | 18.5% | 5.41 |
| 2.48 | 3.56 | 3.09 | 2.37 | 3.00 | 2.48 | 2.61 | 17.5% | 5.12 |
| 3.48 | 3.61 | 3.15 | 2.63 | 3.13 | 2.57 | 2.71 | 16.7% | 4.95 |
| 4.5 | 3.61 | 3.22 | 2.88 | 3.23 | 2.64 | 2.79 | 16.0% | 4.72 |
| 5.53 | 3.50 | 3.25 | 3.01 | 3.28 | 2.69 | 2.84 | 15.6% | 4.73 |
| 6.04 | 3.69 | 3.33 | 3.27 | 3.43 | 2.83 | 2.98 | 16.3% | 4.20 |
| Max ΔEF | 0.49 | 0.47 | 1.38 | 0.78 | 0.63 | 0.67 | | |

Table 1: Summary- Purge Flow Effect on Channel EF

# 32. Conclusions

Within the scope of the tested mass fluxes, at first increasing film cooling suction not only augments heat transfer rate, indicated by the rise in overall EF in Table 1, but also forces the surface temperature distribution to become more uniform, beneficial to prevent thermal gradients and thus thermal fatigue in engine environments, denoted by the drop in EF percent deviation. At higher than 5.53 mass flux ratio, even though the global heat transfer rate continues to increase, the heat transfer distribution begins to be more non-uniform, apparent from the rise in EF deviation to 16.3% at mass flux ratio 6.04, contrary to the general declining trend from suction ration 0 to 5.3. This is indicative of greater susceptibility to thermal fatigue, and suggets an optimum purge rate (mass flux ratio) in between 5.53 and 6.04.

# 33. References on Ribbed Channel with Film Extraction

D1. Aerodynamic Performance Investigation of a Fix Rib-Roughened Internal Cooling Passage. Casarsa, L. s.l. : PhD Thesis, Università degli Studi di Udine, von Karman Institute for Fluid Dynamics, 2003.

D2. Heat Transfer to Reattached Fluid Flow Downstream of a Fence. Zukauskas, V.A. and Pedisius, K.A. s.l. : Wärme- und Stoffübertagung, 21, 125-131, 1987.

D3. A Review on Subsonic Turbulent Flow Reattachment. Eaton, J.K. and Johnston, J.P. s.l. : AIAA J., 19, 9, 1093-1100, 1981.

D4. Momentum, Heat and Mass Transfer in Backward-Facing Step Flows. Armaly, B.F., Durst, F. and Kottke, V. s.l. : Proceedings of 3rd Symposium on Turbulent Shear Flows, Davis, CA, 1981.

D5. Combined heat Transfer and Fluid Dynamic Measurements Downstream of a Backward-Facing Step. Eaton, J.K. and Vogel, J.C. s.l. : ASME, 107, 922, 1985.

D6. Relation Between the Points of Flow Reattachment and Maximum Heat Transfer for Regions of Flow Separation. Sparrow, E.M., Kang, S.S. and Chuck, W. s.l. : Int. J. Heat Mass Transfer, 30, 7, 1237-1246, 1987.

D7. Large Eddy Simulation of the Turbulent Flow Past a Backward-facing Step With Heat Transfer and Property Variations. Avancha, R.V.R. and Pletcher, R.H. s.l. : Int. J. Heat Fluid Flow, 23, 601-614, 2002.

D8. Unsteady Fow Events and Mechanisms Leading to Heat Transfer Enhancement in a Ribbed Channel. Jourdain, C., Escriva, X. and Giovannini, A. s.l. : Proceedings Eurotherm Seminar 55: Heat Transfer in Single Phase Flow, 1997.

D9. A Model for the Backflow Mean Velocity Profile. Simpson, R.L. s.l. : AIAA J., 21, 1, 142-143, 1983.

D10. Turbulent Flow Reattachment: An Experimental Study on the Flow and Structure Behind a Backward-Facing Step. Eaton, J.K. and Johnston, J.P. s.l. : Rept. MD-39, Dept. of Mech. Eng. Stanford University, 1980.

D11. A New Probe for Measurements of Velocity and Wall Shear Stress in Unsteady, Reversing Flow. Westphal, R.V., Eaton, J.K. and Johnston, J.P. s.l. : J. Fluids Eng., 102, 2, 478-482, 1981.

D12. Experimental and numerical investigation of conjugate heat transfer in rib-roughened duct, Final Report on CFD activity. Benocci, C., Rambaud, P., 2011